Diss. ETH n° 15090

Environmental influences on the magnetic properties of lake sediments

A dissertation submitted to the
Swiss Federal Institute of Technology, Zürich
for a degree of
Doctor of Natural Science

presented by

RAMON EGLI
Dipl. Natw. ETH Zürich

born November 18, 1971
citizen of Luzern (LU)

accepted on the recommendations of

Prof. Dr. William Lowrie, examiner
Dr. Michael Sturm, co-examiner
Dr. Andrew Newell, co-examiner
Dr. Luca Lanci, co-examiner

2003

Seite Leer /
Blank leaf

Contents

Seite Leer /
Blank leaf

Abstract

Lake sediments are among those environmental archives with the highest possible temporal resolution, and have been used to reconstruct the environmental history in lake-catchment areas and to asses continental climate changes since the last glaciation. Magnetic methods offer the possibility of a fast and non-destructive characterization of sediments, and are used to develop so-called magnetic proxies for the reconstruction of the environmental history. However, the relation between the magnetic minerals, their magnetic properties and the environment is complex and not completely understood. The present work is concerned with the improvement of basic knowledges about the properties of magnetic particles in sediments as well as with the development of a quantitative method for the characterization of magnetic mineral sources. Representative sediment samples from various continental, marine and lacustrine environments have been analyzed in order to investigate the effects of natural processes on their magnetic properties. The magnetic mineral sources could be divided into few categories with characteristic magnetic properties and a common process of formation. These sources include detrital particles transported by water and air, ultrafine magnetite formed in soils and marine or lacustrine sediments, two types of magnetite particles produced by magnetotactic bacteria, maghemite produced in loesses by weathering processes, and a mixture of fly-ash and metallic particles associated to the urban pollution. The magnetic components formed by detrital particles, ultrafine magnetite and magnetite produced by magnetotactic bacteria have been identified in lake sediments. The effect of the environment on the production and dissolution of these components has been investigated in detail with the sediments of a swiss lake, Baldeggersee. This lake was formed more than 15000 years ago after the retreat of the Reuss glacier at the end of the Würm glaciation. Its sediments are of special interest, because they represent a Holocene record with an interesting sequence of biogenic varves, turbitites, and homogeneous marl layers. During the last century, human activities in the catchment area induced a severe eutrophication of the lake, which culminated in the seventies with an almost complete oxygen depletion in the deep water. A model has been developed to explain the observed changes of the magnetic signature during eutrophication events, as well as the influence of the nutrient load and the water mixing. A strong nonlinear relation between the magnetic signature and progressive changes in the environment of the catchment area has been observed. As a consequence, the possibility of a chaotic response of magnetic proxies to gradual climatic changes has to be taken into consideration. The new techniques developed in this work for the analysis of lake sediments have a wide range of applications in evironmental magnetism, including the possibility of a cheap monitoring of urban pollution with magnetic methods.

Seite Leer /
Blank leaf

Zusammenfassung

Unter den verschiedenen Umweltarchiven sind Seesedimente diejenigen mit der höchsten zeitlichen Auflösung. Detaillierte Rekonstuktionen von Umweltänderungen im Einzugsgebiet der Seen erlauben somit einen Rückschluss auf das kontinentale Klima seit der letzten Eiszeit. Magnetische Methoden bieten die Möglichkeit einer schnellen zerstörungsfreien Charakterisierung der Sedimente und werden für die Gewinnung von so genannten magnetischen Proxydaten, die zur Rekonstruktion der Umweltgeschichte dienen, eingesetzt. Die genauen Zusammenhänge zwischen den magnetischen Mineralien, deren magnetischen Eigenschaften und der Umwelt sind komplex und noch nicht gut verstanden. Die vorliegende Arbeit beschäftigt sich sowohl mit der Verbesserung des Grundwissens über die Eigenschaften magnetischer Teilchen in Sedimenten, als auch mit der Entwicklung einer quantiativen Methode zur Quellen-diskriminierung magnetischer Mineralkomponenten. Es wurden repräsentative Proben von verschiedenen kontinentalen, marinen und lakustrinen Sedimenten analysiert, um die Einflüsse natürlicher Prozesse wie Verwitterung oder Eutrophierung auf die magnetischen Eigenschaften der Sedimente zu untersuchen. Die Quellen der magnetischen Mineralkomponenten lassen sich in einige wenige Kategorien einteilen. Jeder Kategorie hat spezifische magnetische Eigenschaften, die von dem jeweiligen Entstehungsprozess geprägt sind. Die Quellkategorien umfassen: wasser- und lufttransportiertes detritisches Material, sehr feinkörnigen Magnetit, der bei Bodenbildungsprozessen, aber auch in marinen und lakustrinen Sedimenten entsteht, zwei Arten von Magnetit die beide von magnetotaktischen Bakterien produziert werden, Maghemit in Löss der durch Verwitterung entsteht und eine Mischung von Flugasche und ferromagnetischen Verbindungen, die mit städtischen Schwebestaubimmissionen assoziiert werden können. Die Magnetisierung der Seesedimente wird im wesentlichen von detritischem Material, sehr feinkörnigem Magnetit und bakteriellem Magnetit getragen. Die Umwelteinflüsse, die zu Kristallisation und Auflösung dieser Komponenten führen, sind an den Sedimenten eines Schweizer Sees, des Baldeggersees, detailliert untersucht worden. Dieser See entstand vor mehr als 15000 Jahren nach dem Rückzug des Reuss-Gletschers am Ende der Würmeiszeit. Die Sedimente dieses Sees sind von besonderem Interesse, da sie holozänen Alters sind und Abfolgen von Warven, Turbiditen und homogenen Mergelschichten enthalten. Im letzten Jahrhundert stand das Einzugsgebiet unter starkem anthropogenen Einfluss, was zu einer starken Eutrophierung des Sees führte. Diese erreichte ihren Höhepunkt in den siebziger Jahren mit dem fast völligen Verschwinden von Sauerstoff aus dem Tiefenwasser des Sees. Es wurde ein Modell entwickelt, dass die beobachteten Änderungen der magnetischen Eigenschaften des Sediments während der Eutrophierung erklärt; beeinflusst und ausgelöst von dem sich ändernden Nährstoffeintrag und wechselnder Durchmischung. Es wurde eine stark nichtlineare Beziehung zwischen den magnetischen Eigenschaften der Sedimente und den progressiven Umweltänderungen im Einzugsgebiet gefunden. Folglich, muss die Möglichkeit einer chaotischen Antwort magnetischer Proxydaten auf allmähliche klimatische Änderungen in Betracht gezogen werden. Die in dieser Arbeit neu

entwickelten Methoden begrenzen sich nicht nur die Erforschung von Seen, sie eignen sich vielmehr für eine breite Anwendung im Umweltmagnetismus, insbesondere für eine kostengünstige Überwachung städtischer Schwebestaubimmissionen.

Chapter 1

Introduction

Seite Leer /
Blank leaf

" *Unfortunately very few earth science processes are understood well enough to permit the application of deterministic models.* "

E. H. Isaaks and R. M. Srivastava

Seite Leer /
Blank leaf

1. Introduction

The present thesis is an interdisciplinary work on specific aspects of rock magnetism and environmental magnetism, which involved the development of new techniques for the characterization of geological materials, with special regard to lake sediments. It contains the final results of the ETH research project 0-20556-00, entitled "Environmental influences on the magnetic properties of lake sediments in Switzerland".

In the following, the present work is introduced in a general scientific frame, and the main subjects of investigation are discussed.

1.1. Electromagnetism – Geomagnetism – Rock Magnetism – Environmental Magnetism

Magnetism belongs to the four fundamental interactions in nature: gravity, electromagnetism, weak interaction, and strong interaction. The attraction of iron to loadstone (magnetite ore) was observed long before recorded history began, and was probably the first observation of a long-range force. The first known report is by the Greek philosopher Thales of Miletus (about 585 B.C.), who said loadstone attracts iron because it has a soul. The first magnetic instrument, the compass, is an old Chinese invention, probably first made during the Quin dynasty (221-206 B.C.). Chinese fortunetellers used loadstones to construct their fortune telling boards, until someone noticed that these boards were better at pointing out real directions, leading to the first magnetic compass. Magnetized needels used as direction pointers appeared between 850 and 1050 AD in China as a common navigation device on ships. The first reference to a compass in Europe was written in 1175 AD by Alexander Neckem, an English monk of St. Albans, and Petrus Peregrinus gave the first description of a working compass in 1269. Already at that time, magnetism was intimately mixed with superstition: it was widely belived that garlic weakened magnets, as first mentioned in Pliny (23-79 AD). This statement was probably a later transcription error due to the confusion of "alio" (other) with "allio" (garlic). Sailors looking after the compass avoided garlic and onions even into the 1600's as a result. Nevertheless, science was developing, and the first man who began the science of magnetism in earnest was the Queen Elizabeth's Court Physician William Gilbert (1540-1603). In his book *De Magnete* (1600) he reported that the earth itself is a giant magnet. As a proof, he constructed a 'little earth' (*terrella* in Latin), a magnetized sphere of loadstone, and observed the direction pointed by a small compass at many points on the surface of the sphere. He also concluded that measuring the dip could give sailors the latitude. With his observations, Gilbert was the founder of geomagnetism, a discipline dedicated to the study of the Earth magnetic field. Gilbert was a scientist of astonishing modernity, and showed clearly how science might be fruitfully pursued. He wrote:

Many modern authors have written about amber and jet attracting chaff and other facts unknown to the generality with the result of their labours bookseller's shops are crammed full. Our generation has produced many volumes about recondite, abstruse and occult causes and

wonders, and in all of them amber and jet are represented as attracting chaff; but never a proof from experiment, never a demonstration do you find in them. The writers deal only in words that involve in thicker darkness subject-matter; they treat the subject esoterically, miracle-mongeringly, abstrusely, reconditely, mystically. Hence such philosophy bears no fruits; for it rests simply on a few Greek or unusual terms – just as our barbers toss off a few Latin words in the hearing of the ignorant rabble in token of their learning, and thus win reputation – bears no fuit, because few of the philosophers are themselves investigators, or have any first-hand acquaintance with things ...

The two centuries after Gilbert's discovery were characterized by a continuous progress in the study of electricity, which culminated with the invention of the electric battery by the Italian scientist Alessandro Volta in 1800. The discovery of the electric battery allowed for the first time the generation of a steady current and lead to the fully unexpected discovery of the relation between electricity and magnetism – a nice example of serendipity in science. In 1802, the Italian jurist Gian Domenico Romagnosi observed that an electric current flowing in a wire affects a nearby magnet. The discovery was reported in the local newspaper *Gazzetta di Trentino*, and was ignored by the scientific community. Romagnosi himself did not attach importance to his discovery. Some years later, in 1819, the Danish physicist and philosopher Hans Christian Oersted (1777-1851) repeated Romagnosi's discover accidentally while performing a demonstration for his students. Oersted did not suggest any satisfactory explanation of the phenomenon, nor did he try to represent the phenomenon in a mathematical framework. Oersted's paper about the discover, originally written in Latin, led to a flurry of activity in electrodynamic research, with the fundamental research of André Marie Ampère in France (Ampère's law, 1820) and the experimental work of Michael Faraday in England (Faraday induction law, 1821).

A definitive theory of electromagnetism was developed by the Scottish physicist James Clerk Maxwell (1831-1879). Maxwell codified earlier work on electricity and magnetism by Michael Faraday, André Marie Ampere, and others into a linked set of twenty equations, which have been simplified down to four differential equations, known as Maxwell's equations, by Oliver Heaviside (1850-1925).

The work of Oersted and Ampére drew to the study of magnetism one of the sharpest minds of Europe, that of Carl Friedrich Gauss (1777-1855). Gauss was a professor of mathematics at the German university of Göttingen and rarely traveled away from home, but in 1828 he attended a conference in Berlin, and stayed there as house guest of the naturalist Alexander von Humboldt (1769-1859). During this visit he showed Gauss his collection of magnetic instruments and encouraged him to apply his talents to magnetism. That Gauss did, together with his young assistant Wilhelm Weber (1804-91), contributing greatly to the understanding of the Earth's magnetic field. In 1832 Gauss and Weber devised a clever method to measure the direction and the intensity of the Earth's magnetic field, and in 1834 they started setting up

an international network of observatories and established the "Göttingen Magnetic Union" (Göttingen Magnetischer Verein). By 1841 much of the world-wide network was actually in operation. The first world-wide survey had begun, a flood of magnetic data began arriving, and modern geomagnetism was born.

The most lasting contribution of Gauss was the use of a precise mathematical method to represent the global magnetic field of the Earth and to combine observations at many locations. That was spherical harmonic analysis, previously used for analyzing gravitational fields in celestial mechanics and introduced to geomagnetism by the French mathematician Simeon Denis Poisson (1781-1840). The new tool of spherical harmonic analysis provided the first quantitative description of the Earth's magnetic field, both its direction and strength. Since then, magnetic surveys have been carried out repeatedly. Spherical harmonic analysis has shown that Gilbert's dipolar "terrella" has always been a good approximation to the Earth's magnetic field.

Even if the theory of magnetism and electricity was completed by the end of the 19th century, the behaviour of matter in a magnetic field was not yet understood. The intriguing ability of iron and other ferrimagnetic materials to retain a spontaneous magnetization was investigated first by the French physicist Pierre Ernest Weiss (1865-1940). Hypothesizing a molecular magnetic field acting on individual atomic magnetic moments, he was able to construct a mathematical description of ferromagnetism and discovered microscopic regions of uniform magnetization, called Weiss domains. He also investigated the temperature dependence of magnetization, known as the Curie-Weiss law, and discovered the quantum nature of the atomic magnetic moments. The origin of Weiss molecular field was explained by Werner Heisenberg in 1928. Landau and Lifschits (1935) formulated a theory to explain the dimension of magnetic domains and domain walls. A fundamental contribution to the theory of ferromagnetism in metals and fine grains came from the French physicist Louis Néel (1904-2000). For his work he won the Nobel Prize in 1970. His studies on the magnetic properties of fine particles are a mile piece for understanding the acquisition of a remanent magnetization by natural rocks.

Earth magnetism and ferromagnetism developed independently until Koenigsberger (1938), Thellier (1938), Nagata (1943) and Néel (1949) attempted to reproduce and understand the process by which igneous rocks are magnetized in nature. The new science was given a name with the publication of the book *Rock Magnetism* by Nagata in 1953. Rock magnetism is the theoretical basis for understanding the mechanism of remanent magnetization acquisition by ancient rocks in the Earth's field. The study of the magnetic remanence of ancient rocks was initiated by Alexander von Humboldt. Bernhard Brunhes (1867-1910) first observed a reverse magnetization in ancient lava flows, a result that has been confirmed later by Motonori Matuyama (1884-1958). These pioneer studies on the remanent magnetization of ancient rocks lead to the fundamental discovery that the Earth magnetic field switched its polarity several times

in the past. A new research field was born: paleomagnetism. Paleomagnetism gave also a definitive confirmation of Alfred Wegner's theory of continental drift, which was first published in 1915.

After Néel's work on fine magnetic particles, studies on ferromagnetic materials and on rock magnetism has been carried out almost independently. After World War II, physicists concentrated their attention on the magnetization process of recording materials, focussing on the interaction between close-packed particles. At present time, the last frontier of solid-state magnetism is represented by the investigation of spin glasses, thin films and nanometric structures. In rock magnetism, contributions of Stacey, Dunlop, Merrill and other authors dealt with the complex dependence of the magnetic properties of natural iron oxides and iron sulphides on their physical properties, such as the grain size. In contrast to magnetism research in physics, rock magnetic experiments are carried out on natural materials, which are difficult to synthesize in laboratory and whose properties depend on many parameters, most of them unknown. Nevertheless, rock magnetism theories have been used successfully to explain the natural magnetization of many kinds of rocks and sediments. Despite the relative simplicity of the fundamental laws of magnetism, the study of natural and artificial magnetic materials is still a big challenge, 150 years after the formulation of Maxwell's equations. Not all the magnetic properties of natural materials are yet explained, and in some cases the existing theories fail in the quantitative explanation of apparently simple observations.

The study of natural rocks and sediments gave soon evidence of a connection between the amount and the type of magnetic mineral contained in geological materials on one side, and environmental factors on the other. Environmental factors such as climate, geological events and human activities have a great effect on the growth, the transport, the transformation and the deposition of magnetic minerals. Since a relatively long time, the relation between environment and magnetic properties of sediments, soils, atmospheric particulates and biologic materials has been investigated. This new discipline grew out of numerous interdisciplinary studies involving sediments of British lakes, but soon expanded to include sediments in other natural archives that also retain record of environmental changes. It received an official name only in 1986, when Roy Thompson and Frank Oldfield published a book entitled *Environmental Magnetism*. An important aspect of environmental magnetism is that its techniques are relatively rapid, simple, non-destructive and inexpensive. In addition, they allow to address problems that may be inaccessible using other physical and chemical techniques. As a counterpart, the underlying theory to understand the relation between (1) measurable magnetic parameters, (2) concentration and composition of magnetic grains, and (3) environmental processes, is often complex and still incomplete. Nevertheless, environmental magnetic methods have been used successfully in various fields, such as climatology, ecology, geomorphology hydrology, land-use studies, limnology, oceanography, sedimentology and soil science. Since Tompson and Oldfield's book appeared, more than 600 articles on

environmental magnetism have been published, demonstrating the dynamic character on this young discipline.

1.2. An interdisciplinary study between rock magnetism and environmental magnetism

The successful interpretation of magnetic measurements relies on the understanding of the fundamental magnetic properties of natural minerals. Many studies on synthetic and natural materials highlighted the complexity of the magnetization process and its dependence on various physical and chemical parameters, most of them unknown or difficult to measure. There is a fundamental difference between the approach of physicists and rock magnetists to the investigation of magnetization processes. Physicists study homogeneous, idealized materials with complex mathematical tools. On the other hand, rock magnetists deal with complex materials, such as rocks and sediments, with basic physical and mathematical tools and a multidisciplinary approach. Sometimes, both strategies fail in giving a satisfying quantitative description of the magnetic properties of natural materials. Great efforts have been undertaken by various authors to find an "exact" approach to rock magnetism, for example by calculating the magnetization of a grain with a direct numerical solution of Maxwell's equations, a method called micromagnetic modelling. This "brute force" approach was made possible after the diffusion of fast computers, which are able to undertake billion of arithmetic operations within a reasonnable time. Nevertheless, it is almost impossible to explore all possible solutions of micromagnetic modelling, which are given by different configurations and compositions of the magnetic grains. The first part of the present work (Chapter 2) presents an analytical model to explain the acquisition of a particular kind of magnetization, called anhysteretic remanent magnetization (ARM), by very small magnetic grains. ARM was a subject of numerous studies between 1960 and 1970 because of its application in the recording tape technology, where it has been developed as a technique to impart a magnetization that is stable in time. In environmental magnetism, ARM has been used to investigate the magnetic granulometry, since the efficiency of this kind of magnetization is extremely sensitive to the grain size, and is particularily high for fine magnetic particles produced by bacteria. Fine magnetic particles play an important role in the magnetization of sediments, because they are very efficient remanence carriers. Their magnetic properties have been investigated since the early history of rock magnetism, but some aspects related to the magnetization acquired in weak fields could not be modelled in a satisfactory way. The model developed in Chapter 2 is able to explain the behaviour of fine particles in a magnetic alternating field. Some classical rock magnetic parameters have been revisited, offering a different interpretation in terms of statistic properties. The importance of the statistical distribution of grain sizes and shapes in the determination of bulk magnetic properties has been highlighted for the first time.

An important task in environmental magnetism is the determination of different magnetic mineral sources in sediments, known as the unmixing problem. The solution of the unmixing

problem is intimately related to the knowledge of the magnetic properties of each source mineral. On the other hand, since natural sediments are often a complex mixture of different mineral sources, the characterization of the rock magnetic properties of a single source is based on the solution of the unmixing problem. The interdependence between rock magnetic properties of individual mineral sources and the analysis of mineral mixtures creates a vicious circle, which has often been overcome with the measurement of synthetic samples with known properties. However, it is extremely difficult to reproduce assemblages of natural magnetic grains in the laboratory. Chapter 3 of the present work describes the development of a new approach to the unmixing problem, which does not need the a-priori knowledge of the mineral sources. This method is a generalization of an earlier work of Robertson and France (1994), which allows its application to all types of natural magnetic mineral mixtures.

The method developed to solve the unmixing problem has been applied to the investigation of natural geologic materials from various environments, which include lake sediments, marine sediments, limestones, loess deposits, ancient and recent soils, glacial deposits, and samples of atmospheric particulate matter. Results of this systematic investigation are reported in Chapter 4. A comparison of these results allows establishing the magnetic properties of individual magnetic mineral sources, and their dependence on environmental factors. A sort of database of magnetic mineral sources has been created, which can be used as a reference for environmental studies based on various geologic materials. The completeness of this database was limited by time span of the present work, however, further results may be added in the future. The computer programs used to analyse the measurements are available to the scientific community and are supplied with the present work.

A detailed rock magnetic study of individual magnetic mineral sources has been carried out in Chapter 5 in order to find characteristic parameters for the identification and the quantification of the magnetic mineral sources in complex mixtures. Special interest is dedicated to the establishment of a minimum number of independent magnetic parameters, which is necessary for a complete characterization of an individual mineral source.

The results of Chapters 3, 4 and 5 are based on extremely precise measurements, which fully exploit the precision of the facilities of a high-standard rock magnetic laboratory. The measurements were time-consuming, typically a week for each of the investigated samples. The measurement precision allowed a deep insight into the rock magnetism of natural materials, and new, unexpected properties have been discovered. However, such time-consuming experiments are unsuitable for the systematic investigation of a large number of samples, which is required in environmental magnetism studies. Chapter 6 is concerned with effective strategies that can be used to solve correctly the unmixing problem with simple and fast measurements, typically less than 20 minutes for each sample. The practical feasibility of this approach is demonstrated by its application on a detailed investigation of Baldeggersee, a small lake located in Switzerland. The sediments of Baldeggersee are of special interest, because they

represent a Holocene record with an interesting sequence of different sedimentological units, which reflect environmental changes triggered by the climate and by human activities. During the last century, human activities produced a severe eutrophication of the lake, which culminated in 1970 with an almost complete oxygen depletion of the deep water. In 1982, a restoration program has been started, which included the installation of an artificial areation system on the bottom of the lake. This eutrophication event offers the possibility to investigate in detail the biogeochemical processes that control the growth and the dissolution of magnetic minerals in a lake. The fundamental role of magnetite produced by bacteria has been highlighted. Existing theories has been confirmed, and new, unexpected findings extend our knowledge about the iron cycle in lake and its strongly non-linear reaction to gradual environmental changes.

The new methods presented in this work have been tested on samples of atmospheric particulate matter as well. These samples have been collected at various places in Switzerland to measure the concentration of particles emitted by various pollution sources. Usually, air pollution monitoring is performed with expensive and sophisticated methods. Magnetic methods are of particular interest, because they represent an inexpensive alternative to traditional measurements for an extensive and systematic pollution mapping of urban areas. Emissions of combustion processes and vehicle brakes contain various magnetic minerals, whose contribution to the magnetic signal is superimposed to that of natural dust. The same methodology used for natural sediments has been adopted to analyse these samples and characterize the properties of magnetic minerals produced by pollution sources. The relative contribution of these minerals to the magnetic signal is a measure for the air pollution, which can be performed on samples of dust accumulated passively on exposed surfaces.

Chapter 2

Anhysteretic remanent magnetization of fine magnetic particles

This paper has been published in: *Journal of Geophysical Research*, vol. 107 (B10), 2002.

Seite Leer /
Blank leaf

" We should make things as simple as possible, but not simpler. "

Albert Einstein (1879-1955)

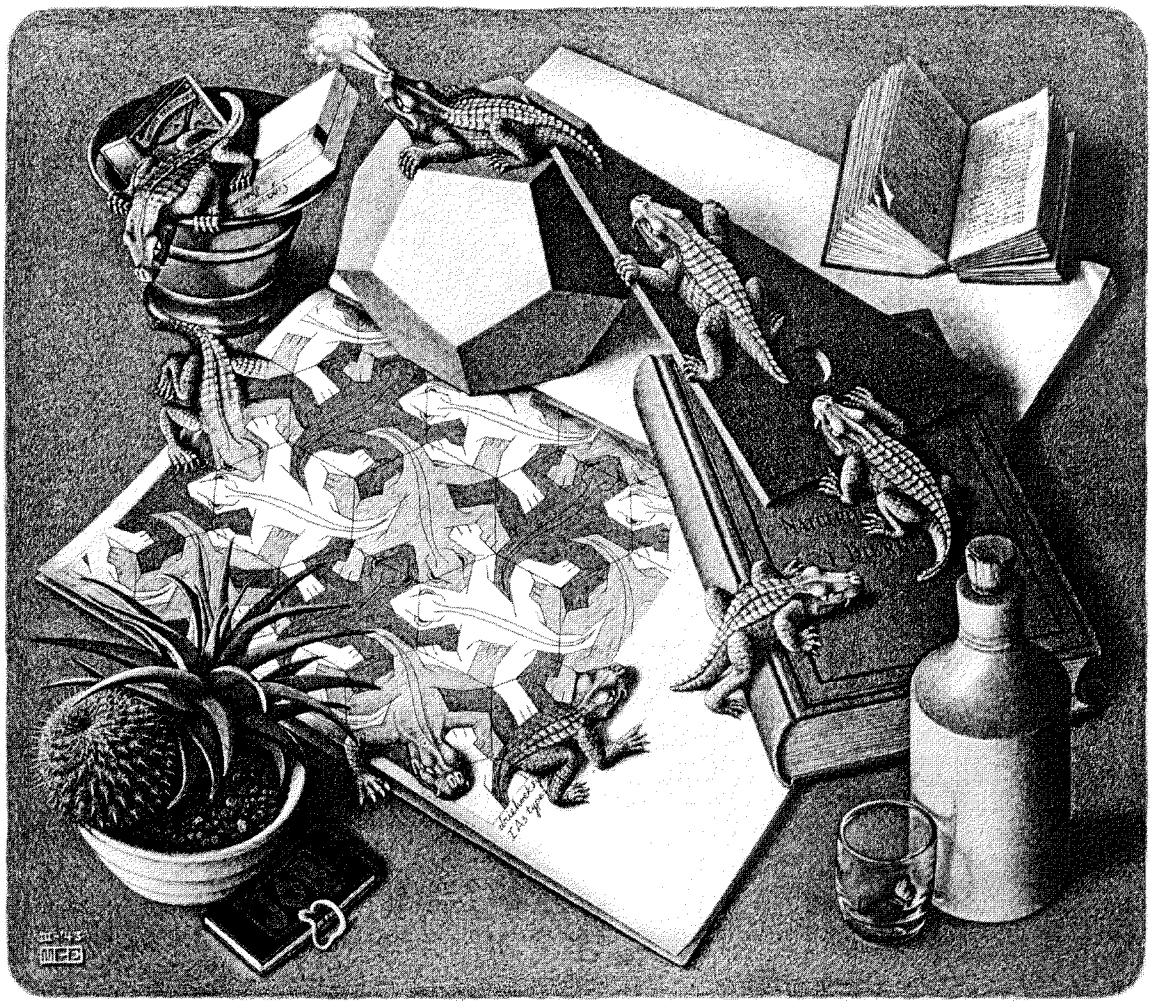

Maurits Cornelis Escher: *Reptiles*, lithography (1943)

The anhysteretic remanent magnetization of fine magnetic particles

R. Egli and W. Lowrie
Institute of Geophysics, ETH Hönggerberg, CH 8093 Zürich

Received 15 June 2001; revised 25 January 2002; accepted 30 January 2002; published 3 October 2002.

Various magnetic parameters are in common use for estimating the grain size of magnetic particles. Among these, the ratio of the intensity of anhysteretic remanent magnetization (ARM) to that of isothermal remanent magnetization (IRM), as well as their alternating field (AF) demagnetization curves are used as an indicator of the domain state of the particles. Several models have been proposed to describe physically the acquisition of ARM in a biased AF field. *Jaep* [1969] first developed a semiquantitative theory based entirely on the thermal fluctuation analysis developed by *Néel* [1949, 1954, 1955]. Significant discrepancies were found between his model and experimental results on magnetite. A new, general theory of ARM based on the work of Jaep is presented here, with particular regard to the influence of various parameters like grain size, coercivity and mineralogy on ARM intensity. An analytical expression for ARM intensity in the special case of very fine particles was derived from this theory, and a good agreement with experimental results and data from the literature was found. A new estimation of the atomic reorganization time was obtained from ARM measurements on a sample of the Yucca Mountain Tuff, which has well known mineralogy and grain size distribution. The results are in agreement with the value proposed by *McNab et al.* [1968] for magnetite. Some authors considered magnetic interactions as the key to understanding the ARM in fine particles, and this is certainly true for strongly interacting samples. In this case, ARM would be useless for the characterization of magnetic grains. However, many sediments have a very low concentration of well-distributed magnetic grains. For these samples, the explanation of an ARM in terms of intrinsic properties of the grains, as qualitatively proposed by other authors, is more suitable.

INDEX TERMS: 1540 Geomagnetism and Paleomagnetism: Rock and mineral magnetism; 1512 Geomagnetism and Paleomagnetism: Environmental magnetism; *KEYWORDS:* thermal fluctuations, ARM, single domain, coercivity, Lowrie-Fuller test.

Citation: Egli, R., and W. Lowrie, Anhysteretic remanent magnetization of fine particles, *J. Geophys. Res.*, *107*(B10), 2209, doi: 10.1029/2001JB000671, 2002.

1. Introduction

In studies of environmental magnetism the variations in grain size are conveniently described by magnetic parameters. Among these, it is common to use the ratio of anhysteretic remanent magnetization (ARM) to bulk susceptibility or to isothermal remanent magnetization (IRM). Interpretation of variations in these parameters is inhibited by lack of fundamental theoretical understanding of how they relate to grain size. The interpretation of many magnetic profiles in sediments is largely empirical, based upon experimental observations made on sized fractions of selected magnetic minerals. A comparison between the demagnetization characteristics of ARM and IRM was proposed as a discriminant between single domain (SD) and multidomain (MD) carriers of remanence [*Johnson et al.*, 1975]. However, an adequate theory of ARM has not yet been developed. In this paper we address the theory of ARM in SD particles.

Several theoretical studies have been made of ARM in fine particles, because of its importance in the recording process on magnetic tapes [*Wolfarth*, 1964; *Jaep*, 1969]. Assuming ARM as a proxy for TRM, *Bailey and Dunlop* [1977] proposed its application in paleointensity determinations as a non-destructive alternative.

In a series of studies [*Wolfarth*, 1964; *Kneller*, 1968] of ARM in SD particles the classical Stoner-Wolfarth theory [*Stoner and Wolfarth*, 1948] was used. This theory ignores the effect of thermal energy fluctuations on the magnetic moment of the particles. It predicts an infinite susceptibility of ARM for non-interacting SD particles. However, experimental values are finite, and to account for this the effect of magnetic interactions between the particles was introduced [*Wolfarth*, 1964; *Dunlop and West*, 1969]. Consequently, *Kneller* [1968] proposed that ARM measurements could be used to study the interaction fields. *Eldridge* [1961] showed that intuitive interaction models, which assume the mean interaction field to be proportional to the magnetization [*Néel*, 1954], fail to predict a finite susceptibility of ARM. In order to explain the finite susceptibility of ARM in SD particles more complex interaction models, based on the Preisach-Néel theory were developed [*Wolfarth*, 1964; *Dunlop and West*, 1969].

These models do not take into account thermodynamic effects. The theory of thermoremanent magnetization (TRM) and its coercivity parameters in single-domain particles depends strongly on the concept of a fluctuation field, which was first introduced by *Néel* [1955] and later utilized by *Dunlop* [1965] and *Kneller and Wolfarth* [1966]. The fluctuation field is a key factor in explaining the dependence of coercivity parameters on temperature, particle volume and time. For example, it allowed *Kneller and Wolfarth* [1966] to predict how ARM intensity varies with the temperature of acquisition.

The approach to the problem of thermodynamic effects on the magnetization of SD particles is based on the thermal fluctuation analysis of *Néel* [1949]. Several later studies based on more general physical models of thermally induced activation processes resulted in improved

versions of the Néel theory [*Brown*, 1959; *Brown*, 1963], but for practical proposes lead to substantially the same results [*Brown*, 1959].

Jaep [1969] first proposed a semiquantitative model for ARM in SD particles, based entirely on thermal fluctuation analysis, which predicts a finite ARM susceptibility even in the non-interacting case. According to this model, thermodynamic fluctuation theory is not merely an additional factor that affects ARM, it is the key mechanism in understanding the acquisition process. Later, Jaep evaluated the effect of magnetic interactions in his thermodynamic model, focussing on materials used for magnetic tapes. In these materials interactions play a major role because of the high volume concentration of magnetic particles [*Jaep*, 1971].

The following paper presents a strictly quantitative theory of ARM acquisition in SD particles. Based on Jaep's approach and on the thermal fluctuation analysis of Néel, it demonstrates that the intensity of ARM is strongly controlled by thermodynamic conditions. The theory is extended to alternating field (AF) demagnetization and includes calculation of the fluctuation field. Finally, measurements on natural samples are presented as an experimental confirmation of the theory. The possible results of the modified Lowrie-Fuller test [*Johnson et al.*, 1975] for non-interacting SD particles with different volume and microcoercivity distributions are also discussed.

2. ARM acquisition without thermal activation

In this paper the following notations will be used for the alternating (AC) and direct (DC) field components (Figure 1):

H_{DC} DC field, superimposed on the AC field
$\tilde{H}$ amplitude of the AC field
$\tilde{H}_0$ maximum amplitude of the AC field
f_{AC} frequency of the AC field
$\Delta\tilde{H}$ decay rate of the AC field in field units per half-cycle

Common values in real ARM experiments are $H_{DC} = 0.1...1$ mT, $\tilde{H}_0 = 10...300$ mT, $f_{AC} = 50...400$ Hz, $\Delta\tilde{H} = 1...10$ μT/half-cycle. In the following calculations we assume $H_{DC} > \Delta\tilde{H}$, which is generally valid in real ARM experiments.

Consider the acquisition of ARM by a uniaxial SD particle in an assemblage of non-interacting grains. We model the behaviour of this particle in a magnetic field H with the Stoner-Wolfarth theory [*Stoner and Wolfarth*, 1948]. Assume that its magnetization is homogeneous and that it defines an angle θ with the easy axis, which in turn defines an angle φ with the applied field H, as in Figure 2.

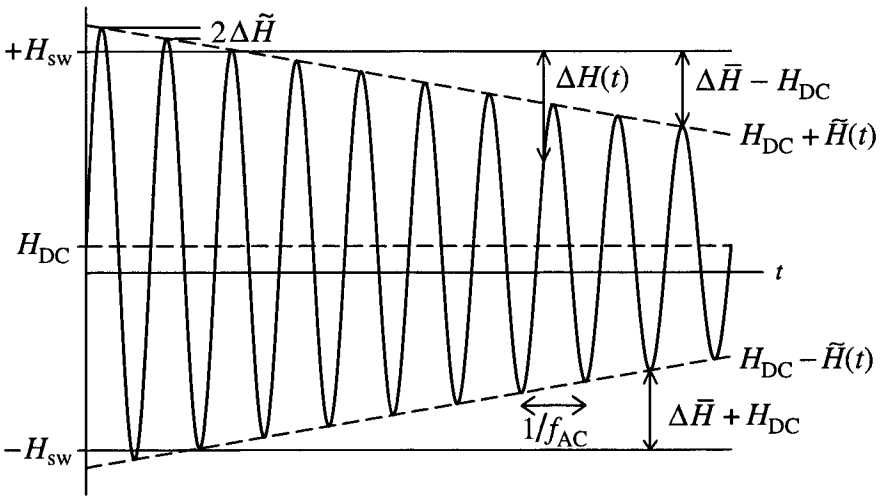

Figure 1: *The applied field during an ARM cycle. Notations are explained in the text.*

Let $m = M_s V$ be the magnetic moment of the particle with volume V and saturation magnetization M_s, and let H_K be its microcoercivity. The free energy E of this particle in a field H is given by:

$$E/E_0 = \sin^2\theta - 2h\cos(\varphi - \theta) \tag{1}$$

with $E_0 = \mu_0 m H_K/2$ and $h = H/H_K$. Let $\varepsilon = E/E_0$ be the reduced free energy. At equilibrium, θ defines a local minimum in ε, according to the conditions $\partial\varepsilon/\partial\theta = 0$ and $\partial^2\varepsilon/\partial\theta^2 > 0$ for the orientation of m. Note that, in the Stoner-Wolfarth model expressed in (1), the thermal energy kT is neglected. The magnetic moment component $m_{\|}$ parallel to the applied field gives a hysteresis loop. The absolute value of the field H_{sw} at which $m_{\|}$ is discontinuous and changes sign will be called the switching field. The shape of the hysteresis loop and the value of H_{sw} depend on φ. Some examples are given by *Dunlop and Özdemir* [1997].

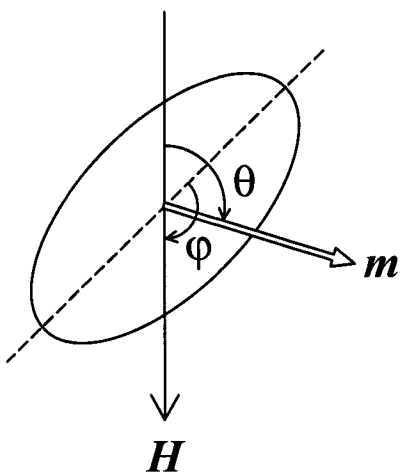

Figure 2: *The magnetization of a SD particle in the Stoner-Wolfarth model. The dashed line indicates the easy-axis of the particle.*

At $H = H_{sw}$ the local minima of equation (1) disappears, and $\partial^2\varepsilon/\partial\theta^2 = 0$, with following solution:

$$h_{sw} = \frac{\sqrt{1 - t^2 + t^4}}{1 + t^2}, \quad t = \tan^{1/3}\varphi$$
$$\tan\theta_{sw} = \frac{\sqrt{3} - \sqrt{4h_{sw}^2 - 1}}{2\sqrt{1 - h_{sw}^2}} \tag{2}$$

where $h_{sw} = H_{sw}/H_K$ and θ_{sw} is the value of θ at which switching occurs [*Stoner and Wolfarth*, 1948]. Generally, $0.5 < h_{sw} < 1$.

We consider now the behaviour of such a SD particle with switching field H_{sw} during an ARM represented in Figure 3a. The arrows represent the direction of $m_{\parallel}$, parallel (↑) or antiparallel (↓) to the applied DC field. If $H_{sw} < \tilde{H}_0$, $m_{\parallel}$ is always parallel to the applied DC field at the end of the ARM acquisition, independently of the initial state of the particle. Extending the model to all particles with different switching fields, we conclude that all particles with $H_{sw} \leq \tilde{H}_0$ are reoriented with a positive $m_{\parallel}$ during the ARM.

According to this model, the ARM acquired by all the particles is identical to an IRM given in a DC field equal to $\tilde{H}_0$. However, it is well known experimentally that ARM intensities are always a fraction of the IRM, even for an assembly of SD non-interacting particles. Moreover, according to this model the ARM intensity is independent of H_{DC}, and gives an infinite ARM susceptibility, in contradiction with experimental observations.

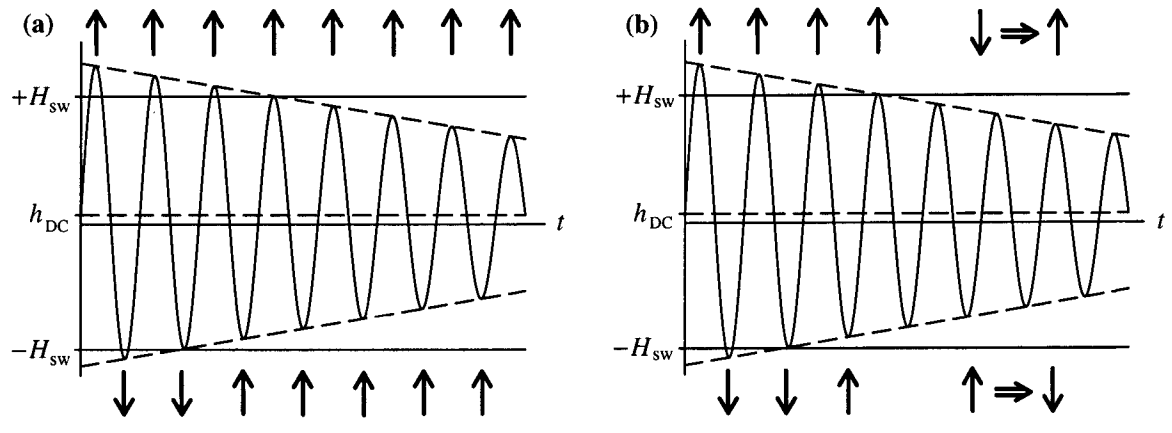

Figure 3: *Magnetic moment of a particle during an ARM cycle (a) according to the Stoner-Wolfarth model and (b) according to a thermodynamic model. Arrows represent the direction of the magnetic moment parallel (↑) or antiparallel (↓) to the DC field. In (a) the moment is frozen-in once the amplitude of the AC field becomes smaller than the switching field. In (b) thermodynamically activated switching events occour when the AC field is smaller than the switching field.*

3. ARM acquisition with thermal activation

We extend now the model of section 1 in order to take into account the thermal energy kT of the particles, and develop the kinetic equations for SD particles in a biased AC field.

3.1 Previous studies

Néel [1949] developed the kinetic equations for an array of aligned non-interacting particles, in order to model thermoremanent magnetization. *Jaep* [1969] applied the work of Néel to anhysteretic magnetization processes. Later he introduced the effect of magnetic interactions through the thermodynamic formalism and obtained the following expression for the acquisition of ARM by aligned interacting particles:

$$\frac{M}{M_{\mathrm{rs}}} = \tanh\left[\frac{\mu_0 m}{kT}\left(\beta H_{\mathrm{DC}} - \lambda M/M_{\mathrm{rs}}\right)\right]$$
$$\beta = \frac{(M_{\mathrm{s}})_{\mathrm{B}}}{M_{\mathrm{s}}}\left(\frac{T}{T_{\mathrm{B}}}\right)^{1/2} \leq 1 \qquad (3)$$

where M_{s} is the saturation magnetization, M_{rs} the saturation of remanence, T the absolute temperature and $(M_{\mathrm{s}})_{\mathrm{B}}$ the saturation magnetization at the blocking temperature T_{B} of the particles. The parameter λ is a measure of the average interaction field. Equation (3) predicts a finite susceptibility of ARM even in the non-interacting case, but is independent of the characteristics of the AC field (i. e. its frequency f_{AC} and its decay rate per half-cylce $\Delta\tilde{H}$).

Most studies of thermal activation in SD particles assumed an alignment between applied field and easy axis of the particles, to reduce the mathematical complexity of the models used. However, in a set of randomly oriented particles, only a negligible part of them satisfy this condition. *Victora* [1989] pointed out that the energy barrier for randomly oriented particles exhibits a $3/2$-power dependence on the applied field, in contrast to the quadratic dependence for aligned particles. This may introduce significant differences in modeling relaxation processes.

Walton [1990] introduced a new approach to the problem, trying to partially solve the kinetic equations for non-interacting SD particles in an AC field. He also extended his calculations to the more general case of a particle whose easy axis defines an angle φ with the applied field, and obtained the following expression for the susceptibility of ARM:

$$\chi_{\mathrm{ARM}}(\varphi) = \mu_0 \frac{2r}{3\mu_0 q(\varphi) H_{\mathrm{K}}}\left(\frac{\mu_0 m H_{\mathrm{K}}}{2kT}\right)^{1/r} \ln^{1-1/r}\left[\frac{F_0}{2\pi f_{\mathrm{AC}}}\left(\frac{2kT}{\mu_0 m H_{\mathrm{K}}}\right)^{3/2}\right] \qquad (4)$$

where $1 \leq q \leq 2$ and $1.5 \leq r \leq 2$ are functions of φ, and $F_0 \approx 10^9$ Hz is the frequency of the thermal activations. Because of the presence of r as exponent in (4), it is impossible to

generalize this expression for the case of an assembly of randomly oriented particles. However, equation (4) with $r = 1.5$ (and $\varphi = \pi/4$) is very similar to the result of this paper, given by (32) for randomly oriented particles. Equation (4) shows a weak dependence on f_{AC} but curiously no dependence on $\Delta\tilde{H}$. This may be a consequence of some approximations adopted to simplify the calculations.

The results mentioned above are all based on some simplifications which reduce their general validity. For this reason, we here apply the thermal relaxation theory to the most general case of a set of noninteracting randomly oriented particles and solve directly the resulting kinetic equations. A similar result to equation (4) is obtained for the anhysteretic magnetization. However, a well-defined dependence on the moment m, the temperature T and the microcoercivity H_K is found. In addition, our result shows a weak dependence on both frequency and ramp rate of the AC field used for the ARM.

3.2 Derivation of the field-antiparallel switching frequency

We consider again the moment of a particle in the ARM field, as represented in Figure 3. At a given point – when the AC peak field becomes smaller than H_{sw} – the particle moment is "frozen" in a stable position (a local minimum of ε). For several cycles, the applied field reaches values very near to H_{sw}. The energy barrier represented by the difference between the local maximum and minimum is reduced to small values, of the same order of magnitude as the thermal energy.

According to Figure 1, we define:

$$\begin{aligned} H(t) &= H_{DC} + \bar{H}(t)\cos(2\pi f_{AC} t) \\ \Delta H(t) &= \left| H_{sw} - \bar{H}(t)\cos(2\pi f_{AC} t) \right| \\ \Delta\bar{H}(t) &= \left| H_{sw} - \bar{H}(t) \right| \end{aligned} \tag{5}$$

$H(t)$ is the total applied field at instant t during the ARM acquisition. It is the sum of the constant bias field H_{DC} and the amplitude of the alternating field at time t. The energy barrier ΔE to overcome a local minimum in E is a function of ΔH, namely $\Delta E = \Delta E(\Delta H)$; in particular, $\Delta E = 0$ when $\Delta H = 0$. In this situation, if ΔH is small enough, thermally activated switching of m is possible. The frequency of switching is given according to the Gibb's principle of statistical thermodynamics by:

$$f = f_0 \exp[\Delta E(\Delta H)/kT] \tag{6}$$

in which $\tau_0 = 1/f_0 \approx 10^{-9}$ s is the atomic reorganization time (time interval between two thermal excitations), $f_0 = f_0(T, m, H_K, H, \varphi)$ is a function of the temperature T, the particle magnetic moment m, the microcoercivity H_K, the applied field H and its orientation φ

with respect to the easy axis. The frequency f_0 results from the solution of physical equations, which describe thermal activation processes in terms of Brownian motion of the particle moment [*Brown*, 1963]. For $\varphi = 0$ and $\mu_0 m H_K \gg kT$, *Brown* [1963] gives the following approximate solution when the initial magnetization is antiparallel to the applied field:

$$f_0 \approx \frac{\mu_0 \gamma_0}{2} H_K \sqrt{\frac{\alpha}{\pi}} (1+h)(1-h)^2 \left(1 + \frac{1+h}{1-h} e^{-4\alpha h}\right) \tag{7}$$

in which γ_0 is the gyromagnetic ratio, $\alpha = \mu_0 m H_K / kT$ the reduced energy barrier and $h = H/H_K$ the reduced field. *Aharoni* [1964] calculated f_0 numerically for $\varphi = 0$ and different values of α and h, showing that the relative error of (7) is within 30% when $\alpha > 5$ and $h < 0.5$. For $\alpha > 5$ and $h > 0.7$ the relative error of (7) can reach one order of magnitude. *Néel* [1949] gives a similar expression for f_0, based on piezomagnetic induced activation.

In our case, with $H = H_K - \Delta H$, we obtain from (7) for $\Delta H \ll H_K$ and $\alpha > 20$ (SD particles):

$$f_0 \approx \mu_0 \gamma_0 H_K \sqrt{\frac{\alpha}{\pi}} \left(\frac{\Delta H}{H_K}\right)^2 \tag{8}$$

This approximation is not accurate for $\Delta H \to 0$ and is strictly valid only in the special case of $\varphi = 0$. Since an accurate and general solution for f_0 is not reported in the literature, we assume:

$$f_0 = F_0(T, m, H_K)\, \Delta h^q \tag{9}$$

where $\Delta h = \Delta H / H_K$ and q is an exponent which depends on the model chosen to explain thermal activation. For $q = 0$ one has the intuitive model in which $F_0 = 1/\tau_0 =$ constant. Equation (8) is a particular case of (9) with $q = 2$ when the initial magnetization is antiparallel to the applied field. For the same configuration and $\Delta h \ll 1$, *Néel* [1949] gives $q = 3/2$. *Brown* [1959] demonstrated that different theories with q ranging from 1 to 2 lead substantially to the same results, because the dependence of the activation frequency on the exponential term of (6) dominates over the dependence of f_0 on the applied field. We will show later in this section that the calculated ARM is almost independent from the value chosen for q, so that a precise estimation of f_0 is not necessary.

Now, in contrast to section 1, both orientations of the particle moment – parallel ($\uparrow$) and antiparallel ($\downarrow$) to h_{DC} – are possible, even if $|H| < H_{sw}$. This can be considered as a reduction of the effective switching field of the particle by a "fluctuation field", according to *Néel* [1955]. We consider a large number N of identical particles with the same orientation

φ of their easy axis and the same H_K. Let $m_{\parallel}$ be the component of the magnetic moment parallel to the applied field. We assume that $m_{\parallel}$ of a proportion p of these particles ($0 \leq p \leq 1$) is positive ($\uparrow$), and the remainder $(1-p)$ is negative ($\downarrow$). Switching events occur with high probability at minima of the applied field for the positively magnetized part p and at maxima of the applied field for the other part, according to Figure 3b.

The switching frequency $f_{\pm}$ in the two cases is given according to (6), (9) and $h_{DC} = H_{DC}/H_K$ by:

$$f_{\pm} = F_0 \left(\Delta h \pm h_{DC}\right)^q \exp\left(-\frac{\Delta E(\Delta h \pm h_{DC})}{kT}\right) \tag{10}$$

3.3 Estimation of the energy barriers

Let θ_{sw} be the value of θ at which a switching of the moment occurs in the Stoner-Wolfarth model. Except when $\varphi = 0$ and $\varphi = \pi/2$, θ_{sw} represents a horizontal flex point on the plot of $\varepsilon(\theta)$ (Figure 4a). Since the amount of particles whose easy axis define an angle φ with the applied field is proportional to $\sin\varphi$, and their contribution to the remanent magnetization parallel to the applied field is proportional to $\sin\varphi\cos\varphi$, the special cases $\varphi = 0$ and $\varphi = \pi/2$ do not contribute to the ARM and can be ignored. *Victora* [1989] estimated the energy barrier ΔE to overcome for a moment switching when the applied field is slightly smaller than H_{sw} by setting $\partial E/\partial\theta = \partial^2 E/\partial\theta^2 = 0$ and $\varphi \neq 0, \pi/2$:

$$\Delta E = \varepsilon_{sw}\mu_0 m H_K \Delta h^{3/2} \tag{11}$$

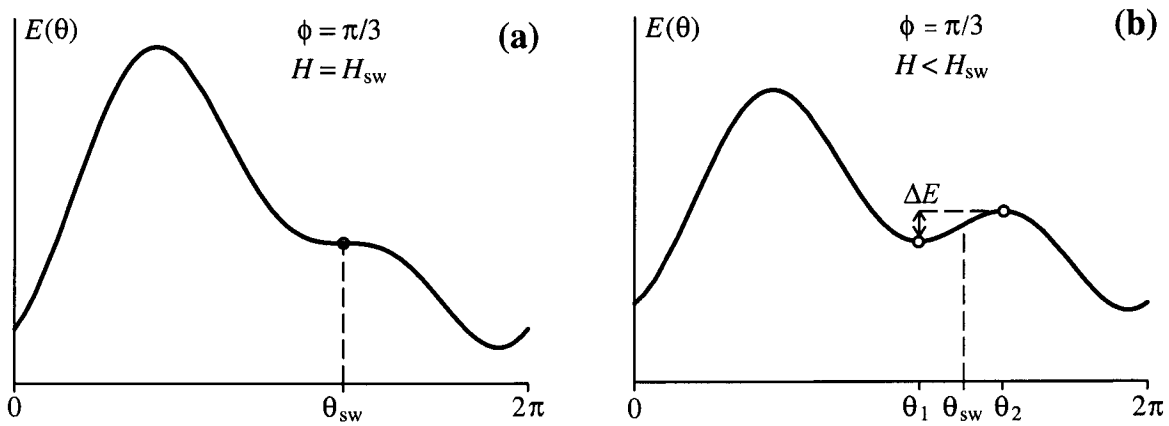

Figure 4: *Free energy of a SD particle as a function of the angle θ of the magnetic moment with respect to the easy-axis (a) when a field equal to the switching field is applied and (b) when a field slightly smaller than the switching field is applied. ΔE is the energy barrier to overcome for a switching event.*

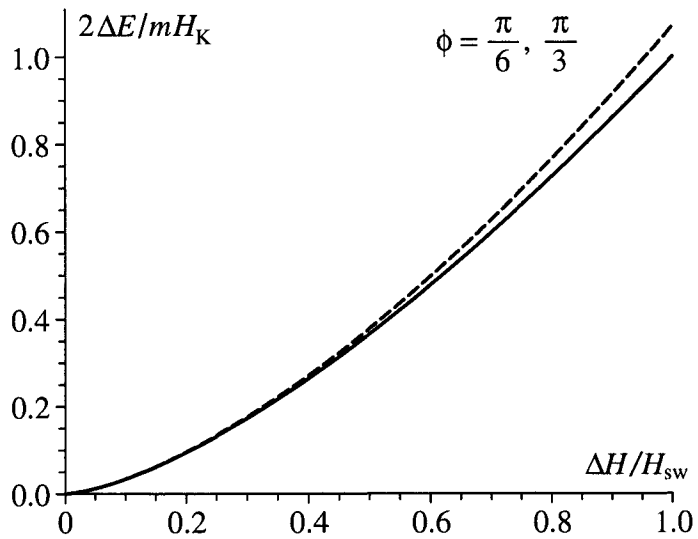

Figure 5: *Energy barrier of a SD particle, which has to be overcome for a switching event, when a field $H_{sw} - \Delta H$ is applied. The solid line represents the exact solution. The analytical approximation given in the text is represented by the dashed line, computed for the symmetrical points $\varphi = \pi/6$ and $\varphi = \pi/3$ in Figure 4b.*

with $\varepsilon_{sw} = (2/3)^{3/2} \sin 2\theta_{sw} / h_{sw}^{3/2}$. This expression is substantially different from the result obtained by *Néel* [1949] for aligned particles: $\Delta E = \mu_0 m H_K \Delta h^2/2$. In Figure 5 the approximate solution for ΔE given in (11) for a small energy barrier is compared to the numerical result obtained directly from equation (1). A very good agreement is found also with higher energy barriers.

3.4 Changes of the particle moment with time in a biased alternating field

Equation (10) can now be rewritten as:

$$f_{\pm} = F_0 \Delta h^q \left(1 \pm \frac{h_{DC}}{\Delta h}\right)^q \exp\left[-\alpha \Delta h^{3/2} \left(1 \pm \frac{h_{DC}}{\Delta h}\right)^{3/2}\right] \tag{12}$$

with $\alpha = \varepsilon_{sw} \mu_0 m H_K / kT$. The switching frequency $f_{\pm}$ is modulated in time by the frequency of the AC field. This allows us to define the mean switching frequency $\overline{f}_{\pm}$. For simplicity, we consider first:

$$f = F_0 \Delta h^q \exp\left(-\alpha \Delta h^{3/2}\right) \tag{13}$$

The switching frequency $f_{\pm}$ can be obtained from (13) by substitution of Δh with $\Delta h \pm h_{DC}$. The modulation in time of $f = f(t)$ according to (13) is represented in Figure 6b over one period. The corresponding mean frequency $\overline{f}$ is given by:

$$\overline{f}(t) = f_{AC} \int_t^{t+f_{AC}^{-1}} f(\tau)\, d\tau \tag{14}$$

Equation (14) cannot be evaluated analytically, except for the limit cases of $\Delta\overline{h} \to 0$ and $\Delta\overline{h} \to h_{sw}$. Since $\Delta\overline{h}$ changes with time, the two limits are reached at the beginning and at

the end of the acquisition process, respectively. The magnetic moment of a particle blocks when $\Delta\bar{h}$ grows from 0 to h_{sw}. Superparamagnetic particles are thermally activated even without the help of an external field: they remain unblocked at the end of the acquisition process, when $\Delta\bar{h} = h_{sw}$, and their magnetization is unstable. In this case, the mean switching frequency is given by (13) when Δh is replaced by $\Delta\bar{h}$:

$$\bar{f}(t) \approx F_0 \Delta\bar{h}^q \exp\left[-\alpha\Delta\bar{h}^{3/2}\right] \tag{15}$$

The moment of larger particles blocks earlier, when $\Delta\bar{h} < h_{sw}$. The limit case of $\Delta\bar{h} \ll h_{sw}$ is a good approximation for large, stable SD particles. In this case, since f decreases rapidly with increasing values of Δh, as shown in Figure 6a, $\Delta h(t)$ can be conveniently approximated by a parabola near the *k*-th minimum, respectively maximum of the field:

$$\Delta h(t) \approx \Delta\bar{h} + \tfrac{1}{2}(h_{sw} - \Delta\bar{h})(2\pi f_{AC} t_k)^2 \tag{16}$$

with $t_k = t - k/f_{AC}$ or $t_k = t - (k+1/2)/f_{AC}$ and equation (13) becomes:

$$\begin{aligned} f(t) &= F_0 \Delta\bar{h}^q \left(1 + bt_k^2\right)^q \exp\left[-a\left(1 + bt_k^2\right)^{3/2}\right] \\ a &= \alpha\Delta\bar{h}^{3/2} \quad b = \frac{h_{sw} - \Delta\bar{h}}{2\Delta\bar{h}}\left(2\pi f_{AC}\right)^2 \end{aligned} \tag{17}$$

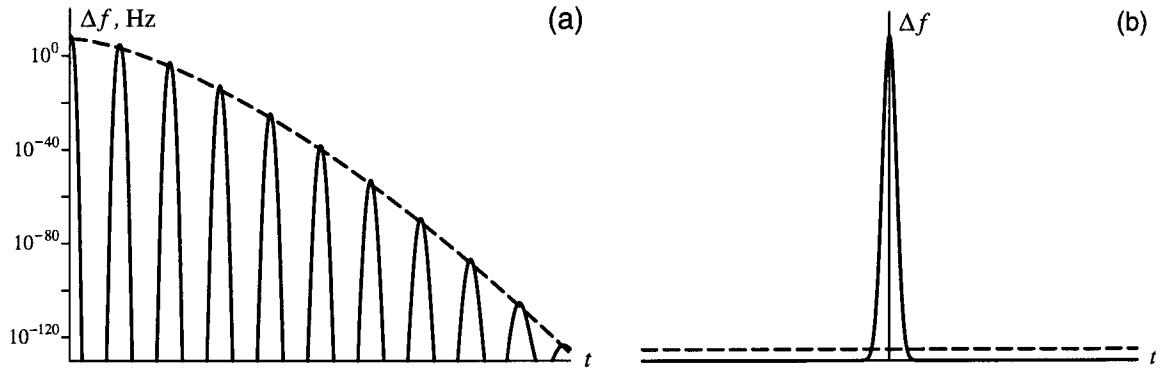

Figure 6: *(a) The instantaneous net switching frequency (solid line) over a complete ARM cycle for a magnetite SD particle and the mean net switching frequency (dashed), averaged over one period of the AF field. The switching frequency was calculated with following data:* $T = 300$ K, $m = 4 \times 10^{-17}$ Am^2, $\mu_0 H_K = 60$ mT *and* $\mu_0 H_{DC} = 100$ μT. *The number of periods over the ARM cycle has been reduced for clarity: an ARM cycle contains typically several hundreds of periods. (b) Calculation of the mean switching frequency (dashed line) over one period. The area under the curve represents the number of switching events over one period, which is identical to that defined by the instantaneous switching frequency (solid line). The scale on the frequency axis is linear.*

The magnetic moment of a particle blocks when $\Delta\bar{h}$ reaches a value $\Delta\bar{h}_0$ given later in this section by equation (25). In general, $a \gg 1$ when $\Delta\bar{h}$ is of the same order of magnitude as $\Delta\bar{h}_0$: $a \approx 14$ with $\mu_0 H_K = 60$ mT and $m = 5\times10^{-17}$ Am^2. For SD magnetite grains that switch by coherent rotation, $\mu_0 H_K < 300$ mT and $m \le 10^{-16}$ Am^2 [*Newell and Merrill*, 1999], and consequently, using (25), $a > 8$. For reasons explained later, the estimation of $f_\pm$ is important only for values of $\Delta\bar{h}$ around $\Delta\bar{h}_0$, and $a \gg 1$ can be assumed in (17). Then (14) has the approximate analytical solution:

$$\bar{f}(t) \approx F\Delta\bar{h}^{q-1/4}\exp\left[-\alpha\Delta\bar{h}^{3/2}\right] \tag{18}$$

valid for the limit case of $\Delta\bar{h} \ll h_{sw}$, whereby $F = F_0(3\pi h_{sw}\alpha)^{-1/2}$. Equations (15) and (18) differ only in the preexponential factor, which has little influence on the final result. Since the measured ARM magnetization is carried mainly by stable particles, equation (18) is adopted as a general solution of (14). From (12) and (18) we have then the mean switching frequency:

$$\bar{f}_\pm(t) = F\left(\Delta\bar{h} \pm h_{DC}\right)^{q-1/4}\exp\left[-\alpha\left(\Delta\bar{h} \pm h_{DC}\right)^{3/2}\right] \tag{19}$$

We assume $h_{DC} \ll \Delta\bar{h}$ for the DC fields normally used in ARM experiments, and in the critical time interval during which the magnetic moment blocks, that is, when $\Delta\bar{h} \approx \Delta\bar{h}_0$. For example, $\mu_0\Delta\bar{H} > 1$ mT for particles with $\mu_0 H_K > 2$ mT and $m < 10^{-16}$ Am^2 (practically all SD magnetites that switch by coherent rotation). When $\Delta\bar{h} \approx \Delta\bar{h}_0$, then $\Delta\bar{h} \gg \alpha^{-2/3}$ and equation (19) simplifies to:

$$\bar{f}_\pm(t) = F\Delta\bar{h}^{q-1/4}\exp\left[-\alpha\Delta\bar{h}^{3/2}\right]\exp\left[\mp\frac{3}{2}\alpha\Delta\bar{h}^{1/2}\,h_{DC}\right] \tag{20}$$

Defining $M_s = Nm$ as the saturation magnetization, the net magnetization $M_\parallel$ parallel to the applied field is given by $M_\parallel = (2p-1)M_s\cos\varphi$ and the net change in time by:

$$\frac{dM_\parallel}{dt} = 2M_s\left[(1-p)f_- - pf_+\right]\cos\varphi \tag{21}$$

Normalizing the magnetization with $\mu = M_\parallel/M_s\cos\varphi$ and substituting (20) in (21) gives the following differential equation in $\mu(\Delta\bar{h})$:

$$\frac{d\mu}{d\Delta\bar{h}} = -a(\mu - \mu_\infty) \tag{22}$$

$$a = \frac{F}{f_{AC}\Delta\tilde{h}}\Delta\bar{h}^{q-1/4}\frac{\cosh\left[3\Delta\bar{h}^{1/2}\,\alpha\,h_{DC}/2\right]}{\exp\left[\Delta\bar{h}^{3/2}\alpha\right]}, \quad \mu_\infty = \tanh\left[\frac{3}{2}\alpha\Delta\bar{h}^{1/2}h_{DC}\right]$$

which does not have an analytical solution. Equation (22) is an approximation of the general kinetic equation. Its validity is discussed in detail in the Appendix. The coefficients of (22) depend on time through $\Delta\bar{h}(t) = 2f_{AC}\Delta\tilde{h}\,t$. To find an approximate solution of (22), we solve first the stationary case, in which $\Delta\bar{h}$ is constant. Thus, we put $\Delta\bar{h} = \Delta\bar{h}_0$ on the right side of (22) and obtain with the initial condition $\mu = 0$ at $t = 0$ the solution:

$$\mu(\Delta\bar{h},\Delta\bar{h}_0) = \mu_\infty\left[1 - \exp\left(-a(\Delta\bar{h}_0)\Delta\bar{h}\right)\right] \tag{23}$$

Thermodynamic equilibrium is given by the value $\mu_\infty(\Delta\bar{h}_0)$ of μ as $t \to \infty$, and is reached after a characteristic time, which corresponds to $\Delta\bar{h}_{eq} = 1/a$. If the time-dependend coefficient a in (22) does not change significantly over the characteristic time which corresponds to $\Delta\bar{h}_{eq}$, that is, when $\Delta\bar{h}_0 \gg \Delta\bar{h}_{eq}$, the asymptotic solution $\mu = \mu_\infty(\Delta\bar{h}_0)$ in (23) is a good approximation of the general solution, and the magnetization is in thermodynamical equilibrium with the applied field. As time proceeds, $\Delta\bar{h}_0$ increases and the coefficient a becomes progressively smaller. As a consequence, also the change in magnetization with time becomes smaller, until a final value of μ is reached. Because of the exponential dependence of a on time, the blocking process is sharp, and we can assume the final magnetization to represent the thermodynamic equilibrium μ_∞ reached just before it becomes frozen in. We assume that this occurs when $\Delta\bar{h}_0 = \gamma\Delta\bar{h}_{eq}$, where γ is an unknown constant in the order of 1. This leads to the following trascendental equation in $\Delta\bar{h}_0$:

$$\Delta\bar{h}_0 = \frac{\gamma f_{AC}\Delta\tilde{h}}{F}\Delta\bar{h}_0^{1/4-q}\frac{\exp\left[\alpha\Delta\bar{h}_0^{3/2}\right]}{\cosh\left[3\alpha\Delta\bar{h}_0^{1/2}\,h_{DC}/2\right]} \tag{24}$$

With $\alpha \gg 1$ and assuming $q = 3/4$, for reasons explained later, equation (24) has the approximate solution:

$$\Delta\bar{h}_0 \approx \alpha^{-2/3}\ln^{2/3}\left[\frac{5.7F_0}{\gamma f_{AC}\Delta\tilde{h}\;h_{sw}^{1/2}\alpha^{3/2}}\right] \tag{25}$$

Details about the solution of (24) are given in the Appendix. Inserting this result in (22) gives the final magnetization μ_∞ as $t \to \infty$:

$$\mu_\infty \approx \tanh\left[\frac{3}{2}\alpha^{2/3}\ln^{1/3}\left(\frac{5.7F_0}{\gamma f_{AC}\Delta\tilde{h}\;h_{sw}^{1/2}\alpha^{3/2}}\right)h_{DC}\right] \tag{26}$$

To estimate a numerical value of γ we linearize equation (22) for $h_{DC} \to 0$ and obtain:

$$\frac{d\mu}{d\Delta\bar{h}} = -\frac{F}{f_{AC}\Delta\tilde{h}}\Delta\bar{h}^{q-1/4}\exp\left[-\frac{3}{2}\alpha\Delta\bar{h}^{3/2}\right]\left(\mu - \frac{3}{2}\alpha\Delta\bar{h}^{1/2}\,h_{DC}\right) \tag{27}$$

Equation (27) can be scaled as follows:

$$y' = -\kappa\tau^{2q+1/2}\left(y - \frac{3}{2}\tau\right)\exp(-\tau^3)$$
$$\kappa = \frac{2F_0}{\sqrt{3\pi h_{sw}}\, f_{AC}\Delta\tilde{h}\,\alpha^{1+2q/3}} \qquad (28)$$

where $\tau = \alpha^{1/3}\sqrt{\Delta\tilde{h}}$ is the scaled time, $y = \alpha^{-2/3}h_{DC}^{-1}\mu$ is the scaled magnetization and κ a parameter of the equation (see the Appendix for details). Equation (28) is not analytically solvable, and has non-constant coefficients. Numerical solutions of equation (28) for different values of κ, ranging from 100 to 10^{14}, and for $q = 0, 1, 3/2, 2$ were computed with the software Mathematica, starting form the initial condition $y(\tau = 0) = 0$, until saturation was reached, at $\tau \approx 5$. Results for $q = 0$ are plotted in Figure 7a. For high values of κ the sharp transition from thermodynamic equilibrium to a "frozen" situation is evident. The asymptotic value for $\tau \to \infty$ from the numerical solutions, which represents the final ARM acquisition, is plotted in Figure 7b. The $\ln^{1/3}$-term in equation (26) is confirmed by the numerical solutions. A linear interpolation of the solutions of Figure 7b gives:

$$y^3(\tau \to \infty) \cong c_1 + c_2 \ln\kappa$$
$$c_1 = -4.918 + 4.196q\,,\quad c_2 = 3.275 + 0.135q \qquad (29)$$

for $0 \le q \le 2$. Table 1 gives the numerical solutions of $y(\tau \to \infty)$ for typical SD magnetite with $m = 4\times10^{-17}\,\mathrm{Am}^2$, $\mu_0 H_K = 60$ mT, $T = 300$ K, $f_{AC} = 400$ Hz and $\mu_0\Delta\tilde{H} = 5\ \mu$T, and different thermal activation models. Models with different values of q, representing significantly different activation models, result in very similar solutions for $y(\tau \to \infty)$ ranging from 3.1 to 3.9.

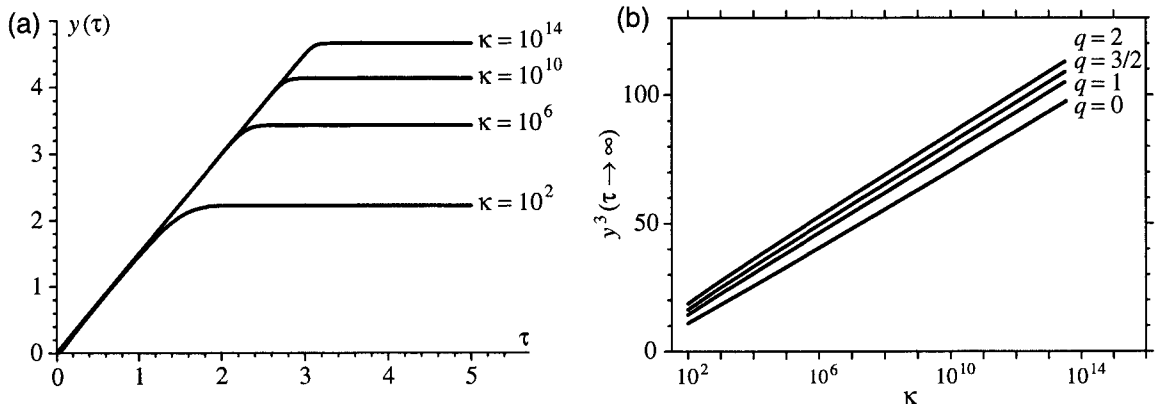

Figure 7: *(a) Solutions of equation (29) for different values of the parameter κ. The parameter τ is an expression for the time during an ARM cycle, and $y(\tau)$ an expression of the acquired magnetization. The flat part of the curves represents the final magnetization, and is a function of κ. (b) The final value of the magnetization as a function of the parameter κ for different switching models expressed by the parameter q. The solutions show only a weak dependence on q.*

Table 1: Comparison of the numerical solutions of different activation models.

activation model	q	F_0 in GHz	Estimation source:	$y(\tau \to \infty)$
intuitive model	0	1...10	*Butler and Banerjee* [1975]	3.7...3.9
gyrom. precession	1	1...10	*Brown* [1959]	3.3...3.5
magnetostriction	1.5	10000	*Néel* [1955]	3.9
brownian motion	2	20...200	*Brown* [1959]	3.1...3.4

3.5 Solution for ARM from the kinetic equation

We adopt below the solution given by $q = 3/4$, because of its algebraic simplicity. For $h_{\mathrm{DC}} \to 0$ we then obtain from (29) the approximate solution:

$$\mu_\infty = \frac{3}{2}\alpha^{2/3}\ln^{1/3}\left[\frac{1.18F_0}{f_{\mathrm{AC}}\Delta\tilde{h}\,h_{\mathrm{sw}}^{1/2}\alpha^{3/2}}\right]h_{\mathrm{DC}} \tag{30}$$

The solutions given in (26) and (30) are almost identical for $h_{\mathrm{DC}} \to 0$. We recall that these solutions are valid for a given direction φ of the easy axis with respect to the applied field. For an isotropic assembly of particles the distribution density of their easy axis is given by $\sin\varphi$. The contribution of all orientations to the bulk magnetization parallel to the applied field is then given by:

$$M = 0.5\,M_{\mathrm{s}}\int_0^{\pi/2}\mu_\infty(\varphi)\sin 2\varphi\;\mathrm{d}\varphi \tag{31}$$

which gives together with (30): $M = \chi_{\mathrm{ARM}}H_{\mathrm{DC}}$, and a finite susceptibility of ARM:

$$\chi_{\mathrm{ARM}} = 1.797\mu_0 M_{\mathrm{rs}}\left(\frac{m}{kT\sqrt{\mu_0 H_{\mathrm{K}}}}\right)^{2/3}\ln^{1/3}\left[\frac{0.35F_0}{f_{\mathrm{AC}}\Delta\tilde{H}\sqrt{\mu_0 H_{\mathrm{K}}}}\left(\frac{kT}{m}\right)^{3/2}\right] \tag{32}$$

being $M_{\mathrm{rs}} = 0.5M_{\mathrm{s}}$. Equation (32) is formally equivalent to a special case of (30) with $h_{\mathrm{sw}} = 0.528$, which corresponds to $\varphi = 61°$. It is also very similar to equation (4) with $\varphi = \pi/4$. According to the result of section 1, where thermodynamic activation was ignored, $\chi_{\mathrm{ARM}} \to \infty$ for $T \to 0$.

Considering (30) as a limit case of (26), we obtain the final expression for the ARM acquisition curve:

$$M(H_{\mathrm{DC}}) = M_{\mathrm{rs}}\tanh\left(\chi_{\mathrm{ARM}}H_{\mathrm{DC}}/M_{\mathrm{rs}}\right) \tag{33}$$

Equation (32) is extremely weakly dependent on the parameters of the AC field: a change of a factor 10 in frequency or decay rate produces a change of only 4% in χ_{ARM} of typical SD magnetite.

The results of this section were obtained assuming uniform rotation of the magnetization during the switching of the particle moment. However, several studies [e. g. *Aharoni and Shtrickman*, 1958] have shown that the magnetization of large SD grains during a moment switching is non-uniform, and exhibits a so-called curling or vortex configuration. This configuration lowers the energy barrier necessary to switch the moment and consequently the coercivity of the particle. Results of micromagnetic calculations of the energy barrier in magnetite cubes by *Enkin and Williams* [1994] are reproduced in Figure 12 in section 5, and show a drop of the energy barrier for sizes larger than 60 nm. As result, the energy barrier calculated in (11) may be considered as an upper limit, especially for grain sizes near the SD/PSD boundary. Other expressions for the field dependence of the energy barrier do not affect the form of the differential equation (22), which leads to the same kind of solution as in (32). A lower energy barrier increases the relative importance of the thermal energy and is therefore equivalent to an apparent increase of temperature. This produces a decrease of the suceptibility of ARM, so that equations (32) and (33) have to be considered as an upper limit for the ARM acquisition of SD particles.

Equation (32) predicts an increase of the susceptibiltiy of ARM with grain size in the SD range. For SD magnetite, according to the coherent rotation model, H_K is independent of the grain size, and thus, the susceptibility of ARM is proportional to d^2, where d is the diameter of the particles. The dependence of ARM on the grain size for particles smaller than 60 nm will be verified experimentally in sections 5 and 6.

4. The fluctuation field

4.1 Previous studies

The field which is necessary to reverse the magnetic moment of a SD particle by overcoming the energy barrier due to anisotropy was called switching field H_{sw} in section 2. Thermal activation is responsible for the moment switching even when the applied field is smaller than H_{sw}. It has the effect of reducing H_{sw} by an amount H_q, which *Néel* [1949] called a "fluctuation field". The fluctuation field depends on the moment of the particle and the time needed to switch its direction. In the literature a distinction is made between H_{sw}, often called the "microscopic coercive force H_c", and the field at which a moment-reversal occurs under specified conditions of time and temperature. The latter is called the "unblocking field H_B" and is the difference between H_c and H_q; that is, $H_B = H_c - H_q$ [*Dunlop and West*, 1969]. Simple calculations based on the application of thermal activation theory to a set of

oriented particles give the following commonly quoted expression for H_q [*Dunlop and West*, 1969]:

$$H_q = H_K \sqrt{\frac{2kTH_K}{\mu_0 m H_K} \ln\left(\frac{F_0 \tau}{2} \frac{H_q^2}{H_K^2}\right)} \tag{34}$$

where τ is the time necessary to switch the magnetic moment. In case of AF demagnetization, $\tau \approx 1/f_{AC}$ [*Kneller and Wolfarth*, 1966].

4.2 The fluctuation field of identical, aligned particles

In this paragraph we define the fluctuation field on the base of AF demagnetization curves as the difference between the real median destructive field and the theoretical value obtained by ignoring thermal activation effects. AF demagnetization can be conveniently described in a similar way as in section 3 by considering it to be a special case of ARM with $H_{DC} = 0$. An expression is obtained for the fluctuation field of randomly oriented particles, which shows important differences in comparison to (34).

Again we consider the behavior of non-interacting SD particles in the magnetic field of Figure 1, but now $H_{DC} = 0$. The particles are identical and have a given orientation φ of their easy axes with respect to the applied field. If thermodynamic effects are neglected, the initial magnetization M_0 remains unaffected if the initial amplitude $\tilde{H}_0$ of the alternating field is less than the switching field $H_{sw} = h_{sw}(\varphi) H_K$. For $\tilde{H}_0 \geq H_{sw}$, the sample is fully demagnetized, leading to a final magnetization $M = 0$.

Thermal activation is responsible for the switching of the particle moments even when $\tilde{H}_0 < H_{sw}$. The problem of thermal activation in a decaying AC field was analyzed in section 3, leading to the differential equation (22). The special case $h_{DC} = 0$ of equation (22):

$$\frac{d\mu}{d\Delta\bar{h}} = \frac{-F}{f_{AC}\Delta\tilde{h}} (\Delta\bar{h})^{q-1/4} \exp\left[-\alpha \Delta\bar{h}^{3/2}\right] \mu \tag{35}$$

describes the time evolution of the normalized magnetization μ during the demagnetization. We assume an initial magnetization $\mu = 1$, when $\Delta\bar{h}(t = 0) = \Delta\bar{h}_0$. Integration of (35) gives:

$$\ln \mu(\Delta\bar{h}) = \frac{-F}{f_{AC}\Delta\tilde{h}} \int_{\Delta\bar{h}_0}^{\Delta\bar{h}} u^{q-1/4} \exp\left(-\alpha u^{3/2}\right) du \tag{36}$$

Equation (36) has an analytical solution in the special case of $q = 3/4$. Since equation (22) is almost independent of q, as demonstrated in section 3, we choose $q = 3/4$ as an exellent

approximation for the general case, and obtain:

$$\mu(\Delta\bar{h}_0,\Delta\bar{h}) = \exp\left[\frac{2F}{3f_{AC}\Delta\tilde{h}\,\alpha}\left(\exp(-\alpha\Delta\bar{h}^{3/2}) - \exp(-\alpha\Delta\bar{h}^{3/2})\right)\right] \tag{37}$$

The end of the demagnetization process can be identified with $\Delta\bar{h} \to \infty$, leading to the final magnetization expressed by:

$$\mu_\infty(\Delta\bar{h}_0) = \exp\left[-\frac{2F}{3f_{AC}\Delta\tilde{h}\,\alpha}\exp\left(-\alpha\Delta\bar{h}_0^{3/2}\right)\right] \tag{38}$$

The final magnetization μ_∞ as a function of the initial value $\Delta\bar{h}_0$ of $\Delta\bar{h}$ is plotted in Figure 8 for different values of H_K and m and is characterized by a sharp transition from $\mu_\infty \to 1$ for small values of $\Delta\bar{h}_0$ to $\mu_\infty \to 0$ for small values of $\Delta\bar{h}_0$. We define the fluctuation field H_q as the value of $\Delta\bar{h}_0$ for which the magnetization is reduced to half its initial value. Since the transition is sharp, the choice of the fraction of initial magnetization is not relevant. From (38) we obtain then the equation $\mu_\infty(H_q) = 0.5$, with solution:

$$H_q = \left(\frac{kT}{\mu_0 f_{sw} m}\right)^{2/3} \ln^{2/3}\left[\frac{2F_0}{3\ln 2\sqrt{3\pi\mu_0 h_{sw} H_K} f_{AC}\Delta\tilde{H}}\left(\frac{kT}{f_{sw} m}\right)^{3/2}\right] \tag{39}$$

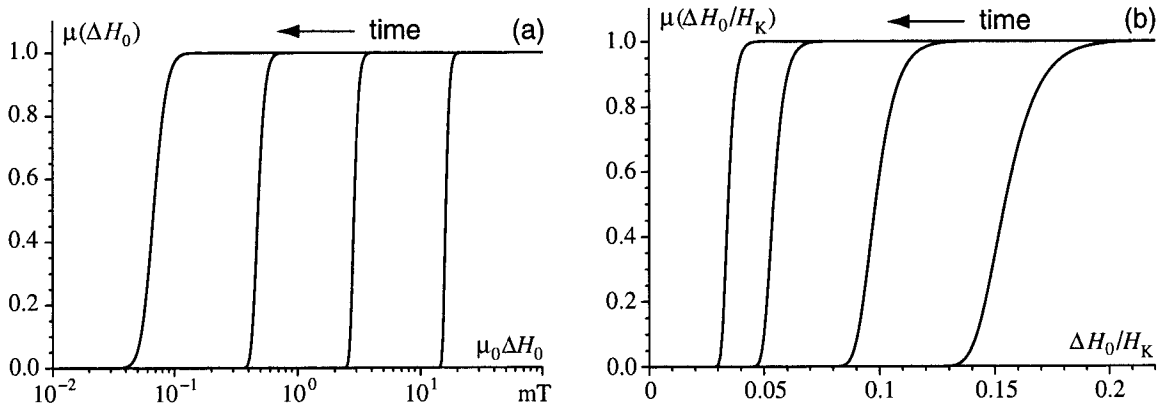

Figure 8: *Normalized magnetization of an oriented assemblage of non-interacting SD particles with microcoercivity H_K, after AF demagnetization with an initial peak field equal to $H_{sw} - \Delta H_0$, H_{sw} being the switching field. (a) The dependence of H_q on the particle moment, and (b) the dependence on the microcoercivity. The value of ΔH_0, at which $\mu = 0.5$, is defined as the fluctuation field H_q of the particles. For large moments the fluctuation field is very small and the particles behave according to the Stoner-Wolfarth theory. The magnetization is calculated with equation* (38) *with following parameters: $T = 300$ K, $f_{AC} = 400$ Hz, $\mu_0\Delta\tilde{H} = 5$ μT, $\varphi = \pi/3$, and (a) $\mu_0 H_K =$ 60 mT with $m = 5\times10^{-18}$, 5×10^{-17}, 5×10^{-16}, 5×10^{-15} Am^2 from left to right, (b) $m =$ 5×10^{-17} Am^2 with $\mu_0 H_K = 100$, 50, 20, 10 mT from left to right.*

4.3 The fluctuation field of identical, randomly oriented particles

We generalize now to the case of a sample with identical randomly oriented particles. Let $\mu(\varphi)\cos\varphi\sin\varphi$ be the contribution of all particles with orientation φ to the total magnetization. In case of an IRM, $\mu(\varphi) = 1$. In case of an ARM, $\mu(\varphi)$ is given by equation (30) when $h_{DC} \to 0$. The total magnetization $\mu_\infty^{tot}(\Delta\bar{h}_0)$ after the AF demagnetization is given by:

$$\mu_\infty^{tot}(\Delta\bar{h}_0) = \int_0^{\pi/2} \mu(\varphi)\exp\left[-\kappa\exp\left(-\alpha\Delta\bar{h}_0^{3/2}\right)\right]\sin 2\varphi\,\mathrm{d}\varphi \tag{40}$$

Equation (40) cannot be evaluated analytically. Numerical solutions for SD grains with different moments and $H_K = 60$ mT, $f_{AC} = 400$ Hz, $\Delta\tilde{H} = 5$ μT are represented in Figure 9 as a function of the maximun AC peak field $\tilde{H}$.

Defining again H_q as the solution of the equation $\mu_\infty^{tot}(H_q) = 0.5$, one has the numerical results of Table 2, given for different values of the particle moment with $H_K = 60$ mT and the same parameters as Figure 9. The value of φ in equation (39) which gives the calculated H_q in (40) is also given in Table 2: it has a mean of $\varphi = 62°$ and differs by no more than 1° when the particle moment varies by over 3 orders of magnitude. We assume therefore equation (40) with $\varphi = 62°$ as an exellent approximation of the fluctuation field of an assembly of random oriented SD particles and get finally:

$$H_q = 0.801\left(\frac{kT\sqrt{H_K}}{\mu_0 m}\right)^{2/3}\ln^{2/3}\left[\frac{F_0}{3.8 f_{AC}\Delta\tilde{H}\sqrt{\mu_0 H_K}}\left(\frac{kT}{m}\right)^{3/2}\right] \tag{41}$$

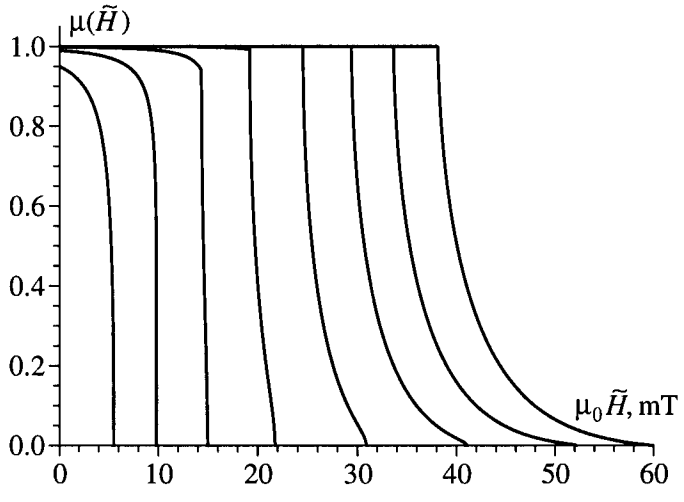

***Figure 9**: Normalized AF demagnetization curves of randomly oriented, non-interacting magnetite SD particles with $\mu_0 H_K = 80$ mT and different magnetic moments, from left to right: 2×10^{-18}, 2.4×10^{-18}, 3×10^{-18}, 4×10^{-18}, 6×10^{-18}, 1×10^{-17}, 2×10^{-17}, 1×10^{-16} Am². The last curve on the right is the AF demagnetization without thermal activation, according to the classic Stoner-Wohlfarth model. Other parameters are: $T = 300$ K, $f_{AC} = 400$ Hz and $\mu_0\Delta\tilde{H} = 5$ μT. The difference between the median destructive field of the curves with and without thermal activation can be identified with the fluctuation field of the particles. According to the Néel relaxation theory a moment of 2.4×10^{-18} Am² has a relaxation time of 10 s.*

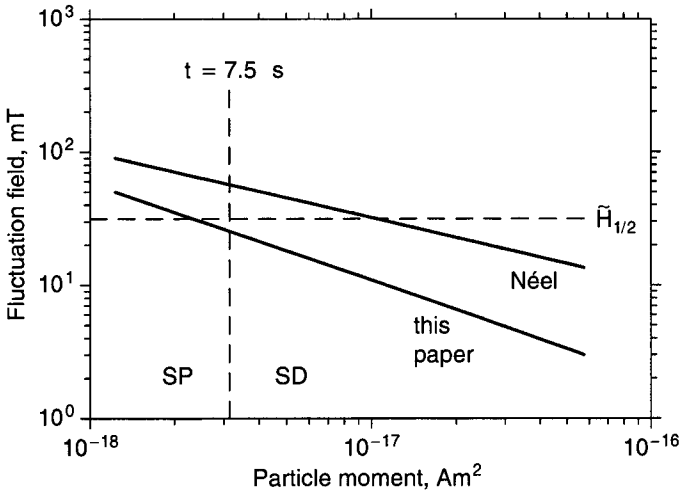

Figure 10: *Comparison between the fluctuation field predicted by Néel theory and by the present theory for randomly oriented SD particles with* $\mu_0 H_K = 60$ mT, *as a function of the particle moment. The horizontal dashed line represents* $\tilde{H}_{1/2}$ *according to the Stoner-Wolfarth model, the vertical dashed line represents particles with a time constant* $\tau = 7.5$ s, *which is the time required by the AF field to decrease from* $\tilde{H}_{1/2}$ *to zero. A fluctuation field larger than* $\tilde{H}_{1/2}$ *represents an impossible solution.*

Equations (34) and (41) have the same qualitative dependence on T, H_K and m, but give quite different results. We choose as example SD particles with $H_K = 60$ mT and following parameters: $T = 300$ K, $\Delta\tilde{H} = 5$ μT, $f_{AC} = 400$ Hz. Results for H_q from (34) and (41) as a function of the particles moment are shown in Figure 10. Equation (34) gives systematically higher values for H_q, especially near the SD/PSD limit, where the difference in H_q can reach up to one order of magnitude. There are three reasons for this difference. First, our definition of H_q is related to the effect of thermal activations on the median destructive field, whereas the definition of Néel is based on the time dependence of the coericivity. Second, equation (41) is the direct solution of the kinetic equations of a SD particle in an alternating field. Third, equation (34) is strictly valid only in the very special case of particles with their easy axes oriented parallel to the field, whereby these particles do not contribute significantly to the total magnetization of an isotropic sample.

Table 2: *Numerical calculation of the fluctuating field for different particle moments.*

mag. moment Am^2	Demagnetization of IRM		Demagnetization of ARM		Eq. (34)
	H_q, mT	φ in eq. (39)	H_q, mT	φ in eq. (39)	H_q, mT
2.4×10^{-18}	32.3	60.5	32.2	60.1	75.4
4.0×10^{-18}	22.3	60.9	22.3	66.8	57.6
6.0×10^{-18}	16.6	61.0	16.7	61.4	46.6
1.0×10^{-17}	11.4	60.5	11.5	61.6	35.6
2.0×10^{-17}	6.78	59.9	6.75	62.5	24.6
5.0×10^{-17}	3.39	58.8	3.60	64.5	15.2
1.0×10^{-16}	2.00	58.3	2.21	67.1	10.5

For classic Stoner-Wolfarth particles, the median destructive field of a demagnetization curve is given by $H_{1/2} = 0.524\,H_K$. If the mean switching field H_{sw} of a set of identical particles is identified with $H_{1/2}$, in case of thermal fluctuations one has $H_{sw} = 0.524\,H_K - H_q$. The shape of a demagnetization curve for a set of particles with different microcoercivities is then given by the distribution of the values of H_{sw}.

5. The range of anhysteretic SD behaviour of fine particles

The stability range of SD particles of magnetite and other minerals has been investigated in several theoretical and experimental studies [*Dunlop and West*, 1969; *Butler and Banerjee*, 1975; *Diaz-Ricci and Kirschvink*, 1992; *Newell and Merrill*, 1999]. Often, single critical sizes are assumed to define the size range of SD particles. In reality, the critical sizes depend on the magnetic property under consideration. For example, grains can have a SD saturation remanent state and then develop domain walls in reverse fields [*Halgedahl and Fuller*, 1980].

In the following we consider the stability range of SD particles with shape-controlled anisotropy from the point of view of anhysteretic processes, i.e. ARM and AF demagnetization. We equate the stability range with the validity range of the equations derived in section 3 for the ARM. As already pointed out, the calculations of this paper assume a uniform rotation as reversal mechanism for the particle moment. *Newell and Merrill* [1999] used nucleation theory to calculate the upper-limit volume of ellipsoidal magnetite particles which reverse by uniform rotation in a magnetic field parallel to their easy axis. As discussed in section 3, only a negligible part of all particles in an isotropic sample satisfy this condition. However, the application of nucleation theory in the general case is complex and still unsolved. We assume therefore the results of *Newell and Merrill* [1999] as an initial approximation. Their upper limit for uniform rotation is almost independent of the shape of the ellipsoid and varies between 50 and 70 nm in size. For larger volumes, the particles can still exhibit a SD remanence, but they reverse in the curling mode and this leads to smaller values of the susceptibility of ARM. For comparison, *Butler and Banerjee* [1975] give grain sizes between 100 nm and 1 μm as the upper limit of SD magnetite prisms.

On the other hand, a reduction of the volume increases the fluctuation field, and lowers therefore all coercivity parameters (H_c, H_{cr} and $\tilde{H}_{1/2}$). In the extreme case when a coercivity parameter is reduced to zero, the particle can be considered to be effectively superparamagnetic (SP). To define the SP/SD boundary we choose the volume at which $\tilde{H}_{1/2} = 0$. The results, plotted in Figure 11a, are slightly smaller in comparison to those of *Butler and Banerjee* [1975] for a time constant of 100 s.

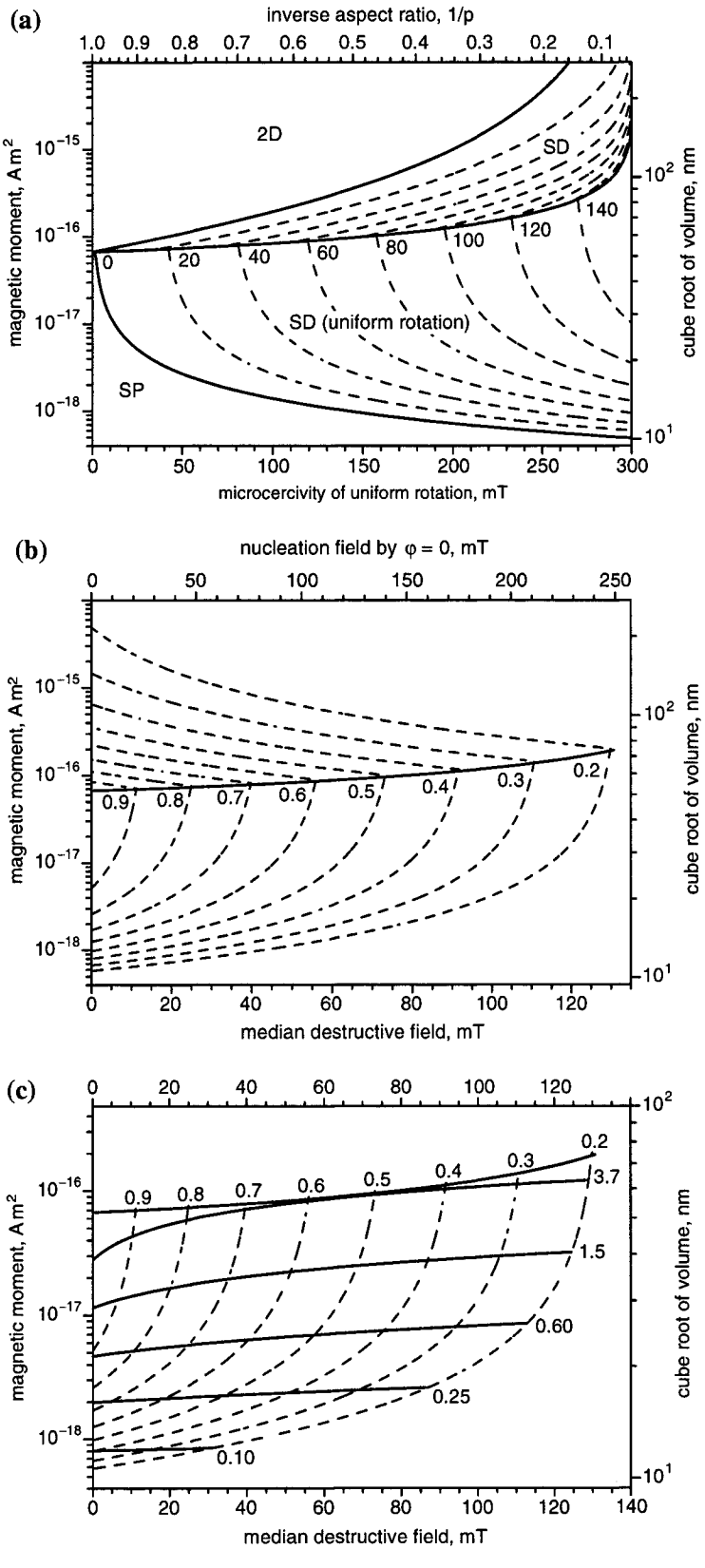

Figure 11: *Theoretical stability range for prolate ellipsoids of magnetite with shape anisotopy only. (a) Solid lines represent in order from bottom to top: upper limit for SP particles ($H_q = \tilde{H}_{1/2}$ in this paper); upper limit for a moment reversal by uniform rotation; upper limit for stable SD remanence (both after Newell and Merrill [1999]). Dashed lines represent the median destructive field for randomly oriented particles in the lower part of the stability diagram ($H_{1/2} = H_{sw} - H_q$ in this paper), and the nucleation field H_{curl} for curling in aligned particles in the upper part (after Newell and Merrill [1999]). Numbers in the plot refer to $H_{1/2}$ and to $0.524H_{curl}$, respectively. (b) The solid line represents the upper limit for a moment switching by uniform rotation. Dashed lines represent curves of constant particle elongation p; numbers refer to $1/p$. The lower part of the stability field represents the smallest volume of randomly oriented SD particles with elongation p as a function of their median destructive field. The upper part of the stability range represents the maximum volume of aligned particles with SD remanence as a function of the nucleation field for a moment switching by curling. (c) Same plot as (b) for the region of moment switching by coherent rotation. Solid curves represent particles with same values of $\chi_{ARM}/SIRM$, expressed in 10^{-3} m/A by the numbers on the right. These values range from 10^{-4} to 2×10^{-3} m/A for common SD particles; the same values are measured in natural samples with SD grains.*

Stability ranges are commonly plotted as a function of the inverse shape parameter $1/p$, where p is the ratio of the largest to the shortest axis of a grain. For better characterization of the properties of SD magnetite, the stability range is plotted in Figure 11b as a function of the median destructive field or nucleation field. This method of plotting demonstrates more clearly than Figure 11a the transitional nature of the SP/SD and SD/PSD boundaries.

The range of stability of SD particles increases with the shape parameter p, from $p = 0$ (a sphere) to $p = \infty$ (an infinite cylinder). Grains with large values of p are less likely to be observed in nature: often $0 \leq p \leq 2$. Magnetosomes have $p \approx 1$ (equant), $p \approx 1.5...2$ (prismatic) or $p \approx 3$ (bullet-shaped); fine-grained magnetite in soils has $p < 1.5$. Acicular magnetite can reach $p \approx 5$, as in the sample described in section 6. The parameter $\chi_{\mathrm{ARM}}/SIRM$ can be calculated with equation (32) as a function of the magnetic moment m and the microcoercivity H_{K}, or the corresponding median destructive field. In Figure 11c, lines with constant $\chi_{\mathrm{ARM}}/SIRM$ are plotted together with the stability diagram of Figure 11b. For common SD magnetite ($0 \leq q \leq 2$) and no interactions, $\chi_{\mathrm{ARM}}/SIRM$ ranges from 2×10^{-4} m/A (for $m = 1.3 \times 10^{-18}$ Am^2 and $\mu_0 \tilde{H}_{1/2} = 20$ mT) to 3.7×10^{-3} m/A (for $m = 1 \times 10^{-16}$ Am^2 and $\mu_0 \tilde{H}_{1/2} = 70$ mT). Values between 2×10^{-4} m/A and 2.5×10^{-3} m/A are commonly measured in natural inorganic magnetite [*Moskowitz et. al.*, 1993; *Maher*, 1988] and values up to 3.8×10^{-3} m/A have been reported in samples of intact magnetosomes [*Moskowitz et. al.*, 1993].

Magnetic interaction between grains generally lowers the values of $\chi_{\mathrm{ARM}}/SIRM$. This occurs with increasing concentration of the magnetic particles and has been observed experimentally [*Banerjee and Mellema*, 1974; *Sugiura*, 1979; *Maher*, 1988; *Dunlop*, 1981; *Yamazaki and Ioka*, 1997]. The effect of interactions cannot be neglected in synthetic samples, where clustering of the magnetite particles is very difficult to avoid. Therefore, ARM experiments on synthetic samples may not be representative for the situation encountered in natural samples with a low concentration of well-distributed magnetic grains.

As already mentioned, the range of validity of equations (32) and (33) is limited to grain sizes related to a moment switching by coherent rotation. As demonstrated with micromagnetic calculations, the energy barrier of the moment switching drops significantly for grain sizes > 60 nm (Figure 12). A significant change in the microcoercivity is also expected. If the grains still exhibit SD remanence when the AF field is removed, new estimates of both microcoercivity and energy barrier allow to extend the thermal activation model toward larger grain sizes. Above the upper limit for SD remanence, magnetic grains can exhibit different remanence states which are influenced by the past history of the grain. The field applied during an ARM may induce the remanence state which minimizes the magnetic energy of the grain in the DC field, and this state is not influenced by thermal activation effects. The acquisition process of such grains is therefore fundamentally different.

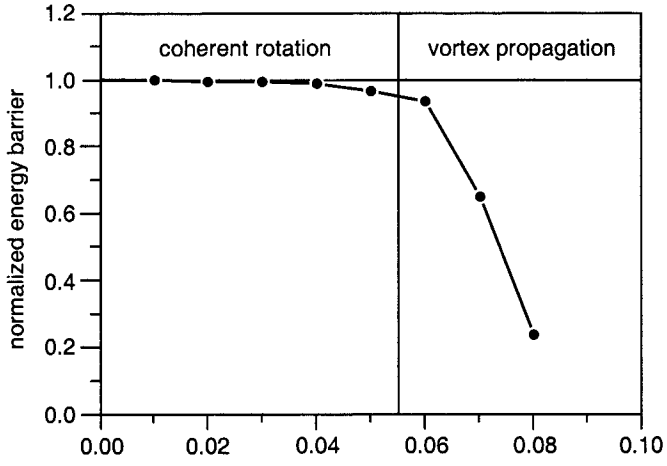

Figure 12: *Energy barrier to magnetic moment reversal as a function of grain size in magnetite cubes. Incoherent rotation lower the energy barrier over 60 nm grain size (from Enkin and Williams, [1994]).*

A summary of experimental results for ARM acquisition in magnetite samples is shown in Figure 13a. Particles with grain sizes < 60 nm exhibit the d^2-dependence on grain size predicted by the model of this paper. A drastic change in the grain size dependence of ARM occurs for $d > 60$ nm, as expected from micromagnetic calculations. Between 60 and 200 nm, the ARM intensity decreases as $d^{-0.8}$ with grain size d. In this grain size range, the ARM may be controlled by thermal activations of non-uniform reversal modes. Above 200 nm (the upper limit for SD remanence), the ARM intensity depends weakly on grain size, and is related to a multidomain remanence. Experimental results for the median destructive field of SIRM and ARM are summarized in Figure 13b. The coercivity of small particles is reduced by the fluctuation field, and the observed trend for particles smaller than 100 nm is compatible with the result predicted by equation (41).

6. An experimental proof

In this section, the theory of the ARM acquisition by non-interacting SD particles is verified experimentally on a sample from the Yucca Mountain Tuff [*Worm and Jackson*, 1999]. The Yucca Mountain Tuff is an ashflow tuff from the Tiva Canyon member of the Paintbrush Tuff at Yucca Mountain (Nevada). It contains small titanomagnetite grains with a narrow size distribution over the SP and finest SD range. The concentration of the magnetic grains is low ($< 0.5\%$ by weight) and is not affected by clustering, so that magnetostatic interactions are expected to be small. The grains are Ti-poor titanomagnetites with a Curie temperature of 521 °C, which corresponds to an ulvospinel content of $x = 0.1$. A room-temperature saturation magnetization of 407 kA/m is assumed for the grains, according to *Worm and Jackson* [1999].

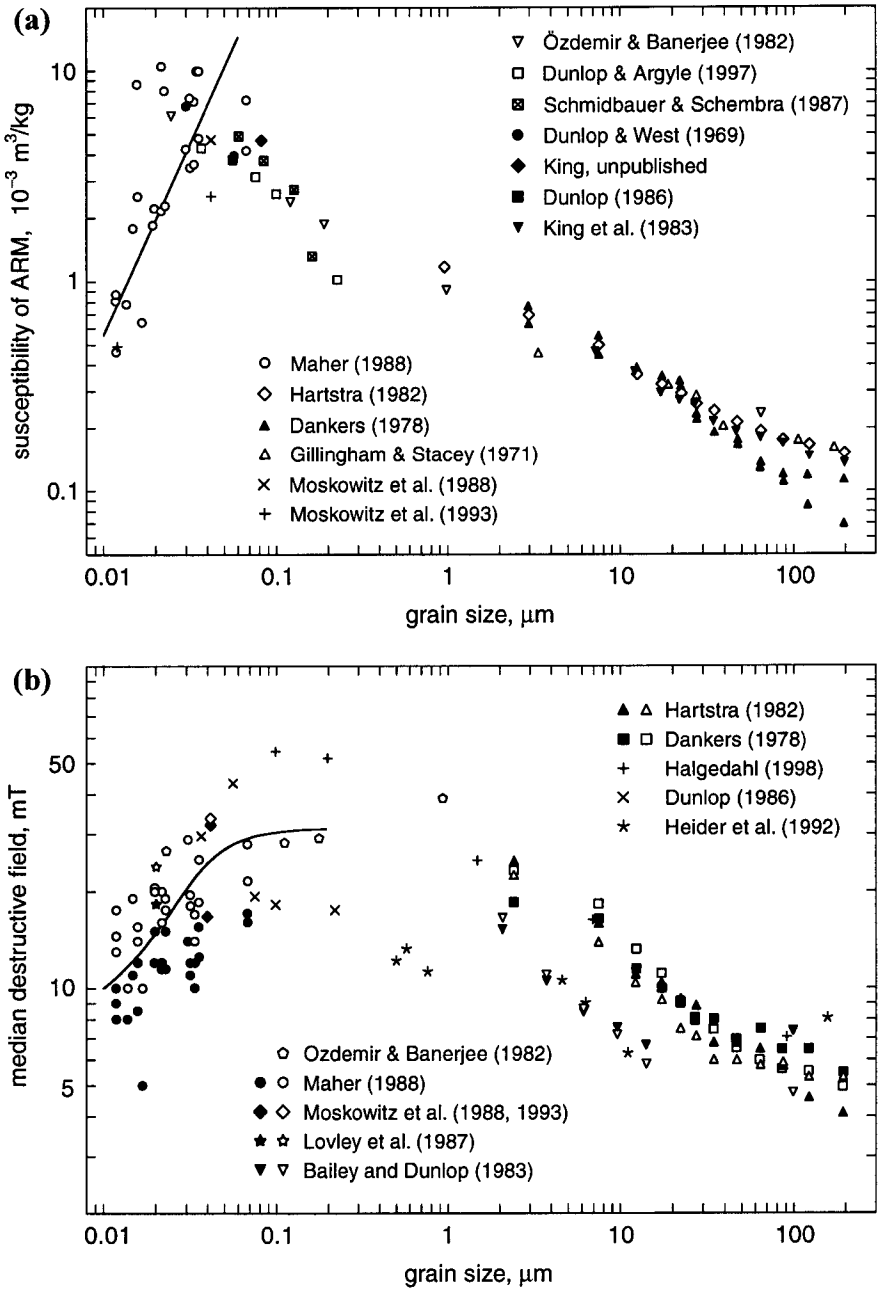

Figure 13: *Summary of experimental results for ARM and IRM magnetizations in synthetic magnetite samples as a function of grain size. (a) Susceptibility of ARM. Data of Schmidbauer and Schembra [1987] are corrected to a magnetite concentration of* $\approx 1\%$ *according to the experimental dependence of the ARM on concentration reported by Sugiura [1978]. The solid line represents the quadratic dependence of the ARM on the grain size, predicted by the theory of this paper for SD particles. Experimental results are compatible with the theory for grain sizes up to* 50 nm, *close to the limit of* 60 nm *reported by Enkin and Williams [1994] for a magnetic moment reversal by coherent rotation. (b) Median distructive fields of SIRM (sybols left in the legend) and ARM (symbols right in the legend). The solid line represent the median destructive field calculated with the theory of this paper assuming a lognormal grain size distribution for each sample. The disperison parameter of the lognormal distribution (*$\sigma = 0.37$*) is a best-fit of the grain size distributions reported for the samples of Maher [1988].*

Among the three samples mentioned in *Worm and Jackson* [1999], the more coarse-grained (CS914) is investigated here for its ARM properties. CS914 is the only sample with a significant amount of particles in the SD state at room temperature. According to electron microscopy and X-ray diffraction analysis, the grains have uniaxially prolate shapes with mean dimensions of 8.5×45 nm. The grains are much smaller than the upper limit for the SD state, and are therefore expected to switch by coherent rotation, with a microcoercivity of 221 mT. According to the properties illustrated above, the sample is therefore expected to behave as predicted by the model presented in this paper.

The experimental proof is divided in two parts. In the first part, the dependence of the ARM intensity on the ramp rate of the AF field predicted by equation (32) is verified experimentally. The experiments allow a new estimation of the atomic reorganisation time at room temperature. In the second part, the grain volumes distribution calculated by *Worm and Jackson* [1999] from thermal demagnetization curves is used to predict the ARM properties of the sample, which are then compared with the measurements.

6.1. The dependence of ARM intensity on the decay rate of the AF field

The ARM model of this paper can be tested by investigating the predicted dependence of the ARM intensity on parameters which can be experimentally varied, like the temperature and the AF field decay rate. The product $f_{AC}\Delta\tilde{H}$ in equation (32) is equivalent to half the decay rate α, expressed in T/s, which represents the drop of the AC peak field per unit time. The dependence on the decay rate is expected to be extremely weak, on the order of 30% when α changes over three orders of magnitude. The temperature dependence is stronger, however, its interpretation is difficult, because the intrinsic properties of the magnetic grains (e.g. saturation magnetization and microcoercivity) are temperature-dependent as well. In addition, in samples with a high proportion of SP particles, as is the case with the Yucca Mountain Tuff, an appreciable amount of particles becomes blocked or unblocked with little temperature change. For these reasons, the temperature dependence cannot be predicted with the necessary precision.

The experimental verification of the dependence of the ARM intensity on the decay rate allows experimental evaluation of the atomic reorganization time, expressed by the frequency F_0 in equation (32). This estimation is important, since the atomic reorganization time depends on several experimental conditions, and the values given in the literature vary from 10^{-8} to 10^{-11} s [*Brown*, 1959; *McNab*, 1968].

In order to measure the weak effect of the field decay rate, the widest range of decay rates made possible by the laboratory instrumentation was tested. Two types of demagnetization apparatus were used for this purpose: a GSD-1 Schoensted specimen demagnetizer with selectable nominal decay rates between 0.1 and 5 μT/half-cycle and an operating frequency of 400 Hz, and a custom-built 2G degausser system with selectable decay rates between 9 and

78 μT/half-cycle and an operating frequency of 150 Hz. The systems have overlapping decay rates from 0.059 to 24 mT/s, which cover three orders of magnitude. The 2G degausser system has a built-in facility for ARM acquisition. A supplementary coil was built around the Schoensted demagnetizer, in order to produce a DC field. The coil was connected to a high-precision current generator through an inductive filter, in order to avoid feedback effects with the demagnetization coil. Ramp rate, DC field, initial AF peak field and frequency were measured at each ARM acquisition. Because of the weak effect to be tested, extreme precision was required for the experiment. A comparison between the ARM acquisition with different ramp rates has to be performed at constant temperature. For this reason, special care was taken to avoid temperature changes during the acquisition process. The time required for the ARM acquisition at the lowest ramp rate (20 min) was long enough to transfer the Joule heat loss of the coil to the sample. For this reason, coil and sample were pre-heated with several AF cycles to achieve an equilibrium temperature before starting the acquisition. The temperature was controlled within $\pm 2^{\circ}\mathrm{C}$, so that the related temperature effect was $< 0.5\%$ of the total ARM. The ARM acquisitions were repeated 9 times for each decay rate, in order to increase the precision and estimate the experimental errors. The results are plotted in Figure 14.

In order to linearize the dependence of χ_{ARM} on the decay rate α, equation (32) can be rewritten as follows:

$$\left(\frac{\chi_{\mathrm{ARM}}(\alpha)}{\chi^{0}_{\mathrm{ARM}}}\right)^{p} = a + b\log\alpha$$

$$p = 3\,; \quad a = 1 + \frac{\ln\alpha_0}{\ln\left[\dfrac{0.7F_0}{\alpha_0\sqrt{H_{\mathrm{K}}}}\left(\dfrac{kT}{m}\right)^{3/2}\right]} \quad ; \quad b = \frac{-\ln 10}{\ln\left[\dfrac{0.7F_0}{\alpha_0\sqrt{H_{\mathrm{K}}}}\left(\dfrac{kT}{m}\right)^{3/2}\right]} \tag{42}$$

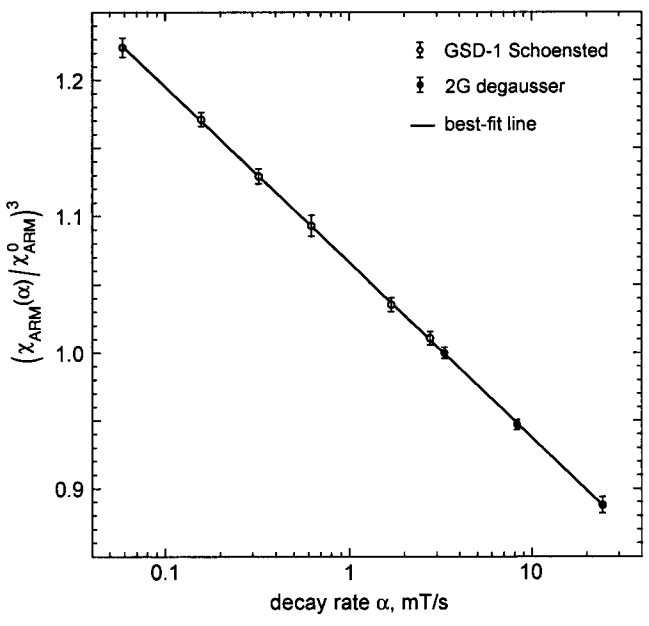

Figure 14: *Dependence of the ARM intensity on the decay rate of the AF field for sample CS914. The error bars represent the double standard deviation of 9 identical measurements for each point. The ARM intensity is normalized by its value for a decay rate of* 3.31 mT/s, *which is normally used in our laboratory.*

whereby α_0 is a reference value of α and $\chi^0_{\mathrm{ARM}} = \chi_{\mathrm{ARM}}(\alpha_0)$. A comparison of equation (42) with the experimental results allows verification of the expected linear relation and to estimate the constants a and b with least-squares fitting. The linearity of (42) was tested by fitting the measurements of Figure 14 with different values of the exponent p. The effect of the measurement errors was simulated by adding an adequate Gaussian noise to each measurement. The result of 10,000 simulations gives $q = 3.11 \pm 0.12$, in good agreement with the theoretical value $p = 3$.

The frequency F_0 can be estimated from (42):

$$F_0 = 1.44\,\alpha_0 \sqrt{H_{\mathrm{K}}}\, 10^{1/b} \left(\frac{m}{kT}\right)^{3/2} \tag{43}$$

The mean values of m and H_{K} for the Yucca Mountain Tuff can be deduced from *Worm and Jackson* [1999]: $m = 2.1 \times 10^{-18}$ Am^2 and $H_{\mathrm{K}} = 220$ mT. These values were taken as starting parameters of equation (43). From the measurements plotted in Figure 14, $\alpha_0 = 3.31$ mT/s and $b = 0.129 \pm 0.00002$. A better estimation of m and H_{K} can be obtained with the AF demagnetization curve of ARM discussed in section 6.2. Equation (32) can be solved with respect to m, obtaining:

$$m = kT \sqrt{H_{\mathrm{K}}} \left(\frac{\chi_{\mathrm{ARM}}}{1.797 \mu_0 M_{\mathrm{rs}}}\right)^{3/2} \ln^{-1/2}\left[\frac{0.696 F_0}{\alpha}\left(\frac{kT}{m}\right)^{3/2}\right] \tag{44}$$

As first estimation, $H_{\mathrm{K}} = 1.91(\tilde{H}_{1/2} + H_{\mathrm{q}})$ was chosen, with $\tilde{H}_{1/2}$ being the median destructive field of the AF demagnetization curve of ARM. Equations (41), (43) and (44) were then iteratively evaluated in order to get better estimates of m and H_{K}. The final values obtained are $m = (2.8 \pm 0.7) \times 10^{-18}$ Am^2 and $H_{\mathrm{K}} = 184 \pm 40$ mT, in good agreement with the initial values taken from *Worm and Jackson* [1999]. Finally, equation (43) gives the following estimate: $F_0 = (1.3 \pm 0.4)$ GHz or $\tau_0 = (7.7 \pm 2) \times 10^{-10}$ s, in good agreement with the values found in the literature. *McNab et al.* [1968] estimated $\tau_0 = (9.5 \pm 1.5) \times 10^{-10}$ s for superparamagnetic magnetite grains using Mössbauer spectra, which is compatible with the result of this paper within the error range. For comparison, *Worm and Jackson* [1999] estimated $F_0 \approx 10^9 \ldots 10^{11}$ Hz by modelling the frequency dependence of the susceptibility on the same sample. Their lower estimation limit of $F_0 \approx 10^9$ Hz fits better the measured susceptibility at low frequencies (0.1...1 Hz), which is controlled mainly by relatively stable particles with time constants of 1...10 s. These particles are only slightly smaller than the stable SD particles, which are contributing to the ARM. The reason for the apparent dependence of F_0 on the particles size in CS914 is not clear: it is maybe due to the difficulty of modelling the susceptibility of particles near the SP/SD boundary.

6.2. A comparison between calculated and measured ARM properties

In section 3, a relation between the microscopic properties of fine particles (magnetic moment and microcoercivity) and ARM was found. The Yucca Mountain Tuff is a suitable material for testing this relation, since size, shape and mineralogy of the magnetic grains is well-known.

Knowledge of the distribution of volumes and microcoercivities of the grains (magnetic granulometry: *Dunlop* [1976]) allow us to predict their magnetic properties, including the ARM. In this section, the magnetic granulometry will be deduced from IRM experiments. The results will be then used to calculate the ARM properties with equation (32), (33) and (41), which are then compared with the ARM measurements.

Worm and Jackson [1999] calculated the volume distribution of the magnetic particles in sample CS914 using thermal demagnetization curves of IRM. Their result is shown in Figure 15a for volumes up to 6×10^{-24} m^3. The shape of the volume distribution suggests the presence of larger particles. In order to extrapolate the contribution of larger volumes, the distribution was fitted in the SD region ($V > 2 \times 10^{-24}$ m^3) with two lognormal functions.

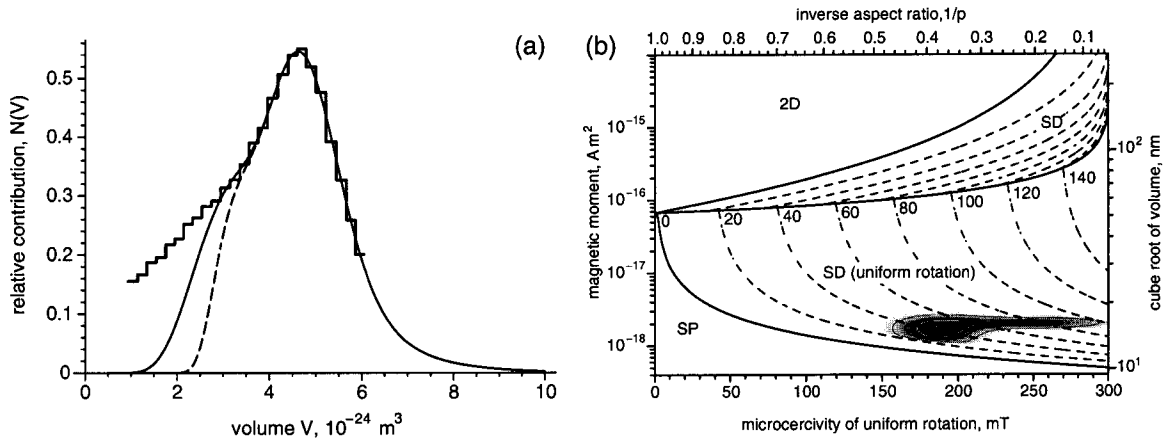

Figure 15: *(a) Volumes distribution of the magnetite particles in sample CS914. The stepped line is the volume distribution calculated from the thermal demagnetization of IRM (from Worm and Jackson, [1999]). The solid line is a best-fit of the volume distribution in the SD range ($V > 2.5 \times 10^{-24}$ m^3) with two lognormal distributions. The dashed line is the volume distribution of all particles that can carry a remanence at room temperature. (b) Distribution of volumes and microcoercivities in sample CS914 (contours and shaded surface), plotted together with the stability range for SD particles. This distribution gives a best fit to both thermal and AF demagnetization curves of SIRM. The density of the distribution is proportional to the contribution of all particles with given volume and microcoercivity to the SIRM. The dashed lines in the SD range represent all particles with the same coercivity, indicated by the numbers in the plot field. A typical coercivity of* 45 mT *can be deduced from the plot: this value coincides with the median destructive field of the AF demagnetization.*

Since the measurements of this paper are performed at room temperature, a misfit below the SP/SD boundary is irrelevant. The extrapolated distribution suggests significant amounts of particles with volumes up to 8×10^{-24} m^3. Assuming a mean microcoercivity of 220 mT from microscopic observations of the grain shapes, and with equation (41), the coercivity of the particles is expected to range from 0 to 110 mT. This broad coercivity distribution is controlled by the strong dependence of the fluctuation field on the volume of fine SD particles. It is reasonable to assume some kind of variations in the grain shape, which is related to a distribution of microcoercivities around 220 mT. This distribution can be deduced from the volume distribution and from the coercivity distribution calculated with IRM acquisition or demagnetization curves. Let $N(H_K,V)$ and $M'(H_{sw})$ be the distributions of H_K, V and the switching field H_{sw}, respectively. Further, $H_{sw} = 0.524H_K - H_q(H_K,V)$, as discussed in section 4. The distribution $N(H_K,V)$ was called magnetic granulometry by *Dunlop* [1976]. The relation between magnetic granulometry and coercivity distribution is then given approximatively by:

$$M'(H_{sw}) = \int_0^\infty \frac{N(H_K,V)}{0.524 - \mathrm{d}H_q/\mathrm{d}H_K} M_s V \,\mathrm{d}V \tag{45}$$

Exept the SP/SD boundary, $\mathrm{d}H_q/\mathrm{d}H_K \ll 1$, and (45) reduces to:

$$M'(H_{sw}) \cong 1.91 M_s \int_0^\infty N(H_K,V) V \,\mathrm{d}V \tag{46}$$

The AF demagnetization curve of SIRM is shown in Figure 16a, the related coercivity distribution $M'(H_{sw})$ is given by the first derivative. In order to solve (45), $N(H_K,V)$ is assumed to be the sum of two distributions, which are expressed with log-normal functions of V, and gaussian functions of H_K. The parameters of the functions were varied until the best agreement with the volume distributions of *Worm and Jackson* [1999] and with $M'(H_{sw})$ was reached. The resulting magnetic granulometry is plotted in Figure 15b, together with the SD boundaries calculated in section 5. The mean values of volume and microcoercivity are $\bar{V} = 4.3 \times 10^{-24}$ and $\bar{H}_K = 190$ mT, in good agreement with *Worm and Jackson* [1999]. From Figure 15b, a typical coercivity of 40 mT can be deduced, and this value corresponds to the median destructive field of the AF demagnetization curve of Figure 16a. Notice that ARM properties were not used to estimate the magnetic granulometry.

In order to calculate the ARM properties for sample CS914, an artificial set of 50,000 particles was created according to the magnetic granulometry of Figure 15. With this set of particles, AF demagnetization curves of SIRM and ARM were calculated assuming a negligeable degree of magnetic interactions.

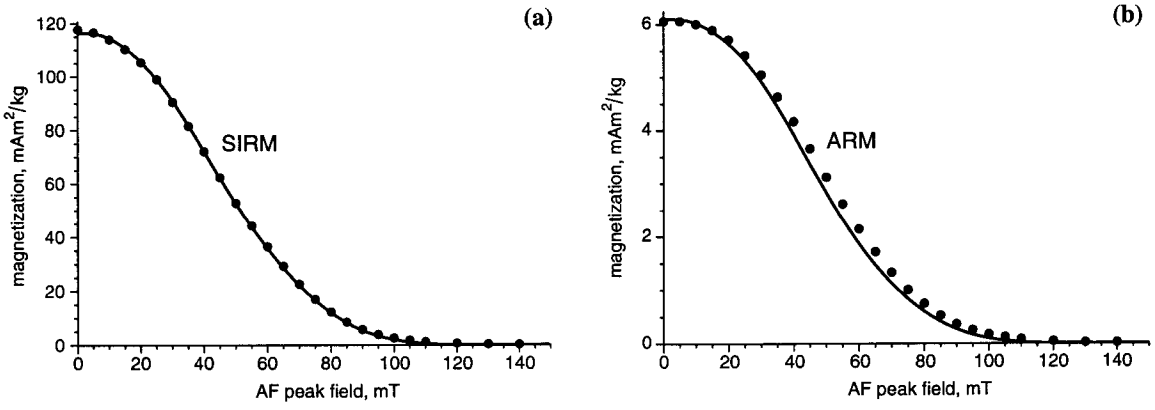

Figure 16: *Comparison between measured and modeled AF demagnetization curves of SIRM and of ARM, both for sample CS914. The modeled curves are calculated from the distribution of volumes and microcoercivities of Figure 15b. (a) AF demagnetization of room-temperature SIRM. Dots are measured points, the solid line is the model. (b) AF demagnetization curve of room-temperature ARM (*0.1 mT *DC field,* 300 mT *AF peak field). Dots are measured points, the solid line is the model. Both curves have similar shape and identical amplitude. This agreement is excellent, considering that the magnetic properties of the particles were deduced only from IRM measurements.*

The ARM curve was calculated using equation (32) with the atomic reorganization frequency estimated in 6.1. The calculated demagnetization curve of ARM is in excellent agreement with the measurements (Figure 16b), both in intensity and shape. The calculated ARM intensity differs only by 1% from the measured value. Differences between modeled and measured coercivity distributions of ARM are within 10% over all the coercivity range.

Furthermore, the dependence of the ARM on the DC-field predicted by equation (32) was also calculated with the magnetic granulometry assumed in Fig. 15b. Considering the small grain sizes, saturation of ARM is expected to occur at relatively high values of the DC field. An ARM with 80 mT AC peak field and different DC field values up to 4 mT was given to the sample. Since the ARM model discussed in section 3 assumes $H_{DC} \ll H_K$, the magnetization of the particles that do not satisfy this condition was removed with a 40 mT AF demagnetization. The results are shown in Figure 17. The initial part of the acquisition curve is controlled only by the susceptibility of ARM, and is in excellent agreement with the model of this paper. A disagreement is found in the range of saturation, above 1 mT. This may be due to interaction effects.

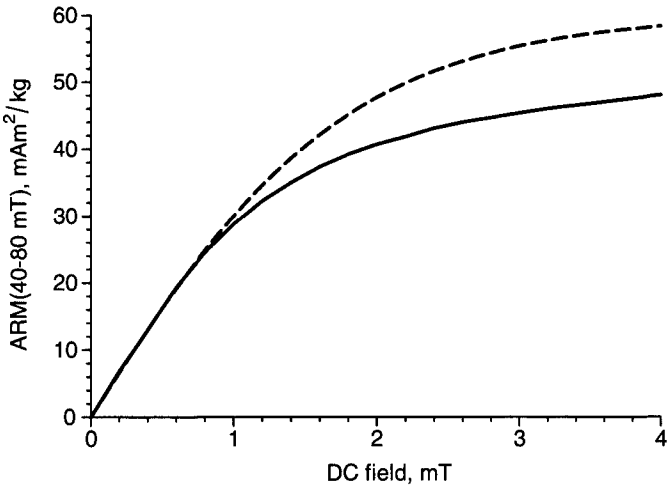

Figure 17: *ARM intensity of sample CS914 as a function of the DC field. The sample was given an ARM with* 80 mT *AF peak field, and subequently it was demagnetized with* 40 mT *AF peak field in order to measure the magnetization of all particles with coercivities between* 40 *and* 80 *mT. The ARM model of this paper assume the DC field to be much smaller than the coercivity of the particles. Since DC fields up to* 4 mT *are necessary to approach saturation, the* 40 mT *AF demagnetization will allow us to compare the measurements (solid line) with the modeled curve (dashed line). The ARM model is able to predict the value of the ARM susceptibility within an error of* 1%. *Disagreement between model and measurements in the saturation range, for DC fields* > 1 mT, *may be due to interaction effects.*

7. Interpretation of the modified Lowrie-Fuller test for SD particles

Experiments based on ARM and IRM acquisition and their demagnetization curves are commonly used as an indicator for the domain state of the particles. In the original Lowrie-Fuller test [*Lowrie and Fuller*, 1971] a comparison of normalized AF demagnetization curves of TRM and SIRM was used to distinguish between SD and MD grains. For multidomain carriers of remanence, saturation IRM is relatively more stable than weak-field TRM; for single domain carriers, the opposite is true. Soon after the test was proposed, *Schmidt* [1976] predicted that MD grains could pass the SD criterion and vice-versa. Later, the more easily produced ARM was substituted for TRM, and a modified Lowrie-Fuller test based on ARM characteristics was proposed [*Johnson et al.*, 1975]. *Newell* [2000] calculated that the Lowrie-Fuller test for SD particles can give opposite results, depending on such particle properties as volume and coercivity. A similar result for the ARM is shown in this section. Also, cases of MD particles which show SD-type behaviour are reported in the literature [*Hartstra*, 1982; *Bailey and Dunlop*, 1983; *Heider et al.*, 1992]. *Xu and Dunlop* [1995] modelled the result of the Lowrie-Fuller test for MD particles and came to the conclusion that the Lowrie-Fuller test is sensitive not only to the grain size of the particles: other factors like the density of dislocations in the crystals and the microcoercivity distribution are also important. They therefore replaced the confusing terms "SD-type" by "L-type" (low-field remanence is more stable), and "MD-type" by "H-type" (high-field remanence is more stable).

Results of the modified Lowrie-Fuller test for a set of identical, randomly oriented and non-interacting SD particles are shown in Figure 18.

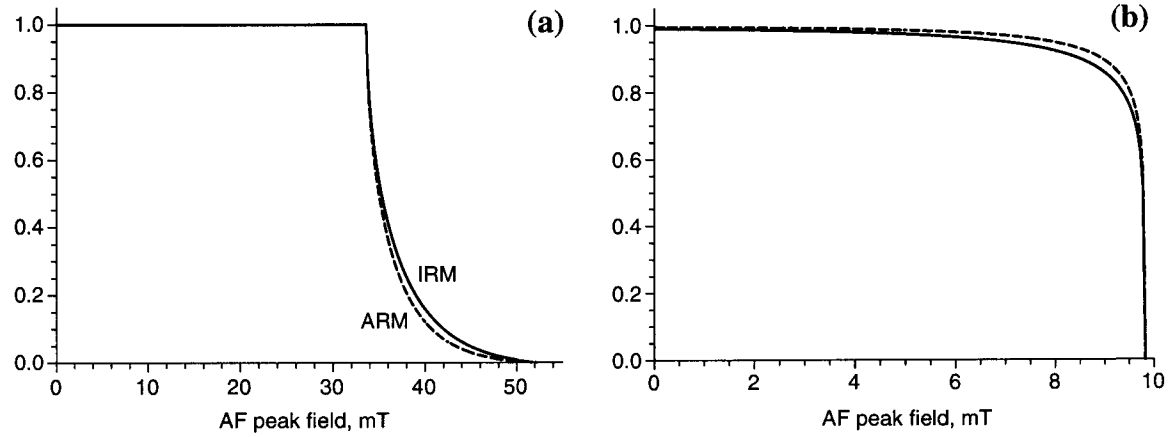

Figure 18: *Normalized AF demagnetization curves of ARM (dashed lines) and IRM (solid lines) for a set of identical, randomly oriented and non-interacting SD particles with* $\mu_0 H_K = 80$ mT. *Particles with a moment of (a)* 2×10^{-17} Am^2 *and (b)* 2.4×10^{-18} Am^2 *show opposite relative stabilities of ARM and IRM in the modified Lowrie-Fuller test, although both sets are SD particles.*

The shapes of the normalized demagnetization curves of ARM and IRM are practically identical. According to the classical interpretation of the Lowrie-Fuller test, the small differences in the shapes of the demagnetization curves are characteristic for SD particles only if their volume is very close to the SP boundary. Significant and systematic differences in the shape of the demagnetization curves cannot arise from a set of identical, non-interacting SD particles. The result of the modified Lowrie-Fuller test for SD particles is therefore not related to their intrinsic magnetic properties.

Significant differences in the shape of normalized AF demagnetization curves of ARM and IRM can be produced with a combination of different populations of SD particles. Results of the modified Lowrie-Fuller test obtained from synthetic sets of non-interacting SD particles with different volumes and microcoercivities are shown in Figure 19. In general, the result of the modified Lowrie-Fuller test depends on the statistical relation between the volume and the coercivity distribution of the particles. If the volume and the coercivity distribution are statistically uncorrelated, the normalized demagnetization curves of ARM and IRM do not differ systematically. In case of a positive correlation between the two distributions, the size of the particles increases as the coercivity increases. Since the ARM to IRM ratio depends mainly on the volume of the particles, large particles acquire a relatively strong ARM, and the related demagnetization curve is steeper at large coercivities and flatter at small coercivities, if compared to the demagnetization of IRM. Consequently, the normalized demagnetization curve of ARM lies above the demagnetization curve of IRM. In other words, the ARM is apparently more resistant against demagnetization than IRM, and the modified Lowrie-Fuller test is positive for SD particles.

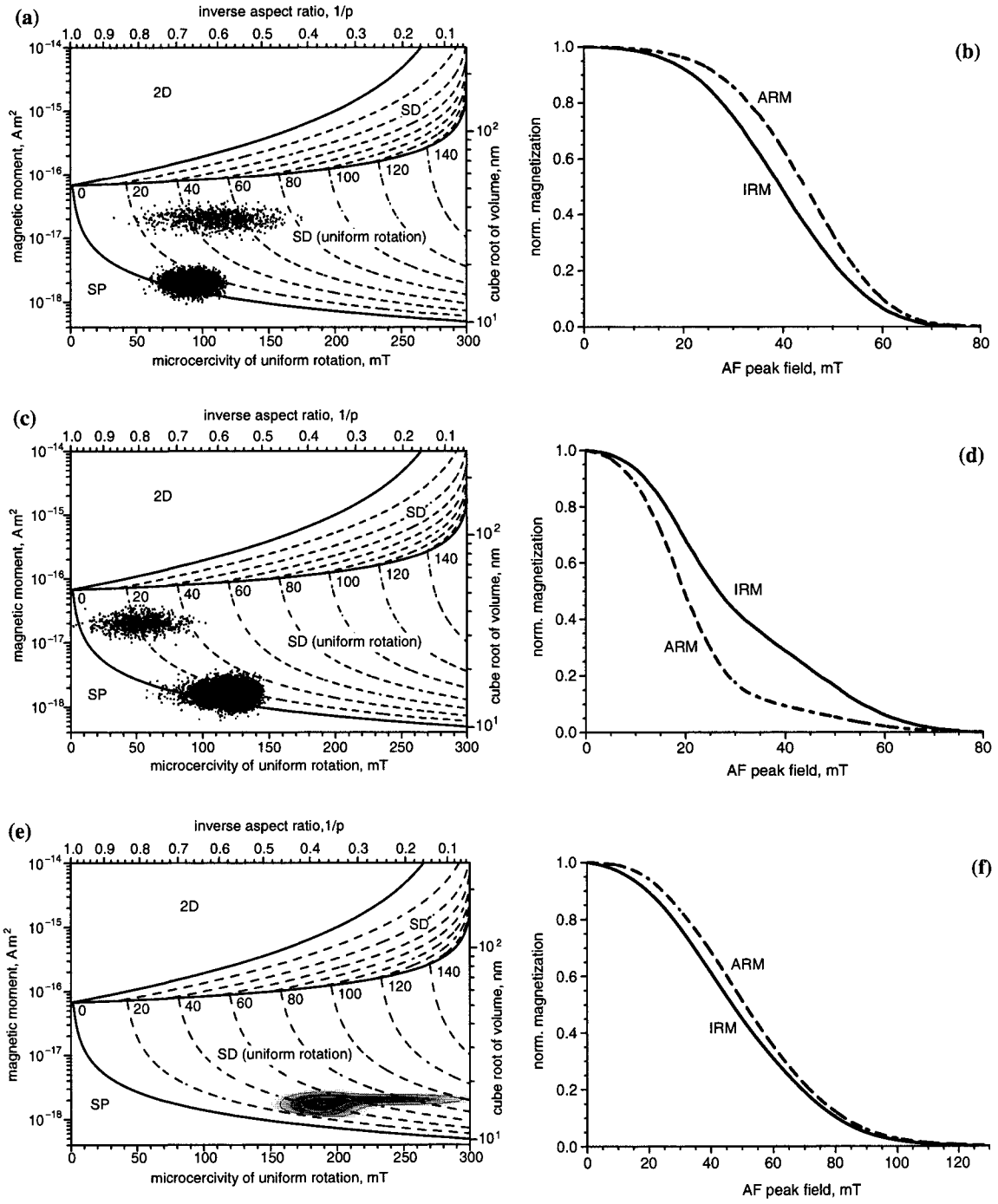

Figure 19: *Results of the modified Lowrie-Fuller test (right) for three sets of 12,000 non-interacting SD particles with different volumes and microcoercivities (left). Each point in the left plots indicates the volume and the microcoercivity of a single particle. The sum of the two particle populations in (a) gives a positive test for SD particles, plotted in (b). The opposite result is obtained in (d) with another combination of SD particles, plotted in (c). For comparison, the result of the modified Lowrie-Fuller test for sample CS914 is plotted in (f). The corresponding volume and microcoercivity distribution is plotted in (e).*

On the other hand, in the case of a negative correlation between the volume and the coercivity distribution, the opposite situation occurs, and the ARM is apparently less resistant against demagnetization than IRM. The result of the modified Lowrie-Fuller test would indicate the presence of multidomain particles. Mixed situations where the two demagnetizazion curves cross each other are also possible.

From the considerations above, it seems that the result of the modified Lowrie-Fuller test for SD particles can be either negative or positive, depending on their volume and coercivity distributions. On the other hand, many experimental observations [*Dunlop and West*, 1969; *Johnson et al.*, 1975] suggest that the result of the modified Lowrie-Fuller test is generally consistent with the domain state of the particles. This consistence can be explained if a positive correlation between the volume and the coercivity distribution is assumed to be a typical feature of SD particles. In Figure 20 it is shown how this correlation can be generated with no assumption about the intrinsic magnetic properties of the particles other than a mean value for the distribution of volumes and microcoercivities.

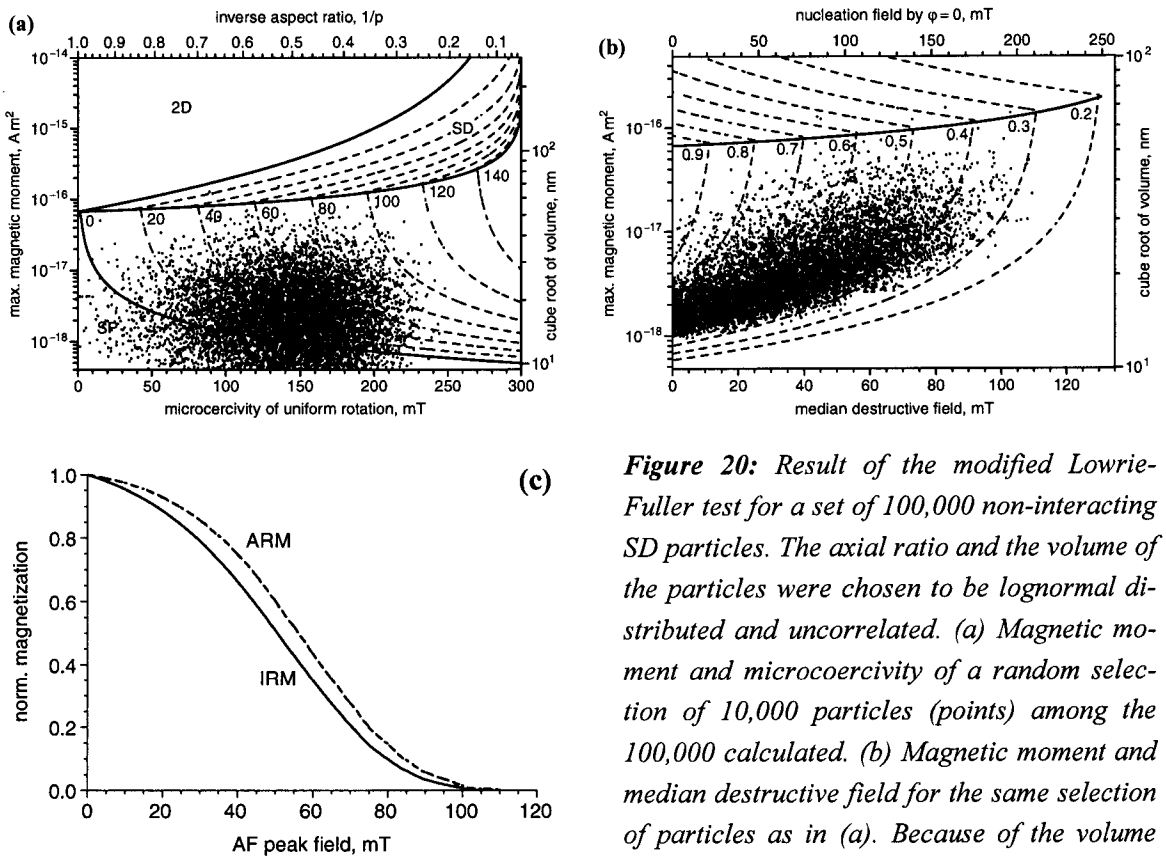

Figure 20: *Result of the modified Lowrie-Fuller test for a set of 100,000 non-interacting SD particles. The axial ratio and the volume of the particles were chosen to be lognormal distributed and uncorrelated. (a) Magnetic moment and microcoercivity of a random selection of 10,000 particles (points) among the 100,000 calculated. (b) Magnetic moment and median destructive field for the same selection of particles as in (a). Because of the volume dependence of the fluctuation field, the magnetic moment and the median destructive field are correlated. (c) Normalized AF demagnetization curves of ARM (dashed line) and IRM (solid line) calculated for the entire set of 100,000 particles.*

First, an artificial set of 100,000 particles was generated. The volume and the axial ratio of the particles were chosen to be lognormally distributed and uncorrelated. The resulting microcoercivity distribution is also not correlated to the volumes. Consider now two particles with identical shape (microcoercivity) and different volumes. The smaller particle has a larger fluctuation field and conesquently a smaller coercivity. In this way, volumes and coercivities of a random set of particles are positively correlated, and the modified Lowrie-Fuller test is positive for SD particles, as shown in Figure 20c. The shape difference between the normalized demagnetization curves of ARM and IRM increases with the amount of dispersion of the volume distribution: particles with similar volumes produce demagnetization curves of ARM and IRM with similar shape.

Magnetic interaction effects can also produce systematic differences between the normalized demagnetization curves of ARM and IRM. Interaction models based on the Preisach-Néel theory predict that the ARM acquisition of particles with a small coercivity is reduced by the interaction field produced by the particles with large coercivity [*Wolfarth*, 1964]. This process is equivalent to a volume reduction by an amount which increases as the coercivity decreases or, in other words, to a positive correlation between volumes and coercivities. Therefore, magnetic interactions apparently increase the relative resistance of ARM against demagnetization. The modified Lowrie-Fuller test is also affected by the fact that the size at which the coercivity of a SD grain is maximum differs from the maximum size a grain can be uniformly magnetized in zero field [*Newell and Merrill*, 1999].

To conclude, a relation between the result of the modified Lowrie-Fuller test and the domain state of the particles does not necessarily exist. Shape differences between the normalized demagnetization curves of ARM and IRM are related to the statistical distribution of the intrinsic magnetic properties of the particles and not to the properties themselves. Some volume and microcoercivity distributions of SD particles can produce H-type properties. On the other hand, a random distribution of well-dispersed volumes and microcoercivities in the SD range is always of L-type. Therefore, the modified Lowrie-Fuller test is effective in the identification of one population of SD particles, but can fail with special combinations of two or more populations of SD particles. Figure 21 summarizes various results of the modified Lowrie-Fuller test as a function of the grain size. The result of the test is represented by the parameter $MDF_{\mathrm{ARM}}/MDF_{\mathrm{IRM}}$, which is the ratio between the median destructive fields of ARM and SIRM. A general trend toward the classical interpretation of the test is evident: all SD samples are of L-type. On the other hand, the majority but not all MD samples are of H-type. The SD samples have highly scattered values of $MDF_{\mathrm{ARM}}/MDF_{\mathrm{IRM}}$, although they all contain a single population of particles. The theory of this paper predicts values slightly larger than 1 for those samples. The observed scattering is probably due to magnetic interaction effects: samples with virtually no interactions (CS914 in this paper, and *Moskowitz et al.*, [1988]) have MDF ratios between 1 and 1.1, whereas the others can reach MDF ratios up to 2.2.

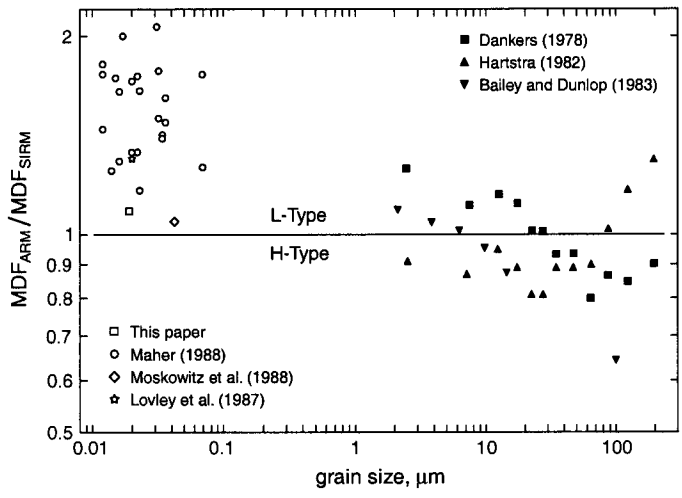

Figure 21: *Summary of experimental results of the modified Lowrie-Fuller test in synthetic and natural magnetite samples as a function of the grain size. On the vertical axis, the ratio between the median destructive fields of ARM and SIRM is shown. Values > 1 of this ratio denote a L-type behaviour (see text), wich is conisdered typical for SD particles. The opposite is true for a H-type behaviour. Not all MD particles are characterized a H-type behaviour.*

An increase of the MDF ratio due to interaction effects is predicted by the Preisach-Néel theory.

A conclusive statement about the result of the Lowrie-Fuller test for small SD particles is the following: (1) SD particles with a random distribution of volumes and microcercivities have an L-type behaviour, which is eventually enhanced by magnetic interactions and (2) samples that contain different populations of SD particles with a sufficiently high negative correlation between volumes and microcoercivities can show an H-type behaviour.

8. Conclusions

The ARM acquisition process in small non-interacting SD particles can be explained in terms of thermal activation processes. Equations (32) and (33) describe the dependence of ARM on the properties of the particles. The ARM intensity depends on the grain size ($\propto d^2$), the microcoercivity ($\propto H_K^{-1/3}$), the temperature ($\propto T^{-2/3}$) and weakly on the ramp rate α of the alternating magnetic field ($\propto \ln^{1/3}(10^4\alpha^{-1})$). These dependences are valid in a range where the grains switch their moment by coherent rotation. Other reversal modes occur in grains larger than 60 nm. Various ARM measurements performed by different authors confirm the d^2-dependence of the ARM for $d < 60$ nm. For larger grain sizes up to the upper limit for SD remanence, the thermal activation model discussed in this paper may still be valid, but microcoercivities and energy barriers have to be recalculated for the case of non-uniform moment switching. A decrease of the ARM intensity with grain size is expected over 60 nm.

The thermal activation model presented in this paper allowed also a new estimation of the fluctuation field, given in (41), and consequently also of the coercivity of SD grains. The model was tested with a natural sample of well-dispersed acicular magnetite grains. Precise ARM measurements confirmed the results predicted by equations (32) and (33) within an error of 1%. Measurements of the dependence of the ARM intensity on the AF field decay

rate allowed a precise estimation of the atomic reorganization time, in agreement with values given by *McNab* [1968].

This paper demonstrates that ARM of well-dispersed fine SD particles is controlled by intrinsic properties such as grain size and shape. Magnetic interactions are not necessary to explain the ARM acquisition process of SD grains. However, as shown by different authors, interactions can play a dominant role in samples with a high concentration of clustered grains, as likely occur in some natural rocks and in many artificial samples. The ARM/SIRM ratio can therefore be a useful parameter for the characterization and identification of populations of well-dispersed magnetic particles over the entire range of grain sizes.

It has also been shown that the modified Lowrie-Fuller test for small non-interacting SD particles does not depend on their intrinsic properties, and can give contradictory results. However, the calculated result of the modified Lowrie-Fuller test for a random distribution of volumes and microcoercivities is compatible with the results reported in *Johnson et al.* [1975].

Acknowledgements

We have benefited from useful discussions with Luca Lanci about the origin of ARM in SD particles. Horst-Ulrich Worm kindly provided us with sample CS914. We are grateful to Andrew Newell for an informal review of section 3, and to Ron Merrill and an anonymous reviewer for their constructive comments. ETH Research Project 0-20556-00.

References

Aharoni, A. and S. Shtrikman, Magnetization Curve of the Infinite Cylinder, *Phys. Rev.*, *109*(5), 1522-1528, 1958.

Bailey, M. E. and D. J. Dunlop, Alternating field characteristics of pseudo-single-domain (2-14 μm) and multidomain magnetite, *Earth Planet. Sci. Lett.*, *63*, 335-352, 1983.

Bailey, M. E. and D. J. Dunlop, On the use of anhysteretic remanent magnetization in paleointensity determination, *Phys. Earth Planet. Inter.*, *13*, 360-362, 1977.

Banerjee, S. K. and J. P. Mellema, A new method for the determination of paleointensity from the ARM properties of rocks, *Earth Planet. Sci. Lett.*, *23*, 177-184, 1974.

Brown, W. F., Relaxation behavior of fine particles, *J. Appl. Phys.*, *30*, 1305-1325, 1959.

Brown, W. F., Thermal fluctuation of a single-domain particle. *Phys. Rev.*, *130*(5), 1677-1686, 1963.

Butler, R. F. and S. K. Banerjee, Theoretical single-domain grain size range in magnetite and titanomagnetite, *J. Geophys. Res.*, *80*, 4049-4058, 1975.

Dankers, P. H. M., Magnetic properties of dispersed natural iron-oxides of known grain-size, Ph.D. thesis, Univ. of Utrecht, Netherlands, 1978.

Diaz Ricci, J. C. and J. L. Kirschvink, Magnetic domain state and coercivity predictions for biogenic greigite (Fe_3S_4): a comparison of theory with magnetosome observations, *J. Geophys. Res.*, *97*, 17309-17315, 1992.

Dunlop, D. J., Grain distributions in rocks containing single-domain grains, *J. Geomagn. Geoelectr.*, *17*, 459-471, 1965.

Dunlop, D. J. and G. West, An experimental evaluation of single-domain theories, *Rev. Geophys.*, *7*, 709-757, 1969.

Dunlop, D. J., Thermal fluctuation analysis: A new technique in rock magnetism, *J. Geophys. Res.*, *81*, 3511-3517, 1976.

Dunlop, D. J., The rock magnetism of fine particles, *Phys. Earth Planet. Inter.*, *26*, 1-26, 1981.

Dunlop, D. J., Coercive forces and coercivity spectra of submicron magnetites, *Earth Planet. Sci. Lett.*, *78*, 288-295, 1986.

Dunlop, D. J. and K. S. Argyle, Thermoremanence, anhysteretic remanence and susceptibility of submicron magnetites: Nonlinear field dependence and variation with grain size, *J. Geophys. Res.*, 102, 20199-20210, 1997.

Dunlop, D. J. and Özdemir, *Rock Magnetism*, Cambridge Univ. Press, Cambridge, 1997.

Eldridge, D. F., Quantitative Determination of the Interaction Fields in Aggregates of Single-Domain Particles, *J. Appl. Phys.*, *32*, 247S-249S, 1961.

Enkin, R. J. and W. Williams, Three-dimensional micromagnetic analysis of stability in fine magnetic grains, *J. Geophys. Res.*, *99*, 611-618, 1994.

Gillingham, E. W. and F. D. Stacey, Anhysteretic remanent magnetization (ARM) in magnetite grains, *Pure Appl. Geophys.*, *91*, 160-165, 1971.

Halgedahl, S. L. and M. Fuller, Magnetic domain observations of nucleation processes in fine particles of intermediate titanomagnetite, *Nature*, *288*, 70-72, 1980.

Halgedahl, S. L., Revisiting the Lowrie-Fuller test: alternating field demagnetization characteristics of single-domain through multidomain glass-ceramic magnetite, *Earth Planet. Sci. Lett.*, *160*, 257-271, 1998.

Hartstra, R. L., A comparative study of the ARM and I_{sr} of some natural magnetites of MD and PSD grain size, *Geophys. J. R. Astron. Soc.*, *71*, 497-518, 1982.

Heider, F., D. J. Dunlop and H. C. Soffel, Low-temperature and alternating field demagnetization of saturation remanence and thermoremanence in magnetite grains (0.037 μm to 5 mm), *J. Geophys. Res.*, *97*, 9371-9381, 1992.

Jaep, W. F., Anhysteretic magnetization of an assembly of single-domain particles, *J. Appl. Phys.*, *40*, 1297-1298, 1969.

Jaep, W. F., Role of interactions in magnetic tapes, *J. Appl. Phys.*, *42*, 2790–2794, 1971.

Johnson, H. P., W. Lowrie and D. Kent, Stability of anhysteretic remanent magnetization in fine and coarse magnetite and maghemite particles, *Geophys. J. R. astr. Soc. 41*, 1-10, 1975.

King, J. W., S. K. Banerjee, and J. Marvin, A new rock-magnetic approach to selecting sediments for geomagnetic paleointensity studies: application to paleointensity for the last 4000 years, *J. Geophys. Res.*, *88*, 5911-5921, 1983.

Kneller, E. and E. P. Wolfarth, Effect of Thermal Fluctuations on the Anhysteretic Process in Ferromagnetic Fine-Particle Assemblies, *J. Appl. Phys.*, *37*, 4816-4818, 1966.

Kneller, E., Magnetic-interaction effects in fine-particle assemblies and thin films, *J. Appl. Phys.*, *39*, 945-955, 1968.

Lovley, D. R. et al., Anaerobic production of magnetite by a dissimilatory iron-reducing microorganism, *Nature*, *330*, 252-254, 1987.

Lowrie, W. and M. Fuller, On the alternating field demagnetization characteristics of multidomain thermoremanent magnetization in magnetite, *J. Geophys. Res.*, *76*, 6339-6349, 1971.

Maher, B. A., Magnetic properties of some synthetic sub-micron magnetites, *Geophys. J.*, *94*, 83-96, 1988.

McNab, T. K., R. A. Fox, and J. F. Boyle, Some Magnetic Properties of Magnetite (Fe_3O_4) Microcrystals, *J. Appl. Phys.*, *39*, 5703-5711, 1968.

Moskowitz, B. M. et al., Magnetic properties of magnetotactic bacteria, *J. Magnet. Mag. Mat.*, *73*, 273-288, 1988.

Moskowitz, B. M., R. Frankel, and D. Bazylinski, Rock magnetic criteria for the detection of biogenic magnetite, *Earth Planet. Sci. Lett.*, *120*, 283-300, 1993.

Néel, L., Théorie du trainage magnétique des ferromagnétiques en grains fins avec applications aux terres cuites, Ann. Geophys., 5, 99-136, 1949.

Néel, L., Remarques sur la théorie des propriétés magnétiques des substances dures, *Appl. Sci. Res.*, *4*, 13-24, 1954.

Néel, L., Some theoretical aspects of rock magnetism, *Advances in Physics*, *4*, 191-243, 1955.

Newell, A. J. and R.T. Merrill, Single-domain critical sizes for coercivity and remanence, *J. Geophys. Res.*, *104*, 617-628, 1999.

Newell, A. J., The Lowrie-Fuller test: single-domain and micromagnetic theory, *Earth Planet. Sci. Lett.*, *183*, 335-346, 2000.

Özdemir, Ö. and S. K. Banerjee, A preliminary magnetic study of soil samples from west-central Minnesota, *Earth Planet. Sci. Lett.*, *59*, 393-403, 1982.

Schmidbauer, E. and N. Schembra, Magnetic hysteresis properties and anhysteretic remanent magnetization of spherical Fe_3O_4 particles in the grain size range 60-160 nm, *Phys. Earth Planet. Inter.*, *46*, 77-83, 1987.

Schmidt, V. A., The variation of the blocking temperature in models of thermoremanence (TRM), *Earth Planet. Sci. Lett.*, *29*, 146-154, 1976.

Stoner, E. C. and E. P. Wohlfarth, A mechanism of magnetic hysteresis in heterogeneous alloys, *Phil. Trans. R. Soc. London*, *240*, 599-602, 1948.

Sugiura, N., ARM, TRM, and magnetic interactions: concentration dependence, *Earth Planet. Sci. Lett.*, *42*, 451-455, 1979.

Victoria, R. H., Predicted time dependence of the switching field for magnetic materials, *Phys. Rev. Lett.*, *63*, 457-460, 1989.

Walton, D., A theory of anhysteretic remanent magnetization of single-domain grains, *J. Magnet. Mag. Mat.*, *87*, 369-374, 1990.

Wohlfarth, E. P., A Review of the Problem of Fine-Particle Interactions with Special Reference to Magnetic Recording, *J. Appl. Phys.*, *35*, 783-790, 1964.

Worm, H.-U. and M. Jackson, The superparamagnetism of Yucca Mountain Tuff, *J. Geophys. Res.*, *104*, 25415-25425, 1999.

Xu, S. and D. J. Dunlop, Toward a better understanding of the Lowrie-Fuller test, *J. Geophys. Res.*, *100*, 22533-22542, 1995.

Appendix

This appendix is the result of fruitful discussions with Andrew Newell. He undertook a careful revision of section 3, focussing on many mathematical derivations, which have been kept as short as possible for publishing reasons. In the following, the main assumptions and mathematical simplifications of the paper are discussed in detail.

Derivation of equation (22)

We assume that the equilibrium is frozen when $\Delta\bar{h}_0 = \gamma\Delta\bar{h}_{eq}$, with $\Delta\bar{h}_{eq} = 1/a$. This gives following equation:

$$\Delta\bar{h}_0 = \frac{\gamma f_{AC}\Delta\tilde{h}}{F}\Delta\bar{h}_0^{1/4-q}\frac{\exp\left[\alpha\Delta\bar{h}_0^{3/2}\right]}{\cosh\left[3\alpha\Delta\bar{h}_0^{1/2}h_{DC}/2\right]} \tag{A1}$$

The atomic reorganization time is only weakly dependent on q: for algebraic simplicity we choose $q = 3/4$. Then:

$$\Delta\bar{h}_0 = \frac{\gamma f_{AC}\Delta\tilde{h}}{F}\Delta\bar{h}_0^{-1/2}\frac{\exp\left[\alpha\Delta\bar{h}_0^{3/2}\right]}{\cosh\left[3\alpha\Delta\bar{h}_0^{1/2}h_{DC}/2\right]} \tag{A2}$$

For an ideal ARM acquisition process, $h_{DC} \to 0$ and $\cosh(3\alpha\Delta\bar{h}_0^{1/2}h_{DC}/2) = 1$. The solution of equation (A2) will be used later to show that $1 < \cosh(3\alpha\Delta\bar{h}_0^{1/2}h_{DC}/2) < 1.2$ in real ARM acquisition experiments. A maximal error of 20% is introduced in equation (A2) by setting $h_{DC} = 0$. This error can be accounted by the factor γ. Accordingly:

$$\Delta\bar{h}_0 = \frac{\gamma f_{AC}\Delta\tilde{h}}{F}\Delta\bar{h}_0^{-1/2}\exp\left[\alpha\Delta\bar{h}_0^{3/2}\right] \tag{A3}$$

The substitution of F gives:

$$\Delta\bar{h}_0^{3/2} = \frac{\gamma f_{AC}\Delta\tilde{h}}{F_0}\sqrt{3\pi h_{sw}\alpha}\exp\left[\alpha\Delta\bar{h}_0^{3/2}\right] \tag{A4}$$

The right term of equation (A4) depends strongly on $\Delta\bar{h}_0$, and an approximate solution is given by following recursive approach. As a first step:

$$\exp\left[\alpha\Delta\bar{h}_0^{3/2}\right] = \frac{F_0}{\gamma f_{AC}\Delta\tilde{h}\sqrt{3\pi h_{sw}\alpha}}\Delta\bar{h}_0^{3/2} \tag{A5}$$

and the logarithm of (A5) gives:

$$\Delta\bar{h}_0 = \alpha^{-2/3}\ln^{2/3}\left[\frac{F_0}{\gamma f_{AC}\Delta\tilde{h}\sqrt{3\pi h_{sw}\alpha}}\Delta\bar{h}_0^{3/2}\right] \tag{A6}$$

Then, $\Delta\bar{h}_0$ on the right side of (A6) is substituted with (A6):

$$\Delta\bar{h}_0 = \alpha^{-2/3}\ln^{2/3}\left[\frac{F_0}{\gamma f_{AC}\Delta\tilde{h}\sqrt{3\pi h_{sw}\alpha}}\alpha^{-1}\ln(\ldots)\right] \tag{A7}$$

With $F_0 = 10^9$ Hz, $\mu_0 f_{AC}\Delta\tilde{H} \approx 2$ mT/s, $\mu_0 H_K = 60$ mT, $10^{-18} < m < 10^{-16}$ Am^2 for SD magnetite, and $h_{sw} \approx 0.5$, one has $\ln(\ldots) \approx 16$ and:

$$\Delta\bar{h}_0 = \alpha^{-2/3}\ln^{2/3}\left[\frac{5.7F_0}{\gamma f_{AC}\Delta\tilde{h}\,h_{sw}^{1/2}\alpha^{3/2}}\right] \tag{A8}$$

If $\ln(\ldots)$ is neglected in (A7), the resulting $\Delta\bar{h}_0$ is affected by a relative error given by $2(\ln 16)/(3\times 16) \approx 0.1$. Thus, the error of (A8) is about 10%. It is now possible to verify the assumption $1 < \cosh(3\alpha\Delta\bar{h}_0^{1/2}h_{DC}/2) < 1.2$ used to simplify equation (A2). Using (A8):

$$\frac{3}{2}\alpha\Delta\bar{h}_0^{1/2}h_{DC} \approx \frac{3}{2}\alpha^{2/3}h_{DC}\ln^{1/3}\left[\frac{5.7F_0}{\gamma f_{AC}\Delta\tilde{h}\,h_{sw}^{1/2}\alpha^{3/2}}\right] \tag{A9}$$

The ARM theory of the paper assumes that the magnetic moment of a grain switches by coherent rotation, which is approximatively true for magnetite particles < 60 nm. Under these conditions, and at room temperature:

$$\alpha = \frac{\mu_0 m H_K}{k_B T} < 2.5\times 10^4\mu_0 H_K \tag{A10}$$

Inserting (A10) in (A9) gives:

$$\frac{3}{2}\alpha\Delta\bar{h}_0^{1/2}h_{DC} < \frac{3(2.5\times 10^4)^{2/3}}{2(\mu_0 H_K)^{1/3}}H_{DC}\ln^{1/3}\left[\frac{5.7F_0}{\gamma f_{AC}\Delta\tilde{h}\,h_{sw}^{1/2}(2.5\times 10^4\mu_0 H_K)^{3/2}}\right] \tag{A11}$$

A reasonable lower limit for the microcoercivity of SD magnetite is $\mu_0 H_K > 10$ mT. In real ARM experiments $\mu_0 H_{DC} < 0.1$ mT, and equation (A11) gives $3\alpha\Delta\bar{h}_0^{1/2}h_{DC}/2 < 0.6$. Since $\cosh 0.6 \cong 1.19$, the simplification of (A2) obtained by setting $\cosh(3\alpha\Delta\bar{h}_0^{1/2}h_{DC}/2) = 1$ is justified.

Validity of equation (22)

In the paper, equation (22) is obtained after the calculation of the mean switching frequencies $\overline{f}_{\pm}$. Andrew Newell used a different approach to obtain a difference equation instead of a differential equation. His approach is based on the fact that the switching frequency of a particle in an alternating field changes enormously during a cycle. He argued that the magnetic moment changes only during short time intervals when the magnetic field is maximal or minimal, since either f_+ or f_- is negligible at any time. Starting from the instantaneous equation for p:

$$\frac{\mathrm{d}p}{\mathrm{d}t} = (1-p)f_-(t) - p\,f_+(t) \tag{A12}$$

and defining $t_n = n/f_{\mathrm{AC}}$ as the time at the beginning of the n-th cycle, and $t_{n+1/2}$ as the time in the middle of the n-th cycle, he divided equation (A12) in two equations, for the positive and the negative half-cycle. For the positive half-cycle, $f_- \gg f_+$, and (A12) can be rewritten as:

$$\frac{\mathrm{d}\log(1-p)}{\mathrm{d}t} \approx -f_-(t) \tag{A13}$$

Integration over the time of the positive half-cycle gives:

$$1 - p_{n+1/2} = (1-p_n)\,C_n, \quad C_n = \exp\left(-\int_{t_n}^{t_{n+1/2}} f_-(t)\,\mathrm{d}t\right) \tag{A14}$$

where $p_n = p(t_n)$. Similarly, the kinetic equation over the negative half-cycle is:

$$p_{n+1} = p_{n+1/2}\,D_n, \quad D_n = \exp\left(-\int_{t_{n+1/2}}^{t_{n+1}} f_+(t)\,\mathrm{d}t\right) \tag{A15}$$

Combining the two half-cycles:

$$p_{n+1} = D_n\left[1-(1-p_n)C_n\right] \tag{A16}$$

In terms of the normalized moment $\mu_n = 2p_n - 1$,

$$\mu_{n+1} - \mu_n = 1 - 2D_n + C_nD_n + (1 - C_nD_n)\,\mu_n \tag{A17}$$

Using the definition of $\overline{f}_{\pm}$:

$$\begin{aligned} C_n &= \exp\left[-\overline{f}_-(t_n)/2f_{\mathrm{AC}}\right] \\ D_n &= \exp\left[-\overline{f}_+(t_{n+1/2})/2f_{\mathrm{AC}}\right] \end{aligned} \tag{A18}$$

and assuming $\overline{f}_{\pm} \ll 2f_{\mathrm{AC}}$ following difference equation is obtained:

$$\begin{aligned} \mu_{n+1} - \mu_n &= \frac{\overline{f}_+(t_{n+1/2}) - \overline{f}_-(t_n)}{2f_{\mathrm{AC}}}(\mu_n - \mu_\infty) \\ \mu_\infty &= \frac{\overline{f}_+(t_{n+1/2}) - \overline{f}_-(t_n)}{\overline{f}_+(t_{n+1/2}) + \overline{f}_-(t_n)} \end{aligned} \tag{A19}$$

It is possible to show that the approximations used to get equation (A19) are valid, and that this equation can be approximated by a differential equation, which is identical with equation (22) in the paper. For this purpose, some parameters will be estimated numerically using the results of the paper. If the equations of the paper are valid, the estimations are correct as well.

According to equation (19) of the paper, $\overline{f}_{\pm} = \overline{f}_{\pm}\left(\Delta\overline{h}(t)\right)$, with:

$$\Delta\overline{h}(t_{n+1/2}) = \Delta\overline{h}(t_n) + \Delta\tilde{h} \tag{A20}$$

The critical time during the ARM acquisition is the time when the magnetic moment of a particle is going to be frozen. In the paper, it has been shown that this happens when $\Delta\overline{h} \approx \Delta\overline{h}_0$, where $\Delta\overline{h}_0$ is given by equation (25) of the paper. The ARM theory of the paper assumes that the magnetic moment of a grain switches by coherent rotation, which is approximatively true for magnetite particles < 60 nm. Under these conditions an upper limit for α is given by (A10). After equation (25) of the paper and using (A10), $\Delta\overline{h}_0 > 0.01$. On the other hand, with $\Delta\tilde{H} < 10\ \mu\mathrm{T}/\text{half-cycle}$ and $\mu_0 H_{\mathrm{K}} > 10$ mT, one has $\Delta\tilde{h} < 10^{-3}$ and $\Delta\tilde{h}/\Delta\overline{h} < 0.1$. Using equation (19) of the paper with $h_{\mathrm{DC}} \to 0$:

$$\frac{\overline{f}_+(t_{n+1/2})}{\overline{f}_+(t_n)} = \left(1 + \frac{\Delta\tilde{h}}{\Delta\overline{h}}\right)^{q-1/4} \exp\left[-\alpha\Delta\overline{h}^{3/2}\left(\left(1 + \frac{\Delta\tilde{h}}{\Delta\overline{h}}\right)^{3/2} - 1\right)\right] \tag{A21}$$

Since during the blocking time $\Delta\tilde{h}/\Delta\overline{h} \ll 1$, equation (A21) can be simplified, and:

$$\frac{\overline{f}_+(t_{n+1/2})}{\overline{f}_+(t_n)} \approx \exp\left[-\frac{3}{2}\alpha\Delta\overline{h}^{1/2}\Delta\tilde{h}\right] \tag{A22}$$

During an ideal ARM acquisition experiment $\Delta\tilde{h} \to 0$ and the right side of (A22) is nearly 1. In the following, it will be shown that $\alpha\Delta\overline{h}^{1/2}\Delta\tilde{h} \ll 1$ in real ARM experiments. During the blocking time, $\Delta\overline{h} \approx \Delta\overline{h}_0$, and using equation (25) of the paper:

$$\alpha\Delta\overline{h}^{1/2}\Delta\tilde{h} \approx \alpha^{2/3}\Delta\tilde{h}\ln^{1/3}\left[\frac{5.7F_0}{\gamma f_{\mathrm{AC}}\Delta\tilde{h}\, h_{\mathrm{sw}}^{1/2}\alpha^{3/2}}\right] \tag{A23}$$

Substitution of (A10) in (A23) gives $\alpha\Delta\overline{h}^{1/2}\Delta\tilde{h} < 0.1$ for $\mu_0 H_K > 10$ mT. Thereafter, $\overline{f}_+(t_{n+1/2}) \approx \overline{f}_+(t_n)$ and equation (A19) becomes:

$$\mu_{n-1} - \mu_n = \frac{\overline{f}_+(t_n) - \overline{f}_-(t_n)}{2f_{AC}}(\mu_n - \mu_\infty) \tag{A24}$$

Another assumption to be verified is given by $\overline{f}_\pm / 2f_{AC} \ll 1$ when the magnetic moment of a grain is going to be frozen. An estimate of $\overline{f}_\pm$ during the blocking time can be obtained by replacing $\Delta\overline{h}$ with $\Delta\overline{h}_0$ in equation (20) of the paper, with $h_{DC} \to 0$ and $q = 3/4$:

$$\overline{f}_\pm = \frac{F_0}{\sqrt{3\pi h_{sw}\alpha}} \exp\left(-\alpha\Delta\overline{h}_0^{3/2}\right) \tag{A25}$$

Using the estimation of $\Delta\overline{h}_0$ given by equation (25) of the paper:

$$\overline{f}_\pm = \frac{F_0}{\sqrt{3\pi h_{sw}\alpha}} \alpha^{-1/3} \ln^{1/3}\left[\frac{5.7F_0}{\gamma f_{AC}\Delta\tilde{h}\, h_{sw}^{1/2}\alpha^{3/2}}\right] \frac{\gamma f_{AC}\Delta\tilde{h}\, h_{sw}^{1/2}\alpha^{3/2}}{5.7F_0} \tag{A26}$$

and after some algebraic simplifications:

$$\frac{\overline{f}_\pm}{2f_{AC}} = \frac{\gamma\,\alpha^{2/3}}{11.4\sqrt{3\pi}} \Delta\tilde{h} \ln^{1/3}\left[\frac{5.7F_0}{\gamma f_{AC}\Delta\tilde{h}\, h_{sw}^{1/2}\alpha^{3/2}}\right] \tag{A27}$$

For an ideal ARM acquisition process, $\Delta\tilde{h} \to 0$, and consequently, $\overline{f}_\pm / 2f_{AC} \ll 1$. In fact, $\overline{f}_\pm / 2f_{AC} \ll 1$ on real ARM acquisition processes as well, as it will be shown in the following. Using equation (3) and $\Delta\tilde{h} = \Delta\tilde{H}/H_K$:

$$\frac{\overline{f}_\pm}{2f_{AC}} < 24.4(\mu_0\Delta\tilde{H})(\mu_0 H_K)^{2/3} \ln^{1/3}\left[\frac{2\times10^{-6}F_0}{f_{AC}\Delta\tilde{h}\,(\mu_0 H_K)^{3/2}}\right] \tag{A28}$$

For SD magnetite $\mu_0 H_K < 0.3$ T and equation (A28) can be simplified to:

$$\frac{\overline{f}_\pm}{2f_{AC}} < 30(\mu_0\Delta\tilde{H}) \tag{A29}$$

Usually, $\mu_0\Delta\tilde{H} < 10$ μT in real ARM experiments, and finally:

$$\frac{\overline{f}_\pm}{2f_{AC}} < 0.0003 \tag{A30}$$

As a consequence of (A30), the approximation used to obtain equation (A19) is valid. Furthermore, with $f_{AC} = 1/T$, equation (A24) can be rewritten as:

$$\frac{\mu_{n-1}-\mu_n}{T}=\frac{\overline{f}_+(t_n)-\overline{f}_-(t_n)}{2}(\mu_n-\mu_\infty) \tag{A31}$$

with $\mu_{n+1}-\mu_n \ll 1$. Using the definition of derivative we obtain finally:

$$\frac{\mathrm{d}\mu}{\mathrm{d}t}=\frac{\overline{f}_+-\overline{f}_-}{2}(\mu-\mu_\infty) \tag{A32}$$

Equation (22) in the paper can be obtained easily from (A32) by replacing $\overline{f}_\pm$ with equation (20) of the paper.

Linearization of equation (22)

For $h_{\mathrm{DC}} \to 0$, the equilibrium magnetization is approximatively $\mu_\infty = 3\alpha\Delta\overline{h}^{1/2}h_{\mathrm{DC}}/2$, and equation (22) simplifies to:

$$\frac{\mathrm{d}\mu}{\mathrm{d}\Delta\overline{h}}=\frac{-F}{f_{\mathrm{AC}}\Delta\tilde{h}}\Delta\overline{h}^{q-1/4}\exp\left[-\frac{3}{2}\Delta\overline{h}^{3/2}\alpha\right]\left(\mu-\frac{3}{2}\Delta\overline{h}^{1/2}h_{\mathrm{DC}}\right) \tag{A33}$$

Equation (A33) can be rescaled with $\tau=\alpha^{1/3}\Delta\overline{h}^{1/2}$ and $y=\alpha^{-2/3}h_{\mathrm{DC}}^{-1}\mu$:

$$\frac{\mathrm{d}y}{\mathrm{d}\tau}=\frac{\mathrm{d}}{\mathrm{d}\tau}\left(\alpha^{-2/3}h_{\mathrm{DC}}^{-1}\mu\right)=\alpha^{-2/3}h_{\mathrm{DC}}^{-1}\frac{\mathrm{d}\mu}{\mathrm{d}\tau}=\alpha^{-2/3}h_{\mathrm{DC}}^{-1}\frac{\mathrm{d}\mu}{\mathrm{d}\Delta\overline{h}}\left(\frac{\mathrm{d}\tau}{\mathrm{d}\Delta\overline{h}}\right)^{-1} \tag{A34}$$

Substitution of $\tau=\alpha^{1/3}\Delta\overline{h}^{1/2}$ gives:

$$\frac{\mathrm{d}y}{\mathrm{d}\tau}=\alpha^{-2/3}h_{\mathrm{DC}}^{-1}\left(\frac{1}{2}\alpha^{1/3}\Delta\overline{h}^{-1/2}\right)^{-1}\frac{\mathrm{d}\mu}{\mathrm{d}\Delta\overline{h}}=2\alpha^{-1}h_{\mathrm{DC}}^{-1}\Delta\overline{h}^{1/2}\frac{\mathrm{d}\mu}{\mathrm{d}\Delta\overline{h}} \tag{A35}$$

and using (22):

$$\frac{\mathrm{d}y}{\mathrm{d}\tau}=\frac{-2F}{f_{\mathrm{AC}}\,\Delta\tilde{h}\,\alpha\,h_{\mathrm{DC}}}\Delta\overline{h}^{1/4-q}\exp(-\tau^3)\left(\alpha^{2/3}h_{\mathrm{DC}}\,y-\frac{3}{2}\tau\alpha^{2/3}h_{\mathrm{DC}}\right) \tag{A36}$$

After some algebraic simplifications:

$$\frac{\mathrm{d}y}{\mathrm{d}\tau}=\frac{-2F}{f_{\mathrm{AC}}\,\Delta\tilde{h}\,\alpha^{1/2+2q/3}}\tau^{2q+1/2}\exp(-\tau^3)\left(y-\frac{3}{2}\tau\right) \tag{A37}$$

Equation (A37) is equivalent to equation (28) with:

$$\kappa=\frac{-2F}{f_{\mathrm{AC}}\,\Delta\tilde{h}\,\alpha^{1/2+2q/3}}=\frac{2F_0}{\sqrt{3\pi h_{\mathrm{sw}}}\,f_{\mathrm{AC}}\,\Delta\tilde{h}\,\alpha^{1+2q/3}} \tag{A38}$$

Chapter 3

Analysis of the field dependence of remanent magnetization curves

This paper has been published in: *Journal of Geophysical Research*, vol. 108 (B2), 2003

Seite Leer /
Blank leaf

" *All models are wrong. Some are useful.* "

George E. P. Box

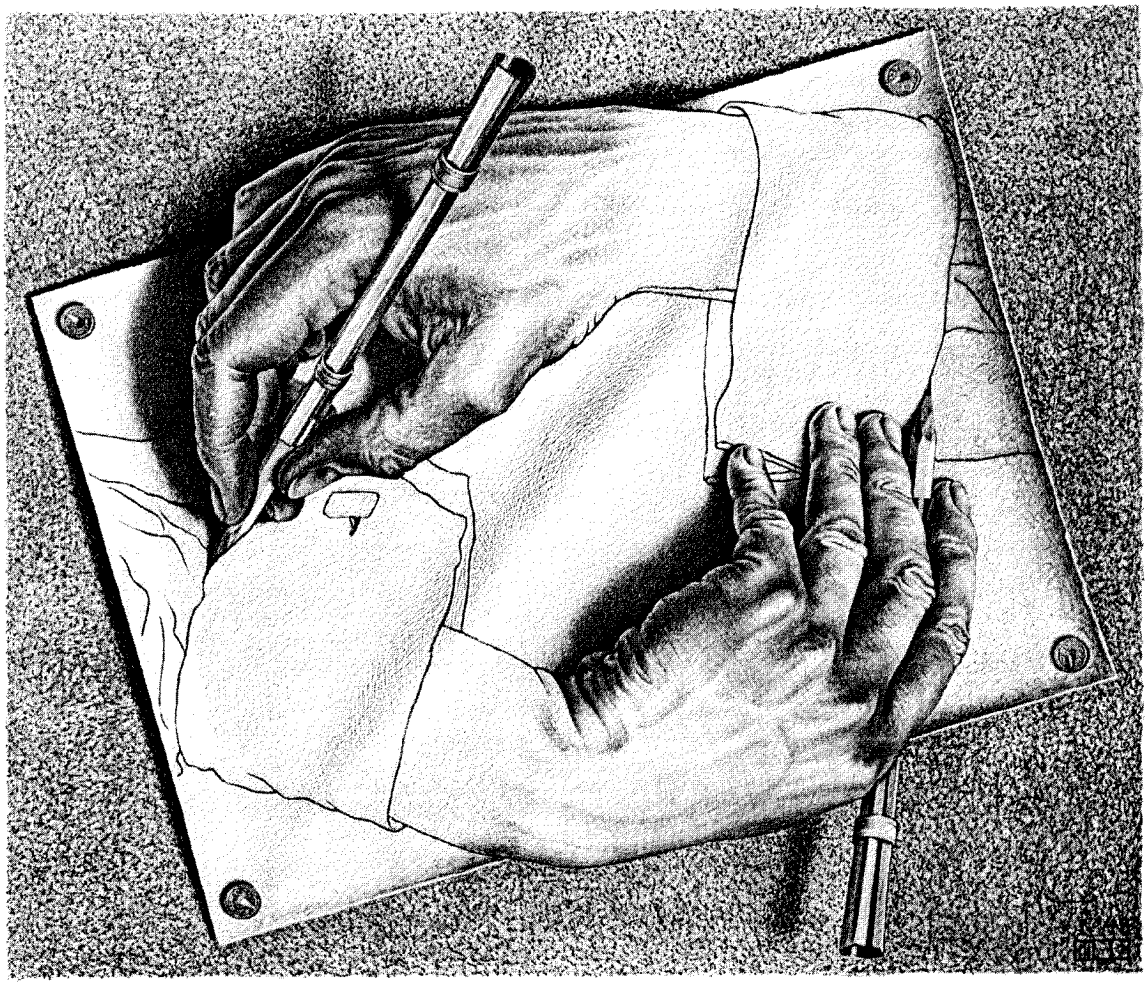

Maurits Cornelis Escher: *Drawing hands*, lithography (1961)


Seite Leer /
Blank leaf

Analysis of the field dependence of remanent magnetization curves

R. Egli
Institut für Geophysik, ETH Hönggerberg, Zürich, Switzerland.

Received 12 June 2002; revised 18 October 2002; accepted 30 October 2002; published 7 February 2003.

A new method to calculate and analyze coercivity distributions of measured acquisition/demagnetization curves of remanent magnetization is presented. The acquisition/demagnetization curves are linearized by rescaling both the field and the magnetization axes. An appropriate filtering of the linearized curves efficiently removes measurement errors prior to evaluating the coercivity distributions. The filtered coercivity distributions are modelled using a set of generalized probability density functions in order to estimate the contributions of different magnetic components. An error estimation is calculated for these functions with analytical and numerical methods, in order to evaluate whether the model is significantly different from the measured data. Three sediment samples from Baldeggersee (Switzerland) and three samples of urban atmosperich particulate matter have been analyzed using this method. It is found that the coercivity distributions of some of the magnetic components show significant and consistent deviations from a logarithmic Gaussian function. Large deviations are found also in the coercivity distributions of theoretical AF demagnetization curves of single-domain and multidomain particles. Constraints in the shape of model functions affect the identification and quantification of magnetic components from remanent magnetization curves, and should be avoided as far as possible. The generalized probability density function presented in this paper is suitable for appropriate modelling of Gaussian and a large number of non-Gaussian coercivity distributions.

INDEX TERMS: 1540 Geomagnetism and Paleomagnetism: Rock and mineral magnetism; 1519 Geomagnetism and Paleomagnetism: Magnetic mineralogy and petrology; 1512 Geomagnetism and Paleomagnetism: Environmental magnetism.

Citation: Egli, R., Analysis of the field dependence of remanent magnetization curves, *J. Geophys. Res.*, *108*(B2), 2081, doi: 10.1029/2002JB002023, 2003.

1. Introduction

Two of the main tasks of environmental magnetism are the identification and the quantification of different magnetic phases in a sample, a procedure usually referred to as the unmixing of magnetic components. Two approaches have been developed for this purpose: multiparameter records [*Thompson*, 1986; *Yu and Oldfield*, 1989; *Verosub and Roberts*, 1995; *Geiss and Banerjee*, 1997] and analysis of magnetization curves [*Thompson*, 1986; *Robertson and France*, 1994; *Carter-Stiglitz et al.*, 2001]. The multi-parameter approach is experimentally simple, and relies on the measurement of different bulk magnetic properties such as isothermal remanent magnetization (IRM), anhysteretic remenent magnetization (ARM), susceptibility and hysteresis parameters. Each parameter is a function of the concentration of the various magnetic components. The concentrations can be estimated if the measured parameters are known individually for each component (forward modelling). However, the relation between the physical and chemical properties of the magnetic grains (e.g. composition, grain size and grain shape) on the one hand, and their magnetic properties on the other, is complex and usually unknown. Many rock magnetic studies are based on synthetic samples, but the magnetic properties of such samples can differ substantially from their natural counterparts. On the other hand, natural magnetic components can rarely be measured alone, since natural samples often represent complex mixtures of more or less altered magnetic crystals with different origins and histories.

The second approach is based on detailed measurement of induced magnetizations (hysteresis loops) or remanent magnetizations (IRM, ARM and TRM) in variable magnetizing or demagnetizing fields. The absolute value of the first derivative of these curves is proportional to the contribution of all magnetic grains with a given intrinsic coercivity to the total magnetization of the sample, and is called the coercivity distribution. If magnetic interactions between the grains of different components are negligible, the magnetization of a sample is a simple linear combination of the contributions of each magnetic component (finite mixture model with linear additivity). The coercivity distribution of each magnetic component is given by a particular (unknown) function of the magnetizing or demagnetizing field (end-member distribution), and the measured coercivity distribution is a linear combination of these model functions. If all end-member distributions are compatible with a parameterized function, such model functions can be used to fit the measured data. If n is the number of components and k the number of parameters of the model function, there are nk parameters which can be adjusted to obtain a model curve that best reproduces the measurements. This operation, called component analysis, is performed with non-linear fitting algorithms [*Heslop et al.*, 2002]. The coefficient which multiplies each model function is a measure of the magnetic contribution of the corresponding component. This approach was first proposed by *Robertson and France* [1994] by assuming that the IRM acquisition curve of each magnetic component can be closely approximated by a cumulative logarithmic Gaussian function with three parameters (amplitude, median destructive field and dispersion parameter). They also proposed a physical

model to explain this assumption. A first application of component analysis with IRM acquisition curves was described by *Eyre* [1996] on Chinese loess samples. The intriguing advantage of this approach is that a detailed knowledge of the magnetic properties of the components is not necessary. The magnetic properties are described by the parameters of the model function used in the component analysis, and the value of these parameters is deduced from the shape of the measured magnetization curve. Furthermore, the same type of magnetization is measured under the same physical conditions for all components, allowing a direct comparison between all magnetic contributions. This approach, however, is limited by its extreme sensitivity to measurement errors and to the shape of the function chosen to model the end-member distributions. *Stockhausen* [1998] handled the effect of measurement noise by introducing goodness-of-fit parameters to indicate how well a measured curve is fitted by a set of model functions. *Kruiver et al.* [2002] proposed a statistical test to compare different models for the component analysis and to decide the number of end-member distributions that are necessary to fit the measured data sufficiently well. They also developed an alternative approach to component analysis, based on a rescaling of the IRM acquisition curve (called LAP: linear acquisition plots) so that a cumulative Gaussian function is transformed into a straight line (called SAP: standardized acquisition plot). The SAP of a mixture of slightly overlapped components with logarithmic Gaussian coercivity distributions is characterized by straight segments separated by inflections.

Another important aspect of component analysis is the modelling of end-member coercivity distributions. Prervious work has shown that natural and artificial end-member distributions can be approximated with logarithmic Gaussian functions [*Robertson and France*, 1994; *Stockhausen*, 1998; *Kruiver et al.*, 2001]. However, this is not necessarily true for all samples, since many factors, including magnetic interactions, affect the shape of magnetization curves. Theoretical AF demagnetization curves of non-interacting single domain particles [*Egli and Lowrie*, 2002] and of multidomain particles [*Xu and Dunlop*, 1995] cannot be modelled with logarithmic Gaussian functions. This also applies for experimental AF demagnetization curves of artificial samples of sized magnetite [*Bailey and Dunlop*, 1983; *Halgedahl*, 1998]. In all the cases mentioned above there is only one magnetic component, however, deviations from a logarithmic Gaussian function could be interpreted as the result of the sum of two components with strongly overlapping coercivities. The latter argument is of fundamental importance in the interpretation of component analysis, since it is directly related to the number of inferred components.

We propose here a new approach to the component analysis of acquisition and demagnetization curves. First, we handle the problem of evaluation and removal of measurement noise without the use of component analysis. In this way, filtered coercivity distributions and confidence margins can be calculated without any assumptions about the magnetic composition of the sample. We then handle the problem of component analysis by introducing the use of generalized probability distribution functions to model end-member coercivity distribu-

tions without any restrictive assumptions about their shape. We also obtain an error estimation for the distribution parameters used for the component analysis. The latter is of fundamental importance when end-member coercivity distributions of different samples are compared. Finally, this approach is tested on three lake sediment samples.

2. Calculation of coercivity distributions

2.1. General properties of coercivity distributions

Coercivity distributions are defined as the absolute value of the first derivative of progressive acquisition or demagnetization curves. We indicate the coercivity distribution with $f_X(H)$, where the index X indicates the original acquisition or demagnetization curve used to calculate f, and H is the magnetic field. Furthermore, $f_X(H)\,\mathrm{d}H$ is the contribution of all coercivities between H and $H + \mathrm{d}H$ to the magnetization indicated by X. Magnetic interactions and thermal activation effects produce differences between the different kinds of magnetizations (IRM and ARM) and the different kinds of demagnetizations (DC or AF), so that a rigorous physical interpretation of $f_X(H)$ is almost impossible. However, coercivity distributions can supply a lot of information about the carriers of magnetization and help in the discrimination between different magnetic components. We define here a magnetic component as a set of particles with identical mineralogy and similar physical properties (e.g. grain size and grain shape, morphology, crystallization degree, concentration of defects): examples are the bacterial magnetosomes [*Moskowitz et al.*, 1988], chemically grown fine magnetite in soils [*Maher and Taylor*, 1988], and detritial magnetite or hematite from a given host rock. The coercivity distribution of a component is characterized by a simple-shaped function (e.g. a lognormal distribution or a negative exponential distribution), whose shape is controlled by the statistical distribution of the magnetic properties of the particles. Often, coercivity distributions of different components cover the same range of coercivities (e.g. different magnetites) or the contribution of one of them is orders of magnitude weaker with respect to the others (e.g. hematite compared to magnetite). For this reason, the contributions of different components are difficult to recognize directly from the acquisition or demagnetization curves, but are evident in the coercivity distributions.

Coercivity distributions are mathematically described by probability distribution functions (PDF) and can be calculated on different field scales for better isolation of different components. The shape of a coercivity distribution changes according to the field scale adopted, because the integration over all coercivities corresponds to the total magnetization of the sample (normalization property). The scale change of a distribution f generates a new distribution f^* defined by the following transformation rule:

$$H^* = g(H)\,; \quad f^*(H^*) = f\big(g^{-1}(H^*)\big)\frac{\mathrm{d}}{\mathrm{d}H^*}g^{-1}(H^*) \tag{1}$$

where H^* is the new field scale, g the transformation rule between the old and the new scale, expressed by an injective function with inverse g^{-1}, and f^* the coercivity distribution with respect to the new scale. For example, the transformation rule from a linear to a logarithmic scale is expressed as follows:

$$H^* = \log H\,; \quad f^*(H^*) = \ln 10 \cdot 10^{H^*} f(10^{H^*}) \tag{2}$$

Another useful transformation is the following:

$$H^* = H^p\,; \quad f^*(H^*) = \frac{(H^*)^{1/p-1}}{p} f((H^*)^{1/p}) \tag{3}$$

where p is a positive exponent. We will refer to this transformation as the power transformation. The power transformation converges for $p \to 0$ to the logarithmic transformation. If $0 < p < 1$, high coercivities are quenched on the field scale, and distributions with large coercivities are enhanced. The same effect is obtained with a logarithmic scale, and the opposite effect with $p > 1$. The effect of the field scale transformation on the shape of a coercivity distribution is illustrated in Figure 1.

2.2. Calculation of coercivity distributions from a measured remanence curve

As pointed out in 2.1, a coercivity distribution is the absolute value of the first derivative of a stepwise acquisition or demagnetization curve. In terms of Fourier analysis, the first derivative is equivalent to a high pass filter, whose effect is to enhance small details of the original curve. For this reason any information contained in the original curve will be more evident in the resulting coercivity distribution. This applies also to the measurement errors, which are generally small in the measured curve, but are enhanced in the resulting derivative. The increase of small measurement errors is the main reason why coercivity distributions have not been used very often in the interpretation of magnetic measurements, despite the potential advantages. Possible sources of measurement errors are discussed in section 2.5. Depending on the curvature of the acquisition/demagnetization curve, a minimum number of steps is required to reproduce the coercivity distribution free from aliasing effects. The amplitude of measurement errors and the number of measured points strongly affect the calculated coercivity distributions, so that changes in the measuring procedure can produce apparently different results. Figure 2 shows the effects of measurement errors on two coercivity distributions of the same sample measured with different degrees of precision.

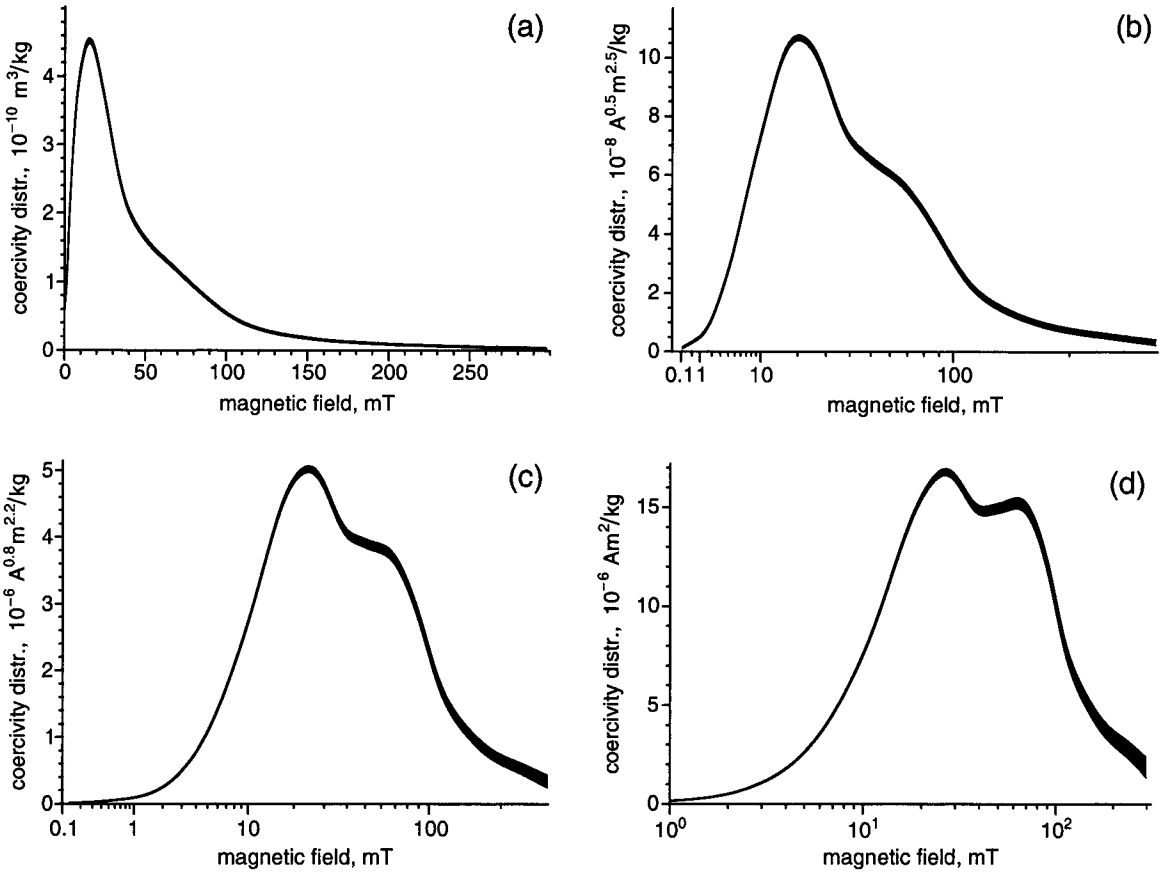

Figure 1: *Effect of field rescaling on the shape of a coercivity distribution (sediment sample G010 from Baldeggersee, Switzerland). Four different field scales were chosen: (a) linear field scale, (b) power field scale according to equation (3) with exponent* $p = 0.5$ *(c) power field scale according to equation (3) with exponent* $p = 0.2$*, (d) logarithmic field scale. Notice how the second peak of the coercivity distribution increases in amplitude when the field scale approaches a logarithmic scale. The thickness of the curve represents the estimated error of the coercivity distribution. The field scale transformation has an effect also on the absolute error of the coercivity distribution.*

Measurement errors are commonly removed by fitting the measured acquisition/demagnetization curve with an arbitrary number of given model curves (cumulative logarithmic Gaussian distributions). These model curves are identified with the magnetic signal of individual components. In this way, the calculation of a coercivity distribution rely on its interpretation in terms of component analysis. A way to calculate coercivity distributions without any further interpretation consists in filtering the measurements or the resulting coercivity distributions in order to remove the measurement noise. Often, the measured curves are asymmetric, and require a different degree of filtering at different fields. A standard low-pass filter would therefore be inefficient in some regions of the curve, while it would significantly affect the shape of the curve in others.

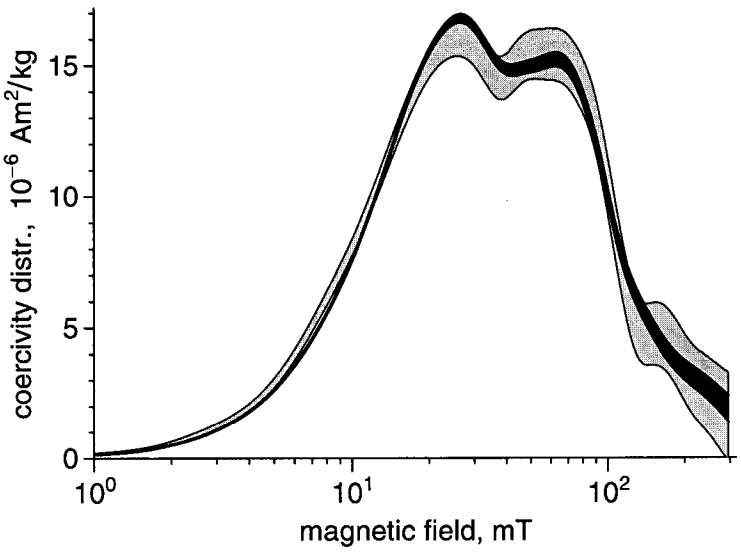

Figure 2: *Effect of the measurement precision on the shape and significance of the resulting coercivity distributions. The black line represents the coercivity distribution calculated from the average of 8 demagnetization curves of the same sample shown in Figure 1 (G010). The thickness of the line is the estimated error of the distribution. The gray band represents the coercivity distribution calculated from only one demagnetization curve of the same sample, its thickness is the corresponding error estimation. The two distributions are identical within the estimated error, indicating the significance of the error estimation. The presence of two peaks in the coercivity distribution is evident already from the result of a single measurement curve. However, a third peak at* 105 mT *is not significant and disappears when more precise measurements are done. This demonstrates the importance of an appropriate error estimation for the correct interpretation of coercivity distributions.*

In the following, we present a technique which permits the removal of the measurement noise homogeneously along the entire curve, and simultaneously estimates the error of the resulting coercivity distribution. The latter is particularly useful to avoid misinterpretations of numerical artefacts. The method presented here is based only on the following assumption: all acquisition/demagnetization curves have two regions where the corresponding coercivity distribution is zero on a logarithmic field scale, one at $H \rightarrow 0$ and the other at $H \rightarrow \infty$. In other words, any acquisition/demagnetization curve has two horizontal asymptotes on a logarithmic field scale. The physical meaning of this assumption for $H \rightarrow \infty$ is obvious: all magnetic minerals have a maximum finite coercivity. For $H \rightarrow 0$ the physical explanation is related to thermal activation processes in SD and PSD particles, and with domain wall motions in MD particles. Measurements with a sufficient number of points near $H = 0$ are necessary in order to obtain a correct coercivity distribution for small fields. Appropriate scaling of field and magnetization allows linearization of the acquisition/demagnetization curve. On the linearized curve each measurement point and the related error have the same relative importance, so that a simple low-pass filter can be applied to remove the measurement noise with the same effectiveness for all coercivities. An acquisition/demagnetization curve $M = M(H)$ can be linearized in a simple way by rescaling the field according to the transformation rule $H^* = M(H)$. However, because of the measurement errors, the function $M(H)$ is unknown. A good degree of linearization is reached when a model function $M_0(H)$

expressed by analytical functions is taken as tranformation rule instead of $M(H)$. The choice of the appropriate model function $M_0(H)$ becomes simpler if field and magnetization are both rescaled. If $M^* = \mu(M)$ and $H^* = g(H)$ are the rescaling functions for the field and the magnetization, respectively, then the model function is given by $M_0(H) = \mu^{-1}(g(H))$. The relation $M^*(H^*)$ between scaled field and scaled magnetization approaches a straight line when the model function $M_0(H)$ approaches the (unknown) noise-free magnetization curve. The curve defined by $\varepsilon(H^*) = M^*(H^*) - H^*$ represents the deviations of $M^*(H^*)$ from a perfect linear relation. We call $\varepsilon(H^*)$ the residual curve. If the model function $M_0(H)$ used for the scaling procedure is identical with the noise-free magnetization curve, then the residual curve contains only the measurement errors. In reality, since it is impossible to guess the noise-free magnetization curve, the residual curve is a superposition of the nonlinear component of $M^*(H^*)$ and the measurement errors. The fundamental advantage of considering the residual curve instead of the original curve is that the measurement errors are highly enhanced in the residual curve and can be homogeneously removed with a low-pass filter. The choice of the filter parameters is not critical, and has little effect on the shape of the resulting coercivity distribution. Under ideal conditions, $\varepsilon(H^*)$ represents the measurement errors, which can be simply removed by fixing $\varepsilon(H^*) = 0$.
The filtered residual curve can be transformed back into a magnetization curve as follows:

$$M(H) = \mu^{-1}\left[\mathscr{L}[\varepsilon(g^{-1}(H))] + g^{-1}(H)\right] \tag{4}$$

where $\mathscr{L}(.)$ is the low-pass filter operator. $M(H)$ is now supposedly free of measurement errors.

2.3. CODICA: a computer program for coercivity spectra calculation

CODICA (COercivity DIstribution CAlculator) is a computer program based on the scaling method described in paragraph 2.2. It calculates a coercivity distribution from an acquisition/demagnetization curve and gives an estimation of the maximal error of the calculated distribution. The latter is important for evaluating the significance of component analysis on the resulting coercivity distribution. CODICA is available from the author on request.

CODICA runs on a *Mathematica* interface and uses several built-in mathematical routines. The functions of the program are discussed step by step in Appendix B. The results of the main processing steps of a real measurement are shown in Figure 3. The original demagnetization curve is shown in Figure 3a, and is characterized by a typical heavy-tailed behaviour at high fields. A first scale transformation is applied to the field axis in order to approach a symmetric sigmoidal function (Figure 3b). The second scale transformation is applied to the magnetization axis in order to linearize the demagnetization curve (Figure 3c). Deviations of the linearized demagnetization curve from a best-fit line are plotted in the next step (Figure 3d): the resulting curve corresponds to the residual curve discussed in section 2.2.

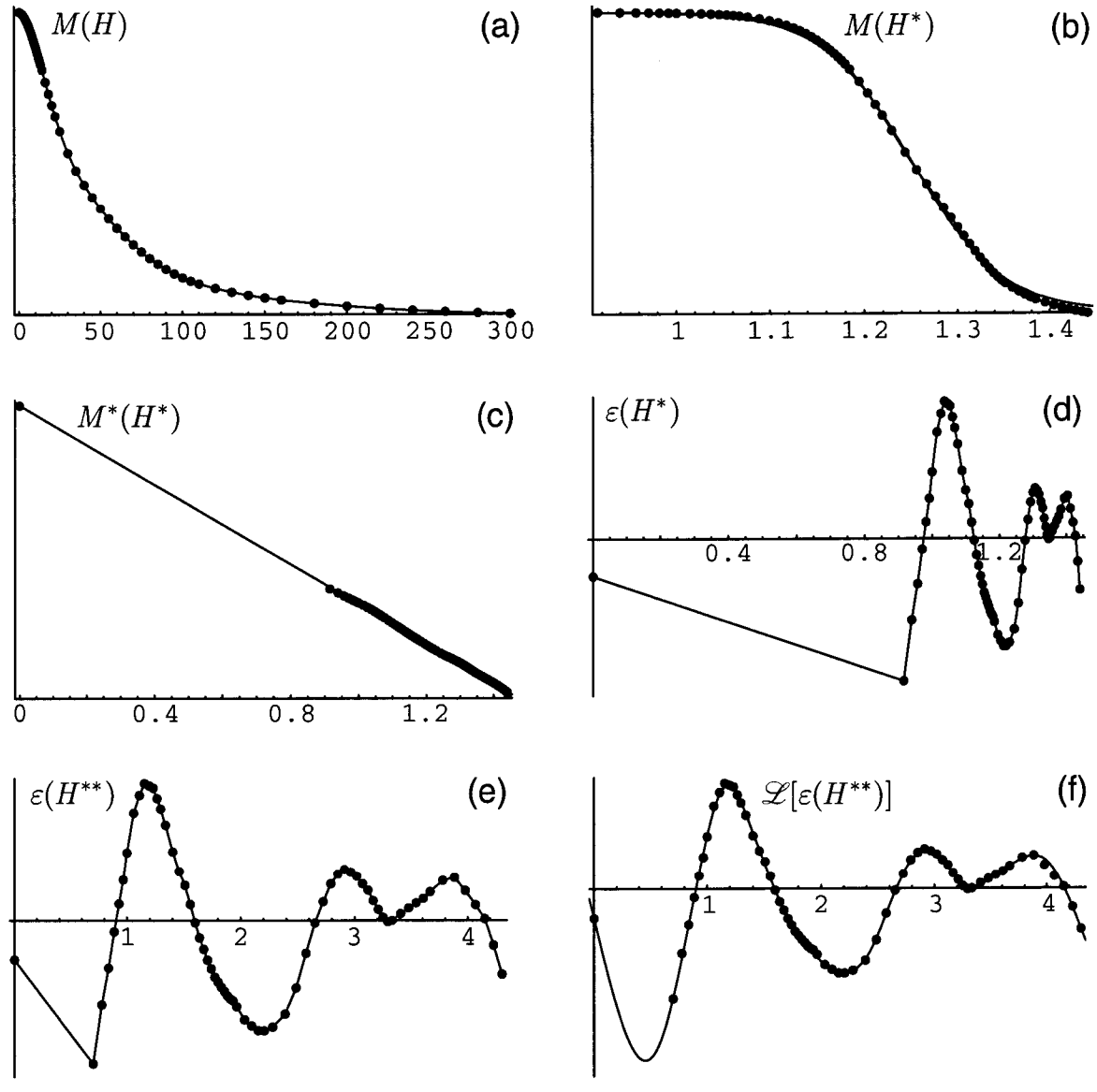

Figure 3: *Calculation of a coercivity distribution using CODICA. Each plot is the original output of a program step, as discussed in the text. (a) Original data for the AF demagnetization of an ARM (sample G010, as in Figure 1,2). (b) Demagnetization curve with rescaled field compared with a best-fitting tanh function (solid line). The scaling exponent was* $p = 0.064$. *(c) Demagnetization curve with rescaled magnetization and best-fitting line. (d) Residual curve. (e) The residual curve in (d) was rescaled in order to approach a sinusoidal curve. (f) A low pass filter was applied to the residual curve in order to remove the measurement errors. A back-transformation of the filtered residuals through the steps shown in (d), (c) and (b) and subsequent numerical derivation gives the coercivity distribution plotted in Figure 1.*

Further rescaling of the field axis allows to obtain a residual curve which is almost sinusoidal (Figure 3e). Its Fourier spectrum is concentrated in a narrow band around a dominant wavelength, so that a simple low-pass filter easily removes the high-frequency measurement noise with little effect on the final shape of the filtered demagnetization curve. Finally, the filtered residuals (Figure 3f) are converted back to the original demagnetization curve by reversing

the previous rescaling steps. The result is a demagnetization curve, which is supposed to be free from measurement errors. A coercivity distribution is obtained from the first derivative of the filtered demagnetization curve (Figure 1). The error estimation is displayed as an error band on the plot (Figure 1), and in a separated plot as a relative error.

2.4. Testing CODICA

CODICA has been tested using a synthetic coercivity distribution given by: $f(\log H) = N(\log H, 24, 0.36) + 0.04N(\log H, 56, 0.12) + 0.01w(\log H)$, where $N(x, \mu, \sigma)$ is a Gaussian function with median μ in mT and dispersion parameter σ, and $w(x)$ is a Gaussian white noise with variance 1 (Figure 4). This coercivity distribution is the sum of two components with overlapping coercivities and different concentrations, which are similar to those encountered in the natural samples presented later in this paper. The efficiency of CODICA in removing the measurement errors is compared with a common low-pass filter. Different cutoff-frequencies were chosen, and the mean square difference between the filtered and the noise-free distributions was calculated. The results are given in Figure 5a. Because the distorting effects introduced by a low-pass filter are mostly avoided after rescaling the magnetization curve, better results are obtained with CODICA. The distorting effects introduced by the application of low-pass filters were further tested by comparing the component analysis of the noise-free and the filtered coercivity distributions. Changes in the shape of the coercivity distribution are related to changes in the fitting parameters. The difference between the original parameters of the synthetic coercivity distribution and the best-fit parameters of the filtered distributions are plotted in Figure 5b. Optimum removal of the measurement noise can be obtained without significant changes of the fitting parameters. Consequently, the results of a component analysis are not affected by the filtering procedure of CODICA.

2.5. Measurement errors

Measurement errors are the main limiting factor in the interpretation of finite mixture models. Some knowledge about the measurement errors is useful to evaluate the significance of a component analysis and to optimize the measurement procedure. Measurement errors may arise from: 1) errors in the magnetization measurement, 2) errors in the application of the magnetization/demagnetization field, 3) errors induced by viscosity effects if the time interval between the application of the field and the measurement is not the same for all steps, 4) errors induced by mechanical unblocking of magnetic particles under application of high magnetic fields on unconsolidated samples. These error sources generate different noise signals which affect the measurement. Simple error propagation equations can be used to estimate the amplitude of the errors; some results are listed in Appendix A.

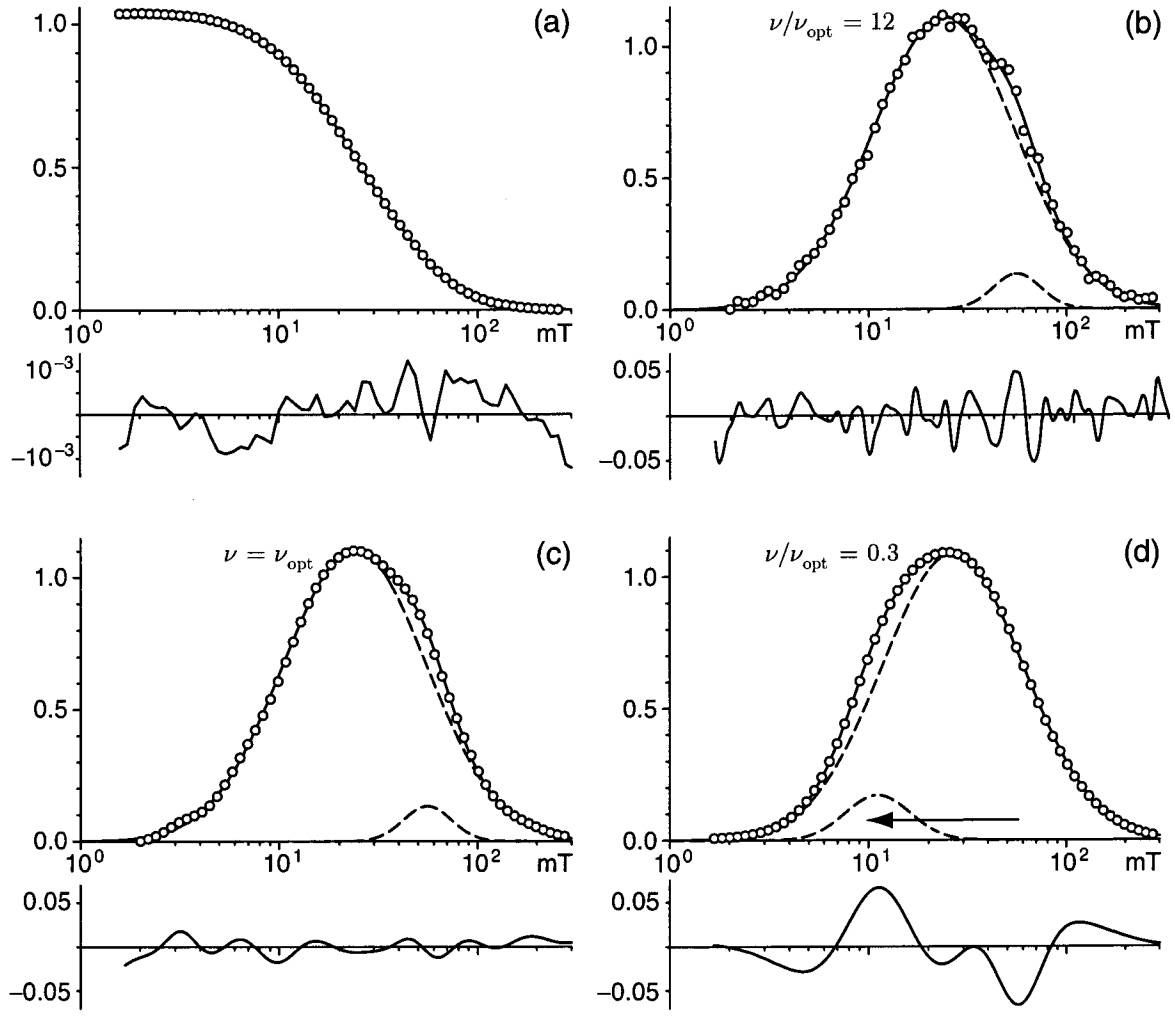

Figure 4: *A synthetic example of measurement noise removal with the procedure described in the text. A synthetic coercivity distribution was generated according to the text. The coercivity distribution is the sum of two components with overlapping coercivities and different concentrations. The demagnetization curve in (a) was calculated by numerical integration of* $f(\log H)$. *This curve was then rescaled according to the procedure described in the text, and subsequently low-pass filtered with different cutoff frequencies. The corresponding coercivity distributions (open circles) in (b), (c) and (d) are the numerical differentiation of the filtered curves. A component analysis has been performed on these coercivity distributions; the single components are dashed. At the bottom of each plot, the difference between the original noise-free coercivity distribution and the coercivity distribution calculated from the filtered curves is presented as well. In (b) the cutoff frequency* ν *was too large, and the measurement errors have not been removed. In (d) the cutoff frequency was too small: the measurement errors have been removed completely, but the shape of the coercivity distrbution is altered (arrow). In (c) the cutoff frequency* ν_{opt} *was sufficient to remove the measurement errors without a significant alteration of the coercivity distribution. The difference between noise-free and calculated coercivity distribution is minimal, and the result of component analysis is unaffected.*

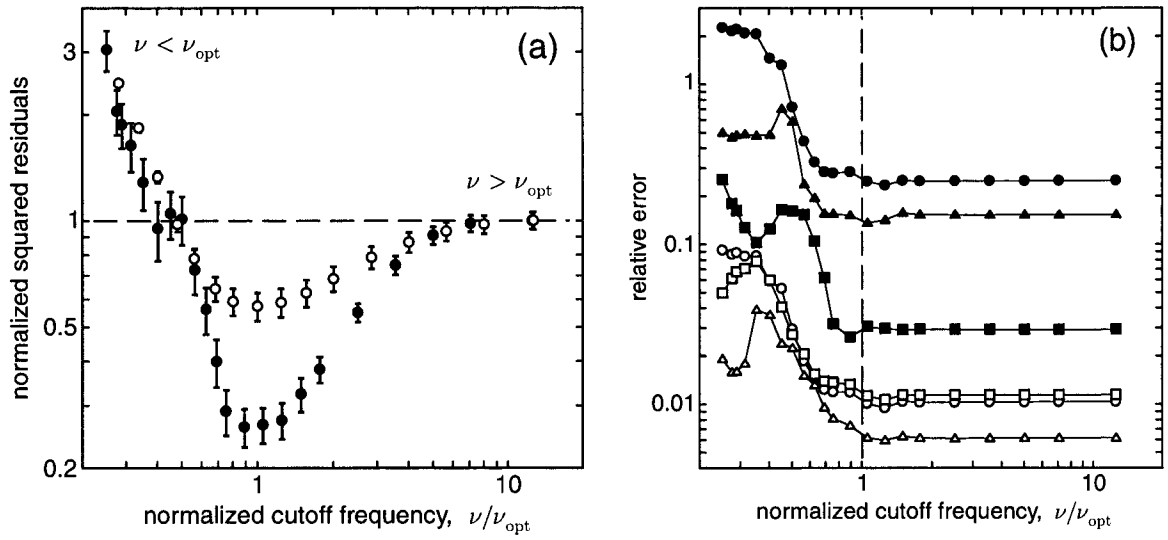

Figure 5: *Comparison between measurement noise removal with and without the rescaling procedure described in the text. The same coercivity distribution of Figure 4 was calculated and the operation was repeated 1000 times with different simulations of the measurement error* $w(\log H)$. *Each of the 1000 distributions was filtered in the same way as in Figure 4. In (a), the mean squared difference between the filtered and the noise-free distributions has been plotted as a function of the normalized cutoff frequency* ν *of the low-pass filter. Filled symbols refer to the output of CODICA, open symbols to the results obtained by filtering the data without the rescaling procedure of CODICA. The normalizing factor for the cutoff frequency is chosen to be identical with the value of the cutoff frequency which minimizes the squared residuals. The noise removal is more efficient after the rescaling procedure. In (b) the relative error of the best-fit parameters* m, μ *and* σ *of the two Gaussian distributions are plotted as a function of the normalized cutoff frequency of the low-pass filter. For* $\nu < 0.7\,\nu_{opt}$ *a low-pass filter induces significant distortions in the shape of the coercivity distribution. Open symbols refer to the best-fit parameters of the component defined by* $m = 0.04$, $\mu = 56$ mT, $\sigma = 0.12$, *solid symbols to the other component. Circles refer to* m, *squares to* μ *and triangles to* σ.

The effect of the four measurement error sources on the calculation of a coercivity distribution is simulated graphically in Figure 6. Mechanical unblocking effects can account for large errors at high fields, which are occasionally observed in some unconsolidated samples obtained by pressing a powder in plastic boxes. Magnetic grains that are electrostatically attached to larger clay particles are good candidates for such undesired effects. Mixing the sample powder with nonmagnetic wax before pressing it has been found to be a good solution to reduce measurement problems at high fields (S. Spassov, personal communication).

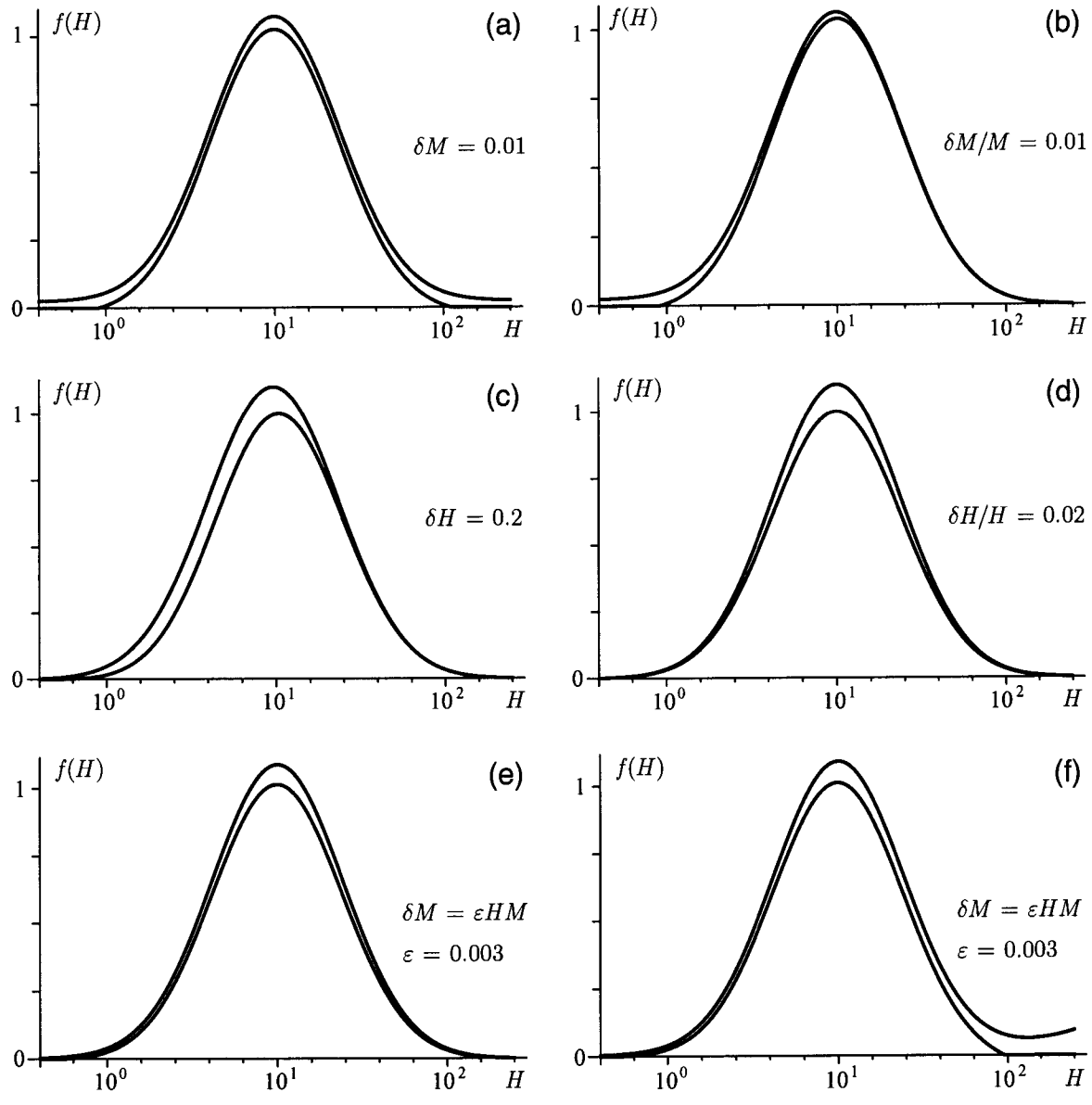

Figure 6: *Simulated effect of some measurement error sources on the calculation of a coercivity distribution with following parameters:* $m = 1$, $\mu = 10$ mT *and* $\sigma = 0.38$, *according to the calculations of Appendix A. The two curves of each plot give the upper and lower limit of a coercivity distribution calculated from a demagnetization curve measured at fixed field intervals of* 0.2 *on a logarithmic field scale (*$\Delta H/H \approx 0.585$*). Mesurements are performed with (a) an absolute measurement error* $\delta M = 0.01$, *(b) a relative measurement error* $\delta M/M = 0.01$, *(c) an absolute error of* 0.2 mT *affecting the applied peak field, (d) a relative error of* 2% *affecting the applied peak field. In (e) and (f), measurement errors arise from mechanical unblocking of a part* $\varepsilon = 0.3\%$ *of all magnetic particles in an unconsolidated sample. In (f), a magnetically harder component (e. g. hematite) with an unremoveable magnetization of* 5% *is added to the soft component.*

3. Component analysis with coercivity distributions

In section 2 we have shown how measurement noise in acquisition/demagentization curves can be filtered so that errors affecting the calculation of coercivity distributions are minimized. Now we turn to the problem of component analysis.

3.1. The finite mixture model

Consider a sample which contains a mixture of n different magnetic components (finite mixture model). Each component has a probability distribution $f_i(H \mid \boldsymbol{\theta}_i)$ for the intrinsic coercivity, which depends on a set of distribution parameters $\boldsymbol{\theta}_i = (\theta_{i1},\ldots,\theta_{il})$. If the magnetization of each component adds linearly to the others (linear additivity), the bulk coercivity distribution of the sample is given by:

$$f(H) = \sum_{i=1}^{n} c_i M_{ri} f_i(H \mid \boldsymbol{\theta}_i) \tag{5}$$

where c_i and M_{ri} are the concentration and the saturated magnetization of the i-th component, respectively. The bulk magnetization is given by the sum of the magnetizations of each component. Generally, $f_i(H \mid \boldsymbol{\theta}_i)$ is modelled with a logarithmic Gaussian function [*Robertson and France*, 1994].

In case of interactions, linear additivity no longer holds. The shape of $f(H)$ depends on the magnetization process, and may differ for acquisition and demagnetization curves [*Cisowski*, 1981]. Linear additivity is destroyed by interaction effects which may easily occur in synthetic mixtures [*Lees*, 1997]. *Carter-Stiglitz et al.* [2001] avoided this problem in their synthetic samples by dispersing potentially interacting pure components in a diamagnetic matrix before mixing them. Their dispersed pure samples were taken as end-member components for their unmixing tests. A particular case is given in samples where each magnetic component is formed by clusters of similar particles. Consequently, strong interactions exist within but not between the clusters, provided the volume concentration of the clusters is low enough. In this case, equation (5) can be rewritten to:

$$f_{\mathrm{int}}(H) = \sum_{i=1}^{n} c_i M_{ri}(C_i) f_i^*(H \mid \boldsymbol{\theta}_i, C_i) \tag{6}$$

where C_i is the volume concentration of the grains of the i-th component within the clusters. Linear additivity is preserved in this case. Equation (6) may apply for the synthetic samples of *Carter-Stiglitz et al.* [2001] and in natural samples.

3.2. Generalized coercivity distributions

Except for artificial samples, the end-member coercivity distributions of a mineral mixture are unknown, and model functions $f(x \mid \theta)$ with a set θ of parameters are used instead. A log-normal function is commonly assumed for $f(x \mid \theta)$. In this case $\theta = (H_{1/2}, DP)$, where $H_{1/2}$ is the median destructive field and DP the dispersion parameter [*Robertson and France*, 1994; *Kruvier et al.*, 2001; *Heslop et al.*, 2002]. On a logarithmic field scale, the log-normal function coincide with the Gauss distribution. Accordingly, an end-member distribution is forced to be symmetrical about $\log H_{1/2}$ and to have a fixed "curvature". Skewed, more "squared" or less "squared" distributions cannot be represented in this way. Deviations of $f(x \mid \theta)$ from a logarithmic Gaussian function are possible, since the relation between chemical and geometric properties of the grains on the one hand, and magnetic properties on the other, are rather complex and non-linear. In this paper we will demonstrate the existence of consistent and systematic deviations from the logarithmic Gaussian distribution model in some natural and artificial samples. These deviations can significantly affect the results of unmixing models.

As shown in 3.1, an end-member coercivity distribution is conveniently described by a probability distribution function (PDF) called $f(x)$ in the following. The shape of $f(x)$ is controlled by a set of distribution centers μ_n with related dispersion parameters σ_n, with $n \in \mathbb{N}$ [*Tarantola*, 1987]. Special cases are given when $n = 1$ (μ_1 is the median, σ_1 the mean deviation), $n = 2$ (μ_2 is the mean, σ_2 the standard deviation), and $n \to \infty$ (μ_∞ is the mid-range and σ_∞ the half-range). The parameters $H_{1/2}$ and DP used by *Robertson and France* [1993] correspond to μ_2 and σ_2 on a logarithmic field scale. The symmetry of a PDF is described by the coefficient of skewness s, where $s = \sigma_3^3/\sigma_2^3$ [*Evans et al.*, 2000]. Symmetric distributions are characterized by $s = 0$ and $\mu_n = \mu_2$. The curvature of a PDF is described by the coefficient of excess kurtosis k, where $k = \sigma_4^4/\sigma_2^4 - 3$ [*Evans et al.*, 2000]. The Gaussian PDF is characterized by $k = 0$.

The description of small deviations from a Gaussian PDF involves the use of functions with more than two independent parameters. It is of great advantage if such functions maintain the general properties of a Gauss PDF: the n-th derivative should exist over $\mathbb{R}$ and $\sigma_n < \infty$ for all values of $n \in \mathbb{N}$. Furthermore, the Gaussian PDF should be a particular case of such functions. A good candidate is the generalized Gaussian distribution *GG* [*Tarantola*, 1987], known also as the general error distribution [*Evans et al.*, 2000]. The Gaussian PDF is a special case of *GG* distirbutions. Other special cases are the Laplace distribution and the box distribution. The *GG* distribution is symmetric: $s = 0$.

Skewed distributions can be obtained from a symmetric PDF through an appropriate variable substitution $x^* = g(x, q)$, where q is a parameter related to the skewness and $g(x, q_0) \equiv x$ for a given value q_0 of q. If these conditions are met, the variable substitution generates a set

of distributions with parameter q, wherein the original PDF is a special case. A suitable transformation applied to the *GG* distribution gives the following function:

$$SGG(x,\mu,\sigma,q,p) = \frac{1}{2^{1+1/p}\sigma\,\Gamma(1+1/p)} \frac{\left|qe^{qx^*} + q^{-1}e^{x^*/q}\right|}{e^{qx^*} + e^{x^*/q}} \exp\left[-\frac{1}{2}\left|\ln\left(\frac{e^{qx^*} + e^{x^*/q}}{2}\right)\right|^p\right] \qquad (7)$$

with $x^* = (x-\mu)/\sigma$ and $0 < |q| \leq 1$. We will call this PDF the Skewed Generalized Gauss Distribution (*SGG*). The *GG* distribution is a special case of (7) for $q = 1$, and the Gauss distribution is a special case of (7) for $q = 1$ and $p = 2$. Approximate relations between the distribution parameters and μ_2, σ_2, s and k for $p \to 2$, $q \to 1$ are listed in Appendix A. Some examples of SGG distributions are shown in Figure 7. The four parameters of a *SGG* distribution have a hierarchic structure: μ and σ control the most evident properties of the PDF, namely the position along the x-axis and the "width". On the other hand, q and p influence the symmetry and the curvature of the PDF.

The need of generalized distribution functions to model the coercivity distribution of a magnetic component is evident on the examples shown in Figure 8 and Figure 9. Figure 8a shows the theoretical AF demagnetization curve of an ARM for an assemblage of non-interacting, uniaxial signle domain magnetite particles with lognormally distributed volumes and microcoercivities [*Egli and Lowrie*, 2002].

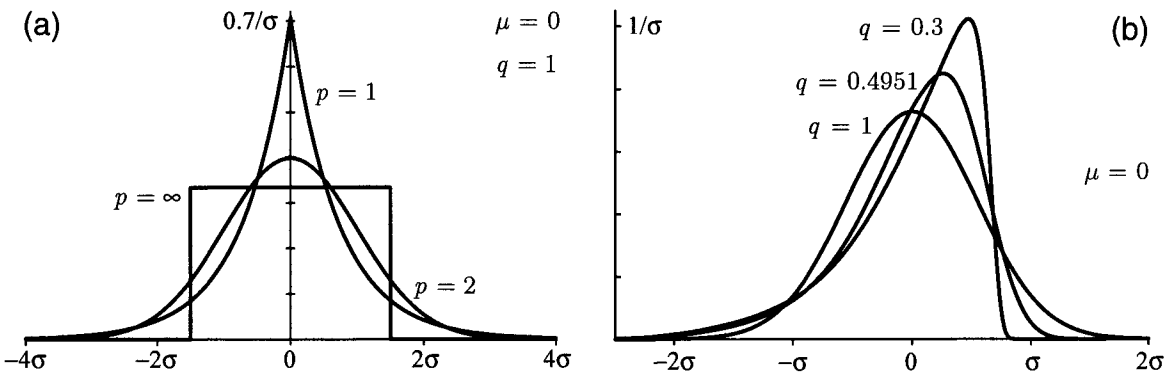

Figure 7: *Examples of SGG distributions, given by* $f(x) = SGG(x,\mu,\sigma,q,p)$. *(a) Some particular cases with* $\mu_2 = 0$, $\sigma_2 = 1$, $q = 1$ *are plotted. The skewness of all curves is zero. Furthermore,* $p = 1$ *for a Laplace distribution;* $p = 2$ *for a Gauss distribution and* $p \to \infty$ *defines a box distribution. (b) Some left-skewed SGG distributions with* $\mu_2 = 0$ *and* $\sigma_2 = 0.5484$ *are plotted. Right-skewed distributions with the same shape can be obtained by changing the sign of* q. *Demagnetization curves of multidomain magnetite can be modelled with exponential functions. The corresponding coercivity distribution on a logarithmic field scale can be approximated by a SGG distribution with* $\sigma = 0.6656$, $q = 0.4951$ *and* $p = 2.3273$, *plotted in (b). The difference between an exponential PDF and its approximation by a SGG distribution is smaller than the thickness of the curves.*

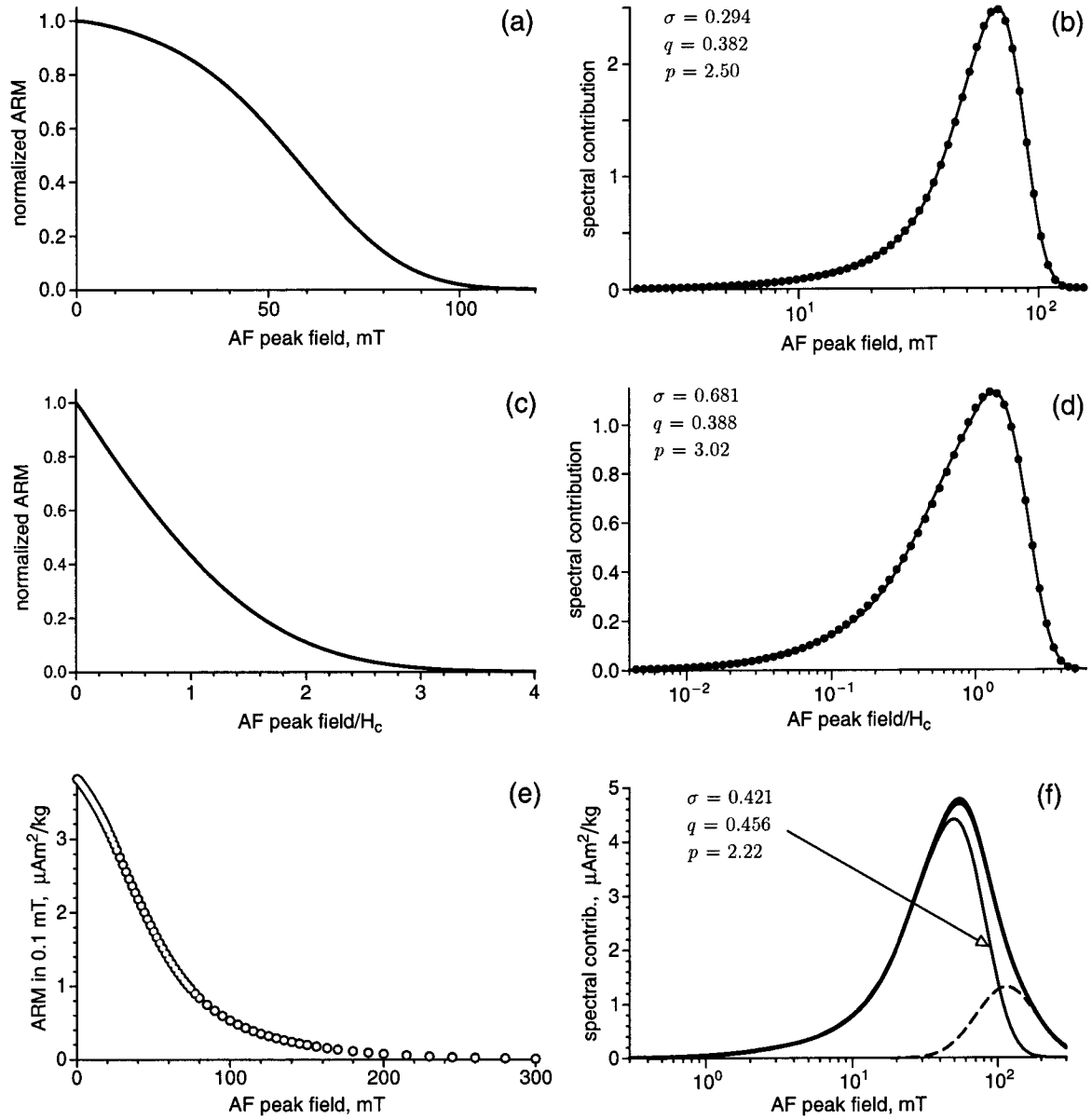

Figure 8: *Examples of significant deviations of calculated and measured coercivity distributions from a logarithmic Gaussian function. (a) Theoretical AF demagnetization curve of an ARM imparted to a set of random oriented, non-interacting single domain magnetite particles (from Egli and Lowrie [2002]). The particles have lognormally distributed volumes and microcoercivities. The corresponding coercivity distribution (b) is plotted with points and the solid line is the best-fitting SGG function. (c) Theoretical AF demagnetization curve of an ARM imparted to a set of multidomain particles with Gaussian distributed microcoercivites (redrawn from Xu and Dunlop [1995]). The corresponding coercivity distribution (d) is plotted with points and the solid line is the best-fitting SGG function. (e) AF demagnetization curve of an ARM imparted to an ODP sediment sample (leg 145) taken in the North Pacific (courtesy of M. Fuller). The corresponding coercivity distribution is shown in (f) together with a component analysis performed with SGG functions. The coercivity distribution of the soft component (solid line) clearly differs from a log-Gaussian function.*

Figure 8c shows the theoretical AF demagnetization curve of an ARM for multidomain particles with a Gaussian distribution of microcoercivities [*Xu and Dunlop*, 1995]. Both cases can be regarded as a single magnetic component. The related coercivity distributions are not Gaussian on a logarithmic field scale, but can be fitted well with a SGG distribution. Similar coercivity distributions are also found in natural sediments, as the ODP sample of Figure 8e,f. The magnetic materials presented in Figure 8 are very different; nevertheless, they have similar coercivity distributions with a negative skewness of -1.3 to -1.7. Similar results are obtained also from AF demagnetization curves of SIRM. Both the magnetic interactions and the magnetic viscosity generally increase the initial slope of an AF demagnetization curve, because they affect mainly low coercivity contributions to the total magnetization. As a consequence, the related coercivity distributions are left-skewed, and the crossing point between normalized acqusition and demagnetization curves is < 0.5 [*Cisowski*, 1981]. However, magnetic interactions and magnetic viscosity can be excluded in the model demagnetization curves of Figure 8a,c. In this case, the skewness of the related coercivity distributions is controlled by intrinsic properties of the magnetic grains. In single domain grains, thermal activation effects produce an asymmetrical shift of the coercivitiy distribution toward lower fields [*Egli and Lowrie*, 2002], so that a symmetrical distribution of microcoercivities ($s = 0$) generates a left-skewed coercivity distribution ($s < 0$). In multidomain grains, the negative exponential distribution (Figure 7b) plays a critical rule. *Bailey and Dunlop* [1983] have shown that magnetic grains with a multidomain-type result of the modified Lowrie-Fuller test [*Johnson et al.*, 1975] have a microcoercivity distribution which is more convex than the negative exponential distribution. These coercivity distributions are characterized by $s < -1$. Left-skewed coercivity distributions are also needed to fit AF demagnetization curves of a SIRM in artificial samples of sized magnetite with grain sizes between 0.1 and 100 μm [*Bailey and Dunlop*, 1983; *Halgedahl*, 1998], as shown in Figure 9. The coercivity distributions of all grain sizes have a skewness of $s = -0.93 \pm 0.1$, which is close to that of a negative exponential distribution ($s = -0.997$). However, the importance of magnetic interactions in these samples is not clear.

3.3. Error estimation

Component analysis can be extremely sensitive to measurement errors, especially in case of magnetic components with highly overlapped coercivity distributions. Thus, some distribution parameter estimates may not be siginificant at all, even if the quality of the measurement is excellent for the usual standards in rock magnetism. An error estimation of each distribution parameter is important to avoid misinterpretations. This problem was first recognized by *Stockhausen* [1998]: he attempted to evaluate the significance of his results by introducing parameters that indicate how well a measured curve is fitted by a set model functions. *Kruvier et al.* [2002] proposed a statistical test to compare different models for the component analysis.

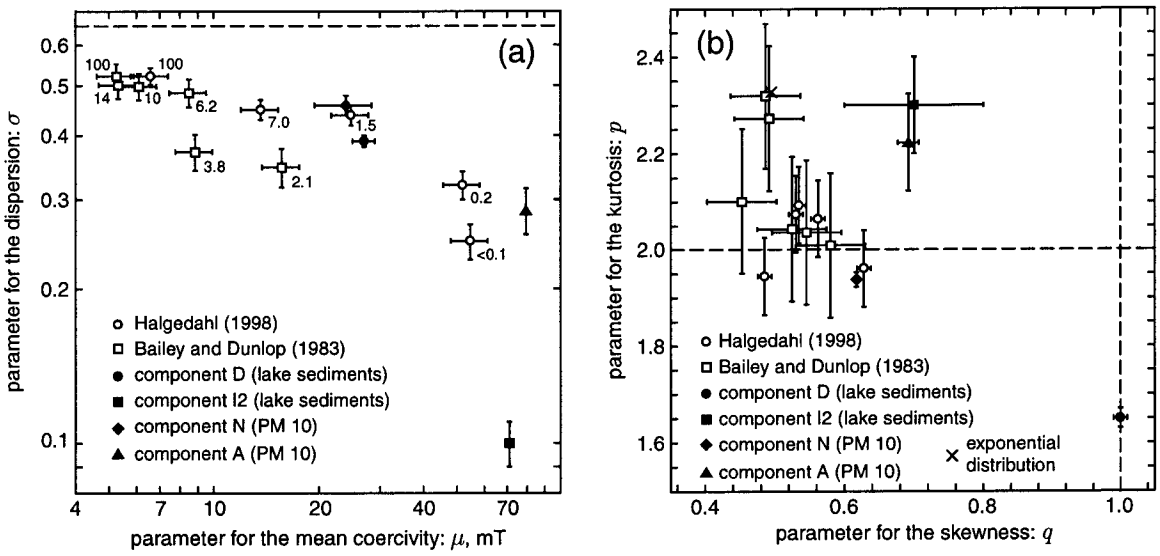

Figure 9: *Coercivity distribution parameters μ, σ, q and p (see text) for the AF demagnetization of IRM in various synthetic samples of sized magnetite. The magnetic components identified in lake sediments and PM10 dust samples are also shown for comparison. Numbers beside each point indicate the grain size in μm. (a) scatter plot of μ and σ, which are a measure of the median and the width of a coercivity distribution, respectively. The dashed line indicates the value of σ for a negative exponential distribution (Figure 7). Large grains are characterized by small values of μ and large values of σ. Notice the extremely small value of σ measured for component I2 (probably bacterial magnetite). An inverse correlation between μ and σ is evident. (b) scatter plot of q and p, which are related to the skewness and the kurtosis of a coercivity distribution, respectively. The cross point of the dashed lines corresponds to the values of q and p for a log-Gaussian distribution. All samples of sized magnetite show values of q which are significantly different from those of a log-Gaussian distribution. They group around mean values of $q \approx 0.46$. All parameters of the sized magnetites are intermediate between those of a log-Gaussian distribution and those of a negative exponential distribution. The coercivity distribution of larger grain sizes approaches an exponential distribution.*

However, these approaches are useful to evaluate the overall significance of component analysis (see section 3.4), but do not provide any information about the single components. The latter is obtained with an error estimation for each distribution parameter. Error estimates for each parameter are provided in the following for a general PDF $f(x \mid \theta)$.

We assume the measured distribution to be given by $y_i = f(x_i) + \delta y_i$, where (x_i, y_i) is a measurement point and δy_i the related measurement error. Several methods can be used to obtain an unbiased estimation $\hat{\theta}$ of θ [*Stockhausen*, 1998; *Kruiver et al.*, 2001; *Heslop et al.*, 2002]. A best-case error estimate is obtained by means of the Rao-Cramér-Frechet inequality (RCF). If $f(x \mid \theta)$ is a Gauss distribution with variance σ^2, measured at regular intervals Δx of x, and if $\delta y_i = \delta y$ is independent of x_i, the variance of one unknown distribution parameter θ is given by:

$$\mathrm{var}(\hat{\theta}) \geq \frac{2\pi^{1/2}\sigma\Delta x(\delta y)^2}{\int_X \frac{[\partial_\theta f(x \mid \theta)]^2}{f(x \mid \theta)}\mathrm{d}x} \tag{8}$$

A proof of equation (8) starting from the standard formulation of the RCF inequality is given in Appendix C. Equation (8) can be used to estimate the minimum errors of the parameter estimates of a *SGG* distribution with $p \rightarrow 2$ and $q \rightarrow 1$. The results are listed in Appendix A. More precise anlytical error estimations which apply asymptotically to all unbiased parameter estimates are obtained with error propagation methods, however, only in the limiting case of one component. Then, the variance of an unknown distribution parameter θ is given by:

$$\mathrm{var}\,\theta = \frac{\Delta x(\delta y)^2}{\int_X [\partial_\theta f(x \mid \theta)]^2 \mathrm{d}x} \tag{9}$$

A proof of equation (9) is given in Appendix C. Errors of the unbiased parameter estimates for one SGG distribution are listed in Appendix A.

3.4. Significance tests

The finite mixture model of equation (6) has $n(l+1)$ independent parameters. If a smaller number of parameters is assumed, the mixture model will not fit well the measured data. There are two possibilities for increasing the number of model parameters. The first one consists of adding more components to the model, as discussed in the literature (*Robertson and France* [1994]: 2 components; *Eyre* [1996]: 4 components; *Stockhausen* [1998]: 2 components; *Kruiver et al.* [2001]: up to 3 components; *Heslop et al.* [2002]: up to 4 components). The second possibility is presented in this paper, and consists of a better definition of the end-member PDF. Both strategies can suggest wrong conclusions, as discussed in section 4, if the unmixing results are not evaluated critically. The problem of finite mixing models is related to the fundamental question of how many parameters should be used to fit experimental data. The addition of new parameters always improves the goodness of fit of a mixture model; however, this improvement is not necessarily significant. *Kruiver et al.* [2001] proposed a combination of statistical tests to determine whether the addition of extra parameters significantly improves the goodness of fit. They apply an *F*-test and a *t*-test to the squared residuals of one fit model with respect to another model to decide if the two models are significantly different. We propose here the use of a Peason's χ^2 goodness of fit test [*Cowan*, 1998], which allows us to test if an experimental probability distribution is compatible with a given model distribution $f(x \mid \boldsymbol{\theta})$ with l unknown parameters $\theta_1 \ldots \theta_l$. According to this test, the two distributions are incompatible at a confidence level α (generally $\alpha = 0.05$) if $\chi^2(\boldsymbol{\theta}) > \chi^2_{n-l-1;1-\alpha}$, where $\chi^2_{n-l-1;1-\alpha}$ is the value of the χ^2 distribution with $n-l-1$

degrees of freedom, evaluated at $1-\alpha$. A coercivity distribution calculated with the method presented in section 2 can be used as reference distribution for the Peason's χ^2 goodness of fit test, since this method is not based on finite mixture models.

A statistical test alone is not sufficient to evaluate the significance of a mixing model, as demonstrated in section 4. Sometimes, the coercivity distributions of two magnetic components are widely overlapped, and an extremely high measurement precision is required in order to identify these components. A stack of six demagnetization curves with 72 steps each has been used for the analysis of some samples presented in this paper. Such a high measurement precision cannot be used as a standard for systematic investigations. Nevertheless, an integrated approach to this problem is possible, as shown in section 4 on the example of urban atmospheric particulate samples. In this case, the component analysis of an individual sample was very critical. The accurate choice of three samples with extremely different degrees of pollution allowed defining the number of magnetic components and their magnetic properties. Much less precision would be required for an extended study of urban atmospheric particles. The component analysis of 'standard quality' measurements would be supported by the detailed information acquired with the accurate analysis of few reference samples. A similar stratagy has been applied to the measurement of the lake sediments presented in section 4. In this case, different sources of magnetic minerals in the sediments were investigated by accurate measurements of each sedimentary unit and of samples from the catchment area. Then, AF demagnetization curves with 20 steps were measured for the entire sediment column. The measurements were fitted with the coercivity distributions of the magnetic components identified in three reference samples. Changes in the amount of biogenic magnetite during the last 120 years could be reconstructed in this way.

We propose the following set of conditions to apply and test mixing models to a large set of samples:

1. *Choice of reference samples.* Reference samples containing the most varied amounts of the same set of magnetic components should be chosen for detailed and precise measurements. These samples should define the most extreme conditions to be taken into account by the mixing model.
2. *Statistical tests.* The mixing model has to pass a statistical significance test (goodness of fit test) for each reference sample; in other words it should be compatible with the measured data within the experimental errors.
3. *Errors.* All model parameters should be significant, i.e. they should not be affected by large errors.
4. *Consistency.* The coercivity distributions of the same components should be identical within the experimental error, or they alternatively should show variations, which are consistent with some physical or chemical changes. Furthermore, variations in the concentration of each magnetic component should be explained with the help of some independent information (geological setting, chemical and physical processes).

Point 4 implies some knowledge about the potential sources of magnetic minerals (e.g. magnetite formation in soils [*Maher*, 1988], titanomagnetites in volcanic rocks [*Worm and Jackson*, 1999], biogenic magnetite [*Moskowitz et al.*, 1993], maghemite in loess [*Eyre*, 1996]) and about the properties of magnetization and demagnetization curves [*Dunlop*, 1981; *Dunlop*, 1986; *Bailey and Dunlop*, 1983; *Johnson et al.*, 1975; *Halgedahl*, 1998; *Cisowski*, 1980; *Hartstra*, 1982; *Robertson and France*, 1994].

4. Interpretation of coercivity distributions by component analysis

4.1. Comparison between different PDF's

As discussed above, the results of a component analysis depend upon the PDF chosen to model the end-member coercivity distributions, and particularly on the number of parameters assigned to each PDF. In this section we will compare results obtained with a linear combination of Gaussian distributions on the one hand, and a linear combination of SGG distributions on the other. Since finite mixture models with non-Gaussian coercivity distributions have not been reported in the literature, it is not possible to decide from a-priori informations which kind of PDF should be used as a basis for a mixture model. From the mathematical point of view, all PDFs are equivalent, since the goodness of fit that can be reached with a particular model depends only upon the total number of parameters assumed, regardless of how they are assigned to individual components. Starting from these considerations, and from the fact that coercivity distributions of natural and artificial samples are nearly log-Gaussian, one could ask if the use of more complicated PDF's has any physical meaning. We will handle this problem in the following.

To better understand the problem, we first illustrate the strong similarities that exist between a SGG distribution with $p \rightarrow 1$ and $q \rightarrow 2$ on one hand, and a linear combination of two Gaussian distributions on the other. We consider three different situations, which are shown in Figure 10. In the first case, two Gaussian distributions with identical amplitudes and same σ, but slightly different values of μ, are fitted with a SGG distribution with $p = 1$ and $q > 2$. If $\Delta\mu/\sigma > 1$, where $\Delta\mu$ is the difference between the means of the two Gauss distributions, the resulting function has two local maxima and is evidently bimodal. However, as $\Delta\mu/\sigma \rightarrow 0$, the resulting distribution becomes very similar to a slightly squared PDF ($k < 0$). In the second case, a SGG distribution with $q < 2$ is fitted to a linear combination of two Gaussian functions with the same μ, but different values of σ. The two distributions converge to the same function for $q \rightarrow 2$. In the third case, a SGG distribution with $p \neq 1$ is fitted to a linear combination of two different Gaussian functions. Convergence of the two distributions is obtained for $|p| \rightarrow 1$. In all three cases, the SGG distribution and the combination of two Gaussian functions can be very similar.

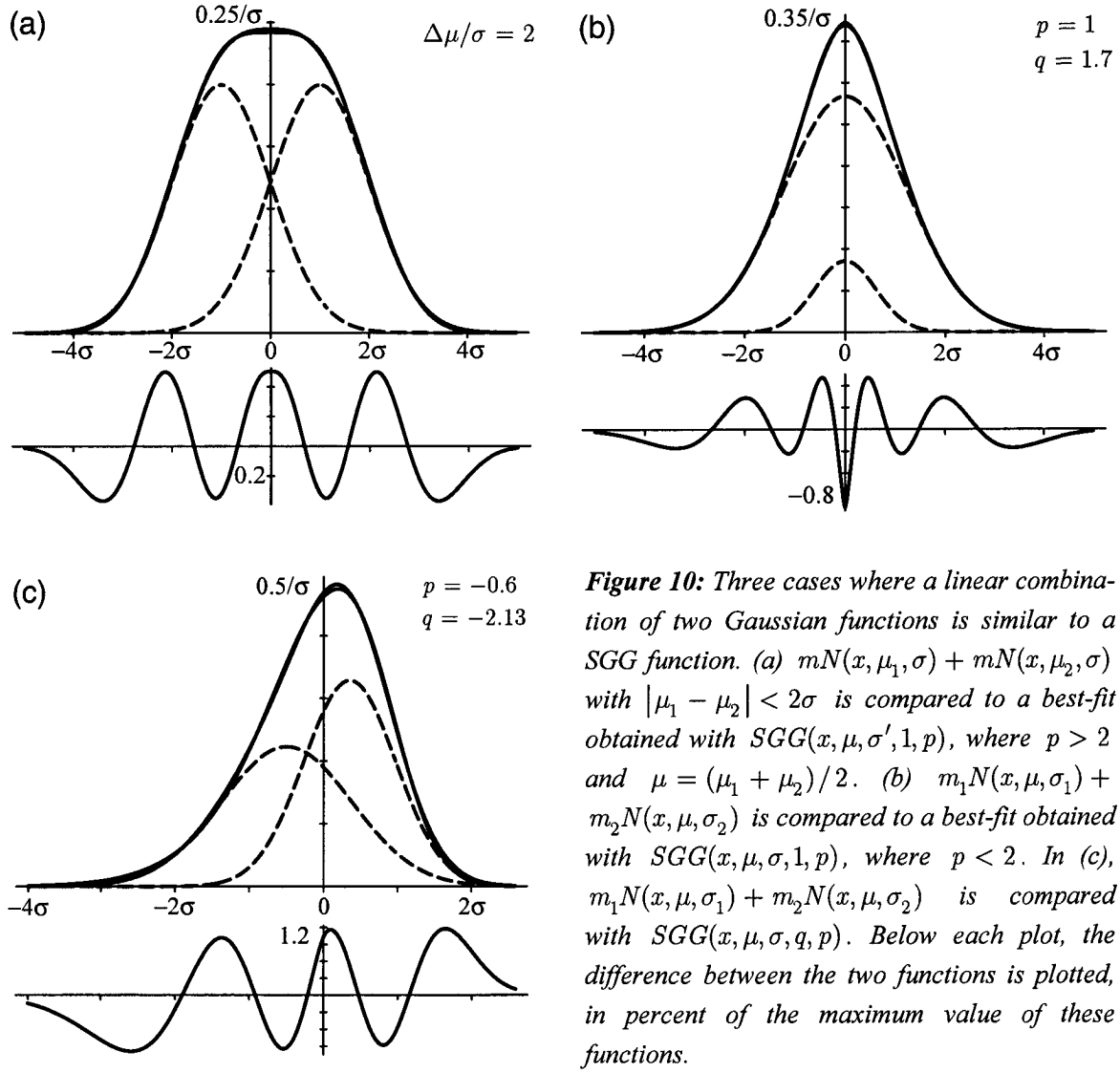

Figure 10: *Three cases where a linear combination of two Gaussian functions is similar to a SGG function. (a)* $mN(x,\mu_1,\sigma)+mN(x,\mu_2,\sigma)$ *with* $|\mu_1-\mu_2|<2\sigma$ *is compared to a best-fit obtained with* $SGG(x,\mu,\sigma',1,p)$*, where* $p>2$ *and* $\mu=(\mu_1+\mu_2)/2$*. (b)* $m_1N(x,\mu,\sigma_1)+m_2N(x,\mu,\sigma_2)$ *is compared to a best-fit obtained with* $SGG(x,\mu,\sigma,1,p)$*, where* $p<2$*. In (c),* $m_1N(x,\mu,\sigma_1)+m_2N(x,\mu,\sigma_2)$ *is compared with* $SGG(x,\mu,\sigma,q,p)$*. Below each plot, the difference between the two functions is plotted, in percent of the maximum value of these functions.*

The possibility of distinguishing two overlapping Gaussian functions from a SGG distribution depends on the noise level of the data to be fitted and can be tested with a Pearson's χ^2 goodness of fit test. If the test is not passed, the fitting models are mathematically equivalent, but the corresponding interpretations are drastically different, since the number of inferred components is not the same. Generally, the use of more complicated PDFs for the end-member coercivity distributions has the effect of reducing the number of components needed to fit a measurement with a sufficient degree of precision. Two components with widely overlapping coercivity distributions may be modeled with one SGG distribution, and vice-versa, a single component with $k \neq 0$ or $s \neq 0$ may be modeled with a combination of two Gaussian distributions. In both cases, incorrect interpretation may result. An example is given by the samples described in section 4.2, which contain magnetic components whose coercivity distribution are similar to the functions plotted in Figure 10b,c.

If two overlapping PDFs cannot be resolved at the given confidence level, the sum of the estimated contributions may still be significant, despite the fact that the individual values of the estimates are not significant. In this case, the two PDF are conveniently modeled as a single component, eventually by substituting them with a more complex PDF. The use of PDFs with more distribution parameters, instead of a large number of distributions with fewer distribution parameters leads to results of the fitting model which are more stable against measurement errors. The stable behavior of a fit with SGG distributions can be explained by the fact that small deviations from an ideal coercivity distribution, which arise from measurement errors, are taken into account by variations in skewness and kurtosis, rather than by variations in the contributions of the single components. Obviously, the values obtained for skewness and kurtosis may not be significant at all. A similar stability can be obtained with Gaussian functions if some of them are grouped as if they were one component. However, it is not always evident which distributions group together, and multiple solutions are often possible, as illustrated by the examples described in the following section.

In the following, measurements of lake sediments and urban atmospheric particulate matter are presented as examples.

4.2. Lake Sediments

Lake sediment samples were taken from Baldeggersee, Switzerland. This lake is situated on the Swiss Plateau at 463 m asl, it has a surface area of 5.2 km^2 and a maximum water depth of 66 m. The catchment area (67.8 km^2) has been used intensively for agriculture since the nineteenth century. The lake was formed more than 15,000 years ago after the retreat of the Reuss glacier. Hills around the catchment area protect the lake from winds and facilitate oxygen depletion in deep waters. Several packets of varves indicate these depletion periods during the last 6000 years. The last and most severe eutrophication event started in 1885, triggered by the development of human activities in the catchment area. The depth to anoxic water column was 60 m in 1885, and rose to 10 m in 1970 [*Wehrli et al.*, 1997]. A 1.2 m long gravity core was taken in 1999 at the center of the lake and sampled every centimetre. The samples were immediately freeze-dried to prevent oxidation and pressed into cylindrical plastic boxes. The core covers the last 200 years of sedimentation [*Wehrli et al.*, 1997]. Magnetite is the major magnetization carrier, with small amounts of a high-coercivity material, probably fine-grained hematite. The analysis of coercivity distributions is used here to separate the detrital component of the magnetic signal from the authigenic component (the magnetic particles produced by chemical and biological processes in the lake). In order to identify the detrital component, a sediment sample from a small river delta of the lake was taken. Since the catchment area is geologically and anthropogenically homogeneous all around the lake, this sample is expected to be representative of the detrital input. The sample was sieved in acetone in order to isolate the fraction $< 20\ \mu m$, which is the one that more easily reaches the center of the lake under normal conditions. In order to separate the

individual contributions to the magnetic signal of the sediments and their variation during the last eutrophication event, AF demagnetization curves of ARM were measured on a selected number of samples distributed across the transition zone between the oxic and the anoxic part of the core. The same measurements were also performed on the sample taken from the river delta. After preliminary AF demagnetization with a 300 mT peak field, each sample was given an ARM using a 0.1 mT DC field and a 300 mT AF peak field. The samples were then stepwise AF demagnetized with increasing peak fields up to 300 mT. From each demagnetization curve, a coercivity distribution was calculated with CODICA (see section 2). Figure 11 shows detailed coercivity distributions and analyzed coercivity components of three samples, labelled G010, G044 and U03F. Sample G010 was taken at a depth of 11 cm from the most anoxic level of the gravity core, and sample G044 corresponds to a depth of 44.5 cm, far below the onset of eutrophication. Sample U03F is the < 20 μm fraction of silt, collected from the small river delta. Different fitting models were used to analyze these samples; some results for G010 are summarized in Table 1. At least three magnetic components can be distinguished directly from the shape of the filtered coercivity distributions: a low-coercivity component (hereafter called component D), a component with intermediate coercivity values (component I) and a high-coercivity component, which is not saturated at 300 mT (component H). In sample G044, the intermediate component seems to be composed of two PDFs with similar values of median destructive field.

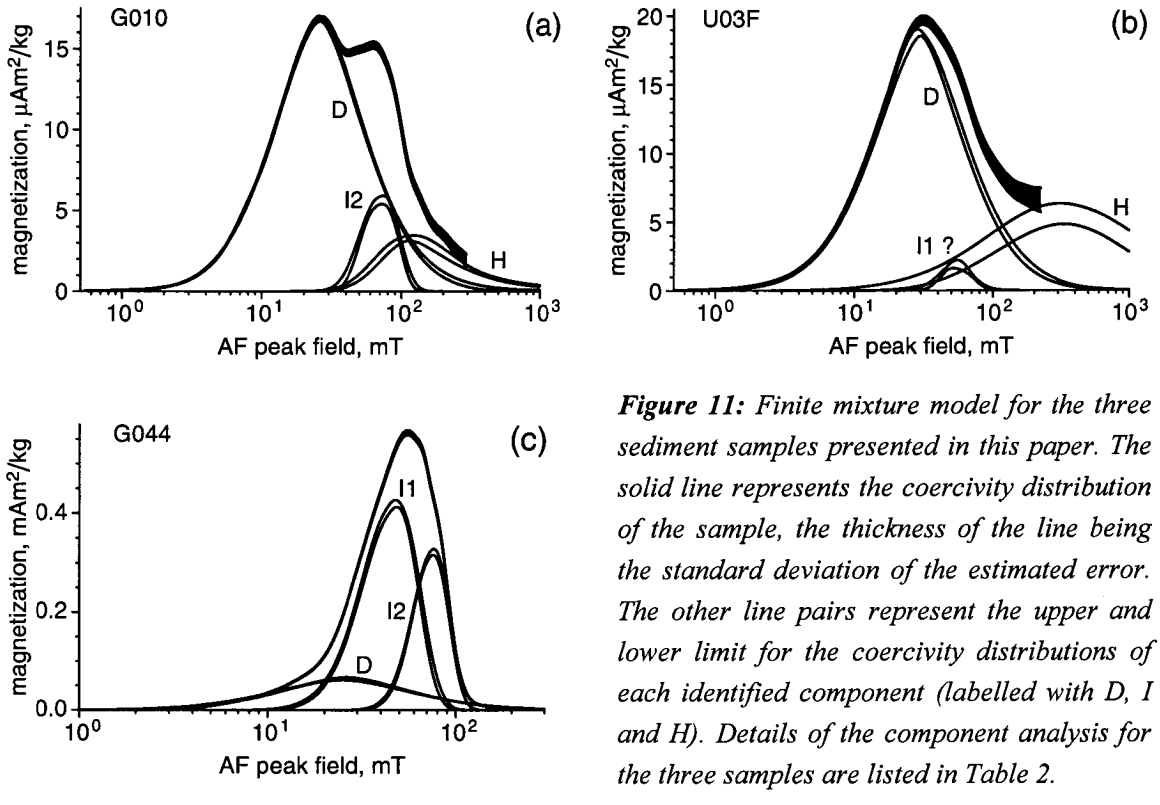

Figure 11: *Finite mixture model for the three sediment samples presented in this paper. The solid line represents the coercivity distribution of the sample, the thickness of the line being the standard deviation of the estimated error. The other line pairs represent the upper and lower limit for the coercivity distributions of each identified component (labelled with D, I and H). Details of the component analysis for the three samples are listed in Table 2.*

Table 1: *Component analysis of sample G010 (anoxic lake sediment), based on the AF demagnetization of an ARM acquired in a* 0.1 mT *bias field. The corresponding coercivity distribution has been plotted in Figure 11a. The following PDFs were assumed as end-member distributions: 3 Gaussian distributions, 5 Gaussian distributions, 3 SGG distributions, 4 SGG distributions. The second column gives the result of a Pearson's* χ^2 *goodness of fit test, and the other colums give the distribution parameters of the end-member coercivity distributions. The last row shows the final interpretation in terms of three components.*

fitting PDF	χ^2 **of fitting** ($\chi^2_{0.95}$)	**norm. contr.** $\frac{m \pm \delta m}{M_{300\,\mathrm{mT}}}$	**MDF** $\mu_2 \pm \delta\mu_2$ mT	**st. deviation** $\sigma_2 \pm \delta\sigma_2$	**skewness** $s \pm \delta s$	**kurtosis** $k \pm \delta k$	**comment**
1 G	611± 35	0.812 ± 0.004	27.1 ± 0.1	0.358 ± 0.002	0	0	1
1 G	(68.7)	0.104 ± 0.005	75.3 ± 0.5	0.122 ± 0.002	0	0	
1 G		0.088 ± 0.006	169 ± 6	0.23 ± 0.01	0	0	
total		1.005 ± 0.003					
2 G	71 ± 22	0.63 ± 0.2	23 ± 2	0.33 ± 0.04	−0.09 ± 0.1	0.2 ± 0.1	2
2 G	(61.7)	0.12 ± 0.02	71 ± 1	0.124 ± 0.006	−0.01 ± 0.06	−0.3 ± 0.1	
1 G		0.27 ± 0.2	95 ± 50	0.35 ± 0.09	0	0	
total		1.02 ± 0.003					
1 SGG	76 ± 20	0.79 ± 0.01	26 ± 1	0.38 ± 0.02	0.07 ± 0.2	0.5 ± 0.3	3,4
1 SGG	(61.7)	0.10 ± 0.01	69 ± 1	0.120 ± 0.004	−0.20 ± 0.06	−0.3 ± 0.1	
1 SGG		0.14 ± 0.02	170 ± 10	0.40 ± 0.04	1.3 ± 0.3	3.5 ± 1	
total		1.03± 0.006					
1 SGG	61 ± 20	0.77 ± 0.02	26 ± 1	0.38 ± 0.01	0.05 ± 0.1	0.5 ± 0.1	3,4
2 SGG	(55.7)	0.11 ± 0.04	72 ± 2	0.12 ± 0.01	0.1 ± 0.3	−0.4 ± 0.1	
1 SGG		0.14 ± 0.04	130 ± 20	0.33 ± 0.06	0.2 ± 0.2	0.1 ± 0.4	
total		1.01 ± 0.006					
comp. 1		0.79 ± 0.01	26 ± 1	0.38 ± 0.02	0 ± 0.2	0.5 ± 0.2	
comp. 2		0.11 ± 0.04	70 ± 2	0.12 ± 0.01	?	−0.4 ± 0.1	
comp. 3		0.14 ± 0.04	150 ± 20	0.36 ± 0.06	?	?	
total		1.03 ± 0.01					

[1] Significantly different from the measurements; [2] Numerically unstable, single components are not real; [3] Numerically stable; [4] Slight deviations from Gaussian PDF, some are significant.

Adequate mixture models are obtained with three or four SGG functions. Component H has generally low quality parameter estimates, because the available maximum field of 300 mT was not sufficient to saturate it. For each mixture model, a Pearson's χ^2 goodness of fit test was performed. The standard error of the distribution parameters was also estimated using the following procedure. An appropriate noise signal, which corresponds to the measurement error estimated by CODICA, was added to the coercivity distribution by means of a random number generator. The component analysis was then performed on the resulting distribution, and new values were obtained for each distribution parameter. The procedure was repeated many times (generally 100) in order to sample a significant set of estimates of the distribution parameters, which allow the calculation of the standard deviation for each parameter. The results are summarized in Table 2. Each end-member coercivity distribution can be normalized to have a unit saturation remanence and can be drawn separately, as shown in Figure 13. In this way, the comparison of end-member coercivity distributions is facilitated.

Table 2: *Summary of distribution parameters of the magnetic components found in samples G010, G044 and U03F from Baldeggersee, Switzerland.*

Parameter	U03F	G010	G044	comment
$m \pm \delta m$, $\mu Am^2/kg$	16 ± 0.6	14 ± 0.2	59 ± 3	**Detrital soft component:** μ_2, σ_2, s and k are almost identical
$100(m \pm \delta m)/M_{rs}$	67 ± 3	77 ± 1	20 ± 1	
$\mu_2 \pm \delta\mu_2$, mT	29 ± 1	26 ± 1	25.5 ± 0.5	
$\sigma_2 \pm \delta\sigma_2$	0.389 ± 0.006	0.38 ± 0.02	0.40 ± 0.01	
$s \pm \delta s$	0 ± 0.08	0 ± 0.1	0 ± 0.002	
$k \pm \delta k$	0.54 ± 0.04	0.5 ± 0.2	0.42 ± 0.05	
$m \pm \delta m$, $\mu Am^2/kg$	7.3 ± 0.6	2.5 ± 0.7	1.8 ± 0.6	**Hard component:** significant differences in all parameters.
$100(m \pm \delta m)/M_{rs}$	30 ± 3	14 ± 2	0.6 ± 0.2	
$\mu_2 \pm \delta\mu_2$, mT	320 ± 50	150 ± 20	180 ± 20	
$\sigma_2 \pm \delta\sigma_2$	0.52 ± 0.05	0.36 ± 0.06	0.18 ± 0.03	
$m \pm \delta m$, $\mu Am^2/kg$	6 ± 3		59 ± 3	**Intermediate component 1:** Relatively soft. Small DP. Maybe not the same component in U03F and G044.
$\mu_2 \pm \delta\mu_2$, mT	54 ± 2		41.8 ± 0.5	
$\sigma_2 \pm \delta\sigma_2$	0.11 ± 0.02		0.153 ± 0.002	
$s \pm \delta s$	?		−0.55 ± 0.04	
$k \pm \delta k$	?		0.33 ± 0.08	
$m \pm \delta m$, $\mu Am^2/kg$		1.9 ± 0.3	77 ± 4	**Intermediate component 2:** Relatively hard. Very small DP. μ_2 and σ_2 are almost identical.
$\mu_2 \pm \delta\mu_2$, mT		70 ± 2	71.3 ± 0.6	
$\sigma_2 \pm \delta\sigma_2$		0.12 ± 0.01	0.095 ± 0.002	
$s \pm \delta s$		?	−0.41 ± 0.04	
$k \pm \delta k$		−0.4 ± 0.1	0.14 ± 0.07	

Models with < 6 Gaussian PDFs do not fit the measured data sufficiently well. On the other hand, models with ≥ 6 Gaussian PDFs are not realistic, and the interpretation of each PDF in terms of magnetic components would be problematic. Models with three or four SGG distributions fit the measurements sufficiently well and provide significant estimates for m, μ and σ of each component. Skewness and kurtosis are not significant for all components. However, the coercivity distribution of component D is similar to the function plotted in Figure 10b and shows consistent and systematic deviations from a Gaussian PDF: for all three samples $s = 0$ and $k \approx 0.5$, which corresponds to $p \approx 1.6$.

4.3. Urban atmospheric particulate matter

Urban atmospheric particulate matter (PM) is the subject of several studies because of its negative effects on human health [*Harrison and Yin*, 2000]. Magnetic properties of urban PM have been recently investigated by several authors [e.g., *Shu et al.*, 2001; *Muxworthy et al.*, 2002] because of the high concentration of magnetic minerals in urban pollution. The identi-

fication of various sources of magnetic particles in urban PM would be of great interest for environmental studies. Three samples of urban PM < 10 μm (called PM10 in the following) were taken in the region of Zürich (Switzerland) with a high-volume air sampler DIGITEL DHA-80. Each sample was taken during a 24 h run by pumping 720 m^3 of air through a filter. All samples were taken during summer 2001 under dry weather conditions. Heavy industries are absent from the region, and the heating systems of buildings were not working during that period. Under these conditions, the major sources of urban PM in the city center of Zürich are represented by motor vehicles and waste combustion products [*Hüglin*, 2000].

Sample GMA was taken in a green area adjacent to our paleomagnetic laboratory outside the city of Zürich. The area is located far away from any heavily travelled road and a small amount of urban pollution is therefore expected to be found in this sample. The measured daily mean PM10 concentration was 14 $\mu g/m^3$. Sample WDK was taken in the city center of Zürich near a heavily travelled road (Wiedikon). The daily mean PM10 concentration was 66 $\mu g/m^3$, and a large amount of pollution produced by motor vehicles is expected. Sample GUH was taken inside a 3.5 km long highway tunnel near Zürich (Gubrist tunnel). The pollution by motor vehicles is expected to be highest in this sample, with a daily mean PM10 concentration of 91 $\mu g/m^3$. The samples were measured with the same procedure as the lake sediments. Results of the component analysis are summarized in Table 3 and the coercivity distributions are plotted in Figure 12. The coercivity distribution of the GMA sample is similar to the distribution plotted in Figure 10c, and it is well fitted with one SGG function. This fitting would pass a significance test with the measurement results of a common AF demagnetization experiment.

Table 3: *Summary of distribution parameters of the magnetic components found in PM10 samples.*

Parameter	GMA	WDK	GUH	comment
$m \pm \delta m$, $\mu Am^2/kg$	338 ± 2	590 ± 2	316 ± 5	**Natural mineral dust (N):** Coercivity distributions of GMA and WDK are similar. GUH was collected in a tunnel.
$100(m \pm \delta m)/M_{rs}$	73 ± 1	41 ± 1	31 ± 1	
$\mu_2 \pm \delta\mu_2$, mT	23.8 ± 0.1	19.6 ± 0.1	15.9 ± 0.3	
$\sigma_2 \pm \delta\sigma_2$	0.456 ± 0.001	0.438 ± 0.001	0.343 ± 0.01	
$s \pm \delta s$	−0.58 ± 0.02	−0.65 ± 0.01	−1.05 ± 0.03	
$k \pm \delta k$	0.76 ± 0.01	0.928 ± 0.001	1.756 ± 0.02	
$m \pm \delta m$, $\mu Am^2/kg$	128 ± 2	864 ± 2	709 ± 2	**Vehicles pollution dust (A):** All coercivity distributions are similar.
$100(m \pm \delta m)/M_{rs}$	27 ± 1	59 ± 1	69 ± 1	
$\mu_2 \pm \delta\mu_2$, mT	77.3 ± 0.2	74.7 ± 0.2	77.5 ± 0.3	
$\sigma_2 \pm \delta\sigma_2$	0.245 ± 0.001	0.275 ± 0.001	0.23 ± 0.01	
$s \pm \delta s$	−0.20 ± 0.02	−0.65 ± 0.01	−0.2 ± 0.1	
$k \pm \delta k$	−0.19 ± 0.01	0.785 ± 0.002	−0.12 ± 0.01	

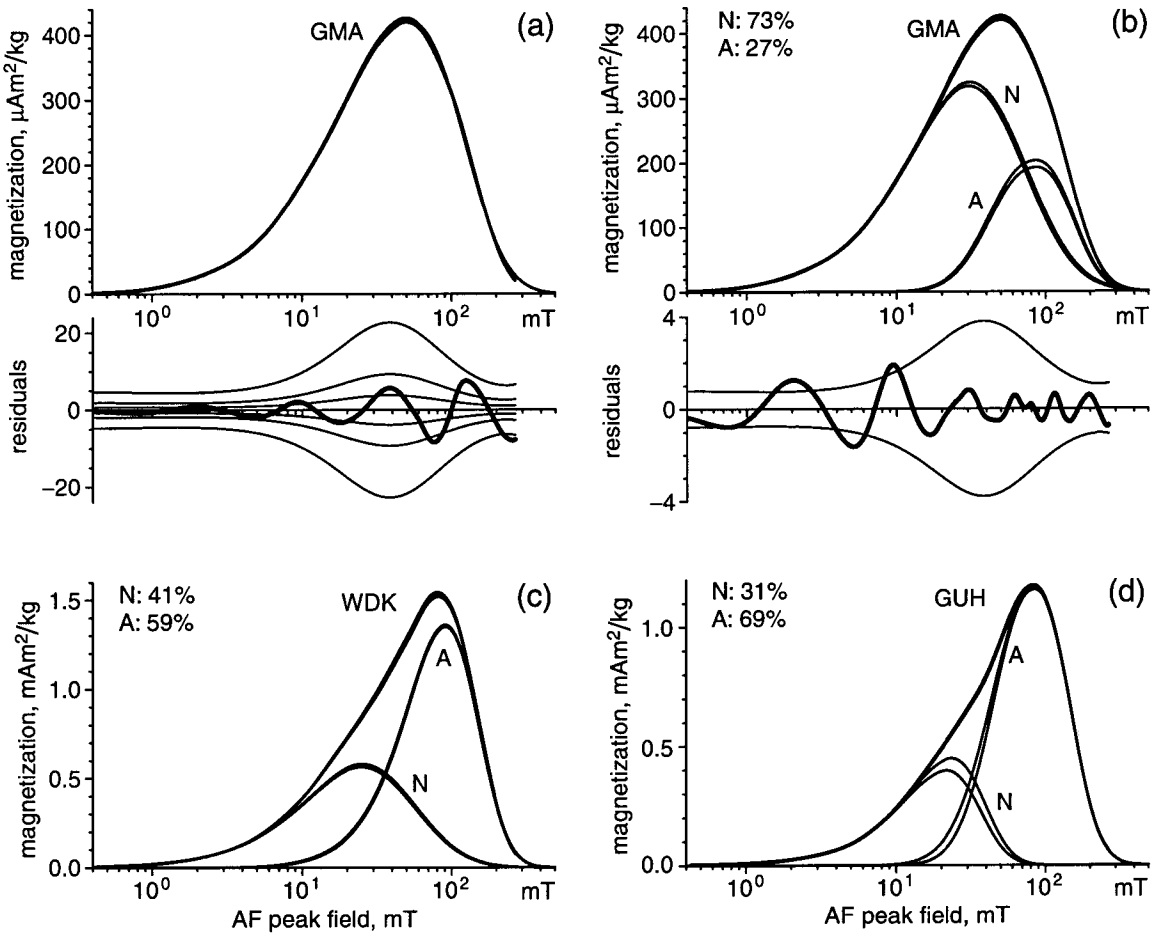

Figure 12: *Example of integrated approach to the component analysis of coercivity distributions. (a) Coercivity distribution of a PM10 sample (GMA) collected in a green area near the city of Zurich (Switzerland). The thickness of the line is the standard deviation of the estimated error. The coercivity distribution is fitted with one SGG distribution. The difference between measured and fitted curve is plotted below (thick line), together with the measurement error estimation provided by CODICA (thin line pairs). The smallest error estimation refers to the real measurement of six demagnetization curves of ARM with 72 steps each. The largest error estimation is calculated for the measurement of one demagnetization curve with 12 steps. The intermediate error estimation refers to the measurement of six demagnetization curves with 12 steps each, or one demagnetization curve with 72 steps. The modelled curve is incompatible with the highest precision measurement; therefore, two magnetic components are used for the component analysis shown in (b). In this case, the coercivity distribution is well fitted within the error of the highest precision measurement. Line pairs represent the upper and lower limit for the coercivity distribution of each component. An alternative approach to high-precision measurements was the investigation of similar samples. In (c) and (d) the coercivity distributions of other two PM10 dust samples are shown. These samples were collected near a high-traffic road in the center of Zürich (WDK) and inside a highway tunnel near Zürich (GUH). The presence of two magnetic components (called N and A) is evident in these samples. Furthermore, the contribution of component A to the total ARM is related to the degree of pollution of the area (in increasing order: GMA, WDK and GUH).*

However, two components are needed to model the results of a high-precision measurement consisting in six stacked AF demagnetization curves with 72 steps each. The GMA sample can be considered as an experimental example of the interpretation problems discussed in section 4.1.

The presence of two magnetic components in the WDK and GUH samples is evident already from a visual inspection of the coercivity distributions calculated with CODICA. The contribution of the component with higher coercivity (component A in the following) to the total magnetization is related to the amount of urban pollution in the sampling area. Therefore, we identify component A with the urban PM. The component with smaller coercivity (component N) shows the opposite trend and can be associated to the magnetic minerals contained in natural dust.

4.4. Discussion

The end-member coercivity distributions of all samples analyzed in this paper are compared in Figure 13. The coercivity distributions of component D are identical within the measurement error in all lake sediments. The absolute contribution of this component varies moderately among the three samples, if compared with the contribution of the intermediate component. Thus, it is reasonable to assume that the magnetization of component D is carried by the same set of magnetic particles, whose magnetization is dominant in sample U03F, which should be representative for the detrital input into the lake. Component I has extremely low values of the dispersion parameter: $\sigma < 0.15$. In the sample with strongest magnetization (G044) it is evident that component I is composed by at least two sub-components, which can be found individually in the other samples at lower concentration. The magnetization of component I vary from $6\ \mu Am^2/kg$ in U03F (2.6% of the bulk magnetization) to $136\ \mu Am^2/kg$ in G044 (80% of the bulk magnetization). The coercivity distribution of component I is comparable to that of samples containing intact cells of magnetotactic bacteria [*Moskowitz et al.*, 1988]. Intact and broken chains of magnetosomes were observed under the electron microscope in sample G044. Therefore component I is identified as magnetite grains of bacterial origin. The magnetic signal of component I may reflect changes in the production rate of biogenic magnetite or a possible reductive dissolution process of fine magnetite grains during eutrophication periods. Component H is badly resolved, because saturation was not reached in any of the three samples. The highest contribution of this component is found in sample U03F. The parameters μ and σ of components D, I and H in all three samples are drawn in a scatter plot in Figure 14. The three components are well grouped in three different regions of the plot. Component I is compatible with the magnetic properties of pure single-domain magnetite, whereas component D contains a small but significant amount of magnetic particles with coercivities $> 300\ mT$, probably representing oxidized magnetite. Component H is associated with a magnetically hard mineral.

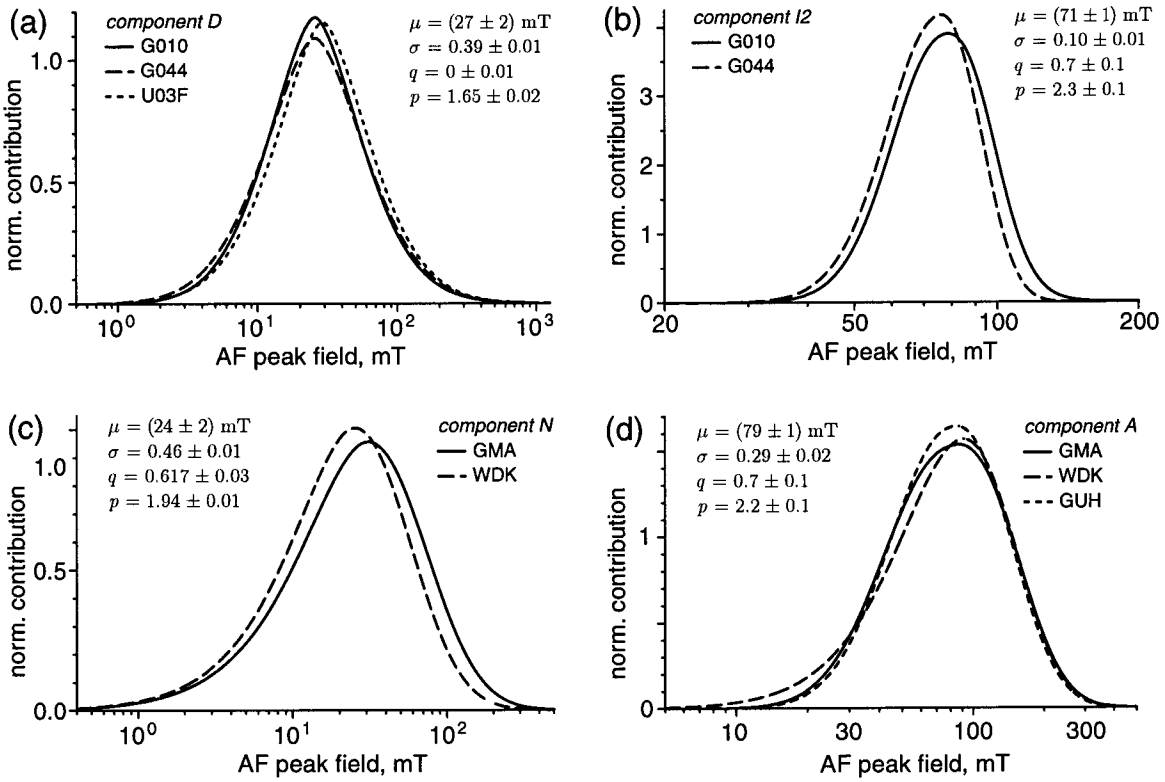

Figure 13: *Coercivity distributions of the magnetic components found in the samples analyzed in this paper. The coercivity distributions are normalized so that the saturation remanence (area under the curve) equals to 1, to facilitate the comparison between different samples. (a) Component D of lake sedinent samples G010, G044 and U03F. The coercivity distribution of this component is identical in all three samples, within the confidence levels given by the measurement errors. This component may represent detrital particles transported toward the center of the lake. (b) Component I2 of lake sediment samples G010 and G044. The coercivity distribution of this component is identical in both samples, within the confidence levels given by the measurement errors. The relatively high coercivity and the extremely small value of σ are indicative for intact magnetosomes, either isolated or arranged in chains. (c) Component N of the PM10 samples GMA and WDK. The coercivity distribution of this component is slightly different in the two samples. This component may represent the magnetic minerals contained in the mineral part of natural dust. (d) Component A of PM10 samples GMA, WDK and GUH. This component may represent the magnetic minerals associated with the pollution products of motor vehicles.*

The coercivity distributions of components A and N are similar in all PM samples, indicating common sources of magnetic minerals which are transported by wind without significant mechanisms of alteration or sorting.

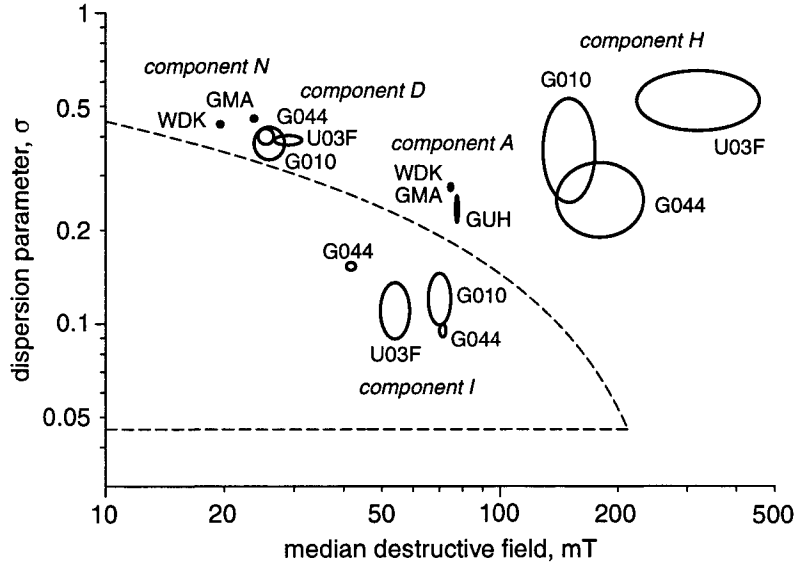

Figure 14: *Summary of the mean properties of the magnetic components found in the samples presented in this paper. For each component, the median destructive field and the dispersion parameter have been plotted. The ellipses indicate the standard error of the estimated parameters. The dashed line delimitates the range of values of the MDF and the DP for pure magnetite. The lower limit for the DP is defined by the coercivity distribution of a set of identical, uniaxial and randomly oriented magnetite particles, according to the Stoner-Wolfarth model. The upper limit is defined by all coercivity distributions that reach 99% saturation at 300 mT.*

5. Conclusions

The component analysis of coercivity distributions offers a way to estimate the contribution of different magnetic materials to the total magnetization of a sample. Component analysis is very sensitive to measurement errors and to the shape of the function used to model the end-member distributions. Nevertheless, it allows to discriminate and quantify different magnetic components of the same mineral, a result that is impossible to achieve with standard rock magnetic investigations based on bulk measurements. Careful experimental design and data treatement allow to reduce the effect of measurement errors into acceptable limits. Unjustified constrains on the shape of the model functions used for component analysis should be avoided. For this reason, generalized distribution functions have been introduced, which are able to fit a large number of different statistical distributions. In this way, a precise estimation of magnetite components with widely overlapped coercivity distributions was possible on lake sediments. Different aspects related to the calculation and the interpretation of coercivity distributions were analyzed and tested on synthetic and natural coercivity distributions. The results of these tests can be summarized into the following points:

1. Not all end-member coercivity distributions can be modelled using a logarithmic Gaussian function. Generalized distributions with five parameters can take into account variations in the symmetry (skewness) and the curvature (kurtosis). End-member coercivity distributions with significant and systematic deviations from a logarithmic Gaussian function are needed to interpretate theoretical AF demagnetization curves of single domain and multidomain magne-

tite, as well as measured demagnetization curves of synthetic samples containing sized magnetite grains.

2. The significance of the component analysis of coercivity distributions should be evaluated with statistical tests and with an error estimation of each distribution parameter. Analytical expressions for the error estimations have been developed.

3. Multiple solutions for the component analysis are possible. In this case, other informations are needed to identify the correct solution. A comparison between the component analysis of different sediments which belong to the same ecological system is useful for the identification of magnetic components.

4. Component analysis is applicable to large sets of samples with standard precision measurements, providing the number of magnetic components and their coercivity distribution parameters is known from detailed measurements on a selection of few, adequate reference samples.

Aknowlergenents

I would like to thank S. Spassov for testing CODICA and suggesting many useful improvements. I thank him and M. Fuller for providing me with some test samples. I am grateful to R. Enkin and M. Jackson for their constructive reviews, and W. Lowrie for helping me with the writing task. This work was supported by the ETH research project 0-20556-00.

References

Bailey, M. E. and D. J. Dunlop, Alternating field characterisitcs of pseudo-single-domain (2-14 μm) and multidomain magnetite, *Earth Planet. Sci. Lett.*, *63*, 335-352, 1983.

Carter-Stiglitz, B., B. Moskowitz and M. Jackson, Unmixing magnetic assemblages and the magnetic behaviour of bimodal mixtures, *J. Geophys. Res.*, *106*, 26397-26411, 2001.

Cowan, G., *Statistical data analysis*, Oxford University Press, New York, 1998.

Cisowski, S., Interacting vs. non-interacting single-domain behaviour in natural and synthetic samples, *Phys. Earth Planet. Inter.*, *26*, 56-62, 1981.

Dunlop, D. J., The rock magnetism of fine particles, *Phys. Earth Planet. Inter.*, *26*, 1-26, 1981.

Dunlop, D. J., Coercive forces and coercivity spectra of submicron magnetites, *Earth Planet. Sci. Lett.*, *78*, 288-295, 1986.

Egli, R. and W. Lowrie, The anhysteretic remanent magnetization of fine magnetic particles, *J. Geophys. Res.*, *107*, 2209-2229, 2002.

Evans, M, N. Hastings and B. Peacock, *Statistical distributions*, John Wiley, New York, 2000.

Eyre, J. K., The application of high resolution IRM acqusition to the discrimination of remanence carriers in Chinese loess, *Studia geoph. et geod.*, *40*, 234-242, 1996.

Geiss, C. E. and S. K. Banerjee, A multi-parameter rock magnetic record of the last glacial-interglacial paleoclimate from south-central Illinois, USA, *Earth Planet. Sci. Lett.*, *152*, 203-216, 1997.

Halgedahl, S. L., Revisiting the Lowrie-Fuller test: alternating field demagnetization characteristics of single-domain through multidomain glass-ceramic magnetite, *Earth Planet. Sci. Lett.*, *160*, 257-271, 1998.

Harrison, R. M. and J. Yin, Particulate matter in the atmosphere: which particle properties are important for its effects on health?, *Sci. Total Environ.*, *249*, 85-101, 2000.

Hartstra, R. L., A comparative study of the ARM and I_{sr} of some natural magnetites of MD and PSD grain size, *Geophys. J. R. Astron. Soc.*, *71*, 497-518, 1982.

Heslop, D., M. J. Dekkers, P. P. Kruiver and I. H. M. van Oorschot, Analysis of isothermal remanent magnetization acquisition curves using the expectation-maximization algorithm, *Geophys. J. Int.*, *148*, 58-64, 2002.

Hüglin, C., Anteil des Strassenverkehrs an den PM10- und PM2.5-Immissionen, Bericht C4 des NFP 41, 2000.

Johnson, H. P., W. Lowrie and D. Kent, Stability of anhysteretic remanent magnetization in fine and coarse magnetite and maghemite particles, *Geophys. J. R. astr. Soc. 41*, 1-10, 1975.

Kruiver, P. P., M. J. Dekkers and D. Heslop, Quantification of magnetic coercivity components by the analysis of acquisition curves of isothermal remanent magnetization, *Earth Planet. Sci. Lett.*, *189*, 269-276, 2001.

Lees, J. A., Mineral magnetic properties of mixtures of environmental and synthetic materials: linear additivity and interaction effects, *Geophys. J. Int.*, *131*, 335-346, 1997.

Maher, B. A. and R. M. Taylor, Formation of ultrafine-grained magnetite in soils, *Nature*, *336*, 368-370, 1988.

Moskowitz, B. M. et al., Magnetic properties of magnetotactic bacteria, *J. Magn. Magn. Mat.*, *73*, 273-288, 1988.

Moskowitz, B. M., R. Frankel, and D. Bazylinski, Rock magnetic criteria for the detection of biogenic magnetite, *Earth Planet. Sci. Lett.*, *120*, 283-300, 1993.

Muxworthy, A. R., E. Schmidbauer and N. Petersen, Magnetic properties and Mössbauer spectra of urban atmospheric particulate matter: a case study from Munich, Germany, *Geophys. J. Int.*, *150*, 558-570, 2002.

Robertson, D. J. and D. E. France, Discrimination of remanence-carrying minerals in mixtures, using isothermal remanent magnetisation acqusition curves, *Phys. Earth Planet. Inter.*, *82*, 223-234, 1994.

Shu, J., J. A. Dearing, A. P. Morse, L. Yu and C. Li, Magnetic properties of daily sampled total suspended particulates in Shangai, *Environ. Sci. Tech.*, *34*, 2393-2400, 2001.

Stockhausen, H., Some new aspects for the modelling of isothermal remanent magnetization acquisition curves by cumulative log Gaussian functions, *Geophys. Res. Lett.*, *25*, 2217-2220, 1998.

Tarantola, A., *Inverse problem theory*, Elsevier, Amsterdam, 1987.

Thompson, R., Modelling magnetization data using SIMPLEX, *Phys. Earth Planet. Inter.*, *42*, 113-127, 1986.

Verosub, K. L. and A. P. Roberts, Environmental magnetism: past, present and future, *J. Geophys. Res.*, *100*, 2175-2192, 1995.

Wehrli, B., A. F. Lotter, T. Schaller and M. Sturm, High-resolution varve studies in Baldeggersee (Switzerland): project overview and limnological background data, *Aquatic Sciences*, *57*, 360-386, 1997.

Worm, H.-U. and M. Jackson, The superparamagnetism of Yucca Mountain Tuff, *J. Geophys. Res.*, *104*, 25415-25425, 1999.

Xu, S. and D. J. Dunlop, Toward a better understanding of the Lowrie-Fuller test, *J. Geophys. Res.*, *100*, 22533-22542, 1995.

Yu, L. and F. Oldfield, A multivariate mixing model for identifying sediment source from magnetic measurements, *Quaternary Res.*, *32*, 168-181, 1989.

Appendix A: Error calculations

Table 1 summarizes the effect of different measurement error sources on the calculation of a coercivity distribution. The numerical calculation of a coercivity distribution from an acquisition/demagnetization curve with finite differences is given in the first row. In the second row, general equations for the error estimation are given by assuming an error δM in the measurement of the magnetization M, and an error δH in the applied field H. In the other rows, error estimations are given for particular cases where the absolute or the relative error of M or H are described by a white noise of amplitude ε. The last row gives an error estimation in the case where a small part ε of all magnetic particles which are not magnetically unblocked by the applied field becomes mechanically unstable and rotates under the influence of a torque $T \propto H$. The amount of these particles is assumed to be proportional to T and thus to H. The corresponding magnetization is then proportional to $HM(H)$, where $M(H)$ is the magnetization of all magnetically blocked particles.

Table 2 summarizes the properties of the SGG distribution and the relative error estimations. The following notations are used: n is the number of measurements, l the number of estimated parameters, u_α the α-quantile of the standartized Gaussian distribution ($u_{0.95} = 1.6$). Other notations are explained in the paper. The second column gives approximate estimations of some distribution properties when $p \to 1$ and $q \to 2$. The third column gives the minimum error estimations of all distribution parameters, according to the Rao-Cramér-Frecht inequality (RCF). The last column gives the error estimations of the minimum χ^2 fitting method, when only one parameter is unknown.

Table 3 summarizes some error estimations for the parameters of a SGG distribution. The errors are calcuated analytically and numerically for the minimum χ^2 fitting method. The numerical error estimation is obtained by fitting 1000 simulated SGG distributions. These distributions are obtained by adding a Gaussian noise signal of known amplitude, to a standardized SGG distribution ($m = 1$, $\mu = 0$, $\sigma = 1$, $q = 1$, $p = 2$). The numerical estimates are reported as the ratio beween the results of the numerical simulation and the analytical equations reported in the second column. The second and the third column refer to a minimum χ^2 fitting with one unknown parameter (m, μ, σ, q or p), the fourth and fifth column to a minimum χ^2 fitting with three unknown parameters (m, μ and σ), and the last colum to a minimum χ^2 fitting where all parameters are unknown.

Table 1.

Error Source	Magnetization curve	Coercivity distribution
General, $h = H/\Delta H$	$M_i = M(H_i) + \Delta M$ $\Delta M =$ total error	$f_i = \frac{H_{i+1} + H_i}{2} \frac{M_{i+1} - M_i}{H_{i+1} - H_i}$
Measurement error: δM Applied field error: δH	$(\Delta M)^2 = (\delta M)^2 + f^2(\delta H)^2$	$(\Delta f)^2 = 2h^2(\delta M)^2 + 2f^2(\delta H)^2$
Absolute measurement error: $\delta M = \varepsilon$ Relative measurement error: $\delta M/M = \varepsilon$	$\Delta M = \varepsilon$ $\Delta M/M = \varepsilon$	$\Delta f = \sqrt{2}h\varepsilon$ $\Delta f = \sqrt{2}h\varepsilon M$
Absolute applied field error: $\delta H = \varepsilon$ Relative applied field error: $\delta H/H = \varepsilon$	$\Delta M = \varepsilon f$ $\Delta M = \varepsilon f H$	$\Delta f/f = \sqrt{2}h\varepsilon/H$ $\Delta f/f = \sqrt{2}h\varepsilon$
Mechanical instability: $\delta M = \varepsilon HM$	$\Delta M = \varepsilon HM$	$\Delta f = \sqrt{2}h\varepsilon HM$

Table 2.

Distribution properties	Relation with the distribution parameters	RCF inequality	Minimum χ^2 fitting (1 unknown parameter)
Optimized $\chi^2(\theta)$: α-confidence limits: for $n - l \gg 1$:	$n - l - 1$ $[\chi_{n-l-1;\alpha}, \chi_{n-l-1;1-\alpha}]$ $(n-l) \pm u_\alpha\sqrt{2(n-l)}$		
General parameter θ		$\Delta\theta \geq \frac{\sqrt{2}\pi^{1/4}\delta y\sqrt{\sigma\Delta x}}{\left[\int_{-\infty}^{\infty}\left(\frac{\partial f(x)}{\partial\theta}\right)^2\frac{dx}{f(x)}\right]^{1/2}}$	$\Delta\theta = \frac{\delta y\sqrt{\Delta x}}{\left[\int_{-\infty}^{\infty}\left(\frac{\partial f(x)}{\partial\theta}\right)^2 dx\right]^{1/2}}$
Amplitude m		$\delta m \geq \sqrt{2}\pi^{1/4}\delta y\sqrt{\sigma\Delta x}$	$\delta m = \sqrt{2}\pi^{1/4}\delta y\sqrt{\sigma\Delta x}$
Mean $\mu_2 = E(x)$	$\mu + \frac{s}{6}(1 + 0.856k)$	$\delta\mu_2 \geq \sqrt{2}\pi^{1/4}\frac{\delta y}{m}\sqrt{\sigma^3\Delta x}$	$\delta\mu_2 = 2\pi^{1/4}\frac{\delta y}{m}\sqrt{\sigma^3\Delta x}$
Standard deviation: $\sigma_2^2 = E[(x-\mu_2)^2]$	$\sigma^2(1 + 0.856k)\cdot$ $(1 - \lvert s\rvert/3)$	$\delta\sigma_2 \geq \pi^{1/4}\frac{\delta y}{m}\sqrt{\sigma^3\Delta x}$	$\delta\sigma_2 = 2\sqrt{\frac{2}{3}}\pi^{1/4}\frac{\delta y}{m}\sqrt{\sigma^3\Delta x}$
Skewness s: $E[(x-\mu_2)^3]/\sigma_2^3$	$-6\operatorname{sgn} q(1-q)^2\cdot$ $(1 + 1.856k)$	$\delta s \geq 4(2\pi)^{1/4}\frac{\delta y}{m}\sqrt{\sigma\Delta x}$	$\delta s = \frac{48}{\sqrt{13}}\pi^{1/4}\frac{\delta y}{m}\sqrt{\sigma\Delta x}$
Kurtosis k: $E[(x-\mu_2)^4]/\sigma_2^2 - 3$	$2 - p$	$\delta k \geq 3.204\frac{\delta y}{m}\sqrt{\sigma\Delta x}$	$\delta k = 8.243\frac{\delta y}{m}\sqrt{\sigma\Delta x}$

Table 3.

Distribution moments	Minimum χ^2 fitting (with $l = 1$)	Num. est. ($l = 1$)	Minimum χ^2 fitting (with $l = 3$)	Num. est. ($l = 3$)	Num. est. ($l = 5$)
Amplitude m	$\delta m = \sqrt{2}\pi^{1/4}\delta y\sqrt{\sigma\Delta x}$	0.993	$\delta m = \sqrt{3}\pi^{1/4}\delta y\sqrt{\sigma\Delta x}$	1.203	1.293
Mean μ_2	$\delta\mu_2 = 2\pi^{1/4}\frac{\delta y}{m}\sqrt{\sigma^3\Delta x}$	0.990	$\delta\mu_2 = 2\pi^{1/4}\frac{\delta y}{m}\sqrt{\sigma^3\Delta x}$	1.021	1.032
Standard deviation σ_2	$\delta\sigma_2 = \sqrt{\frac{8}{3}}\pi^{1/4}\frac{\delta y}{m}\sqrt{\sigma^3\Delta x}$	0.997	$\delta\sigma_2 = \pi^{1/4}\frac{\delta y}{m}\sqrt{\sigma^3\Delta x}$	1.139	2.643
Skewness s	$\delta s = \frac{48}{\sqrt{13}}\pi^{1/4}\frac{\delta y}{m}\sqrt{\sigma\Delta x}$	0.883			1.411
Kurtosis k	$\delta k = 8.243\frac{\delta y}{m}\sqrt{\sigma\Delta x}$	0.698			2.032

Appendix B: a short guide to CODICA

The processing of an acquisition/demagnetization curve with CODICA consits in the following steps.

1. Data checking (Figure 3a)

The measurement curve is always displayed as a demagnetization curve (Figure 3a): this does not affect the calculation of the coercivity distribution. The user is asked to enter an estimation of the measurement error (if known). This estimate may come from inspection of the measurement curve and/or experimental experience with the instruments used. A combination of a relative and an absolute error is assumed to affect the measurements and the AF field. Systematic errors, like magnetization offsets and temperature effects on the sample and on the AF coil do not affect significantly the shape of the measured curve and may not be included. The calculation of a coercivity distribution and the related error is independent of the error estimate entered by the user. This first estimate is needed by the program in order to display a rough estimation of the confidence limits of the measured curve, which should help the user through the following steps of the program.

2. Scaling the magnetic field (Figure 3b)

As discussed in paragraph 2.2, an acquisition/demagnetization curve is supposed to have a sigmoidal shape on a logarithmic field scale. However, the measured curves are not symmetrical. Often, they show a long tail at high fields. In case of lognormal coercivity distributions, the measured curve represented on a logarithmic field scale becomes symmetric. In all other cases the curve is asymmetric on both a linear and a logarithmic field scale. An appropriate scale change which offers a set of intermediate scales between linear and logarithmic is defined by the power function $H^* = H^p$, p being a positive exponent. An appropriate value of p is chosen, so that the scaled curve reaches maximum symmetry. The symmetry of the curve is compared with a reference sigmoidal curve, expressed by an analytical function (a tanh function in our program). The scaled curve is therefore represented together with the best-fitting tanh function. An automatic routine optimizes the scaling exponent p so that the difference between the original curve and the model curve is minimal.

3. Scaling the magnetization (Figure 3c)

A tanh function was chosen as a reference in order to scale the field, because of its mathematical simplicity. It does not have a particular meaning and any other similar function could be used instead. If the measured curve $M(H)$ coincides with a tanh function, the application of the inverse function arctanh to the magnetization values generates a linear relation between scaled field and scaled magnetization. The scale transformation applied to the

magnetization values is based on the following model for the relationship between the scaled field H^* and the measured magnetization $M(H^*)$ in a demagnetization curve:

$$M(H^*) = M_{rs}\left[1 - \tanh\left(a(H^* - H^*_{1/2})\right)\right] + M_0 \qquad \text{(B1)}$$

where M_{rs} has the physical meaning of a saturation remanence (if the measured curve is saturated at the highest field value), M_0 has the physical meaning of a residual magnetization ($M_0 = 0$ if saturation can be reached), $H^*_{1/2}$ is the scaled median destructive field and a is a parameter that controls the steepness of the curve. The following scale transformation

$$M^* = \operatorname{artanh}\left(1 - \frac{M - M_0}{M_{rs}}\right) \qquad \text{(B2)}$$

generates the linear relation $M^* = a(H^* - H^*_{1/2})$ between scaled field and scaled magnetization. The four parameters M_{rs}, $H^*_{1/2}$, M_0 and a have to be chosen in a way that the scaled magnetization curve as linear as possible. The program optimizes the parameters $H^*_{1/2}$ and a automatically using a Levenberg-Marquard algorithm for non-linear fitting. The parameters M_0 and $M_0 + M_{rs}$ represent the asymptotic values of the magnetization curve. Their optimization is controlled by the user, since it was found that the optimization is very unstable with respect to these parameters. The scaled curve is represented together with a least-squares linear fitting. Deviation from the least-squares line can be minimized with an appropriate choice of M_0 and $M_0 + M_{rs}$. In general, too small values of M_0 or too high values of $M_0 + M_{rs}$ produce a flattening at the right and left end of the scaled curve, respectively. In contrast, too high values of M_0 or too small values of $M_0 + M_{rs}$ produce a steepening of the scaled curve at the right and left end of the scaled curve, respectively. Random deviations from the least-squares line indicate the presence of measurement noise, systematic smooth deviations indicate a divergence of the measured curve from equation (B1). Best results are achieved using samples in which one magnetic component is dominant or in which different components have a wide range of overlapping coercivities. In both cases the choice of 5 independent parameters for the two scaling operations (p, M_{rs}, $H^*_{1/2}$, M_0 and a) is sufficient to achieve an exellent linear relationship between scaled field and scaled magnetization. In case of populations with drastically different coercivity ranges (i.e. magnetite and hematite) the scaling method is less effective, but in this case the separation of the different components is also less critical, and can be performed even directly on the measured curve.

4. Plotting the residuals (Figure 3d)

Once the measured curve is scaled with respect to field and magnetization, the deviation of the scaled curve from the least-squares line is plotted. We will call this deviation the residuals curve. At this step, measurement errors are enormously enhanced, as can be seen by

comparing the residuals with the original measured curve (not shown in Figure 3d). The estimated maximum measurement error is plotted in the form of a band around the residual curve. If the error estimation entered by the user was correct, the amplitude of the random oscillations of the residual curve should show the same order of magnitude as the displayed errors.

5. Scaling the residuals (Figure 3e)

Generally, the residuals generate a sinusoidal curve, which is more or less "quenched" at one end. As in step 2, the field axis can be rescaled with a power transformation in order to approach a quite regular sinusoidal curve, which later can be filtered in a more effective way. After this new rescaling step, the residual curve is almost sinusoidal. Its Fourier spectrum is concentrated in a narrow band around a dominant wavelength, so that a simple low-pass filter would easily remove the high-frequency measurement noise.

6. Filtering the residuals (Figure 3f)

The residual curve is now ready to be filtered in order to remove the measurement noise. The filter applied by the program is a modified Butterworth low-pass filter, defined by:

$$F(\nu) = \frac{1}{\left(1 + \nu_0^b / \nu^b\right)^{1/2b}} \tag{B3}$$

where ν is the frequency of the spectrum, ν_0 the so-called cutoff frequency, and $b \geq 1$ the order of the filter. The filter parameters ν_0 and b are chosen by the user. Details of the residual curve with an extension smaller than $1/\nu_0$ on the field axis are filtered out. The sharpness of the filter is controlled by its order b: $b \rightarrow \infty$ gives a cut-off filter. The filter parameters should be chosen so that the measurement error is suppressed without changing the global shape of the curve. This condition is met by choosing the smallest value of ν_0, by which the difference between the filtered and the unfiltered curve attains the same maximal amplitude as the estimated measurement errors. The choice of larger values of ν_0 leads to a coercivity spectrum that fits the measured curve better but still contains an unremoved component of the measurement errors. The choice of larger values of ν_0 may produce a change in the shape of the curve and suppress significant details.

7. Calculating the filtered demagnetization curve

Now, the filtered residuals are converted back to the original curve by applying the steps 2 to 5 in reverse order. The result is a demagnetization curve, which is supposed to be free of measurement errors.

8. Calculating and plotting the coercivity distribution

The coercivity distribution is calculated as the absolute value of the derivative of the filtered demagnetization curve obtained at point 7. The user can choose between a linear, a logarithmic and a power field scale. The maximum amplitude of the error of the coercivity distribution is estimated in the program by comparing the measurement curve with the filtered curve. The error estimation is displayed as an error band on the plot (Figure 1).

Appendix C: Error estimation

A measured distribution is given by $y_i = f(x_i) + \delta y_i$, where (x_i, y_i) is a measurement point and δy_i the related measurement error. In following we assume the measurement error to be ergodic (i.e. statistically independent of x)

The Rao-Cramér-Frechet theorem

Let $f(x \mid \theta)$ be a PDF with distribution parameter θ, and $\{X_1,\ldots,X_N\}$ a set of N realizations of the statistic variate X. The variance $\operatorname{var}\hat{\theta}$ of the parameter $\hat{\theta}$ estimated with this set of realizations obey the RCF inequality [*Cowan*, 1998]:

$$\operatorname{var}(\hat{\theta}) \geq \frac{1}{N\sum_{i=1}^{N} f(x_i \mid \theta)\left[\partial_\theta \ln f(x_i \mid \theta)\right]^2} \tag{C1}$$

We use the RCF inequality to calculate $\operatorname{var}\hat{\theta}$ when $f(x \mid \theta)$ is measured directly, instead of $\{X_1,\ldots,X_N\}$. For this propose, we imagine that $f(x_i \mid \theta)$ is calculated from a set of N realizations by counting the numbers N_i of realizations which belong to given intervals of amplitude Δx_i around a set of reference points $\{x_1,\ldots x_n\}$. Consequently, $y_i = N_i/\Delta x_i$, and $y_i \to f(x_i \mid \theta)$ for $N \to \infty$, $\Delta x_i \to 0$. The probability distribution of N_i is a Poisson distribution with expected value $E(N_i) = Nf(x_i)\Delta x_i$ and variance $\operatorname{var}(N_i) = E(N_i)$. Because $\operatorname{var}(N_i)/E^2(N_i) = \operatorname{var}\delta y_i / y_i^2$, we obtain $E(N_i) = y_i^2/\operatorname{var}\delta y_i$. Inserting the sum of all N_i into (C1) gives:

$$\operatorname{var}(\hat{\theta}) \geq \frac{1}{\sum_{i=1}^{n}\left(\frac{y_i}{\operatorname{var}\delta y_i}\right)^2 \sum_{i=1}^{n}\frac{\left[\partial_\theta f(x_i \mid \theta)\right]^2}{f(x_i \mid \theta)}} \tag{C2}$$

For equally spaced reference points, $x_{i+1} - x_i = \Delta x$, and if $\Delta x \to 0$ the summands in (C2) are conveniently replaced by integrals:

$$\mathrm{var}(\hat{\theta}) \geq \frac{\Delta x}{\int_{-\infty}^{\infty} \frac{f^2(x \mid \theta)}{\mathrm{var}\,\delta y(x)}\mathrm{d}x \int_{-\infty}^{\infty} \frac{[\partial_\theta f(x \mid \theta)]^2}{f(x \mid \theta)}\mathrm{d}x} \tag{C3}$$

A further simplification is obtained by assuming the measurement error $\{\delta y_i\}$ to be ergodic. Then, $\mathrm{var}\,\delta y_i = (\delta y)^2$ and:

$$\mathrm{var}(\hat{\theta}) \geq \frac{\Delta x (\delta y)^2}{\int_{-\infty}^{\infty} f^2(x \mid \theta)\mathrm{d}x \int_{-\infty}^{\infty} \frac{[\partial_\theta f(x \mid \theta)]^2}{f(x \mid \theta)}\mathrm{d}x} \tag{C4}$$

If $f(x \mid \theta)$ is a Gauss distribution with variance σ^2, simplifies finally to equation (8).

Error estimation with unbiased fitting methods

Both the maximum likelihood (ML) and the minimum χ^2 fitting method are asymptotically identical and absolute efficient for $n \to \infty$, where n is the number of measured points [*Cowan*, 1998]. We handle therefore only the minimum χ^2 method, which is directly related to the Pearson's χ^2 goodness of fit test (see section 2.3). Consider a set of N realizations $\{X_1,\ldots,X_N\}$ of the statistic variate X, and a model distribution $f(x \mid \boldsymbol{\theta})$, which depends on the distribution parameters $\boldsymbol{\theta} = (\theta_1,\ldots,\theta_k)$. The χ^2 estimator is given by:

$$\chi^2(\boldsymbol{\theta}) = \sum_{i=1}^{n} \frac{[N_i - \Delta x_i f(x_i \mid \boldsymbol{\theta})]^2}{\Delta x_i f(x_i \mid \boldsymbol{\theta})} \tag{C5}$$

where N_i is the number of realizations which belong to an interval of amplitude Δx_i around a given value x_i. The minimum χ^2 estimate $\hat{\boldsymbol{\theta}}$ is the value of $\boldsymbol{\theta}$ which minimizes $\chi^2(\boldsymbol{\theta})$. In our case, the individual realizations are unknown, but a measure of $f(x,\boldsymbol{\theta})$ is given. As shown before, each measurement y_i of $f(x_i,\boldsymbol{\theta})$ is related to a number $n_i = y_i^2/\mathrm{var}\,\delta y_i$ of realizations. In this case, (C5) can be written as:

$$\chi^2(\boldsymbol{\theta}) = \sum_{i=1}^{m} \frac{[y_i - f(x_i \mid \boldsymbol{\theta})]^2}{\mathrm{var}\,\delta y_i} \tag{C6}$$

If the measurement error is ergodic, $\mathrm{var}\,\delta y_i = (\delta y)^2$, and (C6) simplifies to:

$$\chi^2(\boldsymbol{\theta}) \cong \frac{1}{(\delta y)^2} \sum_{i=1}^{m} [y_i - f(x_i \mid \boldsymbol{\theta})]^2 \tag{C7}$$

Equation (C7) is proportional to the mean quadratic error, and the χ^2 fitting method converge to a simple least-squares fitting. It should be noted that this result holds only as far as $\delta y(x)$ is independent of x, and $|\delta y_i| \ll f(x_i \mid \boldsymbol{\theta})$. If for instance the relative error $\delta y_i / y_i$ is ergodic instead of δy_i, $\chi^2(\boldsymbol{\theta})$ is no longer related to the mean quadratic error. The minimization of $\chi^2(\boldsymbol{\theta})$ is performed by setting:

$$\partial \chi^2(\boldsymbol{\theta}) / \partial \theta_i = 0 \quad , i = 1 \ldots k \tag{C8}$$

The estimate $\hat{\boldsymbol{\theta}}$ is a solution of (C8). The variance $\operatorname{var} \hat{\boldsymbol{\theta}}$ of $\boldsymbol{\theta}$ is obtained by linearizing (C8) for $\boldsymbol{\theta} \rightarrow \hat{\boldsymbol{\theta}}$:

$$\begin{aligned} &\operatorname{var} \mathbf{p} = [\mathbf{J}^{\mathrm{T}} \mathbf{J}]^{-1} (\mathbf{J}\, \mathbf{y}) \\ &\mathbf{J} = [\mathbf{J}_1, \ldots, \mathbf{J}_n]^{\mathrm{T}} \quad , \mathbf{y} = [\delta y_1^2, \ldots, \delta y_n^2] \\ &\mathbf{J}_i = [J_{i1}^2, \ldots, J_{ik}^2] \quad , J_{ij} = \frac{\partial f(x_i \mid \boldsymbol{\theta})}{\partial p_j} \end{aligned} \tag{C9}$$

If $\mathbf{y}$ is ergodic and the measuring points are equally spaced, (C9) can be conveniently approximated with integrals:

$$\begin{aligned} &\operatorname{var} \mathbf{p} = \Delta x (\delta y)^2 \boldsymbol{\Psi}^{-1} \boldsymbol{\Lambda} \\ &\boldsymbol{\Psi} = [\boldsymbol{\Psi}_1, \ldots, \boldsymbol{\Psi}_k]^{\mathrm{T}} \quad , \boldsymbol{\Psi}_i = [\Psi_{i1}^2, \ldots, \Psi_{ik}^2] \quad , \boldsymbol{\Lambda} = [\Psi_{11}, \ldots, \Psi_{kk}] \\ &\Psi_{ij} = \int_X \frac{\partial f(x \mid \boldsymbol{\theta})}{\partial p_i} \frac{\partial f(x \mid \boldsymbol{\theta})}{\partial p_j} \, \mathrm{d}x \end{aligned} \tag{C10}$$

A particularly simple case of (C10) is equation (9), where only one parameter is optimized ($\boldsymbol{\theta} = \theta$).

Seite Leer /
Blank leaf

Chapter 4

Characterization of individual magnetic components by analysis of remanence curves,

1. Unmixing natural sediments

This paper has been submitted to *Studia Geophysica et Geodaetica*.

Seite Leer /
Blank leaf

" *Panta rei* "

Heraclitus of Ephesus (535-475 B.C.)

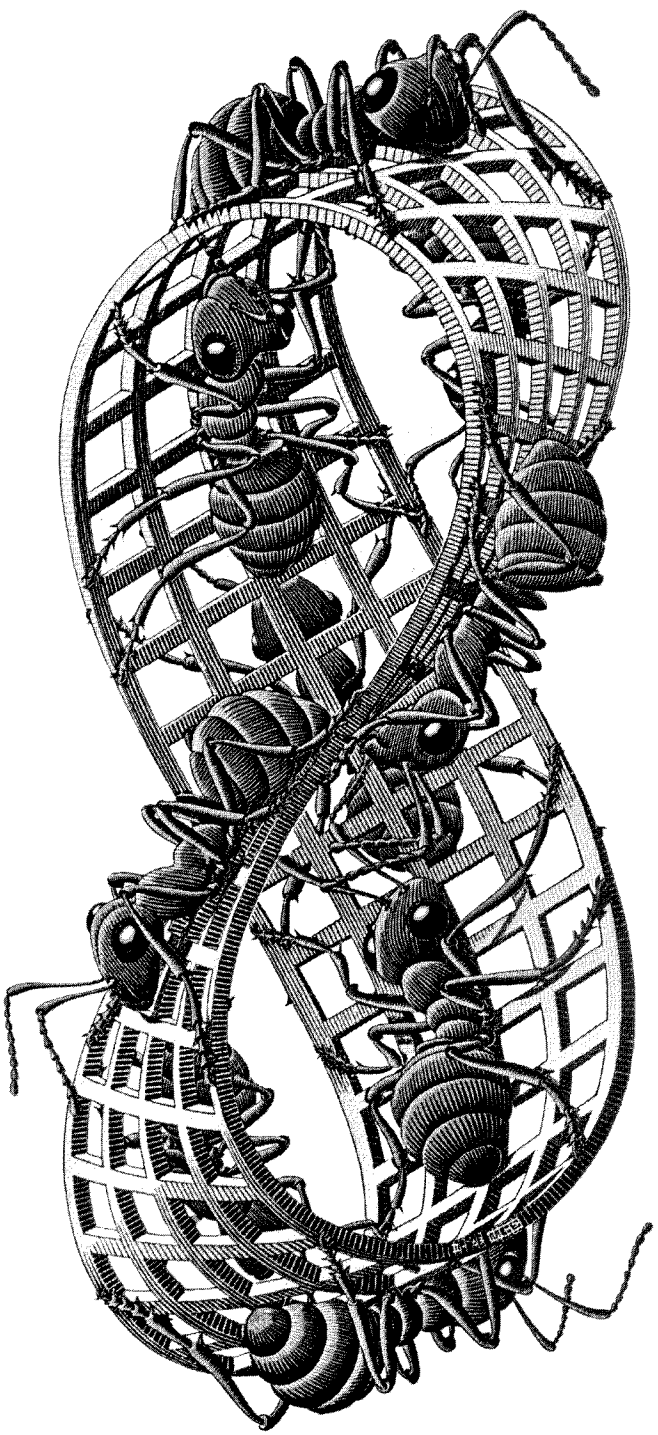

Maurits Cornelis Escher: *Moebius band II*, xylography (1963)

Characterization of individual rock magnetic components by analysis of remanence curves, 1. Unmixing natural sediments

R. Egli
Institut für Geophysik, ETH Hönggerberg, Zürich, Switzerland.

Natural sediments are a complex mixture of magnetic minerals with different origin and different geochemical history, each of which is called a magnetic component. Magnetic components practically never occur in isolated form, and their characterization using bulk magnetic measurements relies on the individuation of the systematic variation of some parameters within a large group of samples. These variations can be interpreted either as a mixing trend or as the result of natural processes, which affect the physical and chemical properties of the magnetic particles. An alternative approach is offered by the analysis of magnetization curves using model functions, which are supposed to represent the magnetic properties of individual components. The success of this approach relies on (1) the accurate choice of model functions, which are effectively able to reproduce the natural properties of a component with sufficient accuracy by varying a minimum number of parameters and (2) on very precise and accurate measurements, which are necessary to overcome the extreme sensitivity of the method to noise. In this paper, the analysis of remanent magnetization curves proposed by *Egli* [2003] is applied to a large set of representative sediments from the most variable environments and to a set of artificial magnetite samples. Despite the variety of materials and natural processes involved in the formation of these sediments, few groups of magnetic components with well-defined and consistent properties could be identified. It has been found that both lacustrine and marine sediments contain two magnetically distinct groups of magnetosomes, which react differently to changes of the redox potential. The effects of some natural processes, such as weathering, and reductive dissolution could be observed on the individual components.

KEYWORDS: magnetite, magnetic mixtures, component analysis, biogenic magnetite.

1. Introduction

The determination of different magnetic mineral sources in sediments, in the following called magnetic components, is an important task in environmental magnetism. Chemical and physical processes, which affect the magnetic properties of these components, are often related to the climatic conditions during sedimentation. This relation has been studied in marine and lacustrine sediments, and in loess deposits [*Verosub and Roberts*, 1995]. Furthermore, human activities constitute an additional source of magnetic components, which can be used for pollution monitoring [*Petrovský and Ellwood*, 1999].

The characterization of magnetic iron spinels in natural rocks and sediments relies often on grain-size related magnetic parameters, i. e. the modified Lowrie-Fuller test [*Johnson et al.*, 1975], the Day plot [*Day et al.*, 1977; *Dunlop*, 2002], the King plot and related plots [*King et al.*, 1982; *Oldfield*, 1994] and crossover plots [*Symons and Cioppa*, 2000]. These parameters are sometimes ambiguous: for example, results of the Day plot which are typical for pseudo-single domain grains have recently been simulated with viscous particles [*Lanci and Kent*, 2003]. The grain-size dependence of magnetic parameters has been calibrated using synthetic samples of sized magnetic materials [*Gillingham and Stacey*, 1971; *Levi and Merrill*, 1976; *Day et al.*, 1977; *Dankers*, 1978; *Harstra*, 1982; *Bailey and Dunlop*, 1983; *Dunlop*, 1986a; *Schmidbauer and Schembra*, 1987; *Heider et al.*, 1992; *de Boer and Dekkers*, 1996; *Heider et al.*, 1996; *Dunlop and Argyle*, 1997; *Halgedahl*, 1998]. However, artificial samples may have different magnetic properties compared to those of similar magnetic grains in sediments. The magnetic properties of artificial samples depend often on the preparation method, and some parameters, like coercivity and anhysteretic remanent magnetization (ARM), are sensitive to magnetostatic interactions between the grains [*Sugiura*, 1979; *Dankers and Sugiura*, 1981, *Yamazaki*, 1997]. Furthermore, weathering processes in sediments and rocks are an additional factor that affects the magnetic properties of natural minerals [*Johnson and Merrill*, 1972; *van Velzen and Zijderveld*, 1995, *Smirnov and Tarduno*, 2000]. The variation of bulk magnetic parameters can always be interpreted as environment-controlled grain size changes of a mineral source as well as a mixing trend of materials from different sources [e. g. *King et al.*, 1982; *Leslie et al.*, 1990; *Geiss and Banerjee*, 1997].

In so-called multi-component mixing models, sediment is considered as a mixture of two or more magnetic components, called also end-members, with different magnetic properties. According to *Thompson* [1986], each component can be linked to a particular source material (mass mixing model, e.g. *Hilton* [1987]) or to a particular mineral (crystal mixing, e.g. *Carter-Stiglitz et al.* [2001]). Multivariate statistics is used to express a set of measured magnetic parameters as a weighted combination of components [*Yu and Oldfield*, 1989]. An important limiting factor of multi-component mixing models is the unknown variability of the individual components, which may arise from the source material itself or from mechanical and chemical processes that alter the magnetic particles during transportation and after deposition. A

systematic investigation of these processes with magnetic bulk measurements is difficult because isolated components are rare in natural samples.

In principle, the problem posed by the variability of single components is overcome by modelling hysteresis loops [*von Dobeneck*, 1996] or acquisition/demagnetization curves of remanent magnetization [*Robertson and France*, 1994] using appropriate model functions. The magnetic contribution of each component is modelled with a parameterized function, generally a cumulative log-Gaussian function (CLG). The variation of the function parameters generates a variety of different curves, which are expected to reproduce the acquisition/demagnetization curve of each component. A mixture of components is modelled using a linear combination of model functions, whose parameters are varied until the difference between the measured and the modelled curve is minimal (minimization procedure). This method has the advantage of avoiding any assumption about the magnetic properties of individual components. Later developments of this method were concerned with the minimization procedure [*Stockhausen*, 1998; *Heslop et al.*, 2002], and the significance of the model, depending on the number of model functions used [*Kruiver et al.*, 2001]. Despite the intriguing flexibility of this method, some limitations might be encountered when attempting to analyze mixtures with highly overlapping coercivity distributions. Furthermore, the use of CLG model functions is not always justified, as demonstrated by *Egli* [2003] on lake sediments and dust samples. *Heslop et al.* [2003] came to the same conclusion by moelling acquisition curves of isothermal remanent magnetization (IRM) with a temperature dependant Preisach-Néel model. Therefore, more general model functions have been introduced, which fit accurately the shape of acquisition/demagnetization curves of individual components [*Egli*, 2003].

A controversial limitation, which may affect multi-component mixing models as well as the analysis of magnetization curves, is given by the assumption that the magnetic contributions of individual components add linearly (linear additivity). Some experiments with artificial mixtures did not show a perfect additivity of some magnetic parameters [*Lees*, 1997], presumably because of magnetostatic interactions. However, other authors obtained linear additivity with artificial mixtures, when avoiding the clumping of grains from different components during sample preparation [*Carter-Stiglitz et al.*, 2001]. *Yu et al.* [2002] reported the linear additivity of partial anhysteretic remanent magnetizations (ARM) in artificial and natural samples. Strong magnetic interactions between different components are not expected in sediments since natural processes are efficient in dispersing small magnetic grains, which are generally attached to large clay minerals. Alternatively, new minerals may grow within the nonmagnetic matrix of sediment. The matrix holds them in a fixed position and avoids the formation of clumps with already existing magnetic grains. Alteration processes, where a magnetic mineral is transformed into another magnetic mineral and both are in close contact, give an exception.

The above discussion suggests the fundamental importance of a detailed and systematic investigation of the magnetic properties of natural components and their variability, as well as the quantification of the effects induced by geochemical processes. This is the scope of the present paper, which presents the results of a detailed investigation carried out on 45 representative samples of lacustrine and marine sediments, loesses, paleosols, recent soils, limestones, magnetotactic bacteria and atmospheric particulate matter. These results are compared with the magnetic properties of 23 artificial magnetite samples, collected from the literature. The low-coercivity magnetic components identified in the natural samples are divided into seven groups according to their magnetic properties. Each group is linked to one of the following processes: airborne- and water-transport, weathering, reductive dissolution, authigenesis, bacterial activity, human activity.

2. Samples

In the following, a brief description of the measured samples and their preparation is given.

2.1. Lake sediments

Lake sediment samples have been collected from three lakes: Baldeggersee and lake Geneva, both in Switzerland, and lake Aral (Uzbekistan/Kazakstan).

A description of Baldeggersee is given by *Wehrli et al.* [1997]. Sediments from Baldeggersee are characterized by a high carbonate content (up to 60%) and the alternation of four main lithologies: (1) brown to dark brown sediments with biogenic varves; (2) light brown sediments with large couplets of lighter and darker layers; (3) homogeneous gray marl beds; (4) turbidite layers [*Lotter et al.*, 1997; *Schaller et al.*, 1997]. Late glacial sediments are made of clastic material (sand and silt). Packets of varved sediments indicate that the hypolymnium of Baldeggersee experienced periods of anoxic conditions long before the onset of anthropogenically induced eutrophication, started in 1885. An artificial aeration system was installed in 1982 at the bottom of the lake in order to reduce the degree of anoxia and restore mesotrophic conditions. A 1.2 m long gravity core (core G) was taken in 1999 at the center of the lake and sampled every centimeter [*Egli*, 2003]. The samples of this core are labeled with 'GXXX', XXX being the depth in cm from the top. A 9 m long piston core (core BA) was taken approximately from the same site of core G in the year 2000. This core covers the last 7000 years and was immediately sampled in slabs with a variable thickness (2 mm to 1 cm), depending on the lithological features. The slabs were freeze-dried and pressed into cylindrical boxes. The samples are labeled with 'BAX-YY', X being the section number of the core (each section has a unit length of 1 m, starting from section 1 on the top) and YY the depth from the top of each section, in centimeters. Earlier piston cores, taken in 1995 and 1997, cover the entire Holocene sedimentation period, and contain late-glacial sediments on the

bottom. These cores are labeled as BAL, and their samples with 'BALX-YY', with the same code as the BA samples. All cores were taken by the EAWAG (Swiss Federal Institute for Environmental Science and Technology). In this paper, several samples from the four main lithologies have been analyzed.

Lake Geneva has been described in detail by *Baster* [2002]. Susceptibility measurements on a sediment core allowed the identification of three main units, with (1) relatively high values at the bottom ($\sim 2\times10^{-5}$ SI); (2) low, constant values in the middle part ($\sim 7\times10^{-6}$ SI); and (3) isolated peaks of very high susceptibility corresponding to thin terrigenous layers [*Baster*, 2002]. Three representative samples have been chosen for further analysis in this paper: LGL, LGN and LGS (courtesy of I. Baster). Sample LGL was taken from the bottom part of the core (784 cm from the top). The lithology of this Late Glacial sediment is characterized by an alternation of gray and yellow laminae of very thin fine sand to silt (rhythmites). The gray laminae are graded and are texturally similar to underflow deposits described in modern proglacial environments. The ungraded yellow laminae have been interpreted as aeolian deposits, which were deposited on the bottom of the lake during ice melting [*Baster*, 2002]. Sample LGN was taken from the middle part of the core (510 cm from the top), and is characterized by greenish-gray clayey silts with several dark layers. Sample LGS was taken in a susceptibility peak at 350 cm, and contains a brown terrigenous rich layer.

Two samples, AR6 and AR23, from piston cores taken in the Aral Sea (Uzbekistan/Kazakstan) have been analyzed as well (courtesy of D. Nourgaliev). The Aral Sea is a rapidly desiccating lake located in the lowlands of Turan. It forms a closed system with main water input from two rivers and no outflow. The Aral Sea experienced several desiccation events in the past [*Nourgaliev et al.*, 2003]. Sample AR6 is a dark brown sediment, which rapidly oxidized in air, while sample AR23 has a more stable greenish-gray color. Both samples were freeze-dried after arrival in Zürich, two month after drilling, and pressed into cylindrical plastic boxes.

2.2. Sediments from the catchment area of Baldeggersee

In order to characterize the detrital input of Baldeggersee, samples were collected from its relatively homogeneous catchment (BALGR and BALWD), and from a small delta formed by one of several small tributaries (U03F). Samples BALGR and BALWD contain material from eroded soils of hill slopes covered by grass and forest, respectively. The samples have been sieved to separate the < 50 μm fraction, which was pressed into cylindrical plastic boxes. The preparation of sample U03F is described in *Egli* [2003].

2.3. Marine sediments and limestones

Two marine sediments from ODP have been kindly provided by M. Fuller and are described in *Fuller et al.* [2002]. The first sample, called here ODPB, is the ODP sediment 1128B-3H-2,

47-49 from Leg 182 in the Great Australian Bight. It is a deep-water pelagic carbonate, which contains biogenic magnetite [*Fuller et al.*, 2002]. The second sample, called here ODPD, is the ODP sediment 1199A-2H3 from Leg 194 on the Marion plateau of NE Australia. It is a dolomitic floatstone with large rhodoliths. A secondary natural remanent magnetization (NRM) was detected in this sample, probably associated with dolomitization [*Fuller et al.*, 2002].

Two pelagic limestones of the Scaglia Bianca formation in the Umbria-Marche Basin, Italy, have been kindly provided by G. Muttoni. This formation shows a striking lithological cyclicity related to the Milankovitch orbital cycles [*De Boer*, 1983; *Erba and Walsworth-Bell*, 2001]. This cyclicity is also evident from magnetic measurements: the IRM oscillates between minimum and maximum values with a saw-tooth pattern (G. Muttoni, personal communication). The two samples, SCBB and SCBD, have been chosen in correspondence to a maximum of the IRM (SCBB), respectively a minimum (SCBD) within the same cycle.

2.4. Loesses, paleosols, red clays and modern soils

Representative samples for a well-developed paleosol (SPS3) and a red clay (RCL) from the Central Chinese Loess Plateau [*Spassov et al.*, in press], have been provided by S. Spassov. Representative samples of a pristine loess (BY55) and a well-developed modern soil (M5A), both from the Western Chinese Loess Plateau, have been kindly provided by F. Heller. A detailed investigation of BY52, a loess sample similar to BY55, demonstrated its low degree of alteration [*Evans and Heller*, 1994].

2.5. Atmospheric particulate matter

Samples of atmospheric particulate matter < 10 μm (called PM10 in the following) have been taken in the region of Zürich (Switzerland). The sampling procedure is described in *Egli* [2003]. Heavy industries are absent from the region, and the heating systems of buildings were not working during the sampling period. Under these conditions, the major sources of urban PM in the city center of Zürich are motor vehicles [*Hüglin*, 2000]. Sample GMA was taken in a green area adjacent to the paleomagnetic laboratory of the ETH, outside the city of Zürich. The area is located far away from any heavily used road and a small amount of urban pollution is therefore expected to be found in this sample. The measured daily mean PM10 concentration was 14 $\mu g/m^3$. Sample KSN was taken in a park near the city center of Zürich, where the daily mean PM10 concentration was 24.5 $\mu g/m^3$. Sample WDK was taken in the city center of Zürich near a very busy road (Wiedikon). The daily mean PM10 concentration was 66 $\mu g/m^3$, and a large amount of pollution produced by motor vehicles is expected. Sample GUB was taken inside a 3.5 km long highway tunnel near Zürich (Gubrist tunnel). The pollution by motor vehicles is expected to be highest in this sample, with a daily mean PM10 concentration of 91 $\mu g/m^3$. Sample MBH was taken along the braking tract of an

underground railway stop in the city center of Zürich. A magnetic contribution from metallic dust produced by the friction of the brakes in expected in this sample.

2.6. Data collected from the literature

Samples that are known to contain only one magnetic component, do not require high-precision measurements for a successful component analysis. Therefore, data from the literature have been collected to characterize samples of cultured bacterial magnetite and synthetic magnetites. Unfortunately, the reported measurements are incomplete in some cases.

Data for the freshwater magnetotactic bacterium *Magnetospirillum Magetotacticum* have been collected from *Moskowitz et al.* [1988] and *Penninga et al.* [1995]. *M. Magnetotacticum* contains a single chain of 10-20 magnetosomes with an average linear dimension of 40-50 nm. The alternating field (AF) demagnetization curve of IRM, and the ratio of the susceptibility of ARM to the IRM for the marine vibroid strain MV1 have been measured by *Moskowitz et al.* [1993]. MV1 produces chains of up to 20 magnetosomes with average dimensions of $53 \times 35 \times 35$ nm. Backfield demagnetization curves for an uncharacterized magnetotactic curved rod (MR) and a many-celled magnetotactic prokaryote (MMP) have been reported by *Penninga et al.* [1995]. MR contains two or more adjacent chains of greigite-containing magnetosomes. The magnetic properties of magnetite particles produced by the dissimilatory iron reducer *Geobacter metallireducens* (GS15) were studied by *Moskowitz et al.* [1993] and *Lovley et al.* [1987]. The grain size distribution of the GS15 magnetite is broad and depends on biogeochemical conditions; typical mean values are 12-15 nm [*Sparks et al.*, 1990]. GS15 is an obligate anaerobe, and produces 5000 times more magnetite by weight than the equivalent biomass of magnetotactic bacteria, however, only few % of this magnetite is able to retain a remanent magnetization.

Data for artificial magnetite samples have been collected from *Levi and Merrill* [1976], *Dankers* [1978], *Bailey and Dunlop* [1983] and *Halgedahl* [1998], which measured detailed AF demagnetization curves of ARM and IRM. Additionally, results for sample CS914 from the Yucca Mountain Tuff have been considered as well [*Worm and Jackson*, 1999; *Egli and Lowrie*, 2002]. This sample, called YU in this paper, contains well-dispersed magnetite grains with a mean diameter of 21 nm. A part of the grain size distribution falls into the SD range and is an ideal reference for weakly interacting SD magnetite.

Clusters of close-packed particles can easily form during sample preparation from powders of pure magnetite. Within this clusters, magnetotstatic interactions are strong and affect the magnetic properties, especially those related to the ARM [*Sugiura*, 1978]. Therefore, interaction effects are expected for all synthetic magnetites and the GS15 sample. Chains of magnetosomes are separated by the cell bodies, which avoid their collapse, and samples of cultured magnetotactic bacteria are therefore expected to be a representative analogue of the bacterial magnetite in natural sediments.

3. Measurement of AF demagnetization curves

The characterization of the magnetic components is based mainly on detailed AF demagnetization curves of both ARM and IRM. Great care was taken to ensure an extremely high precision and reproducibility of the experiments, which are necessary for the analysis of the demagnetization curves described later on. The experiments have been performed using a 2G cryogenic magnetometer and a 2G in-line degausser coil. Some preliminary checks were performed on the calibration of the degausser unit (AF field and bias field), and on the transport unit, to ensure optimal measuring and degaussing positions. The degaussing position is particularly critical, because the region where the field is homogeneous is only as big as a standard paleomagnetic sample. Fluctuations of the degaussing position have been shown to produce a decrease in the quality of the demagnetization curves, which is not noticeable with standard paleomagnetic measurements, but becomes evident when small demagnetization steps are used (1-2 mT). Therefore, a spring was installed to hold the 2G transport system under constant tension and stabilize the degaussing position.

First, each sample was demagnetized along three orthogonal axes with a maximum AF peak field of 300 mT. Then, an ARM was imparted along the *z*-axis, in a 0.1 mT bias field. The maximum peak field was 300 mT, and the AF field decay rate 4 mT/s. After removing the sample and switching off the bias field, the sample holder was AF demagnetized with 300 mT. This step ensured a demagnetization of the coil shield as well. After two minutes, automatic stepwise AF demagnetization was started. The two minutes waiting time ensured an exact reproducibility of the experiment by removing always the same amount of possible viscous component. The AF demagnetization was performed with 76 steps of increasing field intensity along the direction of the ARM (Figure 1). The steps have been chosen to be evenly distributed on a logarithmic scale (0-20 mT every 1 mT, 21.5-26 mT every 1.5 mT, 28-72 mT every 2 mT, 74-80 mT every 3 mT, 85-150 mT every 5 mT, 156 mT, 163 mT, 170-190 mT every 10 mT, 200-260 mT every 15 mT, 280 mT and 300 mT). The *z*-axis reading of the magnetometer with 5 digits was taken as a measure of the magnetization after each demagnetization step. The 5 digits reading was necessary to ensure a good resolution of the demagnetization curve at small fields (0-5 mT), especially with samples rich in bacterial magnetite, which may loose as little as 0.03% of the original ARM at 1 mT. Many measuring programs take only 3 digits from the magnetometer readings, as AUTOCORE in our laboratory does, and a modification of the program was necessary.

The entire procedure of ARM acquisition and demagnetization was repeated 6 times for each sample, and 9 times for weak samples, in order to increase the experimental precision. By comparison of the 6 or 9 measurements, occasionally occurring outliers could be removed, typically 1-2 steps for each measurement. These outliers were probably produced by the interference of the main power with the degaussing unit or the magnetometer. The arithmetic mean of the 'cleaned' measurements was finally taken as a demagnetization curve.

After the ARM measurements, a 300 mT IRM was imparted along the *z*-axis using an electromagnet. Higher fields were not used, in order to avoid the magnetization of grains, which have not been magnetized with the ARM. After two minutes permanence in a shielded room, the sample was demagnetized with the same procedure as for the ARM. The IRM acquisition was repeated 6 times for each sample, including the weak samples. The IRM measurements were also cleaned and averaged, as for the ARM.

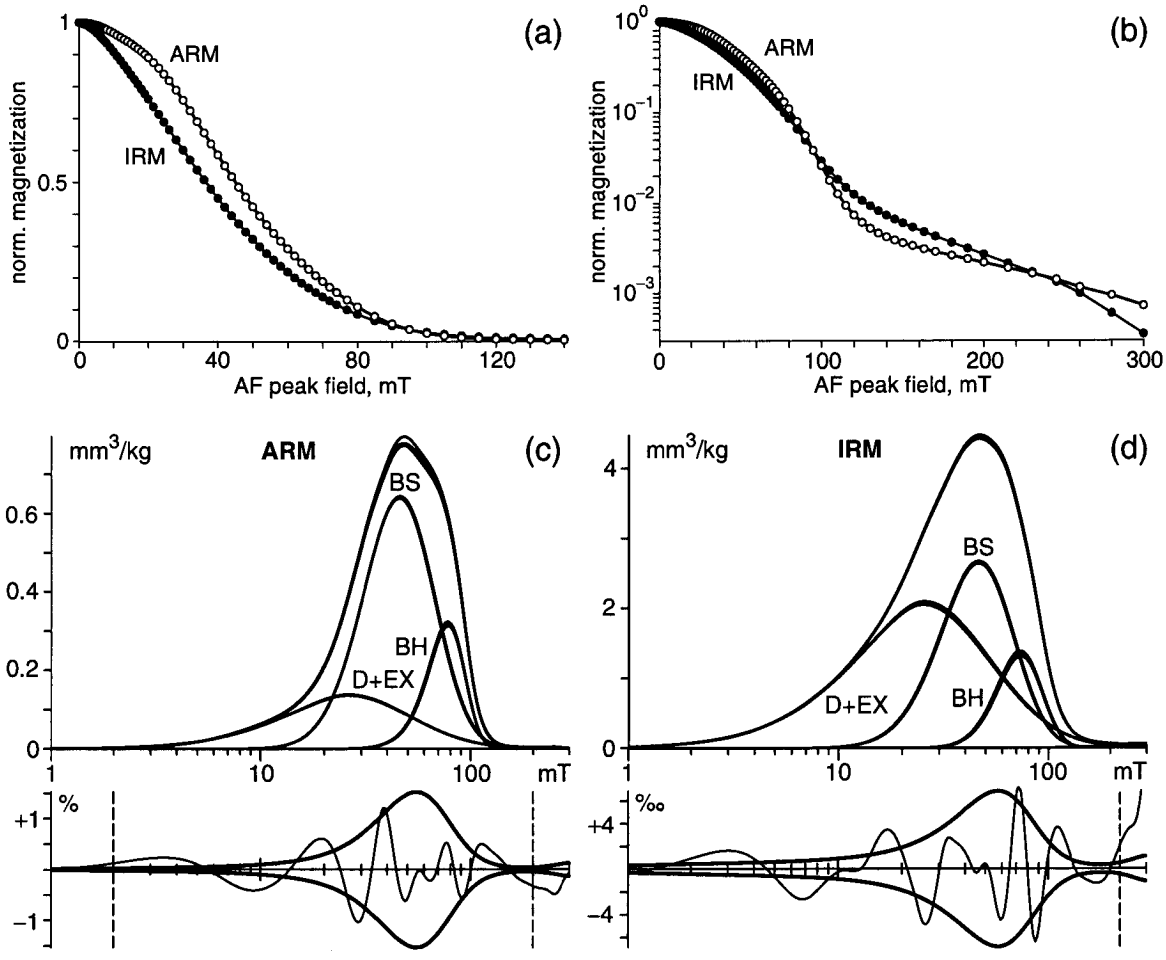

Figure 1. *Example of analysis of AF demagnetization curves (sample G034). (a) Normalized AF demagnetization curves of ARM and IRM. (b) Same as (a), with the magnetization plotted on a logarithmic scale. The presence of more than one magnetic component can be recognized from the slope change of the curves around* 120 mT. *(c,d) Coercivity distributions of ARM and IRM calculated with CODICA, and the result of a component analysis with SGG functions performed with GECA. The coercivity distributions of the isolated magnetic components are labelled with D+EX, BS and BH (see text). All coercivity distributions are plotted together with their confidence limits (thick lines). Below each plot, the estimated error of the sample's coercivity distribution (thick pair of lines) and the difference between this coercivity distribution and the corresponding model (thin line).The range considered for component analysis is limited by the vertical dashed lines.*

The measurement of each demagnetization curve required two hours, and the complete measurement of a sample lasted three days. An example of typical measurement is reported in Fig. 1a. Notice that even if the sample is apparently demagnetized at 120 mT, there is still a small but significant magnetization component, which is evident on the logarithmic plot of Fig. 1b. The demagnetization curves of most samples cover more than three orders of magnitude.

4. Analysis of AF demagnetization curves

The AF demagnetization curves have been analyzed using the method described in *Egli* [2003].

4.1. Coercivity distributions

A coercivity distribution is calculated as the first derivative of the demagnetization curve. This step is performed using CODICA (COercivity DIstribution Analyzer), a dedicated computer program that removes the measurement errors by rescaling and filtering the demagnetization curves [*Egli*, 2003]. It also performs an error estimation, and gives the confidence limits of the calculated coercivity distribution and the maximum number N of independent parameters that define the shape of the curve. The latter is important because it limits the number of model parameters that can be used for component analysis. Coercivity distributions can be calculated on different field scales: a $\log_{10}$ scale has been used for all samples. The scaled field x is given by $x = \log H$, being H the unscaled field.

4.2. Skewed generalized Gaussian functions

The resulting coercivity distribution is modelled using a linear combination of so-called skewed generalized Gaussian distribution functions (SGG), defined as:

$$SGG(x,\mu,\sigma,q,p) = \frac{1}{2^{1+1/p}\sigma\,\Gamma(1+1/p)} \frac{\left|qe^{qx'} + q^{-1}e^{x'/q}\right|}{e^{qx'} + e^{x'/q}} \exp\left[-\frac{1}{2}\left|\ln\left(\frac{e^{qx'} + e^{x'/q}}{2}\right)\right|^{p}\right] \qquad (1)$$

with $x' = (x-\mu)/\sigma$, $0 < |q| \leq 1$ and $p > 0$ [*Egli*, 2003]. The shape of this function depends on the four parameters μ, σ, q and p, where 10^{μ} is identical with the median destructive field (MDF) of the demagnetization curve, σ is related to the standard deviation of the distribution, also called dispersion parameter (DP), q is related to the skewness and p to the kurtosis of the distribution. A Gaussian function is a particular SGG with $q = 1$ and $p = 2$. Symmetrical functions are characterized by $q = 1$, left-skewed functions by $0 < q < 1$ and right-skewed functions by $-1 < q < 0$. More squared functions can be obtained with $p > 2$, less squared with $0 < p < 2$. The shape of a SGG function can be

adapted to every kind of real coercivity distribution by choosing a suitable set of parameters. The relations between σ, q, p on one side, and DP, skewness and kurtosis on the other, is not analytical: approximations are given in *Egli* [2003].

Each coercivity distribution calculated using CODICA was then analyzed with GECA (Generalized Coercivity Analyzer). GECA is a computer program that allows modelling a coercivity distribution with a linear combination of up to four SGG functions. Starting from a set of initial parameters entered by the user for each SGG function, GECA minimizes the difference between modelled and measured coercivity distribution, expressed by a χ^2 estimator, by using a Levenberg-Marquardt algorithm embedded in the software *Mathematica* [*Ratkowsky*, 1983]. It also performs a Pearson's χ^2 goodness-of-fit test to check whether the modelled and the measured distribution are different on a 95% significance level. In addition, the difference between model and measurements is plotted by GECA, together with the measurement error estimation. The user has a visual control over the model optimization performed by the program and can choose some model parameters to be kept constant during the optimization. For example, if $q = 1$ and $p = 2$ are kept constant by the user, GECA uses a Gaussian distribution as model function. A typical output of GECA is plotted in Fig. 1c,d. Other examples are given by *Egli* [2003].

4.3. Goodness of fit tests and free model parameters

The goodness of fit test is a valuable tool that allows the user to decide how many SGG functions are required to model the measurements: is a model based a on given number of SGG function significantly different from the measurements? The number of SGG functions is of fundamental importance in the final interpretation of the component analysis, since each SGG function is assumed to represent the contribution of a specific magnetic component. A SGG function is related to five model parameters: the four shape parameters μ, σ, q and p, and a fifth parameter a, which is the contribution of the coercivity distribution represented by this function to the total magnetization. Thus, the total number m_f of free model parameters is given by $m_f \leq 5n$, where n is the number of components. Additionally, there should not be more free model parameters than independent parameters of the coercivity distribution: $m_f \leq N$. The more SGG functions are included into the model, the more parameters can be adjusted to better approach the measured curve. Thus, the quality of the model is apparently increased. However, not all model parameters are significant if the difference between model and measurements becomes smaller than the measurement errors. As a general rule, a model is acceptable if (1) it does not pass a goodness-of-fit test because it is not significantly different from the measurements and (2) it will pass a goodness-of-fit test the number of free model parameters is reduced. In other words, the minimum amount of free model parameters is chosen, which gives a model that is compatible with the measurements [*Egli*, 2003].

4.4. Convergence of component analysis and multiple solutions

A possible problem of component analysis is represented by multiple solutions, which are equally possible from the mathematical point of view, although only one of them is real. Some unrealistic solutions can be immediately recognized because of the uncommon shape of the related SGG functions. Natural magnetic components should be modelled with $|q| > 0.5$ and $1.6 < p < 2.5$ [*Egli*, 2003]. In case of highly overlapping coercivity distributions, the identification of the correct solution may become impossible. In this case, a higher measurement precision or some additional information about the magnetic properties of one or more components are required. Additional information can be obtained from the measurement of a set of similar samples which contain a mixture of the same magnetic components in different amounts, as shown by *Egli* [2003] on samples of atmospheric particulate matter with different degrees of pollution.

Another important aspect of component analysis is the convergence to a solution. Convergence to a particular solution is possible if the starting parameters of the model are chosen to be close enough to the solution. The choice of the starting parameters is based on a hypothetical model for the magnetic composition of the sample, which is based on sedimentological observations and on the comparison of different coercivity distributions (see section 4.6). The more free parameters are included into the model, the more unpredictable is the convergence behaviour, and distinct solutions can be obtained with relatively small changes of the starting parameters. Convergence to a particular solution can be more easily obtained if some parameters are kept fixed during the first running. The parameters of a SGG function can be ranked according to their meaning. The parameter a is the most important because it represents the magnetic contribution of the corresponding component, followed by μ, which is related to the coercivity. The width of the distribution is controlled by σ, and its symmetry by q. The least important parameter, p, influences the squareness. According to this ranking, only the magnetic contribution a of all components is optimized during a first run. Then, a and μ are optimized, and so on, whereby the model approaches progressively the measured curve. New free parameters are added until the Pearson's goodness of fit test gives a negative result, being the model not significantly different from the measurements. If the Pearson's goodness of fit test is still positive after all parameters have been optimized, a new component is added to the model. New, plausible starting values have to be chosen, and less important parameters are kept fixed during the first runs. The procedure described above has been adopted to perform the component analysis of the samples presented in this paper.

4.5. Error estimation

An analytical error estimation of the model parameters is impossible to perform, except for some simple cases; useful approximations are given in *Egli* [2003]. The error of a model parameter depends not only on the measurement error: in fact, the correlation with other parame-

ters plays an important rule. The more similar are the coercivity distributions of two components, the more their parameters are correlated and the resulting errors become larger. As a consequence, magnetic components with highly overlapping coercivity distributions are difficult to unmix and require accurate measurements. Therefore, a lot of care was taken to obtain the maximum measurement precision with the present laboratory instrumentation. GECA estimates the error of each free model parameter by adding an artificial noise signal to the coercivity distribution, whose amplitude corresponds to the measurement errors estimated by CODICA. The component analysis is performed again on the "noisy" coercivity distribution and new model parameters are calculated. This operation is repeated several times, and a set of values is obtained for each model parameter. The double standard deviation of these values is taken as an estimation of the standard error of the corresponding parameter. This error estimation does not consider the possibility of a convergence to other solutions and should be regarded as a lower limit.

4.6. Component analysis of grouped samples

The following strategy has been adopted to perform a comparative analysis of all samples with uniform criteria.

(1) As a first step, the samples have been divided into the following categories: lake sediments and marine sediments from continental margins, pelagic sediments, limestones, recent soils, paleosols and red clays, loesses, atmospheric particulate matter. The samples of each category are supposed to contain similar magnetic components, which are produced by similar natural processes.

(2) Among the samples of each category, those with extreme properties have been analyzed first, because they are supposed to contain a predominant component. For example, individual bacterial components are already recognizable as distinct peaks of the coercivity distributions (Figure 1). The filtered coercivity distributions obtained with CODICA reveal a variety of details that are completely hidden in the AF demagnetization curve (Figure 1). These details give valuable information for the choice of the starting model parameters.

(3) A component analysis has been performed on this first set of samples according to the procedure described in 4.4. The smallest reasonable number of SGG functions was used first. The optimization of p was generally not necessary, except for the samples with a predominant component: in this case, p relative to this component has been optimized as well. Almost all samples contain a variable amount of high-coercivity antiferromagnets, probably hematite. Although these minerals have generally much higher coercivities than the maximal field of 300 mT used in the experiments, a small part of them has coercivites around 300 mT or smaller, as it can be deduced from IRM acquisition curves of sized hematites [*Thompson*, 1986]. Thus, a high-coercivity component, called component H (hard) in the following, has been included into the model. The coercivity distribution of this component is truncated at

300 mT. Truncated coercivity distributions of magnetite have been investigated with so-called Henkel plots by *Proksch and Moskowitz* [1994]: the shape of the truncated distributions is similar to the whole distribution, with smaller amplitude and different values of MDF and DP. A sharp discontinuity at the truncation field was not observed, independently from the degree of magnetostatic interactions between the particles. Therefore, component H can be modelled with a SGG function as well, like the untruncated components. Since the magnetic contribution of H is small in all samples with some few exceptions, and since its properties are uninteresting for this paper, the fixed parameters $q = 1$ and $p = 2$ have been used to model this component. The starting values of the other parameters were $\mu = 2.2$ and $\sigma = 0.2$. If the contribution of H was particularly small, typically $< 1\%$, μ and σ have been kept fixed as well. Convergence to an acceptable solution was easy to obtain for these samples, since at least one component can be easily identified. The results of the component analysis of these samples have been compared to check whether the same components with consistent magnetic properties could be identified in all selected samples.

(4) The component analysis was then extended to all samples of the same group, using the results obtained for the selected samples as starting parameters for the mixing model. The calculated errors for the model parameters are generally small, typically some few percent. Exceptions have been encountered in mixing models with an unusually high correlation between two or more model parameters. We refer to *Egli* [2003] for an extensive discussion about the parameter errors.

5. Characterization of individual magnetic components

The analysis of ARM and IRM coercivity distributions supply detailed information about the properties of the remanent magnetization of each component. This information is given by the distribution parameters a_{ARM}, μ_{ARM}, σ_{ARM}, q_{ARM}, p_{ARM} for the ARM, and a_{IRM}, μ_{IRM}, σ_{IRM}, q_{IRM}, p_{IRM} for the IRM, respectively. In this section, the relation between these parameters and traditional rock-magnetic measurements will be discussed.

5.1. Saturation ARM and IRM

Saturation ARM (SARM) and saturation IRM (SIRM) refer to ARM and IRM acquired in a maximal field that is sufficient to saturate all magnetic grains. Magnetite, maghemite [*de Boer and Dekkers*, 1996] and greigite [*Dekkers and Schoonen*, 1996] saturate at or below 300 mT. Partially oxidized magnetite may not be entirely saturated at 300 mT [*van Velzen and Dekkers*, 1999]. Therefore, it is possible to model all magnetite, maghemite and gregite components according section 4. Only a very small part of the right tail of their coercivity distributions may be truncated at 300 mT, without consequences for the results of component analy-

sis. Therefore, $a_{\mathrm{ARM}} = \mathrm{SARM}$ and $a_{\mathrm{IRM}} = \mathrm{SIRM}$ can be assumed, and SARM (SIRM) are identical with ARM (IRM) in the following.

5.2. Susceptibility of ARM

The ratio of the susceptibility of ARM to the IRM, k_{ARM}/IRM, is called ARM ratio in the following. The ARM ratio and its reciprocal value have been used as a grain-size indicator [*Oldfield*, 1994; *Yu and Oldfield*, 1989; *Maher*, 1988]. For a single magnetic component $k_{\mathrm{ARM}}/IRM = a_{\mathrm{ARM}}/(a_{\mathrm{IRM}}H_{\mathrm{DC}})$, where H_{DC} is the bias field used for the ARM. High values of k_{ARM}/IRM, around 2-3 mm/A, are characteristic for intact magnetosome chains produced by cultured magnetotactic bacteria [*Moskowitz et al.*, 1993]. A slightly smaller value of 1.4 mm/A has been reported for lake sediments with a high concentration of bacterial magnetite [*Snowball et al.*, 2002]. Synthetic magnetite is characterized by $k_{\mathrm{ARM}}/IRM < 1.8\ \mathrm{mm/A}$. These values, however, are affected by magnetostatic interactions [*Yamazaki*, 1997]. The ARM ratio was successfully used in combination with other magnetic parameters to discriminate different magnetic components in dusts [*Hesse*, 1997], fly ash contaminated dusts [*Oldfield et al.*, 1985], near-shore marine sediments [*Oldfield*, 1994] and magnetite dissolution [*Leslie et al.*, 1990].

The ARM acquisition of non-interacting single domain particles was studied by *Egli and Lowrie* [2002]. They predicted $k_{\mathrm{ARM}}/IRM \propto d^2$, $d < 60\ \mathrm{nm}$ being the grain size, and give values of k_{ARM}/IRM ranging from 0.2 to 3.7 mm/A for typical SD magnetite. The experimental grain size dependence of k_{ARM} for synthetic magnetite samples is discussed in *Egli and Lowrie* [2002]. After reaching its maximum at $d \approx 50\ \mathrm{nm}$, $k_{\mathrm{ARM}} \propto d^{-1}$ between 50 nm and the upper limit for SD remanence, 200 nm. Using $M_{\mathrm{rs}}/M_{\mathrm{s}} \propto d^{-0.5}$ as empirical grain size dependence of the remamence ratio [*Dunlop*, 1986b], $k_{\mathrm{ARM}}/IRM \propto d^{-0.5}$ is obtained between 50 and 200 nm. The grain size dependence of k_{ARM}/IRM is not well known for larger particles. *King et al.* [1983] reported a minimum at $d \approx 2\ \mu\mathrm{m}$ for synthetic samples, followed by an increase toward multidomain grains, which has also been observed by *Gillingham and Stacey* [1971]. However, it is not known how far these results are influenced by a grain size dependence of magnetostatic interactions.

5.3. Median destructive field

The MDF of a single component is simply given by $10^{\mu_{\mathrm{ARM}}}$ or $10^{\mu_{\mathrm{IRM}}}$, and is related to the mean switching field of the magnetic particles. The MDF of IRM belongs to a group of parameters related to the coercivity of remanence H_{cr} [*Fabian and von Dobeneck*, 1997]. Because of thermal activation effects, remanence coercivity parameters are time-dependent, specially for ultrafine magnetic grains [*Dunlop and West*, 1969]. For this reason, μ_{IRM} may depend on the number of steps used for the measurement of a demagnetization curve. However, during AF demagnetization, the switching field of individual particles is

approached slowly. For comparison, the time-dependence of H_{cr} in marine sediments could be detected only on a ms time scale [*Smirnov and Tarduno*, 2001]. Therefore, AF demagnetization curves are independent of the number of demagnetization steps used.

5.4. Dispersion parameter

The dispersion parameter DP of a SGG function is controlled mainly by σ, and $DP = \sigma$ for $q = 1$. GECA calculates the dispersion parameter numerically for each component. The dispersion parameter is not a classic parameter in rock-magnetism, because its definition is related to a coercivity distribution, rather than to the corresponding magnetization curve. A set of identical magnetic particles has an extremely narrow coercivity distribution, with values of DP as low as 0.05 for ideal Stoner-Wohlfarth particles [*Robertson and France*, 1994]. On the other hand, $DP = 0.2...0.5$ for synthetic samples of sized magnetite, $DP = 0.3...0.4$ for magnetite particles of detrital origin and natural dusts, and $DP = 0.1...0.2$ for bacterial magnetite [*Kruiver and Passier*, 2001; *Egli*, 2003]. Therefore, the DP of synthetic and natural magnetic particles reflects a distribution of microcoercivities. The microcoercivity of a magnetic grain is controlled by several factors, i. e. grain size and shape [*Kneller and Luborsky*, 1963], chemical composition, mechanical stress, concentration of crystal defects [*Xu and Dunlop*, 1995] and magnetostatic interactions [*Sprowl*, 1990]. *Fearon et al.* [1990] calculated some coercivity distributions of identical interacting particles, where $DP \approx 3.6\pi$, π being the packing density of the particles.

On the basis of these considerations, the DP of a coercivity distribution can be interpreted as a measure of the variability of the physical and chemical processes that affect the grain microcoercivity. A magnetic component created by a simple process is expected to have a small DP, as for magnetosomes, whose grain size and grain shape is strictly controlled by bacteria. On the other hand, detrital magnetite has been formed in different rocks, was sorted during transport and subjected to weathering, and is therefore characterized by a large DP.

5.5. Skewness

The skewness s of a coercivity distribution is a measure of its asymmetry. Left-skewed distributions are characterized by $s < 0$; the opposite is true of right-skewed distributions. The skewness is intimately related to scale transformations. For example, the right-skewed logarithmic Gaussian distribution is transformed into the symmetric Gaussian distribution on a logarithmic field scale. SGG functions are also generated by the scale transformation of a symmetric distribution [*Egli*, 2003]. There is always a field scale for which a coercivity distribution is symmetric: this scale can be regarded as the natural scale of the distribution. *Egli* [2003] reported relatively small values for the skewness of lake sediments and atmospheric particulate matter. In this paper, we will show that $s \approx -0.4$ is a typical value for natural components. This means that the logarithmic field scale is close to a natural scale for coercivity distributions.

5.6. Kurtosis

The kurtosis κ is a measure of the 'squareness' of a distribution. Distributions that are more squared than a Gaussian function (box-shaped) are characterized by $\kappa < 0$. The kurtosis of a SGG function is controlled mainly by the parameters q and p. *Egli* [2003] found components with a slightly positive kurtosis in lake sediments and in atmospheric particulate matter. A positive kurtosis has been found in synthetic magnetite samples as well. The physical interpretation of κ is unclear. The majority of the samples presented in this paper have been modelled with sufficient accuracy by using $p \approx 2$ for all SGG functions. The opposite procedure, which consists in fixing $q = 1$ and optimizing p, gave very unsatisfactory results. Box-shaped coercivity distributions result from the sum of two components with identical DP and similar MDFs. On the other hand, pointed distributions ($\kappa > 0$) can be obtained with the sum of two components with identical MDFs and different DP. Consequently, distributions with a pronounced kurtosis should be interpreted as the artefact of a component analysis performed with an insufficient number of model functions [*Egli*, 2003].

5.7. Comparison between demagnetization curves of ARM and IRM

The comparison between normalized AF demagnetization curves of ARM and IRM, known as the modified Lowrie-Fuller test [*Johnson* et al., 1975], has been used as a domain state indicator [*Bailey and Dunlop*, 1983; *Halgedahl*, 1998]. The result of this test is of L-type if $MDF_{\mathrm{ARM}} > MDF_{\mathrm{IRM}}$ (Figure 2a), or of H-type, if $MDF_{\mathrm{ARM}} < MDF_{\mathrm{IRM}}$. A mixed result with $MDF_{\mathrm{ARM}} \approx MDF_{\mathrm{IRM}}$ is also possible (Figure 2c). L-type results are considered characteristic for SD particles, and H-type for MD particles. However, the opposite is also possible [*Xu and Dunlop*, 1995; *Egli and Lowrie*, 2002]. *Egli and Lowrie* [2002] demonstrated that the result of the modified Lowrie-Fuller test for non-interacting SD particles depends on the statistical distribution of the volumes and the microcoercivities, rather than on intrinsic properties of the particles. However, a set of non-interacting SD particles with a broad random distribution of volumes and microcoercivties gives a L-type result. Magnetostatic interactions affect the result of the modified Lowrie-Fuller test as well, since they inhibit the ARM acquisition of the low-coercivity grains. Multicomponent mixtures, as for the sample of Figure 1, also influence the result of the Lowrie-Fuller test. The combination of a low-coercivity component with a small ARM ratio, and a high-coercivity component with a large ARM ratio gives a L-type result and vice-versa.

The difference between the shape of ARM and IRM demagnetization curves is an additional tool that can be used to characterize magnetic components. Generally, the result of a modified Lowrie-Fuller test is quantified with $MDF_{\mathrm{ARM}}/MDF_{\mathrm{IRM}}$ [*Xu and Dunlop*, 1995]. However this is not sufficient to characterize mixed-type results, as demonstrated by the example of Figure 2c. Differences between the shape of ARM and IRM curves are better quantified on the corresponding coercivity distributions.

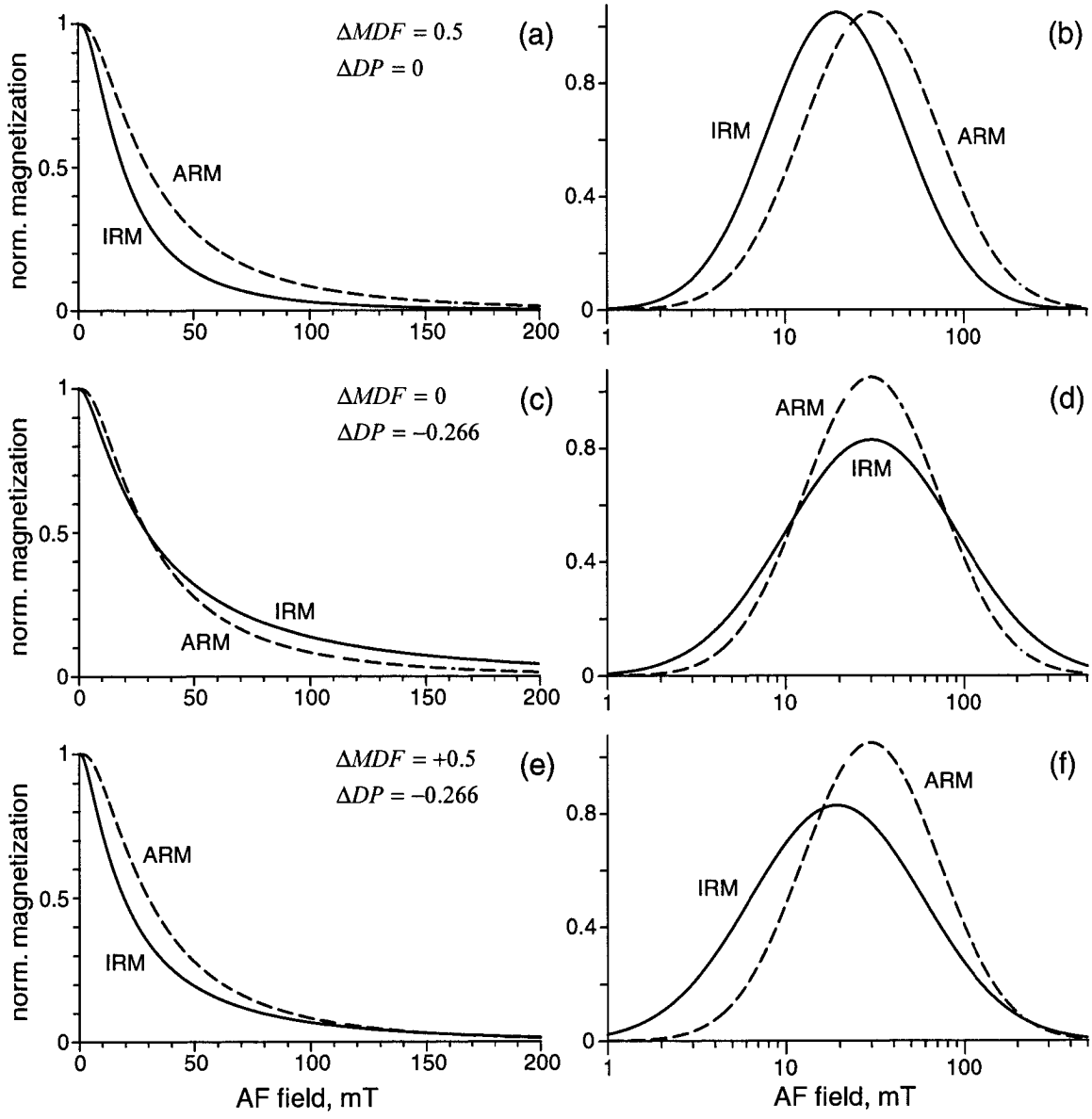

Figure 2. *Relation between the Lowrie-Fuller test (plots on the left) and the corresponding coercivity distributions (plots on the right). Differences between normalized AF demagnetization curves of ARM and IRM are quantified by the relative difference ΔMDF between the median destructive fields of ARM and IRM, and the relative difference ΔDP between the dispersion parameters of ARM and IRM (see text). (a,b) $\Delta DP = 0$ and $\Delta MDF > 0$ generate a L-type result of Lowrie-Fuller test, which is considered typical for SD particles. A H-type result is obtained by changing the sign of ΔMDF: in this case ARM and IRM curves are exchanged. (c,d) $\Delta DP < 0$ and $\Delta MDF = 0$ generate a 'mixed result' which has often been observed in pseudo-single domain particles [Bailey and Dunlop, 1983]. (e,f) The natural magnetic components analyzed in this paper obey the empirical relation $\Delta DP \approx -0.53\Delta MDF$ as for the plotted example. On the other hand, synthetic samples of sized magnetite are characterized by $\Delta DP \approx -0.24\Delta MDF$.*

The coercivity distributions may display different median destructive fields (Figure 2b), different dispersion parameters (Figure 2d), or both (Figure 2f). Let us define ΔMDF and ΔDP as the differences between the corresponding parameters of ARM and IRM, normalized by the DP of ARM, ΔDP_{ARM}:

$$\begin{aligned} \Delta MDF &= (\mu_{\mathrm{ARM}} - \mu_{\mathrm{IRM}})/DP_{\mathrm{ARM}} \\ \Delta DP &= (DP_{\mathrm{ARM}} - DP_{\mathrm{IRM}})/DP_{\mathrm{ARM}} \end{aligned} \quad (2)$$

5.8. Quantitative characterization of a magnetic component

Not all parameters among the 10, which are necessary to model the coercivity distributions with SGG functions (a, μ, σ, q, p for ARM and for IRM) have an immediate relation with classic measurements performed in rock magnetism. Therefore, we propose following parameters as an interpretable 'fingerprint' of a magnetic component: (1) k_{ARM}/IRM as a grain size parameter, (2) μ_{ARM} or μ_{IRM} as a coercivity parameter, (3) DP_{ARM} or DP_{IRM} as a measure of the 'randomness' of natural processes which affect the magnetic grains, (4) ΔMDF and (5) ΔDP as indicators for differences between ARM and IRM, and (6) s_{ARM} or s_{IRM} as a symmetry parameter.

6. Other measurements

For better characterization of some magnetic components, thermal experiments have been performed on a selected group of samples.

For high-temperature experiments, the samples have been powdered and embedded in a special oven cement of the company *Omega CC* in order to fix the magnetic grains. Blank cement samples from the same batch were prepared as well. The samples have been prepared in a shielded room, in order to avoid the orientation of magnetic grains by the Earth's field, and were left one week in a zero field for drying. Then, an IRM at 300 mT was imparted to all samples with an electromagnet. Alternatively, a particular coercivity window $[H_1, H_2]$ was magnetized by giving an IRM at a field H_2 and subsequently demagnetizing the sample with an AF peak field $H_1 < H_2$. The magnetized samples were stored 24 hours in a shielded room to reduce the viscous component of the IRM. Then, they were thermally demagnetized with increasing temperature steps in a shielded ASC oven until the IRM was completely removed. The remanent magnetization of the samples was measured after each temperature step using a 2G cryogenic magnetometer. Since the blank samples have been subjected exactly to the same treatment, the contribution of the cement to the total magnetization could be subtracted.

Low-temperature magnetic properties have been measured on a Quantum Design Magnetic Property measurement system (MPMS-2) at the Institute of Rock Magnetism (University of

Minnesota). Freeze-dried sediment material was taken from the samples and placed into a gelatine capsule. The capsule was then tightly packed in a plastic straw, which is a standard sample holder for the MPMS. Each sample was first cooled to 3 K in a zero magnetic field and then a remanence was imparted by applying a 2.5 T DC field for 60 s, after which the superconducting magnet was quenched to reduce the residual field to $< 1\ \mu\mathrm{T}$. Thermal demagnetization of zero-field-cooled (ZFC) IRM was measured during warming to room temperature (300 K). The sample was next cooled from 300 K to 3 K in the presence of a 2.5 DC field. After quenching the magnet, thermal demagnetization of field-cooled (FC) IRM was measured during warming to room temperature. An additional experiment was performed by imparting an IRM at room temperature in a 2.5 T DC field. After quenching the magnet, the sample was cooled to 50 K in a zero magnetic field and warmed again to room temperature (low-temperature demagnetization LTD). The sample magnetization was measured at fixed temperature intervals during cooling and heating.

7. Results of the component analysis

All results of the component analysis performed with the method described in section 4 are listed in the Appendix. Results of the component analysis for representative samples as well as the magnetic properties of individual components will be discussed in the following.

7.1. Lake sediments

All lake sediments have been modelled using four magnetic components labelled D+EX, BS, BH and H. The components BS (biogenic soft) and BH (biogenic hard) can be easily recognized as distinct, narrow peaks of the ARM coercivity distribution (Figure 3). The shape of the coercivity distributions of BS and BH is constant in all samples: $MDF_{\mathrm{ARM}} \approx 45$ and 73 mT, respectively, and $DP_{\mathrm{ARM}} \approx 0.174$ and 0.106, respectively (Figure 4). The extremely small values of DP, especially for the ARM and for BH, are the most striking property of these components, and allow their unequivocal identification. Components BS and BH have also the highest ARM ratios among all samples analyzed in this paper: typically, $k_{\mathrm{ARM}}/IRM \approx 3\ \mathrm{mm/A}$, a value similar to that of cultured magnetotactic bacteria [*Moskowitz et al.*, 1993] and to the predicted upper limit for non-interacting SD particles [*Egli and Lowrie*, 2002]. However, k_{ARM}/IRM varies over more than one order of magnitude, from 0.1 mm/A to 5 mm/A, whereby all other parameters are relatively constant. The extreme variations of the ARM ratio occur simultaneously for both components: samples with large differences between the ARM ratios of BS and BH have not been found. The behaviour of the ARM ratio is not an artefact of component analysis due to numerical instability of the solutions, since it was observed also in samples where BS and BH account for $> 75\%$ of the total ARM. Furthermore, low values of k_{ARM}/IRM occur systematically in anoxic samples (Figure 5).

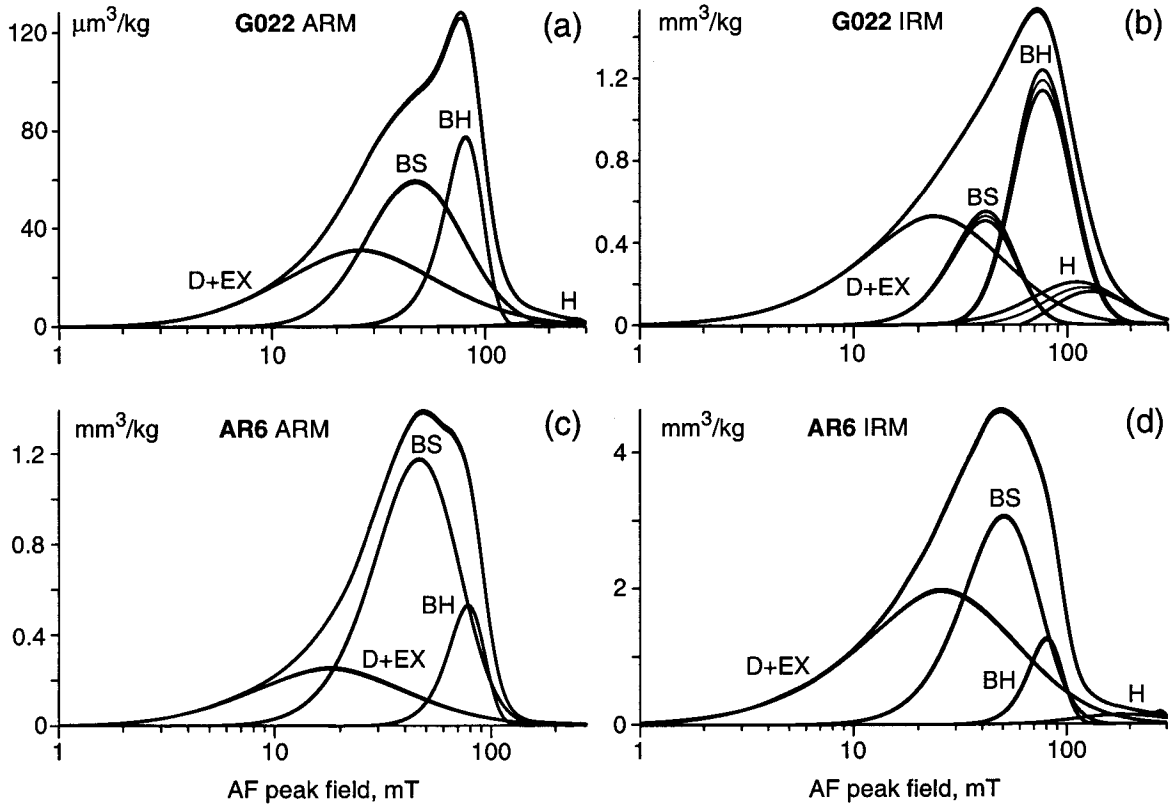

Figure 3. *Examples of component analysis with ARM and IRM coercivity distributions of selected lake sediment samples rich in bacterial magnetite. In both samples, one or more magnetic components are already recognizable as individual peaks of the coercivity distribution. The coercivity distributions of bacterial components are labelled BS and BH. A high-coercivity component probably carried by antiferromagnetic minerals is labelled with H. Component D+EX is probably a mixture of detrital particles and fine-grained extracellular magnetite (see text).*

The thermal demagnetization of a room temperature IRM imparted on a coercivitiy interval which is typical for BS and BH, is shown in Figure 5. Samples with a high ARM ratio are characterized by a narrow distribution of blocking temperatures between 450°C and 580°C, which is typical for stable SD magnetite particles (Figure 5e). From the magnetic properties discussed above for oxic samples we conclude that BS and BH represent two groups of magnetosomes with different coercivities. The same thermal demagnetization experiment has been performed on the anoxic sample G010 (Figure 5f). It shows a peculiar increase of the remanent magnetization between 150°C and 230°C.

An increase of the remanence during thermal demagnetization in a zero-field ambient can be explained only with positive magnetic interactions between magnetic minerals with a different thermal behaviour, since self-reversal mechanisms associated with high-Ti titanomagnetites or -hematites can be excluded in lake sediments.

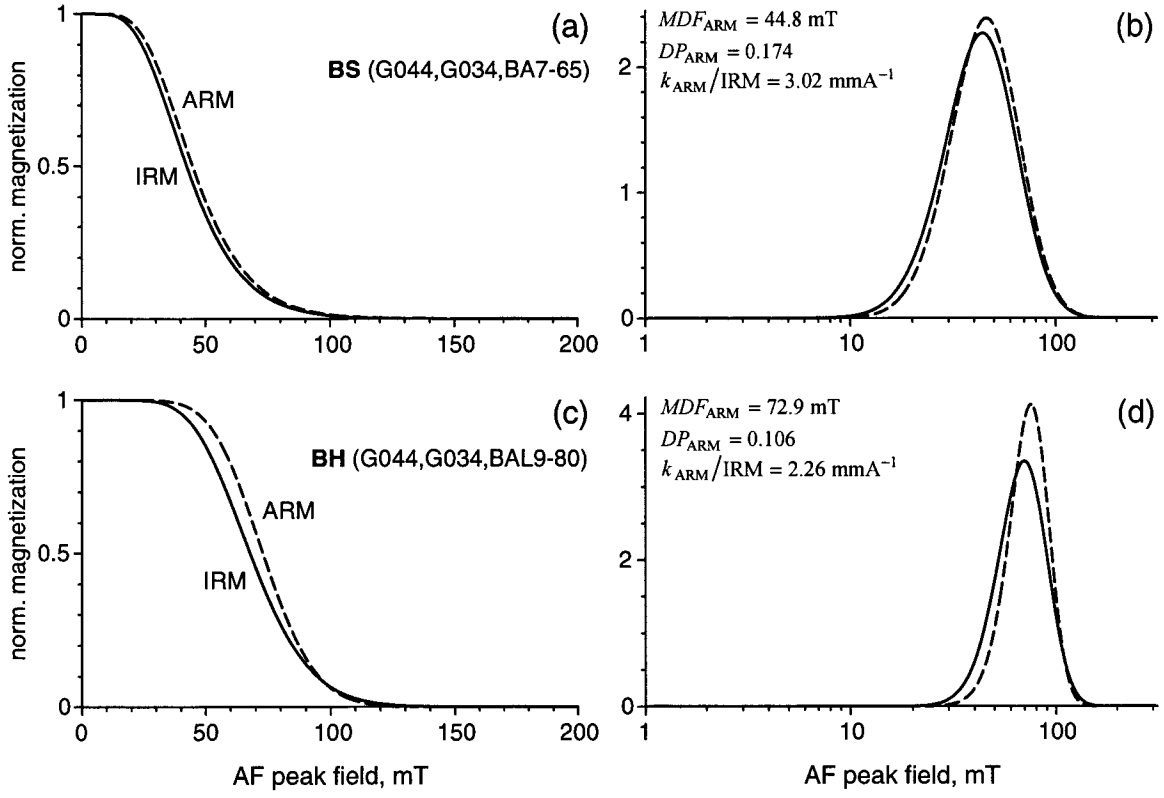

Figure 4. *Typical magnetic properties of ARM and IRM for the bacterial components BH (a,b) and BS (c,d). Left, normalized AF demagnetization curves and right, normalized coercivity distributions of IRM (solid line) and ARM (dashed). Each component was calculated as the average of the parameters found for this component in the samples indicated in parentheses.*

Petersen et al. [1986] and *Vali et al.* [1989] reported electron microscope observations of magnetosome particles that are surrounded by small, superparamagnetic grains. *Tarduno* [1995] observed an increase in the superparamagnetic contribution related to magnetite reduction in pelagic sediments, and *Smirnov and Tarduno* [2000] postulated the existence of magnetite particles surrounded by superparamagnetic grains below the iron redox boundary. *Canfield and Berner* [1987] reported the observation of magnetite particles covered by a pyrite layer. The magnetization peak, which occurs at 230°C during thermal demagnetization of G010, is similar to the result of in-field heating experiments on a mixture of monoclinic pyrrhotite (Fe_7S_8) and hexagonal pyrrhotite (Fe_9S_{10}) [*Schwarz*, 1975; *Rochette et al.*, 1990]. In these experiments, the heating curve shows a characteristic peak at 225°C, which can be explained by the fact that Fe_9S_{10} is ferromagnetic only over a restricted temperature range between the so-called λ transition around 200°C and the Curie point of ≈265°C. During thermal demagnetization in a zero-field, no net magnetization should be acquired by the hexagonal pyrrhotite. However, if this mineral occurs in form of small particles or a layer adhering on the surface of magnetosomes, the magnetic field which surrounds them is able to induce a magnetization during heating above the λ transition.

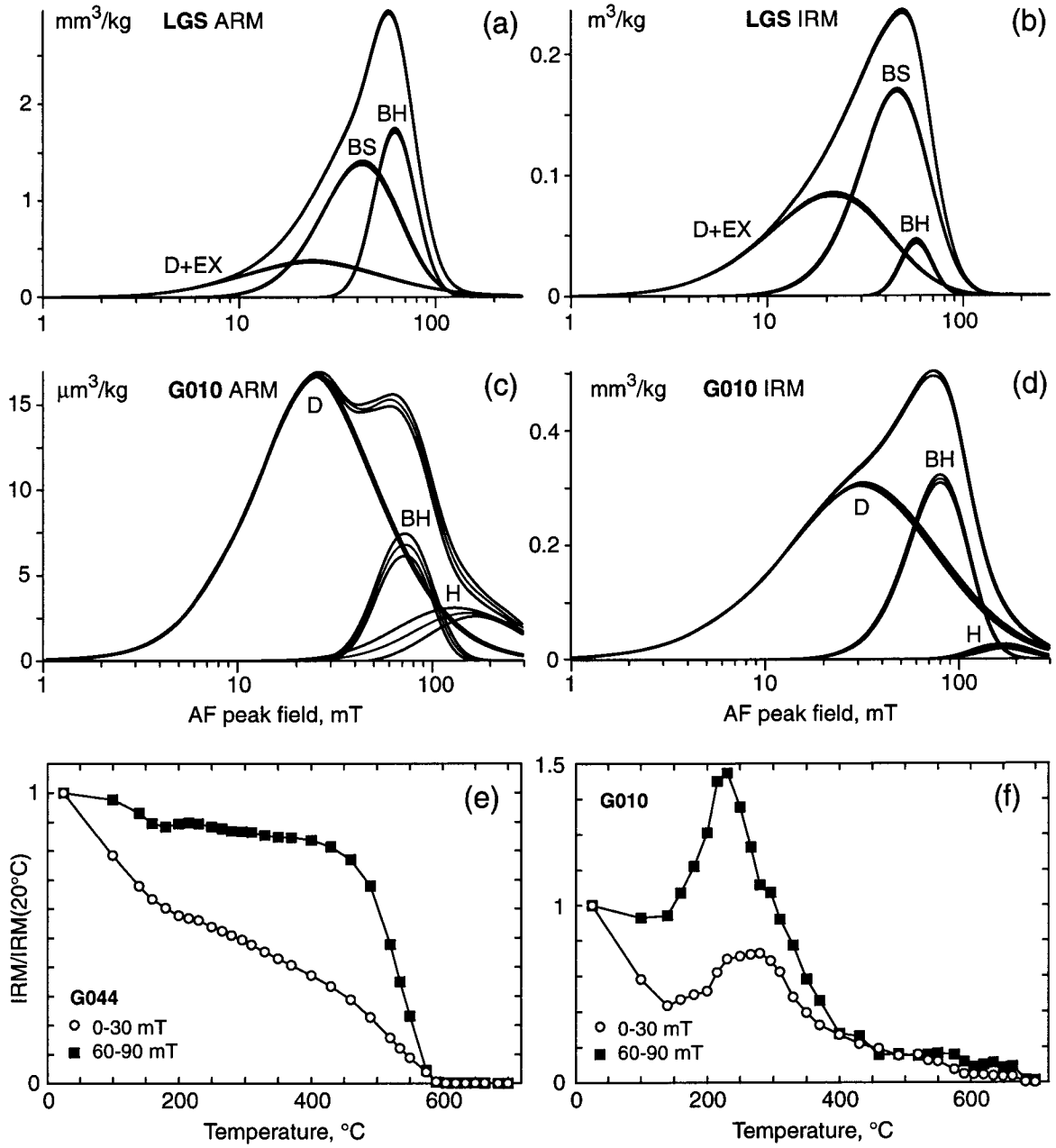

Figure 5. *(a)-(d) Examples of component analysis with ARM and IRM coercivity distributions of two anoxic lake sediment samples. The components are labelled as in Figure 3. In both samples, the bacterial components are characterized by* $k_{\mathrm{ARM}}/IRM < 0.2$ mm/A, *one order of magnitude less than the bacterial components of Figure 3. All other properties, as the MDF and the DP, remain unchanged. In sample G010 the components EX and BS are completely absent. (e), (f) Thermal demagnetisation of IRM for two lake sediment samples. G044 is rich in bacterial magnetite. The coercivity intervals of* 0-30 mT *and* 60-90 mT *were chosen to magnetize mainly the component D+EX and the bacterial component BH, respectively. (e) Component BH is clearly recognizable from its narrow distribution of blocking temperatures below* 580°C. *Component D+EX shows a broader distribution of blocking temperatures below* 580°C. *(f) The bacterial component shows a peculiar increase of the remanent magnetization between* 150°C *and* 220°C, *followed by a rapid decrease up to* 400 °C. *A similar but less pronounced behaviour can be observed in the* 0-30 mT *coercivity interval.*

The magnetization peak at 230°C is more pronounced for the 60-90 mT coercivity interval, which is related to the bacterial components. This observation suggests that hexagonal pyrrhotite is formed during anoxic conditions preferentially on the surface of magnetosomes, which are characterized by a large specific surface area. The stability fields of iron minerals in anoxic marine sediments have been calculated by *Berner* [1964]. The relative position of the stability fields should be similar in lake sediments. Under reducing conditions, magnetite is thermodynamically unstable and may transform into pyrite (FeS_2), pyrrhotite ($Fe_{1-x}S$) or siderite ($FeCO_3$). Pyrite forms only at sulphide concentrations > 1 mM over several hundreds of years [*Canfield and Berner*, 1987], and has been observed in marine sediments and sulfate-rich lakes [*Suits and Wilkin*, 1998] under reducing conditions. The sulphide concentration in Baldeggersee never exceeded 3.5 μM, and pyrite formation has not been detected (M. Sturm, personal communication). Siderite has a Néel temperature of 38 K, a saturation remanence of $\approx 1\ \mathrm{mAm^2/kg}$ below 38 K, and converts to magnetite if heated above 400°C [*Housen et al.*, 1996]. The low-temperature experiments discussed later in this section, give no evidence for the presence of siderite in the lake sediments. The formation of siderite around magnetite particles should result in an increase of the remanence above 400°C, which is not observed (Figure 5f).

The magnetic properties of the low-coercivity component D+EX (detrital and extracellular magnetite) are characterized by a range of values which are distributed between two extremes, given by $MDF_{\mathrm{ARM}} \approx 17$ mT and $k_{\mathrm{ARM}}/IRM \approx 1.6$ mm/A for sediments deposited during periods of high productivity (Figure3), and $MDF_{\mathrm{ARM}} \approx 30$ mT, $k_{\mathrm{ARM}}/IRM \approx 0.35$ mm/A for late glacial samples (Figure 6a,b). In both cases $DP_{\mathrm{ARM}} \approx 0.36$. This trend can be explained by considering D+EX as a binary mixture of two components D and EX with similar coercivity distributions, which can be interpreted as detrital magnetite and extracellular magnetite, respectively. Unfortunately, components D and EX could not be unmixed by component analysis, because of their highly overlapping coercivity distributions and because their total contribution did not exceed 25% in most samples.

The growth of extracellular magnetite is controlled by dissimilatory iron-reducing bacteria through a process called biologically induced mineralization (BIM). During this process, the bacteria modify their local extracellular environment, creating conditions suitable for the chemical precipitation of magnetite [*Moskowitz et al.*, 1993]. Because there is no strict biological control over the particle synthesis, extracellular magnetite is characterized by a broad distribution of grain sizes and irregular shape [*Sparks et al.*, 1990]. The grain size distribution of extracellular magnetite falls mainly in the superparamagnetic range; nevertheless, a small fraction of the particles is large enough to carry a remanence and fall into the SD range. This explains the relatively large ARM ratio and the small MDF, which characterizes D+EX in sediments deposited in highly productive waters. ARM ratios up to 1.6 mm/A have been measured for D+EX in lake sediments, and these values are compatible with those predicted for SD magnetite [*Egli and Lowrie*, 2002]. Similar properties have been measured in synthetic

sub-micron magnetites [*Maher*, 1988], and are typical for well-developed soils and paleosols (see section 7.4).

Component D is the predominant remanence carrier during low-productivity periods, such as the Late Glacial. An example is given by sample LGL in Figure 6a,b. The magnetic properties of component D are similar in all samples where it has been identified, which include material eroded from the catchment area of Baldeggersee (Figure 6c,d), and the fine fraction of sand collected on a delta formed by a small tributary of Baldeggersee (sample U03F). Typical parameters of component D are $MDF_{\mathrm{ARM}} \approx 29$ mT, $DP_{\mathrm{ARM}} \approx 0.36$ and $k_{\mathrm{ARM}}/IRM \approx 0.45$ mm/A (Figure 7). Median destructive field and dispersion parameter are similar to those of dust samples (see section 7.3), while k_{ARM}/IRM is three times higher, probably because of the different grain size. Component D can be interpreted as the magnetic contribution of detrital magnetites and maghemites with a broad distribution of grain sizes and coercivities. A high-coercivity component H, carried by antiferromagnetic minerals, occur together with component D, as expected in materials of lithogeinc origin.

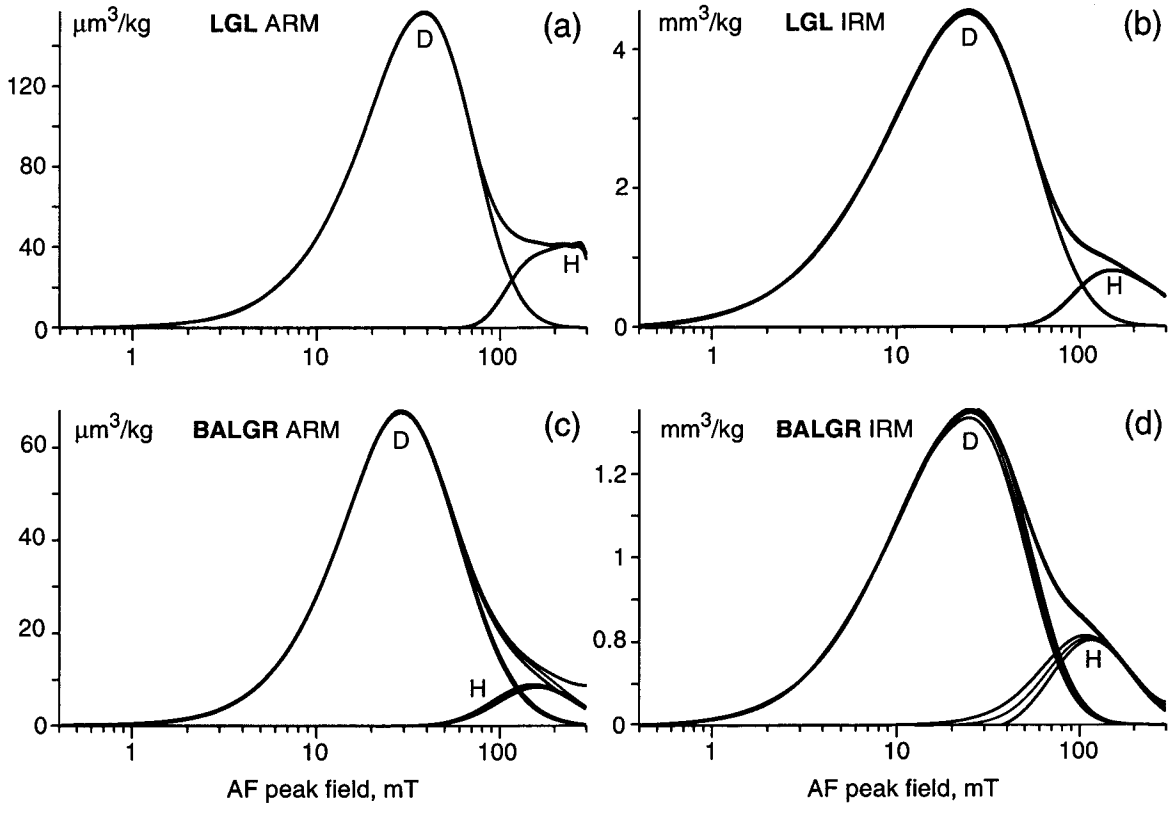

Figure 6. *Examples of component analysis with ARM and IRM coercivity distributions of detrital material from lake sediments (sample LGL), and eroded material from the catchment area (sample BALGR). See the text for more details about the samples. Iron spinels of detrital origin are labelled with D; H is a high-coercivity magnetization carried by antiferromagnetic minerals, probably hematite.*

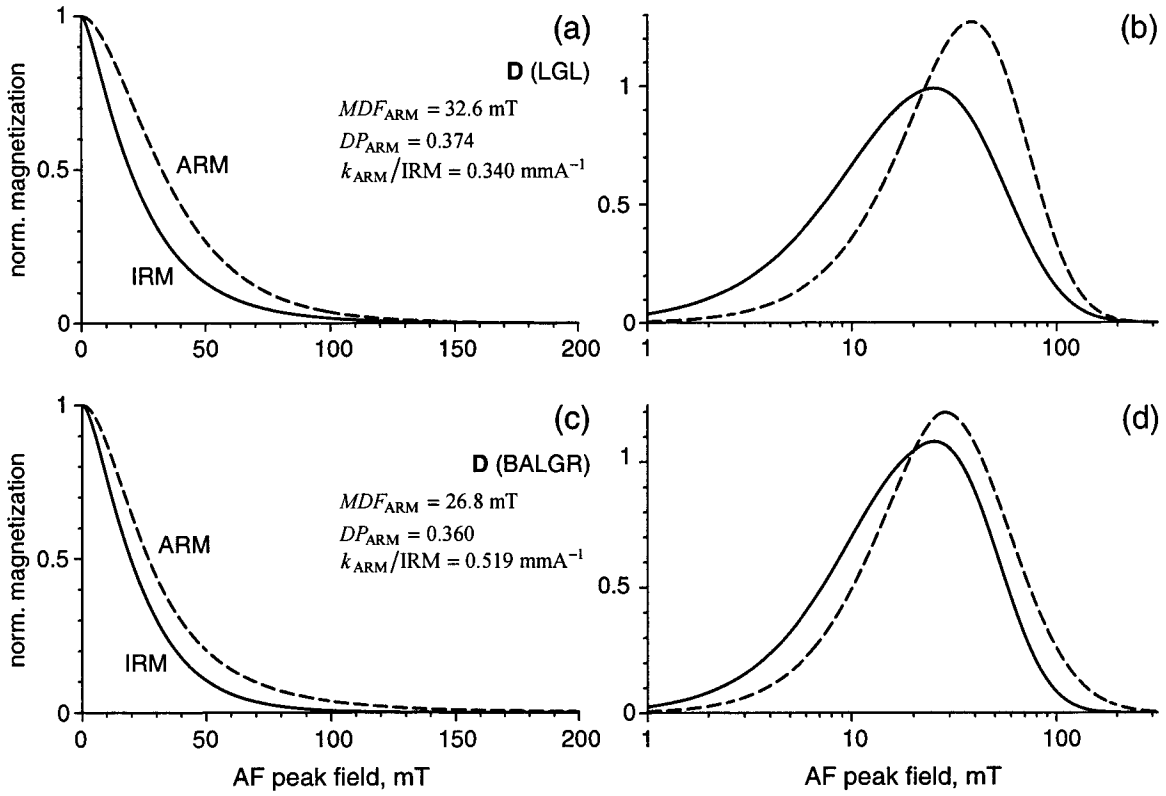

Figure 7. *Typical magnetic properties of ARM and IRM for detrital components D found in a sediment of lake Geneva (a,b), and an eroded soil from the catchment area of Baldeggersee (c,d). Left, normalized AF demagnetization curves and right, normalized coercivity distributions of IRM (solid line) and ARM (dashed).*

Traces of a third component NI similar to bacterial magnetite have been identified in sample U03F. However, the signal of this component is too small to allow its identification. Since U03F was collected in a small river delta, NI could represent a small population of magnetotactic bacteria.

Low-temperature experiments on selected lake sediments are shown in Figure 8. The Vervey transition of magnetite at 110 K can be recognized in all samples. However, the transition is much less pronounced than expected for pure bacterial magnetite [*Moskowitz et al.*, 1993], even in samples where BS and BH account for $> 75\%$ of the total ARM. The suppression of the Vervey transition is due to the low temperature oxidation of magnetite to maghemite, which has been reported for magnetosomes by *Vali et al.* [1987]. It is possible to distinguish three categories of lake sediments according to their different behaviour across the Vervey transition temperature. Sediments deposited during oxic conditions show a less pronounced Vervey transition, and the opposite is true for the anoxic sample G010. Intermediate results are obtained for sediments deposited during sub-oxic conditions.

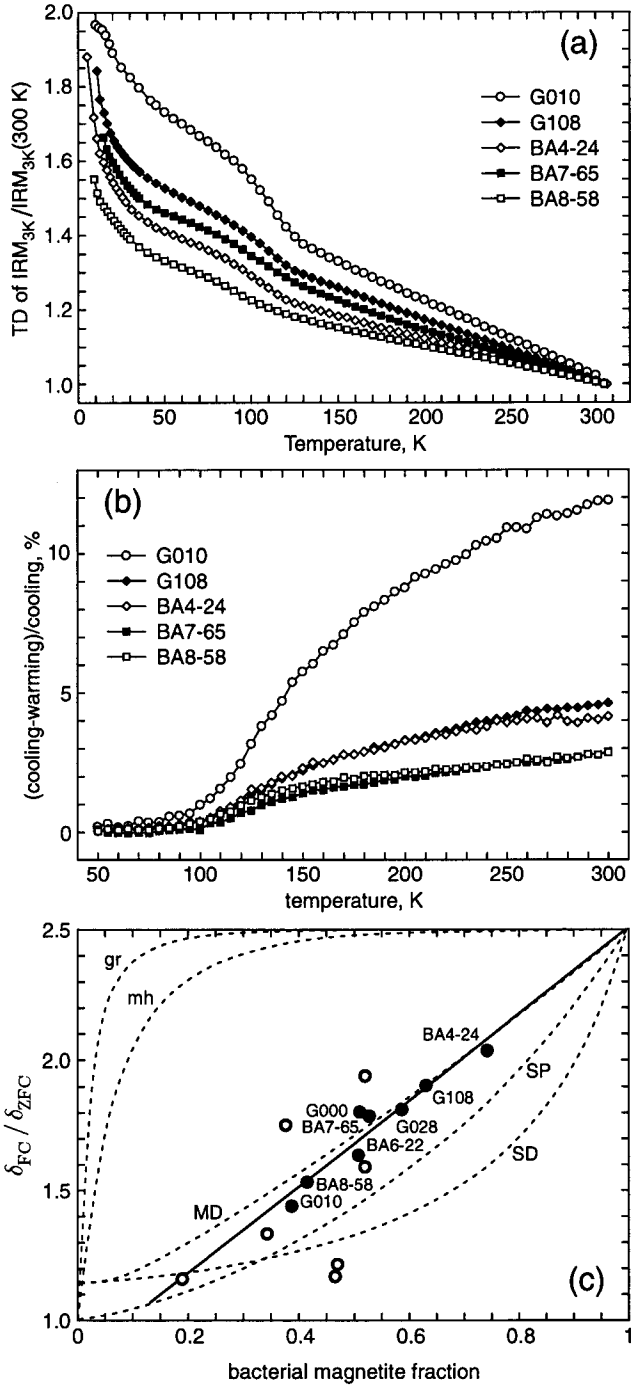

Figure 8. *Low-temperature experiments on lake sediments from Baldeggersee. (a) Thermal demagnetization of a 2.5 T IRM imparted at 3 K. (b) Low-temperature demagnetization of a 2.5 T IRM imparted at room temperature, obtained by cooling the sample down to 50 K and warming it up in zero-field. The difference between the remanence measured during cooling and during warming is plotted. Both experiments give evidence of the Vervey transition of magnetite at 110 K. The Vervey transition is less pronounced in sediments deposited during oxic conditions (BA8-58 and BA7-65), and most pronounced in the anoxic sample G010. (c) Comparison between the bacterial magnetite content, estimated with component analysis, and the parameter $\delta_{FC} / \delta_{ZFC}$, proposed by Moscowitz et al. [1993] as an indicator for intact chains of magnetite magnetosomes. Dotted lines are mixing models with greigite (gr), maghemite (mh), and magnetite in different domain states (SP, SD and MD). Dots are samples from Baldeggersee, open circles are sediments collected above a sapropel layer in the eastern Mediterranean after Kruiver and Passier [2001] and Passier and Dekkers [2002]. The solid line is a linear best-fit of the measurements.*

A similar trend across the iron redox boundary in pelagic sediments has been reported by *Smirnov and Tarduno* [2000]. They interpreted the pronounced Vervey transition in anoxic sediments as an effect of the reductive dissolution of a cation-deficient magnetite shell, which surrounds the oxidized magnetite particles.

Moskowitz et al. [1993] proposed a method to identify intact magnetosome chains on the basis of low-temperature experiments, where the Vervey transition of field cooled (FC) and zero field cooled (ZFC) IRMs is compared. They define $\delta = (IRM_{80\,K} - IRM_{150\,K}) / IRM_{80\,K}$

as the normalized amplitude of the Vervey transition, and take the ratio δ_{FC}/δ_{ZFC} of δ for a FC IRM to that for a ZFC IRM as a diagnostic parameter for intact chains of magnetite magnetosomes. Non-chain magnetite, as well as greigite and maghemite, are characterized by $\delta_{FC}/\delta_{ZFC} \approx 1.15$, intact chains of magnetite magnetosomes by $\delta_{FC}/\delta_{ZFC} \approx 2.5$. Binary mixture models of magnetosome chains with other magnetic grains have been proposed by *Moskowitz et al.* [1993] to estimate the content of bacterial magnetite in natural sediment. Figure 8c shows a plot of the measured δ_{FC}/δ_{ZFC} as a function of the bacterial magnetite content for lake sediment samples from Baldeggersee and for sediments taken above a sapropel layer in the eastern Mediterranean after *Kruiver and Passier* [2001] and *Passier and Dekkers* [2002]. The bacterial magnetite content has been estimated with component analysis after *Egli* [2003] for the Baldeggersee sediments, and with component analysis after *Kruiver et al.* [2001] for the sapropel samples. The empirical dependence of δ_{FC}/δ_{ZFC} on the bacterial magnetite content is linear in the range covered by the samples, and an agreement is found between the results of the present work and those of *Kruiver and Passier* [2001] and *Passier and Dekkers* [2002]. If the linear trend is extrapolated to 100% bacterial magnetite, $\delta_{FC}/\delta_{ZFC} = 2.51$ is obtained, in good agreement with *Moskowitz et al.* [1993]. On the other hand, none of the proposed binary mixture models fits the experimental data, probably because natural sediments are a complex mixture of minerals with different domain states.

7.2. Marine sediments and limestones

A marine sediment, ODPB, is very similar to lake sediments, and similar magnetic components have been identified (Figure 9a,b). Two components, BM and BI, are the marine counterpart of BS and BH, with 30% smaller MDFs, and can be interpreted as bacterial magnetite produced by marine strains of magnetotactic bacteria. The smaller MDFs of BM and BI are probably related to the distinct morphology of these bacteria with respect to those living in lakes.

Only one bacterial component could be identified in the other marine sediment, ODPD, and in the two limestones SCBB and SCBD (Figure 9c,d and Figure 10). This component has a MDF that is similar to BI or BS, and $DP_{ARM} \approx 0.23$, a value 30% larger than DP_{ARM} of BS or BI. The ARM ratio is variable, like for the biogenic components found in lake sediments. It is possible that diagenetic processes, which have been considered to explain the secondary natural remanence of SCBD [*Fuller et al.*, 2002], are responsible for an alteration of the magnetosomes. This alteration could explain the observed higher values of DP_{ARM} with respect to intact biogenic magnetite, since natural processes introduce a certain degree of randomness. In sample SCBD, the biogenic magnetite is characterized by low values of the ARM ratio, which are comparable to those of anoxic lake sediments. This sample belongs to a level of the Scaglia Bianca formation where the IRM is minimal. Some of these levels occur just below black shale layers, so-called Bonarelli precursors, which are indicative of anoxic events [*Erba and Walsworth*, 2001].

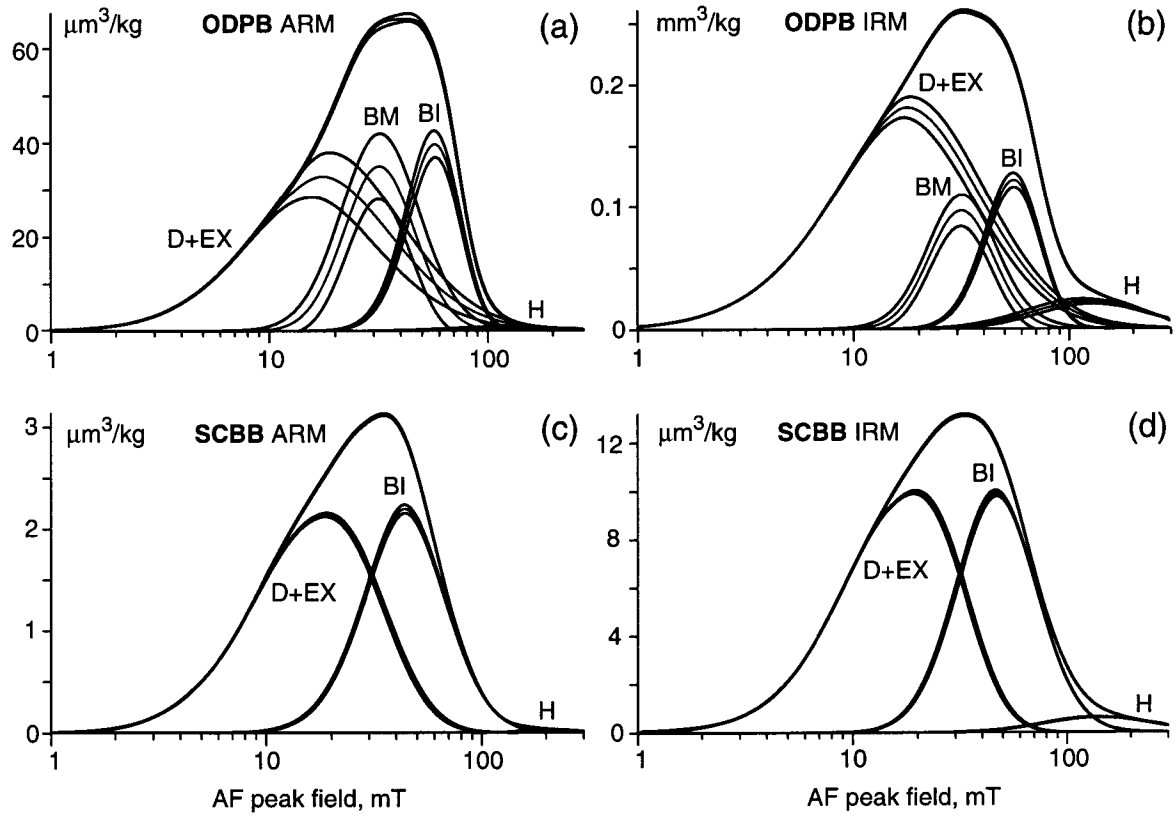

Figure 9. *Examples of component analysis with ARM and IRM coercivity distributions of a deep-water pelagic carbonate (ODPB) and a limestone of the Scaglia Bianca formation (SCBB). Both samples contain bacterial magnetite (components BM and BI) with* $k_{\mathrm{ARM}}/IRM \approx 3-4\ \mathrm{mmA}^{-1}$, *a value that is similar to that of components BS and BH in the lake sediments of Figure 3. However, the median destructive fields are* $\approx 30\%$ *smaller, and reflect some differences in the morphology of magnetosomes produced by marine and fresh-water magnetotactic bacteria. Component BI is present also in the SCBB sample, where it survived diagenentic processes with a little increase of the dispersion parameter. A mixture D+EX of detrital and extracellular magnetite with* $k_{\mathrm{ARM}}/IRM \approx 2-3\ \mathrm{mmA}^{-1}$ *is present in both samples. The high* k_{ARM}/IRM *values are indicative of SD magnetite, and suggest a clear predominance of the fine-grained extracellular magnetite.*

Biogenic magnetite in recent and ancient limestones has been observed under the electron microscope by *Chang et al.* [1987] who postulated its importance as a remanence carrier. Their conclusions are confirmed by the present work, which suggests a biogenic contribution of $> 50\%$ to the remanence carried low-coercivity, soft minerals.

The component D+EX is similar to that of lake sediments. The most extreme properties of D+EX have been found in SCBB, with $MDF_{\mathrm{ARM}} = 16.5\ \mathrm{mT}$, $k_{\mathrm{ARM}}/IRM = 2.85\ \mathrm{mm/A}$. The thermal demagnetization of an IRM imparted at room temperature with a field of 300 mT is shown in Figure 11 for a lake sediment, a marine sediment and the two limestone samples.

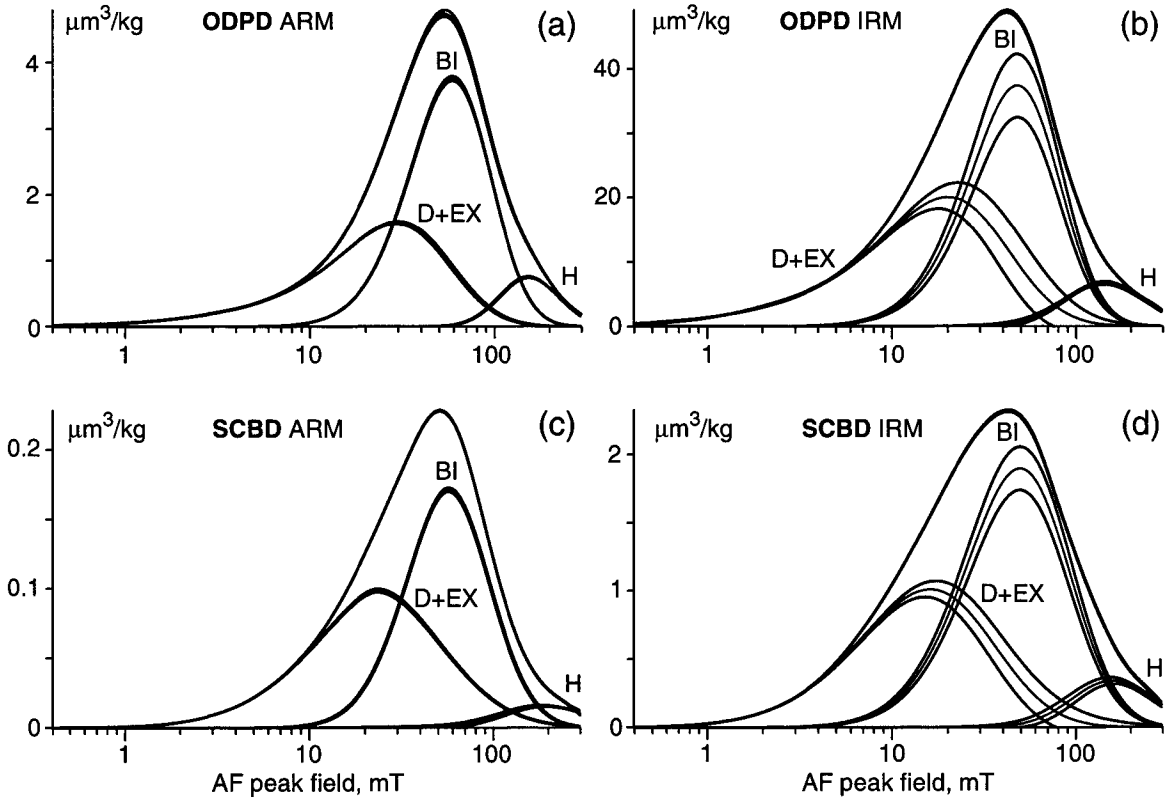

Figure 10. *Examples of component analysis with ARM and IRM coercivity distributions of a sediment from a marine carbonate platform (ODPD) and a limestone of the Scaglia Bianca formation (SCBD). Both samples contain the bacterial magnetite component BI with* $k_{\mathrm{ARM}}/IRM \approx 1\ \mathrm{mmA}^{-1}$, *1/3 of the value found for the bacterial components of Figure 3 and Figure 9. The median destructive fields are approximately the same as for BI in Figure 9. A mixture D+EX of detrital and extracellular magnetite with* $k_{\mathrm{ARM}}/IRM \approx 1-2\ \mathrm{mmA}^{-1}$ *is present in both samples. The high values of* k_{ARM}/IRM *are indicative for SD magnetite, and suggest a predominance of fine-grained extracellular magnetite.*

A broad distribution of blocking temperatures up to 580 °C is evident in both limestones, whereby SCBD is characterized by a steeper decrease below 250°C. Similar thermal demagnetization curves of IRM have been measured by *Lowrie and Heller* [1982] in two shallow-water Jurassic limestones from Bavaria, which differ by a factor 5 in the IRM intensity. The thermal demagnetisation curves of the limestones are different from those of lacustrine and marine sediments, where bacterial magnetite can be easily recognized on the narrow distribution of blocking temperatures below 580°C. This observation is not related to differences in the amount of bacterial magnetite, and reflects a true change of the thermal stability, which is maybe related to an alteration induced by diagenetic processes.

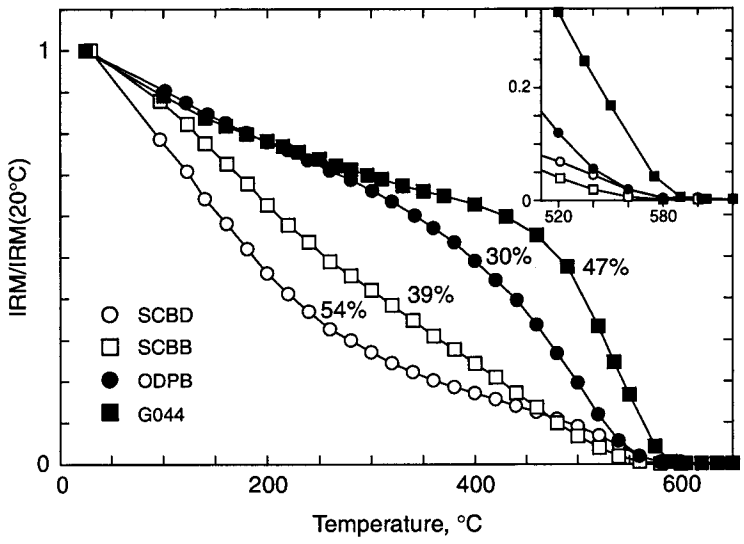

Figure 11. *Thermal demagnetization of IRM for a lacustrine sediment (G044) a marine sediment (ODPB), and two limestones (SCBD and SCBB). These samples are charecterized by a variable amount of bacterial magnetite (percent numbers near each curve), which has been identified with component analysis. A detail of the demagnetization curves near the Curie temperature of magnetite is shown in the small inset. Bacterial magnetite is very clearly recognizable in G044. The narrow distribution of blocking temperatures just below the Curie temperature is characteristic for relatively large, stable SD particles. The differences observed in the shape of the thermal demagnetisation curves are not related to a compositional trend, and may be interpreted as an alteration of the thermal stability of bacterial magnetite. This alteration is particularly evident in the limestones, and is possibly related to diagenetic processes. The maximum blocking tempetature of G044 is 590°C, and can be explained with a partial maghemitization of bacterial magnetite.*

7.3. Loess and atmospheric particulate matter

Three components, ED (eolian dust), L (loess) and H have been identified in the pristine loess BY55, and two components, ED and UP (urban pollution) in the PM10 samples (Figure 12). Component ED is common in both types of samples and has similar properties, especially if the coercivity distribution of IRM is considered: $MDF_{\mathrm{IRM}} \approx 26$ mT and $DP_{\mathrm{IRM}} \approx 0.45$. Very low values of k_{ARM}/IRM, around 0.16 mm/A, are characteristic as well (Figure 13). In BY55, DP_{ARM} of component ED is smaller than in all other samples: it is not clear if it is an artefact produced by the high degree of overlap with component L. Component L is relatively hard, with $MDF_{\mathrm{ARM}} \approx 79$ mT, and an ARM ratio of 0.1 mm/A is one of the smallest among all components identified in this study. The thermal demagnetization of room temperature IRMs of BY55 imparted on different coercivity intervals is shown in Figure 14a. The 0-30 mT coercivity interval was selected to magnetize mainly the component ED; component L was preferentially magnetized in the 70-120 mT coercivity interval. Both components show similar thermal demagnetization curves, whereby the presence of hematite can be recognized in the 70-120 mT coercivity interval. Component L is characterized by a rapid decrease of the magnetization below 270°C and the Curie point of magnetite cannot be recognized. This feature can be interpreted as a consequence of the transformation of maghemite into hematite.

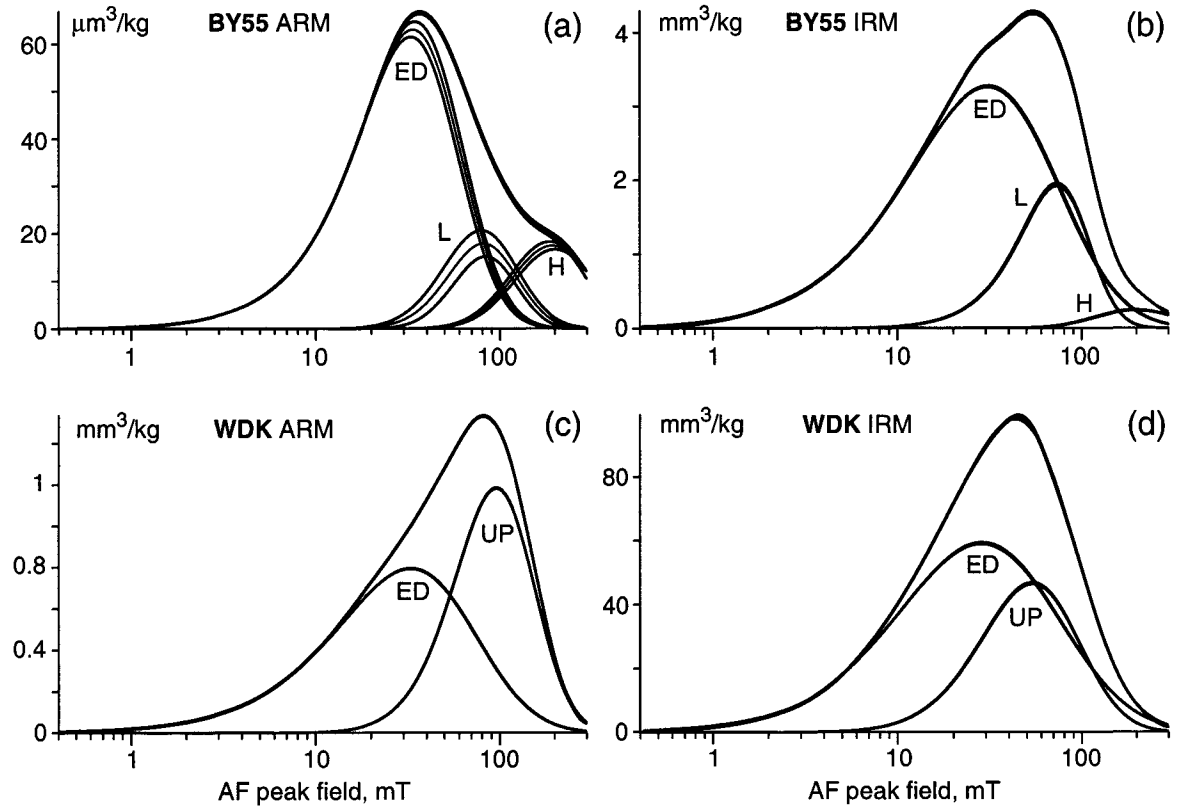

Figure 12. *Examples of component analysis with ARM and IRM coercivity distributions of a pristine loess sample from the Western Chinese Loess Plateau (BY55), and a sample of atmospheric particulate matter collected in the center of Zürich, Switzerland (WDK). Wind-blown natural dust, labelled with ED, is present in both samples and has similar magnetic properties:* $k_{\mathrm{ARM}}/IRM \approx 0.17\ \mathrm{mmA^{-1}}$ *and* $MDF_{\mathrm{ARM}} \approx 28\ \mathrm{mT}$. *A contribution of high-coercivity antiferromagnetic minerals, labelled with H, is present in the loess sample. A third component, L, was also found in BY55: its origin is probably related to the low-temperature oxidation of magnetite (see text). The magnetic contribution of urban pollution, UP, is clearly recognizable in the atmospheric particulate matter sample, which was collected near a highly trafficated road in the city center.*

Various authors reported inversion temperatures of 250-400°C for this transformation [*Dunlop and Özdemir*, 1997]. Furthermore, *Van Velzen and Dekkers* [1999] reported experiments on loess samples, which are compatible with the identification of component L with highly oxidized magnetite. Moderate heating to 150°C removes the effects of low-temperature oxidation of magnetite. In particular, *Velzen and Dekkers* [1999] measured following maximal changes of the magnetic properties after heating to 150°C: k_{ARM}/IRM increases up to 10%, IRM decreases up to 20% and the coercivity of remanence decreases up to 25%. The transformation of maghemite into hematite during heating can be simulated by subtracting the contribution of component L from BY55, with following changes of the bulk magnetic properties: k_{ARM}/IRM increases by 10%, IRM decreases by 21% and MDF_{IRM} decreases by 23%.

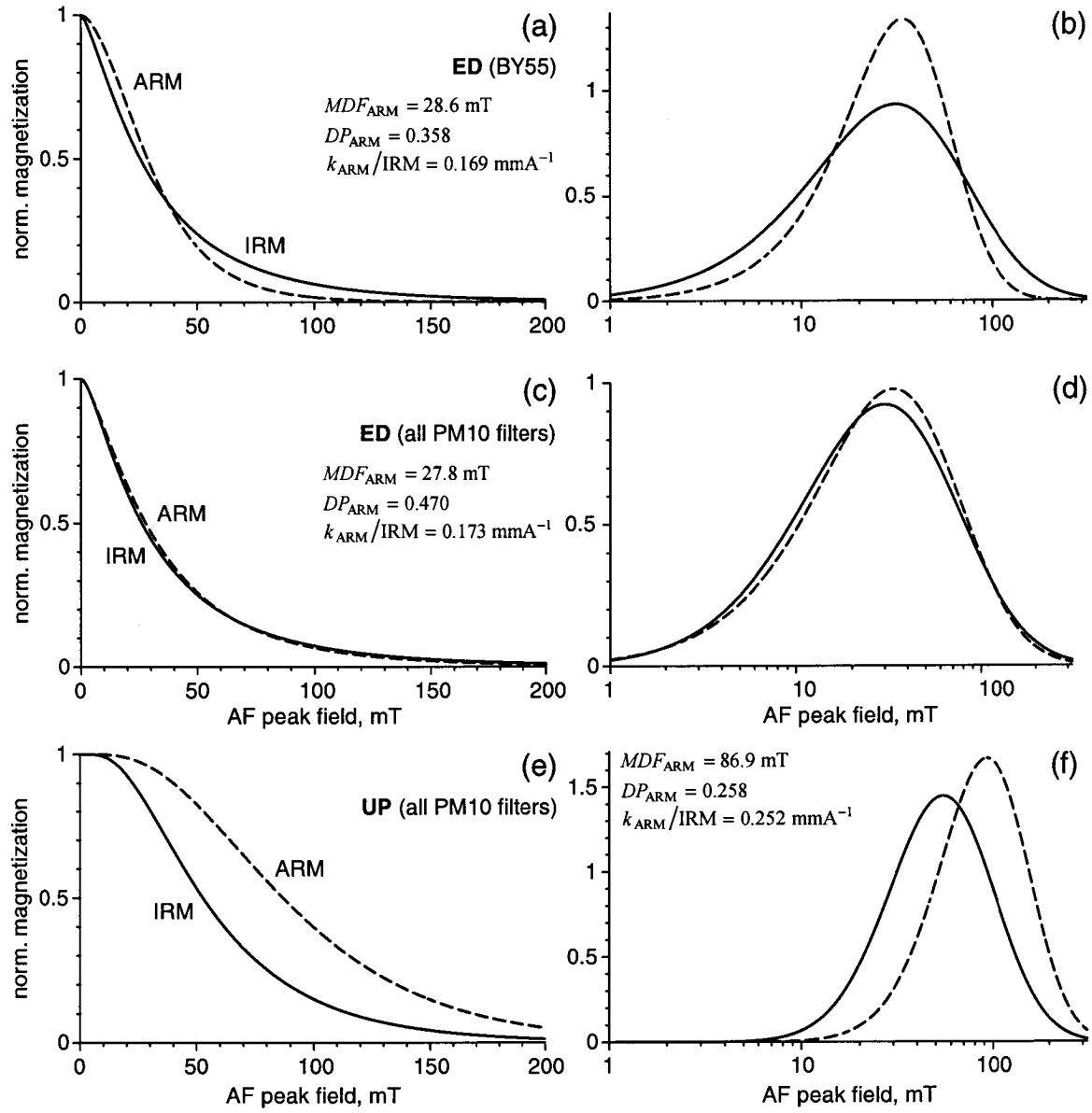

Figure 13. *Typical magnetic properties of ARM and IRM for component ED of a pristine loess (a,b), and of atmospheric PM samples (c,d). The typical properties of the component of atmospheric PM related to the urban pollution (UP), are plotted in (e,f). Left, normalized AF demagnetization curves and right, normalized coercivity distributions of IRM (solid line) and ARM (dashed). Notice the differences between ARM and IRM for component ED in loess and for component UP.*

The similarity between the results of *van Velzen and Dekkers* [1999] and the effect of subtracting component L from BY55 supports the identification of L with highly oxidized magnetite or maghemite. The difference between the coercivity distribution of the ARM of component ED in the loess on one hand and in the PM10 samples on the other, can be explained by the growth of component L at the cost of component ED during weathering processes.

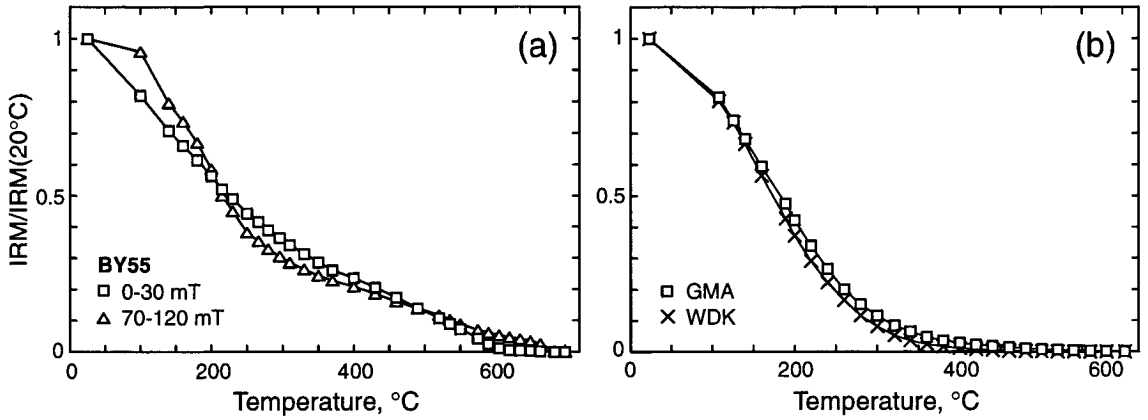

Figure 14. *Thermal demagnetisation of IRM for the pristine loess BY55 (a), and for two samples of atmospheric PM (b). A mixture of magnetite and maghemite with a broad distribution of blocking temperatures characterized the loess sample. The atmospheric PM shows a curious exponential distribution of blocking temperatures, which is more pronounced in the polluted sample WDK. The remanence is almost completely removed at 400 °C.*

The low-temperature oxidation process of magnetite is related to the diffusion of Fe^{2+} ions from the interior of a grain to its surface and is driven by the oxidation gradient [*van Velzen and Dekkers*, 1999]. Since the thickness of the oxidized shell of a grain cannot grow indefinitely, small grains are maghemitized to a higher extent than larger grains. For example, *Haneda and Morrish* [1977] reported a 95% conversion of 0.1 nm magnetite grains into maghemite after 50 days at room temperature. Thus, maghemitization involves preferentially the fine fraction of magnetite, which is the most efficient ARM carrier. As a consequence, the ARM is affected by maghemitization to a larger extent than IRM. The high-coercivity contribution to the ARM, carried by fine SD particles, is transformed into component L, and DP_{ARM} decreases (Figure 12b).

Component UP is characterized by peculiar magnetic properties: $MDF_{\mathrm{IRM}} \approx 87$ mT, which is the highest value among all components except component H, and $DP_{\mathrm{ARM}} \approx 0.25$ (Figure 13e,f). The difference between the MDFs of ARM and IRM is unusually large: MDF_{IRM} is only 61% of MDF_{ARM}. A trend can be recognized for the ARM ratio, which varies from 0.33 mm/A in the less polluted sample GMA to 0.166 mm/A in the highly polluted sample GUB. Component UP can be unambiguously identified with urban pollution dust, since its abundance in the PM10 samples is directly related to the pollution degree of the site. The urban pollution of the region where the samples have been collected is mainly produced by waste incineration and motor vehicles [*Hüglin*, 2000]. At least two sources are responsible for the magnetic signal of component UP: fly-ash particles produced during combustion [*Oldfield et al.*, 1985; *Flanders*, 1994; *Flanders*, 1999; *Kapička et al.*, 2001] and metallic particles released by vehicle brakes [*Flanders*, 1994]. These two sources are expected to produce

particulate matter with different magnetic and aerodynamic properties. The group of smaller particles may be transported to longer distances and is expected to dominate the pollution signal in sites that are located far away from the sources. A dependence of the diameter of fly-ash particles with the distance from fossil power stations was observed by *Flanders* [1999]. The trend observed for k_{ARM}/IRM and the unusually large difference between the MDFs of ARM and IRM can be explained by assuming UP to be a binary mixture of two components with similar coercivities and different values of k_{ARM}/IRM. The magnetization carried by the smaller particles has higher k_{ARM}/IRM values and a smaller coercivity, the opposite is true for the larger particles. In fly ashes, the high values of MDF_{ARM} and MDF_{IRM} are due to the high stress developed during the rapid cooling of the particles after their formation. *Flanders* [1999] reported coercivity values of fly-ash particles, which are 15 times larger than those of slowly cooled magnetite of comparable size. Thermal demagnetization curves of room temperature IRM imparted with a 300 mT field are shown in Figure 14b for the less polluted sample GMA and for the highly polluted sample WDK. The curves are similar and show a kind of exponential decay, which is more pronounced in WDK. The remanent magnetization is almost completely removed at 400°C. However, a small remanence is still present at 650°C, and no Curie temperature point can be recognized up to this temperature. *Muxworthy et al.* [2002] reported Curie temperatures above 650°C from susceptibility heating and cooling curves of urban PM collected in Munich, Germany, which could be explained with the presence of metallic iron. *Kapička et al.* [2001] reported a Curie temperature of about 640°C for unaltered fly ash, which suggested maghemite as the dominant ferrimagnetic phase.

7.4. Modern soils, paleosols and red clays

The coercivity distributions of a modern soil (M5A), a paleosol (SPS3) and a red clay (RCL) have been modeled with three components: PD (pedogenic magnetite), L (loess component) and H (Figure 15). Component PD is predominant in all three samples and accounts for more than 80% of the IRM and 95% of the ARM. The coercivity distributions of PD are characterized by relatively uniform parameters: $MDF_{\mathrm{ARM}} \approx 18$ mT and $DP_{\mathrm{ARM}} \approx 0.32$ (Figure 16). The values of k_{ARM}/IRM are relatively high and scattered, ranging from 0.7 mm/A in the recent soil to 1.7 mm/A in the paleosol. Large values of k_{ARM}/IRM and small coercivities have been reported for pedogenic magnetite and in samples of ultrafine, synthetic magnetite [*Özdemir and Banerjee*, 1982; *Maher*, 1988]. These properties are compatible with those predicted by *Egli and Lowrie* [2002] for ultrafine magnetite. The origin of pedogenic magnetite has been debated: *Maher* [1988] postulated inorganic processes, while *Fassbinder et al.* [1990] observed magnetic bacteria in soils and identified aggregations of ultrafine magnetite with partially dissolved magnetosomes. *Hanesch and Petersen* [1999] obtained an increase of the magnetic susceptibility of a soil over three orders of magnitude 200 days after the addition of a nutrition solution for anaerobic bacteria.

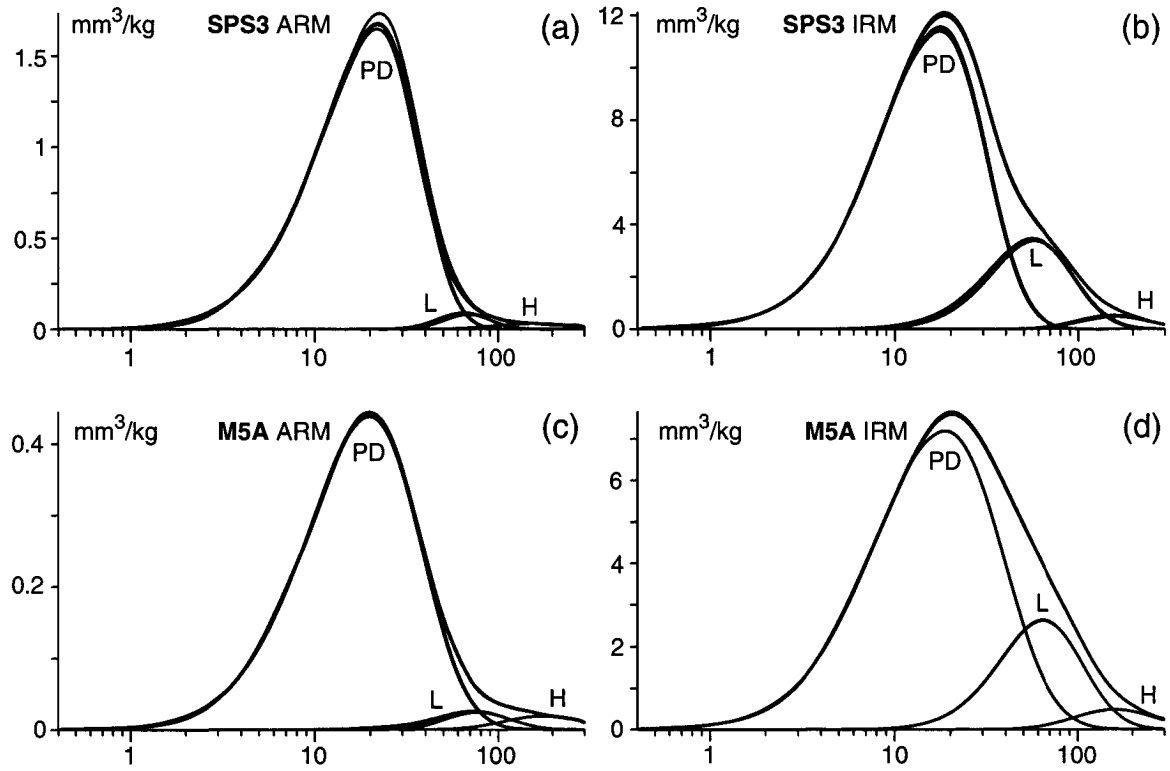

Figure 15. *Examples of component analysis with ARM and IRM coercivity distributions of a well-developed paleosol (SPS3) from the Central Chinese Loess Plateau, and a recent soil (M5A) from the Western Chinese Loess Plateau. Pedogenic magnetite PD is predominant in both samples. Additionally, small contributions of the components L and H (Figure 12) have been identified as well. The magnetic properties of pedogenic magnetite are similar to those of component EX in lacustrine and marine sediment, suggesting similar processes of formation.*

The magnetic properties of component PD are incompatible with those of magnetosomes in oxic and anoxic sediments (components BS, BH or BM, BI). The identification of component PD with biogenic magnetite is therefore excluded. This is not in contradiction with the observation of magnetic bacteria in soils, since their concentration of 100 cells/ml [*Fassbinder et al.*, 1990] is far smaller than the typical value of 10^7 cells/ml reported for lake sediments [*Hilton*, 1987]. The magnetic properties of component PD are very similar to those of component EX, suggesting similar formation processes. The magnetic properties of EX and PD have been modeled assuming ultrafine magnetite particles with logarithmic Gaussian distributions of grain volumes V and microcoercivites H_K. The susceptibility of ARM, $k_{ARM}(V, H_K)$, and the switching field $H_{sw} = h(V, H_K)$ of these particles have been calculated according to *Egli and Lowrie* [2002]. *Sparks et al.* [1990] reported grain size distributions of extracellular magnetite produced by GS15 under various culture conditions, with mean values ranging from 12 to 15 nm and $\sigma_V \approx 0.3$. Volumes distributions with $\langle d \rangle = 10$ to 15 nm, and $\sigma_V = 0.3$ have been assumed.

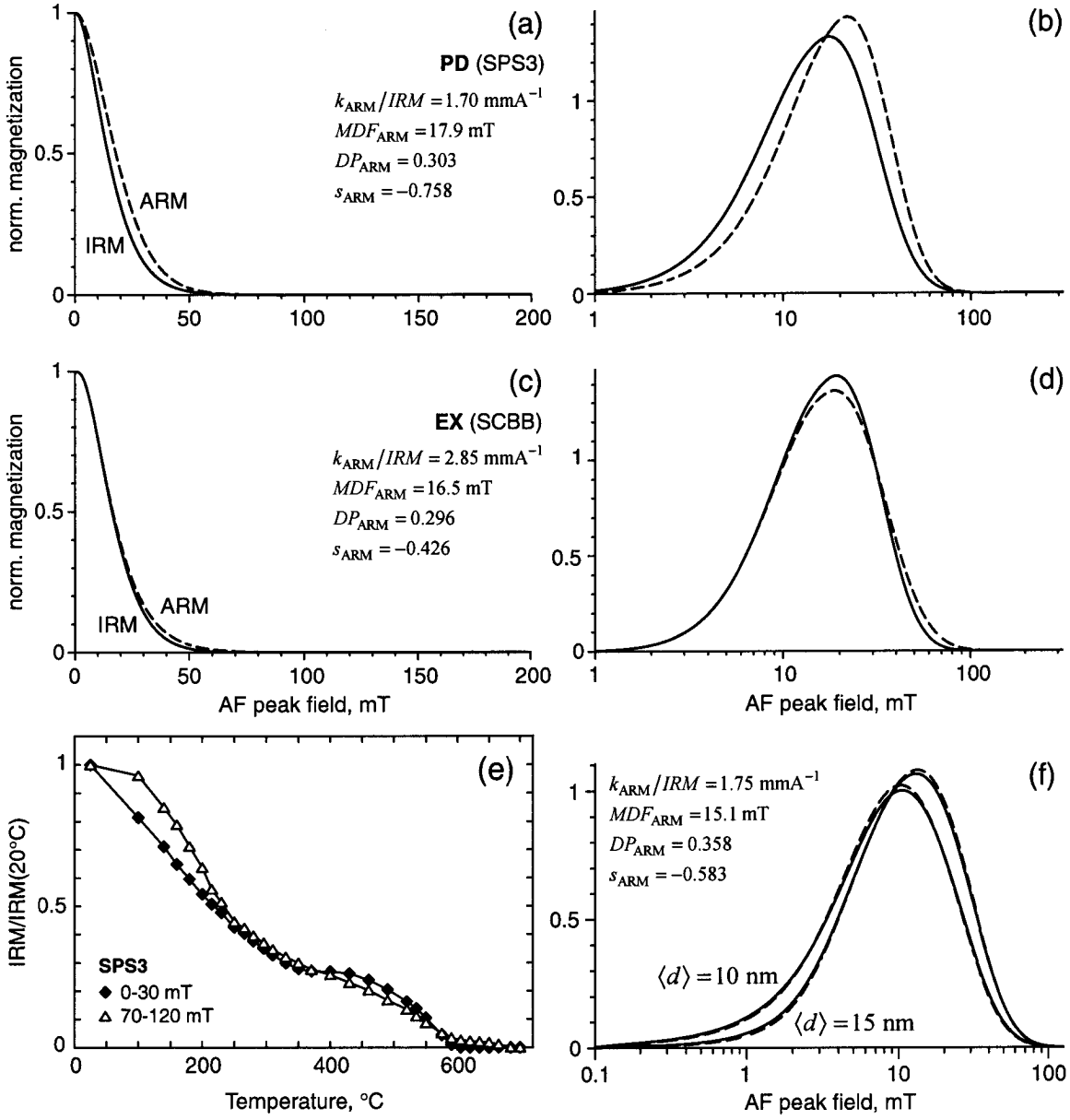

Figure 16. *Typical magnetic properties of ARM and IRM for the pedogenic component PD (a,b), and for component EX from a limestone (c,d). Left, normalized AF demagnetization curves and right, normalized coercivity distributions of IRM (solid line) and ARM (dashed). (e) Thermal demagnetisation of IRM for the well-developed paleosol SPS3. The relatively narrow distribution of blocking temperatures of the pedogenic component between* 400°C *and* 580°C *is superimposed to a broader distribution, probably due to parent material on which the soil developed. Components PD and EX have similar magnetic properties, which are compatible with those of ultrafine, low-coercivity magnetite. (f) Calculated magnetic properties of extracellular magnetites with a lognormal grain size distribution centred at* 10 *and* 15 nm, *respectively. The coercivity distributions of ARM and IRM at room temperature have been calculated after Egli and Lowrie [2002]. The coercivity distribution of the particles with* $\langle d \rangle = 15$ nm *is very similar to that of pedogenic and extracellular magnetites. The ARM ratio is similar as well.*

For the microcoercivity distribution, a mean aspect ratio of 0.8 has been assumed for the shape of the particles, which gives $\bar{H}_K = 50$ mT. Extreme values of 0.5 and 0.95 for the aspect ratio can be deduced from the electron microscope observations of *Sparks et al.* [1990]. These values correspond to microcoercivities of 160 and 16 mT, respectively. The microcoercivity distribution is approximately included between these limits if $\sigma_K = 0.14$. The coercivity distribution of component PD, calculated with the above distribution parameters, is plotted in Figure 16f. Only a small fraction of the particles carry a remanence: $M_{rs}/M_s = 0.014$ for $\langle d \rangle = 15$ nm, and $M_{rs}/M_s = 0.00084$ for $\langle d \rangle = 10$ nm. The coercivity distributions of ARM and IRM are left skewed and almost identical in shape, and the ARM ratio is relatively high. The magnetic properties for $\langle d \rangle = 15$ nm are very similar to those of components PD and EX, and support their identification with ultrafine magnetite similar to that produced by dissimilatory iron-reducing bacteria.

Component L has been identified in the loess sample and interpreted as strongly oxidized magnetite or maghemite. Small contributions of this component can also be observed in the SPS3, M5A and RCL, revealing traces of the parent material on which the soils have formed. The thermal demagnetization of room temperature IRMs imparted on different coercivity intervals of SPS3 is shown in Figure 16e. The 0-30 mT coercivity interval was selected to magnetize mainly the component PD; component L was preferentially magnetized in the 70-120 mT coercivity interval. Component L shows a similar behaviour as in the loess sample. Component PD is characterized by a constant decrease of the remanence up to 400°C, followed by a thermal decay, which is similar to that of magnetosomes (Figure 11). The remanence is totally removed above the Curie temperature of magnetite.

7.6. Summary of the magnetic properties of natural components

The magnetic properties of all natural low-coercivity components identified in this paper are summarized in Figure 17. The components are clearly grouped into few, characteristic clusters. Bacterial magnetite forms two groups, BS and BH, with constant values of MDF_{ARM} but a variable ARM ratio, which is related to the redox potential of the sediments. Components D, PD and EX have overlapping coercivity distributions, which cannot be resolved with component analysis. These components form a mixing trend between end-members defined by relatively coarse-grained detrital magnetite on one side (component D), and ultrafine magnetite on the other (components PD and EX). Distinct groups are formed by wind-blown dust (component D), which contains coarse-grained magnetite, and by a magnetic component (UP) found in atmospheric particulate matter from polluted urban areas. Another component with a relatively high-coercivity (L) occur in samples of loess and soils formed from parent loess, and is formed probably be highly oxidized magnetite.

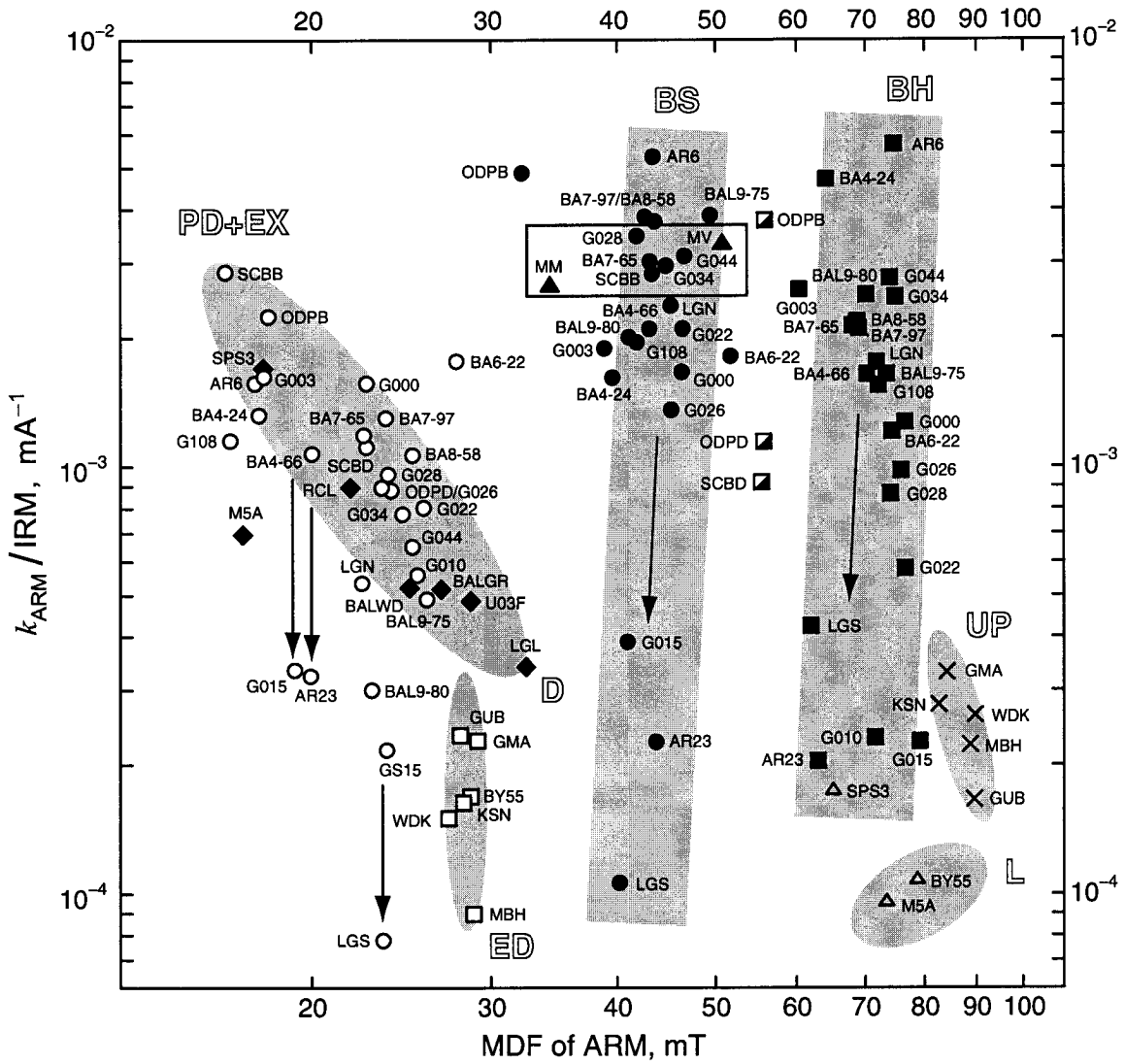

Figure 17. *Summary of the magnetic properties of ARM and IRM for all iron spinel components identified in this paper: MDF_{ARM} and k_{ARM}/IRM. The magnetic components (symbols) group into different clusters, indicated by grey ellipses and rectangles, whose extension is equal to four times the standard deviation of the scattered magnetic properties of the components in each cluster. White letters classify all components into low-coercivity magnetosomes (biogenic soft, BS: dots), high-coercivity magnetosomes (biogenic hard, BH: squares), ultrafine extracellular magnetite (EX: circles), pedogenic magnetite (PD: diamonds), detrital particles transported in water systems (D: diamonds), wind-blown particles (eolian dust, ED: open squares), atmospheric particulate matter produced by urban pollution (UP: crosses), and a maghemite component in loess (L: open triangles). Other components, as BM (dots) and BI (half-filled squares), have been measured in a few numbers of samples and are not labelled. The open rectangle indicates the range of values measured in samples of cultured magnetotectic bacteria (triangles). GS15 labels the measurement of extracellular magnetite particles produced by a cultured dissimilatory iron-reducing microorganism [Lovley et al., 1987; Moskowitz et al., 1993]. Its properties are influenced by the strong magnetostatic interactions: GS15 sediments would probably fall into the cluster labelled with PD+EX. Arrows indicate the decrease of k_{ARM}/IRM observed during anoxic conditions in lake sediments.*

8. Conclusions

A detailed analysis of ARM and IRM demagnetization curves has been performed on 39 samples of sediments from various environments. The results have been compared with 27 reference samples of biogenic and synthetic magnetite. Eight groups of components with consistent magnetic properties could be identified in the sediment samples by unmixing the demagnetization curves.

Biogenic magnetites from lake sediments could be divided into a low- and a high-coercivity group, BS and BH, which correspond to different morphologies of the magnetosomes. The unequivocal characteristic of natural biogenic magnetite is represented by the extremely low DP and not by the high ARM ratio, as wrongly suggested by measurements on cultured bacteria. It has been found that the ARM ratio of natural biogenic magnetite is controlled by the redox potential in the sediment, and ranges from 0.1 mm/A under anoxic conditions to 5 mm/A under sub-oxic conditions. The magnetosomes of Baldeggersee are surrounded by hexagonal pyrrhotite during anoxic conditions, which indicates their partial dissolution.

Biogenic magnetites from marine sediments are similar to their freshwater counterpart, with 30% smaller coercivities. The smaller coercivities are probably related to the different morphology of magnetosomes produced by marine magnetotactic bacteria. Bacterial magnetite is an important remanence carrier in limestones: its contribution to the IRM has been quantified to >50% in the measured limestones.

Extracellular magnetite (EX) has been characterized in lacustrine and marine sediments, as well as in limestones. It is very similar to the pedogenic component (PD) of soils, paleosols and red clays. The similarity between the magnetic properties of EX and PD in such different sedimentary environments suggests a common process of formation, related to the nucleation and growth of SP magnetite grains in the matrix of the sediment. Coercivity distributions of ARM and IRM for EX and PD can be modeled with the magnetic properties calculated for extracellular magnetite produced by dissimilatory iron-reducing bacteria, suggesting similar grain sizes distributions and particle shapes.

The detrital component of lake sediments (D) has been characterized using samples of Late Glacial sediments, samples from the catchment, and samples from a river delta. Component D has relatively homogeneous magnetic properties that seem to be poorly influenced by the ecology of the catchment area. Components D and EX have highly overlapping coercivity distributions that cannot be unmixed by component analysis. However, their ARM ratios are quite different, and can be used to estimate the magnetic contribution of each component.

Magnetic properties of dusts (ED) have been investigated in pristine loess and in samples of atmospheric particulate matter. Component ED in loess is affected by low-temperature oxidation of magnetite, which produces a high-coercivity maghemite component. The magnetic properties of ED are similar in all analyzed samples, despite the different souces of dust in

western China and in Switzerland. A magnetic component associated to urban pollution (UP) could be identified in the atmospheric particulate samples. This component is characterized by large MDFs and small ARM ratios. The ARM ratio depends apparently on the degree of pollution and indicates a possible mixing trend of fly ash and metallic particles released by vehicles.

The results of the present paper can be used as a reference for the individuation of magnetic components in sedimentary environments. An exact knowledge of these properties and their variability is of fundamental importance for a correct inversion of multi-component mixing models and for the characterization of natural processes as weathering, transport, dissolution and iron cycling. The future measurement and analysis of a large number of sediments from various regions of the Earth is necessary to extend the present database.

Acknowledgements.

I would like to thank M. Sturm, S. Spassov, F. Heller, I. Baster, D. Nourgaliev, M. Fuller and G. Muttoni for providing the samples measured in the present work, and K. Monecke for her help in sampling the Baldeggersee cores. All lake sediment samples have been freeze-dried at the limnogeology laboratory of the ETH Zürich. Low-temperature measurements have been performed at the IRM laboratory in Minnesota. I am grateful to M. Sturm, I. Baster, K. Monecke and D. Nourgaliev for interesting discussions about lake sediments, and S. Spassov and F. Heller for useful informations about loesses and paleosols. The manuscript has been improved after an informal revision of M. Dekkers. ETH Research Project 0-20556-00.

References

Bailey, M. E. and D. J. Dunlop, Alternating field characteristics of pseudo-single-domain (2-14 μm) and multidomain magnetite, *Earth Planet. Sci. Lett.*, *63*, 335-352, 1983.

Baster, I., Holocene delta in western Lake Geneva and its paleoenvironmental implications: seismic and sedimentological approach, Ph.D. thesis, Univ. of Geneva, Switzerland, 2002.

Berner, R. A., Stability fields of iron minerals in anaerobic marine sediments, *J. Geol.*, *72*, 826-834, 1964.

Canfield, D. E., and R. A. Berner, Dissolution and pyritization of magnetite in anoxic marine sediments, *Geochim. Cosmochim. Acta*, *51*, 645-659, 1987.

Carter-Stiglitz, B., B. Moskowitz and M. Jackson, Unmixing magnetic assemblages and the magnetic behaviour of bimodal mixtures, *J. Geophys. Res.*, *106*, 26397-26411, 2001.

Chang S. R., J. L. Kirschvink and J. F. Stolz, Biogenic magnetite as a primary remanence carrier in limestone deposits, *Phys. Earth Planet. Inter.*, *46*, 289-303, 1987.

Cisowski, S. M., J. R. Dunn, M. Fuller and P. J. Wasilewski, NRM:IRM(s) demagnetization plots of intrusive rocks and the origin of their NRM, *Tectonophysics*, *184*, 35-54, 1990.

Dankers, P. H. M., Magnetic properties of dispersed natural iron-oxides of known grain-size, Ph.D. thesis, Univ. of Utrecht, Netherlands, 1978.

Dankers, P. and N. Sugiura, The effect of annealing and concentration on the hysteresis properties of magnetite around the PSD-MD transition, *Earth Planet. Sci. Lett.*, *56*, 422-428, 1981.

Day, R., M. Fuller and V. A. Schmidt, Hysteresis properties of titanomagnetites: grain-size and compositional dependence, *Phys. Earth Planet. Inter.*, *13*, 260-267, 1977.

De Boer, P. L. Aspects of middle Cretaceous pelagic sedimentation in southern Europe, *Geologica Ultraiectina*, *31*, 1983.

De Boer, C. B. and M. J. Dekkers, Grain-size dependence of the rock magnetic parameters for a natural maghemite, *Geophys. Res. Lett.*, *23*, 2815-2818, 1996.

Dekkers, M. J., and M. A. A. Schoonen, Magnetic properties of hydrothermally synthesized greigite (Fe_3S_4) – I. Rock magnetic parameters at room temperature, *Geophys. J. Int.*, *126*, 360-368, 1996.

Dunlop, D. J. and G. West, An experimental evaluation of single-domain theories, *Rev. Geophys.*, *7*, 709-757, 1969.

Dunlop, D. J., Coercive forces and coercivity spectra of submicron magnetites, *Earth Planet. Sci. Lett.*, *78*, 288-295, 1986a.

Dunlop, D. J., Hysteresis properties of magnetite and their dependence on particle size: a test of pseudo-single-domain remanence models, *J. Geophys. Res.*, *91*, 9569-9584, 1986b.

Dunlop, D. J. and K. S. Argyle, Thermoremanence, anhysteretic remanence and susceptibility of submicron magnetites: Nonlinear field dependence and variation with grain size, *J. Geophys. Res.*, 102, 20199-20210, 1997.

Dunlop, D. J. and Ö. Özdemir, *Rock magnetism*, Cambridge University Press, 573 pp., 1997.

Dunlop, D. J., Theory and application of the Day plot (M_{rs}/M_s versus H_{cr}/H_c), 2: Application to data for rocks, sediments and soils, *J. Geophys. Res.*, *107*, doi 10.1029/2001JB000487, 2002.

Egli, R. and W. Lowrie, The anhysteretic remanent magnetization of fine magnetic particles, *J. Geophys. Res.*, *107*, 2209-2229, 2002.

Egli, R., Analysis of the field dependence of remanent magnetization curves, *J. Geophys. Res.*, 102, doi 10.1029/2002JB002023, 2003.

Erba, E. and B. Walsworth-Bell, Lithological Milankovitch cycles in the Cenomanian of the Scaglia Bianca at Furlo (Umbria-Marche Appennines, Italy). *Multidisciplinary approach to cyclostratigraphy*, International Workshop, Sorrento, Italy, Abstracts Volume, p. 26, 2001.

Evans, M. E. and F. Heller, Magnetic enhancement and paleoclimate: study of a loess/paleosol couplet across the Loess Plateau of China, *Geophys. J. Int.*, *117*, 257-264, 1994.

Fabian, K. and T. von Dobeneck, Isothermal magnetization of samples with stable Preisach function: a survey of hysteresis, remanence, and rock magnetic parameters, *J. Geophys. Res.*, *107*, 17659-17667, 1997.

Fassbinder, J. W. E., H. Stanjek and H. Vali, Occurrence of magnetic bacteria in soil, *Nature*, *343*, 161-163, 1990.

Fearon, M., R. W. Chantrell and E. P. Wohlfarth, A theoretical study of interaction effects on the remanence curves of particulate dispersions, *J. Magnet. Mag. Mat.*, *86*, 197-206, 1990.

Flanders, P. J., Collection, measurement, and analysis of airborne magnetic particulates from pollution in the environment, *J. Appl. Phys.*, *75*, 5931-5936, 1994.

Flanders, P. J., Identifying fly ash at a distance from fossil fuel power stations, *Environ. Sci. Technol.*, *33*, 528-532, 1999.

Fuller, M., T. Kidane and J. Ali, AF demagnetization characteristics of NRM, compared with anhysteretic and saturation isothermal remanence: an aid in the interpretation of NRM, *Phys. Chem. Earth*, *27*, 1169-1177, 2002.

Geiss, C. E. and S. K. Banerjee, A multi-parameter rock magnetic record of the last glacial-interglacial paleoclimate from south-central Illinois, USA, *Earth Planet. Sci. Lett.*, *152*, 203-216, 1997.

Gillingham, E. W. and F. D. Stacey, Anhysteretic remanent magnetization (ARM) in magnetite grains, *Pure Appl. Geophys.*, *91*, 160-165, 1971.

Halgedahl, S. L., Revisiting the Lowrie-Fuller test: alternating field demagnetization characteristics of single-domain through multidomain glass-ceramic magnetite, *Earth Planet. Sci. Lett.*, *160*, 257-271, 1998.

Haneda, K. and A. H. Morrish, Magnetite to maghemite transformation in ultrafine particles, *J. Physique*, *38*, suppl. C1, 321-323, 1977.

Hanesch, M. and N. Petersen, Magnetic properties of a recent parabrown-earth from Southern Germany, *Earth Planet. Sci. Lett.*, *169*, 85-87, 1999.

Hartstra, R. L., A comparative study of the ARM and I_{sr} of some natural magnetites of MD and PSD grain size, *Geophys. J. R. Astron. Soc.*, *71*, 497-518, 1982.

Heider, F., D. J. Dunlop and H. C. Soffel, Low-temperature and alternating field demagnetization of saturation remanence and thermoremanence in magnetite grains (0.037 μm to 5 mm), *J. Geophys. Res.*, *97*, 9371-9381, 1992.

Heider, F., A. Zitzelsberger and K. Fabian, Magnetic susceptibility and remanent coercive force in grown magnetite crystals from 0.1 μm to 6 mm, *Phys. Earth Planet. Inter.*, *93*, 239-256, 1996.

Heslop, D., M. J. Dekkers, P. P. Kruiver and I. H. M. van Oorschot, Analysis of isothermal remanent magnetization acquisition curves using the expectation-maximization algorithm, *Geophys. J. Int.*, *148*, 58-64, 2002.

Heslop, D., G. McIntosh, and M. J. Dekkers, Using time and temperature dependant Preisach models to investigate the limitations of modelling isothermal remanent magnetisation acquisition curves with cumulative log Gaussian functions, submitted to *Geophys. J. Int.*, 2003.

Hesse, P. P., Mineral magnetic 'tracing' of aeolian dust in southwest Pacific sediments, *Palaeogeography, Palaeoclimatology, Palaeoecology, 131*, 327-353, 1997.

Hilton, J., A simple model for the interpretation of magnetic records in lacustrine and ocean sediments, *Quaternary Res., 27*, 160-166, 1987.

Housen, B. A., S. K. Banerjee and B. M. Moskowitz, Low-temperature magnetic properties of siderite and magnetite in marine sediments, *Geophys. Res. Lett., 23*, 2843-2846, 1996.

Hüglin, C., Anteil des Strassenverkehrs an den PM10- und PM2.5-Immissionen, Bericht C4 des NFP 41, 2000.

Johnson, H. P. and R. T. Merrill, Magnetic and mineralogical changes associated with low-temperature oxidation of magnetite, *J. Geophys. Res., 77*, 334-341, 1972.

Johnson, H. P., W. Lowrie and D. Kent, Stability of anhysteretic remanent magnetization in fine and coarse magnetite and maghemite particles, *Geophys. J. R. astr. Soc. 41*, 1-10, 1975.

Kapička, A., N. Jordanova, E. Petrovský and S. Ustjak, Effect of different soil conditions on magnetic parameters of power-plant fly ashes, *J. Appl. Geophys., 48*, 93-102, 2001.

King, J., S. K. Banerjee, J. Marvin and Ö. Özdemir, A comparison of different magnetic methods for determining the relative grain size in natural materials: some results from lake sediments, *Earth Planet. Sci. Lett., 59*, 404-419, 1982.

Kneller, E. F. and F. E. Luborsky, Particle size dependence of coercivity and remanence of single-domain particles, *J. Appl. Phys., 34*, 656-658, 1963.

Kruiver, P. P., M. J. Dekkers and D. Heslop, Quantification of magnetic coercivity components by the analysis of acquisition curves of isothermal remanent magnetization, *Earth Planet. Sci. Lett., 189*, 269-276, 2001.

Kruiver, P. P., and H. F. Passier, Coercivity analysis of magnetic phases in sapropel S1 related to variations in redox conditions, including an investigation of the *S* ratio, *Geochem. Geophys. Geosys.*, 14 december 2001, paper number 2001GC000181, 2001.

Lanci, L. and D. V. Kent, Introduction of thermal activation in forward modeling of hysteresis loops for single-domain magnetic particles and implications for the interpretation of the Day diagram, *J. Geophys. Res., 108*, doi 10.1029/2001JB000944, 2003.

Lees, J. A., Mineral magnetic properties of mixtures of environmental and synthetic materials: linear additivity and interaction effects, *Geophys. J. Int., 131*, 335-346, 1997.

Leslie, B. W., S. P. Lund, and D. E. Hammond, Rock magnetic evidence for the dissolution and authigenic growth of magnetic minerals within anoxic marine sediments of the California Continental Borderland, *J. Geophys. Res., 95*, 4437-4452, 1990.

Levi, S. and R. Merrill, A comparison of ARM and TRM in magnetite, *Earth Planet. Sci. Lett., 32*, 171-184, 1976.

Leslie, B. W., S. P. Lund and D. E. Hammond, Rock magnetic evidence for the dissolution and authigenic growth of magnetic minerals within anoxic marine sediments of the California continental borderland, *J. Geophys. Res.*, *95*, 4437-4452, 1990.

Lotter, A. F., M. Sturm, J. L. Teranes and B. Wehrli, Varve formation since 1885 and high-resolution varve analyses in hypertrophic Baldeggersee (Switzerland), *Aquatic Sciences*, *57*, 305-325, 1997.

Lovley, D. R. et al., Anaerobic production of magnetite by a dissimilatory iron-reducing microorganism, *Nature*, *330*, 252-254, 1987.

Lowrie, W., and F. Heller, Magnetic properties of marine limestones, *Rev. Geophys. Space Phys.*, *20*, 171-192, 1982.

Maher, B. A., Magnetic properties of some synthetic sub-micron magnetites, *Geophys. J.*, *94*, 83-96, 1988.

Maher, B. A., Formation of ultrafine-grained magnetite in soils, *Nature*, *336*, 368-370, 1988.

Moskowitz, B. M. et al., Magnetic properties of magnetotactic bacteria, *J. Magnet. Mag. Mat.*, *73*, 273-288, 1988.

Moskowitz, B. M., R. B. Frankel and D. A. Bazylinski, Rock magnetic criteria for the detection of biogenic magnetite, *Earth Planet. Sci. Lett.*, *120*, 283-300, 1993.

Muxworthy, A. R., E. Schmidbauer and N. Petersen, Magnetic properties and Mössbauer spectra of urban atmospheric particulate matter: a case study from Munich, Germany, *Geophys. J. Int.*, *150*, 558-570, 2002.

Nourgaliev, D., F. Heller, A. Borisov, P. Iassonov, S. Ibraguimov, and M. Froidevaux, Preliminary magnetic and paleomagnetic data from Lake Aral recent sediments: reconstruction of lake history and age of lake sediments, Gent (Belgium), 2003.

Oldfield, F., A. Hunt, M. D. H. Jones, R. Chester, J. A. Dearing, L. Olsson and J. M. Prospero, Magnetic differentiation of atmospheric dusts, *Nature*, *317*, 516-518, 1985.

Oldfield, F., Toward the discrimination of fine-grained ferrimagnets by magnetic measurements in lake and near-shore marine sediments, *J. Geophys. Res.*, *99*, 9045-9050, 1994.

Özdemir, Ö. and S. K. Banerjee, A preliminary magnetic study of soil samples from west-central Minnesota, *Earth Planet. Sci. Lett.*, *59*, 393-403, 1982.

Passier, H. F., and M. J. Dekkers, Iron oxide formation in the active oxidation front above sapropel S1 in the eastern Mediterranean Sea as derived from low-temperature magnetism, *Geophys. J. Int.*, *150*, 230-240, 2002.

Penninga, I., H. de Waard, B. M. Moskowitz, D. A. Bazylinski and R. B. Frankel, Remanence measurements on individual magnetotactic bacteria, *J. Magnet. Mag. Mat.*, *149*, 279-286, 1995.

Petersen, N., T. von Dobeneck and H. Vali, Fossil bacterial magnetite in deep-sea sediments from the South Atlantic Ocean, *Nature*, *320*, 611-615, 1986.

Petrovský, E. and B. B. Ellwood, Magnetic monitoring of air- land- and water-pollution, in Quaternary climates, environments and magnetism, edited by B. A. Maher and R. Thompson, Cambridge University Press, 1999.

Proksch, R. and B. Moskowitz, Interactions between single domain particles, *J. App. Phys.*, *75*, 5894-5896, 1994.

Ratkowsky, D. A., *Nonlinear Regression Modelling, A Unified Practical Approach*, Marcel Dekker, New York, 1983.

Robertson, D. J. and D. E. France, Discrimination of remanence-carrying minerals in mixtures, using isothermal remanent magnetisation acquisition curves, *Phys. Earth Planet. Inter.*, *82*, 223-234, 1994.

Rochette, P., G. Fillion, J.-L. Mattéi and M. J. Dekkers, Magnetic transition at 30-34 Kelvin in pyrrhotite: insight into a widespread occurrence of this mineral in rocks, *Earth Planet. Sci. Lett.*, *98*, 319-328, 1990.

Schaller T., H. C. Moor and B. Wehrli, Sedimentary profiles of Fe, Mn, V, Cr, As, Mo as indicators of benthic redox conditions in Baldeggersee, *Aquatic Sciences*, *57*, 345-361, 1997.

Schmidbauer, E. and N. Schembra, Magnetic hysteresis properties and anhysteretic remanent magnetization of spherical Fe_3O_4 particles in the grain size range 60-160 nm, *Phys. Earth Planet. Inter.*, *46*, 77-83, 1987.

Schwarz, E. J., Magnetic properties of pyrrhotite and their use in applied geology and geophysics, *Geol. Surv. Canada. Prof. Paper*, *74-59*, 1-24, 1975.

Smirnov, A. V. and J. A. Tarduno, Low temperature magnetic properties of pelagic sediments (Ocean Drilling Program Site 805C): traces of maghemitization and magnetic mineral reduction, *J. Geophys. Res.*, *105*, 16457-16471, 2000.

Smirnov, A. V. and J. A. Tarduno, Estimating superparamagnetism in marine sediements with the time dependency of coercivity of remanence, *J. Geophys. Res.*, *106*, 16135-16143, 2001.

Snowball, I., L. Zillén and P. Sandgren, Bacterial magnetite in Swedish varved lake-sediments: a potential bio-marker of environmental change, *Quaternary International*, *88*, 13-19, 2002.

Sparks, N. C. H., S. Mann, D. A. Bazylinski, D. R. Lovley, H. W. Jannasch and R. B. Frankel, Structure and morphology of magnetite anaerobically-produced by a marine magnetotactic bacterium and a dissimilatory iron-reducing bacterium, *Earth Planet. Sci. Lett.*, *98*, 14-22, 1990.

Spassov, S., F. Heller, R. Kretzschmar, M. E. Evans, L. P. Yue and D. K. Nourgaliev, Detrital and pedogenic magnetic mineral phases in the loess/paleosol sequence at Lingtai (Central Chinese Loess Plateau), *Phys. Earth Planet. Inter.*, in press.

Sprowl, D. R., Numerical estimation of interactive effects in single-domain magnetite, *Geophys. Res. Lett.*, *17*, 2009-2012, 1998.

Stockhausen, H., Some new aspects for the modelling of isothermal remanent magnetization acquisition curves by cumulative log Gaussian functions, *Geophys. Res. Lett.*, *25*, 2217-2220, 1998.

Sugiura, N., ARM, TRM, and magnetic interactions: concentration dependence, *Earth Planet. Sci. Lett.*, *42*, 451-455, 1979.

Suits, N. S., and R. T. Wilkin, *Pyrite formation in the water column and sediments of a meromictic lake*, *Geology*, *26*, 1099-1102, 1998.

Symons, D. T. A. and M. T. Cioppa, Crossover plots: a useful method for plotting SIRM data in paleomagnetism, *Geophys. Res. Lett.*, *27*, 1779-1782, 2000.

Tarduno, J. A. Superparamagnetism and reduction diagenensis in pelagic sediments: Enhancement or depletion?, *Geophys. Res. Lett.*, *22*, 1337-1340, 1995.

Thompson, R., Modelling magnetization data using SIMPLEX, *Phys. Earth Planet. Inter.*, *42*, 113-127, 1986.

Vali, H., and J. L. Kirschvink, Magnetofossil dissolution in a paleomagnetically unstable deep-sea sediment, *Nature*, *339*, 203-206, 1989.

Van Velzen, A. J. and J. D. A. Zijderveld, Effects of weathering on single-domain magnetite in early Pliocene marine marls, *Geophys. J. Int.*, *121*, 267-278, 1995.

Van Velzen, A. J. and M. J. Dekkers, Low-temperature oxidation of magnetite in loess-paleosol sequences: a correction of rock magnetic parameters, *Studia Geoph. et Geod.*, *43*, 357-375, 1999.

Verosub, K. L. and A. P. Roberts, Environmental magnetism: past, present and future, *J. Geophys. Res.*, *100*, 2175-2192, 1995.

Von Dobeneck, T., A systematic analysis of natural magnetic mineral assemblages based on modelling hysteresis loops with coercivity-related hyperbolic functions, *Geophys. J. Int.*, *124*, 675-694, 1996.

Wehrli, B., A. F. Lotter, T. Schaller and M. Sturm, High-resolution varve studies in Baldeggersee (Switzerland): project overview and limnological background data, *Aquatic Sciences*, *57*, 360-386, 1997.

Worm, H. U. and M. Jackson, The superparamagnetism of Yucca Mountain Tuff, *J. Geophys. Res.*, *104*, 25415-25425, 1999.

Xu, S. and D. J. Dunlop, Toward a better understanding of the Lowrie-Fuller test, *J. Geophys. Res.*, *100*, 22533-22542, 1995.

Yu, L. and F. Oldfield, A multivariate mixing model for identifying sediment source from magnetic measurements, *Quaternary Research*, *32*, 168-181, 1989.

Yu, Y., D. J. Dunlop and Ö. Özdemir, Partial anhysteretic remanent magnetization in magnetite, 1: Additivity, *J. Geophys. Res.*, *107*, doi 10.1029/2001JB001249, 2002.

Yamazaki, T., Cautionary note on magnetic grain-size estimation using the ratio of ARM to magnetic susceptibility, *Geophys. Res. Lett.*, *24*, 751-754, 1997.

Appendix

Table1. *Component analysis results for all lake sediments analyzed in this paper. Component H is not reported. Values of p given with only two digits were kept fixed during optimization. See the text for more details about the samples.*

sample	comp.	k_{ARM}/IRM mm/A	a Am^2/kg	μ	σ	q	p	MDF mT	DP	s
G000 (~1999) Baldeggersee, dark brown, bioturbated, artificial areation	D+EX	1.560	4.72×10^{-5}	1.355	0.341	0.708	1.8	22.65	0.363	−0.389
			3.79×10^{-4}	1.167	0.357	0.779	1.8	14.69	0.385	−0.212
	BS	1.660	7.66×10^{-5}	1.666	0.186	0.692	2.0	46.34	0.178	−0.361
			5.79×10^{-4}	1.561	0.236	0.707	2.0	36.39	0.226	−0.322
	BH	1.270	1.20×10^{-5}	1.884	0.097	0.620	2.0	76.56	0.092	−0.591
			1.19×10^{-4}	1.829	0.141	0.701	2.0	67.45	0.136	−0.337
G003 (~1984) Baldeggersee, dark brown, bioturbated, artificial areation	D+EX	1.610	4.15×10^{-5}	1.255	0.286	0.786	1.8	17.99	0.309	−0.197
			3.23×10^{-4}	1.124	0.337	0.741	1.8	13.30	0.361	−0.298
	BS	1.880	5.89×10^{-5}	1.590	0.174	0.762	2.0	38.90	0.169	−0.203
			3.93×10^{-4}	1.505	0.226	0.798	2.0	31.99	0.221	−0.144
	BH	2.590	7.20×10^{-5}	1.781	0.134	0.779	2.0	60.39	0.131	−0.173
			3.49×10^{-4}	1.733	0.176	0.733	2.0	54.08	0.170	−0.262
G010 (~1972) Baldeggersee, varved, eutrophic	D	0.558	1.41×10^{-5}	1.405	0.311	0.964	1.679	25.41	0.369	−0.006
			3.16×10^{-4}	1.475	0.413	0.752	1.8	29.85	0.444	−0.271
	BH	0.232	2.37×10^{-6}	1.855	0.147	0.802	2.189	71.61	0.134	−0.117
			1.28×10^{-4}	1.876	0.181	0.644	2.0	75.16	0.172	−0.506
G015 (~1958) Baldeggersee, biogenic varves, eutrophic	D+EX	0.333	1.02×10^{-5}	1.285	0.309	0.723	1.8	19.28	0.330	−0.344
			3.84×10^{-4}	1.266	0.368	0.687	1.8	18.45	0.390	−0.453
	BS	0.387	1.01×10^{-5}	1.613	0.202	0.701	2.0	41.02	0.194	−0.337
			3.27×10^{-4}	1.646	0.220	0.800	2.0	44.26	0.215	−0.140
	BH	0.227	9.32×10^{-6}	1.905	0.138	0.939	2.0	80.35	0.138	−0.012
			5.16×10^{-4}	1.896	0.158	0.698	2.0	78.70	0.152	−0.345
G022 (~1940) Baldeggersee, biogenic varves, eutrophic	D+EX	0.801	2.89×10^{-5}	1.411	0.356	0.961	1.8	25.76	0.393	−0.006
			4.54×10^{-4}	1.340	0.357	0.685	1.8	21.88	0.379	−0.460
	BS	2.100	3.38×10^{-5}	1.667	0.230	0.872	2.0	46.45	0.228	−0.055
			2.02×10^{-4}	1.593	0.169	0.661	2.0	39.17	0.161	−0.452
	BH	0.579	1.87×10^{-5}	1.884	0.119	0.550	2.0	76.56	0.112	−0.904
			4.07×10^{-4}	1.882	0.138	0.891	2.0	76.21	0.137	−0.039
G026 (~1932) Baldeggersee, biogenic varves, eutrophic	D+EX	0.878	4.31×10^{-5}	1.379	0.372	0.924	1.8	23.93	0.410	−0.023
			6.17×10^{-4}	1.367	0.370	0.775	1.8	23.28	0.399	−0.219
	BS	1.360	5.43×10^{-5}	1.656	0.207	0.828	2.0	45.29	0.204	−0.102
			5.03×10^{-4}	1.709	0.220	0.800	2.0	51.17	0.216	−0.140
	BH	0.979	2.36×10^{-5}	1.880	0.104	0.627	2.0	75.86	0.099	−0.565
			3.03×10^{-4}	1.903	0.133	0.863	2.0	79.98	0.132	−0.063
G028 (~1928) Baldeggersee, biogenic varves, eutrophic	D+EX	0.957	7.07×10^{-5}	1.376	0.349	1.005	1.8	23.77	0.385	0.000
			9.28×10^{-4}	1.361	0.373	0.795	1.8	22.96	0.404	−0.179
	BS	3.460	9.85×10^{-5}	1.622	0.192	0.850	2.0	41.88	0.190	−0.077
			3.58×10^{-4}	1.540	0.179	0.635	2.0	34.67	0.170	−0.536
	BH	0.865	4.29×10^{-5}	1.870	0.112	0.623	2.0	74.13	0.106	−0.582
			6.23×10^{-4}	1.835	0.142	0.894	2.0	68.39	0.141	−0.037
G034 (~1914) Baldeggersee, biogenic varves, eutrophic	D+EX	0.774	1.08×10^{-4}	1.390	0.325	0.686	1.8	24.55	0.345	−0.456
			1.75×10^{-3}	1.369	0.355	0.666	1.8	23.39	0.376	−0.524
	BS	2.950	2.75×10^{-4}	1.651	0.177	0.773	2.0	44.77	0.172	−0.184
			1.17×10^{-3}	1.645	0.187	0.715	2.0	44.16	0.180	−0.304
	BH	2.500	7.30×10^{-5}	1.874	0.105	0.614	2.0	74.82	0.099	−0.614
			3.68×10^{-4}	1.850	0.117	0.696	2.0	70.79	0.112	−0.350
G044 (~1890) Baldeggersee, light grey homogeneous marl, mesotrophic	D+EX	0.650	5.56×10^{-5}	1.400	0.332	0.981	1.8	25.12	0.366	−0.001
			1.08×10^{-3}	1.406	0.343	0.700	1.8	25.47	0.365	−0.410
	BS	3.110	1.89×10^{-4}	1.669	0.178	0.663	2.0	46.67	0.169	−0.445
			7.65×10^{-4}	1.658	0.191	0.662	2.0	45.50	0.181	−0.449
	BH	2.760	4.82×10^{-5}	1.869	0.097	0.668	2.0	73.96	0.093	−0.429
			2.19×10^{-4}	1.832	0.118	0.719	2.0	67.92	0.113	−0.294
G108 (<1700) Baldeggersee, light grey homogeneous marl, mesotrophic	D+EX	1.150	2.12×10^{-5}	1.222	0.303	0.827	1.8	16.67	0.329	−0.126
			2.32×10^{-4}	1.136	0.375	0.951	1.8	13.68	0.414	−0.009
	BS	1.950	1.04×10^{-4}	1.622	0.182	0.601	2.0	41.88	0.172	−0.666
			6.70×10^{-4}	1.516	0.277	0.609	2.0	32.81	0.262	−0.636
	BH	1.550	4.09×10^{-5}	1.858	0.101	0.907	2.0	72.11	0.100	−0.028
			3.31×10^{-4}	1.810	0.153	0.939	2.0	64.57	0.153	−0.012
BA4-24 (~760 a.D) Baldeggersee, dark grey homogeneous marl	D+EX	1.310	4.27×10^{-5}	1.250	0.334	0.736	1.8	17.78	0.357	−0.311
			4.09×10^{-4}	1.157	0.339	0.749	1.8	14.35	0.363	−0.279
	BS	1.610	1.14×10^{-4}	1.598	0.178	0.737	2.0	39.63	0.172	−0.255
			8.91×10^{-4}	1.596	0.231	0.740	2.0	39.45	0.223	−0.248
	BH	4.680	1.06×10^{-4}	1.803	0.124	0.719	2.0	63.53	0.119	−0.294
			2.83×10^{-4}	1.784	0.131	0.751	2.0	60.81	0.127	−0.225

Table1. Continued.

sample	comp.	k_{ARM}/IRM mm/A	a Am^2/kg	μ	σ	q	p	MDF mT	DP	s
BA4-66 (~570 a.D) Baldeggersee, dark brown, biogenic varves	D+EX	1.070	1.15×10^{-4}	1.302	0.345	0.646	1.8	20.04	0.365	−0.600
			1.36×10^{-3}	1.205	0.333	0.714	1.8	16.03	0.355	−0.370
	BS	2.090	3.59×10^{-4}	1.635	0.185	0.712	2.0	43.15	0.178	−0.311
			2.16×10^{-3}	1.569	0.200	0.715	2.0	37.07	0.193	−0.302
	BH	1.640	1.44×10^{-4}	1.847	0.110	0.656	2.0	70.31	0.105	−0.467
			1.11×10^{-3}	1.796	0.132	0.724	2.0	62.52	0.127	−0.283
BA6-22 (~670 b.C) Baldeggersee, brown, biogenic varves	D+EX	1.760	1.19×10^{-4}	1.443	0.270	0.643	1.8	27.73	0.285	−0.613
			8.48×10^{-4}	1.400	0.344	0.771	1.8	25.12	0.371	−0.229
	BS	1.810	8.14×10^{-5}	1.714	0.167	0.695	2.0	51.76	0.160	−0.354
			5.65×10^{-4}	1.635	0.252	0.722	2.0	43.15	0.243	−0.286
	BH	1.210	2.98×10^{-5}	1.871	0.094	0.687	2.0	74.30	0.090	−0.375
			3.10×10^{-4}	1.788	0.144	0.692	2.0	61.38	0.138	−0.361
BA7-65 (2300 b.C) Baldeggersee, grey marl	D+EX	1.110	1.12×10^{-4}	1.355	0.324	0.615	1.8	22.65	0.343	−0.729
			1.27×10^{-3}	1.300	0.350	0.688	1.8	19.95	0.371	−0.450
	BS	3.010	2.03×10^{-4}	1.635	0.167	0.850	2.0	43.15	0.165	−0.076
			8.46×10^{-4}	1.581	0.179	0.808	2.0	38.11	0.176	−0.129
	BH	2.130	9.76×10^{-5}	1.833	0.116	0.688	2.0	68.08	0.112	−0.371
			5.75×10^{-4}	1.783	0.138	0.735	2.0	60.67	0.133	−0.258
BA7-97 (2900 b.C) Baldeggersee, dark grey marl	D+EX	1.300	1.38×10^{-4}	1.374	0.304	0.684	1.8	23.66	0.323	−0.464
			1.33×10^{-3}	1.346	0.342	0.710	1.8	22.18	0.364	−0.383
	BS	3.830	1.86×10^{-4}	1.630	0.177	0.739	2.0	42.66	0.171	−0.249
			6.11×10^{-4}	1.596	0.183	0.771	2.0	39.45	0.178	−0.187
	BH	2.100	5.41×10^{-5}	1.839	0.112	0.682	2.0	69.02	0.106	−0.390
			3.23×10^{-4}	1.789	0.137	0.753	2.0	61.52	0.133	−0.221
BA8-58 (4000 b.C) Baldeggersee, light grey homogeneous marl	D+EX	1.060	1.60×10^{-4}	1.400	0.315	0.686	1.8	25.12	0.334	−0.456
			1.89×10^{-3}	1.368	0.341	0.696	1.8	23.33	0.363	−0.424
	BS	3.740	2.43×10^{-4}	1.640	0.169	0.769	2.0	43.65	0.164	−0.191
			8.15×10^{-4}	1.609	0.172	0.871	2.0	40.64	0.171	−0.056
	BH	2.180	9.13×10^{-5}	1.837	0.114	0.680	2.0	68.71	0.109	−0.395
			5.25×10^{-4}	1.787	0.142	0.735	2.0	61.24	0.138	−0.258
BAL9-75 Baldeggersee, late glacial, light grey homogeneous marl	D	0.489	1.48×10^{-5}	1.414	0.337	0.709	1.8	25.94	0.359	−0.386
			3.80×10^{-4}	1.330	0.402	0.676	1.8	21.38	0.426	−0.490
	BS	3.860	2.26×10^{-5}	1.694	0.203	0.778	2.0	49.43	0.198	−0.176
			7.36×10^{-5}	1.630	0.195	1.000	2.0	42.66	0.195	0.000
	BH	1.640	6.12×10^{-6}	1.866	0.116	0.630	2.0	73.45	0.110	−0.555
			4.68×10^{-5}	1.840	0.137	0.911	2.0	69.18	0.137	−0.026
BAL9-80 Baldeggersee, late glacial, silt + minor sand, lack of organic carbon	D+EX	0.300	1.07×10^{-4}	1.360	0.350	0.743	1.8	22.91	0.375	−0.293
			4.47×10^{-3}	1.313	0.407	0.680	1.8	20.56	0.432	−0.475
	BS	2.000	2.05×10^{-4}	1.614	0.183	0.675	2.0	41.11	0.174	−0.408
			1.29×10^{-3}	1.651	0.206	0.887	2.0	44.77	0.205	−0.042
	BH	2.520	1.56×10^{-4}	1.846	0.116	0.721	2.0	70.15	0.112	−0.290
			7.79×10^{-4}	1.812	0.147	0.708	2.0	64.86	0.141	−0.321
AR6 Lake Aral, dark greenish gray	D+EX	1.560	2.31×10^{-4}	1.246	0.352	0.855	1.8	17.62	0.384	−0.087
			1.85×10^{-3}	1.373	0.391	0.679	1.8	23.60	0.415	−0.478
	BS	5.300	5.89×10^{-4}	1.638	0.220	0.663	2.0	43.45	0.209	−0.446
			1.40×10^{-3}	1.673	0.205	0.635	2.0	47.10	0.194	−0.536
	BH	5.670	1.19×10^{-4}	1.873	0.106	0.578	2.0	74.64	0.100	−0.768
			2.62×10^{-4}	1.889	0.097	0.606	2.0	77.45	0.092	−0.647
AR23 Lake aral, dark brown	D+EX	0.324	1.81×10^{-5}	1.300	0.338	0.766	1.8	19.95	0.364	−0.238
			7.01×10^{-4}	1.200	0.306	0.690	1.8	15.85	0.325	−0.442
	BS	0.226	4.44×10^{-5}	1.641	0.263	0.641	2.0	43.75	0.249	−0.518
			2.46×10^{-3}	1.618	0.233	0.635	2.0	41.50	0.221	−0.537
	BH	0.205	1.02×10^{-5}	1.799	0.112	1.000	2.0	62.95	0.112	0.000
			6.28×10^{-4}	1.742	0.105	0.896	2.0	55.21	0.104	−0.036
LGN (~8700 BP) Lake Geneva, greenish grey clayley silt	D+EX	0.536	4.41×10^{-5}	1.350	0.397	1.000	2.0	22.39	0.397	0.000
			1.03×10^{-3}	1.209	0.427	0.607	2.0	16.18	0.403	−0.642
	BS	2.390	1.99×10^{-4}	1.655	0.200	0.681	2.0	45.19	0.191	−0.393
			1.05×10^{-3}	1.590	0.221	0.657	2.0	38.90	0.210	−0.462
	BH	1.760	8.63×10^{-5}	1.856	0.092	0.832	2.0	71.78	0.090	−0.097
			6.17×10^{-4}	1.816	0.137	0.716	2.0	65.46	0.131	−0.302
LGS (~4000 BP) Lake Geneva, brown terrigenous rich layer	D+EX	0.078	7.01×10^{-5}	1.371	0.347	1.001	1.8	23.50	0.383	0.000
			1.13×10^{-2}	1.229	0.309	0.728	1.8	16.94	0.330	−0.332
	BS	0.106	1.46×10^{-4}	1.605	0.214	0.714	2.0	40.27	0.206	−0.307
			1.73×10^{-2}	1.605	0.205	0.679	2.0	40.27	0.196	−0.396
	BH	0.425	9.51×10^{-5}	1.792	0.106	1.000	2.0	61.94	0.106	0.000
			2.81×10^{-3}	1.756	0.088	0.999	2.0	57.02	0.088	0.000
LGL (~15000 BP) Lake geneva, fine sand/silt rhythmites	D	0.340	1.80×10^{-5}	1.512	0.375	0.582	2.046	32.51	0.346	−0.721
			6.64×10^{-4}	1.293	0.495	0.576	2.166	19.63	0.434	−0.683

Table 2. *Component analysis results for all natural samples analyzed in this paper except lake sediments. Component H is not reported. Values of p given with only two digits were kept fixed during optimization. See the text for more details about the samples.*

sample	comp.	k_{ARM}/IRM mm/A	a Am^2/kg	μ	σ	q	p	MDF mT	DP	s
ODPB	D+EX	2.170	2.75×10^{-5}	1.241	0.324	0.857	1.8	17.42	0.354	−0.085
pelagic carbonate,			1.59×10^{-4}	1.232	0.352	0.745	1.8	17.06	0.377	−0.289
ODP Leg 182	BM	4.910	1.42×10^{-5}	1.505	0.161	1.006	2.0	31.99	0.161	0.000
			3.63×10^{-5}	1.500	0.150	1.000	2.0	31.62	0.150	0.000
	BI	3.920	1.23×10^{-5}	1.747	0.130	0.726	2.0	55.85	0.125	−0.279
			3.93×10^{-5}	1.732	0.135	0.749	2.0	53.95	0.131	−0.229
ODPD	D+EX	0.891	1.40×10^{-6}	1.370	0.466	0.502	2.0	23.44	0.447	−1.175
dolomitic floatstone,			1.97×10^{-5}	1.201	0.493	0.531	2.0	15.89	0.468	−1.004
ODP Leg 194	BI	1.140	2.12×10^{-6}	1.746	0.242	0.698	2.0	55.72	0.232	−0.347
			2.33×10^{-5}	1.649	0.271	0.676	2.0	44.57	0.259	−0.406
SCBB	D+EX	2.850	1.57×10^{-6}	1.217	0.335	0.649	2.175	16.48	0.296	−0.426
Scaglia Bianca			6.90×10^{-6}	1.210	0.338	0.600	2.297	16.22	0.283	−0.538
limestone,	BI	2.830	1.05×10^{-6}	1.637	0.189	0.843	1.851	43.35	0.200	−0.097
maximal IRM			4.69×10^{-6}	1.665	0.186	0.998	1.93	46.24	0.192	0.000
SCBD	D+EX	1.180	8.88×10^{-8}	1.352	0.359	0.741	1.774	22.49	0.390	−0.306
Scaglia Bianca			9.43×10^{-7}	1.161	0.405	0.678	2.0	14.49	0.387	−0.400
limestone,	BI	0.919	9.90×10^{-8}	1.744	0.233	0.804	1.918	55.46	0.237	−0.145
minimal IRM			1.35×10^{-6}	1.668	0.303	0.713	2.0	46.56	0.291	−0.308
U03F	D	0.485	1.63×10^{-5}	1.457	0.340	0.729	1.769	28.64	0.370	−0.340
Baldeggersee,			4.22×10^{-4}	1.388	0.437	0.735	1.859	24.43	0.452	−0.294
silt from a delta	NI	0.442	1.79×10^{-7}	1.752	0.089	1.000	2.0	56.49	0.089	0.000
			5.09×10^{-6}	1.659	0.200	0.800	2.0	45.60	0.196	−0.140
BALGR & BALWD	D+PD	0.519	5.68×10^{-5}	1.428	0.345	0.695	1.831	26.79	0.360	−0.414
Eroded soils from			1.38×10^{-3}	1.292	0.469	0.568	2.301	19.59	0.390	−0.657
Baldeggersee	D+PD	0.522	5.25×10^{-5}	1.397	0.297	0.694	1.676	24.95	0.342	−0.493
cathment area			1.26×10^{-3}	1.353	0.480	0.557	2.254	22.54	0.406	−0.725
M5A	PD	0.694	3.48×10^{-4}	1.234	0.365	0.619	2.099	17.14	0.331	−0.549
Modern soil,			6.29×10^{-3}	1.202	0.403	0.636	2.155	15.92	0.358	−0.471
western Chinese	L	0.097	1.18×10^{-5}	1.866	0.191	0.800	2.0	73.45	0.187	−0.140
Loess Plateau			1.54×10^{-3}	1.780	0.251	0.699	2.0	60.26	0.240	−0.343
SPS3	PD	1.700	1.17×10^{-3}	1.254	0.361	0.547	2.274	17.95	0.303	−0.758
Well-developed			8.62×10^{-3}	1.160	0.375	0.573	2.243	14.45	0.319	−0.663
paleosol, central	L	0.176	2.81×10^{-5}	1.814	0.136	0.800	2.0	65.16	0.133	−0.140
Chinese Loess			2.00×10^{-3}	1.720	0.255	0.673	2.0	52.48	0.243	−0.413
RCL	PD	0.895	2.10×10^{-4}	1.339	0.340	0.631	1.97	21.83	0.327	−0.566
Red clay,			2.95×10^{-3}	1.315	0.441	0.662	2.0	20.65	0.420	−0.447
central Chinese	L	0.220	2.39×10^{-6}	2.066	0.085	0.800	2.0	116.41	0.083	−0.140
Loess Plateau			1.36×10^{-4}	1.939	0.171	0.700	2.0	86.90	0.164	−0.340
BY55	ED	0.169	4.71×10^{-5}	1.457	0.358	0.568	2.0	28.64	0.339	−0.815
Pristine loess,			3.50×10^{-3}	1.408	0.489	0.614	2.0	25.59	0.463	−0.615
western Chinese	L	0.109	8.50×10^{-6}	1.896	0.198	0.763	2.0	78.71	0.192	−0.201
Loess Plateau			9.83×10^{-4}	1.821	0.238	0.587	2.0	66.22	0.225	−0.725
GMA	ED	0.228	4.13×10^{-4}	1.464	0.492	0.596	2.0	29.11	0.465	−0.688
PM10 from a forest			2.27×10^{-2}	1.432	0.462	0.680	2.0	27.04	0.442	−0.393
near a city	UP	0.330	1.06×10^{-4}	1.925	0.264	0.702	2.0	84.14	0.253	−0.335
			4.04×10^{-3}	1.734	0.221	1.000	2.0	54.20	0.221	0.000
KSN	ED	0.163	2.82×10^{-4}	1.450	0.500	0.644	2.0	28.18	0.474	−0.507
PM10 from a park			2.17×10^{-2}	1.420	0.472	0.655	2.0	26.30	0.449	−0.470
near a city center	UP	0.278	1.93×10^{-4}	1.917	0.293	0.606	2.0	82.60	0.277	−0.647
			8.74×10^{-3}	1.766	0.266	0.801	2.0	58.35	0.261	−0.139
WDK	ED	0.150	7.95×10^{-4}	1.435	0.464	0.597	2.0	27.23	0.439	−0.682
PM10 from a highly			6.64×10^{-2}	1.401	0.483	0.693	2.0	25.18	0.462	−0.359
trafficated road, city	UP	0.262	6.61×10^{-4}	1.953	0.241	0.685	2.0	89.74	0.230	−0.381
center			3.17×10^{-2}	1.699	0.291	0.700	2.0	50.00	0.279	−0.341
GUB	ED	0.235	5.05×10^{-4}	1.447	0.417	0.619	2.0	27.99	0.395	−0.593
PM10 from the			2.70×10^{-2}	1.411	0.460	0.666	2.0	25.76	0.439	−0.434
middle of a	UP	0.166	5.20×10^{-4}	1.952	0.228	0.726	2.0	89.54	0.219	−0.278
motorway tunnel			3.93×10^{-2}	1.653	0.382	0.581	2.0	44.98	0.361	−0.752
MBH	ED	0.090	8.61×10^{-3}	1.460	0.490	0.515	2.0	28.84	0.467	−1.096
PM10 at a under-			$1.21\times10^{+0}$	1.420	0.489	0.647	2.0	26.30	0.465	−0.496
ground railway stop	UP	0.223	1.08×10^{-2}	1.948	0.262	0.742	2.0	88.72	0.254	−0.243
			6.05×10^{-1}	1.758	0.266	0.810	2.0	57.28	0.261	−0.125

Table 3. *Component analysis results for AF demagnetization curves taken from the literature for cultured biogenic magnetites (A and BR) and samples of magnetite with known grain size (S). Values of k_{ARM}/IRM in parentheses refer to samples affected by magnetostatic interactions.*

sample	comment	comp.	k_{ARM}/IRM mm/A	μ	σ	*q*	*p*	*MDF* mT	*DP*	*s*
GS15	*Geobacter metallireducens*	EX	(0.217)	1.375	0.314	0.593	2.043	23.71	0.291	−0.677
				1.272	0.343	0.545	1.963	18.71	0.332	−0.958
MM	*Magnetosp. magnetotacticum*	BR	2.675	1.536	0.111	0.668	1.783	34.36	0.118	−0.526
				1.515	0.120	0.632	1.737	32.73	0.133	−0.701
MV1	Vibroid strain MV1	BR		1.684	0.082	0.709	1.711	48.35	0.092	−0.421
MR	Greigite magnetosomes			1.486	0.132	0.437	1.983	30.62	0.133	−1.630
MMP	many-celled mag. prokaryote			1.318	0.140	−0.689	1.624	20.80	0.168	+0.544
B2.1	Unannealed grains obtained by crushing natural magnetite crystals. Sieved to different grain-size fractions. (Bailey and Dunlop, 1983)	S		1.214	0.307	0.572	1.925	16.37	0.302	−0.844
				0.951	0.450	0.617	2.149	8.92	0.399	−0.535
B6.2		S		0.925	0.363	0.604	1.976	8.42	0.347	−0.668
				0.951	0.450	0.617	2.149	8.92	0.399	−0.535
B9.7		S		0.869	0.359	0.911	1.833	7.39	0.388	−0.031
				0.894	0.417	0.646	2.073	7.84	0.383	−0.470
B14.3		S		0.817	0.384	0.766	1.817	6.56	0.409	−0.236
				0.866	0.410	0.726	2.002	7.35	0.395	−0.278
B100		S		0.747	0.503	1.000	2.001	5.59	0.503	0.000
				0.867	0.447	0.671	1.820	7.36	0.474	−0.508
H0.2	Glass-ceramic magnetites of different grain size. (Halgedahl, 1998)	S		1.809	0.187	0.496	1.776	64.42	0.208	−1.420
				1.711	0.338	0.465	2.057	51.40	0.320	−1.370
H1.5		S		1.714	0.287	0.581	1.703	51.76	0.327	−0.979
				1.400	0.458	0.566	2.201	25.12	0.395	−0.709
H100		S		0.778	0.358	0.800	2.000	6.00	0.350	−0.140
				0.898	0.478	0.657	1.715	7.91	0.535	−0.609
YU	Yucca Mountain Tuff (Egli, 2002)	S	0.739	1.707	0.263	0.511	2.331	50.93	0.216	−0.902
				1.676	0.328	0.473	2.703	47.42	0.240	−0.921
L0.08	Synthetic and natural magnetites (Levi and Merrill, 1976)	S	ARM	1.796	0.150	1.000	1.750	62.52	0.171	0.000
L0.12		S	ARM	1.424	0.368	0.451	2.194	26.55	0.327	−1.360
L0.21		S	ARM	1.509	0.221	0.579	1.700	32.28	0.252	−0.990
L1.5		S	ARM	1.177	0.611	0.504	2.245	15.03	0.520	−0.992
D5	Unannealed grains obtained by crushing magnetite-bearing rocks. Sieved to different grain-size fractions. (Dankers, 1978)	S		1.357	0.502	0.429	2.807	22.75	0.359	−1.140
				1.288	0.419	0.544	2.105	19.41	0.377	−0.865
D10		S		1.284	0.396	0.615	2.002	19.23	0.374	−0.609
				1.215	0.513	0.461	2.565	16.41	0.391	−1.060
D15		S		1.137	0.428	0.617	2.085	13.71	0.389	−0.563
				1.095	0.472	0.560	2.087	12.45	0.428	−0.799
D20		S		1.075	0.493	0.599	2.301	11.89	0.411	−0.541
				1.041	0.522	0.594	2.400	10.99	0.421	−0.523
D25		S		1.005	0.461	0.652	1.985	10.12	0.441	−0.484
				1.008	0.459	0.596	1.946	10.19	0.446	−0.718
D30		S		0.958	0.472	0.675	2.076	9.07	0.436	−0.384
				0.951	0.457	0.670	2.012	8.93	0.433	−0.418
D55		S		0.913	0.497	0.684	2.118	8.18	0.451	−0.347
				0.890	0.504	0.644	2.099	7.76	0.458	−0.466
D100		S		0.808	0.437	0.896	1.746	6.43	0.495	−0.046
				0.860	0.443	0.727	1.908	7.24	0.446	−0.300
D250		S		0.723	0.423	1.000	1.758	5.29	0.478	0.000
				0.802	0.460	0.694	1.896	6.33	0.463	−0.392

Chapter 5

Characterization of individual magnetic components by analysis of remanence curves, 2. Rock magnetism of individual components

This paper has been submitted to *Physics and Chemistry of the Earth.*

" *Nature loves to hide.* "

Eraclitus of Ephesus (535-475 B.C.)

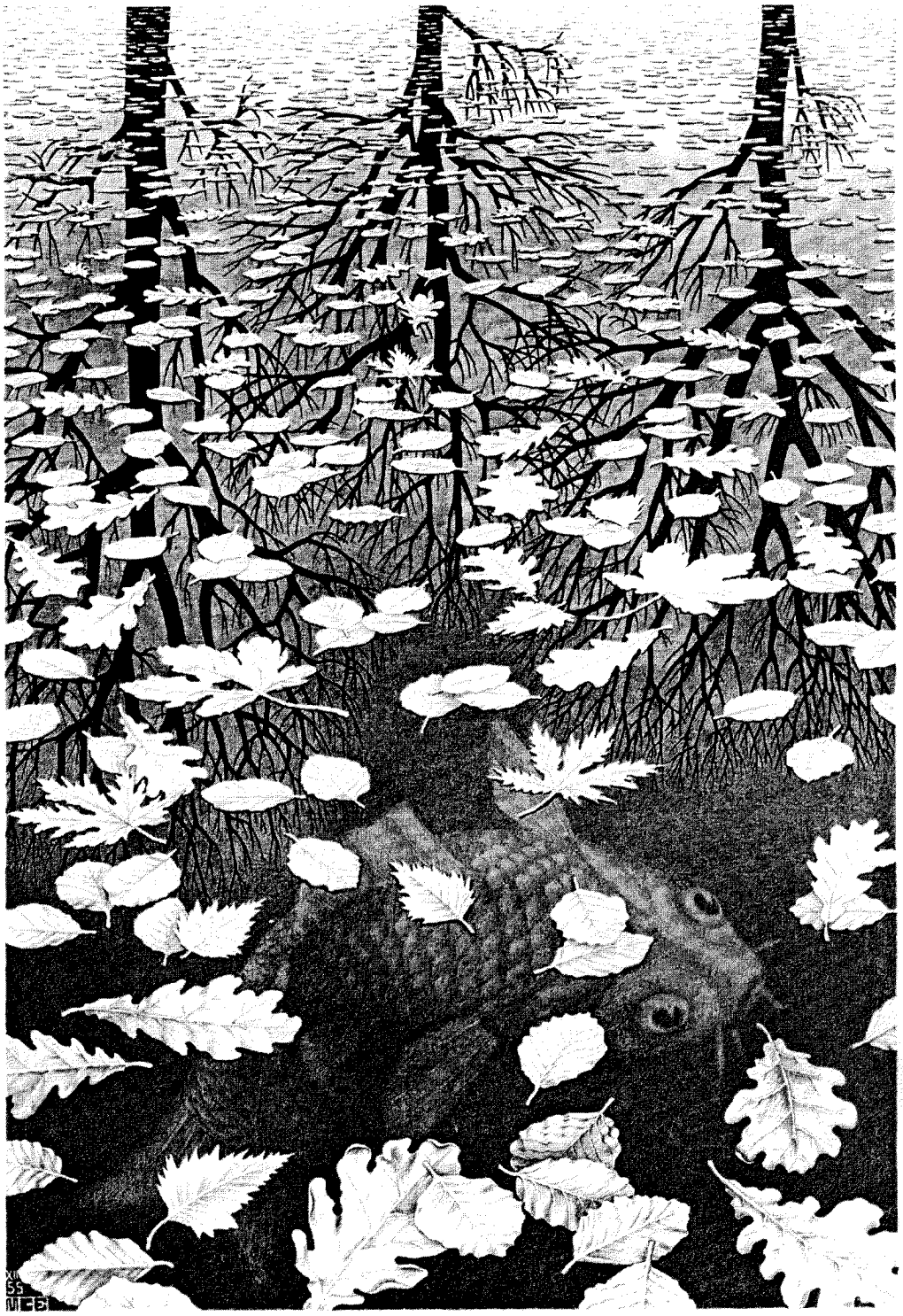

Maurits Cornelis Escher: *Three worlds*, lithography (1955)

Characterization of individual rock magnetic components by analysis of remanence curves, 2. Rock magnetism of individual components

R. Egli
Institut für Geophysik, ETH Hönggerberg, Zürich, Switzerland

The characterization of individual magnetic components in sediments and sedimentary rocks is difficult, since these natural materials are often a complex mixture of magnetic mineral sources. The analysis of magnetization curves with model functions is the only practicable method that allows us to unmix the magnetic components and characterize their magnetic properties, if a-priori information is not available. Unfortunately, such analysis relies on time consuming measurements and on the choice of appropriate model functions. However, once the magnetic properties of individual components have been determined on selected representative samples, a simpler and faster analysis of a large set of similar samples can be performed. The effect of natural processes on the properties of single magnetic components can be investigated on a large number of samples with a simplified component analysis. The simplification of the unmixing problem is closely related to the number of parameters required to fully characterize a magnetic component, and the significance of these parameters in rock magnetic terms. A systematic analysis of synthetic and natural samples shows that a combination of four parameters, so called magnetic fingerprint parameters, is sufficient for this purpose. The fingerprint parameters of magnetic components isolated from a wide range of natural sediments and sedimentary rocks form well-defined groups with specific properties. These groups reflect common processes of formation, transport and dissolution of magnetic particles. A clear distinction can be made between two sorts of biogenic magnetite, atmospheric dust, urban pollution and ultrafine magnetite produced in soils and lacustrine/marine sediments.

KEYWORDS: magnetite, magnetic mixtures, component analysis, bacterial magnetite.

1. Introduction

The knowledge of the rock magnetic properties of all sources of magnetic particles in sediments is of fundamental importance for environmental magnetism. This knowledge is the key for a successful unmixing of multi-component models [*Verosub and Roberts*, 1995; *Thompson*, 1986; *Hilton*, 1987; *Yu and Oldfield*, 1989; *Carter-Stiglitz et al.*, 2001]. Detailed rock magnetic studies, with special regard to the grain size dependence of magnetic parameters, have been performed mainly on artificial samples [*Dunlop*, 1981, 1995; *Hunt et al.*, 1995]. However, severe limitations in the extrapolation of these results to natural samples are given by the sensitivity of some magnetic parameters to magnetostatic interactions [*Sugiura*, 1979; *Dankers and Sugiura*, 1981; *Yamazaki*, 1998], and to the method used to prepare the magnetic crystals [*Hunt et al.*, 1995]. For example, the anhysteretic remanent magnetization (ARM) of artificial samples of single domain (SD) magnetite is only 3% of the value measured in natural samples [*Moskowitz et al.*, 1993; *Egli and Lowrie*, 2002]. Other parameters, like the coercivity of remanence and the remanence ratio, differ at least by a factor two if measured using crushed, respectively grown magnetite grains [*Hunt et al.*, 1995]. Furthermore, the properties of magnetic grains do not depend only on the grain size: other factors, such as grain shape and oxidation state are also important. Further complications arise from the fact that natural magnetic components are grain mixtures with statistically distributed properties. In natural environments, several magnetic components occur simultaneously and form multi-component mixtures that are difficult to characterize using bulk measurements.

In *Egli* [2003b], demagnetization curves of anhysteretic and isothermal remanent magnetizations (ARM and IRM) have been analyzed in detail to characterize the properties of individual magnetic components encountered in various natural sediments. The natural components have been characterized using following parameters: (1) the ratio of the susceptibility of ARM to the IRM, k_{ARM}/IRM, called ARM ratio in the following, as a grain size parameter, (2) the median destructive field of ARM or IRM, MDF_{ARM} or MDF_{IRM}, as a coercivity parameter, (3) the dispersion parameter of ARM or IRM, DP_{ARM} or DP_{IRM}, as a measure for the 'randomness' of a component, (4) ΔMDF and (5) ΔDP as a measure of the differences between ARM and IRM, and (6) s_{ARM} or s_{ARM} as a symmetry parameter for the coercivity distributions of ARM and IRM. The first two parameters are well known in rock magnetism, but the physical meaning of the others is unclear. The variability of the parameters that describe a magnetic component is an important limiting factor to be considered in multi-component mixing models [*Dearing*, 1999]. This variability may reflect random processes, systematic changes in the sedimentary environment [e. g. *King et al.*, 1982; *Geiss and Banerjee*, 1997], or diagenetic processes [e. g. *Leslie et al.*, 1990a; *Leslie et al.*, 1990b; *Karlin*, 1990; *Lu and Banerjee*, 1994]. The results of *Egli* [2003b] will be discussed in detail in the present work in order interpret the six magnetic parameters mentioned above in terms of rock magnetic properties and highlight their relation with natural processes. These results will be compared with synthetic coercivity distributions, calculated on the basis of simple models for

the magnetization process of magnetic particles with a distribution of physical properties. The comparison of natural components with the synthetic simulations allows us to investigate the effect of simple grain properties, such as size and shape, on the coercivity distribution. For example, *Heslop et al.* [2003] used a temperature dependant Preisach-Néel model to model the effect of magnetostatic interactions on the symmetry of a coercivity distribution. In this context, the use of generalized distribution functions, which have been introduced by *Egli* [2003a] as a model for natural magnetic components, is supported by physical arguments.

2. Theoretical coercivity distribution of a magnetic component

The component analysis of *Egli* [2003b] is based on a family of distributions called Skewed Generalized Gaussian functions (SGG), introduced by *Egli* [2003a] to model AF demagnetization curves. The shape of these distributions depends upon four parameters, which include a symmetry parameter, called skewness, and a curvature parameter called squareness, or kurtosis. In this section, we justify the use of such distributions instead of more simple functions with a fixed symmetry, like the logarithmic Gaussian function, by calculating the coercivity distribution of non-interacting magnetic grain assemblages with simple models. We will show that the symmetry of a coercivity distribution depends in a complex manner on the grain size D and the elongation E of the particles. In the following, three different factors which may affect the shape of coercivity distributions are considered: (1) the effect of specific physical parameters such as D and E on the microcoercivity, (2) thermal activation effects, which are modeled in terms of viscosity and time dependence of the coercivity, and (3) defects of the crystal structure and processes related to the surface of the grains, such as weathering.

The coercivity distribution of a set of magnetic particles depends upon geometric parameters, such as D and E, and the orientation φ of their axes of symmetry with respect to the applied field. We define the switching field $H_{sw}(D,E,\varphi)$ as the field at which the saturation magnetization of identical and aligned particles is reduced to zero without thermal activations. The switching field is maximal for a given orientation φ_0: we define $H_K = H_{sw}(D,E,\varphi_0)$ as the microcoercivity of the particle. Furthermore, let H_{cr} indicate the switching field of the particle when thermal activation effects are taken into consideration: according to the original definition of *Néel* [1949], $H_{cr} = H_{sw} - H_q(H_K,D)$, where H_q is called fluctuation field.

In general, for a statistical variable X with a probability distribution $f(X)$, let $x = \log X$ be the logarithm of X, and $\overline{f}(x) = 10^x f(10^x)$ the probability distribution of X on a logarithmic scale. Furthermore, $\overline{k}(h_K)$ is microcoercavity distribution, $\overline{n}(h_{sw})$ is the switching field distribution and $\overline{m}(h_{cr})$ is the coercivity distribution, all on a logarithmic field scale. Finally, the Gaussian function is indicated by $N(x,\mu,\sigma)$.

2.1. Switching field distribution of Stoner-Wohlfarth particles

In the following, the switching field distribution of SD magnetite is calculated with the simplest model for magnetic particles, the so-called Stoner-Wohlfarth model [*Stoner and Wohlfarth*, 1948]. If the magnetic anisotropy of a SD grain is controlled by its shape, the microcoercivity is given by $H_K = (1-N)M_s/2$, M_s being the saturation magnetization of the particle and N the demagnetizing factor along the easy axis. The demagnetizing factor depends upon the elongation E, as shown in Figure 1a [*Stacey and Banerjee*, 1974]. The resulting dependence of H_K on E is shown in Figure 1b, and can be approximated by $\mu_0 H_K \approx 0.3(1-1/E)$. If $\rho(E)$ is the elongation distribution, the microcoercivity distribution is given by $\overline{k}(h_K) = \overline{\rho}(e)\mathrm{d}E/\mathrm{d}h_K$. Using the approximation given above for $H_K(E)$:

$$\overline{k}(h_K) \approx \frac{10^{\mu_0 h_K}}{0.3 - 10^{\mu_0 h_K}}\overline{\rho}(e) \tag{1}$$

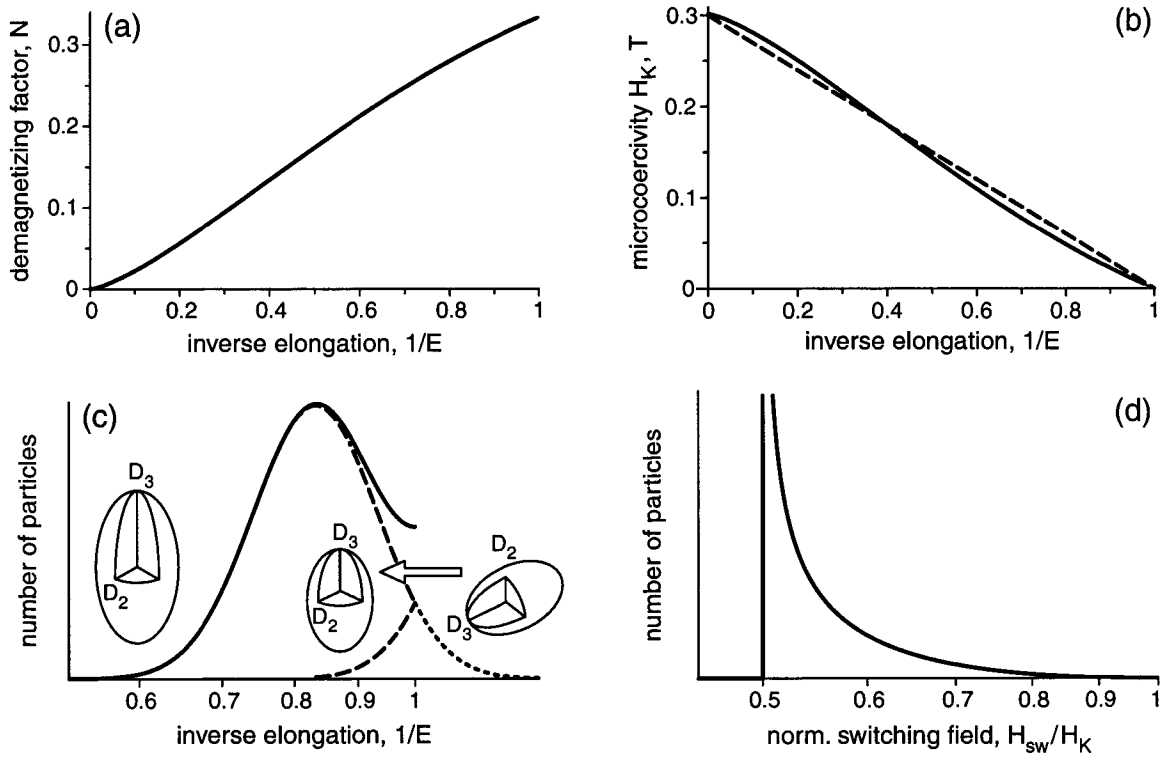

Figure 1. *Magnetic properties of Stoner-Wohlfarth particles. (a) Relation between the elongation E of an ellipsoidal particle and the demagnetization factor N along the longest axis (after Stacey and Banerjee, [1974]). (b) Relation between elongation and microcoercivity, calculated for shape anisotropy. The dashed line is an approximation given by $\mu_0 H_K \approx 0.3(1-1/E)$. (c) The elongation distribution (solid line) is the distribution of the ratio of the axis D_2 to the axis D_3 of the ellipsoid (dashed line). The axes are exchanged if $D_2 > D_3$, because $E \geq 1$ by definition, (short-dashed line). (d) Switching field distribution of a set of identical, randomly oriented Stoner-Wohlfarth particles.*

If a Stoner-Wohlfarth particle is modeled with a rotation ellipsoid whose axes lengths are given by $D_1 = D_2 < D_3$, then $E = D_3/D_2$. According to this model, the microcoercivity distribution depends ultimately only upon the distribution of D_3/D_2, which is related to the grain size distributions $v(D_2)$ and $v(D_3)$. Different models for grain size distributions in rocks and sediments have been proposed [*Korvin*, 1992], and among these the logarithmic Gaussian function:

$$lN(x,\mu,\sigma) = \frac{1}{\sqrt{2\pi}\sigma x}\exp\left[-\frac{\ln^2(x/\mu)}{2\sigma^2}\right] \tag{2}$$

and the Weibull distribution:

$$W(x,\sigma,\alpha) = \frac{x^{\alpha-1}}{\sigma}\exp[-(x/\sigma)^{\alpha}] \tag{3}$$

If a logarithmic Gaussian function is used to model the grain size distribution, the ratio R of two axes of a grain is characterized by a logarithmic Gaussian distribution as well [*Evans et al.*, 2000], and $\log R \sim N(r,\mu,\sigma)$. Since $E \geq 1$ by definition, $E = R$ if $r \geq 1$ and $E = 1/R$ else. Accordingly, the distribution function of $e = \log E$, $e \geq 0$, is given by $\overline{\rho}(e) = N(e,\mu,\sigma) + N(e,-\mu,\sigma)$ and is plotted in Figure 1c. This result can be extended to any kind of distribution of R by replacing $N(r,\mu,\sigma)$ with a convenient function.

In order to calculate the switching field distribution for a given $\overline{k}(h_K)$, let $s(H_{sw}/H_K)$ be the switching field distribution for a set of identical, randomly oriented particles, which takes into account the angular dependence of H_{sw}. The switching field distribution related to $\overline{k}(h_K)$ is given by the convolution of $\overline{k}$ with $\overline{s}$:

$$\overline{n}(h_{sw}) = (\overline{s} * \overline{k})(h_{sw}) = \int_{-\infty}^{\infty} \overline{s}(h_{sw} - h_K)\,\overline{k}(h_K)\,\mathrm{d}h_K \tag{4}$$

as shown in the Appendix. This result has a general validity. For a set of Stoner-Wohlfarth particles, $\overline{s}$ is given by:

$$\overline{s}(u) = \begin{cases} 4\ln 10\dfrac{u^2}{(1-u)(1+u^3)}, & -\log 2 < u < 0 \\ 0 & \text{, else} \end{cases}$$

$$u = \frac{1+2h^2-\sqrt{3(4h-1)}}{2(1-h^2)},\ h = H_{sw}/H_K \tag{5}$$

(Figure 1d), as shown in the Appendix. With (1), (4) and (5) it is possible to calculate the switching field distribution for a variety of Stoner-Wohlfarth particle assemblages with

different elongation distributions. The results of these calculations are shown in Figure 2. The skewness of the switching field distribution is intermediate between the skewness of $\overline{k}(h_K)$, which is negative in the Stoner-Wohlfarth model discussed above, and the positive skewness of $\overline{s}$.

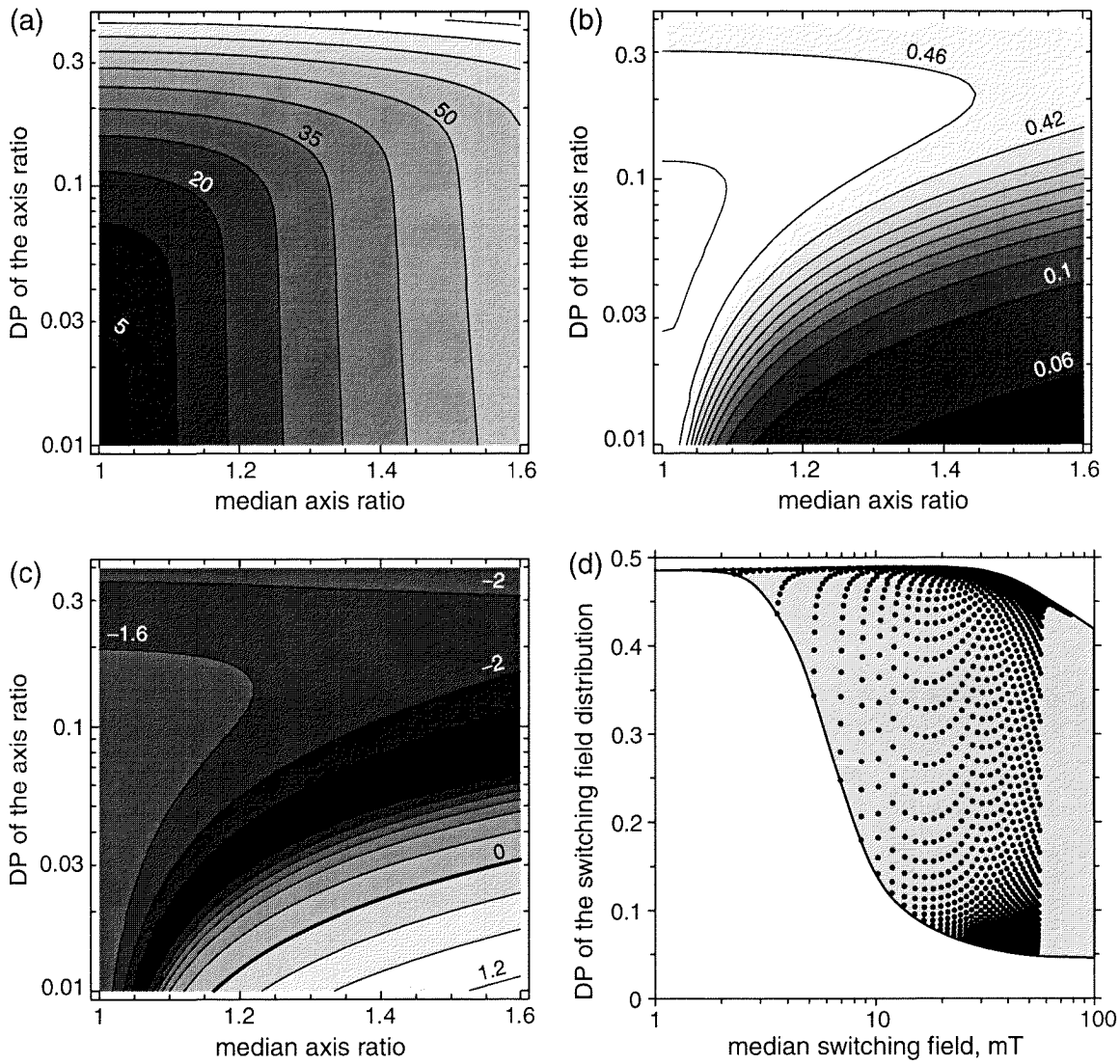

Figure 2. *Dependence of the switching field distribution of Stoner-Wohlfarth particles on their elongation distribution. (a) Median, (b) DP and (c) skewness of the switching field distribution as a function of the median and the DP of logarithmic Gaussian distributed axis ratios. Contours are equally spaced, fields are expressed in* mT. *Stoner-Wohlfarth particles with strongly scattered elongations are characterized by a left-skewed switching field distribution. On the other hand, the switching field distribution of almost identical, moderately elongated particles is right-skewed. The DP of the axis ratio is* > 0.05 *for synthetic and natural magnetite particles, and their elongation does not exceed 1.6, except for acicular particles. Consequently, the switching field distribution of SD magnetite is expected to be negative. (d) Range of possible switching field distributions for magnetite (shaded area); each point is a numerical value calculated in (a) and (b).*

A positive value of the skewness parameter is obtained only for a set of almost identical, moderately elongated particles, which is unlikely to occur in nature. The absolute values of the skewness parameter plotted in Figure 2 are too high, compared to the skewness reported in *Egli* [2003b] for synthetic and natural samples of SD magnetite. The reason for this discrepancy resides in the failure of the Stoner-Wohlfarth model in accounting for the coercivity of elongated and round grains. Incoherent reversal modes occur preferentially in elongated grains and lower their coercivity [*Enkin and Williams*, 1994; *Newell and Merrill*, 1999]. The microcoercivity of round grains is controlled by the crystalline anisotropy and by crystal defects. Therefore, the dependence of the microcoercivity on the elongation of a particle is expected to be weaker than predicted by the Stoner-Wohlfarth model, and the resulting microcoercivity distribution less skewed.

2.2. Thermal activation effects

Thermal activation effects on the shape of a (de)magnetization curve can be divided into: (1) effects on the acquisition of a magnetization, (2) viscosity of the acquired magnetization and (3) effects on the coercivity of the particles. Effects on the acquisition of a magnetization can be taken into account by a factor $\mu(H_K, D)$, which we define as the ratio between the acquired magnetization and the saturation remanence M_{rs0} without thermal activations. An example is shown in Figure 3a with the ARM acquired by a set of SD particles, which has been calculated after *Egli and Lowrie* [2002]. In this case, $\mu(D, H_K)$ is proportional to the ARM ratio. Differences between the normalized demagnetization curve of IRM and of a weak-field magnetization, such as the ARM, are considered in the original Lowrie-Fuller test [*Lowrie and Fuller*, 1971] and its modified version [*Johnson et al.*, 1975]. Viscosity effects are expressed through the time dependence of the acquired magnetization. In a zero field, this dependence is given by $\exp(t/\tau)$, where $\tau = \tau(D, H_K)$ is a time constant. For single-domain particles, $\tau(D, H_K)$ is given by *Néel* [1949]. On the other hand, the time dependence of the coercivity is taken into account by the fluctuation field H_q.

Let $p(H_K, D)$ be the joint distribution of microcoercivities and grain sizes. The coercivity distribution is then given by:

$$\overline{m}(h_{cr}) = H_{cr} D \int_{h_K(h_{sw})}^{\infty} \frac{\overline{p}(h_K, d)}{\left|\partial H_q / \partial D\right|} \mu(h_K, d) e^{-t/\tau} \Big|_{H_q = H_{sw} - H_{cr}} \mathrm{d}h_K \qquad (6)$$

For SD particles, H_q has been calculated by *Egli and Lowrie* [2002]. Inserting their result for H_q in (6) gives the following approximation:

$$\overline{m}(h_{cr}) \approx 0.48 H_{cr} \int_{\log \frac{H_{cr}+H_q}{0.524}}^{\infty} \overline{p}(d, h_K) 10^{2d - h_K/3} \mu(d, h_K) e^{-t/\tau} \Big|_{H_q = 0.524 H_K - H_{cr}} \mathrm{d}h_K \qquad (7)$$

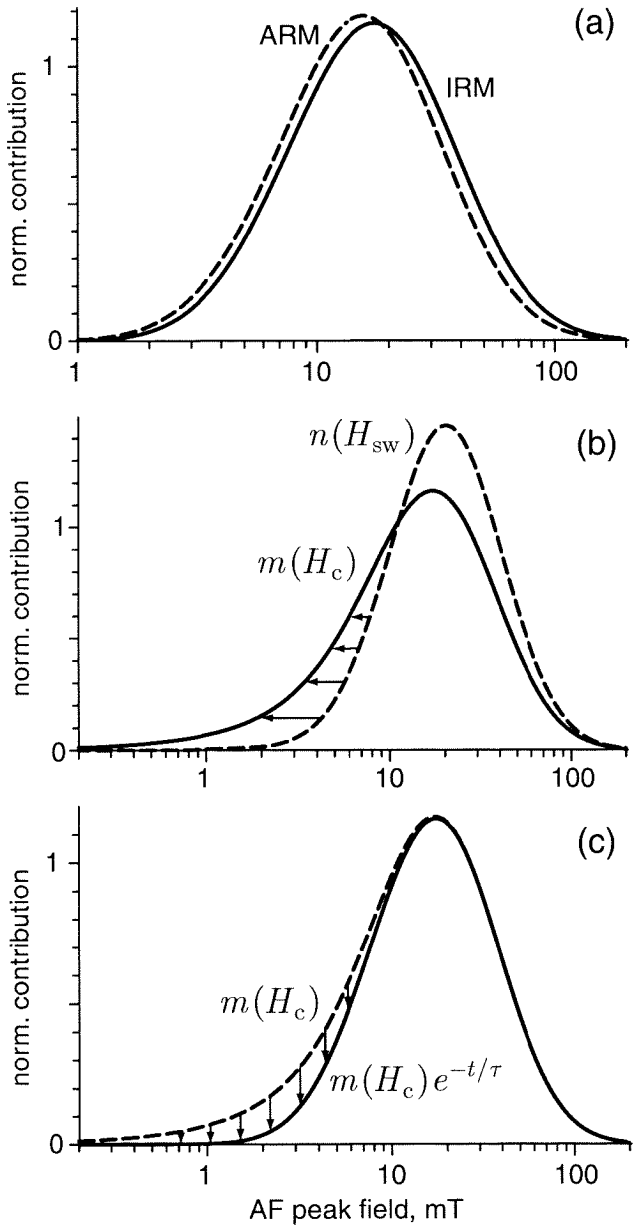

Figure 3. *Calculated effects of thermal activation processes on the coercivity distribution of a set of SD particles with a logarithmic Gaussian distribution of microcoercivities and grain sizes, according to Egli and Lowrie [2002]. Following parameters have been chosen:* $\mu = 30$ nm, $DP = 0.2$ *for the grain size, and* $\mu = 40$ mT, $DP = 0.3$ *for the microcoercivity. (a) Thermal activations account for the difference between a strong field magnetization, such as the IRM, and a weak field magnetization, such as the ARM. (b) Thermal activations reduce the switching field of a particle by a quantity called fluctuation field,* H_q *(arrows). The fluctuation field depends on the volume of a particle and on its microcoercivity* H_K. *The effect is stronger for small values of* H_K, *and the left tail of the coercivity distribution is expanded. (c) Viscous particles loose the magnetization soon after the acquisition of a magnetization. Only a fraction of this magnetization, given by* $\exp(-t/\tau)$, *can be measured after a time* t. *The time constant* τ *depends on the grain size and on the microcoercivity of the particle, and is positively related to* H_K. *Accordingly, the left tail of a coercivity distribution is suppressed (arrows). The two processes illustrated in (b) and (c) have opposite effects on the skewness of a coercivity distribution.*

whith $\mu_0 H_q \approx 2000(\mu_0 H_K)^{1/3} D^{-2}$, where $\mu_0 H_K$ expressed in mT, and D in nm. Details about the calculation of (6) and (7) are shown in the Appendix.

The effect of thermal activation processes on the symmetry of a coercivity distribution can be investigated by assuming $p(H_K, D) = k(H_K)v(D)$, where $v(D)$ and $k(H_K)$ are logarithmic Gaussian functions. The distributions $\overline{v}(d) = N(d, \mu_d, \sigma_d)$ and $\overline{k}(h_K) = N(h_K, \mu_k, \sigma_k)$ are symmetric on a logarithmic scale, and represent the simplest case to consider. The skewness of the resulting coercivity distribution has been calculated with (7) for SD particles, and is plotted in Figure 4 for various combinations of grain size and microcoercivity distributions.

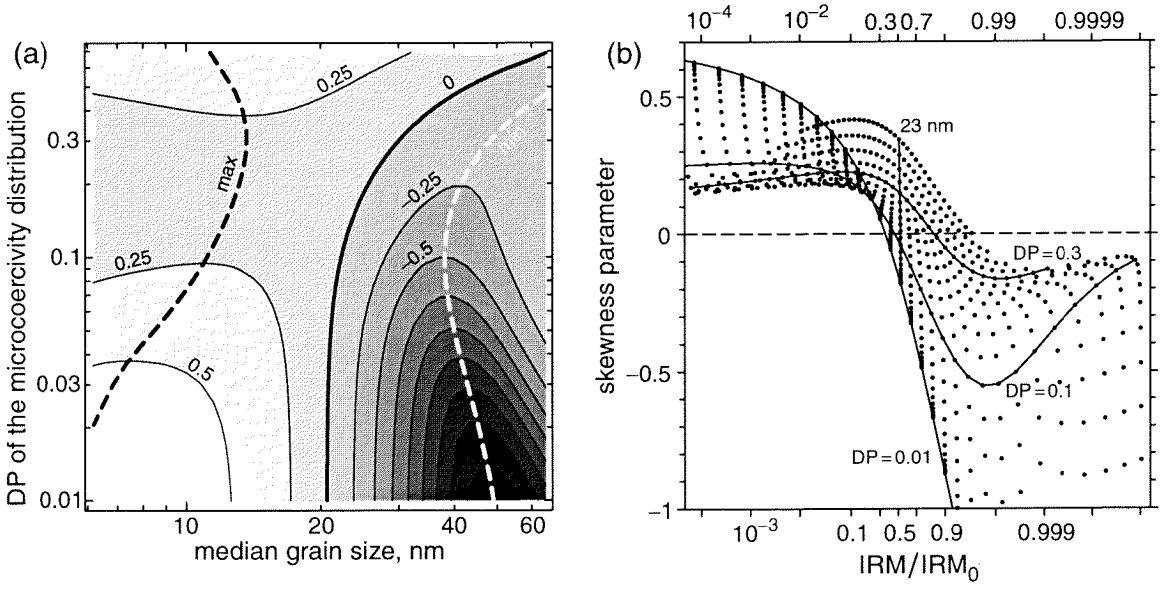

Figure 4. *Systematic investigation of the effect of thermal activation processes on the coercivity distribution of SD particles with logarithmic Gaussian grain size and microcoercivity distributions:* $\log(D) \sim N(d, \mu_D, 0.1)$ *and* $\log \mu_0 H_K \sim N(h_K, \log 40, \sigma_K)$, *D in nm and* H_K *in mT. (a) The skewness of the coercivity distribution has been calculated for various combinations of the median grain size* μ_D *and the DP* σ_K *of the microcoercivity distribution. The skewness parameter is positive for very small grains and negative for stable SD grains. Contours of constant skewness are drawn every* 0.25. *The thick contour represents symmetric coercivity distributions; maxima and minima of the skewness are marked with dashed lines. (b) Skewness of the coercivity distribution as a function of the ratio between the saturation remanence with and without thermal activations,* IRM/IRM_0. *If most of the particles are SP,* IRM/IRM_0 *is small and the skewness is positive. The opposite is true for stable SD particles. The SP/SD boundary can be fixed at a median grain size* 23 *nm, where* $IRM/IRM_0 \approx 0.5$.

Thermal activation processes are effective in particles with a small microcoercivity, which contribute especially to the left tail of a coercivity distribution. Consequently, the symmetry of a coercivity distribution is altered. As shown in Figure 3, viscosity effects tend to produce coercivity distributions with a positive skewness; on the other hand, the effect of H_q is opposite. For stable SD particles, viscous effects can be neglected, and the resulting coercivity distribution is left-skewed. If the grain size of those particles is reduced, the role of viscous effects becomes important, and the coercivity distribution is right-skewed below a critical size, which corresponds approximatively to the boundary between superparamagnetic (SP) and SD particles. Hence, right-skewed coercivity distributions are generated by assemblages of particles with a median grain size that falls into the SP range. The saturation remanence of such particles is very low, since only a small part of them is SD (Figure 4b). Consequently, they are easily masked by other components in natural samples, unless their concentration is very high.

2.3. Effect of defects and surface-controlled processes

Let us consider a set of identical particles with microcoercivity H_K. Small defects in the crystal structure, cracks and chemical processes on the surface of the grains act as a perturbation factor, which may produce small, random changes of the microcoercivity. An example of a microcoercivity distribution produced by such defects is shown in Figure 5. If these changes represent an additive process, the perturbed microcoercivity can be written as $H_K + dH_K$, being $dH_K = \pm \delta$ a small change in H_K. Thus, after the introduction of the first defect, the distribution of microcoercivities is split into the two values $H_K + \delta$ and $H_K - \delta$ with equal probability $p = 1/2$.

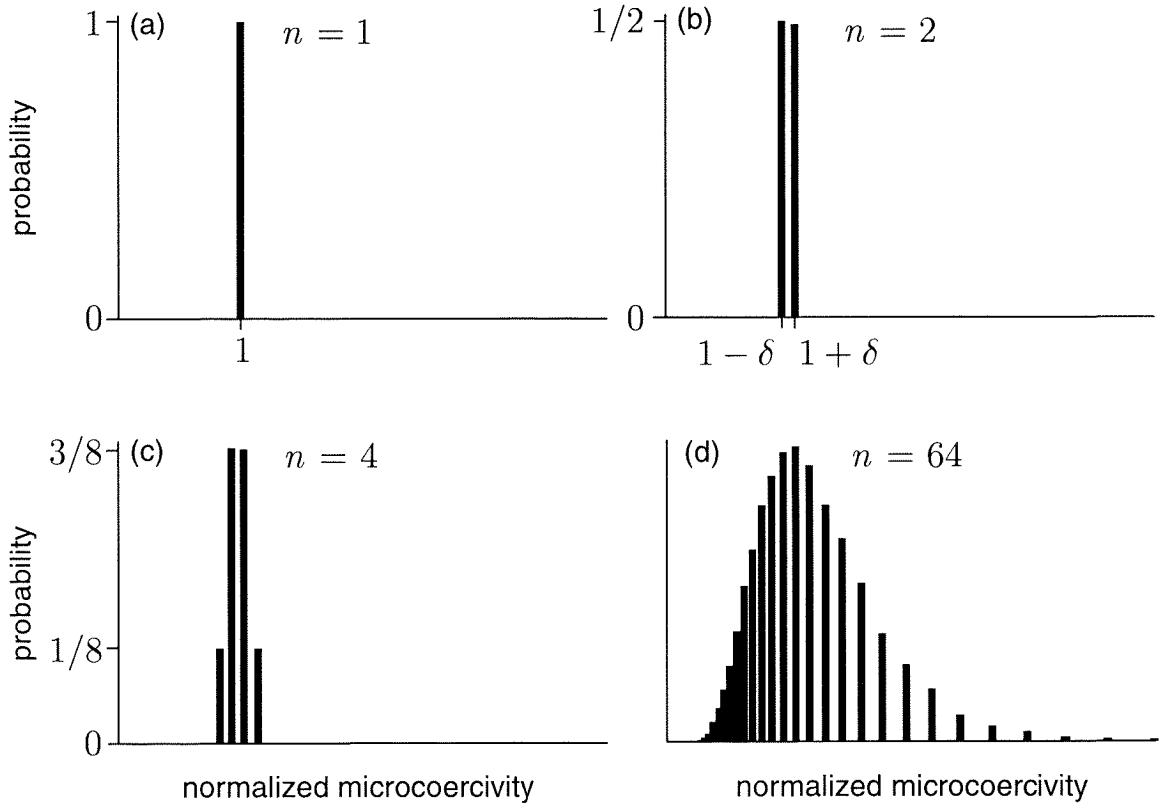

Figure 5. *A mathematical simulation that illustrates the generation of a logarithmic Gaussian microcoercivity distribution with small multiplicative perturbation processes. (a) Identical particles have the same microcoercivity H_K. (b) A random perturbation process induces a small relative change $-\delta$ of the microcoercivity in 50% of the particles, and $+\delta$ in the other 50%. The microcoercivity distribution is now given by the two values $H_K - \delta H_K$ and $H_K + \delta H_K$. (c) The procedure is repeated for each of the new values of the microcoercivity. After each step, a new microcoercivity is added to the coercivity distribution. (d) The microcoercivity distribution after 64 steps is very similar to a logarithmic Gaussian function. Other distribution functions can be easily obtained when a small perturbation is combined with the microcoercivity through different mathematical laws.*

The introduction of additional defects produces the same change $\mathrm{d}H_K$ in $H_K + \delta$ and $H_K - \delta$, and the following microcoercivities are obtained after this step: $H_K + 2\delta$, H_K, $H_K - 2\delta$ with $p = 1/4$, $p = 1/2$ and $p = 1/4$, respectively. The procedure can be reiterated in order to simulate the nucleation of a large number of defects. According to the central theorem of statistics, the distribution of microcoercivities after many iterations converge to a Gaussian distribution [*Evans*, 2000].

Not all microcoercivity changes produced by a perturbing factor are additive. Some of them may be multiplicative, and in this case, the perturbed microcoercivity can be written as $H_K(1 + \mathrm{d}H_K)$. Hence,

$$\log H_K(1 + \mathrm{d}H_K) = \log H_K + \log(1 + \mathrm{d}H_K) \approx h_K + \mathrm{d}H_K \tag{8}$$

with $h_K = \log H_K$ and $\mathrm{d}H_K \to 0$, and the process is additive with respect to h_K. According to the central theorem of statistics, h_K tends to have a Gaussian distribution, which corresponds to a logarithmic Gaussian distribution of H_K (Figure 5).

Depending on the mathematical law used to combine a small perturbation $\mathrm{d}H_K$ with H_K, there is always a variable transformation $H_K^* = g(H_K)$ according to which the perturbation process is additive with respect to H_K^*, and the distribution function of H_K^* is symmetric. For example, let consider the anisotropy energy of uniaxial SD particles, which is given by $E_K = \mu_0 M_s V H_K / 2$ [*Dunlop*, 1997], where M_s is the saturation magnetization and V the volume of the particles. A small perturbation of the anisotropy energy, which is produced by surface processes, is proportional to the surface of the grain, given by $V^{2/3}$. Since E_K is proportional to V, one has $\mathrm{d}E_K \propto E_K^{2/3}$. The same applies to the microcoercivity, since $H_K \propto E_K$, and the perturbed microcoercivity may be written as $H_K + H_K^{2/3}\mathrm{d}H_K$. It is easy to show that this process is additive with respect to $H_K^* = H_K^{1/3}$:

$$(H_K + H_K^{2/3}\mathrm{d}H_K)^{1/3} = H_K^{1/3}(1 + H_K^{-1/3}\mathrm{d}H_K)^{1/3} \approx H_K^{1/3} + \frac{1}{3}\mathrm{d}H_K \tag{9}$$

The resulting coercivity distribution is a Gaussian function if represented on a field scale given by $H_K^{1/3}$. By analogy, it can be shown that perturbation processes that depend on the volume of the particle, such as crystal defects, can be modeled with $H_K + H_K \mathrm{d}H_K$, and are symmetric on a logarithmic field scale. Natural random processes may be controlled in part by the surface and in part by the volume of the grain, and the resulting coercivity distribution is symmetric on a field scale given by $H_K^* = H_K^\alpha$, with $0 < \alpha < 1/3$. This distribution is always left-skewed on a logarithmic field scale.

2.4. Effect of the grain size dependence of the coercivity

The grain size dependence of common magnetic parameters has been investigated in detail on synthetic magnetite samples (see *Dunlop* [1981] for a review). Despite the complexity of the

results, a common feature is represented by the maximum stability of magnetite grains with a diameter of ≈ 60 nm. This grain size corresponds to the lower limit for the nucleation of incoherent reversal modes, which lower the energy barrier and the related coercivity of remanence, H_{cr} [*Enkin and Williams*, 1994]. Above this limit, H_{cr} decreases roughly as $H_{cr} \propto D^{-0.36}$ for synthetic magnetite [*Dunlop*, 1981]. The proportionality factor and the exponent depend on the sample preparation. Below 40 nm, thermal activation processes become effective, and H_{cr} decreases progressively to zero as the SP/SD limit is approached. It is evident from the above considerations, that $H_{cr}(D)$ is a convex function with its maximum around 60 nm. A similar behavior characterizes the remanence ratio M_{rs}/M_s, with $M_{rs}/M_s \propto D^{-0.45}$ for $D > 60$ nm [*Dunlop*, 1986]. Consider now a set of particles whose coercivity of remanence depends only on the grain size: $H_{cr} = H_{cr}(D)$. Accordingly, a set of particles with a distribution of grain sizes $v(D)$ has a coercivity distribution given by:

$$m(H_{cr}) = (M_{rs}/M_s)(H_{cr})\, v(D(H_{cr}))\left|\mathrm{d}D/\mathrm{d}H_{cr}\right| \tag{10}$$

It is easy to show that if $H_{cr}(D)$ and $(M_{rs}/M_s)(D)$ follow a power law and $v(D)$ is a logarithmic Gaussian function, then $m(H_{cr})$ is a logarithmic Gaussian distribution as well. Consequently, the symmetry of a coercivity distribution remains unaffected by the power dependence of H_{cr} and M_{rs}/M_s on the grain size. However, the coercivity distribution becomes negatively skewed if H_{cr} is limited by a maximum value. To demonstrate this effect, we consider following model for the grain size dependences: $H_{cr} \propto D$ and $M_{rs}/M_s \propto D^2$ for $D \leq 60$ nm, $H_{cr} \propto D^{-0.36}$ and $M_{rs}/M_s \propto D^{-0.45}$ for $D > 60$ nm (Figure 6a). The grain size dependences below 60 nm have been chosen so, that $H_{cr} \approx 0$ and $M_{rs}/M_s \approx 0$ at the SP/SD boundary. The skewness of the coercivity distribution of various sets of particles with a logarithmic Gaussian distribution of grain sizes has been calculated according to the grain size dependences given above (Figure 6b). The skewness parameter is always negative, with a minimum around 60 nm. Therefore, we conclude that the grain size dependence of the magnetic parameters tends to generate coercivity distributions that are negatively skewed on a logarithmic scale.

2.5. Squareness of a coercivity distribution

The SGG functions used in *Egli* [2003b] for modeling the coercivity distribution of individual magnetic components depend upon a parameter p, which controls the squareness. If $p = 2$, SGG functions are obtained from a Gaussian distribution with a simple scale transformation [*Egli*, 2003a]. Almost all components in paper 1 have been fitted with $p \approx 2$ to a sufficient precision. The optimization of p was necessary only for the component analysis of few samples where the magnetic contribution of one component was predominant. For these componetns $1.6 \leq p \leq 2.3$.

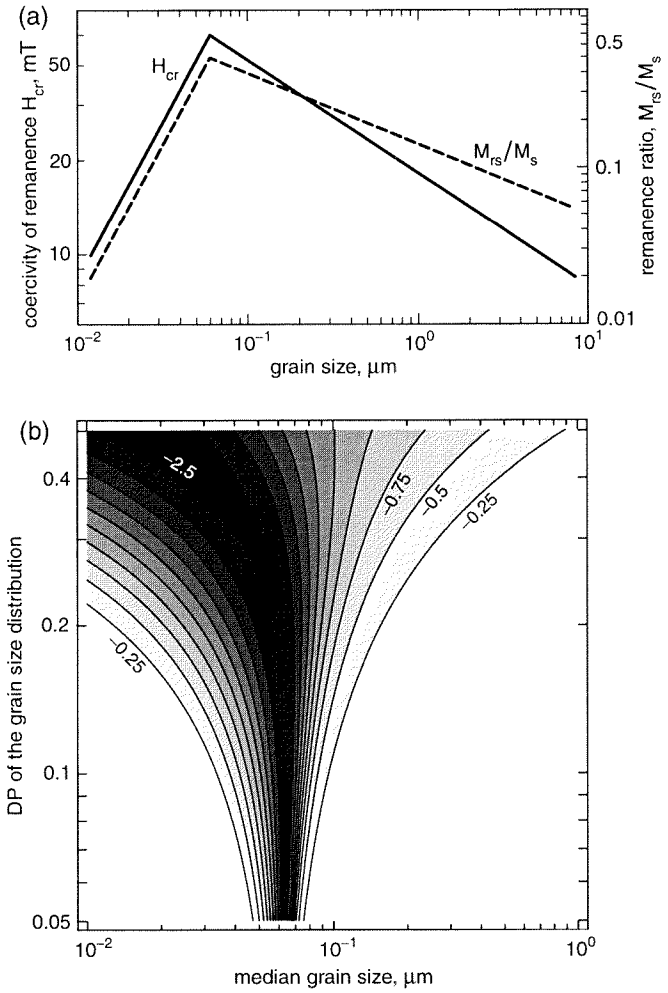

Figure 6. *Effect of the grain size dependence of the coercivity of remanence on the symmetry of a coercivity distribution. (a) A simplicistic model for the grain size dependence of the remanence coercivity* H_{cr} *and the remanence ratio* M_{rs}/M_s. *Both parameters are maximal at* 60 nm, *which is the lower limit for the nucleation of incoherent reversal models after Enkin and Williams [1994]. Following dependences have been assumed:* $H_{cr} \propto D$ *and* $M_{rs}/M_s \propto D^2$ *for* $D \leq 60$ nm, $H_{cr} \propto D^{-0.36}$ *and* $M_{rs}/M_s \propto D^{-0.45}$ *for* $D > 60$ nm. *Grain size dependences above* 60 nm *have been inferred from measurements on synthetic magnetite reported by Dunlop [1981,1986]. The discontinuity observed between* 200 nm *and* 1 µm *in the coercivity of remanence has been ignored. Grain size dependences below* 60 nm *are controlled by thermal activations. They have been chosen so, that the magnetization of SP particles* < 20 nm *is negligible. (b) Skewness of the coercivity distribution of magnetic particles modelled with (a) and a logarithmic Gaussian grain size distribution. The skewness is systematically negative, with a minimum around* 60 nm. *Similar results can be obtained with other models for the coercivity of remanence and the saturation remanence, provided these parameters are limited to a maximum value for a given grain size.*

In the following, we investigate the default value of p that should be used if the precision of the measurements does not allow its optimization. SGG functions are obtained trough a generalization of the Gaussian function $N(x,\mu,\sigma)$ with two additional parameters q and p, where q controls the skewness of the distribution [*Egli*, 2003a]. The generalization of $N(x,\mu,\sigma)$ imply the addition of some information, expressed by q and p. This additional information can be quantified with the so-called Shannon's information content. The Shannon's information content $I_{2,1}$ of a probability density function $f_2(x)$ with respect to another probability density function $f_1(x)$, both defined on the probability space Ω, is given by:

$$I_{2,1} = \int_{\Omega} f_2(x) \log \frac{f_2(x)}{f_1(x)} \mathrm{d}x \tag{11}$$

[*Tarantola*, 1987]. In our case, the additional information $I(q,p)$ related to the generalization of $N(x,\mu,\sigma)$ is given by (11), with $f_2 = SGG(\mu,\sigma,q,p)$, $f_1 = N(\mu,\sigma)$ and $\Omega = \mathbb{R}$. If p is not going to be optimized, a reasonable criterion for choosing p is to minimize the information added by the generalization of $N(x,\mu,\sigma)$. In this case, p is the solution of the minimization problem $I(q,p) = \min$ with a fixed q (Figure 7). The approximate solution of the minimization problem is given by:

$$p(q) \approx 2 - 1.533\,|1-q|^{2.082} + 5.725\,|1-q|^{3.527} \tag{12}$$

Some well-defined natural and artificial components analyzed in *Egli* [2003b] have been modeled by optimizing all the four shape parameters and the results for q and p are plotted in Figure 7. The resulting empirical relation between q and p is affected by the high sensitivity of these parameters to measurement errors; nevertheless, the observed trend is compatible with equation (12). To conclude, $SGG(\mu,\sigma,q,p(q))$, where $p(q)$ is given in (12), is a minimum information (or maximum entropy) model function which can be used for an adequate modeling of skewed coercivity distributions with three shape parameters. In the following, we will refer to $SGG(\mu,\sigma,q,p(q))$ as the maximum entropy SGG function.

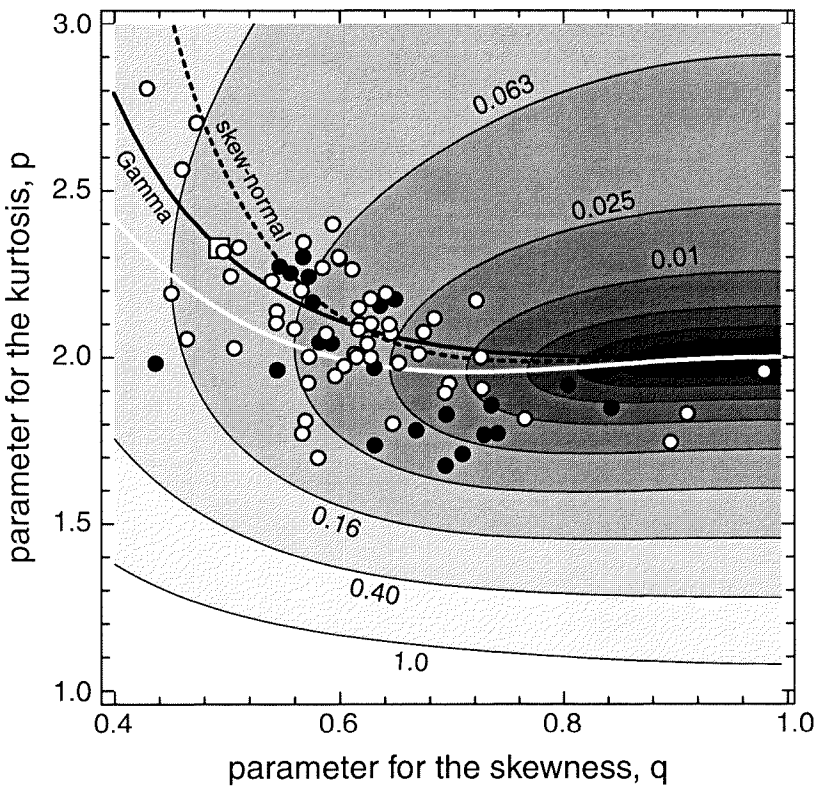

Figure 7. *Shannon's information content calculated for $SGG(x,\mu,\sigma,q,p)$ with respect to $N(x,\mu,\sigma)$, as a function of the parameters q and p (see text). Contour levels are equally spaced on a logarithmic scale. The white line indicates the value of p that minimizes the information content for a given q. SGG functions that plot along this line are maximum entropy functions with a given skewness. The solid line, the short-dashed line and the open square represent best-fit SGG functions of Gamma, Weibull and skew-normal distributions, respectively [Azzalini, 1985; Evans et al., 2000]. Best-fit SGG functions of individual natural (dots) and artificial (circles) components reported by Egli [2003b] are plotted for comparison.*

3. Coercivity distributions of natural magnetic components

In the following, the magnetic properties of the sedimentary components characterized in *Egli* [2003b] are discussed, with special regard to their interpretation in terms of classic rock magnetism. It will be shown that four parameters, derived from the parameters used to model the coercivity distributions of ARM and IRM, can be regarded as a characteristic 'fingerprint' of a magnetic component. The properties of all ninety-four sedimentary components identified in *Egli* [2003b], and those of 23 artificial magnetite samples collected from the literature, are plotted in Figures 8-11. We refer to *Egli* [2003b] for a detailed discussion of the individual components.

3.1. Median destructive field and k_{ARM}/IRM

The two most important parameters of ARM and IRM demagnetization curves, MDF and k_{ARM}/IRM, are plotted in Figure 8 for all natural components. The components are clearly grouped into different clusters. A similar plot can be obtained by using MDF_{IRM} instead of MDF_{ARM}. The components, however, are slightly less well grouped because of the systematically higher values of the dispersion parameter DP obtained from the coercivity distributions of IRM with respect to the ARM (see section 3.2). Since DP is a measure for the 'randomness' of a component, a better grouping of the ARM properties is expected, because low-field magnetizations are carried preferentially by SD particles.

Bacterial components found in freshwater sediments, BS and BH, form two distinct groups, probably related to different morphologies of the magnetosomes. The ARM ratio of magnetosomes displays a clear trend, from large values, which characterize oxic and suboxic sediments, as well as cultured magnetotactic bacteria, toward much smaller values observed in the anoxic sediments. Only small changes can be observed in the MDFs, which are characterized by mean values of 45 and 73 mT, respectively. It is evident that k_{ARM}/IRM cannot always be considered a diagnostic parameter for biogenic magnetite. Few data are available for biogenic components from marine sediments. However, similar trends are observed, with systematically smaller values of the MDF.

Other well-grouped components are the urban pollution, UP, and airborne dust, ED. Both have moderately scattered ARM ratios, but constant MDFs of 28 and 87 mT, respectively. The scattered ARM ratios of UP have been interpreted as a mixing trend of fly ash and metallic particles in *Egli* [2003b].

Extracellular magnetite, EX, and pedogenic magnetite, PD, form a mixing trend together with the detrital component of lake sediments, D. These components could not be unmixed, because their coercivity distributions overlap widely and are similar in shape. However, in some samples the magnetic contribution of one component is predominant and defines an end-member of the group formed by D, EX and PD.

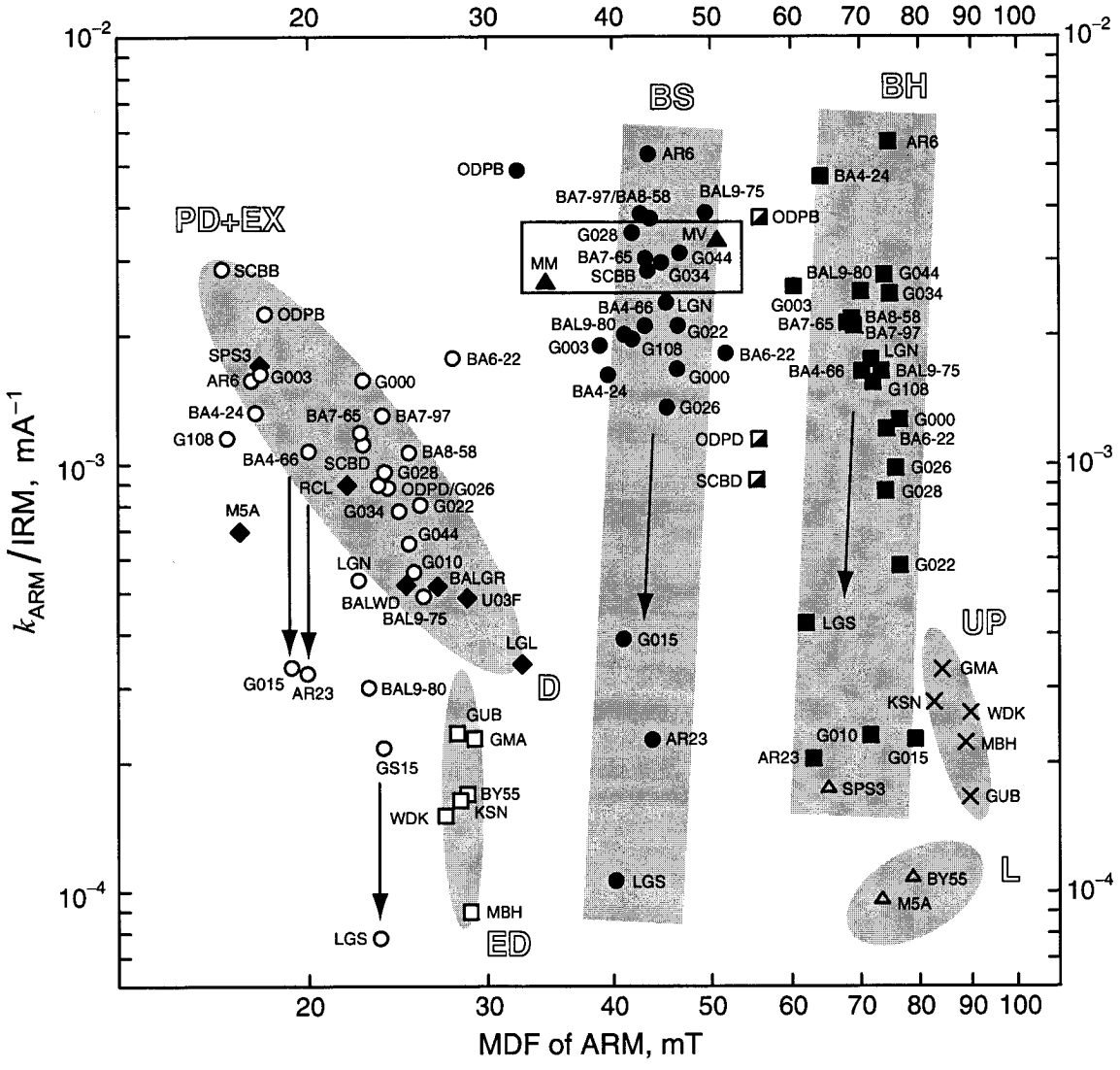

Figure 8. *Summary of the magnetic properties of ARM and IRM for all iron spinel components identified in Egli [2003b]:* MDF_{ARM} *and* k_{ARM}/IRM *. The magnetic components (symbols) group clearly into different clusters, indicated by grey ellipses and rectangles, whose extension is equal to four times the standard deviation of the scattered magnetic properties of the components in each cluster. White letters classify all components into low-coercivity magnetosomes (biogenic soft, BS: dots), high-coercivity magnetosomes (biogenic hard, BH: squares), ultrafine extracellular magnetite (EX: circles), pedogenic magnetite (PD: diamonds), detrital particles transported in water systems (D: diamonds), wind-blown particles (eolian dust, ED: open squares), atmospheric particulate matter produced by urban pollution (UP: crosses), and a maghemite component in loess (L: open triangles). Other components, as BM (dots) and BI (half-filled squares), have been measured in a few numbers of samples and are not labelled. The open rectangle indicates the range of values measured in samples of cultured magnetotectic bacteria (triangles). GS15 labels the measurement of extracellular magnetite particles produced by a cultured dissimilatory iron-reducing microorganism [Lovley et al., 1987; Moskowitz et al., 1993]. Its properties are influenced by the strong magnetostatic interactions: GS15 in sediments would probably fall into the cluster labelled with PD+EX. Arrows indicate the decrease of* k_{ARM}/IRM *observed during anoxic conditions in lake sediments.*

The magnetic contribution of the detrital component is predominant in samples LGL and U03F, with $MDF_{ARM} \approx 30$ mT and $k_{ARM}/IRM =$ 0.1-0.2 mm/A. Extracellular and pedogenic magnetites have similar magnetic properties, with $MDF_{ARM} \approx 17$ mT and $k_{ARM}/IRM > 1.5$ mm/A. These properties have been modelled with ultrafine magnetite in *Egli* [2003b].

3.2. The dispersion parameter

The dispersion parameter of ARM is plotted in Figure 9 as a function of MDF_{ARM} for all natural and artificial components characterized in *Egli* [2003b]. In general, DP_{ARM} is inversely related to MDF_{ARM}. The reason for this trend can be explained as follows. Each magnetic mineral has a maximum intrinsic coercivity $H_{c,max}$, which can be regarded as a mineralogic constant. For magnetite $H_{c,max} \approx 300$ mT, according to the Stoner-Wohlfarth theory of SD particles [*Stoner and Wohlfarth*, 1948]. Therefore, the coercivity distribution of every set of particles is equal to zero for fields above $H_{c,max}$. On the other hand, the function $SGG(H_c, \mu, \sigma, q)$ used in *Egli* [2003b] to model coercivity distributions is > 0 for all fields. However, for the symmetric case given by $q = 1$, the magnetic contribution of all fields H_c with $\log H_c > \mu + 3\sigma$ is only 0.14% of the total magnetization, and with good approximation, we assume $f(H_c) \equiv 0$ for $\log H_c > \mu + 3\sigma$. A simple relation between the median destructive field μ and the dispersion parameter σ of all coercivity distributions of the same mineral is obtained by setting $\mu + 3\sigma < \log H_{c,max}$. A more general result is obtained by considering skewed coercivity distributions $SGG(H_c, \mu, \sigma, q)$ with $0 < q < 1$ (Figure 9). This result accounts for the trend observed in natural and artificial components, and is compatible with all coercivity distributions of synthetic magnetite. Many natural components exceed the limit of pure magnetite, indicating the presence of other minerals, like maghemite in component ED or maghemite and metallic iron in component UP. Natural and artificial magnetite components follow trend lines defined by coercivity distributions with a maximum switching field of 160 mT.

All natural low-coercivity components except bacterial magnetite and the urban pollution fall into the same group, characterized by $MDF_{ARM} = 15...30$ mT and $DP_{ARM} = 0.3...0.45$. This suggests an underlying similarity between magnetite/maghemite components that are not directly grown by living organisms. Chemical weathering, transport by air or in water, and authigenic or pedogenic processes produce a similar dispersion of coercivities in a similar coercivity range. For comparison, mean and standard deviation of some parameters which influence MDF_{ARM} and DP_{ARM} are listed in Table 1 for natural and synthetic magnetites.

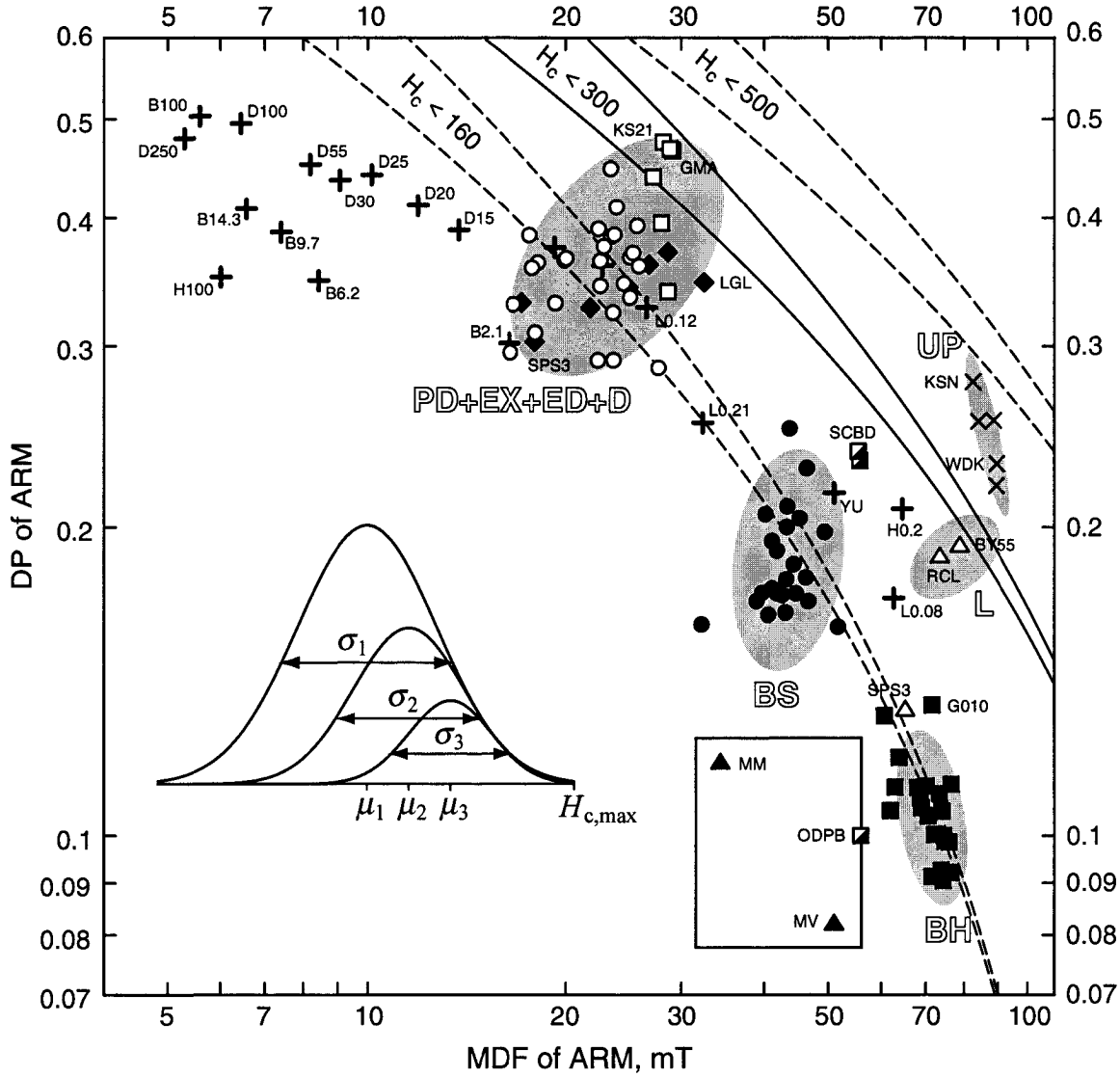

Figure 9. *Summary of the magnetic properties of ARM and IRM for all iron spinel components identified in Egli [2003b]:* MDF_{ARM} *and* DP_{ARM}*. Same labels and definitions as in Figure 8. For comparison, results collected from the literature for samples of sized synthetic magnetites are reported as well ("+" symbols, labelled with L: Levi and Merrill [1978], D: Dankers, [1978], B: Bailey and Dunlop [1983], H: Halgedahl [1998], followed by the grain size in* μm*). All natural components except UP and the biogenic magnetites, fall into the same cluster, suggesting an underlying similarity between natural processes which are not directly controlled by living organisms. The solid and the dashed lines represent the maximum possible DP, for which the coercivity distribution can be approximated with zero above a given maximum field* $H_{c,max}$ *(small inset). Coercivity distributions of minerals with a maximal intrinsic switching field* $H_{c,max}$ *plot below these lines. For pure magnetite,* $H_{c,max} = 300$ mT *according to the Stoner-Wohlfarth theory for SD particles [Stoner and Wohlfarth, 1948] and all artificial magnetite samples plot effectively below the limit given by the solid lines. Many natural components exceed this limit, indicating the presence of other minerals, like maghemite.*

Table 1. *Median grain size D, standard deviation of the grain size, $\sigma(\log D)$, median elongation E, and standard deviation of the elongation, $\sigma(\log E)$, all weighted by volume, for some synthetic and natural magnetite particles. Median destructive field and dispersion parameter of the ARM are listed as well for comparison.*

Magnetite sample	vol. weighted mean grain size D, μm	$\sigma(\log D)$	vol. weighted mean elongation E	$\sigma(\log E)$	MDF_{ARM} mT	DP_{ARM}
Pfizer BK-5099	0.330 [1]	0.126 [1]				
Columbian Carbon Company	0.275 [1]	0.123 [1]			32 [1]	0.252 [1]
Elmore	0.172 [1]	0.140 [1]			27 [1]	0.327 [1]
Submicron magnetites	0.023 [2]	0.148 [2]			≈15 [2]	≈0.32 [8]
	0.025 [2]	0.107 [2]			≈20 [2]	≈0.32 [8]
Synthetic magnetite	0.059 [3]	0.108 [3]				
	0.083 [3]	0.079 [3]				
	0.123 [3]	0.081 [3]				
	0.160 [3]	0.085 [3]				
Synthetic magnetite	0.240 [4]	0.123 [3]				
Mapico	0.256 [5]	0.116 [5]	1.31 [5]	0.202 [5]	≈30 [8]	≈0.3 [8]
Wright Company	24 [5]	0.166 [5]	1.56 [5]	0.456 [5]	≈10 [8]	≈0.4 [8]
Dissimilatory iron reducer GS15	15.1 [6]	0.076 [6]			≈20 [8]	≈0.32 [8]
	14.9 [6]	0.115 [6]			≈20 [8]	≈0.32 [8]
	12.6 [6]	0.090 [6]			≈20 [8]	≈0.32 [8]
Yucca Mountain tuff (CS914)	14.8 [9]	0.12 [10]	5.3 [9]		50.9 [10]	0.216 [10]
Magnetosomes from MV-1	0.044 [6]	0.073 [6]	1.55 [6]	0.049 [6]	≈50 [7]	0.092 [7]

[1] *Levi and Merrill* [1978]; [2] *Maher* [1988]; [3] *Schmidbauer and Schembra* [1987]; [4] *Schmidbauer and Keller* [1996]; [5] *Yu et al.* [2002]; [6] *Sparks et al.* [1990]; [7] *Moskowitz et al.* [1993]; [8] Approximated values from Figure 8 and Figure 9; [9] *Worm and Jackson* [1999]; [10] *Egli and Lowrie* [2002].

3.3. Skewness

The skewness s of a coercivity distribution is a measure for its symmetry, and is plotted in Figure 10a for all components characterized in *Egli* [2003b]. The components are scattered along a line defined by identical values for the skewness of ARM and IRM. This means that the symmetry of a coercivity distribution is independent of the type of acquired magnetization. Part of the scattering of the results is due to the sensitivity of the skewness parameter to measurement errors. All components are negatively skewed with values between –0.8 and 0, and a mean of –0.4. The relation between the symmetry of a coercivity distribution and the physical parameters of the grains has been discussed in section 2. Generally, all models considered in section 2 predict a negative skewness, except in some special case that are unlikely to occur in nature.

According to section 2.3, random perturbations of the intrinsic coercivity of a particle induced by defects may affect the shape of the observed coercivity distributions. In this case, the coercivity distribution becomes symmetric if plotted on an appropriate field scale, given by $H^* = H^\alpha$. On a logarithmic field scale, the skewness depends on α and is approximately proportional to the DP.

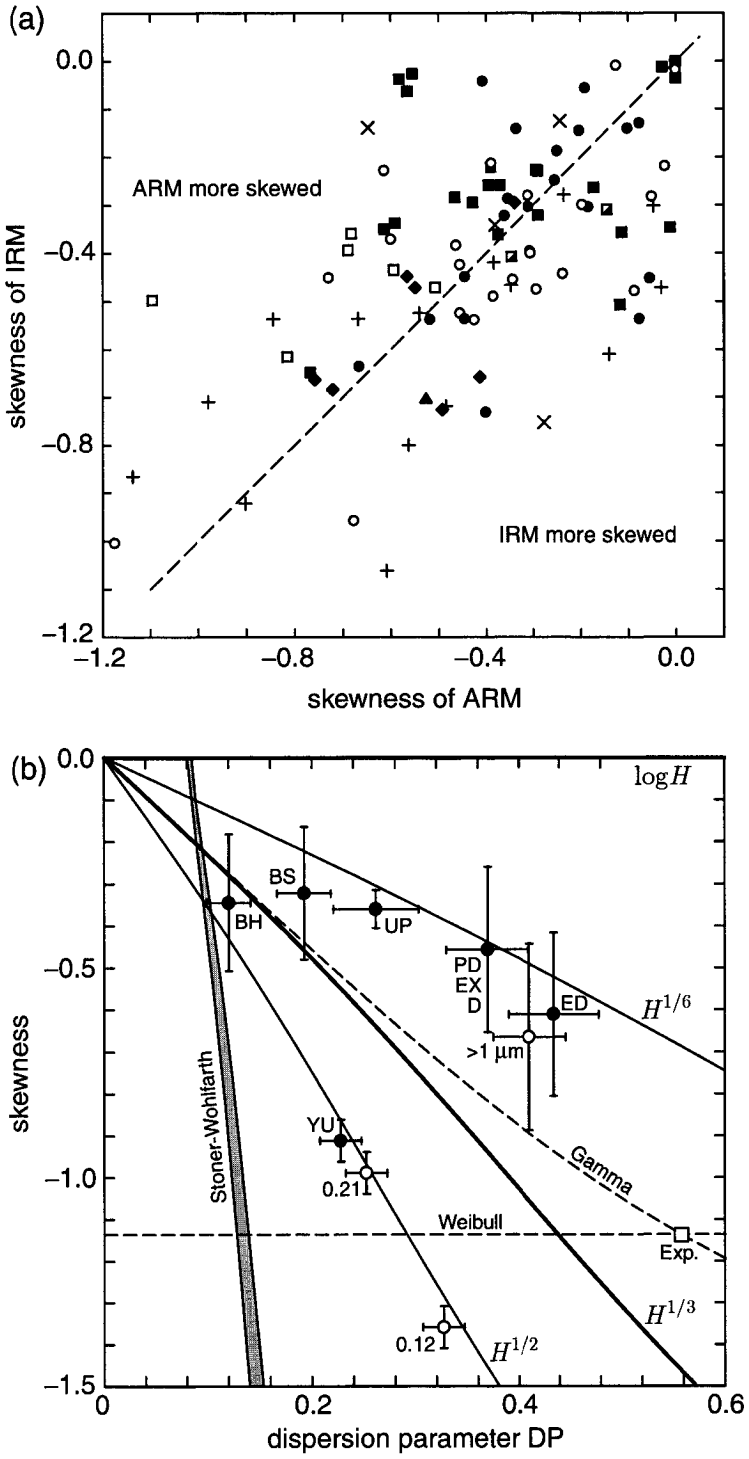

Figure 10. *(a) Summary of the magnetic properties of ARM and IRM for all iron spinel components identified in paper Egli [2003b]: skewness of ARM and IRM. Same symbols as in Figure 8 and Figure 9. The dashed line separates components with a more skewed ARM from those with a more skewed IRM. Natural components and artificial samples are scattered along this line suggesting a similar symmetry of ARM and IRM coercivity distributions. (b) Scatter plot of the DP and the skewness of ARM and IRM coercivity distributions. Open symbols indicate artificial samples, and error bars the standard deviation of all components of a specific group. Solid lines are trends expected for distributions that are symmetric on a field scale given by H^{α}. Natural components and artificial magnetite samples > 1 μm are intermediate between coercivity distributions generated by random processes related to the volume ($\alpha \rightarrow 0$) and random processes related to the surface ($\alpha = 1/3$) of the particles. Ultrafine magnetite approaches the trend predicted by the Stoner-Wohlfarth theory (shaded area). Dashed lines indicate the trend defined by positive distribution functions such as the Weibull and the Gamma distribution.*

A scatter plot of DP and s for natural and artificial components is given in Figure 10b, together with the theoretical dependence of s on DP, which results from distributions that are symmetric on $H^* = H^{\alpha}$. The trend observed for natural samples suggests values of α which are intermediate between $\alpha \rightarrow 0$, which is characteristic for processes that depend on the

volume of the particles, and $\alpha = 1/3$, which is expected for surface-controlled processes. On the other hand, the coercivity distributions of ultrafine synthetic and natural magnetite plot along a line given by $\alpha = 1/2$. This line approaches the behaviour calculated for Stoner-Wohlfarth particles in section 2.1.

3.4. Comparison between ARM and IRM

As discussed in *Egli* [2003b], differences between the shape of demagnetization curves of ARM and IRM can be quantified with the parameters ΔMDF and ΔDP, given by:

$$\begin{aligned} \Delta MDF &= (\log MDF_{\mathrm{ARM}} - \log MDF_{\mathrm{IRM}}) / DP_{\mathrm{ARM}} \\ \Delta DP &= (DP_{\mathrm{ARM}} - DP_{\mathrm{IRM}}) / DP_{\mathrm{ARM}} \end{aligned} \tag{13}$$

These parameters are plotted in Figure 11 for artificial and natural components. Both the natural and the artificial components show a linear relation between ΔMDF and ΔDP, with different proportionality coefficients. In natural components $\Delta DP \approx -0.532\,\Delta MDF$, with the only exception of the urban pollution. The different behaviour of the artificial samples arises probably from interaction effects. The linear relation between ΔMDF and ΔDP can be explained by taking into account the statistical distribution of intrinsic properties such as the grain size and the microcoercivity. Consider first a set of particles with identical volumes and a microcoercivity distribution. Since k_{ARM}/IRM depends mainly on the grain size, the coercivity distributions of ARM and IRM are very similar: $\Delta MDF \approx 0$ and $\Delta DP \approx 0$. Consider now a set of particles with a volume distribution and a microcoercivity distribution. Microcoercivity and k_{ARM}/IRM are maximal in SD grains of ≈60 nm size [*Egli and Lowrie*, 2002]. Since both parameters have an upper limit for the same grain size, a positive correlation exists between them. As a consequence, the coercivity distribution of ARM is shifted toward higher fields and $\Delta MDF > 0$. Furthermore, the ARM 'sees' preferentially a narrow range of grain sizes around 50 nm, which is equivalent to a narrow range of coercivities. Consequently, the dispersion parameter of the ARM coercivity distribution becomes smaller, and $\Delta DP < 0$. In this way, a negative correlation between ΔMDF and ΔDP is obtained by varying the grain size distribution.

3.5. Switching field and ARM ratio for magnetic grains of the same component

The dependence of k_{ARM}/IRM on the switching field H_{sw} for magnetic grains of the same component is obtained by calculating the ratio of the coercivity distribution of ARM to the coercivity distribution of IRM. This ratio has been calculated for a selected group of natural components and the results are shown in Figure 12. Two distinct categories can be clearly distinguished. SD particles of biogenic and non-biogenic origin are characterized by large maximum values of k_{ARM}/IRM and a weak dependence on H_{sw}: $(k_{\mathrm{ARM}}/IRM)_{\max} \approx H_{\mathrm{sw}}^{0.28}$, with k_{ARM}/IRM expressed in mm/A and H_{sw} in mT.

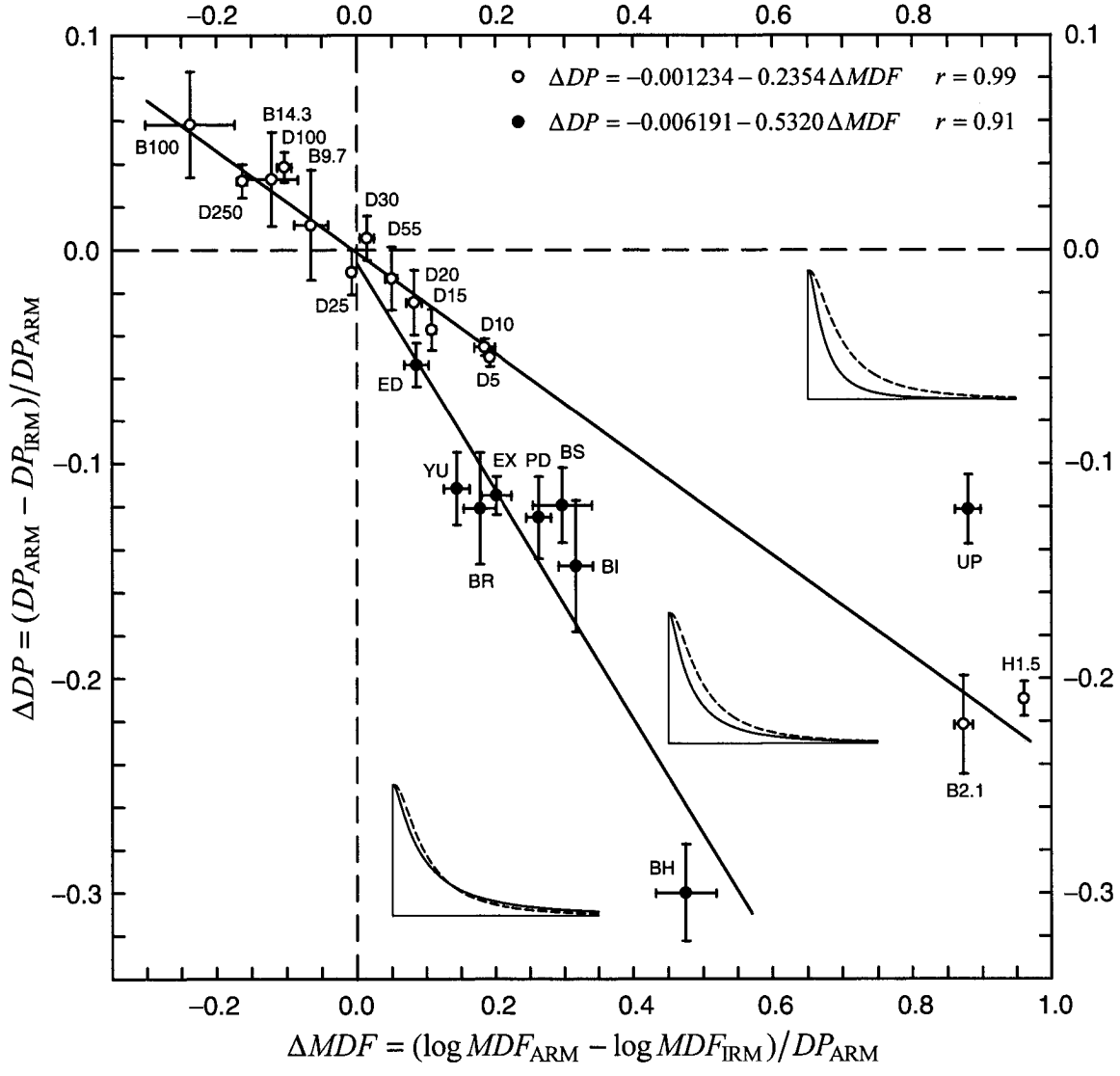

Figure 11. *Summary of the magnetic properties of ARM and IRM for all iron spinel components identified in Egli [2003b]: modified Lowrie-Fuller test. In the modified Lowrie-Fuller test, the shapes of normalized AF demagnetization curves of ARM and IRM are compared. In this plot, the differences between demagnetization curves of ARM and IRM are quantified by means of the relative difference* ΔMDF *between the median destructive fields, and the relative difference* ΔDP *between the dispersion parameters. For reasons of clarity, averaged values are plotted for each of the groups of components described in Figure 8 (dots). The error bars indicate the standard deviation of all components that belong to a particular cluster. BR indicates all samples of cultured magnetotactic bacteria. For comparison, results for the synthetic magnetite samples reported in Figure 9 are also shown (open symbols). Error bars indicate the standard error. Small inserts represent the typical result of the modified Lowrie-Fuller test for the region of the plot where they are placed. A 'mixed type' result is obtained if* $\Delta MDF = 0$ *(vertical dashed line). Results which are considered typical for SD particles fall along the diagonal of the lower right quadrant defined by the dashed lines. Results that are considered typical for MD particles fall along the same diagonal, but in the upper left quadrant. Natural components and synthetic magnetite samples are distributed according to two different trends, indicated by best-fit lines. In both cases, the relation between* ΔMDF *and* ΔDP *is linear.*

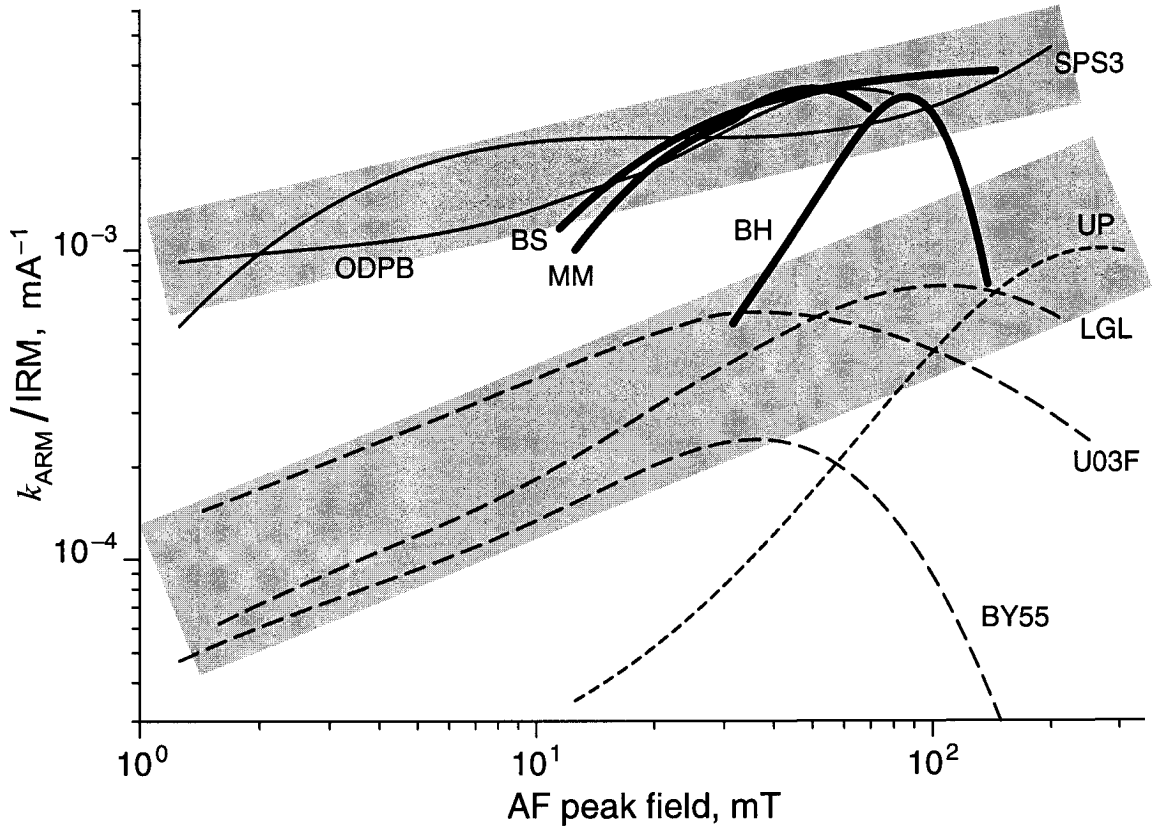

Figure 12. *Dependence of k_{ARM}/IRM on the switching field for individual magnetic components. The switching field is equal to the AF peak field during AF demagnetization experiments. Solid thick lines are averaged values for the bacterial components BS and BH, and for a sample of cultured Magnetospirillum Magnetotacticum [Moskowitz et al., 1988]. Solid thin lines are values obtained for the authigenic component of a pelagic sediment (ODPD) and the pedogenic component of a paleosol from the Central Chinese Loess Plateau (SPS3). These components and the bacterial components contain single domain magnetite particles, and are characterized by large values of k_{ARM}/IRM. Long-dashed lines are values obtained for the detrital component D of lake sediments (LGL and U03F) and for component ED of a pristine loess from the Western Chinese Loess Plateau (BY55). Components D and ED contain relatively coarse-grained magnetites and maghemites, and are characterized by small values of k_{ARM}/IRM. Averaged results for the urban pollution component (UP) are plotted with a short-dashed line. The maximum value of k_{ARM}/IRM for SD magnetite shows a weak dependence on the switching field H_{sw} (upper grey rectangle): $(k_{\mathrm{ARM}}/IRM)_{\mathrm{max}} \approx H_{\mathrm{sw}}^{0.28}$, with k_{ARM}/IRM expressed in mmA^{-1} and H_{sw} in mT. The maximum value of k_{ARM}/IRM for all the other components is more strongly dependent on the switching field (lower grey rectangle): $(k_{\mathrm{ARM}}/IRM)_{\mathrm{max}} \approx 0.1 H_{\mathrm{sw}}^{0.5}$, with k_{ARM}/IRM expressed in mmA^{-1} and H_{sw} in mT.*

Smaller values of k_{ARM}/IRM characterize the other components, together with a stronger dependence of k_{ARM}/IRM on H_{sw}. For these components, $(k_{\mathrm{ARM}}/IRM)_{\mathrm{max}} \approx 0.1 H_{\mathrm{sw}}^{0.5}$, with k_{ARM}/IRM expressed in mm/A and H_{sw} in mT. The dependence of k_{ARM}/IRM on the switching field influences the shape of a Fuller diagram (Figure 13), in which the

logarithm of a weak field magnetization, as the ARM or a natural remanence, is plotted against the IRM [*Fuller et al.*, 1988; *Cisowski et al.*, 1990; *Fuller et al.*, 2002].

3.6. The four fingerprint parameters

In the previous paragraphs, the relations existing between the coercivity distribution parameters of ARM and IRM have been highlighted. Some parameters are correlated, as s_{ARM} and s_{IRM}, s_{ARM} and DP_{ARM}, or ΔMDF and ΔDP, and only one of them is necessary to characterize a magnetic component. The four parameters given by k_{ARM}/IRM, MDF_{ARM} DP_{ARM} and ΔMDF are sufficient to describe the remanence properties of all natural components identified in *Egli* [2003b]. In the following, these parameters will be called fingerprint parameters, since they characterize unambiguously a magnetic component. The fingerprint parameters have a physical meaning: k_{ARM}/IRM is sensitive to the grain size, MDF_{ARM} is a measure for the 'hardness' of the particles and DP_{ARM} for their 'randomness', and ΔMDF is an expression for the relation between the switching field and k_{ARM}/IRM. The other distribution parameters can be expressed with the fingerprint parameters as follows:

$$\begin{aligned} \log MDF_{\mathrm{IRM}} &\approx \log MDF_{\mathrm{ARM}} - DP_{\mathrm{ARM}}\Delta MDF \\ DP_{\mathrm{IRM}} &\approx DP_{\mathrm{ARM}}(1 + c_1\,\Delta MDF) \\ s_{\mathrm{ARM}} &\approx s_{\mathrm{IRM}} \\ s_{\mathrm{ARM}} &\approx c_2 DP_{\mathrm{ARM}} \end{aligned} \tag{14}$$

with $c_1 \approx 0.53$ for natural components, $c_1 \approx 0.235$ for synthetic magnetite, $c_2 \approx -1.43$ for natural and artificial magnetite components $> 1\ \mu\mathrm{m}$, $c_2 \approx -3.75$ for ultrafine magnetite.

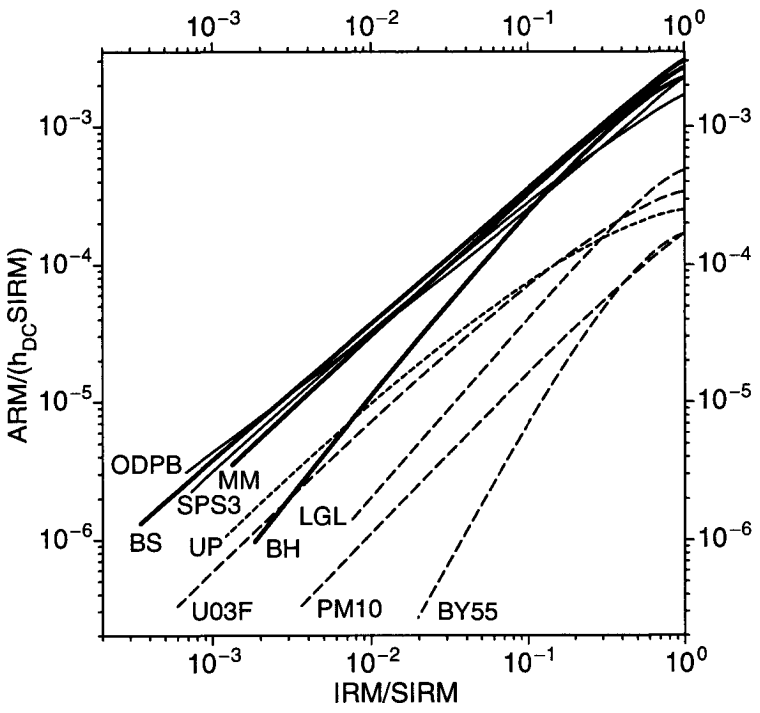

Figure 13. *Fuller diagram for the same components and labels of Fig. 12. Components that contain SD particles (solid lines) plot along almost straight lines with unit slope, because of the weak field dependence of k_{ARM}/IRM. All other components are more or less concave.*

If the natural scatter of the fingerprint parameters of each group of components identified in *Egli* [2003b] is taken into account, a maximum of six groups of components can be distinguished with MDF_{ARM}, four groups with k_{ARM}/IRM, four groups with DP_{ARM} and four groups with ΔMDF (Figures 8, 9, and 11). Considering the relation between MDF_{ARM} and DP_{ARM} discussed in section 3.2, a combination of all four fingerprint parameters offers the possibility of discriminating up to 64 different components.

4. Conclusions

The remanence properties of a component can be summarized by the parameters used to fit the coercivity distributions of ARM and IRM with the model functions described in *Egli* [2003b]. Some of these parameters, which are directly related to the magnetization curves, are of common use in rock magnetism. The other parameters are related to the shape of a coercivity distribution, and their physical meaning has been discussed in section 3. Different models to explain the shape of a coercivity distribution have been discussed in section 2. All models predict left-skewed coercivity distributions on a logarithmic field scale, in concert with the measurement of natural and artificial magnetic components performed in *Egli* [2003b].

The characterization of magnetic component with skewed coercivity distributions requires the use of model functions with three shape parameters, such as maximum entropy SGG functions. The ARM and the IRM of a component are fully described by six shape parameters (three for each type of magnetization) and a seventh parameter that account for the ratio between ARM and IRM. It has been found that only four of the seven parameters are independent. A combination of the four independent parameters is sufficient to characterize unambiguously the remanent magnetization properties of a component, and can be regarded as a kind of 'fingerprint'. The complexity of the unmixing problem is greatly reduced by this knowledge, since there are much less degrees of freedom to consider for a solution. A further simplification is obtained if the fingerprint parameters of all components occurring in sediments, and their dependence on natural processes, are known in advance from detailed measurements on a set of samples used as reference.

Acknowledgements. ETH Research Project 0-20556-00. I am grateful to Simo Spassov for interesting discussions about modeling coercivity distributions.

References

Azzalini, A., A class of distributions which includes normal ones, *Scand. J. Stat.*, *12*, 171-178, 1985.

Bailey, M. E. and D. J. Dunlop, Alternating field characteristics of pseudo-single-domain (2-14 μm) and multidomain magnetite, *Earth Planet. Sci. Lett.*, *63*, 335-352, 1983.

Carter-Stiglitz, B., B. Moskowitz and M. Jackson, Unmixing magnetic assemblages and the magnetic behaviour of bimodal mixtures, *J. Geophys. Res.*, *106*, 26397-26411, 2001.

Cisowski, S. M., J. R. Dunn, M. Fuller and P. J. Wasilewski, NRM:IRM(s) demagnetization plots of intrusive rocks and the origin of their NRM, *Tectonophysics*, *184*, 35-54, 1990.

Dankers, P. H. M., Magnetic properties of dispersed natural iron-oxides of known grain-size, Ph.D. thesis, Univ. of Utrecht, Netherlands, 1978.

Dankers, P. and N. Sugiura, The effect of annealing and concentration on the hysteresis properties of magnetite around the PSD-MD transition, *Earth Planet. Sci. Lett.*, *56*, 422-428, 1981.

Dearing, J. A., Holocene environmental change from magnetic proxies in lake sediments, in *Quaternary climates, environments and magnetism*, edited by B. A. Maher and R. Thompson, Cambridge University Press, 1999.

Dunlop, D. J., The rock magnetism of fine particles, *Phys. Earth. Planet. Inter.*, *26*, 1-26, 1981.

Dunlop, D. J., Hysteresis properties of magnetite and their dependence on particle size: a test for pseudo-single-domain remanence models, *J. Geophys. Res.*, *91*, 9569-9584, 1986.

Dunlop, D. J., Magnetism in rocks, *J. Geophys. Res.*, *100*, 2161-2174, 1995.

Dunlop, D. J., and Ö. Özdemir, *Rock magnetism: fundamentals and frontiers*, Cambridge University Press, 1997, 573 pp.

Egli, R. and W. Lowrie, The anhysteretic remanent magnetization of fine magnetic particles, *J. Geophys. Res.*, *107*, 2209-2229, 2002.

Egli, R., Analysis of the field dependence of remanent magnetization curves, *J. Geophys. Res.*, 102, 2081, doi 10.1029/2002JB002023, 2003a.

Egli, R., Characterization of individual rock magnetic components by analysis of remanence curves, 1. Unmixing natural sediments, submitted to *Studia Geophysica et Geodaetica*, 2003b.

Enkin, R. J., and W. Williams, Three-dimensional micromagnetic analysis of stability in fine magnetic grains, *J. Geophys. Res.*, *99*, 611-618, 1994.

Evans, M., N. Hastings, and B. Peacock, *Statistical distributions*, John Wiley, New York, 2000, 221 pp.

Fuller, M., S. Cisowski, M. Hart, R. Haston and E. Schmidtke, NRM:IRM(S) demagnetization plots; an aid to the interpretation of natural remenent magnetization, *Geophys. Res. Lett.*, *15*, 518-521, 1988.

Fuller, M., T. Kidane and J. Ali, AF demagnetization characteristics of NRM, compared with anhysteretic and saturation isothermal remanence: an aid in the interpretation of NRM, *Phys. Chem. Earth*, *27*, 1169-1177, 2002.

Geiss, C. E. and S. K. Banerjee, A multi-parameter rock magnetic record of the last glacial-interglacial paleoclimate from south-central Illinois, USA, *Earth Planet. Sci. Lett.*, *152*, 203-216, 1997.

Halgedahl, S. L., Revisiting the Lowrie-Fuller test: alternating field demagnetization characteristics of single-domain through multidomain glass-ceramic magnetite, *Earth Planet. Sci. Lett.*, *160*, 257-271, 1998.

Heslop, D., G. McIntosh, and M. J. Dekkers, Using time and temperature dependant Preisach models to investigate the limitations of modeling isothermal remanent magnetization acquisition curves with cumulative log Gaussian functions, submitted to *Geophys. J. Int.*, 2003.

Hilton, J., A simple model for the interpretation of magnetic records in lacustrine and ocean sediments, *Quaternary Res.*, *27*, 160-166, 1987.

Hunt, C. P., B. M. Moskowitz, and S. K. Banerjee, Magnetic properties of rocks and minerals, Rock physics and phase relations, A handbook of physical constants, AGU Reference Shelf 3, 1995.

Johnson, H. P., W. Lowrie, and D. Kent, Stability of anhysteretic remanent magnetization in fine and coarse magnetite and maghemite particles, *Geophys. J. R. Astronom. Soc.*, *41*, 1-10,1975.

Karlin, R., Magnetite diagenesis in marine sediments from the Oregon Continental Margin, *J. Geophys. Res.*, *95*, 4405-4419, 1990.

King, J., S. K. Banerjee, J. Marvin and Ö. Özdemir, A comparison of different magnetic methods for determining the relative grain size in natural materials: some results from lake sediments, *Earth Planet. Sci. Lett.*, *59*, 404-419, 1982.

Korvin, G., *Fractal models in the Earth sciences*, Elsevier, 396 pp., 1992.

Leslie, B. W., S. P. Lund and D. E. Hammond, Rock magnetic evidence for the dissolution and authigenic growth of magnetic minerals within anoxic marine sediments of the California continental borderland, *J. Geophys. Res.*, *95*, 4437-4452, 1990a.

Leslie, B. W., D. E. Hammond, W. M. Berelson, and S. P. Lund, Diagenesis in anoxic sediments from the California Continental Borderland and its influence on iron, sulfur and magnetite behaviour, *J. Geophys. Res.*, *95*, 4453-4470, 1990b.

Levi, S. and R. Merrill, Properties of single-domain, pseudo-single-domain and multidomain magnetite, *J. Geophys. Res.*, *83*, 309-323, 1978.

Lovley, D. R. et al., Anaerobic production of magnetite by a dissimilatory iron-reducing microorganism, *Nature*, *330*, 252-254, 1987.

Lowrie, W., and M. Fuller, On the alternating field demagnetisation characteristics of multi-domain thermoremanent magnetization in magnetite, *J. Geophys. Res.*, *76*, 6339-6349, 1971.

Lu, R., and S. K. Banerjee, Magnetite dissolution in deep sediments and its hydrologic implication: a detailed study of sediments from site 808, leg 131, *J. Geophys. Res.*, *99*, 9051-9059, 1994.

Maher, B. A., Magnetic properties of some synthetic sub-micron magnetites, *Geophys. J.*, *94*, 83-96, 1988.

Moskowitz, B. M., R. B. Frankel and D. A. Bazylinski, Rock magnetic criteria for the detection of biogenic magnetite, *Earth Planet. Sci. Lett.*, *120*, 283-300, 1993.

Néel, L., Théorie du trainage magnétique des ferromagnétiques en grains fins avec application aux terres cuites, *Ann. Geophys.*, *5*, 99-136, 1949.

Newell, A. J., and R. T. Merrill, Single-domain critical sizes for coercivity and remanence, *J. Geophys. Res.*, *104*, 617-628, 1999.

Schmidbauer, E. and N. Schembra, Magnetic hysteresis properties and anhysteretic remanent magnetization of spherical Fe_3O_4 particles in the grain size range 60-160 nm, *Phys. Earth Planet. Inter.*, *46*, 77-83, 1987.

Schmidbauer, E. and R. Keller, Magnetic hysteresis properties and rotational hysteresis of Fe_3O_4 and γ-Fe_2O_3 particles ~250 nm in diameter, *J. Mag. Magnet. Mat.*, *152*, 99-108, 1996.

Sparks, N. C. H., S. Mann, D. A. Bazylinski, D. R. Lovley, H. W. Jannasch and R. B. Frankel, Structure and morphology of magnetite anaerobically-produced by a marine magnetotactic bacterium and a dissimilatory iron-reducing bacterium, *Earth Planet. Sci. Lett.*, *98*, 14-22, 1990.

Stacey, F. D. and S. K. Banerjee, *The physical principles of rock magnetism*, Elsevier, Amsterdam, 1974, 195 pp.

Stoner, E. C. and E. P. Wohlfarth, A mechanism of magnetic hysteresis in heterogeneous alloys, *Phil. Trans. Roy. Soc. London, A240*, 599-642, 1948.

Sugiura, N., ARM, TRM, and magnetic interactions: concentration dependence, *Earth Planet. Sci. Lett.*, *42*, 451-455, 1979.

Tarantola, A., *Inverse problem theory*, Elsevier, Amsterdam, 1987, 613 pp.

Thompson, R., Modelling magnetization data using SIMPLEX, *Phys. Earth Planet. Inter.*, *42*, 113-127, 1986.

Thompson, R., Modelling magnetization data using SIMPLEX, *Phys. Earth Planet. Inter.*, *42*, 113-127, 1986.

Verosub, K. L. and A. P. Roberts, Environmental magnetism: past, present and future, *J. Geophys. Res.*, *100*, 2175-2192, 1995.

Worm, H. U. and M. Jackson, The superparamagnetism of Yucca Mountain Tuff, *J. Geophys. Res.*, *104*, 25415-25425, 1999.

Yamazaki, T. and H. Kawahata, Organic carbon flux controls the morphology of magnetofossils in marine sediments, *Geology*, *26*, 1064-1066, 1998.

Yu, L. and F. Oldfield, A multivariate mixing model for identifying sediement source from magnetic measurements, *Quaternary Research, 32*, 168-181, 1989.

Yu, Y., D. J. Dunlop and Ö. Özdemir, Partial anhysteretic remanent magnetization in magnetite, 1: Additivity, *J. Geophys. Res., 107*, 2244, doi 10.1029/2001JB001249, 2002.

Appendix

Calculation of the switching field distribution.

The switching field distribution is given by:

$$m(H_{sw}) = \int_0^\infty s(H_{sw}/H_K)\, k(H_K)\, \mathrm{d}H_K \tag{A1}$$

With the variable transformation $h_K = \log H_K$, (A1) is given by:

$$m(H_{sw}) = \int_0^\infty s(H_{sw}/10^{h_K})\, \overline{k}(h_K)\, \mathrm{d}h_K \tag{A2}$$

By definition, $\overline{n}(h_{sw}) = n(10^{h_{sw}})10^{h_{sw}} \ln 10$, and

$$m(H_{sw}) = \int_{-\infty}^\infty 10^{h_{sw}} \ln 10\, s(10^{h_{sw}-h_K})\, \overline{k}(h_K)\, \mathrm{d}h_K \tag{A3}$$

With $\overline{s}(h) = s(10^h)10^h \ln 10$ equation (4) is obtained. The switching field of a Stoner-Wohlfarth particle is given by:

$$\overline{H}_{sw} = \frac{H_{sw}}{H_K} = \frac{(1 - t^2 + t^4)^{1/2}}{1 + t^2},\ t = \tan^{1/3}\varphi \tag{A4}$$

where φ is the angle between the applied field and the easy axis of the particle [*Stoner and Wohlfarth*, 1948]. The probability density function for the orientation φ of randomly oriented particles is given by:

$$f(\varphi) = \sin 2\varphi = \frac{2t^3}{1 + t^6} \tag{A5}$$

and the switching field distribution by:

$$n(H_{sw}) = f(\varphi(H_{sw}))\left|\frac{\mathrm{d}\varphi}{\mathrm{d}H_{sw}}\right| \tag{A6}$$

Inserting the derivative of (A4) with respect to t in (A6) gives:

$$n(\bar{H}_{sw}) = \frac{4t^4(1+t^2)^2(1-t^2+t^4)^{1/2}}{(1-t^2)(1+t^6)^2} \tag{A7}$$

Equation (5) is obtained from (A7) with $\bar{h}_{sw} = \log \bar{H}_{sw}$, $u = t^2$ and the solution of (A4) with respect to t.

Calculation of the coercivity distribution

Consider the probability density function $f(x,y)$ of the two random variables X and Y. A third variable is given by $Z = g(X,Y)$. The probability density function f_Z of Z is given by:

$$f_Z(z) = \int_X \left. \frac{f(x,y)}{|g_y(x,y)|} \right|_{g(x,y)=z} \mathrm{d}x \tag{A8}$$

where $g_y(x,y)$ is the derivative of $g(x,y)$ with respect to y. In our case $f(x,y)$ is given by $\bar{p}(h_K,d)$, and $g(x,y)$ by:

$$h_{cr}(h_K,d) = \log[H_{sw} - H_q(h_K,d)] \tag{A9}$$

The derivative of (A9) is:

$$\frac{\partial h_{cr}}{\partial d} = H_{cr}^{-1} D^{-1} \frac{\partial H_q}{\partial D} \tag{A10}$$

and equation (6) is obtained from (A8) and (A10). *Egli and Lowrie* [2002] give following expression for H_q of SD grains:

$$H_q = 0.524 H_K - H_{sw} = 0.801 \left(\frac{k_B T \sqrt{H_K}}{\mu_0 M_s V} \right)^{2/3} \ln^{2/3} \left[\frac{F_0}{1.9\,\alpha \sqrt{\mu_0 H_K}} \left(\frac{k_B T}{M_s V} \right)^{3/2} \right] \tag{A11}$$

where k_B is the Boltzmann constant, T the absolute temperature in K, M_s the saturation magnetization in A/m, V the particle volume in m^3, α the decay rate of the alternating field in T/s, and $F_0 \approx 1.3$ GHz the atomic reorganization frequency. For typical SD magnetite, $5.3 < \ln^{2/3}(...) < 6.8$ in (A11), and an approximation for magnetite at room temperature is given by:

$$\mu_0 H_q \approx 2000 (\mu_0 H_K)^{1/3} D^{-2} \tag{A12}$$

where $\mu_0 H_q$ and $\mu_0 H_K$ are expressed in mT, and D in nm. The derivative of (A12) with respect to D is given by:

$$\left|\frac{\mathrm{d}H_q}{\mathrm{d}D}\right| = \frac{H_q}{D}\left\{2 + 3\ln^{-1}\left[\frac{F_0}{1.9\,\alpha\sqrt{\mu_0 H_K}}\left(\frac{k_B T}{M_s V}\right)^{3/2}\right]\right\} \tag{A13}$$

For typical SD magnetite, $2 + 3\ln^{-1}(\ldots) \approx 2.1$. According to equation (6) and the approximation given by (A12), we obtain:

$$\overline{m}(h_{cr}) = H_{cr} D \int_{\log\frac{H_{cr}+H_q}{0.524}}^{\infty} \frac{\overline{p}(h_K, d)}{2.1 H_K^{-1/3} D^{-1}} \mu(h_K, d) e^{-t/\tau}\Big|_{H_q = 0.524 H_K - H_{cr}} \mathrm{d}h_K \tag{A14}$$

which is equivalent to equation (7).

Seite Leer /
Blank leaf

Chapter 6

Characterization of individual magnetic components by analysis of remanence curves, 3. Bacterial magnetite and natural processes in lakes

This paper has been submitted to *Physics and Chemistry of the Earth.*

Seite Leer /
Blank leaf

" *In the circumference of a circle,*
the beginning and the end are common. "

Heraclitus of Ephesus (535-475 B.C.)

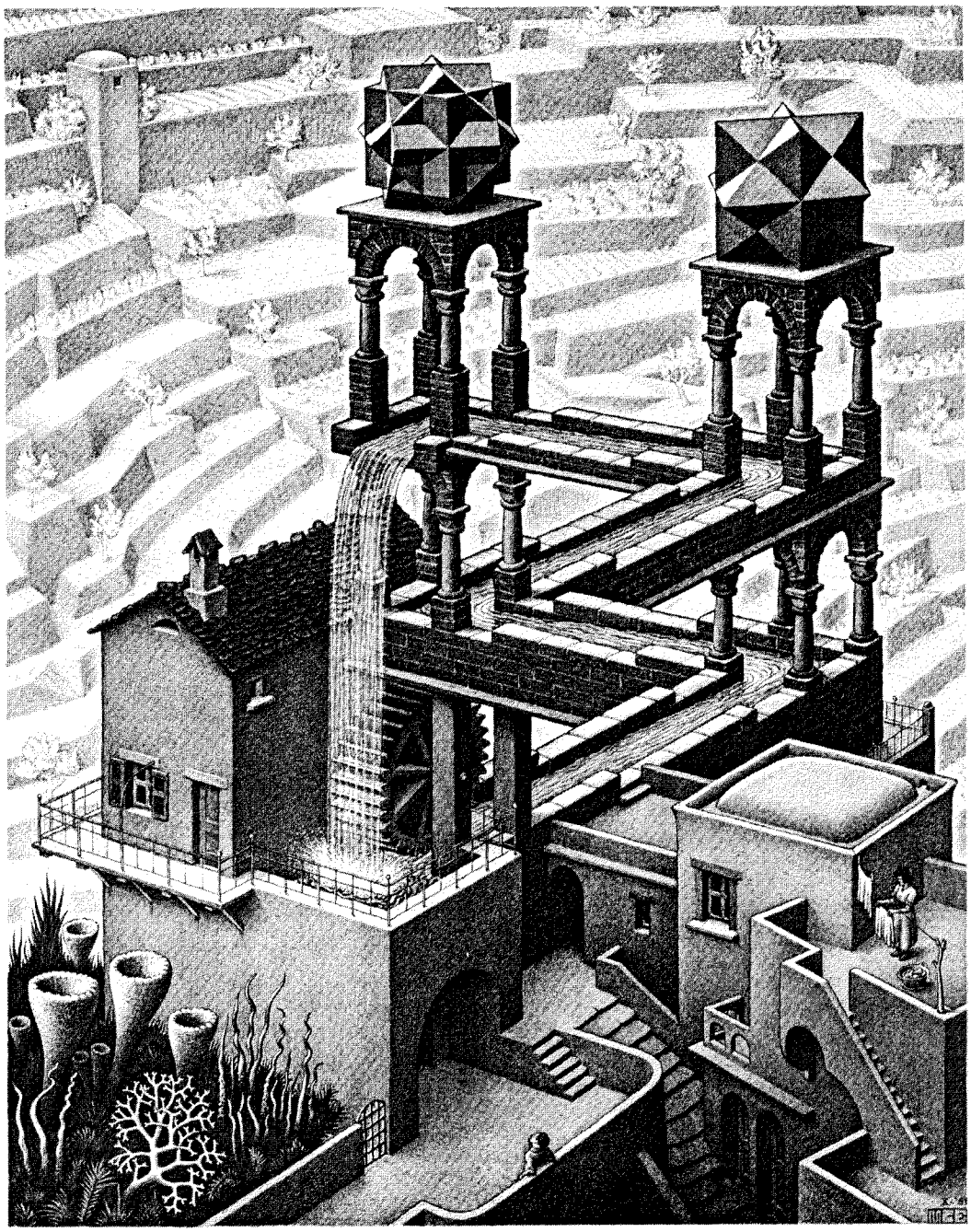

Maurits Cornelis Escher: *Waterfall*, lithography (1961)

Characterization of individual rock magnetic components by analysis of remanence curves, 3. Bacterial magnetite and natural processes in lakes

R. Egli
Institut für Geophysik, ETH Hönggerberg, Zürich, Switzerland

The analysis of magnetization curves with model functions has been proposed independently in several works as a method to unmix and characterize magnetic minerals assemblages in sediments and sedimentary rocks. Unfortunately, a successful result of such analysis relies on time-consuming measurements and on the choice of appropriate model functions. However, once the magnetic properties of individual magnetic components have been determined on a small set of selected samples, a simpler and faster analysis of similar samples is possible. The fast analysis of a large number of samples allows investigation of the effect of natural processes on the properties of single magnetic components. The simplification of the unmixing problem proposed in this paper is based on an iterative linearization procedure, which considers the variability of magnetic components. Any simplification of the unmixing problem is limited by a minimum number of parameters, which are required to fully characterize a magnetic component. It has been shown in *Egli* [2003b] that a combination of four parameters, so-called magnetic fingerprints, is sufficient for a complete characterization of the remanent magnetization of a component. The usefulness of magnetic fingerprints in tracking natural processes is demonstrated exemplarily for lake sediments. The response of Baldeggersee (Switzerland) to environmental changes has been investigated, with special regard to the role of bacterial magnetite in the iron cycle and its possible use as a sensitive paleoredox indicator. The relation between the magnetic properties of lake sediments on one hand, and climatic, tectonic- and human-driven environmental changes on the other, is strongly non-linear. Therefore, a classic correlation between so-called magnetic proxies and environmental signals should be considered with care.

KEYWORDS: magnetite, magnetic mixtures, component analysis, biogenic magnetite.

1. Introduction

Several magnetic components occur simultaneously in natural sediments, and form multi-component mixtures that are difficult to characterize using bulk measurements. In *Egli* [2003a], demagnetization curves of anhysteretic and isothermal remanent magnetizations (ARM and IRM) have been analyzed in detail to characterize the magnetic properties of individual magnetic components encountered in various natural sediments and sedimentary rocks. A detailed study of the magnetic properties of individual components, performed in *Egli* [2003b], allows the definition of four parameters, called magnetic fingerprint parameters, which are sufficient to fully characterize the remanent magnetization of a component. The fingerprint parameters are: (1) the ratio k_{ARM}/IRM of the susceptibility of ARM to the IRM, (2) the median destructive field of the ARM, MDF_{ARM}, (3) the dispersion parameter of the ARM coercivity distribution DP_{ARM}, (4) The difference ΔMDF between the MDFs of ARM and IRM. These parameters characterize fully the coercivity distributions of ARM and IRM.

The variability of the magnetic parameters that describe a component is an important limiting factor to be considered in multi-component mixing models [*Dearing*, 1999]. However, the problem of unmixing magnetic components using magnetization curves can be simplified if the properties of the components and their variability are known in advance. The solution of the simplified unmixing problem relies on a small number of unknown parameters and comes out with simple measurements. It can therefore be used for the systematic investigation of a large number of samples that contain a certain number of known components in variable amounts. A simple example of such simplified unmixing problem is given by the so-called *S* ratio, which is the ratio of an IRM imparted at 300 mT to the saturation IRM [*Thompson and Oldfield*, 1986]. The *S* ratio is considered an indicator of the amount of low-coercivity minerals, such as magnetite, and can be regarded as a particular solution of the simplified unmixing problem discussed in this work.

The systematic component analysis of a large number of samples is a valuable tool for the investigation of natural processes, and is of fundamental importance for the calibration of so-called magnetic proxies. Magnetic proxies calculated from bulk measurements have been used to establish a relation between sediment magnetism on one side, and environmental changes [*Hunt*, 1986; *Heller et al.*, 1993; *Geiss and Banerjee*, 1997; *Hesse*, 1997; *Hu et al.*, 2001; *Snowball et al.*, 2002] and human impact [*Oldfield et al.*, 1985; *Muxworthy et al.*, 2001; *Hanesch and Scholger*, 2002] on the other. The interpretation of magnetic proxies is sometimes ambiguous, because different magnetic particle assemblages may be characterized by the same bulk properties [*Lanci and Kent*, 2003], and some earlier works have been revised recently [*Dearing*, 1999].

An example of systematic component analysis on lake sediment samples is discussed in the present work. This analysis points out the strongly non-linear relation between the occurrence

of individual magnetic components in lake sediments and environmental conditions. Recent developments in environmental sciences describe many natural ecosystems, like lakes, oceans and deserts, which are characterized by a non-linear response to gradual climate changes [*Scheffer et al.*, 2001]. These systems switch abruptly between different stable states, a behavior that is also reflected in the magnetic properties of sediments.

2. Simplified component analysis

The method of analyzing demagnetization curves described in *Egli* [2003a] requires time-consuming detailed measurements and complex data processing. It is therefore rather impractical for a systematic analysis of a large number of samples. However, if the magnetic properties of all components of a group of similar samples are known, simpler measurements can be used to solve the unmixing problem and estimate the magnetic contribution of each component. In the following, a suitable linearization of the unmixing problem is developed and tested on samples of atmospheric particulate matter, which are a binary mixture of two components with fixed magnetic properties [*Egli*, 2003a]. A more complex example of linearized component analysis is tested on lake sediments, which are a mixture of four components [*Egli*, 2003a]. Some of the magnetic properties of these components depend on the redox state of the lake. In this case, an iterative approach is used to characterize the components and obtain an estimate of their contribution to the total magnetization with fast measurements.

2.1. Linearization the component analysis

The coercivity distribution of a mixture of N non-interacting magnetic components is given by:

$$m(H) = \sum_{i=1}^{N} c_i m_i(H) \tag{1}$$

where c_i is the magnetic contribution of component i and $m_i(H)$ its coercivity distribution. If the magnetic parameters of $m_i(H)$ are known, (1) becomes a linear equation with the unknowns c_i. To solve this equation, N values of $m(H)$ should be known. Since $m(H)$ is not directly measurable, equation (1) is integrated to obtain the magnetization of the mixture as a function of the magnetizing or demagnetizing field H. Let define N coercivity intervals $[H_k^-, H_k^+]$, $1 \le k \le N$, delimited by a set of fields H_k^- and H_k^+. The magnetic contribution of all components to the magnetization ΔM_k of the k-th interval is given by:

$$\Delta M_k = M(H_k^-) - M(H_k^+) = \sum_{i=1}^{N} c_i A_{ki} \quad , A_{ki} = \int_{H_k^-}^{H_k^+} m_i(H)\,\mathrm{d}H \tag{2}$$

$M(H)$ being the acquisition or demagnetization curve (Figure 1a). Equation (2) can be written with matrix notation:

$$\Delta \boldsymbol{M} = \mathbf{A}\boldsymbol{c} \quad ,$$
$$\Delta \boldsymbol{M} = (\Delta M_1, \cdots, \Delta M_N), \quad \boldsymbol{c} = (c_1, \cdots, c_N) \tag{3}$$
$$\mathbf{A} = \begin{pmatrix} A_{11} & \cdots & A_{1N} \\ \vdots & \ddots & \vdots \\ A_{N1} & \cdots & A_{NN} \end{pmatrix}$$

and has the following general solution:

$$\boldsymbol{c} = \mathbf{A}^{-1}\Delta \boldsymbol{M} \tag{4}$$

with $\mathbf{A}^{-1}$ being the inverse of $\mathbf{A}$. Theoretically, N measurements of an acquisition or demagnetization curve, obtained by setting $H_k^+ = H_{k+1}^-$, are sufficient to calculate $\Delta \boldsymbol{M}$ and solve equation (4). However, the choice of the coercivity intervals is not free, and has a great influence on the sensitivity of equation (4) to the error sources. The error sources are given by: (1) measurement errors $\delta M(H)$, and (2) deviations $\delta m_i(H)$ of the real coercivity distribution of a component from its model $m_i(H)$, called model error in the following. Model errors arise from a residual variability of the individual components, which is not taken into consideration by $m_i(H)$.

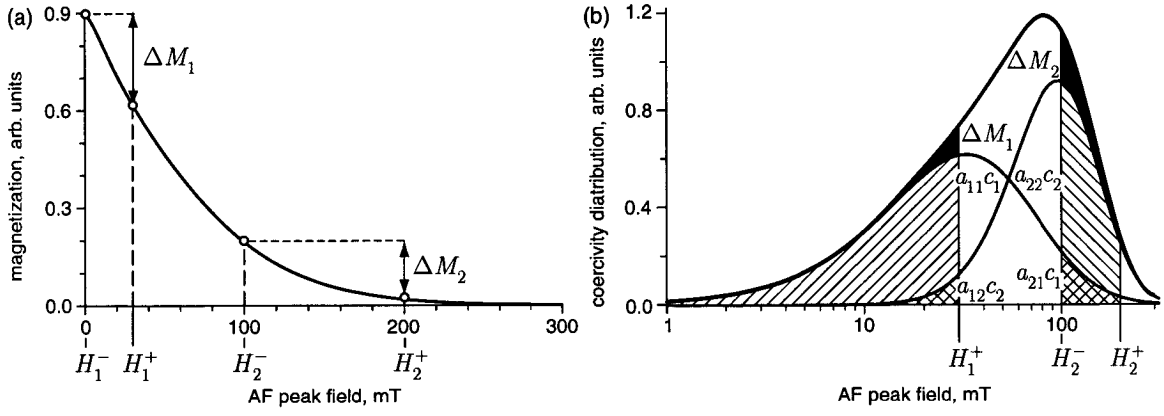

Figure 1. *Definition of the coercivity intervals for a linearized component analysis. The example of this figure is based on the AF demagnetisation curve of a sample of atmospheric particulate matter (sample WDK, see Egli [2003a]) (a) The demagnetization curve is measured on few selected points (dots), which correspond to AF peak fields $H_k^{+,-}$. (b) The fields $H_k^{+,-}$ define the k-th coercivity intervals $[H_k^-, H_k^+]$ and the contributions $a_{ki}c_i$ of i-th magnetic component to this interval (dashed regions). The total magnetization ΔM_k of the k-th coercivity interval (black regions) corresponds to the difference between consecutive points of the demagnetisation curve (a).*

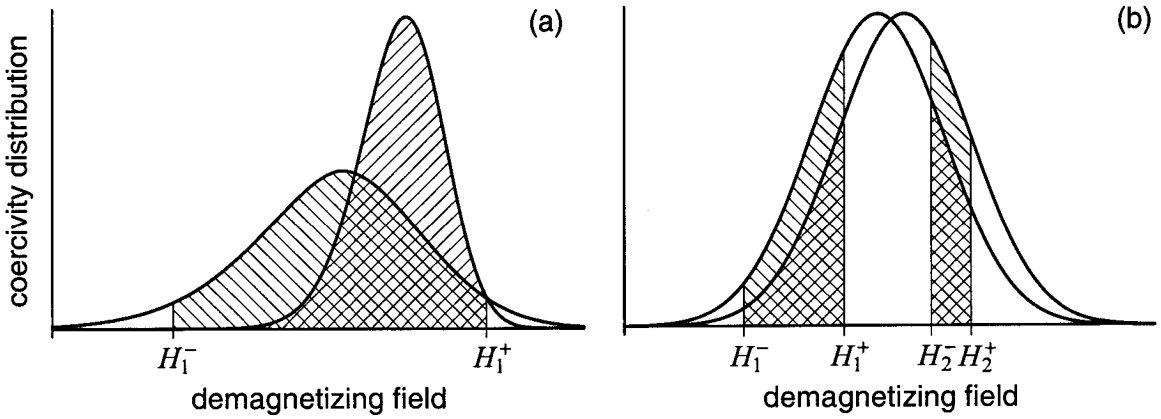

Figure 2. *Two cases where the coercivity intervals are not selective to individual components, and give a solution of the linearized component analysis which is very sensitive to measurement errors and to the choice of the model functions. (a) A coercivity interval, which is wider than the DP of the distributions is 'blind', because it defines similar contributions of all normalized components. (b) Two widely overlapping distributions define similar contributions in all coercivity intervals. Unlike (a), the resulting unmixing problem is intrinsically badly conditioned, regardless of the coercivity intervals chosen.*

A bad choice of the coercivity intervals (Figure 2a), as well as widely overlapped coericivty distributions (Figure 2b), defines a matrix $\mathbf{A}$ whose coefficients A_{ki} have all similar values. In the following, the effect of the two error sources is considered, when equation (4) is solved for a matrix of similar coefficients $A_{ki} = A(1 + a_{ki})$, with $|a_{ki}| < a \ll 1$. Let ε be the maximum measurement error, or the maximum error of the coefficients A_{ki}. Since $\mathbf{A}^{-1}$ is inversely proportional to the determinant $\det \mathbf{A}$ of the matrix, and since $\det \mathbf{A} \propto a^{N-1}$, the following error estimation is obtained:

$$\delta m \propto \frac{\varepsilon}{a^{N-1}} \tag{5}$$

For example, with $N = 3$ and $a = 0.2$, the error sources are enhanced by a factor 25. Equation (5) demonstrates the importance of choosing the coercivity intervals so that each interval is focussed mainly on the contribution of one component. In the ideal case, $\mathbf{A}$ has a nearly diagonal form, with $A_{ki} \ll A_{kk}$ if $k \neq i$.

In the following, the linearization of component analysis is discussed on the example of ARM measurements of atmospheric particulate matter samples, described in *Egli* [2003a]. These samples contain variable amounts of two magnetic components (ED and UP) with fixed magnetic properties (Table 1), and represent an ideal situation for testing the choice of optimal coercivity intervals. The high-coercivity component UP is related to the exposure of the sampling site to motor vehicles emissions, and has therefore been identified with the magnetic signal of urban pollution sources.

Table 1: *Results of a complete component analysis performed with two maximum entropy SGG functions after Egli [2003b] on coercivity distributions of atmospheric PM measured by Egli [2003a].*

sample	k_{ARM}	Component ED				Component UP				linearized	
	$\mu m^3/kg$	c_1	μ_1	σ_1	q_1	c_2	μ_2	σ_2	q_2	c_1	c_2
CHM	5.00	4.447	*1.525*	*0.511*	*0.591*	0.584	*1.808*	*0.208*	*0.998*	4.14	0.55
GMA	6.50	5.890	1.520	0.511	0.581	0.660	1.965	0.235	0.659	5.54	1.00
KSN	5.96	4.175	1.514	0.507	0.647	1.828	1.934	0.261	0.625	4.09	1.98
WDK	18.27	10.546	1.461	0.470	0.607	7.789	1.958	0.235	0.694	11.23	7.37
GUB	17.21	8.619	1.461	0.420	0.647	8.586	1.948	0.230	0.712	8.91	7.85
mean			**1.489**	**0.477**	**0.621**		**1.951**	**0.240**	**0.672**		
sd			**0.032**	**0.042**	**0.032**		**0.012**	**0.014**	**0.039**		

On the other hand, the low-coercivity component ED is dominant in the samples collected far from eventual pollution sources, and its magnetic properties are similar to those of unweathered loess [*Egli*, 2003a]. Therefore, this component is identified with wind-blown mineral dust.

The two coercivity intervals to be determined are given by $[H_1^-, H_2^+]$ and $[H_2^-, H_2^+]$. The relative magnetic contribution of component ED is large at small fields, therefore $H_1^- = 0$ is chosen. Component UP is predominant at large fields, and H_2^+ can be as large as the saturation field. The maximum available AF field for ARM experiments was 300 mT, and $H_2^+ = 200$ mT has been chosen because truncation effects may affect the coercivity distribution just below the field used to impart a magnetization [*Kruiver et al.* 2001]. In order to optimize the choice of H_1^+ and H_2^-, a classical error propagation calculation has been performed for different combinations of H_1^+ and H_2^-. An average value of 0.2% has been assumed for δM_i from empirical determinations of the measurement errors. The δA_{ki} have been calculated from the standard deviation (sd) of the mean parameters of each component, reported in Table 1. Results of this error calculation are shown in Figure 3. Accordingly, $H_1^+ = 20$ mT and $H_2^- = 100$ mT have been chosen, because the error of the linearized component analysis is minimal for these values. With the coercivity intervals defined by $[0,20]$ mT and $[100,200]$ mT, equation (4) can be solved to obtain the contributions of ED and UP to the ARM, with:

$$\mathbf{A}^{-1} = \begin{pmatrix} +2.983 & -0.075 \\ -0.643 & +2.729 \end{pmatrix} \tag{6}$$

A good agreement is found between the results of the complete component analysis after *Egli* [2003b] and the linearized approximation with (4) and (6) (Table 1 and Figure 3).

Unrealistic negative values for the c_i's may result from unmixing highly overlapped or weakly magnetized components with equation (4).

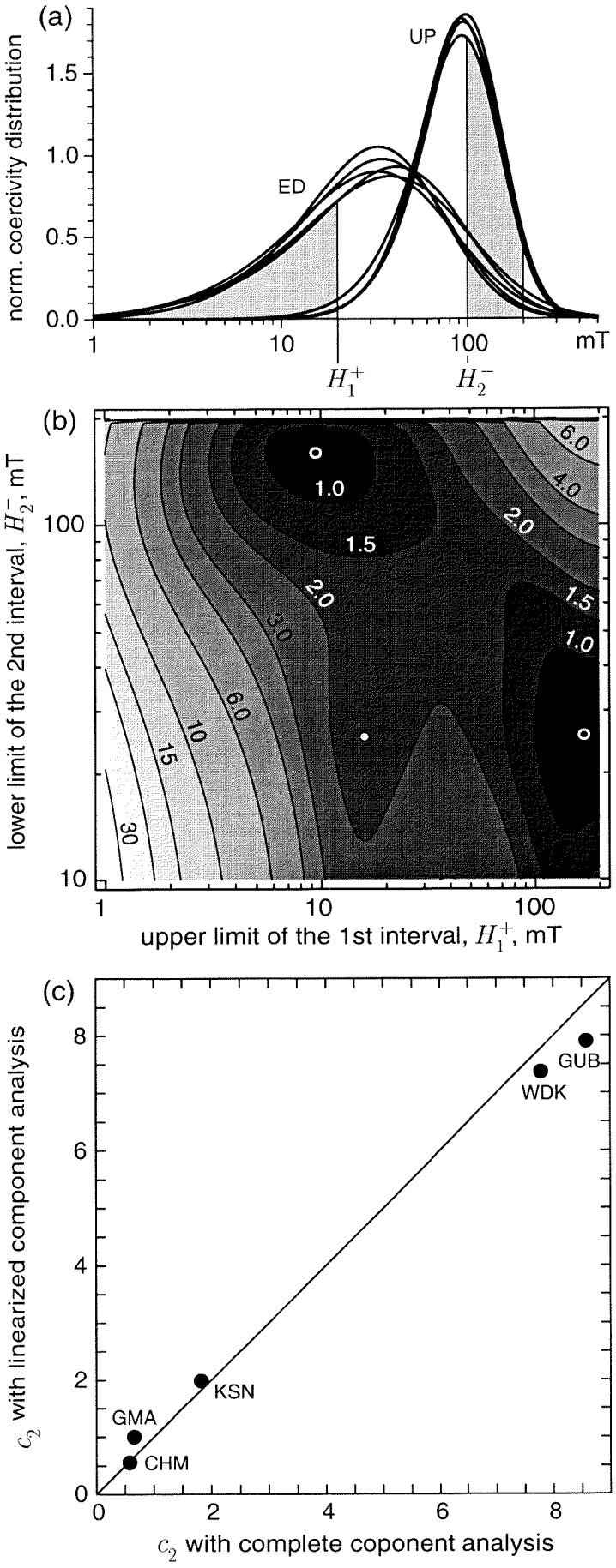

Figure 3. *Example of linearized component analysis on samples of atmospheric particulate matter. (a) A detailed component analysis performed after Egli [2003b] allowed the identification of two magnetic components, labelled with ED and UP. The coercivity distributions of these components are similar in all samples, and the small differences are random. The magnetic contribution of the coercivity intervals used for a linearized component analysis is marked in grey. (b) Simple error propagation laws have been used to calculate the effect of measurement and model errors on the estimation of the magnetic contribution of component UP with a linearized component analysis. A relative measurement error of* 0.2% *has been deduced from multiple measurements. Model errors have been estimated from the standard deviation of the parameters of each component (Table 1). The standard error of the estimated magnetic contribution of UP, expressed in %, has been plotted as a function of the upper and the lower limit of the first and the second coercivity interval, respectively. Local minima of the error are highlighted by circles. (c) Comparison between the magnetic contribution* c_2 *of component UP, estimated with a complete component analysis reported in Table 1 and with the linearized component analysis described in this paper.*

The superposition of a positive and a negative component with highly overlapping coercivities is formally equivalent to a single component with a variable shape, which includes the model errors $\delta m_i(H)$. The effect of model errors $\delta m_i(H)$ cannot be removed with a linearized component analysis. A method to deal with the natural variability of the magnetic components is discussed in the following section.

2.2. Iterative linearization of component analysis

The linearization of the unmixing problem relies on the knowledge of the coercivity distributions of all components. These can be determined with a detailed analysis of the (de)magnetization curves of some selected samples. In the simplest case, a group of samples with a common geological history is expected to contain a mixture of the same components with fixed magnetic properties. Examples are given by dust or soil samples from the same region, or sediment samples within the same sedimentary column. In this case, the scatter of the real coercivity distributions with respect to the model functions is a possible error source, which will introduce some random 'noise' in the result of the unmixing problem. However, the use of magnetic components with fixed properties is not always justified, as it has been shown by *Egli* [2003a] with lake sediments. The effect of natural processes on the magnetic properties of one or more components has to be considered in this case. The major variability of lake sediment components is observed on the ratio of the ARM susceptibility to the IRM, k_{ARM}/IRM, which is particularly sensitive to the redox potential. Variations of this parameter do not affect a linearized component analysis, since the shape of the coercivity distributions is not directly concerned. Nevertheless, other magnetic properties, such as the median destructive field, MDF, are weakly dependent on the redox state of the sediment, and on the lake productivity. This is especially true for those magnetic components, which are formed by groups of particles with a different origin that could not be resolved as individual components. In this case, changes of MDF and dispersion parameter (DP) arise from variations of the relative amounts of the two groups of particles with slightly different magnetic properties. The magnetic contributions c_i are the only variables of the linearized component analysis. Their ratios $r_i = (k_{\mathrm{ARM}}/IRM)_i$ can be used as an indicator for natural processes that affect other parameters, such as the MDF or the DP, which are fixed in the linearized component analysis. The relation between r_i and the fixed parameters can be investigated with the help of a detailed component analysis performed on selected samples, as shown in *Egli* [2003a].

The variability of the components considered for the unmixing problem can be taken into account with the following iterative approach. Let us assume that the model functions $m_i(H)$ have a well-known dependence on r_i, which is taken into account by replacing $m_i(H)$ with $m_i(H, r_i)$ in equation (1). The linearized component analysis described in section 2.1 is first performed with initial values $r_{0,i}$ of r_i, which are known from a detailed analysis of ARM and IRM coercivity distributions of selected samples. The resulting solution can be used to

calculate new values $r_{1,i}$ of r_i, which define better model functions $m_i(H, r_{1,i})$. These functions are used in the next step and so on. The j-th iterative solution is then given by:

$$\boldsymbol{c}_j = \mathbf{A}^{-1}(\boldsymbol{r}_{j-1})\,\Delta\boldsymbol{M} \tag{7}$$

If the dependence of $m_i(H, r_i)$ on r_i is not too strong, (7) converges to the true solution after few iteration steps.

3. An example of iterative linearization of component analysis on lake sediments

In the following, an example of iterative linearization of component analysis is discussed. This example is based on the systematic measurement of all samples of core G from Baldeggersee, which is described in *Egli* [2003a].

Figure 4 shows the choice of the coercivity intervals and the model functions for the four components identified in *Egli* [2003a]: D+EX (detrital and extracellular magnetite), BS (magnetosomes with $MDF_{\mathrm{ARM}} \approx 45$ mT), BH (magnetosomes with $MDF_{\mathrm{ARM}} \approx 73$ mT) and H (high-coercivity minerals, such as hematite). The four coercivity intervals require the measurement of seven demagnetization steps for both the ARM and the IRM. These steps have been chosen as follows: 0, 14, 35, 55, 100, 130 and 160 mT for the ARM, and 0, 12, 30, 50, 90, 130 and 160 mT for the IRM (Figure 4a), according to the criteria discussed in section 2.1 to maximize the contribution of a single component in each coercivity interval. Using a 2G cryogenic magnetometer, the magnetization and the stepwise demagnetization of both ARM and IRM requires 24 min for each sample, and 20 samples can be measured during a working day.

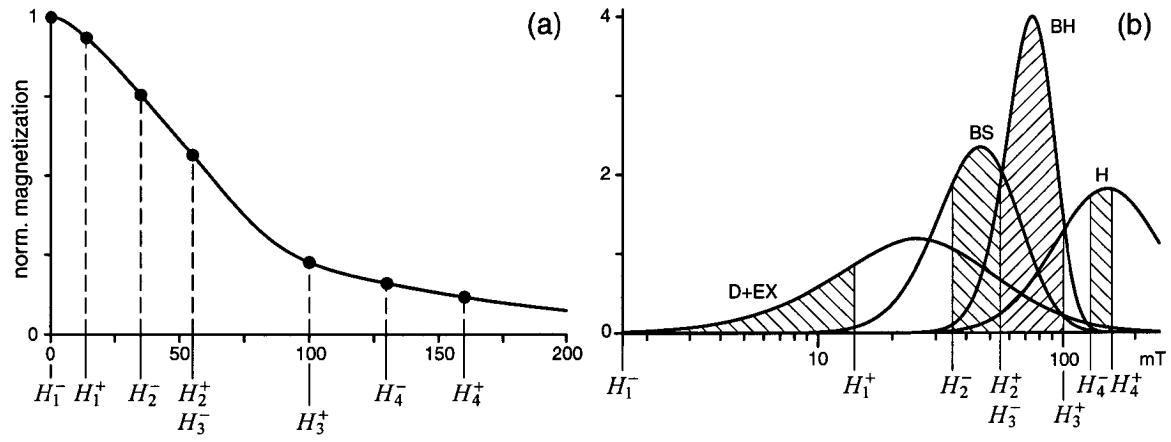

Figure 4. *Definition of the coercivity intervals for the iterative linearized component analysis of lake sediments. Each coercivity interval (a) has been chosen to focus mainly on the contribution of one component. Labels D+EX, BS, BH and H refer to the magnetic components individuated in lake sediments by Egli [2003a].*

Table 2. *Relation between some magnetic parameters and the ARM ratios r_D und r_B for the magnetic components found in lake sediments. D+EX is the contribution of detrital and extracellular magnetite, which cannot be modeled as individual components because of their highly overlapped coercivity distributions. BS and BH are two contributions of different magnetosomes, and H is the contribution of a high coercivity mineral, probably hematite. These components have been analyzed in Egli [2003a], and n is the number of lake sediment samples analyzed to characterize these components. Correlation coefficients are given in the right column for each component except H, for which fixed parameters have been chosen. Bold numbers indicate correlations coefficients, which are significant at a 90% confidence level.*

	D+EX, $n = 28$		**BS**, $n = 22$		**BH**, $n = 22$		H
μ_{ARM}	$1.026 - 0.289 \log r_D$	**0.85**	$1.654 + 0.016 \log r_B$	**0.36**	$1.875 + 0.025 \log r_B$	**0.42**	2.18
μ_{IRM}	$0.994 - 0.264 \log r_D$	**0.58**	$1.618 + 0.0022 \log r_B$	0.02	$1.818 + 0.002 \log r_B$	0.00	2.15
σ_{ARM}	$0.328 - 0.0064 \log r_D$	0.11	$0.151 - 0.0436 \log r_B$	**0.72**	$0.100 - 0.013 \log r_B$	**0.42**	0.22
σ_{IRM}	$0.372 - 0.0002 \log r_D$	0.00	$0.198 - 0.0069 \log r_B$	0.14	$0.133 - 0.0028 \log r_B$	0.06	0.22
q_{ARM}	$0.79 + 0.035 \log r_D$	0.10	$0.74 + 0.024 \log r_B$	0.21	$0.54 - 0.20 \log r_B$	**0.74**	1
q_{IRM}	$0.70 + 0.012 \log r_D$	0.06	$0.75 + 0.043 \log r_B$	0.34	$0.72 - 0.064 \log r_B$	0.23	1

Empirical relations between

$$r_D = ARM_{D+EX,0.1\ mT} / IRM_{D+EX}$$
$$r_B = (ARM_{BS} + ARM_{BH})_{0.1\ mT} / (IRM_{BS} + IRM_{BH}) \quad (8)$$

and the other parameters can be obtained from the measurements of *Egli* [2003a], and are listed in Table 2 together with the correlation coefficients ρ. The most significant correlations have been found between MDF and ARM ratio (Figure 5). The generally small values of ρ show the weak variability of most magnetic properties of individual components. A major exception is represented by component D+EX, which is a binary mixture of detrital particles, supposed to be almost constant in all samples, and extracellular magnetite. The abundance of extracellular magnetite depends on the productivity of the lake and the redox potential. An iterative linearization of the component analysis according to section 2.2 has been performed with equations (7) and (8). Five iterations were sufficient to approach a stable solution. The results are shown in Figure 6. Well-defined trends reflecting the onset of anoxic conditions demonstrate the reliability of the performed analysis. These results are discussed in the following section.

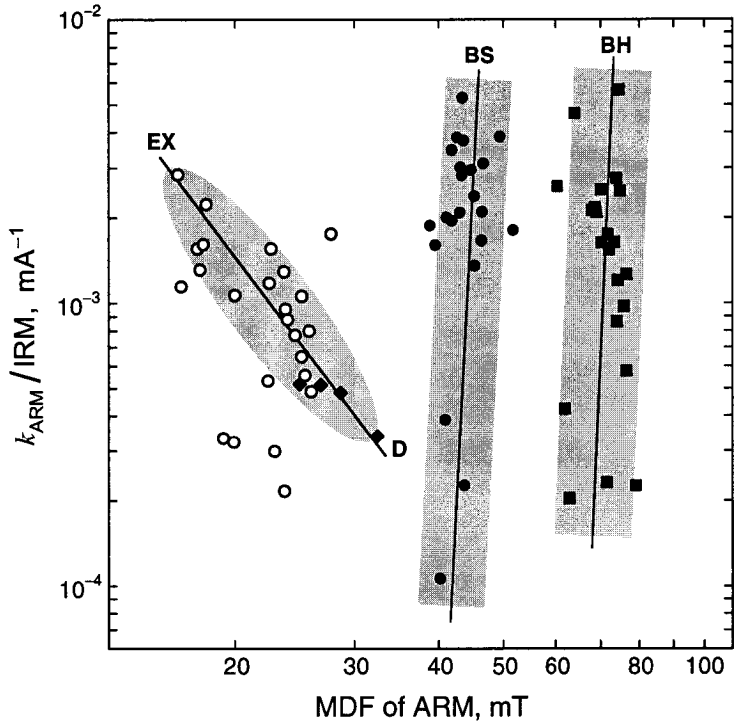

Figure 5. *Summary of the magnetic properties of ARM and IRM for all iron spinel components identified in lake sediments after Egli [2003b]. The magnetic components (symbols) group clearly into different clusters, indicated by grey ellipses and rectangles, whose extension is equal to four times the standard deviation of the scattered magnetic properties of the components in each cluster. All components are classified into low-coercivity magnetosomes (biogenic soft, BS: dots), high-coercivity magnetosomes (biogenic hard, BH: squares), ultrafine extracellular magnetite (EX: circles), detrital particles transported in water systems (D: diamonds). Best-fit lines indicate the correlation existing between MDF and ARM ratio. This correlation is particularly evident for the binary mixture of detrital and extracellular magnetite (D+EX), which cannot be resolved with component analysis because of the highly overlapped coercivity distribution.In the case of bacterial magnetite (BS and BH), the correlation depend on reductive dissolution processes that occur in anoxic sediments.*

4. Nonlinearity and redox cycles in lakes: a case study

The fundamental role of chemical and biological processes on the magnetic response of lacustrine and marine sediments to climatic changes has been the object of several studies [*Snowball*, 1993; *Tarduno*, 1994; *Hesse*, 1994; *Geiss and Banerjee*, 1997; *Gruber et al.*, 2000; *Hu et al.*, 2001; *Snowball et al.*, 2002]. Recent studies pointed out that many natural systems, such as lakes, oceans and deserts, are characterized by a strongly nonlinear response to gradual climatic changes [*Manabe and Stouffer*, 2000; *Boyle*, 2000; *deMenocal et al.*, 2000; *Scheffer et al.*, 2001]. Multiple stable states are possible, and natural systems can be characterized by the same stable state under different climatic conditions or by different stable states under the same climatic conditions. Therefore, care should be taken in attempting to establish a correlation between magnetic proxies and climate parameters. Furthermore, the effect of different biogeochemical processes on the magnetic properties of sediments is not always clear. For example, the relation between magnetic mineral reduction and the concentration of superparamagnetic grains has been debated [*Tarduno*, 1995]. The analysis of demagnetization curves described in section 3 is therefore a valuable tool to investigate the effect of biogeochemical processes on the magnetic properties of sediments.

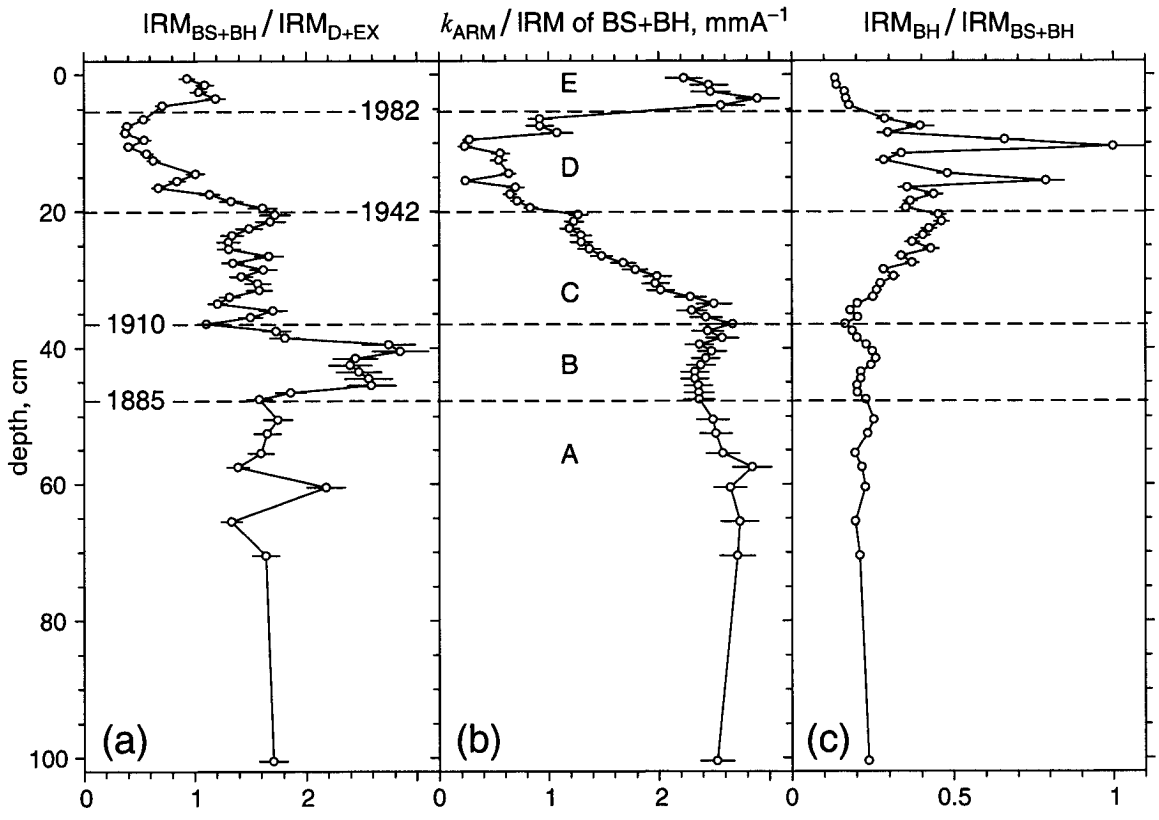

Figure 6. *Downcore results of the iterative component analysis of core G from Baldeggersee. This core is 1 m long and covers an anoxic event produced by human activities around the lake. Approximated dates for some levels in the sediments are highlighted. (a) Relative contribution of the bacterial components to the IRM, (b) ARM ratio for the sum of the two bacterial components, and (c) relative contribution of the bacterial component BH to the total IRM of the bacterial particles. The core can be divided into four main sections. Section A is formed by light grey marls deposited before 1885 during oxic conditions. The magnetic properties are relatively constant and indicate the moderate presence of bacterial magnetite with a large ARM ratio, comparable to that of cultured magnetotactic bacteria. In section B, the abundance of bacterial magnetite increases abruptly, while the ARM ratio decreases slightly. This part of the core is characterized by the alternation of lighter and darker packets of varved sediments. In section C, the abundance of bacterial magnetite is reset to the values prior to 1885. However, the ARM ratio decreases continuously to the half of its initial value, and the relative contribution of BH doubles. The sediments are varved and have a dark brown colour. Section D is composed by fully anoxic, varved sediments. The abundance of bacterial magnetite is reduced to* 20% *of the values prior to 1885 and the ARM ratio dropped by one order of magnitude. The relative contribution of BH increases further and reaches* 100% *of the bioorganic magnetite in some samples. In 1982, an artificial aeration experiment was started to restore the original conditions of the lake. Sediments deposited after this date belong to section E, and are characterized by a tendency toward the properties prior to 1885.*

4.1. Bacterial magnetite

The magnetic properties of some bacterial magnetites obtained from cultured and natural magnetotactic bacteria have been reported in the literature [*Moskowitz et al.*, 1988, 1993; *Penninga et al.*, 1995; *Hanzlik et al.*, 2002]. Coercivities of remanence and MDFs of individual bacterial strains vary between 30 and 80 mT, depending of the morphology of the magnetosomes (equant, prismatic, elongated, rod- and bullet-shaped) and their arrangement in the cells (isolated, in chains, in chain bundles). The reversing mechanism of individual magnetosome chains is different as well: magnetic vibrios do not show intermediate remanence states and behave like a single Stoner-Wohlfarth particle. On the other hand, intermediate remanences are possible in chain bundles and in many-celled magnetotactic prokaryotes, and define a coercivity distribution with $DP \approx 0.043$ (calculated from *Penninga et al.* [1995] and *Hanzlik et al.* [2002]). For macroscopic samples of cultured cells, $DP \approx 0.08 \ldots 0.14$. From these data, variable coercivity distributions are expected for natural samples of bacterial magnetite, since different bacterial strains occur simultaneously in natural sediments. However, the opposite has been observed in lake sediment samples [*Egli,* 2003a] with the occurrence of two distinct groups of bacterial components, BS and BH, characterized by a narrow distribution of coercivites around 45 and 73 mT, and $DP_{\mathrm{ARM}} = 0.174$ and 0.1, respectively. No other bacterial components could be observed in lake sediments. All magnetic properties of the bacterial components, except the ARM ratio, depend weakly on the redox conditions, and remain almost constant even during anoxic events, when small magnetite particles are supposed to undergo reductive dissolution [*Canfield and Berner*, 1987]. In fact, typical corrosion features have been detected on electron microscope observations of natural magnetosomes [*Vali*, 1987; *Vali and Kirschvink*, 1989; *Hilgenfeldt*, 2000], and indirect evidence of magnetite dissolution has been reported by several authors [*Leslie et al.*, 1990a; *Lu and Banerjee*, 1994; *Hilgenfeldt*, 2000]. Magnetite dissolution is also evident in Baldeggersee, as shown in Figure 6 and in *Egli* [2003a].

Micromagnetic models of magnetosome chains predict a dependence of the coercivity of remanence on the distance between the particles and their elongation [*Kuo*, 1988; *Hanzlik et al.*, 2002], but not on their volume. If a magnetosome chain is free to contract during dissolution, the gap between the particles does not increase and the coercivity of remanence remains unchanged. A model for the ARM acquisition in magnetosome chains has not been developed to present. According to classical interaction models [*Wohlfarth*, 1964], the susceptibility of ARM of the positive interacting magnetosome chains should be infinite. However, chains with only two remanent states behave as a single SD particle, and the ARM acquisition may be modeled with thermal activation processes [*Egli and Lowrie*, 2002]. The chain reversal is supposed to nucleate at one end of the chain, where the positive interaction field is only half of that in the center of the chain. Thus, the effective volume to consider for the calculation of the energy barrier is equivalent to the volume of a single magnetosome. According to the thermal activation model of *Egli and Lowrie* [2002], $k_{\mathrm{ARM}}/IRM = 3.7$ mm/A for a

typical magnetosome chain, a value that is very similar to that reported for cultured bacterial magnetite [*Moskowitz et al.*, 1993]. Furthermore $k_{ARM}/IRM \propto d^2$, d being the grain size, and a reduction of d caused by partial dissolution of the magnetosomes is accompanied by a decrease of k_{ARM}/IRM. As shown in Figure 5, the ARM ratio of bacterial magnetite can decrease by up to one order of magnitude. In this case, according to the thermal activation model, the coercivity of remanence of the partially dissolved chains should be only 37% of its initial value, in contradiction with the observed results. The observed decrease of the ARM ratio for partially dissolved bacterial magnetite can be alternatively explained by the possibility of inducing intermediate remanence states even in chains that excluded this possibility under normal conditions. These intermediate states are induced preferentially by the ARM, since they correspond to a global energy minimum, and are characterized by a virtually zero net magnetization. On the other hand, a strong field is still able to induce the maximal remanence, and k_{ARM}/IRM becomes smaller. The corrosion of magnetosome edges and the sediment shrinkage produced by water loss may decrease the elastic stability of a chain. In this case, the chain assumes a 'zig-zag' configuration and possibly collapses [*Shcherbakov et al.*, 1997]. Intermediate remanence states are favored by altered chain configurations. A detailed study on the ARM acquisition in magnetosome chains is necessary to model the change of k_{ARM}/IRM during anoxic conditions.

It is interesting to observe that a similar and less pronounced decrease of the ARM ratio during anoxic conditions is observed for the other magnetite components as well [*Egli*, 2003a], including the relatively coarse-grained detrital magnetite. The dissolution of coarse-grained magnetite should be accompanied by an increase of the ARM ratio, since k_{ARM}/IRM is inversely related to the grain size above 60 nm, but the opposite trend has been observed. Dissolution of the detrital component can be excluded, since it has been measured in the most anoxic sample of Baldeggersee, G010 [*Egli*, 2003a], with the typical parameters that characterize detrital particles in other samples. An alternative explanation for the decrease of k_{ARM}/IRM could be related to the overgrowth of iron sulphides around magnetite particles reported in [*Egli*, 2003a].

The identification of BS and BH with the magnetotactic bacterial strains reported in the literature is not straightforward. Component BH is more resistant against dissolution, at least in Baldeggersee, as shown in Figure 6c. In some anoxic levels, this component accounts for more than 70% of the bacterial particles, compared to 20-30% during normal conditions. It is not clear if this resistance is due to the presence of greigite magnetosomes [*Mann at al.*, 1990; *Penninga et al.*, 1995]. Greigite has similar magnetic properties as magnetite, and undergoes a thermal decomposition between 250 and 350°C [*Roberts*, 1995; *Dekkers and Schoonen*, 1996; *Dekkers at al.*, 2000]. Thus, greigite magnetosomes are expected to have similar coercivity distributions as the magnetite magnetosomes. Greigite could not be identified during thermal demagnetization experiments on lake sediments [*Egli*, 2003a]. In oxic sediments, no significant change in the remanence can be seen at 250-350°C. In the anoxic sediment G010, a

characteristic magnetization peak at 230°C, probably due to hexagonal pyrrhotite, masks the eventual signal of greigite.

A correlation between the abundance of magnetosomes with different morphologies and the IRM has been reported by *Hesse* [1994] in sediments of the Tasman Sea. He found that elongated magnetosomes have been found to be predominant in correspondence of sediment levels with a low IRM, while equant magnetosomes prevail immediately above these levels, where the IRM is maximal. Elongated magnetosomes or chains of elongated magnetosomes are expected to have a large coercivity of remanence if compared with equant or prismatic magnetosomes. *Hanzlik et al.* [2002] calculated a switching field of ≈80 mT for chains of elongated magnetosomes, and ≈40 mT for chains of equant magnetosomes. These values correspond approximatively to the MDFs of BS and BH measured in this paper. Considering that the DP of component BS is 64% larger than that of component BH, it is possible that BS consists of two highly overlapped coercivity distributions, which could not be unmixed. In this case, three magnetic components related to bacterial particles are obtained, which could possibly correspond to the three morphologies reported by *Hesse* [1994]. Equant and prismatic magnetosomes would contribute to component BS, and elongated magnetosomes to component BH. The amount of elongated magnetosomes reported by *Hesse* [1994] ranges form 20% to 80%, and a similar range is found for component BH in Baldeggersee (Figure 6c). From the above discussion, it can be concluded that components BS and BH are related to the morphology of the magnetosomes, rather than to their mineralogy (magnetite or greigite).

4.2. Production and dissolution of bacterial magnetite

The production of magnetosomes by magnetotactic bacteria depends on several geochemical factors, i.e. nutrients (C, N), terminal electron acceptors (NO_3^-), oxygen (O_2) and iron (Fe^{2+}). *Blakemore et al.* [1985] investigated the effect of oxygen and nitrate concentration on the production of bacterial magnetite by *A. Magnetotacticum*. They found that optimum magnetite production occurred under microaerobic conditions ($p_{O2} \approx 1$ kPa), regardless of the nitrate concentration, and that the absence of a terminal electron acceptor other than O_2 reduces the magnetite production by a factor 5. *Snowball* [2002] observed a linear relationship between the total organic carbon content (TOC) and the SIRM of varved lake sediments rich in bacterial magnetite and suggested that the bacterial production of magnetite is controlled primarily by the supply of organic carbon to the sediment. This conclusion is supported by the results of the component analysis reported in *Egli* [2003a]: in late-glacial samples with $TOC < 1\%$ the bacterial magnetite contributes with only 20% to the SIRM, while 75% is reached in samples with higher TOC. Furthermore, a correlation between the abundance of elongated magnetosomes and the organic carbon flux in marine sediments has been observed by *Yamazaki and Kawahata* [1998]. However, TOC is the principal controlling factor for bacterial magnetite production only under oxic and sub-oxic conditions, as it can be observed on core G (Figure 6). This core is characterized by a regular decrease of TOC from 6% at the

top to 2% on the bottom [*Lotter*, 1997], but the abundance of bacterial magnetite is controlled by the onset of anoxic conditions after 1942.

The iron availability depends on the redox potential: the Fe^{3+}/Fe^{2+} redox couple for FeOOH is 0 mV and occurs in the middle of the oxic to anoxic transition zone, OATZ [*Zehnder and Stumm*, 1988]. The iron availability is increased by the ability of magnetotactic bacteria to produce iron-chelating compounds, so-called siderophores, which are capable of dissolving even the most stable iron oxides [*Vali and Kirschvink*, 1989]. Considering that magnetotactic bacteria occur mainly within the OATZ, and that natural sediments are rich in clay minerals and other iron-containing minerals, iron should not be a limiting factor for bacterial magnetite production. With these considerations, the production M_{bio} of bacterial magnetite in the sediment can be modeled with:

$$M_{\text{bio}} = \eta(\text{TOC}, \text{NO}_3^-)\, \varphi(\text{pO}_2) \tag{9}$$

where η is a function of the nutrients and φ is a bell-shaped function of $\text{pO}_2 = -\log[\text{O}_2]$. Magnetite is unstable under reducing conditions, especially in presence of H_2S. *Canfield and Berner* (1987) calculated the following law for the rate of dissolution of magnetite particles:

$$\frac{\text{d}}{\text{d}t}\log[\text{Fe}_3\text{O}_4] = -1.1 \times 10^{-5}\,[\text{S}^{2-}]^{0.5} A \tag{10}$$

where $[\text{Fe}_3\text{O}_4]$ is the concentration of magnetite in grams per gram sediment, $[\text{S}^{2-}]$ is the sulphide concentration in mM and A is the specific surface area of magnetite in cm^2 per gram magnetite. For 1 μm magnetite particles, $A \approx 1000\ \text{cm}^2/\text{g}$, and for typical magnetosomes this value is 150 times higher. Sulphide concentration is regulated by the precipitation of insoluble iron sulphides and measured values should be extrapolated to the past in order to obtain a reliable estimation of the dissolution rate. Deviations from the dissolution rate given in (9) have been observed when $[\text{S}^{2-}] > 1\ \text{mM}$, because a pyrite layer is formed around the magnetite particles, which protect them from further dissolution [*Canfield and Berner*, 1987; *Leslie et al.*, 1990b]. Pyrite formation has not been detected in Baldeggersee (M. Sturm, personal communication); however, indirect evidence of hexagonal pyrrhotite associated to the magnetosomes has been reported in anoxic samples [*Egli*, 2003a]. Therefore, the formation of a protective layer around the magnetosomes during anoxic conditions cannot be excluded. The maximal sulphide concentration in core G is 3.5 μM, in correspondence of the anoxic layers (M. Sturm, personal communication). According to equation (10), a sulphide concentration of 3.5 μM gives a dissolution rate of 0.1/yr and 5.4% of the bacterial magnetite survives after 30 years. For comparison, in the most anoxic part of core G, sedimented in 1972, the bacterial magnetite content is reduced to 30% of the value before 1942 (Figure 6). This discrepancy can only be explained by assuming a lower sulphide concentration in the

past, or by considering the inhibition of the dissolution process produced by a pyrrhotite shell surrounding the magnetosomes.

4.3. Redox cycling in lakes and oceans

A phenomenological model to explain the magnetic properties of marine and lacustrine sediments is shown in Figure 7. Four main stages characterize the response of magnetic minerals to environmental changes. The first stage is characterized by a relatively low concentration of bacterial magnetite in sediments formed under oxic conditions.

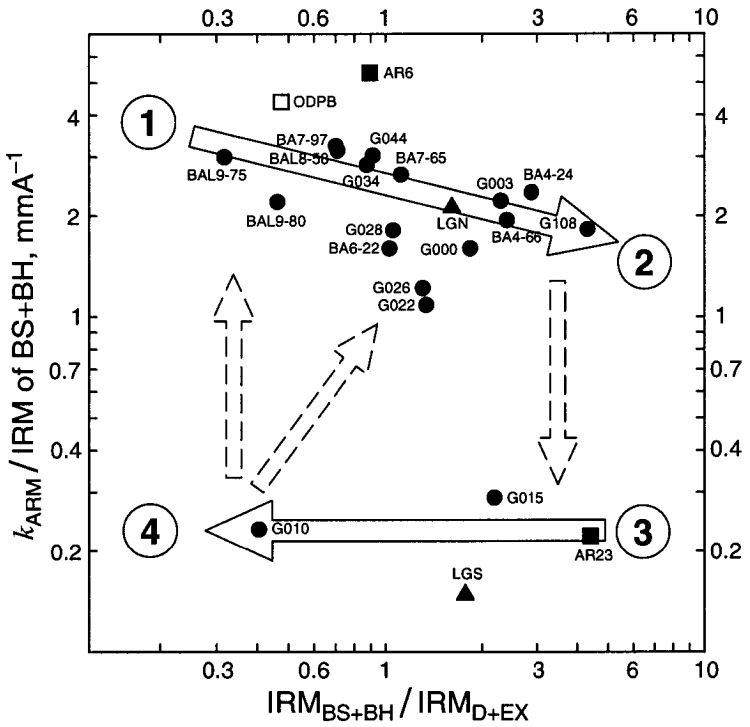

Figure 7. *A phenomenological model for lacustrine and marine sediments. The ratio of the IRM of the bacterial components to the IRM of non-bacterial components is plotted against the total ARM ratio of the bacterial components for samples from lakes and oceans analyzed in Egli [2003a]. Dots are sediments from Baldeggersee, triangles from lake Geneva, squares from the Aral lake, open squares are pelagic sediments. The relative abundance of the bacterial components, plotted along the x-axis, is a measure of the productivity, which is based on the linear relation established between bacterial magnetite and organic carbon content [Snowball et al. 2002]. The ARM ratio gives information about the redox potential in the sediment during and after deposition. Numbers within circles indicate four different states of the sedimentary environment, and arrows indicate environmental changes. In 1 the environment is characterized by low productivity and oxic conditions. When the productivity increases, more bacterial magnetite is produced and the environment becomes sub-oxic (open arrow between 1 and 2). The amount of bacterial magnetite rises to a critical limit, indicated by 2, without significant changes of the ARM ratio. If the productivity exceeds this limit, the sedimentary environment becomes unstable, and local events as a landslide can switch it abruptly to anoxic conditions. Consequently, k_{ARM}/IRM drops by one order of magnitude (dashed arrow between 2 and 3). If the redox potential is further reduced, the fine-grained bacterial magnetite undergoes reductive dissolution, and its concentration decreases (open arrow between 3 and 4). If the productivity is reduced below a critical level or the oxygen supply is increased above a critical level, oxic, respectively sub-oxic conditions are restored (dashed arrows between 4 and 1 or 2).*

At this stage, the production of bacterial magnetite is controlled by the concentration of organic matter, which is in turn related to the productivity of the system. Late Glacial lake sediments belong to this stage. As the productivity is raised by more favorable conditions, the concentration of bacterial magnetite increases. The abundance of organic matter drives the bacterial activity, which is related to oxygen consumption. Since the oxygen supply is limited by the water mixing, deep waters become sub-oxic, and the ARM ratio of bacterial magnetite starts to decrease. These processses can be driven up to a critical productivity level, represented by stage 2. If the productivity exceeds this level, anoxic conditions are set, and the ARM ratio is reduced drastically by one order of magnitude (stage 3). Reductive dissolution of magnetite begins, and the concentration of bacterial magnetite decreases with time, as long as anoxic conditions persist. The formation of a protective iron sulphide layer around the magnetosomes prevents their complete dissolution, and a small amount of bacterial magnetite survives (stage 4). If oxic or sub-oxic conditions are restored, the production of new bacterial magnetite can start, and the cycle is closed.

4.4. Redox cycling in Baldeggersee

The same approach of section 4.3 is used here to discuss the results of core G. A cycle similar to that of Figure 7 is obtained for the last eutrophycation event of Baldeggersee, and is plotted in Figure 8a. The early history of Baldeggersee is characterized by the deposition of Late Glacial sediments with a very low organic matter content. In these sediments, the availibility of organic carbon is the limiting factor for the growth of magnetotactic bacteria. The bacterial magnetite content is very low and accounts for less than 30% of the IRM. During warmer periods, the productivity of the lake rose, more organic carbon was deposited in the sediments and the content of bacterial magnetite became higher (dashed line in Figure 8a). During this stage, the bacterial magnetite content is expected to be proportional to the organic carbon. A slight decrease in k_{ARM}/IRM is observed in the bacterial component, probably related to the increasing percentage of elongated magnetosomes (Figure 8b). Since these particles are produced by magnetotactic bacteria that tolerate less oxygen than those producing equant magnetosomes, a decrease of the redox potential can be inferred. A period of high bacterial magnetite production can be recognized between 1885 and 1910, probably driven by human activities in the catchment area. This period coincides with the abrupt onset of biogenic varves [*Lotter et al.*, 1997], and marks the critical productivity level above which the response of the lake to the environment becomes irreversible. Between 1910 and 1942 the production of bacterial magnetite is apparently reduced to values typical for 1885, while the organic carbon content is still increasing [*Lotter et al.*, 1997]. However, the ARM ratio is now rapidly reduced to <50% of its initial value and indicates the onset of dissolution processes. After 1942, the ARM ratio decreases further, and reaches a minimum value, which is one order of magnitude smaller than for the late-glacial bacterial magnetite.

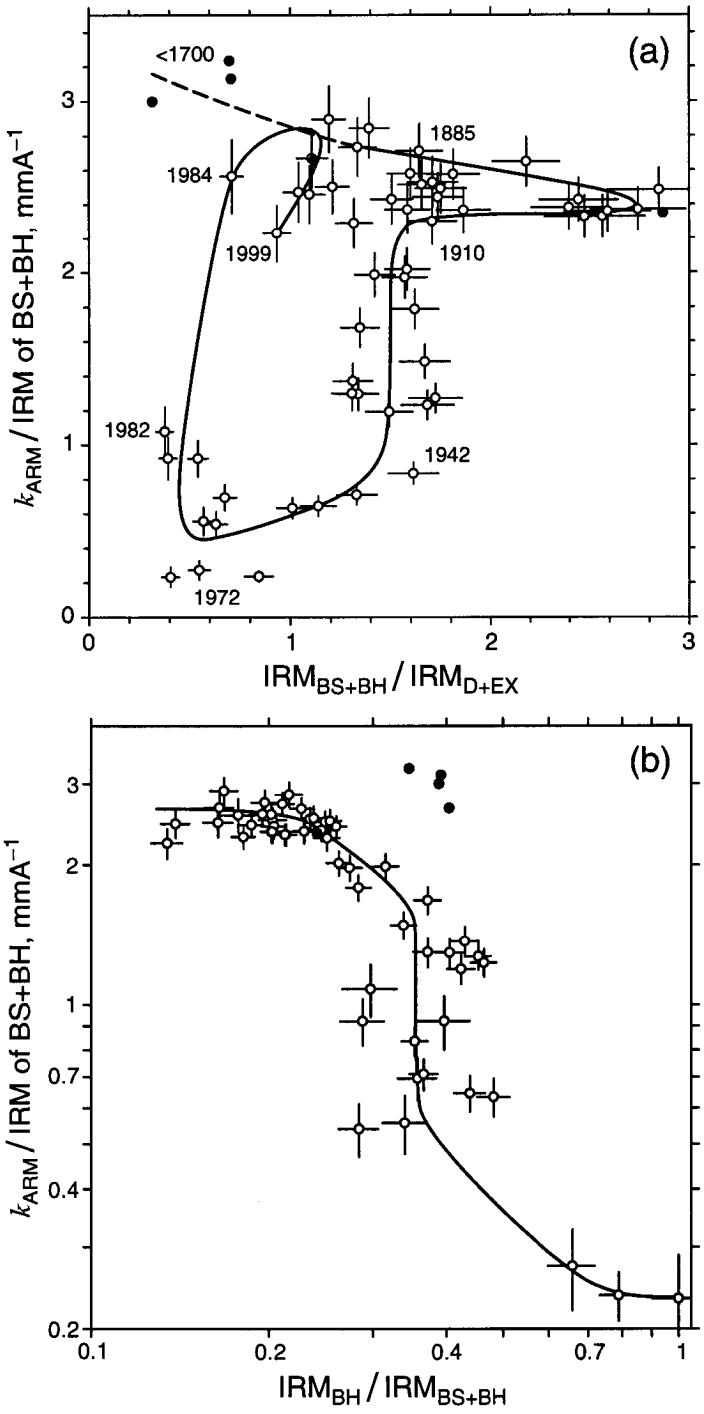

Figure 8. *A phenomenological model for the magnetic properties of the lake sediments of Baldeggersee. Circles are the results of the iterative linearization of the component analysis of core G, dots the results of the complete component analysis reported in Egli [2003a] for some selected samples. (a) The same cycle of Figure 7 is highlighted by the dashed and the solid line. The dashed line refers to sediments taken from other cores of the Baldeggersee. Notice the period of high productivity between 1885 and 1910 (section B in Figure 6), which precedes the onset of anoxic conditions. The open cycle indicates a kind of hysteretic response of the lake to the ambient conditions, which is characteristic for highly non-linear systems [Scheffer et al., 2001]. (b) Relation between the abundance of component BH and the ARM ratio of the bacterial components. Oxic sediments are characterized by a high ARM ratio and less than 30% of component BH. The abrupt change of the ARM ratio indicates the onset of anoxic conditions, accompanied by the dissolution of component BS.*

At this stage, the abundance of bacterial magnetite is drastically reduced as well, and the amount of elongated magnetosomes reaches 100% of the bacterial particles in some samples. The recovering program started in 1982 with the artificial aeration of the water column produced an immediate response of the ARM ratio, which rose to the 'normal' values. On the other hand, the concentration of bacterial magnetite increased only moderately. It is not known if this is because magnetotactic bacteria are still growing in the unconsolidated top of the sediment column. The magnetic contribution of component BH did not increase at all after

1982, as might be expected from magnetosomes produced by bacteria that do not afford high oxygen concentrations. These bacteria may develop later, when the sediment will be covered by a layer of new material, which will limit the oxygen supply. A decreasing trend of the bacterial contribution can be observed since 1982 (Figure 9). This trend coincides with the reduction of the amount of oxygen pumped yearly since the beginning of the experiment (M. Sturm, personal communication). This detail reveals the sensitive response of bacterial magnetite to the redox conditions of the lake.

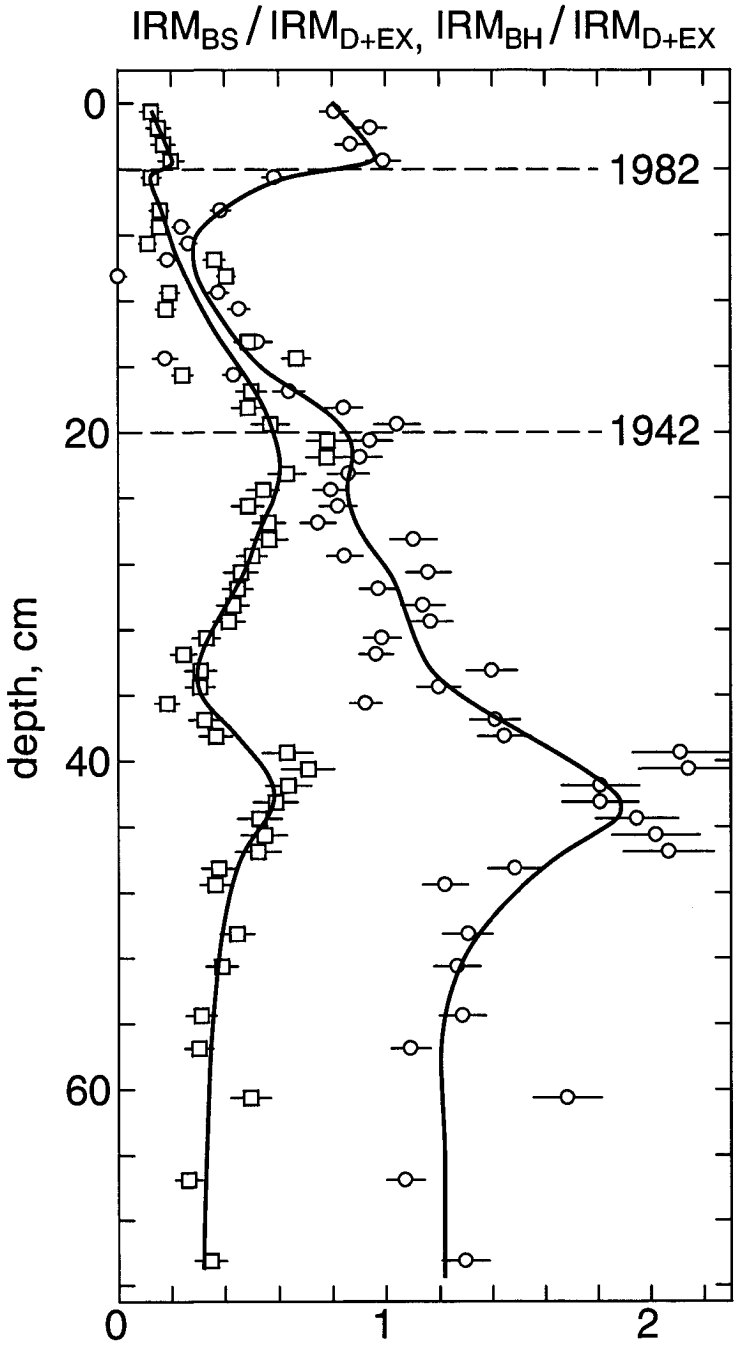

Figure 9. *Downcore variations of the magnetic contributions of components BS (circles) and BH (squares), normalized by the magnetic contribution of component D+EX. The same features of Figure 6 can be recognized. The contribution of BH remains low after the start of the artificial aeration experiment (1982). On the other hand, a drastic increase of BS is observed after 1982, suggesting that BS is produced by magnetotactic bacteria that tolerate higher oxygen concentrations than the BH producing bacteria. The contribution of both components shows a slight decrease toward the top of the core (last four points), which corresponds to a reduction of the amount oxygen pumped into the lake since the beginning of the artificial aeration experiment.*

4.5. A simulation of the reaction of Baldeggersee to environmental changes

The effect of the productivity and the oxygen concentration on the magnetic properties of lake sediments has been investigated in section 4.4. In the following, a simple model for the production and dissolution of bacterial magnetite is developed, in order to test the reaction of Baldeggersee to a climatic signal. The results of this model are shown in Figure 10. The climatic signal has been generated numerically by adding four contributions: (1) a long-term trend, which simulates a global warming effect, (2) short-term climatic oscillations, simulated by a sinusoidal curve, (3) a random noise signal, which reproduces casual year-to-year variations, (4) local extreme events in the catchment area, as landslides produced by anomalous rainy periods (Figure 10a). The climatic signal can be expressed with the nutrient load $N(t)$, which is the total amount of phosphates, nitrates and micronutrients, which are necessary to sustain photosynthetic organisms. According to *Scheffer et al.* [2002], there are two critical nutrient loads, $N_{\text{crit}}^{\max}$ and $N_{\text{crit}}^{\min}$, which are characteristic for a lake. If the nutrient load exceeds $N_{\text{crit}}^{\max}$, the lake turns into anoxic conditions, which are maintained unless the nutrient load falls below $N_{\text{crit}}^{\min}$. Alternatively, anoxic periods are terminated by a strong mixing event, which brings fresh water into the hypolimnium. The state of the lake is expressed by a boolean variable $b(t)$: during anoxic conditions, $b(t) = \text{anox}$, otherwise $b(t) = \text{ox}$. The magnetization $M(t,t_0)$ of a sediment deposited at the time t_0 is given by the sum of a detrital component, $M_{\text{D}}(t_0)$, and a bacterial component $M_{\text{B}}(t,t_0)$, which includes magnetosomes and extracellular magnetite. For simplicity, the detrital component is assumed to be constant with time. This simplification does not introduce a large error, since the magnetization of the sediment is controlled mainly by the abundance of bacterial magnetite. The ARM ratio of the bacterial component is given by $r_{\text{B}}(t,t_0)$.

If $b(t) = \text{ox}$, the magnetization of the bacterial component is proportional to the nutrient load: $M(t,t_0) \propto N(t_0)$, and nothing happens to this component after its deposition. The ARM ratio is expressed by a monotonically decreasing function $f(N)$ of the nutrient load: $r_{\text{B}}(t,t_0) = f(N(t))$. As soon as a local extreme event satisfies the condition given by $N(t) > N_{\text{crit}}^{\max}$, the state of the lake is switched to $b(t) = \text{anox}$. In this case, time-dependent dissolution processes will begin. First, the ARM ratio decreases with time, according to $r_{\text{B}}(t,t_0) = r_{\text{B}}(t_0)\exp(-t/\tau)$, where τ is a characteristic time constant, which depends on the rate of the dissolution process. As long as the ARM ratio does not fall below a critical value $r_{\text{B,crit}} \approx 1\ \text{mm/A}$, which has been deduced from Figure 8a, the bacterial magnetite is not going to be dissolved. When this critical value is reached, reductive dissolution occurs and the concentration of the bacterial magnetite decreases according to equation (9), whose solution is given by $M_{\text{B}}(t,t_0) \propto M(t_0)\exp(-t/\tau)$. The anoxic state is maintained as long as $N(t) > N_{\text{crit}}^{\min}$. A local extreme event, accounted by $N(t) < N_{\text{crit}}^{\min}$, terminates the anoxic state, and $b(t) = \text{ox}$.

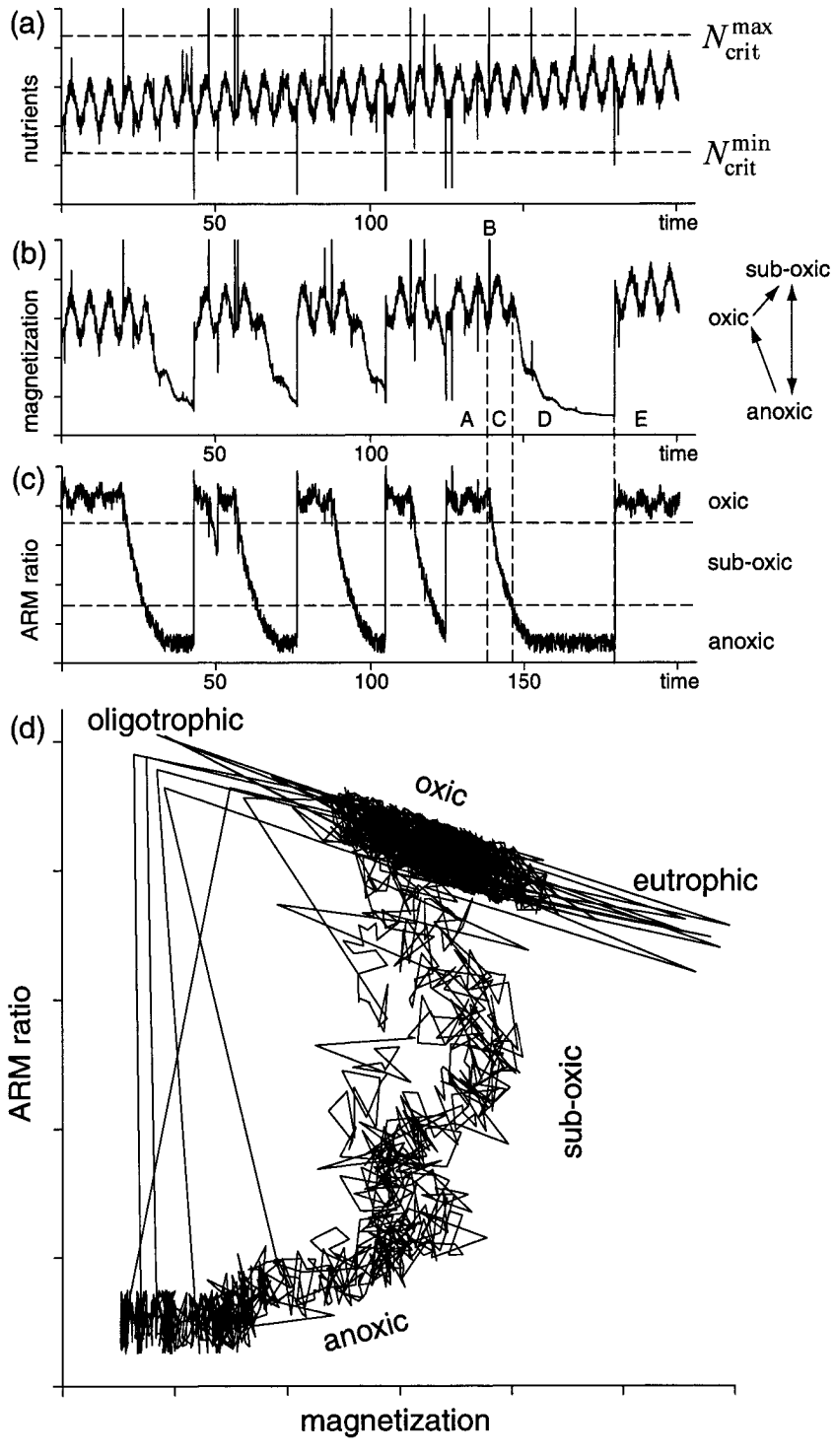

Figure 10. *A simple simulation of the reaction of Baldeggersee to environmental changes, according to the phenomenological model described in the text. (a) The environmental signal is simulated by the nutrient load, which is higher during warm, humid periods. The signal contains a long-term trend (e.g. global warming) and short-term oscillations. Superimposed to this signal, the effect of extreme local events, as landslides induced by anomalous rainy periods, appears as isolated spikes. The two critical values of nutrient load are highlighted with dashed lines (see text). Magnetization (b) and ARM ratio (c) of the sediments depend on the lake productivity and on the redox conditions. Isolated peaks of nutrients load that exceed* N_{crit}^{max} *trigger anoxic events, which are overcome only if the nutrients load fall below* N_{crit}^{min}*. Notice that the magnetic signals are poorly correlated to the environmental signal. Parts of the curves labelled with A, B, C, D, E are similar to the measurements of Figure 6. (d) A scatter plot of the magnetization and the ARM ratio highlights the hysteretic behaviour of the lake, which reacts like a switch to environmental changes. Notice the similarity of this plot with the measured data (Figure 6a).*

The results of this simple model for the magnetization of the sediments and the ARM ratio of the bacterial component are plotted in Figure 10b,c. A saw-tooth pattern results from the onset of anoxic conditions driven by extreme events, which are randomly distributed with time. However, the long-term climatic trend is responsible for progressively longer and frequent periods of anoxia. The magnetic signature has a chaotic behavior, which does not give a classical correlation to the climatic signal. All features recognized in the temporal evolution of the last anoxic event in Baldeggersee (Figure 6, labeled with A, B, C, D, E) are reproduced by the simulation. A scatter plot of the two magnetic parameters of Figure 10b,c highlights the anoxic cycles (Fig. 10d), which are very similar to the real anoxic cycle plotted in Figure 8a.

5. Conclusions

A great simplification of the unmixing problem is obtained if the magnetic properties of all components of a sediment, and their dependence on natural processes, are known in advance from detailed measurements on a set of samples used as reference. In this case, the measurement of magnetization curves with a number of steps equal to twice the number of components is sufficient to obtain a solution of the linearized unmixing problem. The natural variability of magnetic components can be taken into account by an iterative version of the linearized unmixing problem, which has been used to analyze systematically the evolution of the last eutrophication event in Baldeggersee.

A model has been developed to describe the processes of growth and dissolution of magnetite in lacustrine and marine sediments. The amount of bacterial magnetite is proportional to the productivity of a lake up to a critical level, which depends on the morphology and on the chemistry of the lake. Above this level, the concentration of bacterial magnetite does not increase, and the ARM ratio drops by up to one order of magnitude. This change is accompanied by the precipitation of iron sulphides, which may form a shell around magnetite particles. It is not clear whether the decrease of the ARM ratio is caused by the sulphidic shell, or by the onset of dissolution. As long as the ARM ratio decreases, the concentration of bacterial magnetite is approximately constant. When the ARM ratio falls below 1 mm/A, the lake is completely anoxic, and bacterial magnetite starts to be dissolved. The lake tends to preserve the anoxic conditions until an extreme natural event produces a complete mixing of the deep water, which brings oxygen to the bottom. In this case, the production of bacterial magnetite starts again. Two different magnetic components, BS and BH, could be associated to magnetosomes with a different morphology. The relative proportion of these two components is a sensitive indicator of the redox conditions in the lake. Component BS prevails during oxic conditions, and disappears almost completely during anoxic events. Component BH is more resistant to anoxic conditions and its production is suppressed if the oxygen concentration is too high.

The processes summarized above are of fundamental importance to understand the complex relation between the environment and the magnetic properties of sediments, and for the calibration of magnetic proxies, which are used for paleoclimatic reconstructions. The relation between climate and magnetic properties of lake sediments has been simulated in order to test the model developed in section 4. Realistic results that give evidence of the possibility of a chaotic response of lacustrine ecosystems to progressive climatic changes have been obtained.

Acknowledgements. I would like to thank M. Sturm, for providing the core G from Baldeggersee. I am grateful to M. Sturm, I. Baster, K. Monecke and D. Nourgaliev for interesting discussions about lake sediments. ETH Research Project 0-20556-00.

References

Blakemore, R. P., K. A. Short, D. A. Bazylinski, C: Rosenblatt, and R. B. Frankel, Microaerobic conditions are required for magnetite formation within *Aquaspirillum Magnetotacticum*, *Geomicrobiol. J.*, *4*, 53-70, 1985.

Boyle, E. A., Is ocean thermohaline circulation linked to abrupt stadial/interstadial transitions?, *Quat. Sci. Rev.*, *19*, 255-272, 2000.

Canfield, D. E., and R. A. Berner, Dissolution and pyritization of magnetite in anoxic marine sediments, *Geochim. Cosmochim. Acta*, *51*, 645-659, 1987.

Dearing, J. A., Holocene environmental change from magnetic proxies in lake sediments, in *Quaternary climates, environments and magnetism*, edited by B. A. Maher and R. Thompson, Cambridge University Press, 1999.

Dekkers, M. J., and M. A. A. Schoonen, Magnetic properties of hydrothermally synthesized greiginte (Fe_3S_4) – I. Rock magnetic parameters at room temperature, *Geophys. J. Int.*, *126*, 360-368, 1996.

Dekkers, M. J., H. F. Passier, and M. A. A. Schoonen, Magnetic properties of hydrothermally synthesized greigite (Fe_3S_4) – II. High- and low-temperature characteristics, *Geophys. J. Int.*, *141*, 809-819, 2000.

DeMenocal, P., J. Ortiz, T. Guilderson, J. Adkins, M. Sarnthein, L. Baker and M. Yarusinsky, Abrupt onset and termination of the African Humid Period: rapid climate responses to gradual insolation forcing, *Quat. Sci. Rev.*, *19*, 347-361, 2000.

Egli, R. and W. Lowrie, The anhysteretic remanent magnetization of fine magnetic particles, *J. Geophys. Res.*, *107*, 2209-2229, 2002.

Egli, R., Characterization of individual rock magnetic components by analysis of remanence curves, 1. Unmixing natural sediments, submitted to *Studia Geophysica et Geodaetica*, 2003a.

Egli, R., Characterization of individual rock magnetic components by analysis of remanence curves, 2. Rock magnetism of individual components, submitted to *Physics and Chemistry of the Earth*, 2003b.

Geiss, C. E. and S. K. Banerjee, A multi-parameter rock magnetic record of the last glacial-interglacial paleoclimate from south-central Illinois, USA, *Earth Planet. Sci. Lett.*, *152*, 203-216, 1997.

Gruber, N., B. Wehrli and A. Wüest, The role of biogeochemical cycling for the formation and preservation of varved sediments in Soppensee (Switzerland), *J. Paleolimn.*, *24*, 277-291, 2000.

Hanesh, M., and R. Scholger, Mapping of heavy metal loadings in soils by means of magnetic susceptibility measurements, *Environmental Geology*, *42*, 857-870, 2002.

Hanzlik, M., M. Winklhofer and N. Petersen, Pulsed-field-remanence measurements on individual magnetotactic bacteria, *J. Magnet. Mag. Mat.*, *248*, 258-267, 2002.

Heller, F., C. D. Shen, J. Beer, X. M. Liu, T. S. Liu, A. Bronger, M. Suter and G. Bonani, Quantitative estimates of pedogenic ferromagnetic mineral formation in Chinese loess and paleoclimatic implications, *Earth Planet. Sci. Lett.*, *114*, 385-390, 1993.

Hesse, P. P., Evidence for bacterial palaeoecological origin of mineral magnetic cycles in oxic and sub-oxic Tasman Sea sediments, *Marine Geology*, *117*, 1-17, 1994.

Hesse, P. P., Mineral magnetic 'tracing' of aeolian dust in southwest Pacific sediments, *Palaeogeography, Palaeoclimatology, Palaeoecology*, *131*, 327-353, 1997.

Hilgenfeldt, K., Diagenetic dissolution of biogenic magnetite in surface sediments of the Benguela upwelling system, *Int. J. Earth Sci.*, *88*, 630-640, 2000.

Hu, Y., F. Oldfield, F. Manalt and C. Beck, The environmental significance of magnetic measurements of late Pleistocene and Holocene sediments from the Grand Lac d'Annecy, eastern France, *J. Paleolimn.*, *25*, 193-203, 2001.

Hunt, A., The application of mineral magnetic methods to atmospheric aerosol discrimination, *Phys. Earth Planet. Sci. Int.*, *42*, 10-21, 1986.

Kruiver, P. P., M. J. Dekkers and D. Heslop, Quantification of magnetic coercivity components by the analysis of acquisition curves of isothermal remanent magnetization, *Earth Planet. Sci. Lett.*, *189*, 269-276, 2001.

Kuo, P. C., Chain-of-spheres calculation on the coercivities of elongated fine particles with both magnetocrystalline and shape anisotropy, *J. Appl. Phys.*, *64*, 5071-5083, 1988.

Lanci, L. and D. V. Kent, Introduction of thermal activation in forward modeling of hysteresis loops for single-domain magnetic particles and implications for the interpretation of the Day diagram, *J. Geophys. Res.*, *108*, 2142, doi 10.1029/2001JB000944, 2003.

Leslie, B. W., D. E. Hammond, W. M. Berelson, and S. P. Lund, Diagenesis in anoxic sediments from the California Continental Borderland and its influence on iron, sulfur and magnetite behaviour, *J. Geophys. Res.*, *95*, 4453-4470, 1990a.

Leslie, B. W., S. P. Lund and D. E. Hammond, Rock magnetic evidence for the dissolution and authigenic growth of magnetic minerals within anoxic marine sediments of the California continental borderland, *J. Geophys. Res.*, *95*, 4437-4452, 1990b.

Lotter, A. F., M. Sturm, J. L. Teranes and B. Wehrli, Varve formation since 1885 and high-resolution varve analyses in hypertrophic Baldeggersee (Switzerland), *Aquatic Sciences*, *57*, 305-325, 1997.

Lu, R., and S. K. Banerjee, Magnetite dissolution in deep sediments and its hydrologic implication: a detailed study of sediments from site 808, leg 131, *J. Geophys. Res.*, *99*, 9051-9059, 1994.

Manabe, S. and R. J. Stouffer, Study of abrupt climate change by a coupled ocean-atmosphere model, *Quat. Sci. Rev.*, *19*, 285-299, 2000.

Mann, S., N. H. C. Sparks, R. B. Frankel, D. A. Bazylinski, and H. W. Jannash, Biomineralization of ferromagnetic greigite (Fe_3S_4) and iron pyrite (FeS_2) in a magnetotactic bacterium, *Nature*, *343*, 258-261, 1990.

Moskowitz, B. M. et al., Magnetic properties of magnetotactic bacteria, *J. Magnet. Mag. Mat.*, *73*, 273-288, 1988.

Moskowitz, B. M., R. B. Frankel and D. A. Bazylinski, Rock magnetic criteria for the detection of biogenic magnetite, *Earth Planet. Sci. Lett.*, *120*, 283-300, 1993.

Muxworthy, A. R., J. Matzka, and N. Petersen, Comparison of magnetic parameters of urban atmospheric particulate matter with pollution and meteorological data, *Atmospheric Environment*, *35*, 4379-4386, 2001.

Oldfield, F., A. Hunt, M. D. H. Jones, R. Chester, J. A. Dearing, L. Olsson and J. M. Prospero, Magnetic differentiation of atmospheric dusts, *Nature*, *317*, 516-518, 1985.

Penninga, I., H. de Waard, B. M. Moskowitz, D. A. Bazylinski and R. B. Frankel, Remanence measurements on individual magnetotactic bacteria, *J. Magnet. Mag. Mat.*, *149*, 279-286, 1995.

Roberts, A. P., Magnetic properties of sedimentary greigite (Fe_3S_4), *Earth Planet. Sci. Lett.*, *134*, 227-236, 1995.

Scheffer, M., S. Carpenter, J. A. Foley and B. Walker, Catastrophic shifts in ecosystems, *Nature*, *413*, 591-596, 2001.

Shcherbakov, V. P., M. Winkelhofer, M. Hanzlik, and N. Petersen, Elastic stability of chains of magnetosomes in magnetotactic bacteria, *Eur. Biophys. J.*, *26*, 319-326, 1997.

Snowball, I. F., Geochemical control of magnetite dissolution in subartic lake sediments and the implications for environmental magnetism, *J. Quaternary Sci.*, *8*, 339-346, 1993.

Snowball, I., L. Zillén and P. Sandgren, Bacterial magnetite in Swedish varved lake-sediments: a potential bio-marker of environmental change, *Quaternary International*, *88*, 13-19, 2002.

Tarduno, J. A., Temporal trends of magnetic dissolution in the pelagic realm: gauging paleoproductivity?, *Earth Planet. Sci. Lett.*, *123*, 39-48, 1994.

Tarduno, J. A. Superparamagnetism and reduction diagenensis in pelagic sediments: Enhancement or depletion?, *Geophys. Res. Lett.*, *22*, 1337-1340, 1995.

Thompson, R., and F. Oldfield, *Environmental magnetism*, 227 pp., Allen and Unwin, Concord, Mass., 1986.

Vali, H., O. Förster, G. Amarantidis and N. Petersen, Magnetotactic bacteria and their magnetofossils in sediments, *Earth Planet. Sci. Lett.*, *86*, 389-400, 1987.

Vali, H., and J. L. Kirschvink, Magnetofossil dissolution in a paleomagnetically unstable deep-sea sediment, *Nature*, *339*, 203-206, 1989.

Wohlfarth, E. P., A review of the problem of fine-particle interactions with special reference to magnetic recording, *J. Appl. Phys.*, *35*, 783-790, 1964.

Yamazaki, T. and H. Kawahata, Organic carbon flux controls the morphology of magnetofossils in marine sediments, *Geology*, *26*, 1064-1066, 1998.

Zehnder, A. J. B., and W. Stumm, Geochemistry and biogeochemistry of anaerobic habitats, *Biology of anaerobes*, ed. M. Zehnder, pp 1-38, Blackwell Scientific, Boston, 1988.

Seite Leer /
Blank leaf

Chapter 7

Conclusions

" *Science may be described as the art of systematic oversimplification.* "

Karl Popper (1902-1994)

Seite Leer /
Blank leaf

Conclusions

In the following, a brief summary of the principal results of this thesis is given.

1. The magnetic properties of fine particles

The magnetic properties of non-interacting single domain (SD) particles have been modelled with Néel's thermal activation theory. Analytical expressions have been obtained for the susceptibility of the anhysteretic remanent magnetization (ARM) and for the alternating field necessary to reduce the remanent magnetization of the particles to the half. The susceptibility of ARM of non-interacting particles is finite, and depends on their magnetic moment, their shape and their temperature. A weak dependence on the ramp rate of the alternating magnetic field used to impart an ARM has been predicted as well. The susceptibility of ARM is proportional to the square of the grain size, for grain sizes up to 60 nm. The model has been tested with a natural sample that contains pure SD magnetite grains. A detailed investigation of the dependence of the ARM on the ramp rate of the alternating field allowed the estimation of the atomic reorganization frequency of magnetite at room temperature. The estimate is compatible with other results reported in the literature. The dependence of the shape of alternating field demagnetization curves on the intrinsic properties of SD particles has been investigated as well. It has been found that the difference between the demagnetization curves of ARM and of isothermal remanent magnetization (IRM) depends on the statistical distribution of the volume and the elongation of the particles. As a consequence, the comparison of AF demagnetization curves of ARM and IRM, known as the modified Lowrie-Fuller test, is not an absolute test for the domain state of the particles. However, the numerical simulation of a set of SD particles with a broad distribution of volumes and elongations confirms the result expected from the modified Lowrie-Fuller test for SD particles.

2. Analysis of magnetization curves with skewed generalized functions (SGG)

The analysis of magnetization curves with model functions offers a solution of the unmixing problems, which does not need a previous characterization of the magnetic components. The success of this method rely on accurate and detailed measurements, and on the ability of the model functions in fitting the magnetization of each component, or its derivative, called coercivity distribution. In previous works logarithmic Gaussian functions have been chosen as model functions. However, these functions are not always adequate, and many natural magnetic components cannot be correctly modelled. A generalization of these functions with four shape parameters, called SGG function, has been developed in order to control the symmetry and the squareness of a coercivity distribution. Two computer programs have been written for the analysis of magnetization curves with SGG functions. The user's manuals for these programs are given in the Appendix of the thesis. The first program, CODICA (COercivity DIstribution CAlculator), calculates the coercivity distribution of a (de)magneti-

zation curve and filters the measurement errors. The second program, GECA (GEneralized Coercivity Analyzer), is used to fit a coercivity distribution with a linear combination of SGG functions. The program adjusts the parameters of the SGG functions until the difference between the measured and the modelled distribution is minimal. The analysis of demagnetization curves with SGG functions has been tested successfully on lake sediment samples and on samples of atmospheric particulate matter.

3. A systematic investigation of natural sediments with the analysis of magnetization curves

The analysis of coercivity distributions with SGG functions has been used to characterize the magnetic components of 45 representative samples from various sedimentary environments, and 23 artificial magnetite samples. About hundred natural magnetic components have been characterized. These components could be divided into the following groups according to their magnetic properties: (1) water-transported detrital particles from lake catchments, river deltas and late-glacial sediments, (2) dusts from loesses and atmospheric particulate matter, (3) ultrafine magnetites in soils, paleosols and red clays, and ultrafine magnetites in lacustrine and marine sediment, as well as in limestones, (4) low-coercivity magnetic particles produced by magnetotactic bacteria, (5) high-coercivity magnetic particles produced by magnetotactic bacteria, (6) maghemite produced by the low-temperature oxidation of magnetite in loesses, paleosols and soils, and (7) fly-ash and metallic particles from urban pollution. Some unexpected results have been obtained for the bacterial components. First, there are two groups of bacterial particles characterized by distinct coercivities. The first group is probably formed by equant and prismatic magnetosomes, the second group by elongated magnetosomes. The elongated magnetosomes are produced by magnetotactic bacteria that develop under lower concentrations of oxygen with respect to the other bacteria. These two groups could be identified in lacustrine and in marine sediments. The coercivity of the marine magnetosomes is systematically 30% lower than those of fresh-water magnetosomes. Under anoxic conditions, the ratio of the susceptibility of ARM to the IRM in bacterial magnetite drops by one order of magnitude, whereby all other magnetic properties remain unchanged. The reasons of this effect are not clear, however, it has been shown that magnetosomes of anoxic lake sediments are surrounded by a shell of hexagonal pyrrhotite, which protect them from a complete dissolution.

4. Rock magnetism of individual components and magnetic fingerprints

The characterization of the ARM and IRM properties of a magnetic component with SGG functions involves the use of nine parameters: four parameters for the shape of the ARM curve, other four parameters for the shape of the IRM curve, and an additional parameter for the ratio between ARM and IRM. Some of these parameters are well known in rock magnetism, but the physical meaning of the other parameters is not straightforward. Furthermore, not all nine parameters are independent. It was therefore possible to simplify the model for the

coercivity distribution of individual components by establishing empirical relations between shape parameters. These relations depend on fundamental properties of the magnetic minerals and are expected to have a general validity. The coercivity distributions of individual natural components have been compared with synthetic coercivity distributions, which have been calculated with simple rock magnetic models for non-interacting magnetic grain assemblages. It has been found that the symmetry of a coercivity distribution depends in a complex manner on the grain size and the elongation of the particles. Three different factors affects the simmetry of a coercivity distribution: (1) the effect of specific physical properties, such as the grain size, on the microcoercivity, (2) thermal activation effects, which have been modeled in terms of viscosity and time dependence of the coercivity, and (3) defects of the crystal structure and processes related to the surface of the grains, such as weathering. The coercivity distributions of all natural components are characterized by three independent shape parameters, since a precise relation has been found between skewness and squareness. Accordingly, coercivity distributions of individual components can be modelled by so-called maximum entropy SGG functions, which are a special case of SGG functions with three shape parameters. An inverse relation exists between the median destructive field MDF and the dispersion parameter DP, due to the maximal intrinsic coercivity of the mineral. The skewness of a coercivity distribution depends on the DP and on the grain size of the particles. A linear relation has been found between the differences of MDF and DP of ARM demagnetization curves with respect to IRM demagnetization curves. This relation defines all possible results of the modified Lowrie-Fuller test. With the above considerations, two independent parameters (MDF and DP) characterize the shape of a coercivity distribution. An additional parameter, which account for the result of the Lowrie-Fuller test, is necessary to characterize the difference between normalized demagnetization curves of ARM and IRM. A fourth parameter, the ARM ratio, accounts for the susceptibility of ARM. These four parameters have been called fingerprint parameters, because they give a unique identification of a magnetic component.

5. Linearization of the unmixing problem

The analysis of magnetization curves with SGG functions requires time-consuming, accurate measurements, and is therefore not applicable to a large set of samples. The use of magnetic fingerprits allows a substantial simplification the unmixing problem, which has been obtained by reducing the number of parameters necessary to model a magnetic component. A further simplification is obtained if the magnetic properties of the components, as well as their dependence on natural processes, are known. In this case, the unmixing problem can be linearized, and its solution comes out with relatively fast measurements, typically two acquisition or demagnetisation steps for each component.

6. Redox cycles in lake sediments

A linearization of the unmixing problem has been used for the systematic analysis of a sediment core from Baldeggersee. A major eutrophycation event started in 1885 could be investigated in detail, with special regard to the processes of formation and dissolution of magnetite. The following main states of the lake have been identified: (1) During periods of low productivity, as in the Late Glacial, the formation of bacterial magnetite is limited by the availability of organic matter. The magnetic contribution of the bacterial magnetite is about 30%, and the high ARM ratio is typical for oxic conditions. This situation is characteristic for oligotrophic lakes. (2) As the nutrient load increases, the production of organic carbon is enhanced, followed by the concentration of bacterial magnetite. The bacterial activity produces oxygen depletion in the hypolymnium, which is characteristic for sub-oxic conditions. The ARM ratio decreases up to a factor 2, and the relative amount of elongated magnetosomes increases. This trend in maintained up to a specific critical productivity level, above which the lake becomes eutrophic. At this critical level, bacterial magnetite account for 75% of the total magnetization of the sediments. The critical productivity level depends mainly on the mixing rate of the water column. (3) When the productivity of the lake approaches the critical level, extreme events in the catchments area, as a landslide, can trigger the abrupt onset of anoxic conditions, which are characterized by the formation of biogenic varves in the sediment. Initially, the ARM ratio of the bacterial magnetite is reduced progressively by one order of magnitude, but its contribution to the IRM does not change significantly. (4) If anoxic conditions persist, the bacterial magnetite begins to be reductively dissolved and its concentration decreases progressively. The formation of a sulphide shell around the magnetosomes prevents their complete dissolution. The amount of elongated magnetosomes increases up to 100%. Anoxic conditions are terminated only if the productivity of the lake falls below a certain level, or after a complete mixing of the water column.

7. Nonlinear behaviour of lakes and chaotic response to environmental changes

According to the mangetic properties of the sediments, a lake reacts as a kind of 'switch' to progressive environmental changes, showing a hysteretical cycle caused by its nonlinear behaviour. A model to explain the magnetic signature of lake sediments has been tested by simulating the reaction of a lake to a progressive climatic change. The related changes of the magnetic properties show a chaotic behaviour, witch is characterized by several eutrophication periods. During these periods, magnetic properties predicted by the model are similar to those measured in the sediments of Baldeggersee. The chaotic response of the magnetic signature to environmental changes suggests that a classic correlation between so-called magnetic proxies and environmental signals should be considered with care.

Acknowledgements

I would like to thank Prof. William Lowrie for affording the expenses of this thesis inside the magnetic group and for useful improvements of my manuscripts.

The underlying idea of this work has a long story, and arose unconsciously from fruitful discussions with the *vieille garde* of the magnetic group: in chronological order my friend Simo (is the entire universe a black hole?), Mizzo the philosopher (humans are curious), Luca Lanci, also called peripatetic because he managed to walk 5000 km inside the laboratory looking for an inspiration, Giovanni Muttoni (inventore del percasól), the volcanic Marisa (...sabes?), Katrin Monecke (the famous Goldmünzen-layers), Danis Nourgaliev (ja, jaaa) and Ira Baster (il magnetismo è cosí veloce...).

A special thank is devoted to Prof. Friedrich Heller for introducing me with enthusiasm into the world of magnetism and for his constant advice and support.

The realization of this work would not have been possible without the help of Mike Sturm, and his unlucky coring campaign. The piston core has been sampled with the precious help of Katrin Monecke at the limnogeology laboratory of the ETH Zürich. Low-temperature measurements have been performed at the IRM laboratory in Minnesota. I thank M. Sturm, S. Spassov, F. Heller, I. Baster, D. Nourgaliev, M. Fuller and G. Muttoni for providing many samples.

A very special thank is devoted to my friends and colleagues Simo and Fàtima. I spent a lot of time with them, sharing emotions, frustrations, beers, philosophical lucubrations (me, God and the triangle), and joy. Thanks to Fàtima for showing me the many-layers-strategy against temperatures below 29.5°C and for the accurate bibliographic service, and to both for expe-riencing with me the third law of thermodynamics inside the office. Thanks to Simo, for our friendship and fruitful collaboration, which should continue...

I would also thank Mr. Hobla George for some wonderful findings, as DF and many others.

I spent a good time with many guests of the laboratory: Paola Gialannella, Marisa Osete, Francesca Cifelli, Juanjo Villaréz, Marife Bogalo, Kais Mohammed, Giovanni Napoleone. I will miss them.

I would like to mention my colleagues and friends at the institute: Francesca Funiciello, Raffaele di Stefano, Fabio Cammarano, Fabrizio Bernardi, Senén Sandoval Castaño, Remco Muijs and Federica Marone.

Last but not least, a special thank is dedicated to you, Rossella, for affording together with me a difficult and hostile phase of this work, and giving me the necessary endurance and much love.

Curriculum Vitae

1977-1982 Primarschule in Vacallo (Schweiz).

1982-1986 Sekundarschule in Morbio Inferiore (Schweiz).

1986-1990 Gymnasium in Mendrisio (Schweiz), mit Hauptgewicht Naturwissenschaften.

1990-1993 Physikstudium an der Eidgenössischen Technischen Hochschule, ETH Zürich.

1993-1998 Studium in Erdwissenschaften, Fachrichtung Geophysik, an der ETH Zürich.

1998 Diplomarbeit am Institut für Geophysik der ETH Zürich unter der Leitung von Prof. Dr. Friedrich Heller: *Mikromagnetische Feldverteilungsmessungen mit einem Hochtemperatur-SQUID-Magnetometer: Praxis, Programmierung und Anwendung.*

1998 Diplom in Naturwissenschaften (Dipl. Natw. ETH). Auszeichnung für den besten Prüfungsabschluss (5.9/6 im Durchschnitt) und Silbermedaille für die beste Diplomarbeit.

2003 Doktorat an der ETH Zürich unter der Leitung von Prof. Dr. William Lowrie und Assistent am Institut für Geophysik.

Publications

Egli, R. and F. Heller, High-resolution imaging using a high-T_c superconducting quantum interference device (SQUID) magnetometer, *J. Geophys. Res.*, *105*, 25709-25727, 2000.

Egli, R. and W. Lowrie, Anhysteretic remanent magnetization of fine magnetic particles, *J. Geophys. Res.*, *107*, doi 10.1029/2001JB000671, 2002.

Egli, R., Analysis of the field dependence of remanent magnetization curves, *J. Geophys. Res.*, *108*, doi 10.1029/2002JB002023, 2003.

Ravazzi, C., R. Pini, M. Breda, E. Martinetto, G. Muttoni, S. Chiesa, F. Confortini, and **R. Egli**, The lacustrine deposits of Fornaci di Ranica (late Early Pleistocene, Italian Pre-Alps): stratigraphy, palaeoenvironment and geological evolution, *Quat. Int.*, in press.

Egli, R., Characterization of individual rock magnetic components by analysis of remanence curves, 1. Unmixing natural sediments, submitted to *Studia Geophysica Geodaetica.*

Egli, R., Characterization of individual rock magnetic components by analysis of remanence curves, 2. Rock magnetism of individual components, submitted to *Physics and Chemistry of the Earth.*

Egli, R., Characterization of individual rock magnetic components by analysis of remanence curves, 3. Bacterial magnetite and natural processes in lakes, submitted to *Physics and Chemistry of the Earth.*

Spassov, S., **R. Egli**, F. Heller, D. K. Nourgaliev, and J. Hannam, A preliminary study on the quantification of urban pollution sources in atmospheric particulate matter by mean of magnetic measurements, submitted to *Atmospheric Environment.*

Appendix

Reference manuals for the programs CODICA and GECA

Seite Leer /
Blank leaf

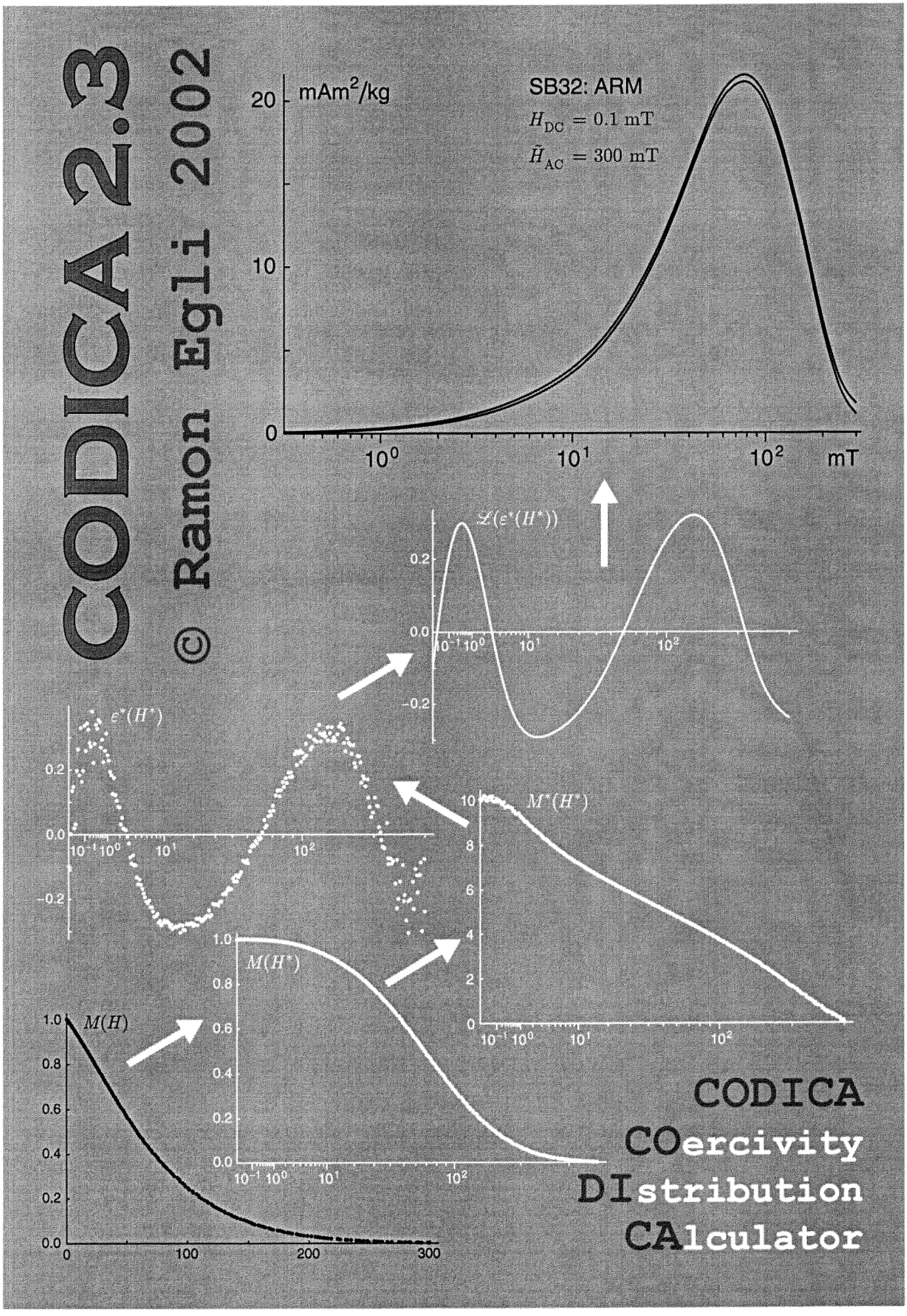
CODICA 2.3
© Ramon Egli 2002
20
mAm²/kg
SB32: ARM
$H_{DC} = 0.1$ mT
$\tilde{H}_{AC} = 300$ mT
10
0
10^0
10^1
10^2
mT
$\mathcal{L}(\varepsilon^*(H^*))$
$\varepsilon^*(H^*)$
$M^*(H^*)$
$M(H^*)$
$M(H)$
CODICA
COercivity
DIstribution
CAlculator

Introduction

CODICA (COercivity DIstribution CAlculator) is a program which efficiently removes the measurement errors from acquisition/demagnetization curves and calculates the corresponding coercivity distribution on different field scales. The efficiency of the measurement errors removal is based on several rescaling procedures which converts the original acquisition/demagnetization curve to a residuals curve. The residuals curve is low-pass filtered and transformed back into an acquisition/demagnetization curve where the noise has been reduced more efficiently than by direct filtering. An error estimation is performed as well, and the coercivity distribution is plotted together with confidence limits.

Read carefully this manual to learn about CODICA. Many steps of CODICA seems complicate, but in reality they are quite intuitive once you are familiar with the program. This manual contains a theoretical part, which gives you the background to understend the basic ideas of CODICA, and a practical part, which guides you through each step of the program. You can practice with the examples delivered together with this program. CODICA is designed to perform an optimized data treatement of acquisition/dempagnetization curves. It allows you to easily recognize and efficiently remove the measurement errors. The parameters you are asked to enter do not directly affect the final result since they only control the efficiency of the measurement errors removal procedure. Therefore, the choice of these parameters is not critical and the results are not "user dependent", as long as the instructions given in this manual are followed. You should always consider that CODICA does not add any information to the original measurements, as any other program for data analysis: bad measurements will give poorly defined coercivity distributions affected by large errors. Nevertheless, CODICA helps you to identify the measurement errors and better redesign the experiment, by optimizing the magnetization/demagnetization steps and stacking more measurements, if necessary.

Click on the following topics to see the contents of this manual:

Theoretical background

Coercivity distributions are defined as the absolute value of the first derivative of acquisition/demagnetization curves. In terms of Fourier analysis, the first derivative is equivalent to a high-pass filter, whose effect is to enhance small details of the original curve (see Fig. 1). For this reason, any information contained in the original curve will be more evident in the resulting coercivity distribution. This applies also to the measurement errors, which are generally small in the measured curve, but are enhanced in the resulting derivative. The enhancement of small measurement errors is the main reason why coercivity distributions have not been used very often in the interpretation of magnetic measurements, despite the potential advantages.

Measurement errors may be removed with an appropriate filter. The measured curves are often asymmetric and they require a different degree of filtering at different fields. CODICA (COercivity DIstribution CAlculator) is a program which removes the measurement errors by appropriately rescaling and filtering the acquisition/demagnetization curve. It calculates the corresponding coercivity distribution on different field scales and estimates the confidence limits. The latter is particularly useful when the significance of a component analysis performed on the coercivity distribution has to be evaluated.

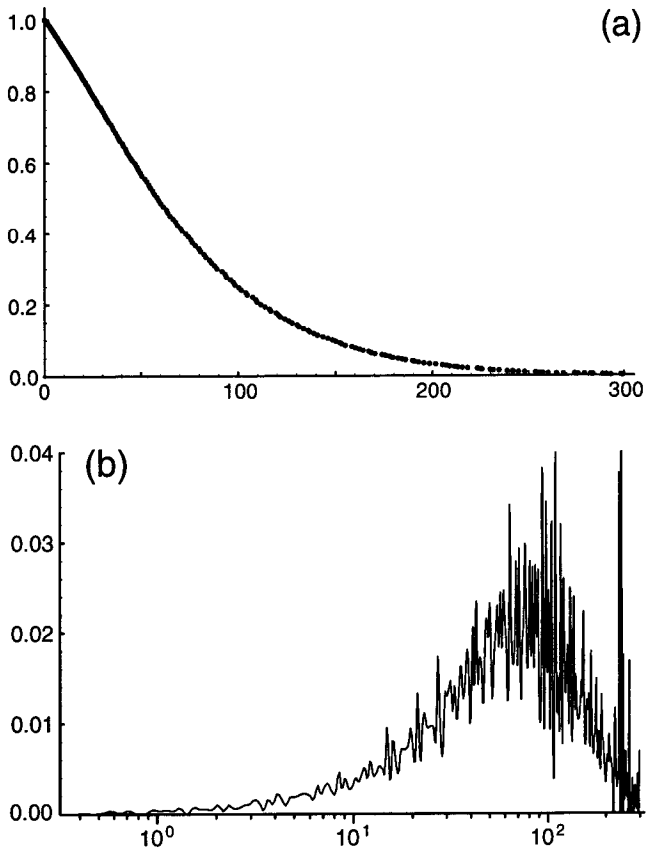

Fig 1: *An AF demagnetization curve* (a), *and the corresponding coercivity distribution* (b), *calculated by numerical differentiation. In* (c), *the coercivity distribution calcualted with CODICA is plotted on a logarithmic field scale. The curve pair indicates the confidence limits. In (d), the efficiency of CODICA in removing the measurement noise (dots) is compared with a conventional low-pass filter (open circles).*

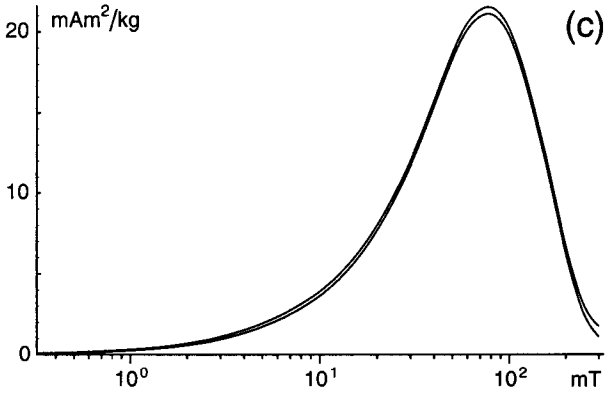

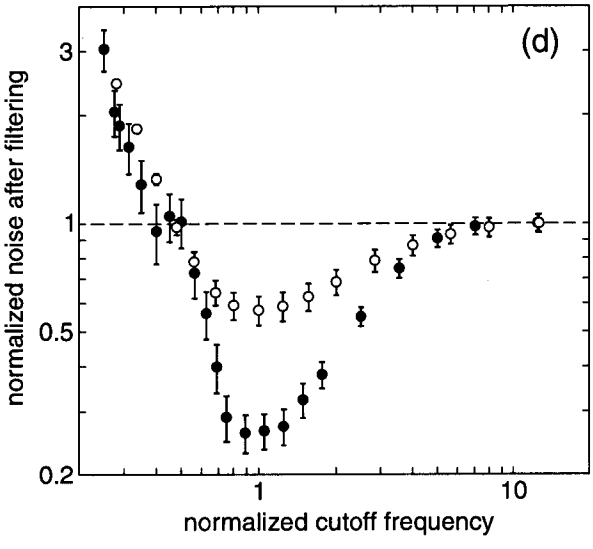

Coercivity distributions are mathematically described by probability distribution functions (PDF) and can be calculated on different field scales for better isolation of different components. The shape of a coercivity distribution changes according to the field scale adopted, because an integration over all coercivities corresponds to the total magnetization of the sample (normalization property). The scale change of a distribution f generates a new distribution f^* defined by the following transformation rule:

$$H^* = g(H)\,; \quad f^*(H^*) = f\big(g^{-1}(H^*)\big)\frac{\mathrm{d}}{\mathrm{d}H^*}g^{-1}(H^*) \tag{1}$$

where H^* is the new field scale, g the transformation rule between the old and the new scale, expressed by an injective function with inverse g^{-1}, and f^* the coercivity distribution with respect to the new scale. For example, the transformation rule from a linear to a logarithmic scale is expressed as follows:

$$H^* = \log H\,; \quad f^*(H^*) = \ln 10 \cdot 10^{H^*} f(10^{H^*}) \tag{2}$$

Another useful transformation is the following:

$$H^* = H^p\,; \quad f^*(H^*) = \frac{(H^*)^{1/p-1}}{p} f((H^*)^{1/p}) \tag{3}$$

where p is a positive exponent. We will refer to this transformation as the power transformation. The power transformation converges to the logarithmic transformation for $p \to 0$. If $0 < p < 1$, high coercivities are quenched on the field scale, and distributions with large coercivities are enhanced. The same effect is obtained with a logarithmic scale, and the opposite effect with $p > 1$. Click here to see the effect of the field scale transformation on the shape of a coercivity distribution.

In the following, the technique used by CODICA to remove the measurement noise homogeneously along the entire curve is presented. It is based only on the following assumption: all acquisition/demagnetization curves have two regions where the corresponding coercivity distribution is zero on a logarithmic field scale, one at $H \to 0$ and the other at $H \to \infty$. In other words, any acquisition/demagnetization curve has two horizontal asymptotes on a logarithmic field scale. The physical meaning of this assumption for $H \to \infty$ is obvious: all magnetic minerals have a maximum finite coercivity. For $H \to 0$ the physical explanation is related to thermal activation processes in SD and PSD particles, and with domain wall motions in MD particles. Measurements with a sufficient number of points near $H = 0$ are necessary in order to obtain a correct coercivity distribution for small fields. Appropriate scaling of field and magnetization allows the linearization of acquisition/demagnetization curve. On the linearized curve, each measurement point and the rela-

ted error have the same relative importance, so that a simple low-pass filter can be applied to remove the measurement noise with the same effectiveness for all coercivities. An acquisition/demagnetization curve $M = M(H)$ can be linearized in a simple way by rescaling the field according to the transformation rule $H^* = M(H)$. However, because of the measurement errors, the function $M(H)$ is unknown. A good degree of linearization is reached when a model function $\tilde{M}(H)$ expressed by analytical functions is taken as tranformation rule instead of $M(H)$. The choice of the appropriate model function $\tilde{M}(H)$ becomes simpler if field and magnetization are both rescaled. If $M^* = \mu(M)$ and $H^* = g(H)$ are the rescaling functions for the field and the magnetization, respectively, then the model function is given by $\tilde{M}(H) = \mu^{-1}(g(H))$. The relation $M^*(H^*)$ between scaled field and scaled magnetization approaches a straight line when the model function $\tilde{M}(H)$ approaches the (unknown) noise-free magnetization curve. The curve defined by $\varepsilon(H^*) = M^*(H^*) - H^*$ represents the deviations of $M^*(H^*)$ from a perfect linear relation. We call $\varepsilon(H^*)$ the *residuals curve*. If the model function $\tilde{M}(H)$ used for the scaling procedure is identical with the noise-free magnetization curve, then the residuals curve contains only the measurement errors. In reality, since it is impossible to guess the noise-free magnetization curve, the residual curve is a superposition of the nonlinear component of $M^*(H^*)$ and the measurement errors. The fundamental advantage of considering the residuals curve instead of the original curve is that the measurement errors are highly enhanced in the residuals curve and can be homogeneously removed with a low-pass filter. The choice of the filter parameters is not critical, and has little effect on the shape of the resulting coercivity distribution. Under ideal conditions, $\varepsilon(H^*)$ represents only the measurement errors, which can be simply removed by fixing $\varepsilon(H^*) = 0$.
The filtered residual curve can be transformed back into a magnetization curve as follows:

$$\bar{M}(H) = \mu^{-1}\left[\mathscr{L}[\varepsilon(g^{-1}(H))] + g^{-1}(H)\right] \tag{4}$$

where $\mathscr{L}(.)$ is the low-pass filter operator. $\bar{M}(H)$ is now supposedly free of measurement errors.

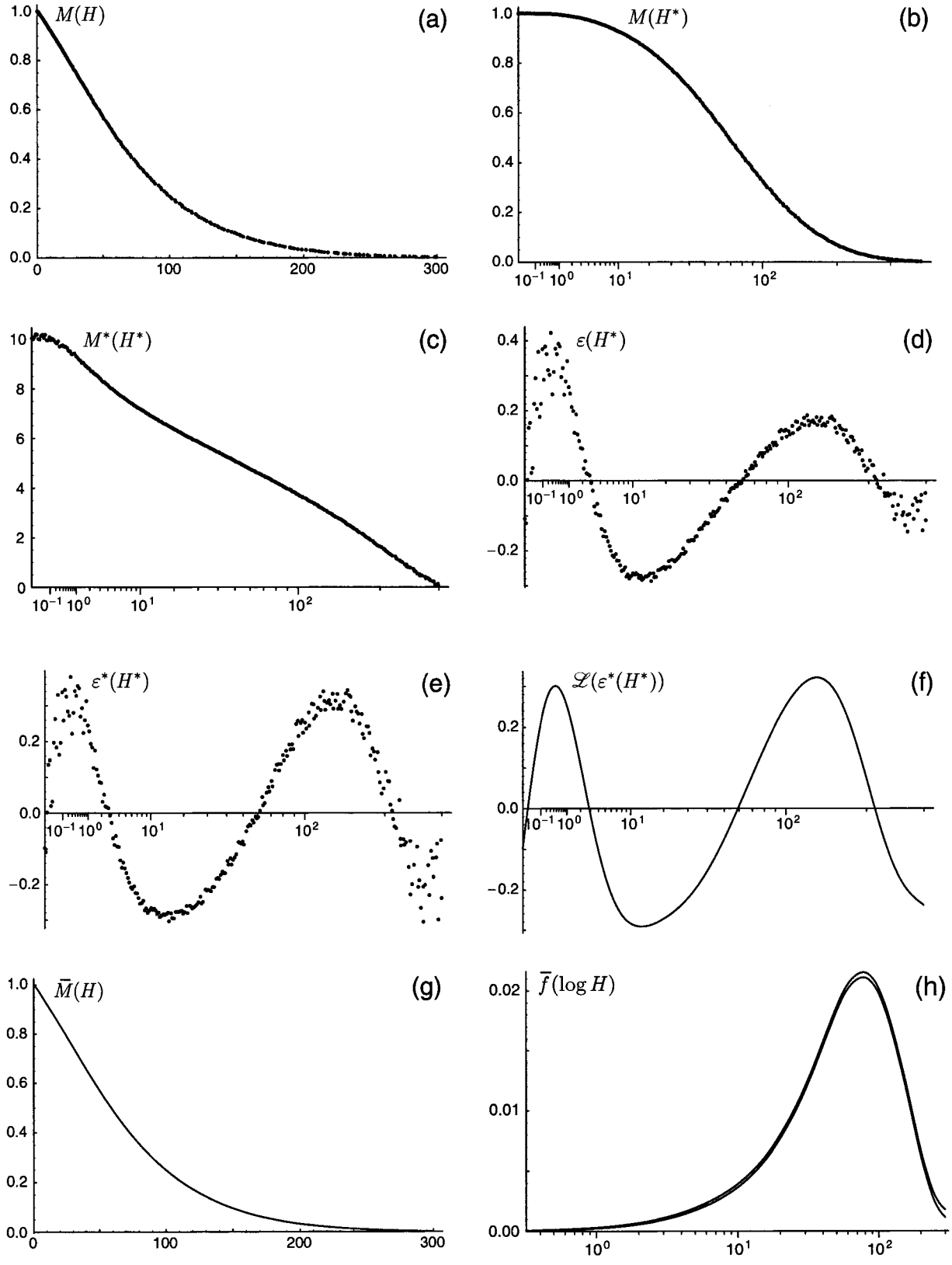

Fig. 2: *Main steps of data processing by CODICA. Original demagentization curve* (a). *Demagnetization curve after rescaling of the field axis* (b), *and the magnetization axis* (c). *Residuals curve before* (d) *and after rescaling* (e). *Filtered residuals* (f), *filtered demagnetization curve* (g) *and coercivity distribution* (h). *See the text for more details.*

CODICA step by step

The processing of an acquisition/demagnetization curve with CODICA consits in the following steps.

1. *Data checking* (figure 2a)
The measurement curve is always displayed as a demagnetization curve: this does not affect the calculation of the coercivity distribution. The user is asked to enter an estimation of the measurement error (if known). This estimate may come from inspection of the measurement curve and/or experimental experience with the instruments used. A combination of a relative and an absolute error is assumed to affect the measurements and the AF field. Systematic errors, like magnetization offsets and temperature effects on the sample and on the AF coil do not affect significantly the shape of the measured curve and may not be included. The calculation of a coercivity distribution and the related measurement error is independent of the error estimate entered by the user. This first estimate is needed by the program in order to display a rough estimation of the confidence limits of the measured curve, which should help the user through the following steps of the program.

2. *Scaling the magnetic field* (figure 2b)
Acquisition/demagnetization curves are supposed to have a sigmoidal shape on a logarithmic field scale. However, the measured curves are not symmetrical. In case of lognormal coercivity distributions, the measured curve represented on a logarithmic field scale becomes symmetric. In all other cases the curve is asymmetric on both a linear and a logarithmic field scale. An appropriate scale change which offers a set of intermediate scales between linear and logarithmic is defined by the power function $H^* = H^p$, p being a positive exponent. An appropriate value of p is chosen, so that the scaled curve reaches maximum symmetry. The symmetry of the curve is compared with a reference sigmoidal curve, expressed by a tanh function. For this porpouse, the scaled curve is therefore represented together with the best-fitting tanh function. An automatic routine optimizes the scaling exponent p so that the difference between the original curve and the model curve is minmal. In most cases, $p \approx 0.3$.

3. *Scaling the magnetization* (figure 2c)
A tanh function was chosen as a reference fuction for scaling the field, because of its mathematical simplicity. It does not have a particular meaning and every other similar function could be used instead. If the measured curve $M(H)$ coincides with a tanh function, the application of the inverse function arctanh to the magnetization values generates a linear relation between scaled field and scaled magnetization. The scale transformation applied to the magnetization values is based on the following model for the relationship between the scaled field H^* and the measured magnetization $M(H^*)$ in a demagnetization curve:

$$M(H^*) = M_{\mathrm{rs}}\left[1 - \tanh\left(a(H^* - H^*_{1/2})\right)\right] + M_0 \tag{5}$$

where M_{rs} has the physical meaning of a saturation remanence (if the measured curve is saturated at the highest field value), M_0 has the physical meaning of an unremoveable magnetization ($M_0 = 0$ if saturation of all minerals can be reached), $H^*_{1/2}$ is the scaled median destructive field and a is a parameter that controls the steepness of the curve. The following scale transformation

$$M^* = \operatorname{artanh}\left(1 - \frac{M - M_0}{M_{\mathrm{rs}}}\right) \tag{6}$$

generates the linear relation $M^* = a(H^* - H^*_{1/2})$ between scaled field and scaled magnetization. The four parameters M_{rs}, $H_{1/2}$, M_0 and a have to be chosen in a way that the scaled magnetization curve becomes as linear as possible. The program optimizes the parameters $H_{1/2}$ and a automatically using a Levenberg-Marquard algorithm for non-linear fitting. The parameters M_0 and $M_0 + M_{\mathrm{rs}}$ represent the asymptotic values of the magnetization curve. Their optimization is controlled by the user, since it was found that the optimization procedure can be very unstable with respect to these parameters. The scaled curve is represented together with a least-squares linear fitting. Deviation from the least-squares line can be minimized with an appropriate choice of M_0 and $M_0 + M_{\mathrm{rs}}$. Instead of M_0 and $M_0 + M_{\mathrm{rs}}$ CODICA uses equivalent parameters, called *relative unsaturation degrees*, defined as:

$$\begin{aligned} u_{\mathrm{U}} &= (M_0 + M_{\mathrm{rs}} - M(0))/M_{\mathrm{rs}} \\ u_{\mathrm{L}} &= (M(H_{\max}) - M_0)/M_{\mathrm{rs}} \end{aligned} \tag{7}$$

where u_{U}, u_{L} are the unsaturation degrees of the upper and lower part of $M(H^*)$, respectively. Furthermore, $M(0)$ and $M(H_{\max})$ are the initial and the final magnetization, respectively. In general, too large values of u_{U}, u_{L} produce a flattening at the left and the right end of $M^*(H^*)$, respectively. On the other hand, too small values of u_{U}, u_{L} produce a steepening of $M^*(H^*)$ at the left and right end of the scaled curve, respectively. Random deviations from the least-squares line indicate the presence of measurement noise, systematic smooth deviations indicate a divergence of the measured curve from equation (5). Best results are achieved by analyzing samples where one magnetic com-

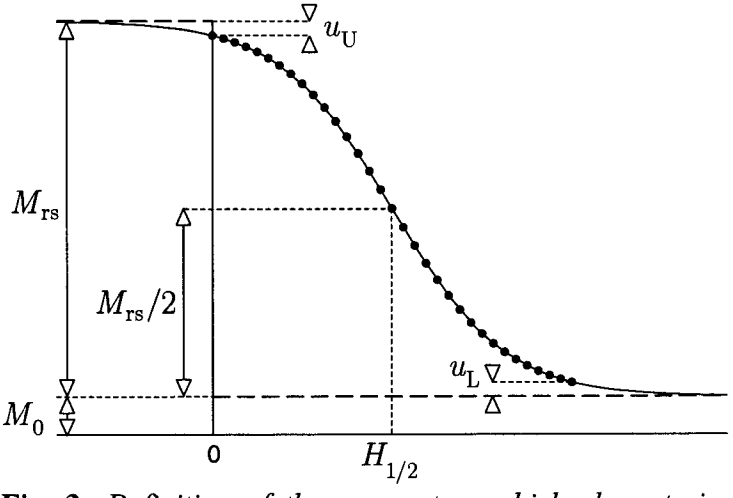

Fig. 3: *Definition of the parameters which charecterize $M(H^*)$. Measured points are indicated by dots.*

ponent is dominant or samples where different components have a wide range of overlapping coercivities. In both cases the choice of 5 independent parameters for the two scaling operations (p, M_{rs}, $H_{1/2}$, M_0 and a) is sufficient to achieve an exellent linear relationship between scaled field and scaled magnetization. In case of components with drastically different coercivity ranges (i. e. magnetite and hematite) the scaling method is less effective, but in this case the separation of the different components is less critical as well, and can be performed even directly on the measured curve.

4. *Plotting the residuals* (figure 2d)
Once the measured curve is scaled with respect to field and magnetization, the deviation of the scaled curve from the least-squares line is plotted. We will call this deviation the residuals curve. At this step, measurement errors are enormously enhanced, as it can be seen by comparing the residuals with the original measured curve.

5. *Scaling the residuals* (figure 2e)
Generally, the residuals generate a sinusoidal curve, which is more or less „quenched" at one end. As in step 2, the field axis can be rescaled with a power transformation in order to approach a quite regular sinusoidal curve. Variations of the amplitude are removed by normalizing the residuals with a mean value caculated from the first three Fourier coeffcient of the residuals curve. After these steps, the rescaled residuals curve $\varepsilon^*(H^*)$ is almost sinusoidal. Its Fourier spectrum is concentrated around a dominant wavelength (Fig. 4) so that a simple low-pass filter would easily remove the high-frequency measurement noise.

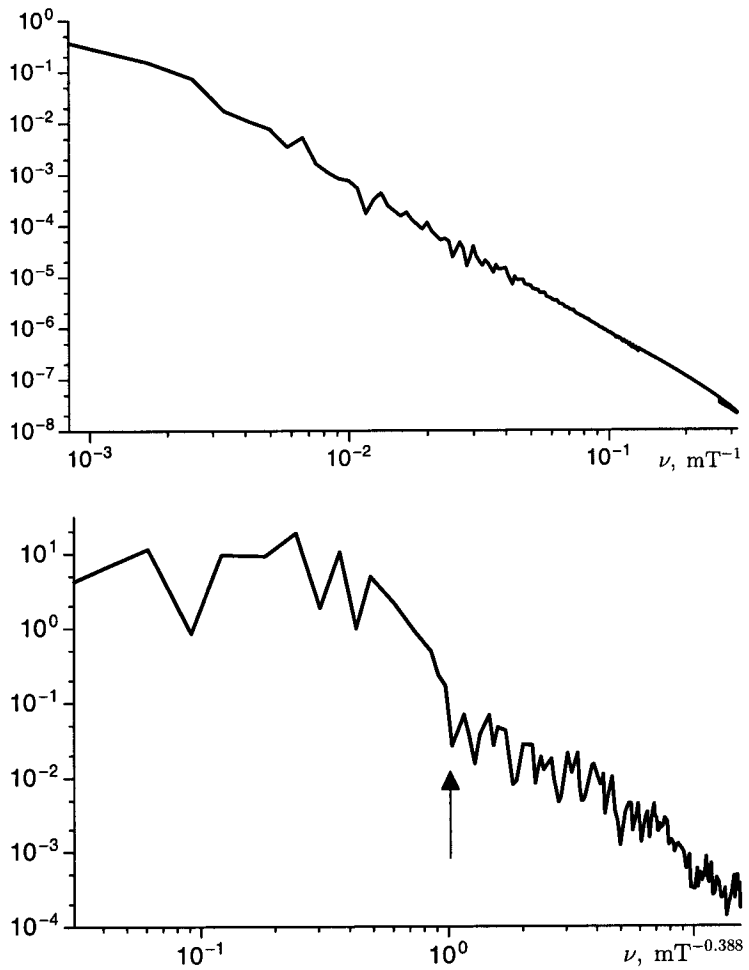

Fig. 4: *Fourier transform of the original measured curve $M(H)$ (top) and of the rescaled residuals curve $\varepsilon^*(H^*)$ (bottom). Few Fourier coefficients dominate the spectrum of $\varepsilon^*(H^*)$ and the contribution of measurement noise is evident above the frequency indicated by the arrow. Contributions of those frequencies can be removed without affecting the shape of $\varepsilon^*(H^*)$. On the other hand, high frequencies are contributing significantly to the shape of $M(H)$ and cannot be removed with a filter.*

6. *Filtering the residuals* (figure 2f)

The residuals curve is now ready to be filtered in order to remove the measurement noise. The filter applied by CODICA is a modified Butterworth low-pass filter, defined by:

$$\mathscr{L}(\nu,\nu_0,n) = \frac{1}{\left(1+\nu_0^n/\nu^n\right)^{1/2n}} \tag{8}$$

where ν is the frequency of the spectrum, ν_0 the so-called cutoff frequency, and n the order of the filter. The filter parameters ν_0 and n are chosen by the user. Details of the residuals curve with an extension smaller than $1/\nu_0$ on the rescaled field axis are filtered out. The sharpness of the filter is controlled by its order n: $n \to \infty$ gives a cutoff filter. Filters with a low order are inefficient, filters with a too high order produce undesired wiggling in the filtered curve. The filter order should be chosen so that the Fourier spectrum of the filtered curve is not sharply cutted around the cutoff frequency. The effect of the filter order on the Fourier transform is shown in Fig. 5.

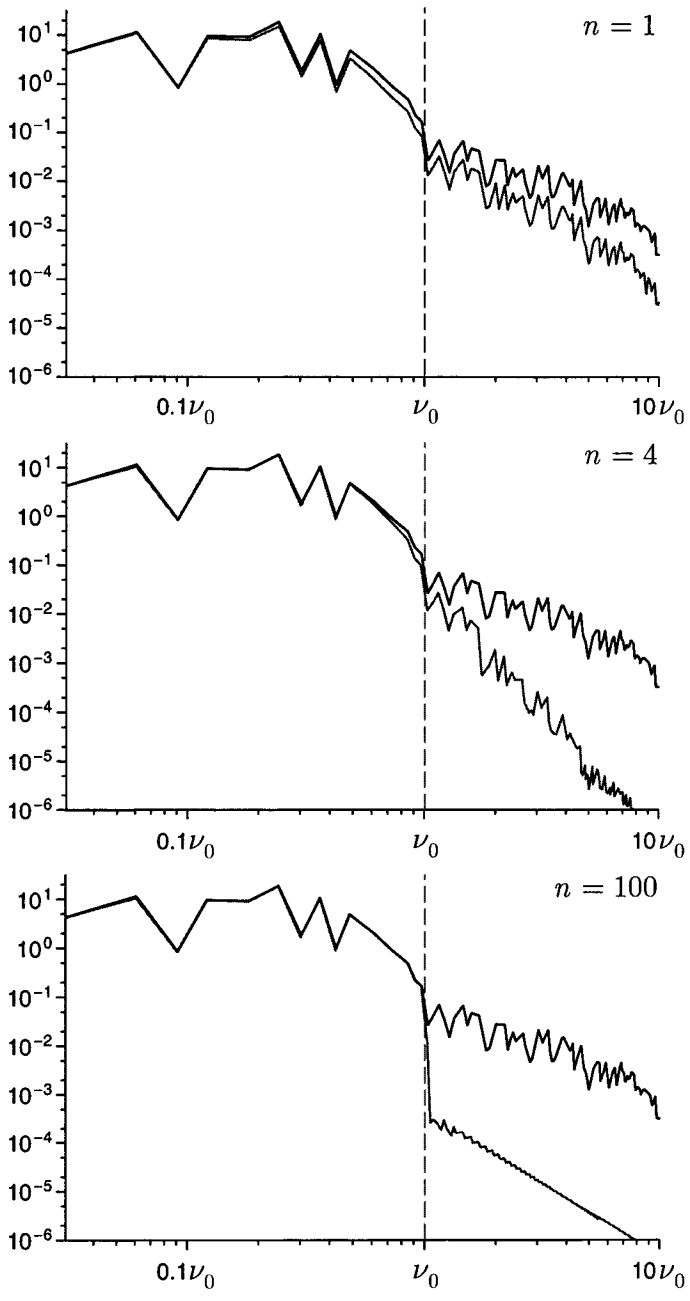

Fig. 5: *Effect of a Butterworth low-pass filter of order n on the Fourier transform of $\varepsilon^*(H^*)$ with $n = 1,4,100$ from top to bottom, and the same cutoff frequency ν_0 (indicated by a dashed line). The Fourier transform of $\varepsilon^*(H^*)$ is plotted for the unfiltered curve (black), and for the filtered curve (red). A filter of order $n = 1$ is inefficient and a filter of order $n = 100$ produces a discontinuity in the Fourier transform.*

The filter parameters should be chosen so that the measurement errors are suppressed without changing the global shape of the curve. This condition is met by choosing the smallest value of ν_0, by which the difference between the filtered and the unfiltered curve attains the same maximal am-

plitude as the estimated measurement errors. The choice of larger values of ν_0 leads to a coercivity spectrum that fits the measured curve better but still contains an unremoved noise component. The choice of smaller values of ν_0 may produce an alteration of the shape of the curve and suppress significant details.

7. *Calculating the filtered demagnetization curve* (figure 2g)
Now, the filtered residuals are converted back to the original curve by inverting steps 2 to 5 in reverse order. The result is a demagnetization curve, which is supposed to be free of measurement errors.

8. *Calculating and plotting the coercivity distribution* (figure 2h)
The coercivity distribution is now calculated as the absolute value of the filtered demagnetization curve obtained at point 7. The user can choose between a linear, a logarithmic and a power field scale to represent the results. The effect of the different field scales on the shape o a coercivity distribution is illustrated in Fig. 6.

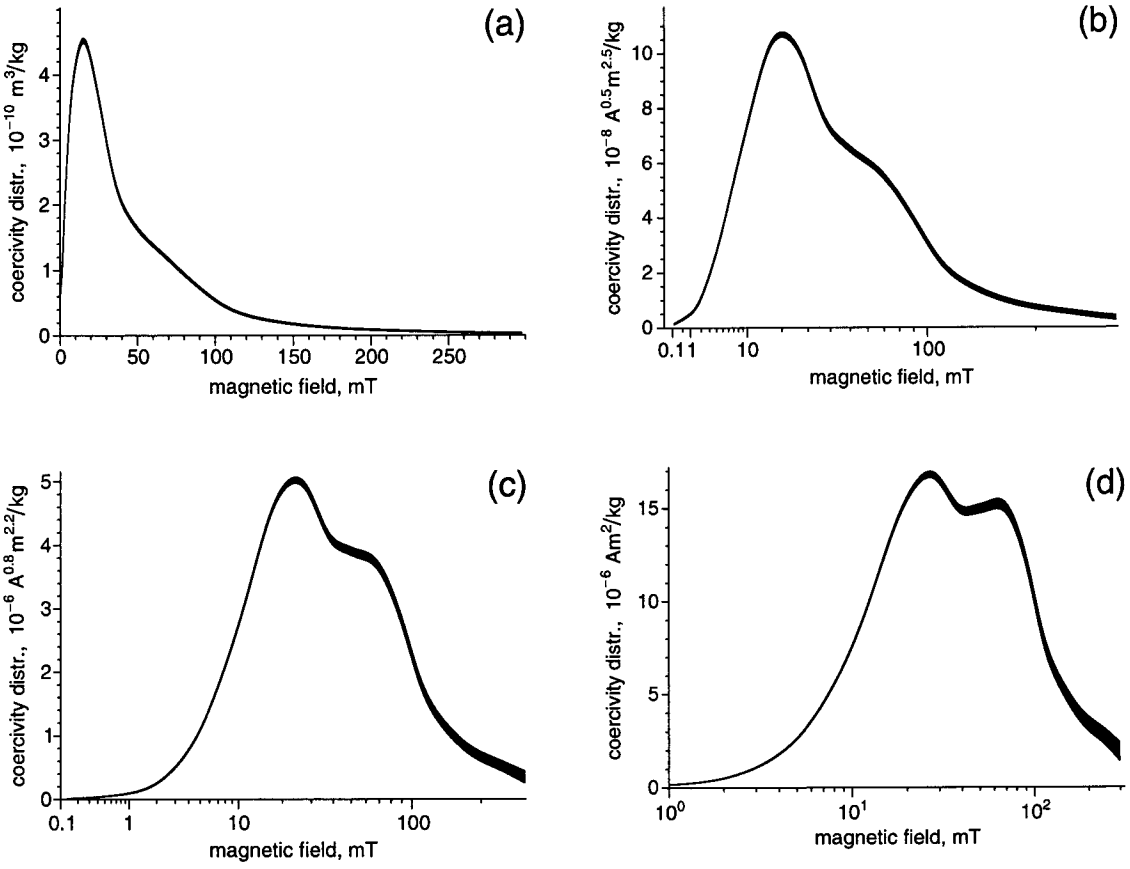

Fig. 6: *Effect of field rescaling on the shape of a coercivity distribution (sediment sample from Baldeggersee, Switzerland). Four different field scales have been chosen:* (a) *linear field scale,* (b) *power field scale according to equation (3) with exponent* $p = 0.5$, (c) *power field scale according to equation (3) with exponent* $p = 0.2$, (d) *logarithmic field scale.*

The maximum error amplitude of the coercivity distribution is estimated by CODICA by comparing the measured curve with the filtered curve. The error estimation is displayed as an error band around the plotted coercivity distribution, and can be considered as a confidence interval of the plotted data.

A program example

```
In[1]:= <<Utilities`Codica`
```

Load the program

```
Program package Codica v.2.3 for Mathematica 3.0 and later versions.
Copyright 2000-2003 by Ramon Egli. All rights reserved.
```

```
In[2]:= Codica
```

Start the program

```
Data from file
C:/users/ramon/papers/fitting/SB32-arm.dat
```

Enter file name

```
Checking double points...
```

Enter the type of measurement

```
Calculating data parameters...
```

Enter sample weight

```
Measurement curve:
```

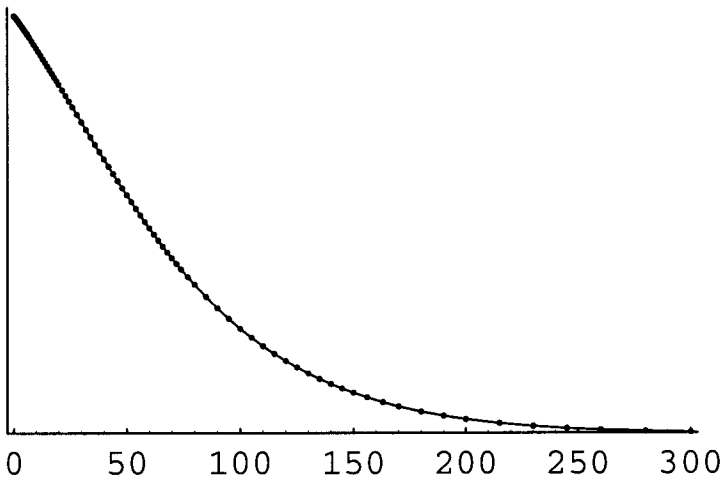


```
Measurement type: cryo6

Assumed measurement errors,
 field:         0.1 mT + 0.2%
 magnetization: 2.3e-8 emu + 0%

Measured curve with scaled field. Scaling exponent: 0.4
```

Rescale the field axis

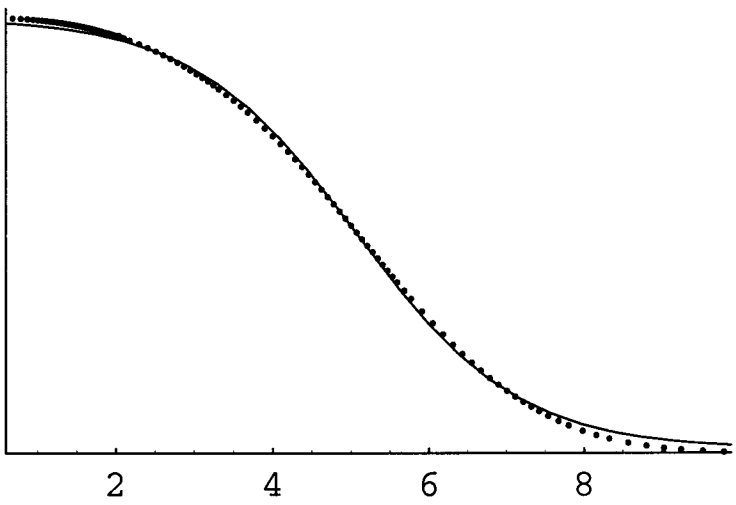

```
Iteration #1: exponent 0.4, residual 0.0001990844346492842
Iteration #2: exponent 0.373225, residual 0.00019330045337513505
Iteration #3: exponent 0.368493, residual 0.0001932552874762185
Optimized exponent: 0.368889
Measured curve with scaled field. Scaling exponent: 0.368889
```

Optimize the field axis rescaling

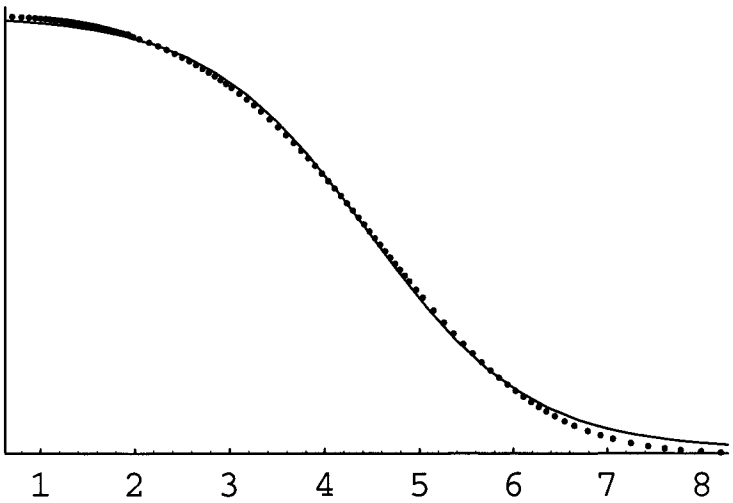


```
Estimating the measurement error...
 upper unsaturation degree: 0.00007028366343771037
 lower unsaturation degree: 0.006469552438032343
Linearized measurement curve with:
 upper unsaturation degree: 0.005
 lower unsaturation degree: 0.017
```

Linearize the measurement curve

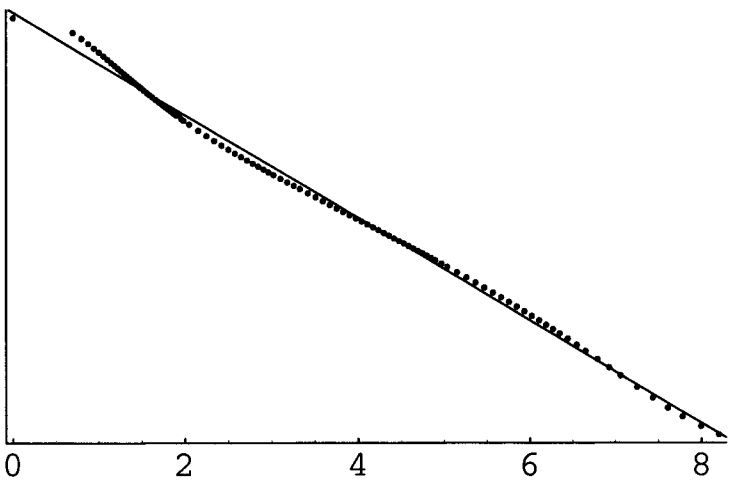

Optimize the linearization

Residuals curve (every 10th point in grey).
Measurement error margins in gray:

Calculate the residuals

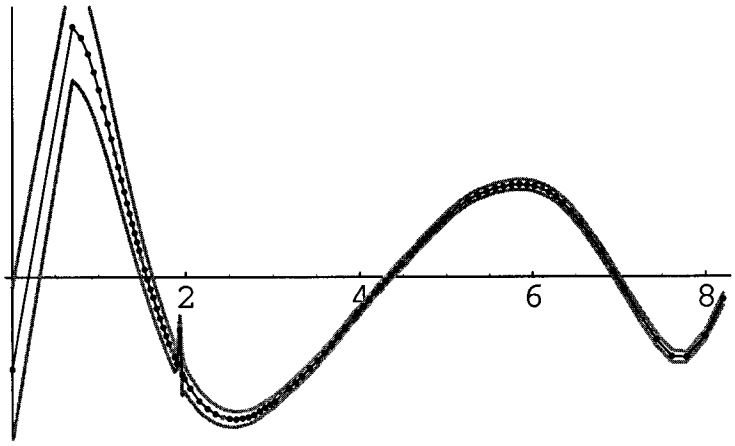

Resuduals curve with rescaled field.
Scaling exponent: 0.368889 × 1. = 0.368889

Rescale the residuals field axis

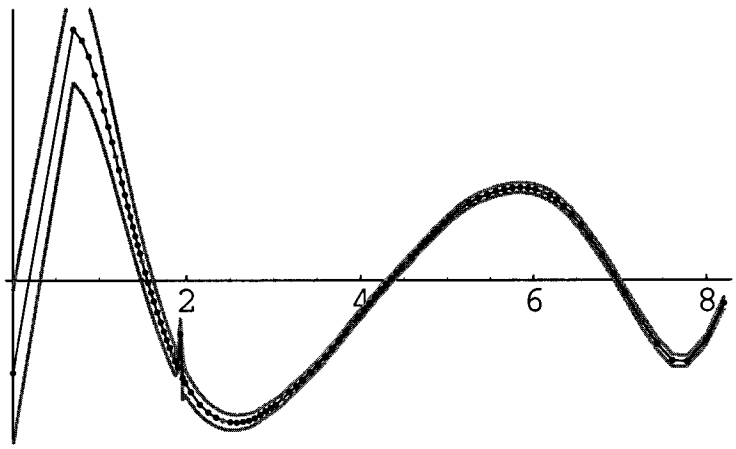

Resuduals curve with removed outlying points (in red):

Remove outlying points

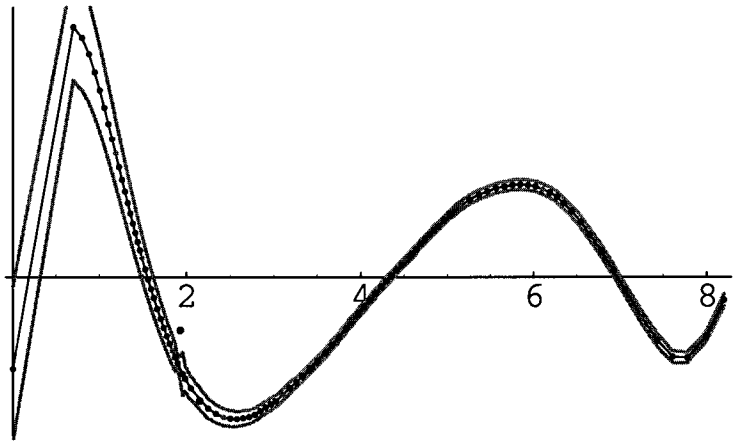

List of cancelled points (red):

Point #	field
33	5.9439
37	8.

Interpolated residuals with minimum curvature, Minimum curvature interpolation
1 interpolated point (in grey) every measured point:

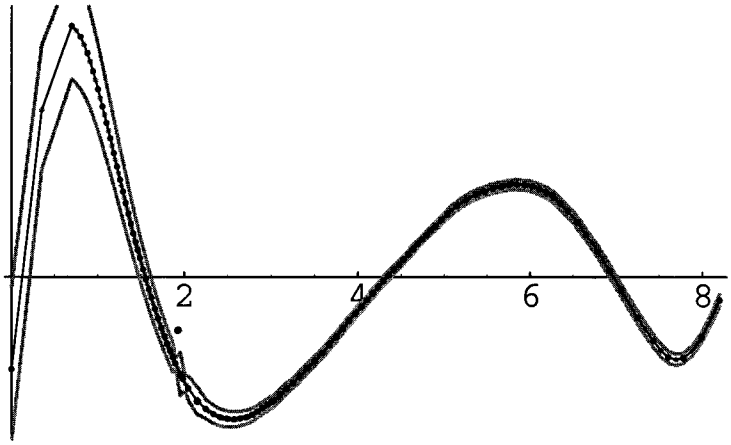

Interpolated residuals with minimum curvature, Minimum curvature interpolation
3 interpolated point (in grey) every measured point:

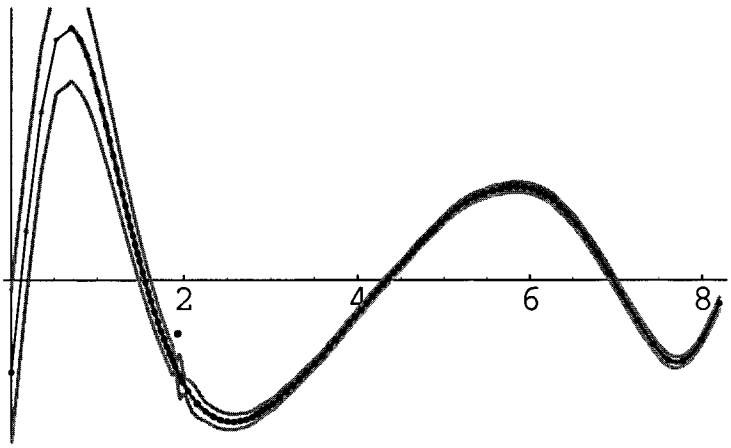

Interpolated residuals with minimum curvature, Minimum curvature interpolation
7 interpolated point (in grey) every measured point:

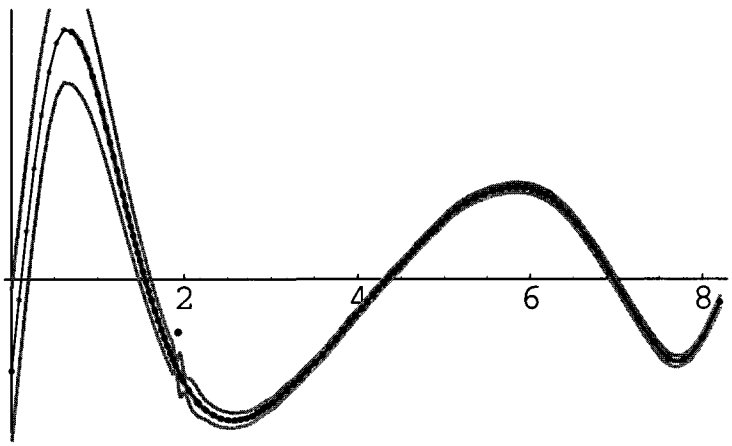

Normalize the residuals to approach a sinusoidal curve... Normalize the residuals

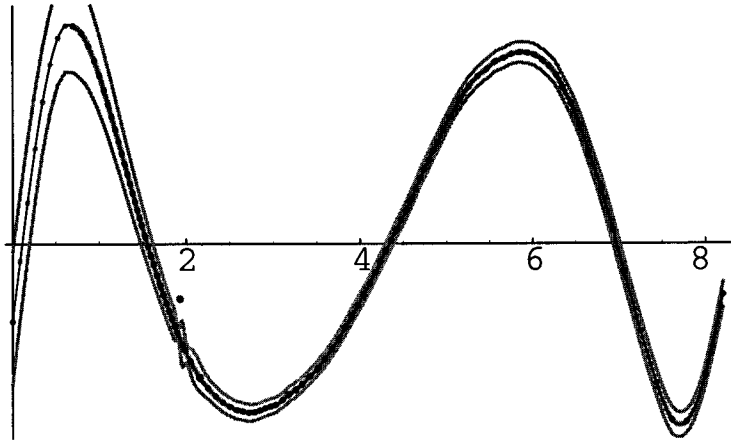

Fourier spectrum of the residuals: Fourier spectrum of the residuals

Dashed vertical lines are the lower/upper limit of the aliasing frequency.

Dashed horizontal line is the measurement noise level of the residuals.

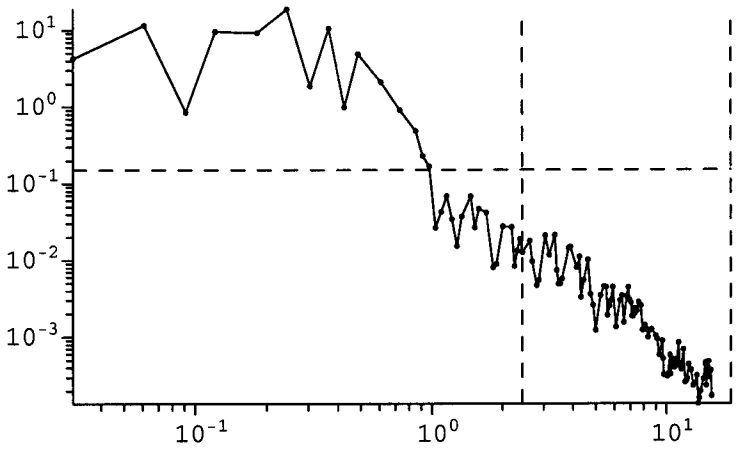

Parameters of the Butterworth low pass filter: Apply a low-pass filter to the residuals

cutoff frequency: 1

order : 4

Filtered residuals (solid line):

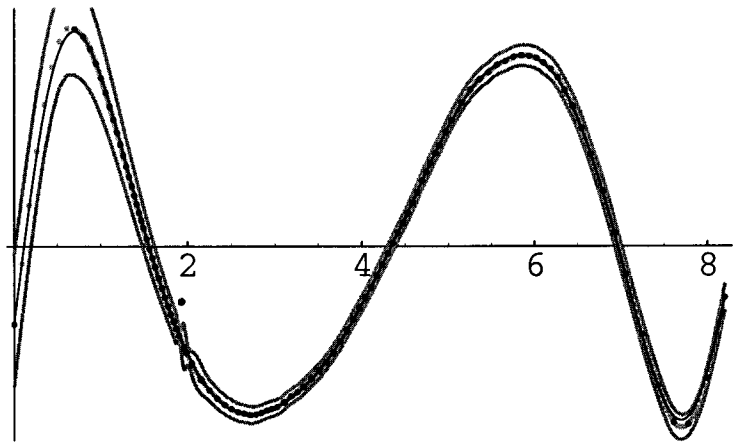

Difference between filtered and unfiltered residuals;
this curve should represent the measurement errors.

Measurement errors

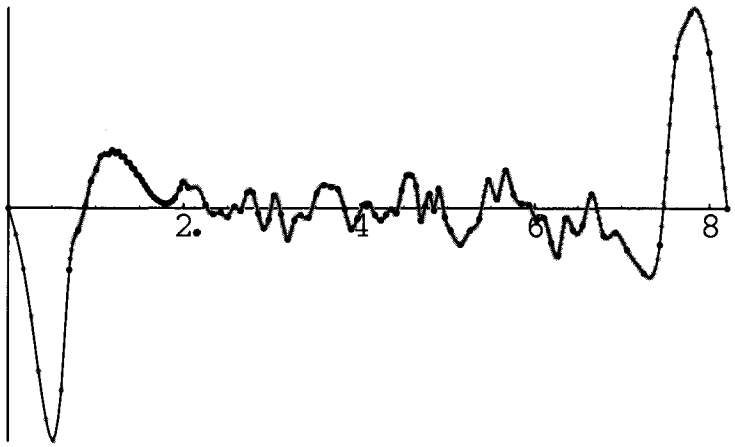

Fourier spectrum of the filtered residuals.
Dashed red line is the corner frequency of the filter:

Fourier spectrum of the filtered residuals

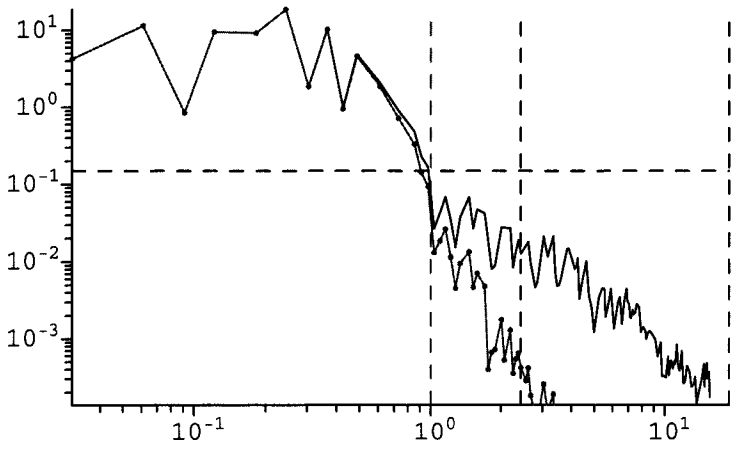

Number of independent parameters for a component analyisis: 16

Number of filtering iterations: 1

Measured points and fitted curve.

Plot the filtered measurements

Units: 10^0 mT 10^{-3} emu

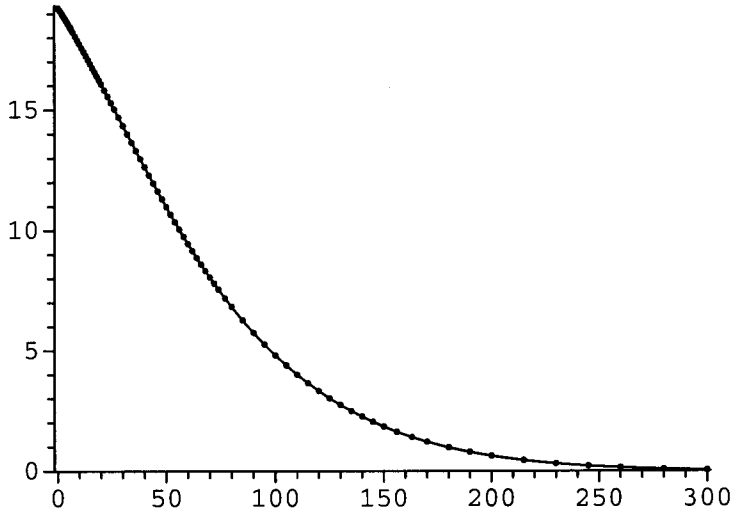

Estimating the fitting error. Please wait...

Estimated maximal absolute error of the fitted curve:

Plot the measurement errors

Units: 10^0 mT emu

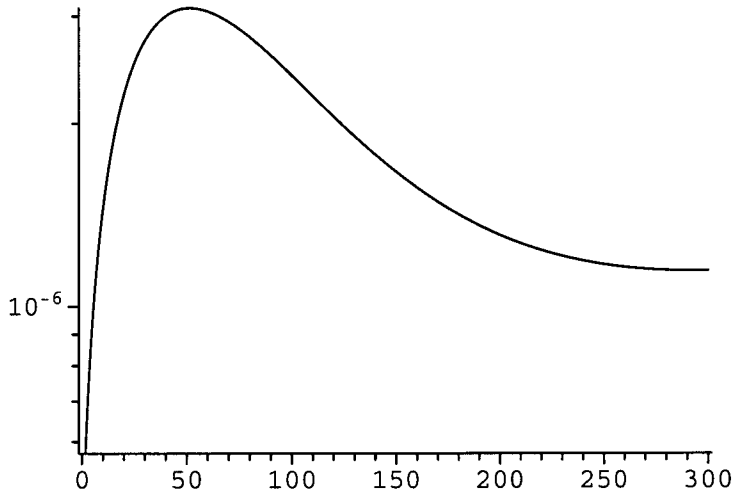

Saving the fitted measurements in file: SB32-arm.cum

Saving the fitted measurements

1. column: field in mT
2. column: magnetization in emu
3. culumn: absolute fitting error in emu

```
Estimating the spectral error. Please wait...

Spectrum with logarithmic field scale.
Dashed lines represent the lower and upper confidence limit.
Units:      mT      10^-3 emu
```

Plotting a spectrum on a log-scale

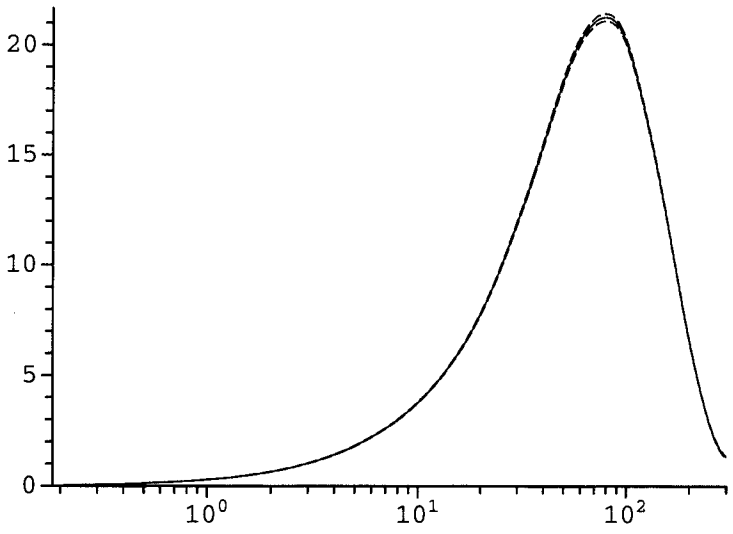


```
Estimated maximal relative error of the spectrum:
```

Relative error of a coercivity distribution

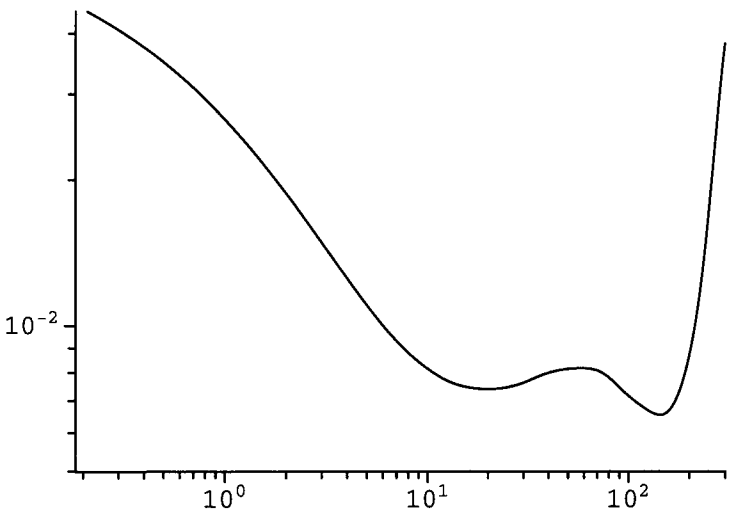


```
Saving logarithmic spectrum in file: SB32-arm.slog
 1. column: field in mT
 2. column: magnetization per field unit, in emu
 3. column: relative fitting error
```

Saving the coercivity distribution

Spectrum with linear field scale (solid line).
Dashed lines represent the lower and upper confidence limit.
Units: 10^0 mT 10^{-5} emu/mT

Plotting a spectrum on a linear scale

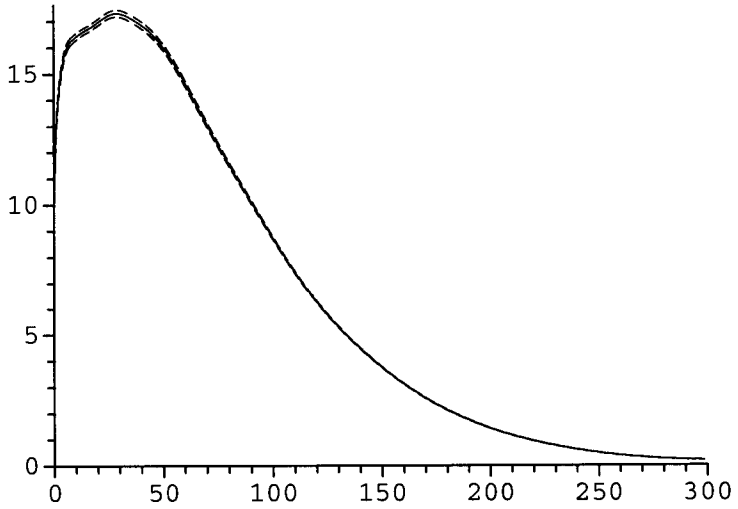

Estimated maximal relative error of the spectrum:

Relative error of a coercivity distribution

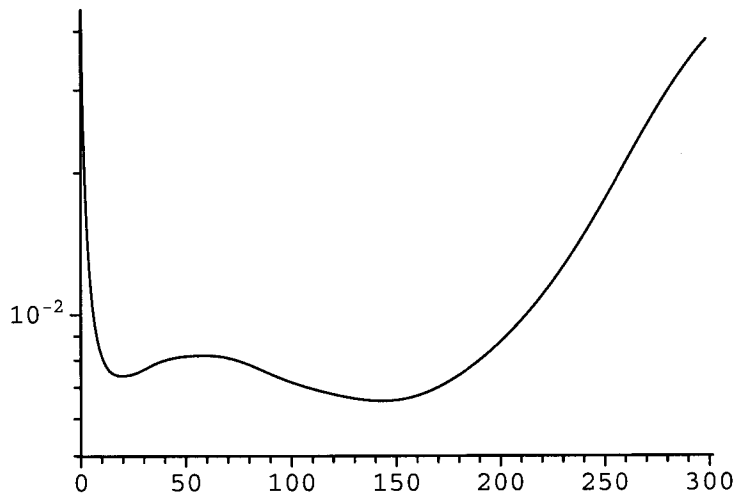

Saving a linear spectrum in file: SB32-arm.slin
1. column: field in mT
2. column: magnetization per field unit, in emu/mT
3. column: relative fitting error

Saving the coercivity distribution

Spectrum with power field scale (solid line).
Dashed lines represent the lower and upper confidence limit.
Units: mT 10^{-4} emu/mT$^{0.5}$

Plotting a spectrum on a power-scale

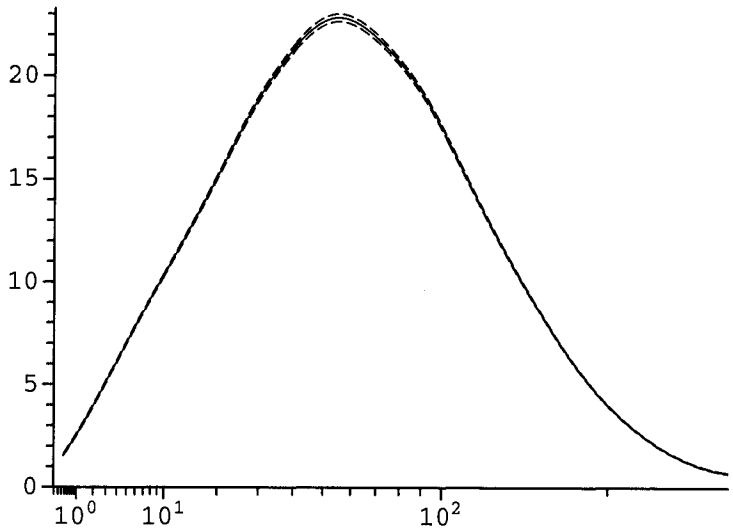

Estimated maximal relative error of the spectrum:

Relative error of a coercivity distribution

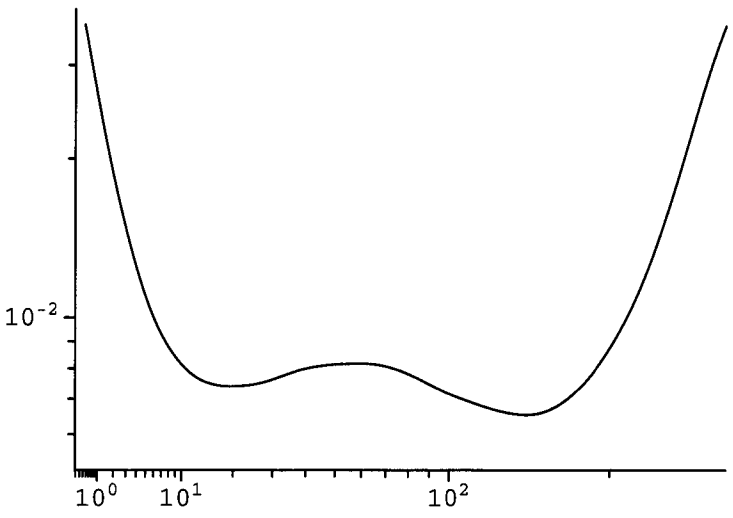

Saving a power spectrum in file: SB32-arm.spow
1. column: field in mT
2. column: magnetization per field unit, in emu/mT^0.5
3. column: relative fitting error

Saving the coercivity distribution

Installing CODICA

To install CODICA, you need to add the files `codica.m`, `codicasets` and `components.txt` to *Mathematica* v.3.0 or later running on a PC. The file `codica.m` contains the source code of CODICA and GECA, and is a so-called *Mathematica package*. The file `codicasets` contains informations about the measurement parameters (units, errors). The file `components.txt` contains informations about the component analysis results of GECA.

Copy `codica.m`, `codicasets` and `components.txt` to:

`C:/.../Programs/Wolfram Research/Mathematica/4.1/AddOns/StandardPackages/Utilities`

Cursive directories depend upon the operating system and the installed version of *Mathematica*. If you copy the files `codicasets` and `components.txt` from a CD, you have then to change the file properties by removing the read-only attributes, otherwise CODICA will not have access to these files.

Loading and running CODICA

To run CODICA, open a new *Mathematica* notebook by clicking on the *Mathematica* program icon. Type `<<Utilities`Codica`` on the input prompt *In[]* and press the keys *Shift* + *Enter* to load CODICA. On the next input prompt, type `Codica` and press the keys *Shift* + *Enter* to start CODICA. From now on, the program asks you to enter specific commands step by step. In the following, all CODICA commands are explained in order of appearance.

Back to the program

Enter the name of the data file

The prompt window on the right asks you to enter the name on the file which contains the measurement data. Type the path of the data file. You can skip intermediate directories if other files with the same name are not stored. The data file should be an ASCII file with two colums of numbers separated by spaces or tabulators. The file should not contain comment lines or text in general. The first column is the applied field, the second column is the magnetic moment or the magnetization.

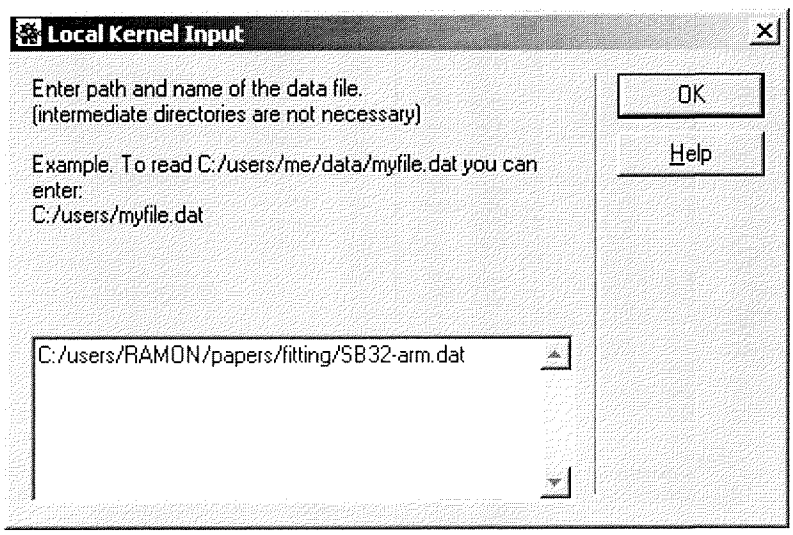

Back to the program

Enter the type of measurement

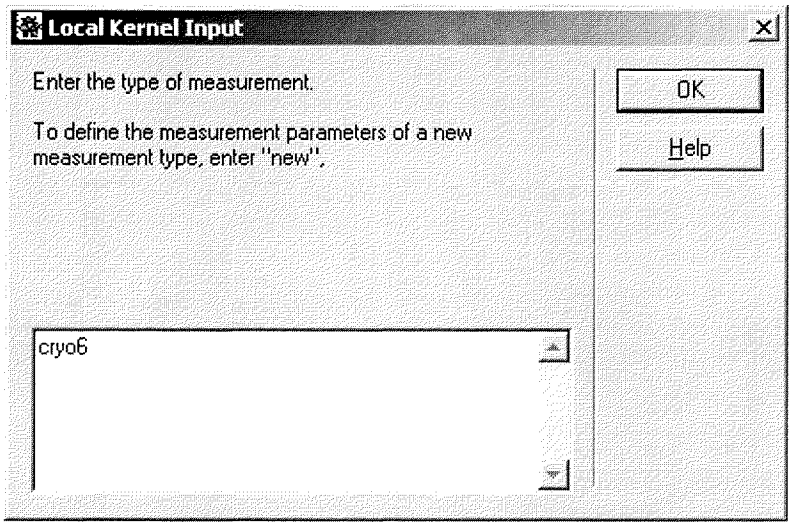

CODICA needs some informations about measurement parameters like the field and the magnetization units and the measurement errors. To avoid you entering every time these parameters, CODICA stores them in a file. The first time you analyze a given type of measurement with CODICA, you can store the measurement parameters and enter a name to recall them whenever you want. Every time you run CODICA you will be asked for the measurement parameters with the prompt window on the right. You can enter the name by which you stored them, or you can type "new" to define the parameters of a new type of measurement. Two measurement types (cryo1 and cryo6) are already stored as a default example. They refer to an automatic AF demagnetization system of 2G entreprises. Type "cryo1" denotes a single measurement, type "cryo6" denotes the mean of six identical AF demagnetization curves. You can view these parameters by opening the program file `codicasets` with a text editor. Each measurement type is a list with following parameters:

```
{"type", {"filed unit", "magnetic moment unit"},
         {absolute error of the field, relative error of the field},
         {absolute error of the measurement, relative error of the measurement}}
```

Store the measurement parameters

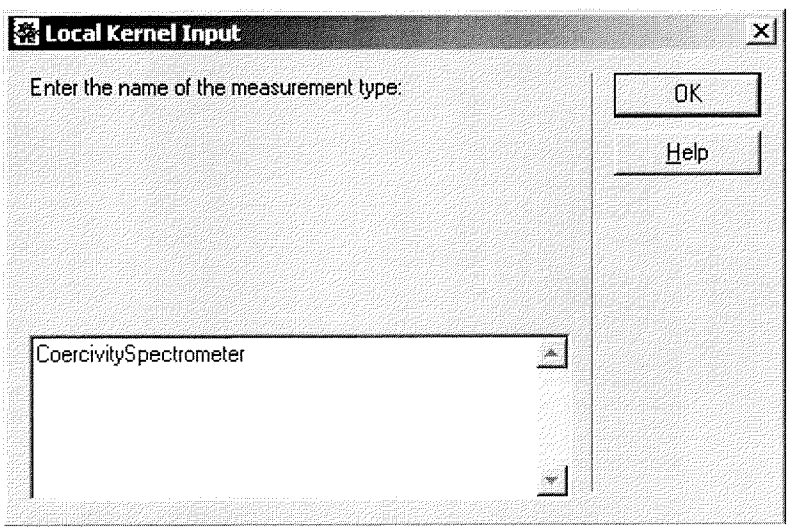

To store new measurement parameters type "new" in the prompt window for entering the type of measurement. You will be asked to enter a new name with which you can recall these measurement parameters next time. You can also change the parameters of an already defined measurement type.

Enter the appropriate units for the field and the magnetization values to store for the measurement type "CoercivitySpectrometer".

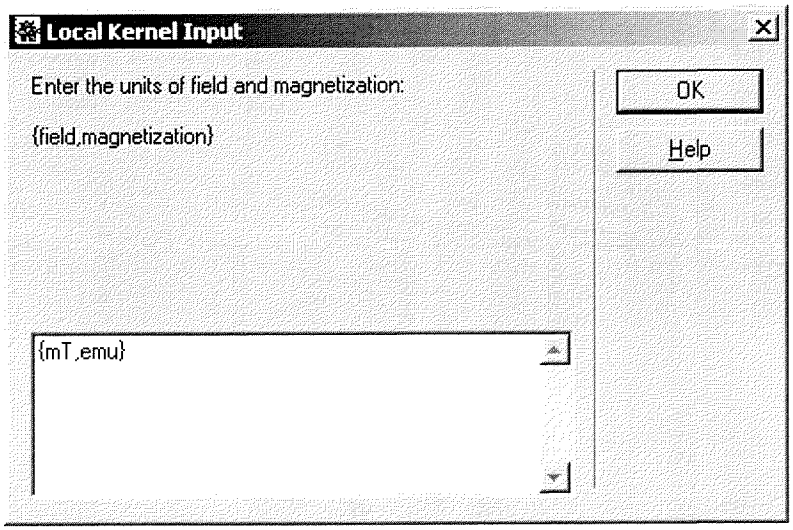

Enter the absolute and relative error of the applied field. If you do not know these parameter, enter indicative values, e.g. 1 mT for the absolute error and 1% for the relative error. The program will use these parametes to help you during the data elaboration, but *not* for estimating the error which affects the final result.

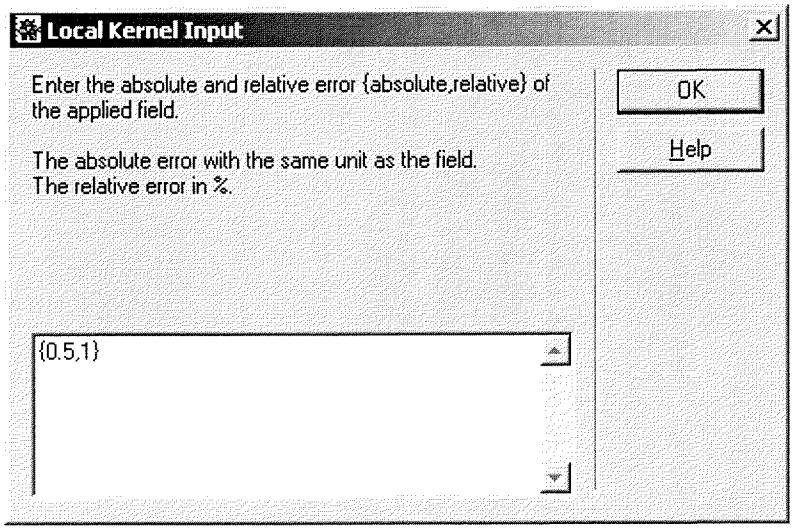

Enter the absolute and relative measurement error. If you do not know these parameter, enter indicative values, e.g. the lower detection limit of the magnetometer for the absolute error and 1% for the relative error. The program will use these parametes to help you during the data elaboration, but *not* for estimating the error which affects the final result. The measurement error refers to the measurement of a *magnetic moment*, regardless of how the measurements are normalized in the original data file.

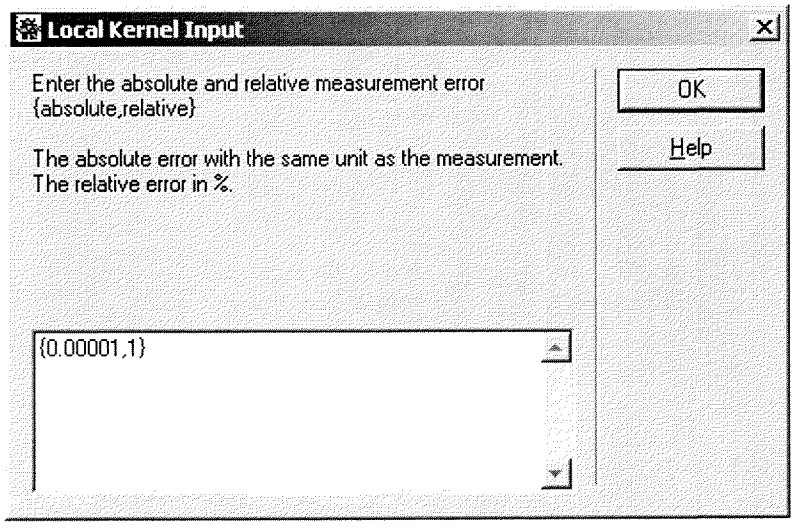

If you want to change the parameters of an existing measurement type, enter its name when you are asked. The prompt window on the right will appear. If you really want to overwrite the parameters of this measurement type, enter "y", and you will be asked for new parameters.
Back to the program

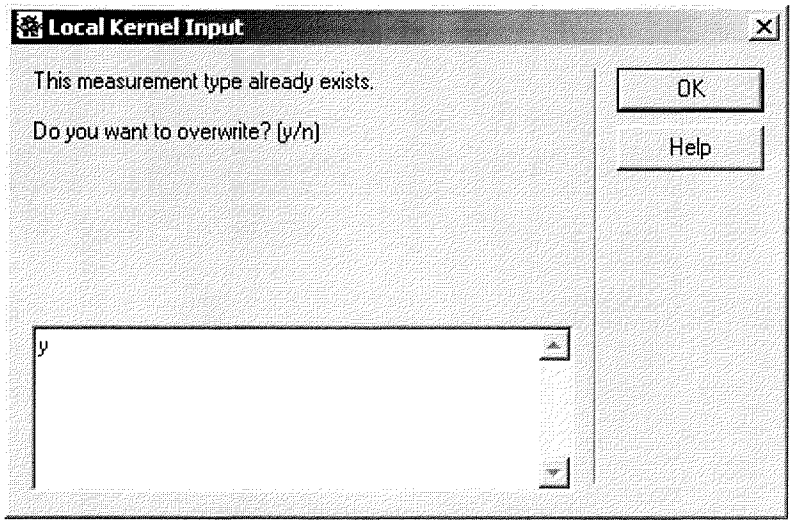

Enter the sample weight

The measurement error is related to the magnetic moment measured by the magnetometer. In general it does not have the same unit as the magnetization values of your data file. To calculate a magnetization, the measured magnetic moment is divided by a normalizing factor, generally the weight or the volume of the sample. Enter this factor in the promt window on the right to normalize the measurement error as well. If the measurement data are not normalized, type "1" in the promt window.
Back to the program

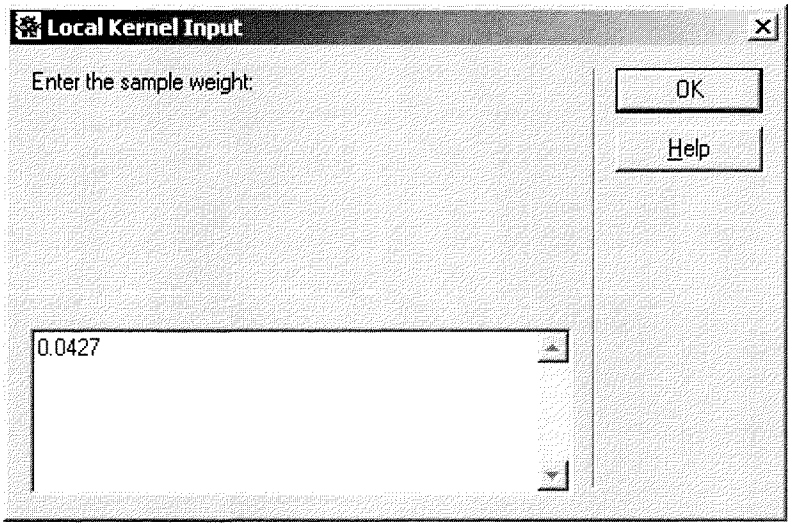

Rescale the field axis

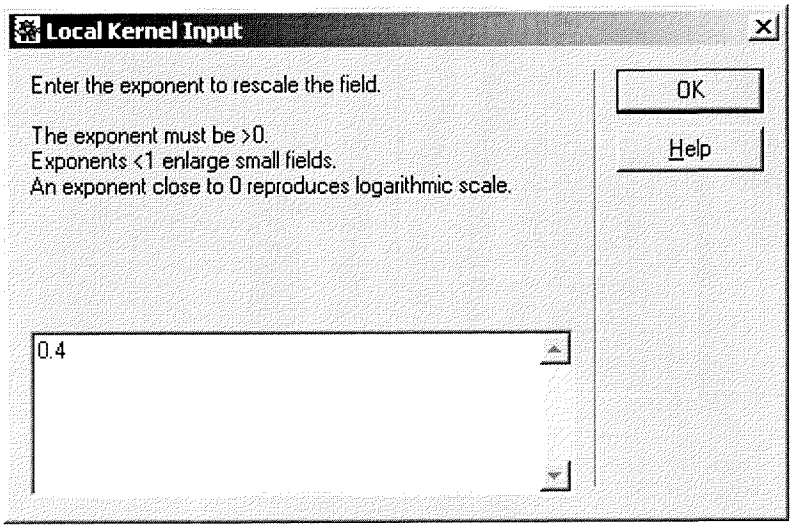

Generally,acquisition/demagnetization curves have a sigmoidal shape. However, they are not symmetrical, and are generally heavy-tailed at high fields. As a first step, CODICA makes the curve symmetrical by applying a rescaling function to the field axis. In case of lognormal coercivity distributions, the measured curve becomes symmetrical on a logarithmic field scale. CODICA uses a power transformation to rescale the field axis. The exponent p of the power transformation offers a set of intermediate field scales between the original linear scale ($p = 1$) and a logarithmic scale ($p \to 0$). An appropriate value of p can be chosen, so that the scaled curve reaches maximum symmetry. The symmetry of the curve is compared with a reference sigmoidal curve (plotted as a solid line). You can enter different values of p until you reach a satisfacting result.

Back to the program

Optimize the field axis rescaling

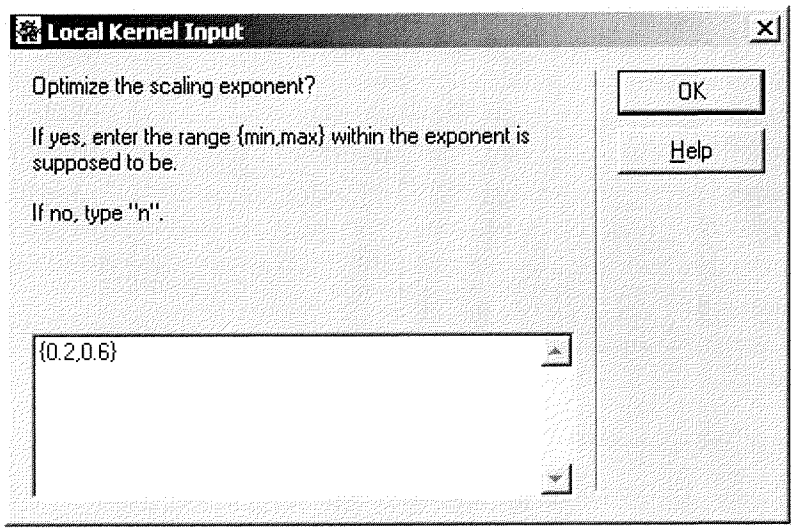

CODICA can automatically optimize the field scaling exponent p so that the scaled curve reaches a maximum symmetry. Enter the range within CODICA should perform the optimization. If the data is very noisy, the optimization may not be possible. In this case a warning message appears and you are asked to enter a scaling exponent.

Back to the program

Linearize the measurement curve

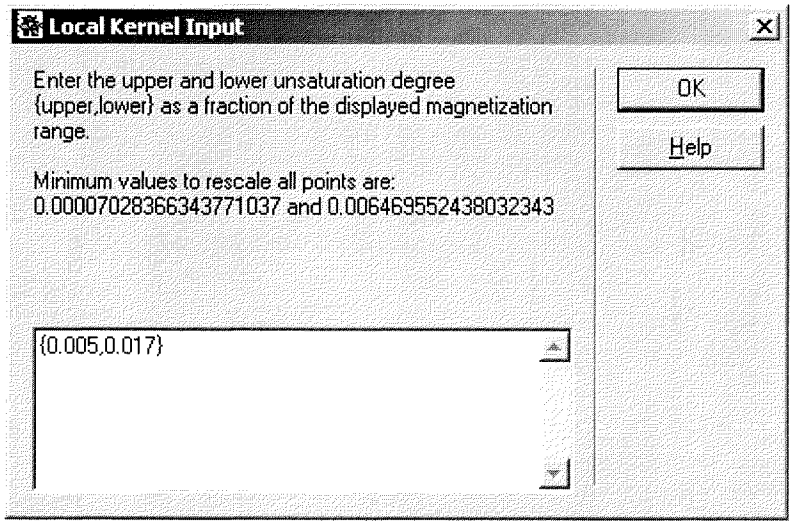

As a second step, CODICA linearizes the scaled measurements. Linearization is performed by modelling the scaled measurements with a symmetric sigmoidal curve. The shape of this curve is controlled by following parameters:
– upper asymptotic magnetization
– lower asymptotic magnetization
– median destructive field
– dispersion parameter
– vertical offset
Median destructive field, dispersion parameter and vertical offset can be easily calculated by the program. An estimation of the upper/lower asymptotic magnetization is more critical, since these values are never reached with real measurements. A good approximation is obtained by measuring a sample in the most wide field range made possible by the instrument. If the field range is not wide enough, the rescaled curve does not approach the asymptotic magnetization values. The gap between the measurements and the asymptotic magnetization values is called upper/lower unsaturation degree. The upper/lower unsaturation degree is expressed as the difference between the absolute maximum/minimum values of the measured curve and the (unknown) upper/lower asymptotic magnetization, normalized by the total magnetization of the sample. You are asked to enter these parameters in the prompt window shown above, where minimum values are suggested. You should not enter smaller values than the suggested limits, otherwise the linearization cannot be performed with all points and a warning message appears. You may enter smaller values if the measurements are very noisy.
To guess suitable values of the unsaturation degrees, start by doubling the minimum values given in the promt window (0.0002 and 0.01 in the example shown above). A linearized curve calculated with these values will be shown, together with a best-fit line. If the upper/lower unsaturation degree is too small, a steepening of the linearized curve results at the left/right end. Vice-versa, a flattening of the linearized curve results from a large unsaturation degree. You are asked to reenter the upper/lower unsaturation degree until you decide to accept the resulting linearization. This operation needs typically 4-10 trials to an experienced user.
Back to the program

Optimize the linearization (not shown)

You can let CODICA optimizing the upper/lower unsaturation degree to minimize the difference between the linearized curve and a best-fit line. In this case you will be asked to enter a range for the upper and the lower unsaturation degree: CODICA performs the optimization within these ranges. An automatic optimization is usually not needed, since the manual linearization performed by an experienced user is already very close to the optimum.
Back to the program

Calculate the residuals

The best-fit line is now subtracted from the linearized curve. The resulting curve will be called residuals curve in the following. The residuals contain both detailed informations about the shape of the acquisition/demagnetization curve, and a noise signal produced by the measurement errors. The latter is highly enhanced by the rescaling procedure, and outlyers can be easily identified. The noise-free residuals curve has generally a sinusoidal shape. The estimated maximum measurement error is plotted in the form of a band around the residuals curve. It should help the user with the further elaboration steps. The error estimation is based on the measurement parameters entered at the beginning. These parameters are not necessarily correct; nevertheless, they should provide a rough estimation of the measurement errors.
Back to the program

Rescale the field axis of the residuals

Often, the residuals curve is similar to a sinusoidal curve "stretched" on one side. An appropriate rescaling of the field axis can bring the residuals closer to a sinusoidal curve. The rescaling is based on a power transformation, exactly as the field axis rescaling of the measurement curve. You can enter a value for the rescaling exponent p until a satisfacting result is attempted. It is important that the rescaled residuals approach a sinusoidal curve. In this way, measurement errors can be filtered more efficiently.
Back to the program

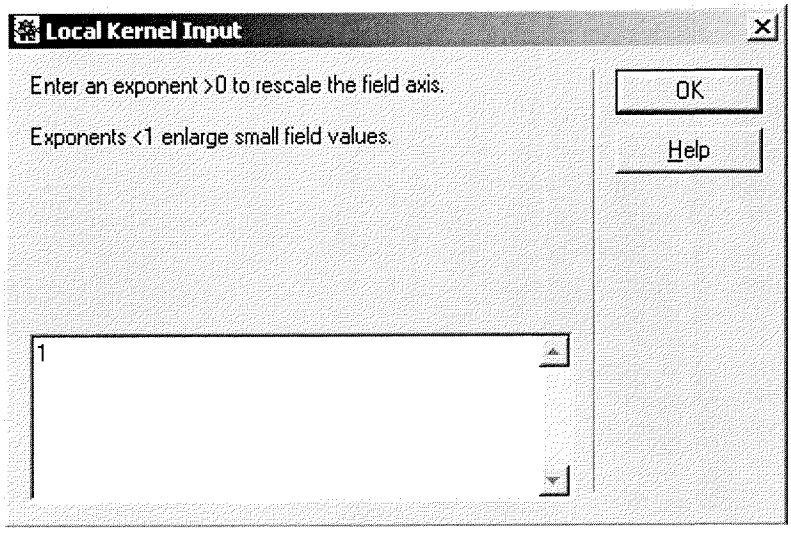

Remove outlying points

Often, the measurements contain some points affected by a particularly large error. The most evident among them can already be identified on the acquisition/demagnetization curve. Other outlyers can be recognized only in the residuals curve. Notice that the outlyers of the program example cannot be recognized on the measurement curve. In the promt window on the right you can enter a list of outlying points to be removed. You indicate each point with a number, 1 being the first point on the left. To facili-

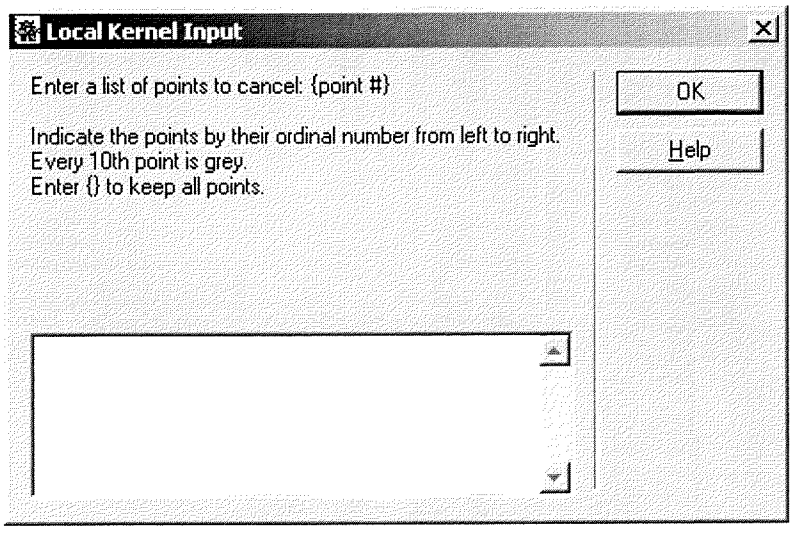

tate the identification of an outlyer, every 10^{th} point is drawn in grey. In the program example, points 33 and 37 are removed.
Back to the program

Minimum curvature interpolation

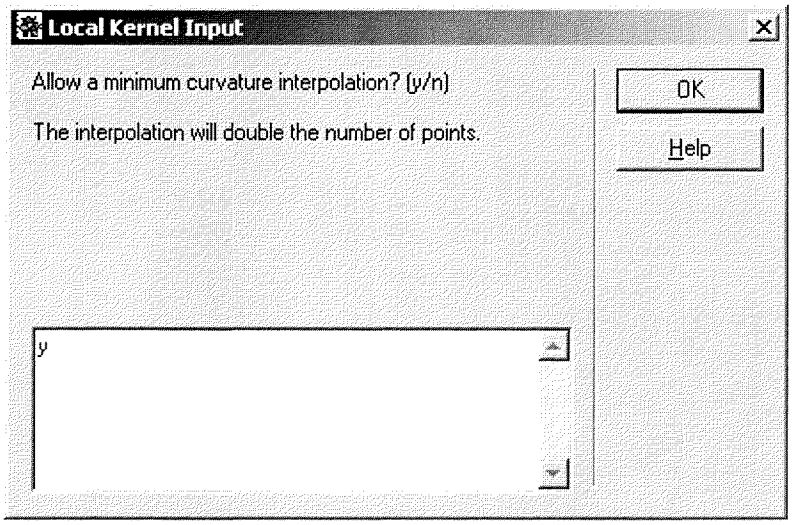

The rescaling procedure described above generally produces a "stretching" of the residuals curve on the left end, where the curve is poorly defined, as it can be seen in the program example. For further elaborations, the residuals curve needs to be interpolated and resampled at regular intervals. Interpolation is performed by adding additional points to the residuals. Each point is added in the middle of two measurements in a way that minimizes the curvature of the residuals. You can repeat this operations until the residuals curve looks smooth. Generally, minimum curvature interpolation is performed one to three times. It is important to know that minimum curvature interpolation, as any other interpolation method, does not add any information to the original curve, and is performed for numerical reasons only. You should avoid minimum curvature interpolation if the residual curve is dominated by measurement errors and has an irregular aspect.
Back to the program

Normalize the residuals

Generally, at this stage the residuals curve is quite similar to a sinusoidal curve. However, the amplitude of the residual curve is not constant over the entire field range. Amplitude variations are removed by normalizing the residuals with a mean value caculated with the first three Fourier coefficients of the residuals curve. After this correction, the noise-free component of the residuals should be almost equivalent to a sinusoidal curve. In this way, measurement errors can be filtered very efficiently.
Back to the program

Fourier spectrum of the residuals

A Fourier spectrum of the residuals is calculated with FFT. To avoid windowing effects, the residuals curve is previously continuated on the left and right side, whereby continuity is guaranteed up to the second derivative over the entire range. On the Fourier transform, the minimum and maximum aliasing frequencies are highlighted with dashed lines. The minimum/maximum aliasing frequencies are calculated as the reciprocal of the maximum/minimum separation between the measurement points of the residual curve. Additional points generated with a minimum curvature interpolation are not considered. Frequencies smaller than the minimum aliasing frequency carry informations about the entire range of the residuals curve. The frequencies between the minimum and the maximum aliasing frequency carry informations only about some parts of the residuals curve. Finally, frequen-

cies larger than the maximum aliasing frequency do not carry *any* real information about the residuals, and have to be considered as interpolation artefacts. The noise content of the residuals is indicated by a horizontal dashed line, whereby a white noise is assumed, whose amplitude is calculated from the measurement parameters entered at the beginning. Fourier coefficient below the noise limit are dominated by the measurement errors. Notice that the calculated noise content is not necessarily correct, nevertheless, it should provide a rough estimation of the measurement errors.
Back to the program

Apply a low-pass filter to the residuals

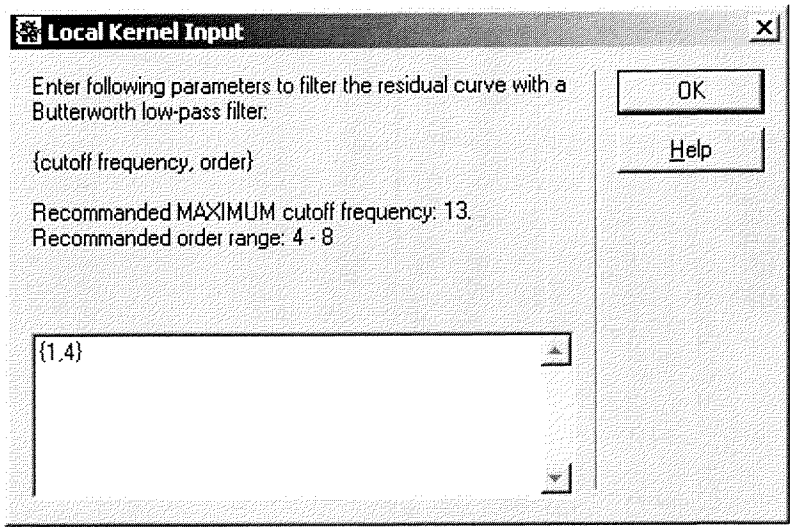

Measurement errors that contribute to the residuals with a white noise signal can be removed with a low-pass filter. A Butterworth low pass filter is used for this porpouse. You are asked to enter the parameters of this filter, e. g. the cutoff frequency and the order. The cutoff frequency should be chosen *below* the minimum aliasing frequency. If the estimate of the measurement errors given with the measurement parameters is correct, you should identify the cutoff frequency with the frequency at which the Fourier spectrum of the residuals crosses the horizontal dashed line which indicates the amplitude of the measurement errors in the last plot. The sharpness of the Butteworth filter is controlled by its order. Filters with a low order are inefficient, filters with a too high order produce undesired wiggling in the filtered curve. The filter order should be chosen so that the Fourier spectrum of the filtered curve is not sharply cutted around the cutoff frequency. Click here to see correct and incorrect filtering examples. The filtered residuals (solid line) are plotted together with the unfiltered residuals (dots). The filtered residuals should be compatible with the error margin defined by a gray band around the measured points.
Back to the program

Measurement errors

Measurement errors are plotted as the difference between the low-pass filtered and the unfiltered residuals. If the parameters of the low-pass filter were correctly chosen, the measurement errors have a cahotic appearance along the entire range. These measurement errors are used for the final error estimation performed by CODICA, regardless of the values given as measurement parameters. You can use the final error estimation performed by CODICA to reenter a better estimation of the measurement errors in the measurement parameters.
Back to the program

Fourier spectrum of the filtered residuals

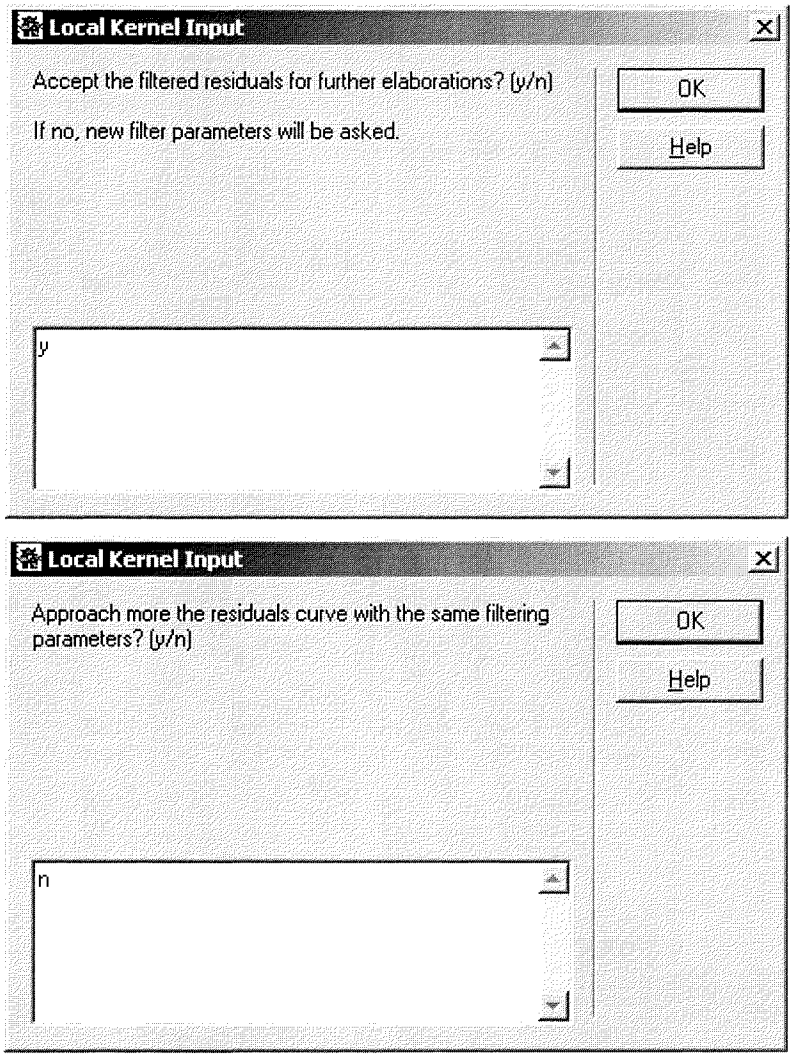

The Fourier transform of the filtered residuals (red) is plotted together with the Fourier spectrum of the unfiltered residuals (black). A dashed line indicates the cutoff frequency of the low-pass filter. The Fourier spectrum of the filtered residuals should not show a sharp drop around the cutoff frequency, otherwise the chosen low-pass filter order was too high. Click here to see Fourier transforms of correctly and incorrectly filtered residuals. The number of Fourier coefficients (red points) below the cutoff frequency, divided by five, is a good indicator for the maximum number of magnetic components which can be inferred in the resulting coercivity distribution. In the program example, there are 16 Fourier coefficients below the cutoff frequency. If the coercivity distribution of each magnetic component is described by 5 parameters (amplitude, mean, standard deviation, skewness and kurtosis), the 16 coefficients are determined by a maximum of 3 magnetic components. The atmospheric particulate sample measured for this example contains two magnetic components: natural dust and motor vehicles combustion products. If you are satisfied with the results of the filtered residual, you can accept them for further calculations. Otherwise you can reenter the low-pass filter parameters and repeat the filtering procedure. If you are not able to remove the measurement errors in a satisfactory way by choosing an appropriate cutoff frequency, you can tell CODICA to low-pass filter the resulting measurement errors curve and add it to the filtered residuals. In this way you can fit the measured residuals with a kind of fractal technique which may give better results for the particular case of a residuals curve which differs strongly from a sinuoidal. This should never occur for measurements of natural samples.

Back to the program

Plot the filtered measurements and save them in a file

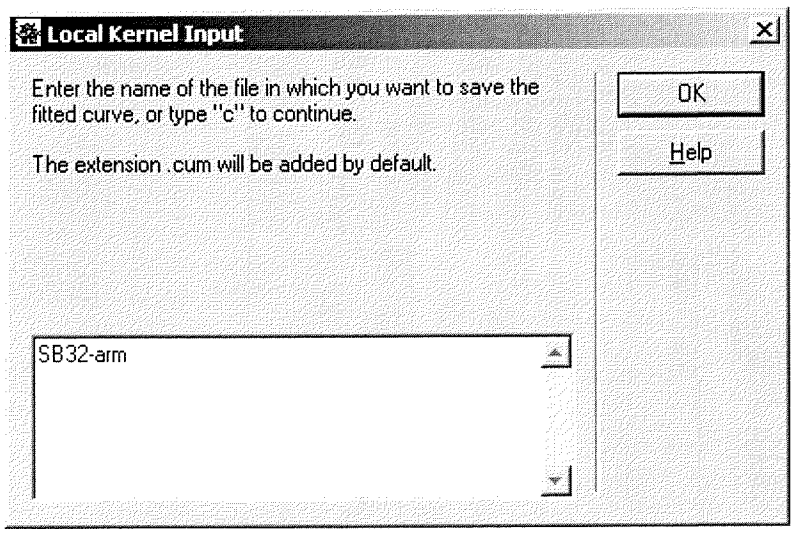

At this point, a filtered measurement curve is calculated from the filtered residuals by inverting all rescaling steps described above. The measurement errors are calculated from the difference between filtered and unfiltered residuals, and are displayed on a separate plot. You can save the result in an ASCII file with three columns. The first column contains the applied field, the second column contains the magnetization and the third column contrains the estimated absolute measurement error.

Back to the program

Plot the coercivity distribution on different field scales

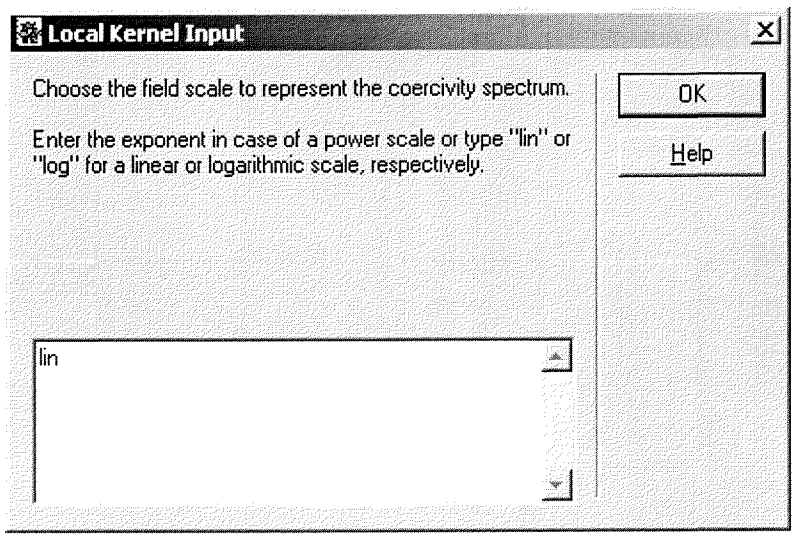

CODICA calculates the coercivity distribution by numerical differentiation of the filtered measurements. You can choose between a linear field scale, a logarithmic field scale and a power field scale. The coercivity distribution is plotted on the requested scale (solid line), together with the confidence limits given by the estimated measurement errors (dashed lines). The maximal relative error affecting the calculated coercivity distribution is displayed on a separated plot. You can save the result on a ASCII file with three colums. The first column contains the applied field, the second column contains the values of the coercivity distribution and the third column contains the estimated relative error of the coercivity distribution.

Back to the program

Cautionary note

CODICA 2.3 has been tested more than 1000 times with measurements of various artificial and natural samples and the most different combinations of initial parameters. Nevertheless, there is a remote possibility that particular uncommon or noisy data or parameter sets will produce evaluation problems. In this case, blue-written warning messages appear on the *Mathematica* front-end. If more than one of these messages is displayed, you may force-quit the Kernel of *Mathematica* as follows: in the top menu bar choose Kernel → Quit Kernel → Local. You can also exit from CODICA at any time just by typing "abort" in any input prompt window.
In case of problems, write to the author (Ramon Egli) at the address given in the `install.txt` file of the installation packet or at the beginning of the source code file `Codica.m`. Please save and send a copy of the Mathematica session you were using when the problem arised, together with the data file you analyzed with CODICA.

Reference

Egli, R., Analysis of the field dependence of remanent magnetization curves, *J. Geophys. Res.*, *102*, doi 10.1029/2002JB002023, 2003.

GECA 1.1

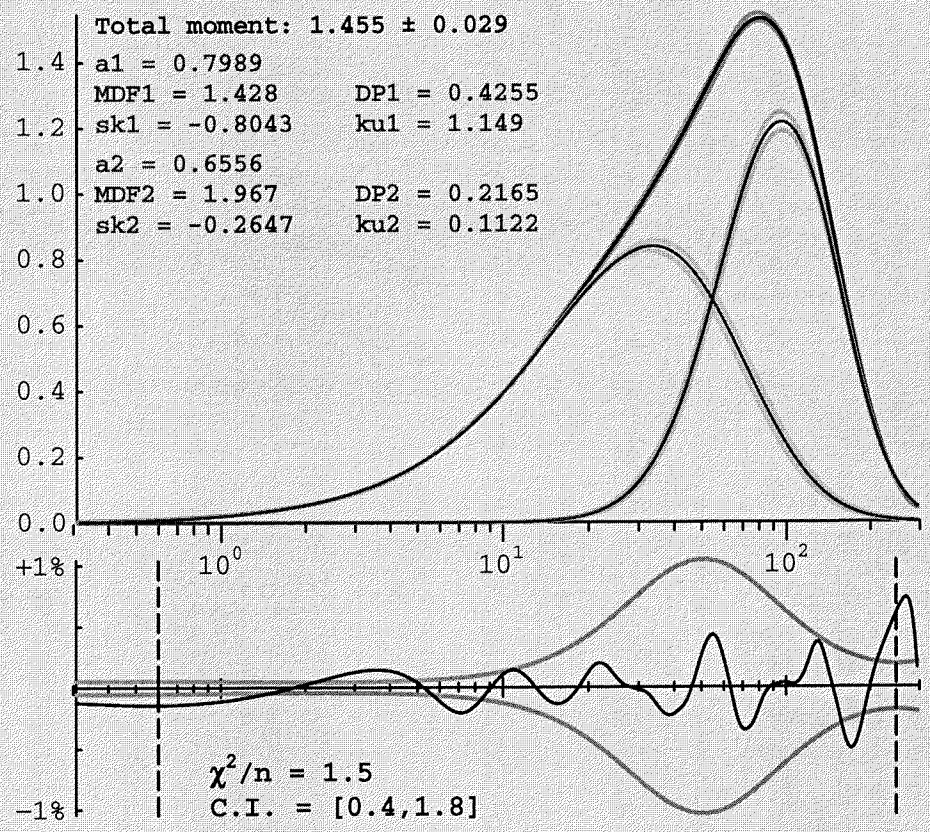

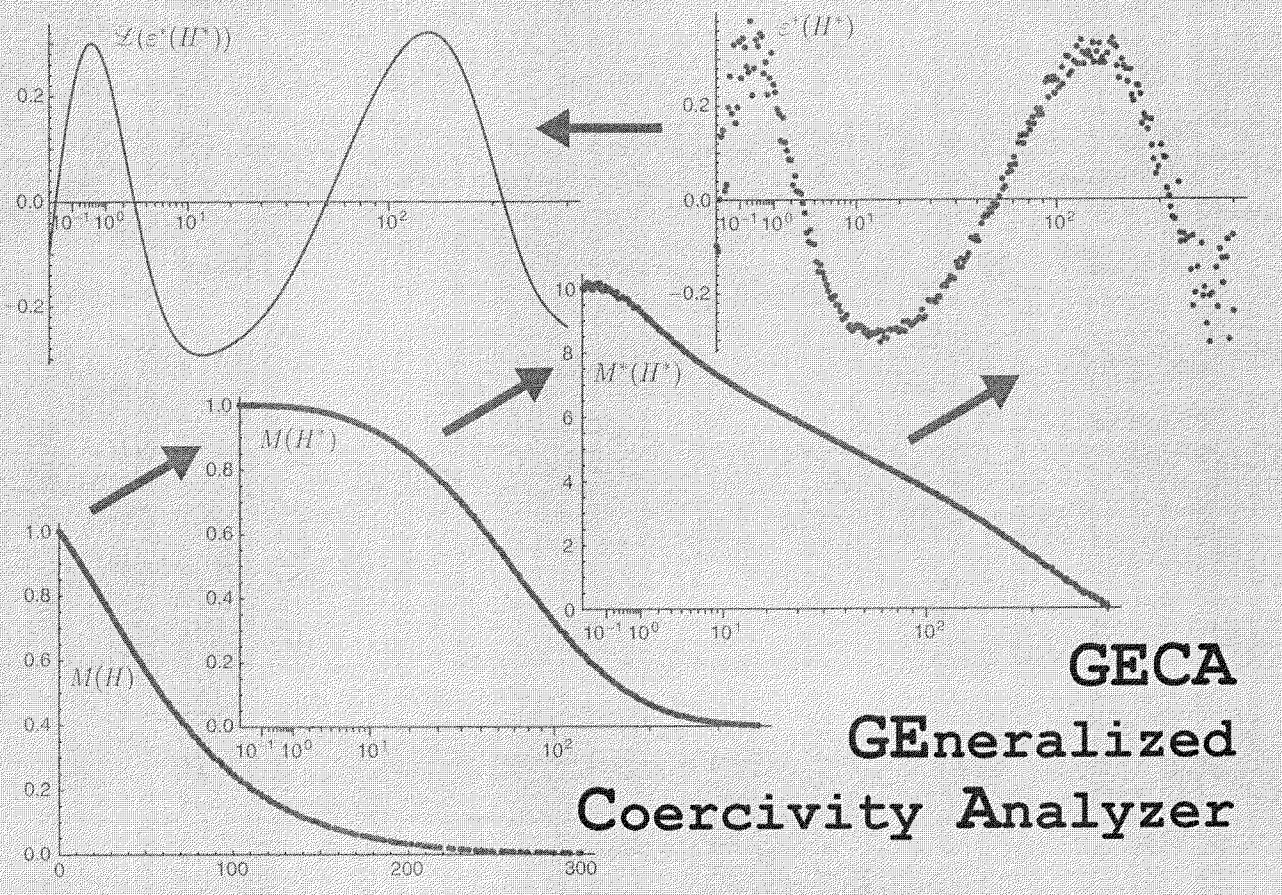

GECA

GEneralized

Coercivity Analyzer

Introduction

The program GECA (GEneralized Coercivity Analyzer) is part of the package CODICA. GECA performs a component analysis based on special generalized functions which can fit the coercivity distributions of natural and artificial magnetic components particularly well. It also performs a Pearson's χ^2 goodness of fit test to evaluate the number of functions required to model a coercivity distribution. Finally, GECA performs an error estimation and calculate the cofindence limits for each model parameter.
Read carefully this manual to learn about GECA and take full advantage from the different possibilities offered by the program to perform a component analysis and verify its significance. This manual contains a theoretical part, which gives you the background to understend the basic ideas of GECA, and a practical part, which guides you through each step of the program. You can practice with the examples delivered together with this program. CODICA is designed to work optimally on coercivity distributions calculated with CODICA and stored in files with extention `.slog`.
Click on the following topics to see the contents of this manual:

Theoretical background: coercivity distributions

A group of magnetic grains with similar chemical and physical properties, distributed around characteristc values, is called a *magnetic component*. Examples of magnetic components are pedogenic magnetite (nanometric magnetite perticles with a wide grain size distribution), and magnetosomes (prismatic magnetite with a very narrow grain size distribution between 40 nm and 80 nm). Magnetic components have a simple-shaped, unimodal distribution of coercivities. Commonly, the coercivity distribution of a single magnetic component is modelled with a logarithmic Gaussian function:

$$G(x,\mu,\sigma) = \frac{1}{\sqrt{2\pi}\sigma x}\exp\left[-\frac{\log^2(x/\mu)}{2\sigma^2}\right] \tag{1}$$

In the literature, x is identified with the magnetic field H, μ is the *median destructive or acquisition field* $H_{1/2}$, called also MDF and MAD respectively, and σ the *dispersion parameter* DP. However, not all coercivity distributions can be modelled appropriately with (1). Experimental and theoretical coercivity distributions of single components are better described by distribution functions with four parameters. The two additional parameters control the skewness and the squareness of the distribution.

The coercivity distribution $f(H)$ of a mixture of different magnetic components may be considered as a linear combination of the coercivity distributions of the single components:

$$f(H) = \sum_{i=1}^{n} c_i M_{ri} f_i(H \mid \theta_i) \tag{2}$$

where c_i and M_{ri} are the concentration and the saturated magnetization of the *i*-th component respectively, and $f_i(H \mid \theta_i)$ is the corresponding coercivity distribution with the parameters $\theta_i = (\theta_{i1},\ldots,\theta_{ik})$. Equation (2) is called a *finite mixture model*, and $f_i(H \mid \theta_i)$ are the so-called *end members*. Equation (2) assumes that the magnetization of all components adds linearly (*linear additivity*). This assumption does not hold in case of magnetic interactions between the magnetic grains of different components. However, magnetic interactions between different components are not likely to occur in natural samples, since each component is expected to have a different origin and to hold different places within a nonmagnetic matrix. On the other hand, magnetic interactions within the same component are possible, but they do not affect the linear additivity law.

Coercivity distributions of single magnetic components are described by *probability density functions* (PDF). The shape of a PDF is controlled by a set of *distribution centers* μ_n with related *dispersion parameters* σ_n, with $n \in \mathbb{N}$. Special cases are given when $n = 1$ (μ_1 is the median, σ_1 the mean deviation), $n = 2$ (μ_2 is the mean, σ_2 the standard deviation), and $n \to \infty$ (μ_∞ is the mid-range and σ_∞ the half-range). The *dispersion parameter* DP corresponds to σ_2 on a logarithmic field scale. The symmetry of a PDF is described by the *coefficient of skewness* s, where

$s = \sigma_3^3/\sigma_2^3$. Symmetric distributions are characterized by $s = 0$ and $\mu_n = \mu_2$. The curvature of a PDF is described by the *coefficient of excess kurtosis* k, where $k = \sigma_4^4/\sigma_2^4 - 3$. The Gaussian PDF is characterized by $k = 0$.

The description of non-Gaussian PDF involves the use of functions with more than two independent parameters. It is of great advantage if such functions maintain the general properties of a Gauss PDF: the n-th derivative should exist over $\mathbb{R}$ and $\sigma_n < \infty$ for all values of $n \in \mathbb{N}$. Furthermore, the Gaussian PDF should be a particular case of such functions. A good candidate is the *generalized Gaussian distribution GG*, known also as the *general error distribution*. The Gaussian PDF is a special case of *GG* distirbutions. Other special cases are the Laplace distribution and the box distribution. The *GG* distribution is symmetric: $s = 0$. In GECA, a particular set of *skewed generalized Gaussian distributions*, called SGG, is used to model single components. A SGG function is given by:

$$SGG(x,\mu,\sigma,q,p) = \frac{1}{2^{1+1/p}\sigma\,\Gamma(1+1/p)} \frac{\left|qe^{qx^*} + q^{-1}e^{x^*/q}\right|}{e^{qx^*} + e^{x^*/q}} \exp\left[-\frac{1}{2}\left|\ln\left(\frac{e^{qx^*} + e^{x^*/q}}{2}\right)\right|^p\right] \tag{3}$$

with $x^* = (x-\mu)/\sigma$, $x = \log H$, and $0 < |q| \leq 1$. The *GG* distribution is a special case of (3) for $q = 1$, and the Gauss distribution is a special case of (3) with $q = 1$ and $p = 2$. The relation between the distribution parameters μ, σ, q, p and some statistical properties is given in Table 1.

Distribution properties	**Definition**	**Relation with the distribution parameters**	**Comments**
Median $x_{x/2}$	$\int_{-\infty}^{x_{1/2}} f(x)\,\mathrm{d}x = \frac{1}{2}$	$x_{1/2} = \mu$	$x_{x/2}$ is also called MDF or MAF
Mean μ_2	$\mu_2 = \int_{-\infty}^{+\infty} f(x)\,x\,\mathrm{d}x$	$\mu_2 \approx \mu + \frac{s}{6}(1+0.856k)$ for $q \to 1$, $p \to 2$	generally not used in the literature
Standard deviation σ_2	$\sigma_2^2 = \int_{-\infty}^{+\infty} f(x)(x-\mu_2)^2\,\mathrm{d}x$	$\sigma_2^2 = \sigma^2(1+0.856k)\left(1-\lvert s\rvert/3\right)$ for $q \to 1$, $p \to 2$	σ_2 is also called DP
Skewness s	$s = \sigma_3^3/\sigma_2^3$ $\sigma_3^3 = \int_{-\infty}^{+\infty} f(x)(x-\mu_2)^3\,\mathrm{d}x$	$s \approx -6\,\mathrm{sgn}\,q\,(1-q)^2\,(1+1.856k)$	$q > 0$: left skewed $q < 0$: right skewed
Kurtosis k	$s = \sigma_3^4/\sigma_2^4 - 3$ $\sigma_4^4 = \int_{-\infty}^{+\infty} f(x)(x-\mu_2)^4\,\mathrm{d}x$	$k \approx 2 - p$	$p > 2$: box-shaped $p < 2$: tip-shaped

Table 1: *Relation between statistical distribution properties and distribution parameters for a SGG function. Exept for the median, the relations are not analytical; approximations are given in the case of small deviations from a Gaussian distribution.*

Examples of *SGG* functions with different parameters are given in Fig. 1. The parameters of the coercivity distribution of some calculated and measured coercivity distributions are plotted in Fig. 2.

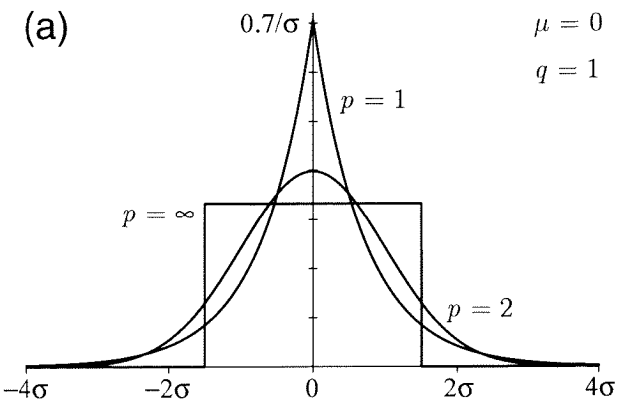

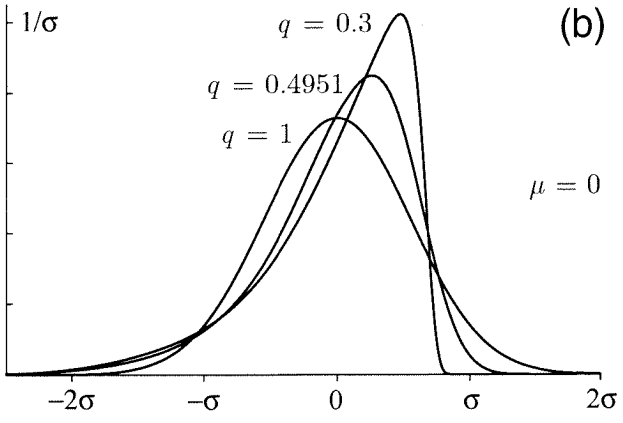

Fig. 1: *Examples of SGG distributions.* (a) *Some particular cases with* $\mu = 0$, $\sigma_2 = 1$ *and* $q = 1$ *are plotted. The skewness of all curves is zero. Furthermore,* $p = 1$ *for a Laplace distribution,* $p = 2$ *for a Gauss distribution and* $p = \infty$ *defines a box distribution.* (b) *Some left-skewed SGG distributions with* $\mu = 0$ *and* $\sigma_2 = 0.5484$ *are plotted. The SGG distribution with* $q = 0.4951$ *is an exellent approximation of the logarithmic plot of a negative exponential distribution.*

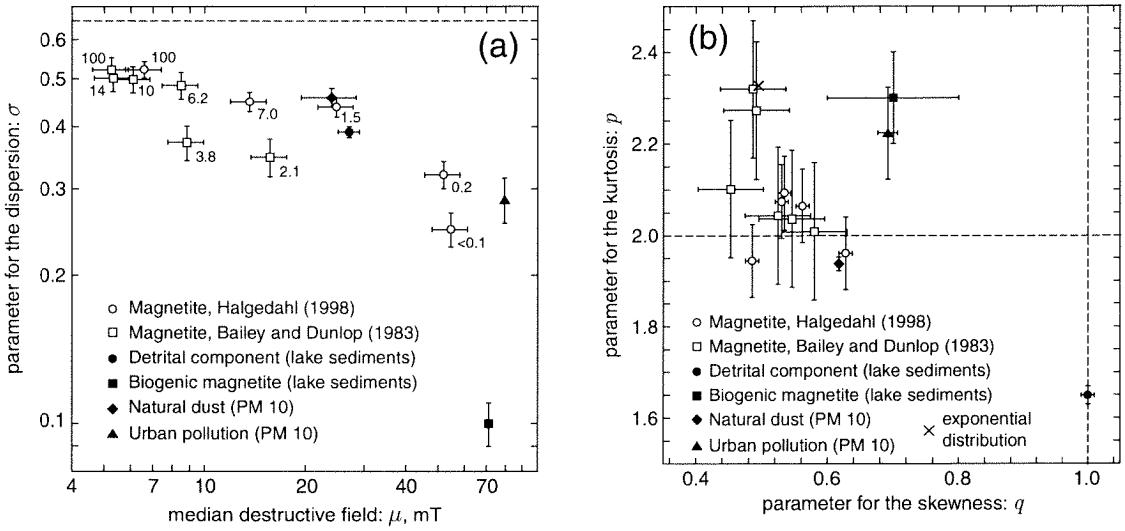

Fig. 2: *Coercivity distribution parameters* μ, σ, q *and* p *for the AF demagnetization of IRM in various synthetic and natural samples. Numbers beside the points indicate the grain size in* μm. (a) *Scatter plot of* μ *and* σ. *The dashed line indicates the value of* σ *for a negative exponential distribution.* (b) *Scatter plot of* q *and* p. *The cross point of the dashed lines corresponds to the values of* q *and* p *for a logarithmic Gaussian distribution. All samples show significant deviation form a logarithmic Gaussian distribution. All parameters of sized magnetite are intermediate between those of a logarithmic Gaussian distribution and those of an exponential distribution.*

Some aspects of component analysis

The result of a component analysis depends upon the PDF chosen to model the end-member coercivity distributions, and particularly on the number of parameters assigned to each PDF. Strong differences exist between the results obtained with a linear combination of Gaussian distributions on the one hand, and a linear combination of SGG distributions on the other. Since finite mixture models with non-Gaussian coercivity distributions have not been reported in the literature, it is not possible to decide from a-priori informations which kind of PDF should be used as a basis for a finite mixture model. From the mathematical point of view, all PDFs are equivalent, since the goodness of fit which can be reached with a particular model depends only upon the total number of parameters assumed, regardless of how they are assigned to individual components. Generally, the use of few PDFs with more distribution parameters, instead of a large number of distributions with fewer distribution parameters leads to results of the fitting model which are more stable against measurement errors. The stable behavior of a fitting with SGG distributions can be explained by the fact that small deviations from an ideal coercivity distribution, which arise from measurement errors, are taken into account by variations in skewness and kurtosis, rather than by variations in the contributions of the single components. Obviously, the values obtained for skewness and kurtosis may not be significant at all. A similar stability can be obtained with Gaussian functions if some of them are grouped as if they were one component. However, it is not always evident which distributions group together, and multiple solutions are often possible. The aspects discussed above are illustrated with the examples of Fig. 3 and Fig. 4. Both figures show the results of a component analysis performed with GECA on the coercivity distribution of a sample of urban particulate matter. In Fig. 3, the component analysis is performed with logarithmic Gaussian functions. Four logarithmic Gaussian functions are needed to fit the measured data so that the misfit between model and data is compatible the measurement errors. However, it is impossible to identify these four distributions with an equivalent number of magnetic components. In Fig. 4, the component analysis is performed with SGG functions. The measurements are already well fitted with one SGG function, however, the measured and the modelled coercivity distributions differens significantly. This model could be adequate to describe low-precision measurements of the same sample. Two SGG functions fit the data within the margins given by the measurement errors. However, multiple solutions are possible, but only one solution minimize the difference between model and measurements. The other solutions imply rather uncommon shapes for the coercivity distribution of the individual components, which are not likely occur in natural samples.

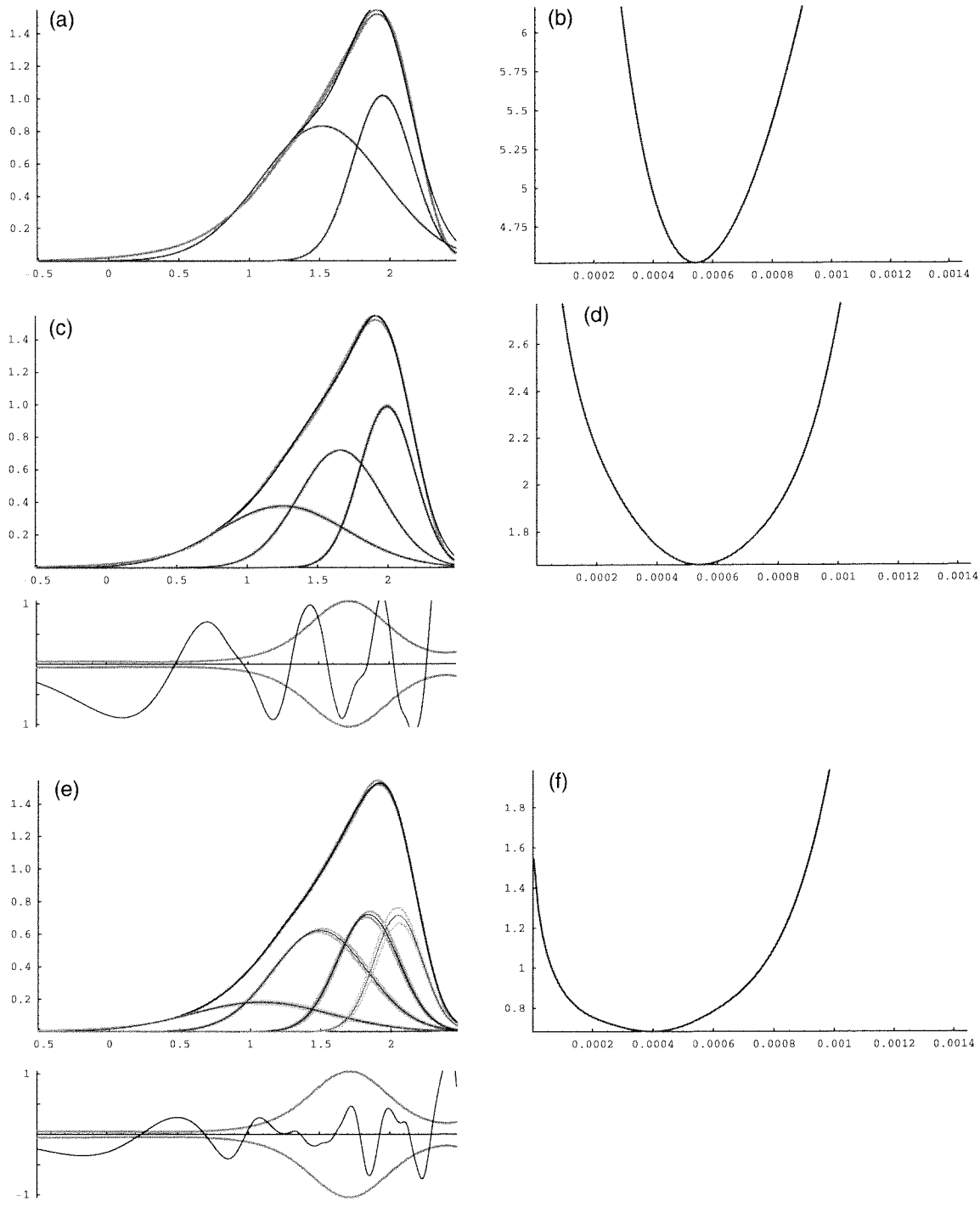

Fig. 3: *Component analysis on a sample of urban atmospheric dust collected in Zürich, Switzerland. The component analysis is performed with logarithmic Gaussian functions. Results of the component analysis are shown in* (a), (c) *and* (e). *The gray pair of line indicates the confidence limits of the measured coercivity distribution. The blue line is the modelled coercivity distribution, expressed as the sum of the logarithmic Gaussian distributions (red, green, violet and light blue). Confidence limits are plotted around each function. Below each plot, the difference between measured and modelled curve is drawn in blue; the gray pair of curves indicates the amplitude of the measurement errors. The mean quadratic residuals of each model are plotted in* (b), (d) *and* (f) *as a function of the amplitude of the logarithmic Gaussian function labelled with the same color. The solutions plotted in* (a), (c) *and* (e) *represents the absolute minima of* (b), (d) *and* (f).

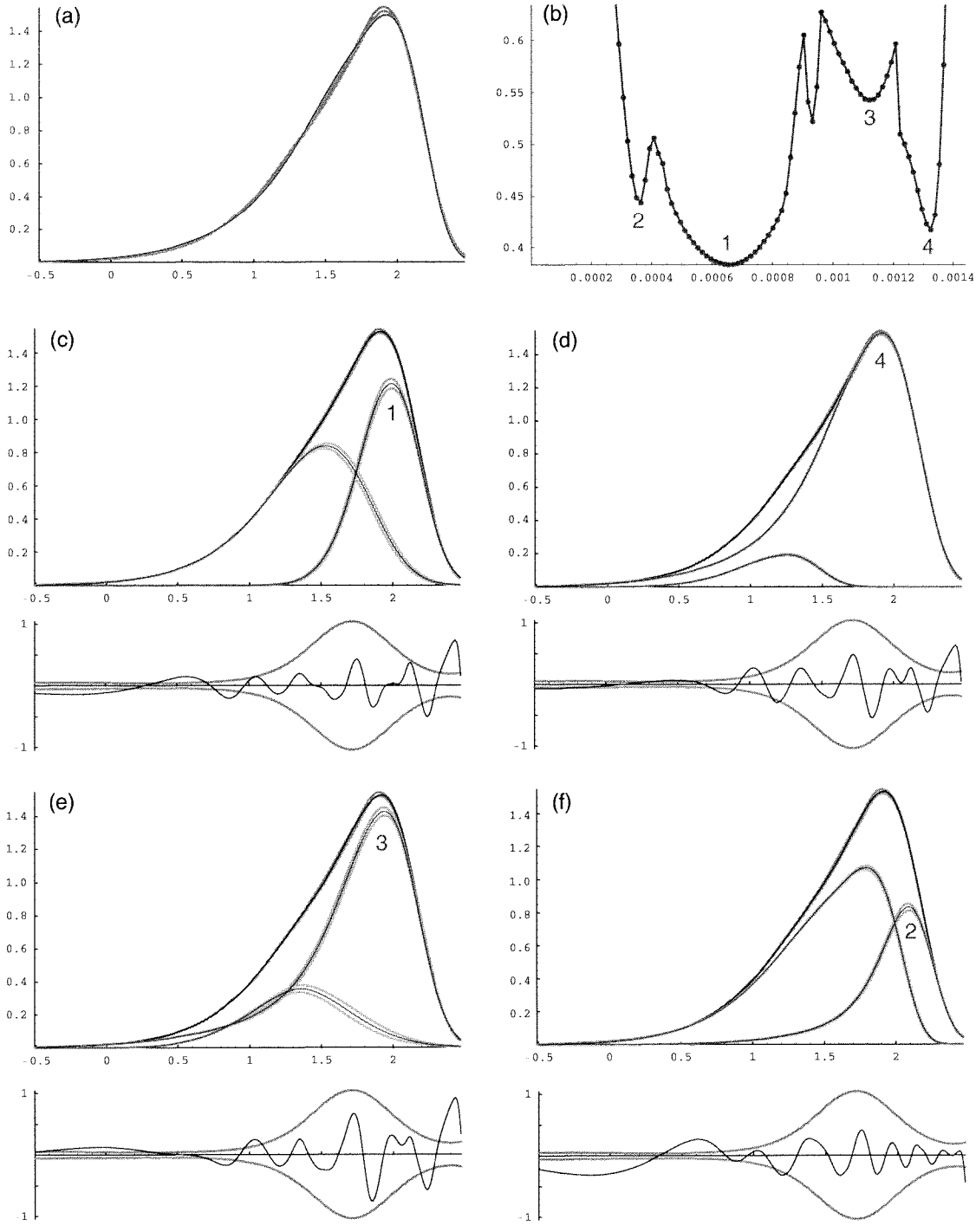

Fig. 4: *Component analysis of the same sample as in Fig. 3. The component analysis is performed with SGG functions. The same notation as in Fig. 3 is used for the plots.* (a) *Component analysis with one SGG function. The modelled coercivity distributions is significantly different from the measured distribution.* (b) *Mean quadratic residuals of a model with two SGG functions, plotted as a function of the amplitude of one function. Different local minima which correspond to stable solutions of the component analysis are labelled with numbers. The corresponding solutions are plotted in* (c), (d), (e) *and* (f). *The solution plotted in* (c) *corresponds to the global minimum of* (b) *and the resulting components are compatible with the coercivity distributions of natural dust (red), and combustion products of motor vehicles (green). The solutions corresponding to the other local minima of* (b) *are not realistic.*

The fundamental questions related to component analysis are:

- How many components are needed to fit a given coercivity distribution?
- Are multiple solutions possible? If yes, which solution is correct?

The answer to these questions is not simple. In the example of Fig. 4 the number of components and the identification of the correct solution among multipe solutions is evident. However, this is not always possible, especially if good measurements are not available, or if the coericivity distributions of individual components are too widely overlapped. In this case, some additional information is needed to put appropriate constraints to the number of end-members and to their distribution parameters.

Performing and testing a component analysis

When component analysis is performed, a modelled coercivity distribution $f(x \mid \theta)$ with parameters $\theta = (\theta_1,\ldots,\theta_n)$ is compared with the measured coercivity distribution, given by a set of numerical values $(x_i, f_i \pm \delta f_i)$ with measurement errors δf_i. A solution of the component analysis is represented by a set of values of θ which minimizes a so-called *merit function* $\varepsilon(\theta)$. The merit function is an estimation of the difference between the modelled and the measured curve: $\varepsilon = 0$ if the model is identical with the measurements. Examples of $\varepsilon(\theta)$ are the mean squared residual:

$$d^2(\theta) = \sum_{i=1}^{N} [f(x_i \mid \theta) - f_i]^2 \tag{4}$$

used for a least-squares fitting, and the χ^2 estimator:

$$\chi^2(\theta) = \sum_{i=1}^{N} \left[\frac{f(x_i \mid \theta) - f_i}{\delta f_i} \right]^2 \tag{5}$$

used for a minimum χ^2 fitting. GECA uses following weighted version of the χ^2 estimator:

$$w^2(\theta) = \sum_{i=1}^{N} r_i^{-2} \left[\frac{f(x_i \mid \theta) - f_i}{\delta f_i} \right]^2 \tag{6}$$

where $r_i = \delta f_i / f_i$ are the relative errors. In this case, measurement points affected by a large relative error are less considered for the component analysis. Equation (6) can be rewritten as:

$$w^2(\theta) = \sum_{i=1}^{N} \left(\frac{\delta f_i}{\sqrt{f_i}} \right)^{-4} [f(x_i \mid \theta) - f_i]^2 \tag{7}$$

If $f(x)$ originates from the sum of a finite number of elementary contributions, f_i is a Poisson distributed variable, and $(\delta f_i)^2 \propto f_i$. An experimental confirmation of this assumption is shown in Fig. 5. After these considerations, $w^2(\theta) \propto d^2(\theta)$ and $d^2(\theta)$ is used by GECA as an improved merit function with respect to (6), since the randomizing effect of the measurement errors on the weighting factors r_i is removed.

Generally, the merit function $\varepsilon(\theta)$ has several local minima $\varepsilon_{\min} = \varepsilon(\theta_{\min})$, which correspond to stable solutions $\theta_{\min}$ of the component analysis. Among these minima, there is an absolute minimum $\varepsilon_{\mathrm{MIN}} = \varepsilon(\theta_{\mathrm{MIN}})$. Depending on the starting values θ_{ini} of θ, one of these solutions is attained by GECA.

If the model used for component analysis is adequate and if there are no measurement errors, $\varepsilon_{\mathrm{MIN}} = 0$. Let n be the number of magnetic components and m the number of end-member functions used in the model. Then, $\varepsilon_{\mathrm{MIN}} > 0$ for $m < n$ and $\varepsilon_{\mathrm{MIN}} = 0$ for $m \geq n$, so that the number of components can be easily guessed (Fig. 6a). In case of an inadequate model, the end-member functions cannot reproduce exactly the coercivity distribution of all magnetic components, and $\varepsilon_{\mathrm{MIN}} > 0$, even without measurement errors.

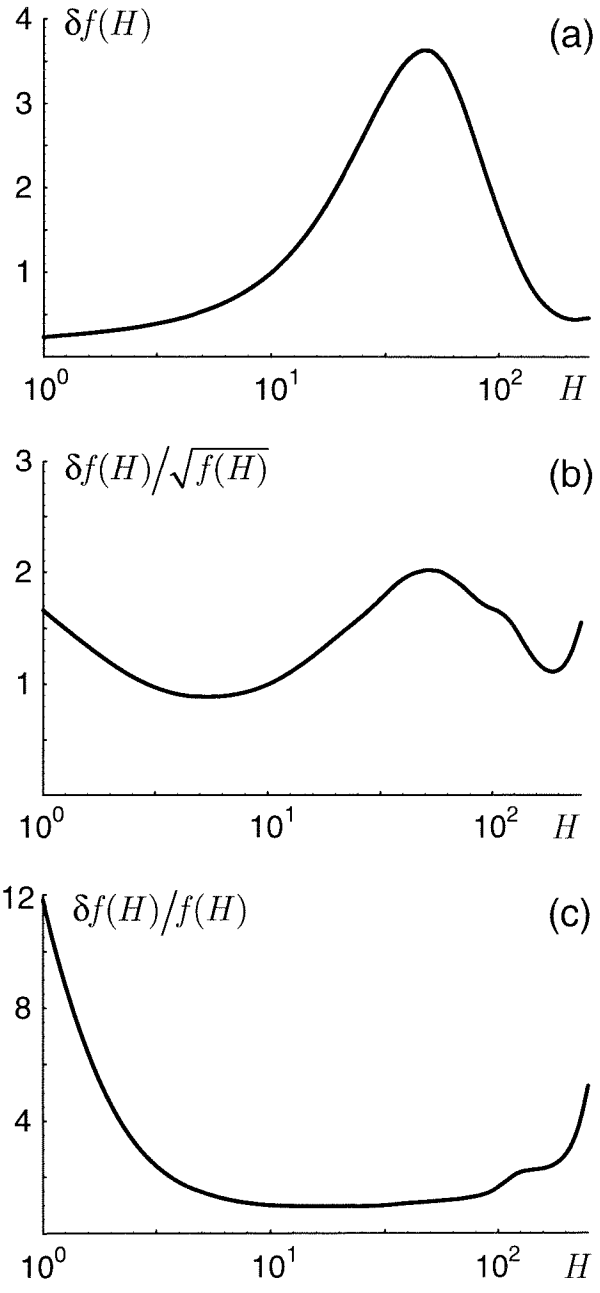

Fig. 5: *Mean measurement error of the coercivity distribution of six samples of loess, soil, lake sediments, marine sediments and athmospheric particulate matter. The absolute error* $\delta f(H)$ *and the relative error* $\delta f(H)/f(H)$ *are plotted in* (a) *and* (c), *respectively. In* (b), *the absolute error is normalized by the square root of* $f(H)$. *The field unit is* mT. *All curves are normalized by their value at* 10 mT.

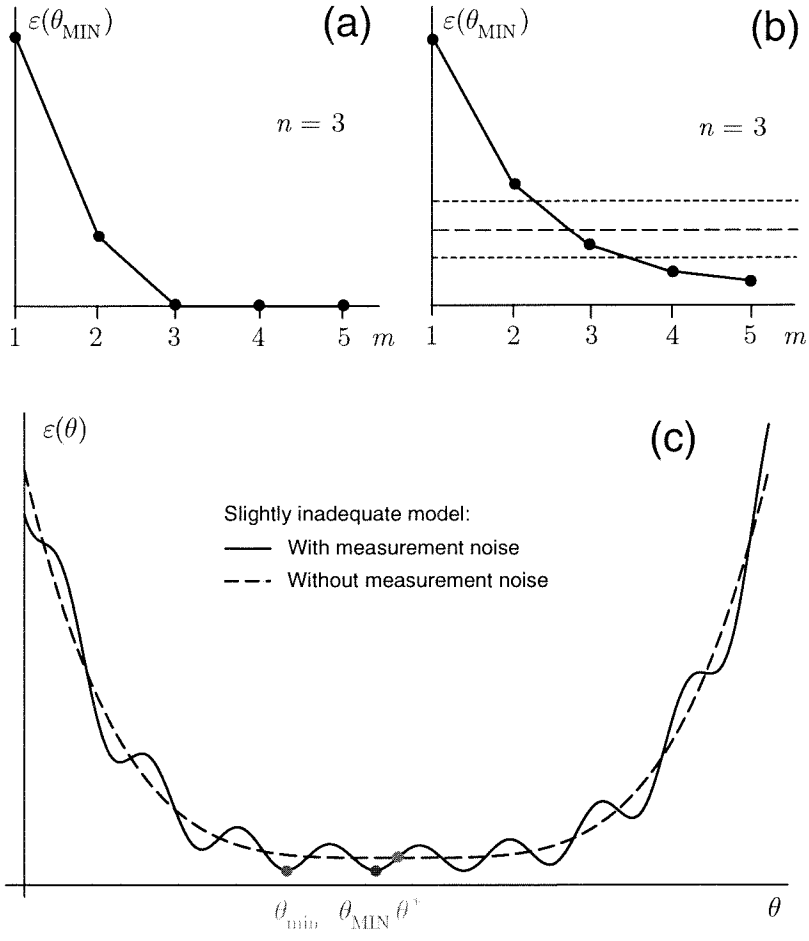

Fig. 6: *Dependence of the merit function* $\varepsilon(\theta)$ *on the parameters of the model chosen for fitting a coercivity distribution. In* (a) *a noise-free coercivity distribution with* $n = 3$ *magnetic components is fitted with an adequate model with* m *end-member functions. The functions are assumed to reproduce exactly the coercivity distribution of each component. If* $m < n$, *some components cannot be considered into the model and* $\varepsilon(\theta) > 0$; *on the other hand* $\varepsilon(\theta) = 0$ *for a given combination* $\theta = \theta_{MIN}$ *of parameters when* $m > n$. *The number of components can be easily guessed. The situation becomes more complex in* (b), *where measurement errors are taken into account. In this case, there is always a misfit between model and measurements, and* $\varepsilon(\theta_{MIN})$ *decreases monotonically as the number of end-members taken into account by the model is increased. In this case, the number of components is guessed with the help of a Pearson's* χ^2 *test. According to this test,* $\varepsilon(\theta_{MIN})$ *is compared with the expected value of* ε *(dashed line). If* $\varepsilon(\theta_{MIN})$ *is compatible with the expected value within given confidence limits (dotted lines), the model is accepted. If* $\varepsilon(\theta_{MIN})$ *is too large, the modelled coercivity distribution is significantly different from the measured coercivity distribution and more parameters should be included in the model. On the other hand, if* $\varepsilon(\theta_{MIN})$ *is too small, the model fits the measured data unrealistically well and random effects produced by the measurement errors are included in some parameters which are not significant. The model is accepted if* $\varepsilon(\theta_{MIN})$ *belongs to the range of values given by the confidence limits. The complex dependence of the merit function on the model parameters is illustrated in* (c) *for the case of a model with a fixed number of end-member functions which approximatively fit the coercivity distribution of all magnetic components. These end-member functions produce a small misfit between model and data, even is the measurement errors are not considered (dashed curve). Nevertheless, there is only one stable solution* θ^* *of the component analysis (green point), which corresponds to an absolute minimum of* $\varepsilon(\theta)$. *If the measurement errors are taken into account, the shape of* $\varepsilon(\theta)$ *becomes rather complex, with numerous local minima* $\varepsilon(\theta_{min})$. *Some of these local minima represent possible solutions which fits the measurements as good as the absolute minimum* $\varepsilon(\theta_{MIN})$, *even if they do not model the coercivity distribution of the real components. The absolute minimum (red point) represents a solution* θ_{MIN} *which is still close to the realitiy. With larger measurement errors, this could not be the case, and a realistic solution may be given by a local minimum of* $\varepsilon(\theta)$.

If an adequate model is used to fit data affected by measurement errors, $\varepsilon_{MIN} > 0$, and $\varepsilon_{MIN} \to 0$ for $m \to \infty$ (Fig. 6b).

Two fundamental questions arise at this point:

1) How many end-member distributions should be considered for a component analysis?

2) Is a particular solution $\hat{\theta}$ close to the (unknown) real solution θ^*?

These questions can be easily answered only if the model chosen for the component analysis is adequate and the measurement errors are sufficiently small. The first condition can be approximatively attained by using a set of SGG functions to model the coercivity distributions of the magnetic components. SGG functions are able to reproduce all fundamental characteristics of the coercivity distribution of a single component (median, dispersion parameter, skewness and kurtosis).

If the measurement errors are small enough, the solution θ_{MIN} which corresponds to a global minimum of $\varepsilon(\theta)$ is close to the real solution θ^* (Fig. 6c). In case of large measurement errors, the real solution θ^* may be close to one or more a local minima of $\varepsilon(\theta)$. In this case, additional independent informations are needed to individuate the correct solution among all possible solutions θ_{min}.

The problem of the number of end-members to consider for a component analysis is evaluated with a *Pearson's* χ^2 *goodness of fit test*. To perform this test, the statistical distribution of the χ^2 estimator given in equation (5) is considered. The χ^2 estimator is a statistical variable which is distributed according to a χ^2 distribution with $N - k - 1$ degrees of freedom, being N the number of *independent* points to fit with a given model, and k the number of model parameters. The expected value of the χ^2 estimator is $N - k - 1$. The confidence limits at a confidence level α (generally $\alpha = 0.95$) are given by $\chi^2_{N-k-1;\alpha}$ and $\chi^2_{N-k-1;1-\alpha}$, with:

$$\int_{\chi^2_{N-k-1;p}}^{\infty} \chi^2_{N-k-1}(t)\,\mathrm{d}t = p \tag{8}$$

If $\chi^2 > \chi^2_{N-k-1;1-\alpha}$, the model differs significantly from the measurements. The model should be refined by adding new parameters, eventually by considering an additional end-member function. If $\chi^2 < \chi^2_{N-k-1;\alpha}$ the differences between model and measurements are unrealistically small. An excessive number of parameters allow the model to include random effects of the measurement errors. Consequently, some of these parameters are not significant. The model should be revised to include a smaller number of parameters, eventually by reducing the number of end-members or by keeping some parameters fixed. If $\chi^2_{N-k-1;\alpha} \le \chi^2 \le \chi^2_{N-k-1;1-\alpha}$ the model is acceptable.

To calculate the χ^2 estimator with equation (5) some knowledge about the measurement errors δf_i and the number of independent data points is necessary. The measurement errors are automatically estimated with CODICA, when a coercivity distribution is calculated from an acquisition/demagnetization curve. The number of independent data points is more difficult to estimate. It is identical with the number of measurements if the measurement errors are equivalent to an ergodic noise signal, that is, when the autocorrelation of the noise signal is equivalent to a Dirac δ-function.

This is often not the case with real measurements, where entire groups of measured points are affected by the same error. Furthermore, the coercivity distributions calculated by CODICA are low-pass filtered, and an autocorrelation of the remaining measurement errors is unavoidable. GECA estimates the degrees of freedom of the fitting model by evaluating the residuals curve which results from the difference between the model and the measurements. The residuals curve contains a certain number of random oscillations around a mean value of zero. To reproduce these oscillations a minimum number l of points is necessary, whose spacing defines the Nyquist frequency of the signal. GECA sets $l-1$ equal to the number of zero crosses of the residuals. Obviously, the shape of the residuals curve depends on the model chosen for component analysis.

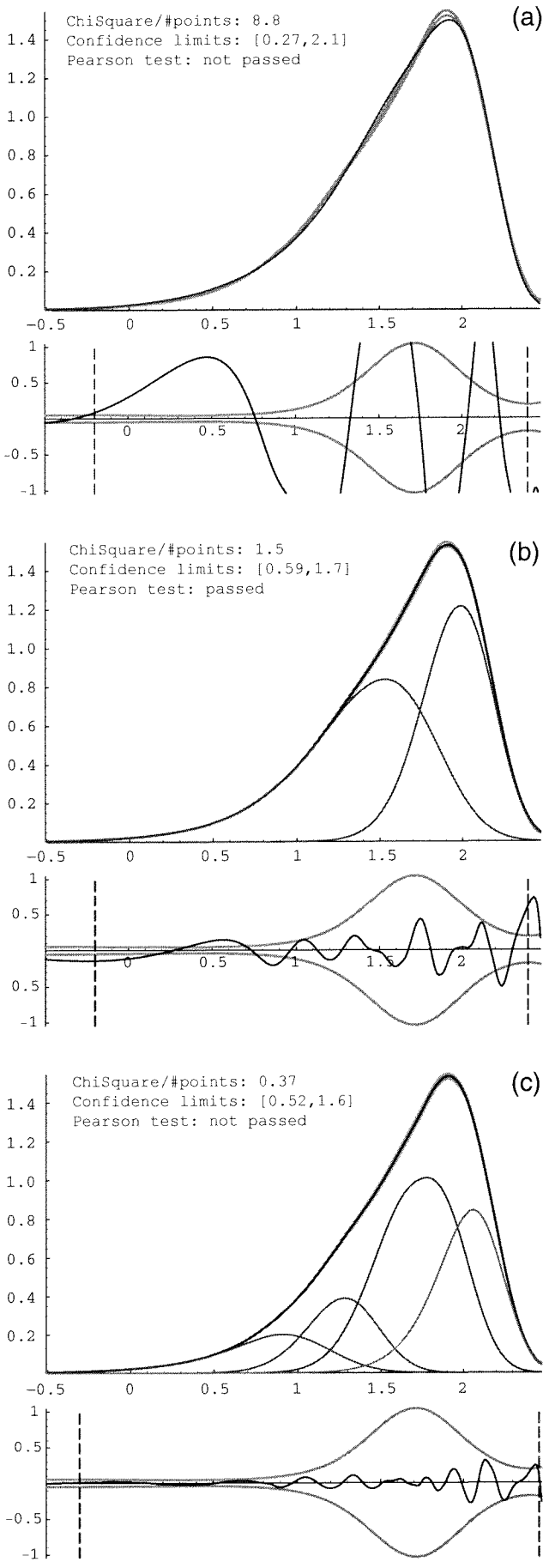

Fig. 7: *Examples of Pearson's χ^2 test on the component analysis of a sample of urban atmospheric particulate matter. The gray and the blue curves are the measured and the modelled coercivity distributions, respectively. Curves labelled with other colors represent the coercivity distributions of individual end-members. Below each plot, the difference between model and measurements is plotted (blue line) together with the measurement errors (pair of gray lines). In* (a)*, a model with one SGG function is evaluated. The differences between model and measurements are too large, and the model is rejected. In* (c) *the a model with four SGG functions is rejected for the opposite reason: the model fits the data unrealistically well for the given measurement errors. A model with two SGG functions is represented in* (b)*. In this case, the χ^2 statistics is compatible with the expected value within at a 95% confidence level, and the model is accepted.*

A model with a small number of parameters produces a residuals curve with few, large oscillations. The more parameters are included in the model, the more oscillations characterize the residuals and the confidence limits of the χ^2 estimator become closer to the expected value. Consequently, models with a too large number of parameters are rejected. An example of Pearson's χ^2 test is shown in Figure 7 with the example of a sample of urban atmospheric particulate matter. In Fig. 7a, the coercivty distribution is fitted with one SGG function. The residulas curve has 5 zero crosses in the range considered for fitting, and GECA assumes $l = 6$ degrees of freedom for the χ^2 distribution. The confidence limits of χ^2/l are 0.27 and 2.1, while $\chi^2/l = 8.8$ for that model, which is rejected. In Fig. 7b, two SGG functions are used for the component analysis. Now, $l = 12$, and the confidence limits of χ^2/l are 0.44 and 1.8. With $\chi^2/l = 1.5$ this model is acceptable. With four SGG functions (Fig. 7c), $l = 18$ and the confidence limits of χ^2/l are 0.52 and 1.6, while $\chi^2/l = 0.37$ for that model, which is rejected.

A program example

```
In[1]:= <<Utilities`Codica`
```

Load the program

```
Program package Codica v.2.3 for Mathematica 3.0 and later versions.
Copyright 2000-2003 by Ramon Egli. All rights reserved.
```

```
In[2]:= Geca
```

Start the program

```
Data from file
```

Enter file name

```
C:/users/ramon/papers/fitting/WDKarm.slog

Checking the coercivity distribution...

Confidence limits of the coercivity distribution:
```

Plot the distribution

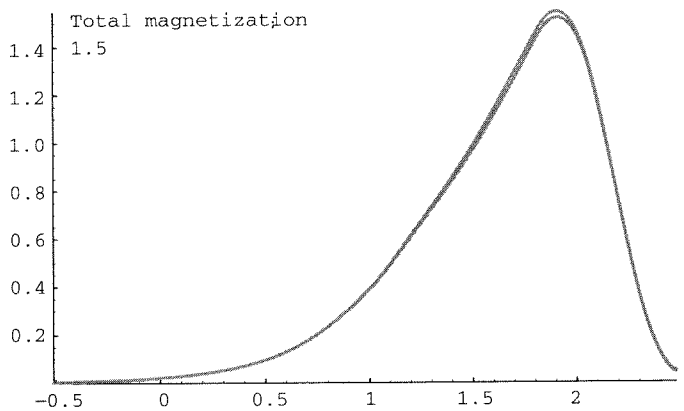


```
Coercivity distribution is significant between -0.5 and 2.474

Fitting is performed in the range between -0.1957 and 2.396
```

Set the fitting range

Enter initial parameters (1)

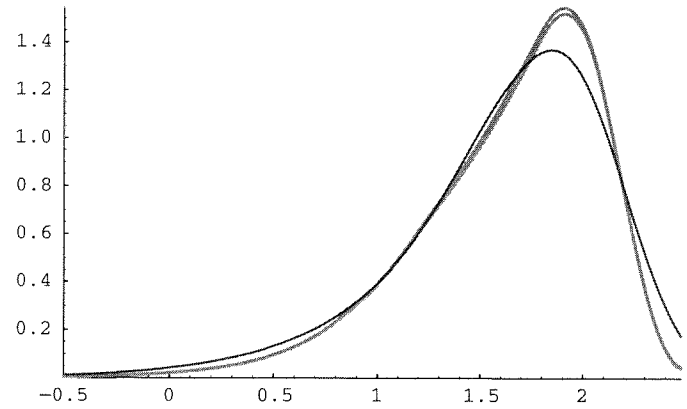

Initial distribution parameters:

a1 = 1.5
m1 = 1.7 s1 = 0.6
q1 = 0.5 p1 = 2.2

Optimizing the distribution parameters. Please wait...

Perform a component analysis (1)

{a1=0.0015, m1=1.7, s1=0.6, q1=0.5, p1=2.2}

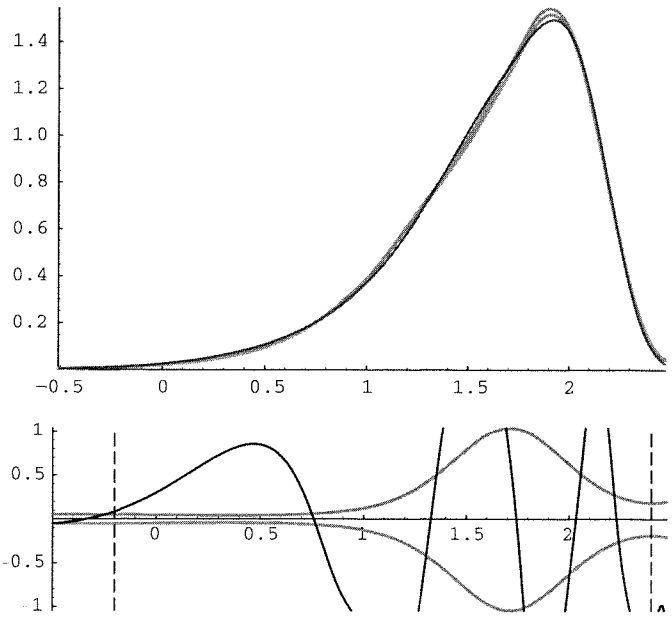

Optimized distribution parameters:

a1 = 1.454
m1 = 1.714 s1 = 0.6875
q1 = 0.4256 p1 = 3.076

Residuals (modelled - measured) and measurement errors
in % of the maximum value of
the coercivity distribution.

Dashed lines delimitate the interval
considered for the component analysis.

ChiSquare/#points: 8.8
Confidence limits: [0.52,1.9]

Model and data are significantly different. Refine your model.

Enter initial parameters (2)

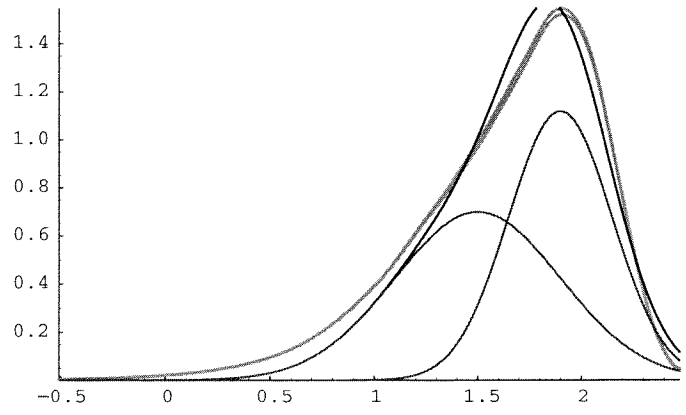


```
Initial distribution parameters:

a1 = 0.7
m1 = 1.5        s1 = 0.4
q1 = 1.         p1 = 2.

a1 = 0.7
m1 = 1.9        s1 = 0.25
q1 = 1.         p1 = 2.
```

```
Optimizing the distribution parameters. Please wait...
```

Perform a component analysis (2)

```
{a1=0.0007,m1=1.5,s1=0.4,a2=0.0007,m2=1.9,s2=0.25}
```

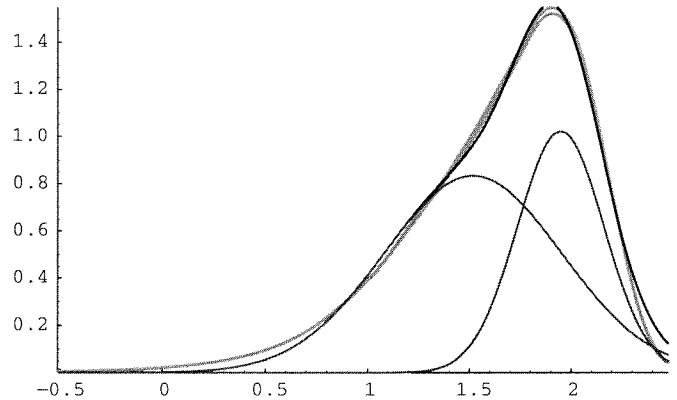


```
Optimized distribution parameters:

a1 = 0.9101
m1 = 1.517      s1 = 0.4363
q1 = 1.         p1 = 2.

a1 = 0.5428
m1 = 1.948      s1 = 0.2124
q1 = 1.         p1 = 2.
```

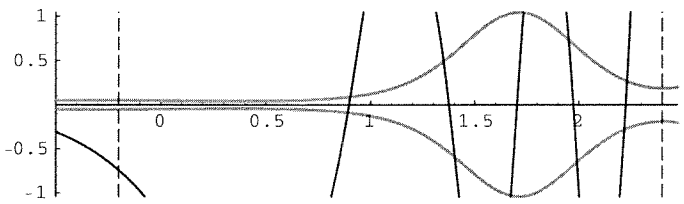


```
Residuals (modelled - measured) and
measurement errors
in % of the maximum value of
the coercivity distribution.

Dashed lines delimitate the interval
considered for the component analysis.

ChiSquare/#points: 27.
Confidence limits: [0.52,1.9]
```

```
Model and data are significantly different. Refine your model.
```

Enter initial parameters (3)

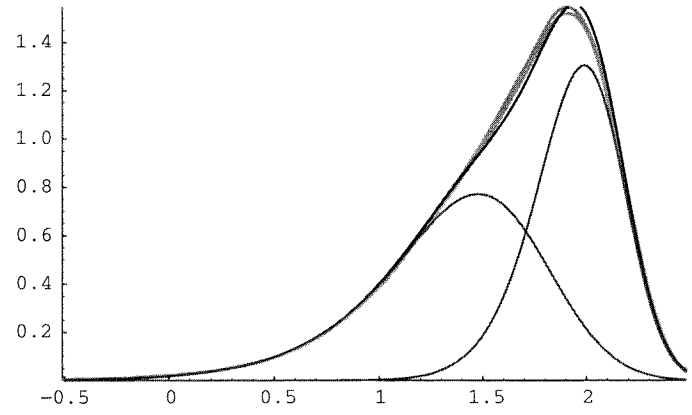

Initial distribution parameters:

a1 = 0.75
m1 = 1.4 s1 = 0.45
q1 = 0.6 p1 = 2.

a1 = 0.7
m1 = 1.957 s1 = 0.235
q1 = 0.663 p1 = 2.

Optimizing the distribution parameters. Please wait...

Perform a component analysis (3)

{a1=0.00075,m1=1.4,s1=0.45,q1=0.6,p1=2.,a2=0.0007}

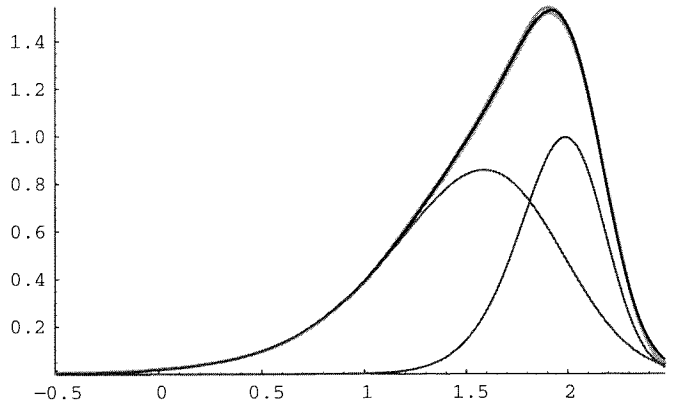

Optimized distribution parameters:

a1 = 0.9217
m1 = 1.509 s1 = 0.4882
q1 = 0.6235 p1 = 2.023

a1 = 0.5348
m1 = 1.957 s1 = 0.235
q1 = 0.663 p1 = 2.

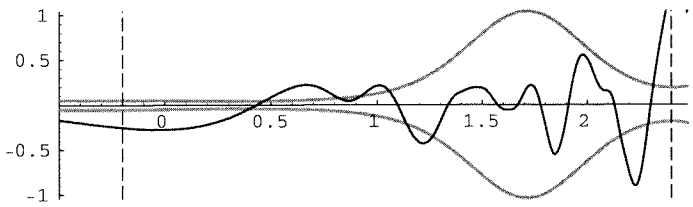

Residuals (modelled - measured) and measurement errors in % of the maximum value of the coercivity distribution.

Dashed lines delimitate the interval considered for the component analysis.

ChiSquare/#points: 2.8
Confidence limits: [0.63,1.6]

Model and data are significantly different. Refine your model.

Enter initial parameters (4)

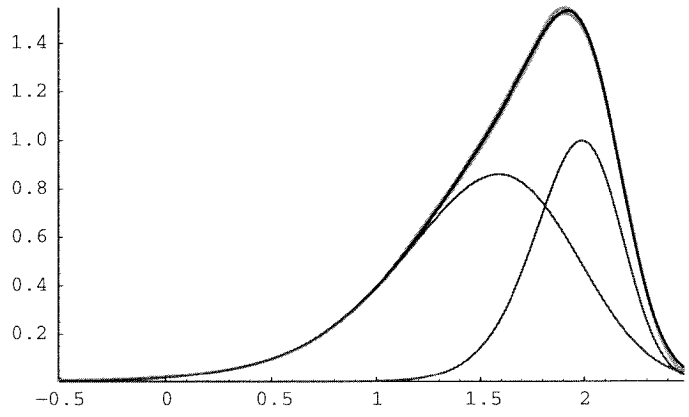


```
Initial distribution parameters:

a1 = 0.9217
m1 = 1.509     s1 = 0.4882
q1 = 0.6235    p1 = 2.023

a1 = 0.5348
m1 = 1.957     s1 = 0.235
q1 = 0.663     p1 = 2.
```

```
Optimizing the distribution parameters. Please wait...
```

Perform a component analysis (4)

```
{a1=0.0009217,m1=1.509,s1=0.4882,q1=0.6235,p1=2.023,
 a2=0.0005348,m2=1.957,s2=0.235,q2=0.663,p2=2.}

FindMinimum::fmlim: The minimum could not be bracketed in 50 iterations.

{a1=0.0006243,m1=1.311,s1=0.4483,q1=0.4878,p1=2.171,
 a2=0.0008625,m2=1.963,s2=0.2331,q2=0.7765,p2=2.107}
```

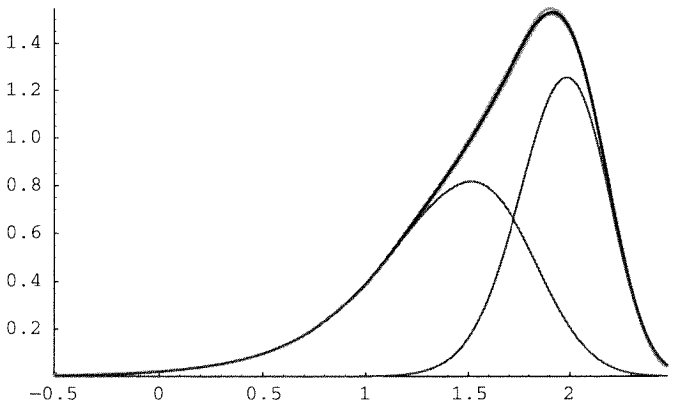


```
Optimized distribution parameters:

a1 = 0.7699
m1 = 1.412     s1 = 0.4699
q1 = 0.5537    p1 = 2.106

a1 = 0.6847
m1 = 1.962     s1 = 0.2329
q1 = 0.7221    p1 = 2.053
```

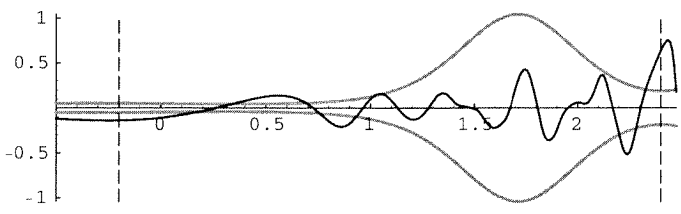


```
Residuals (modelled - measured) and
measurement errors
in % of the maximum value of
the coercivity distribution.
Dashed lines delimitate the interval
considered for the component analysis.
ChiSquare/#points: 1.5
Confidence limits: [0.59,1.7]
```

```
Model and data are compatible. You may accept this component analysis.
```

```
Perform an automatic variation of the contribution of component #2:
This process takes several minutes. Please wait...

Decreasing contribution of component #2...

Increasing contribution of component #2...

Residuals as a function of the contribution of component #2
(Every 10th point in gray, first point is #21, red point is the starting solution)
```

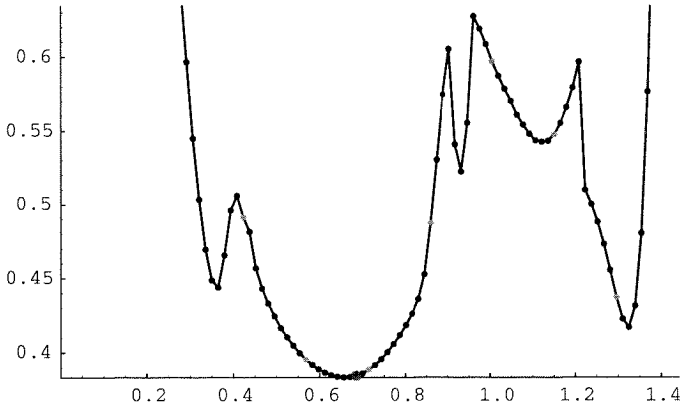

Choose initial parameters

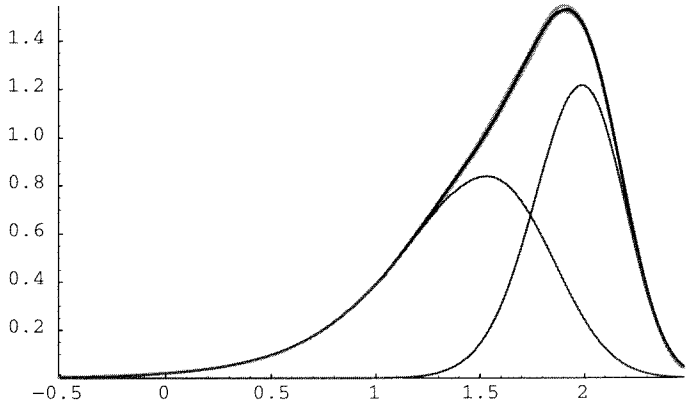

Initial distribution parameters:

a1 = 0.7989
m1 = 1.428 s1 = 0.4739
q1 = 0.5562 p1 = 2.108

a1 = 0.6556
m1 = 1.967 s1 = 0.2297
q1 = 0.7265 p1 = 2.052

Optimizing the distribution parameters. Please wait...

Perform a component analysis (5)

{a1=0.0007989,m1=1.428,s1=0.4739,q1=0.5562,p1=2.108,a2=0.0006556,
m2=1.967,s2=0.2297,q2=0.7265,p2=2.052}

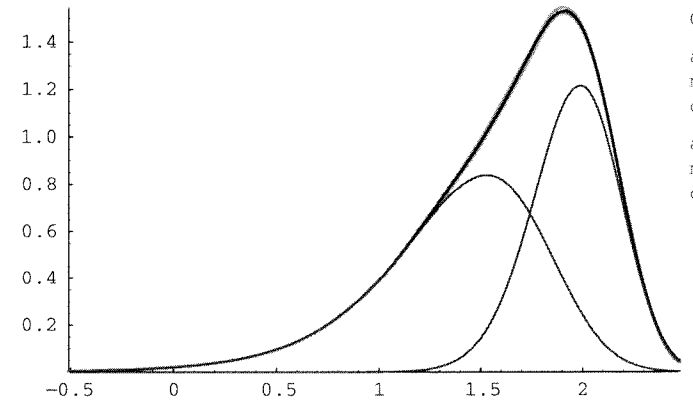

Optimized distribution parameters:

a1 = 0.7989
m1 = 1.428 s1 = 0.4739
q1 = 0.5562 p1 = 2.108

a1 = 0.6556
m1 = 1.967 s1 = 0.2297
q1 = 0.7265 p1 = 2.052

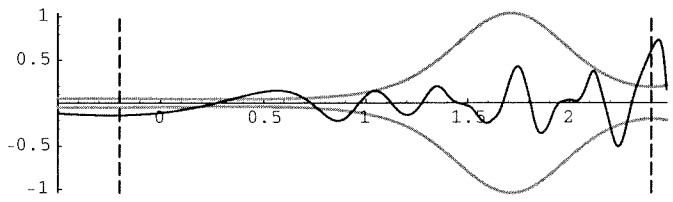

Residuals (modelled - measured) and measurement errors
in % of the maximum value of
the coercivity distribution.
Dashed lines delimitate the interval
considered for the component analysis.

ChiSquare/#points: 1.5
Confidence limits: [0.59,1.7]

Model and data are compatible. You may accept this component analysis.

Calculating statistical parameters of the distributions...

Perform an error estimation

Perform an error estimation of the distribution parameters with 64 error simulations.
Accuracy of the error estimation: 12.%
This process takes several minutes time. Please wait...

Error estimation of the statistical parameters. Please wait...

Calculating the confidence limits of the components. Please wait...

Parameters of component #1:	Parameters of component #2:
a = 0.7989 ± 0.021	a = 0.6556 ± 0.021
μ = 1.428 ± 0.011	μ = 1.967 ± 0.0038
σ = 0.4739 ± 0.0029	σ = 0.4739 ± 0.0029
q = 0.5562 ± 0.0047	q = 0.7265 ± 0.0065
p = 2.108 ± 0.019	p = 2.052 ± 0.0082
MDF = 1.428 ± 0.011	MDF = 1.967 ± 0.0038
mean = 1.374 ± 0.012	mean = 1.957 ± 0.0044
DP = 0.4255 ± 0.0027	DP = 0.2165 ± 0.0024
skewness = -0.8043 ± 0.013	skewness = -0.2647 ± 0.015
kurtosis = 1.149 ± 0.026	kurtosis = 0.1122 ± 0.024

Result of the component analysis:

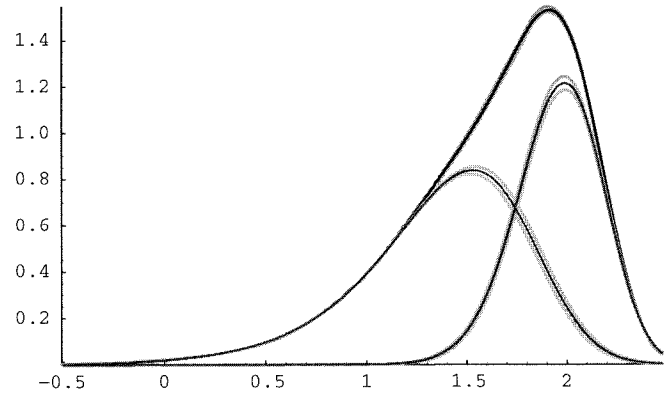

Total magnetization: 1.455 ± 0.029

a1 = 0.7989
MDF1 = 1.428 DP1 = 0.4255
sk1 = -0.8043 ku1 = 1.149

a2 = 0.6556
MDF2 = 1.967 DP2 = 0.2165
sk2 = -0.2647 ku2 = 0.1122

Calculating the confidence limits of each component. Please wait...

Normalized components with confidence limits:

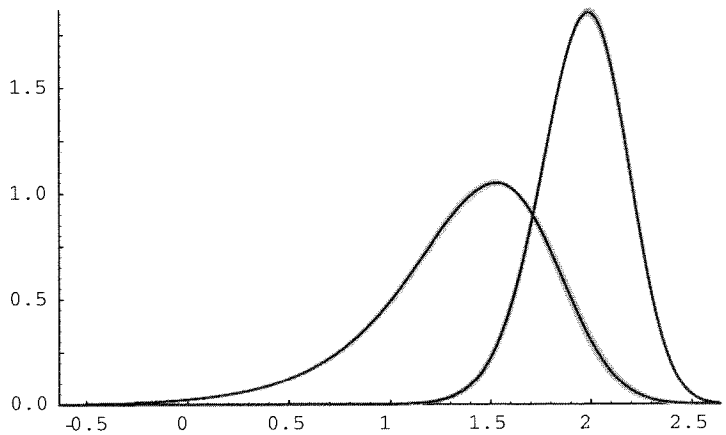

Distribution parameters:

MDF1 = 1.428 DP1 = 0.4255
sk1 = -0.8043 ku1 = 1.149

MDF2 = 1.967 DP2 = 0.2165
sk2 = -0.2647 ku2 = 0.1122

```
Preparing data to an export format. Please wait...

Printing results to:  components.dat

Saving the coercivity distributions to WDKarm.comp :
Column #1: magnetic field,
Column #2: component #1    Column #3: error of component #1
Column #4: component #2    Column #5: error of component #2
END
```

Save results to a log file

Save end-members

Loading CODICA and running GECA

To run GECA, open a new *Mathematica* notebook by clicking on the *Mathematica* program icon. Type `<<Utilities`Codica`` on the input prompt *In[]* and press the keys *Shift* + *Enter* to load CODICA. On the next input prompt type `Geca` and press the keys *Shift* + *Enter* to start GECA. From now on, the program asks you to enter specific commands step by step. In the following, all GECA commands are explained in order of appearance.

Back to the program

Enter the name of the data file

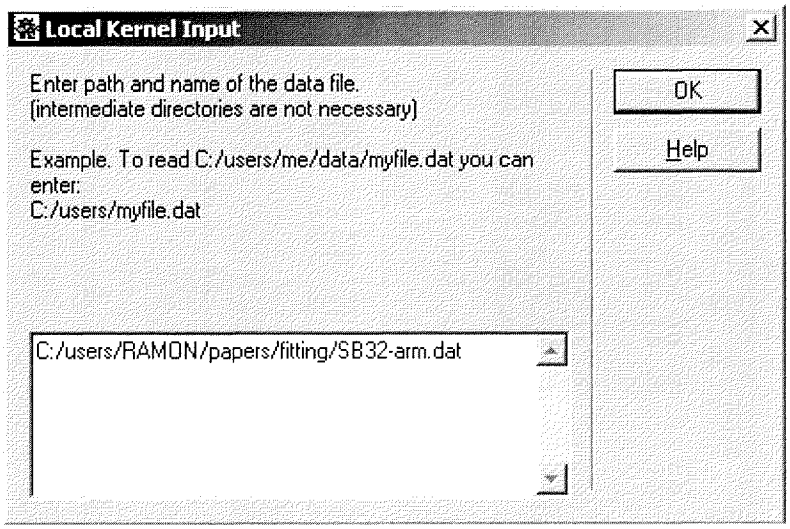

The prompt window on the right asks you to enter the name on the file which contains the coercivity distribution data. Type the path of the data file. You can skip intermediate directories if other files with the same name are not stored. The data file should be an ASCII file with three colums of numbers separated by spaces or tabulators. The file should not contain comment lines or text in general. The first column is the scaled or unscaled field, the second column is the value of the coercivity distribution for the corresponding field. The third column is the relative error of the second column; 0.1 means 10% error. Output files of CODICA with extentions `.slin`, `.slog` and `.spow` are automatically accepted. It is strongly recommanded to run GECA only on CODICA output files with extention `.slog`.

Back to the program example

Plot the coercivity distribution

The coercivity distribution is plotted together with the confidence limits given by the error estimation stored in the file. If the maximal measurement error is less than 5% of the peak value of the coercivity distribution, only the confidence limit are plotted as a pair of gray lines. With errors larger than 5%, the coercivity distribution is plotted as a black line, together with the confidence limits. Within the plot, an estimation of the total magnetization is given. This estimation is obtained by integrating the coercivity distribution over the field range given by the data stored in the file. If saturation is not reached within this range, the calculated value is an underestimation of the total magnetization. You can use the estimation of the total magnetization as a reference when you enter the initial distribution parameters.

Back to the program example

Set the fitting range

GECA estimates a field range where the values of the coercivity distribution are significant. As a significance limit, a maximum relative error of 50% has been chosen for the values of the coercivity distribution . You can enter a different range with the promt window displayed on the right. If the coercivity distribution was calculated from a demagnetization curve, it is recommanded to discard the data near the right end of the field range, because they could be affected by truncation effects. Data outside the range you entered are displayed but are not considered for further calculations.

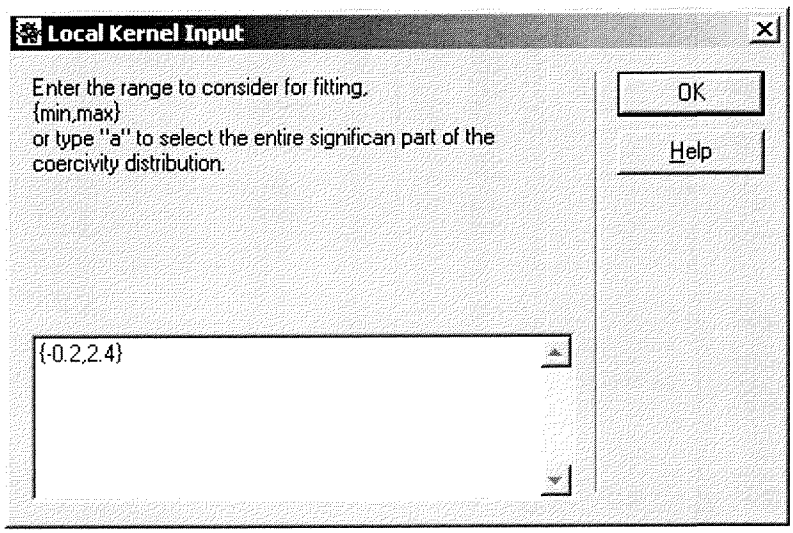

Back to the program example

Enter initial distribution parameters

You are asked to enter initial values for the parameters of the finite mixture model that will be used for the component analysis. GECA uses a set of one to four SGG functions to fit the measured coercivity distribution. Each SGG function is characterized by following five parameters:

- *amplitude* a: the area under the SGG function, which is equivalent to the magnetization of a component whose coercivity distribution is represented by this function.
- *median* μ: this parameter corresponds to the median value of the function, also called median destructive field (MDF) or median acquisition field (MAF).
- *parameter for the standard deviation* σ: this is the principal parameter which controls the standard deviation of the SGG function, also called the dispersion parameter DP.
- *parameter for the skewness* q: this is the principal parameter which controls the skewness of a SGG function, with $-1 \leq q \leq 1$. Positive values of q generate left skewed functions, negative values of q generate right skewed functions. Symmetrical functions are characterized by $q = \pm 1$. Generally, real coercivity distributions are characterized by $0.5 \leq |q| \leq 1$. If you do not have independent informations about the starting parameters, set a vaule of q near 1.
- *parameter for the kurtosis* p: this is the principal parameter which controls the kurtosis of a SGG function. A logarithmic Gaussian distribution is characterized by $p = 2$. More squared functions are generated with $p > 2$, less squared distributions by $p < 2$. Common values for real coercivity distributions are given by $1.6 < p < 2.4$. If you do not have independent informations about the starting parameters, set $p = 2$.

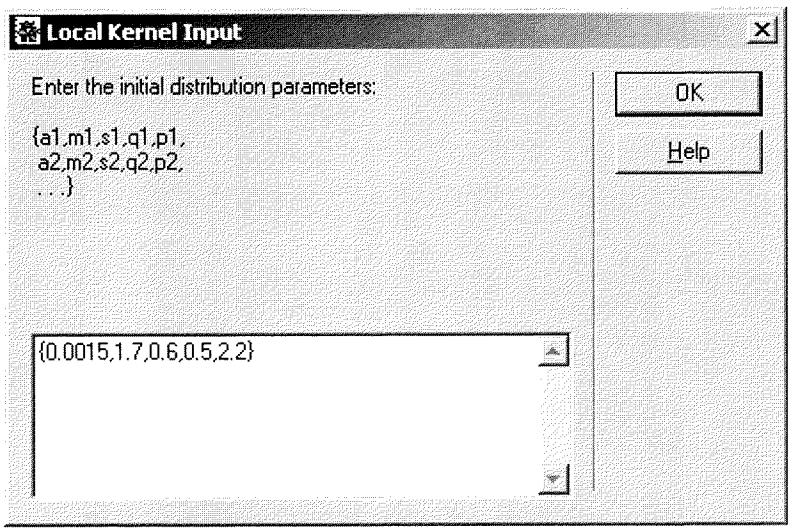

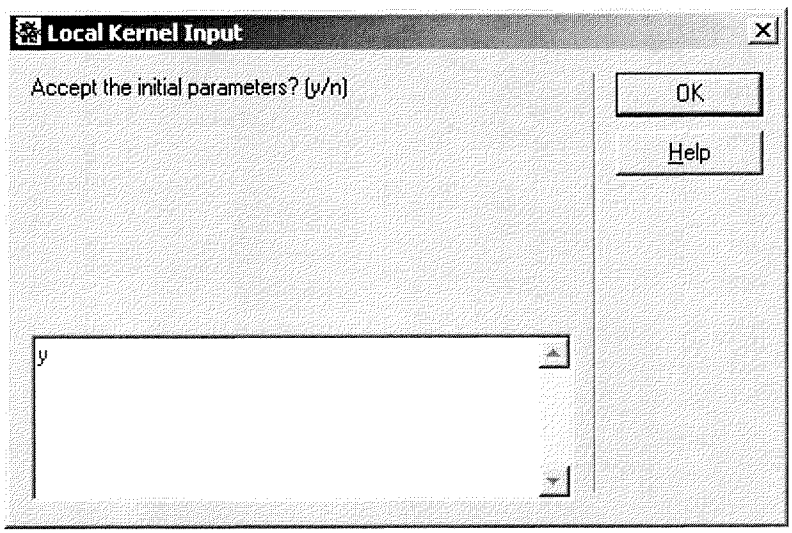

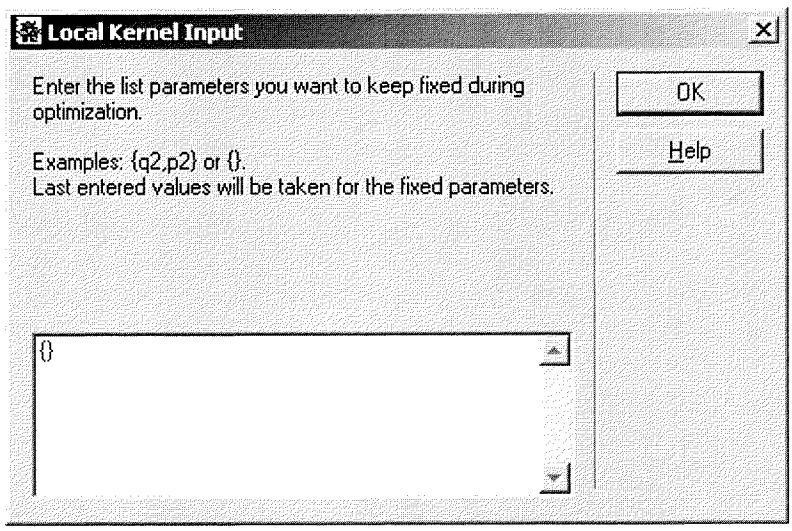

Enter the parameters as an ordered list: a, μ, σ, q and p of the first component, a, μ, σ, q and p of the second component, and so on, as in the example given in the promt window shown to the right. The end-member distributions defined by the initial parameters you entered are plotted with different colors (red, green, violed and light blue). The modeled coercivity distribution is given by the sum of all end-members and is plotted in blue, together with the measured coercivity distribution (black/gray). The initial parameters shoud be chosen so, that the modelled coercivity distribution is as close to the measured coercivity distribution as possible. You can enter the initial parameters either with some knowledge about the magnetic components which are contributing to the measured distribution, or by try and error. In this last case you can reenter new initial parameters until you get a satisfacting result. After entering the initial parameters, you are asked to keep some parameters fixed during the optimization. If you want to oprimize all parameters, type "{}". Otherwise, enter the symbols for the fixed parameters in the next promt window. For example, if you want to use a logaritmic Gaussian function for the second end-member, set $q = 1$ and $p = 2$ as initial values for the corresponding SGG function, and keep these parameters fixed by entering "{q2,p2}" in the following prompt window. You can choose every combination of parameters to keep fixed. If you exactly know the parameters of one magnetic component, you can model this component by an end-member function with fixed values of μ, σ, q and p. Then, only the magnetic contribution of this component, given by a, will be optimized.

It is recommanded to start with a small number of end-members and a small number of parameters, and to use independent informations about the number of magnetic components and their properties. You can then progressively increase the complexity of your model. Keep in mind that the complexity of a model increases exponentially with the number of parameters to optimize. If you

want to perform a component analysis with three SGG functions, you have to deal with a solution space in 15 dimensions. You will not have the possibility to perform a systematic solution search is such a space: if you try 5 initial values for each parameter, you should perform $5^{15} = 3 \times 10^{10}$ optimizations! You would probably find several stable solutions, but only one among them is correct and has a physical meaning. The parameters have a hierachical structure: a controls the amplitude of an end-member, μ the "position" along the field axis, and σ the "width", q the symmetry and p the curvature. The amplitude is the most important parameter, the curvature is the less important. You can start with fixed values of p, or fixed values of q and p. Use logarithmic Gaussian functions to model magnetic components which are not saturated in the field range of the measured coercivity distribution.
In the program example, the measured coercivity distribution is similar to an asymmentric unimodal probability density function. There is no direct evidence for more than one magnetic component. Therefore, initial parameters for one SGG function have been entered in the program example. Since only 5 parameters have to be optimized, the component analysis is relatively simple and only one stable solution is expected. Therefore, it is not necessary to start with a modelled coercivity distribution which is very close to the measured data.
Back to the program example

Perform a component analysis

GECA performs a component analysis by optimizing the initial parameters in a way that minimizes the squared residuals between model and measurements by using a Levenberg-Marquardt algorithm. The parameters to optimize are displayed together with the corresponding initial values. If the initial values were carefully chosen, the search for a solution is performed in a reasonable time with no more than 50 iterations. Otherwise, the search will take more than 50 iterations or it will converge to an absurd solution. If a global or a local minimum of the squared residuals is not reached within 50 iterations, a warning message appears and you will be asked to continue the search or stop it and plot the solution given by the last iteration. It is recommanded to perform at least 200 iterations. The numerical values of the parameters are shown every 50 iterations and you can check how they change and if they converge to a meaningful result.

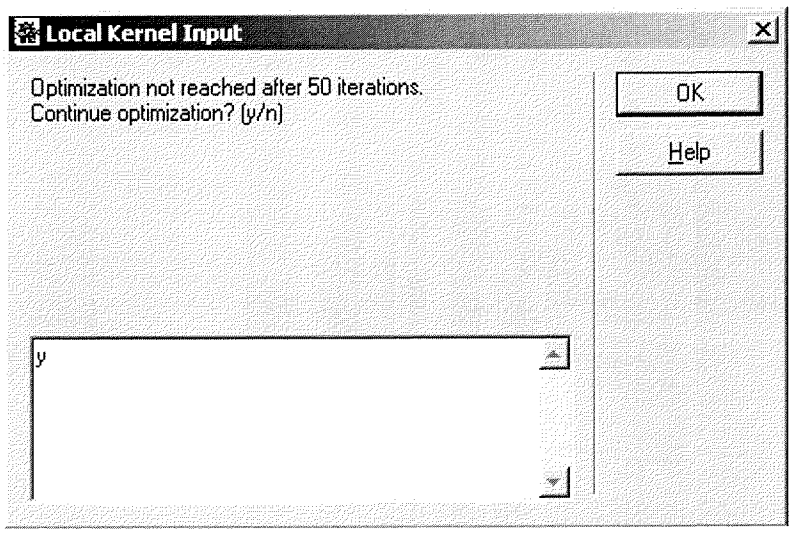

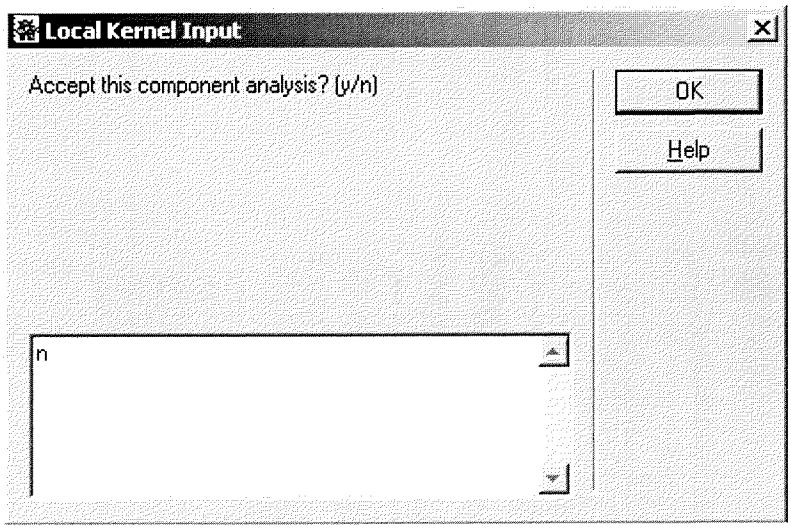

If a convergence to a stable solution cannot be obtained, interrupt the search for a solution by typing "n" in the promt window and choose other initial parameters.

The result of the component analysis is displayed exactly like the initial model. The same colors are used to label the end-members. Additionally, the difference between the model and the measurements (blue line) is plotted below the result of the component analysis, together with the measurement errors (pair of gray lines). The difference between model and measurements (called *misfit* in the following) should be of the same order of magnitude as the estimated measurement error. If the misfit is much larger than the estimated measurement error, the model is not able to account for the measurements: other parameters should be added to reduce the misfit. If the misfit is much smaller than the measurement error, the model chosen for the component analysis is able fo fit the measurements very well but it is not significant: some of the model parameters do not have any physical meaning. In this case you should decrease the number of model parameters by reducing the number of end-members or by keeping some parameters fixed. If the misfit has the same amplitude as the estimated measurement error, the model may be adequate. Nevertheless, more than one solution witch satisfy this condition may exist.

An adequate parameter to test the significance of a component analysis is the χ^2 statistics. GECA gives an estimation of χ^2/l, where l represents the degrees of freedom of the model. For a correct model, $\chi^2_{l;\alpha} \leq \chi^2 \leq \chi^2_{l;1-\alpha}$, where $\chi^2_{l;\alpha}$, $\chi^2_{l;1-\alpha}$ are the confidence limits at a given confidence level (usually 95%). GECA calculates the confidence limits with a 95% confidence level and displays them together with the estimation of χ^2/l. If $\chi^2 > \chi^2_{l;1-\alpha}$, the model is significantly different from the measured data, and GECA suggests you to refine it by adding more parameters. If $\chi^2 < \chi^2_{l;\alpha}$, not all model parameters are significant and a warning message is displayed. In this case you should reduce the number of parameters. If $\chi^2_{l;\alpha} \leq \chi^2 \leq \chi^2_{l;1-\alpha}$, GECA suggests to accept the model.

In the program example, the component analysis with one SGG function is inadequate to model the measurements within the given error margins.

Back to the program example

Enter initial distribution parameters (2 logarithmic Gaussian functions)

Since the component analysis with one component was not adequate, a more complex model with two logarithmic Gaussian functions is used. The initial values for skewness and kurtosis are setted to zero by entering $q = 1$ and $p = 2$ for both components. These parameters are kept fixed by entering "{q1,p1,q2, p2}" in the second prompt window. Initial parameters for a, μ and σ are guessed until a relatively good agreement with the measured data is obtained.

Back to the program example

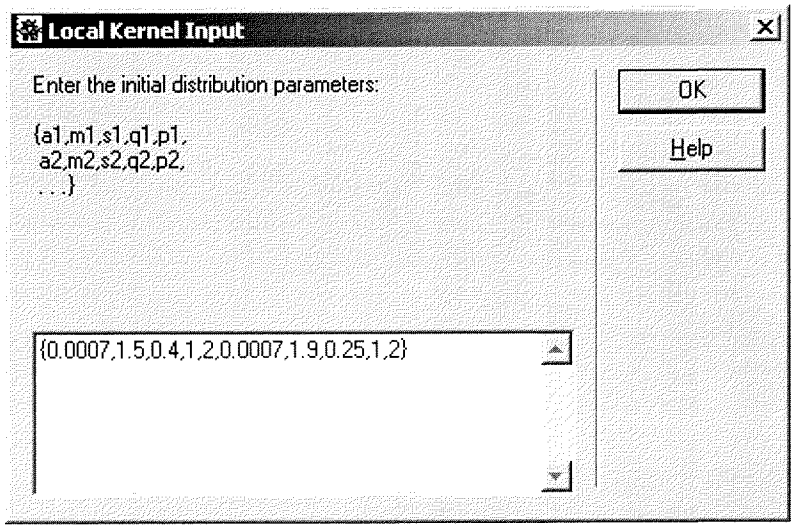

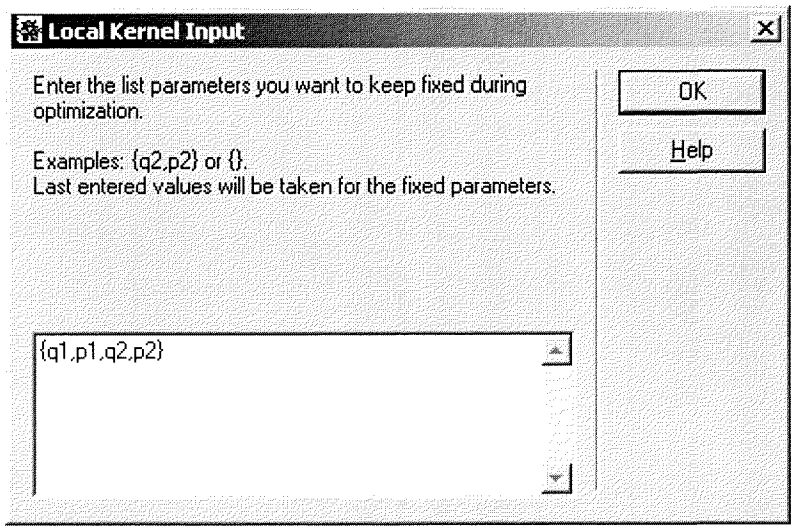

Perform a component analysis (2 logarithmic Gaussian functions)

The component analysis with two logarithmic Gaussian functions is inadequate to model the measurements within the given error margins. The misfit between model and measurements is larger than that obtainend with one SGG function, even if there is one more parameter to optimize. This example shows that logarithmic Gaussian functions are generally not suitable for modelling the coercivity distribution of single magnetic components. A good agreement between measurements and model is achieved only with 4 logarithmic Gaussian functions (Figure 3). Unfortunately, these functions cannot be related to the coercivity distributions or real magnetic components.

Back to the program example

Enter initial distribution parameters (one component is known)

The different sources of magnetic minerals for the sample taken as example are known from independent investigations on urban atmospheric dust samples collected in the same region. The two main sources are given by natural dust and by the products of combustion precesses, mainly from motor vehicles and from waste incineration. The coercivity distribution of the combustion products can be modelled by a SGG function with $\mu = 1.96$, $\sigma = 0.235$, $q = 0.66$, $p = 2$. These parameters are kept fixed during the component analysis. Only the magnetization of the combustion products (given by a) is unknown and is optimized, together with the unknown parameters of natural dust.

Back to the program example

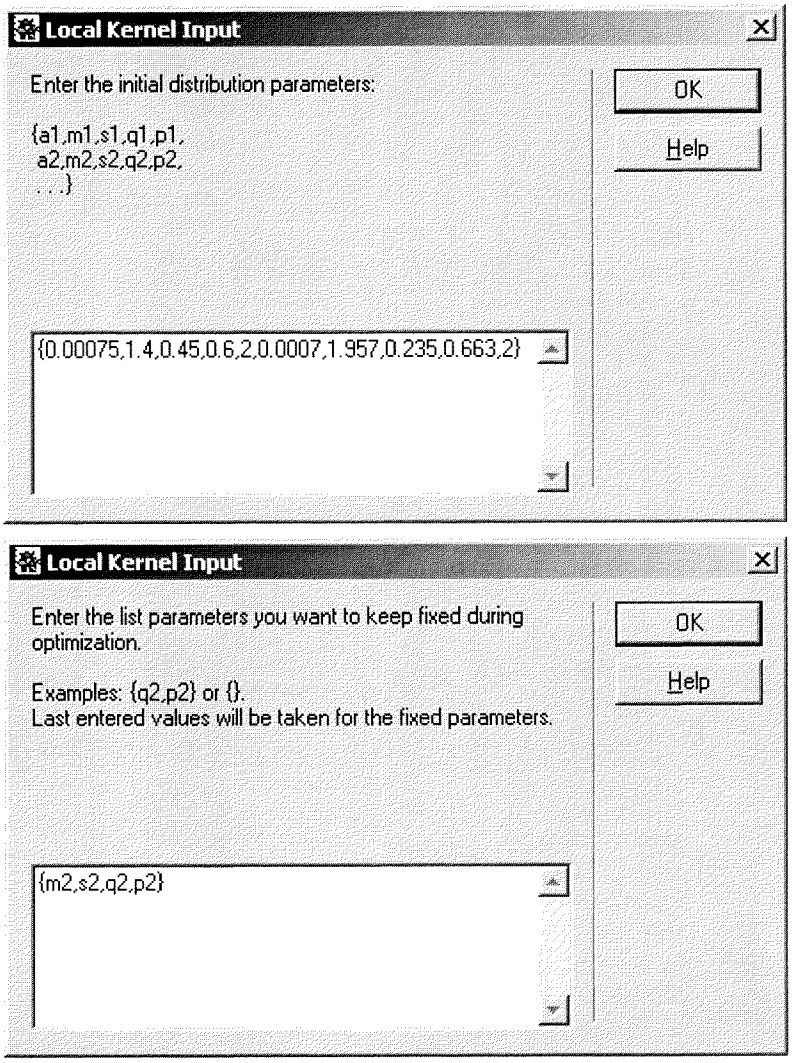

Perform a component analysis (one component is known)

This component analysis is characterized by a much better agreement with the measurements, if compared to the previous results. Six distribution parameters have been optimized. The same number of parameters has been used to perform a component analysis with two logarithmic Gaussian functions: nevertheless, χ^2/l was almost one order of magnitude larger! This model is still significantly different from the measurements. A reason for that could arise from small variations in the properties of the same magnetic component collected from different places.

Back to the program example

Enter initial distribution parameters (2 SGG functions)

To take into account small variations in the magnetic properties of combustion products, the results of the previous component analysis are taken as initial values for a new component analysis where all 10 distribution parameters are optimized.

Back to the program example

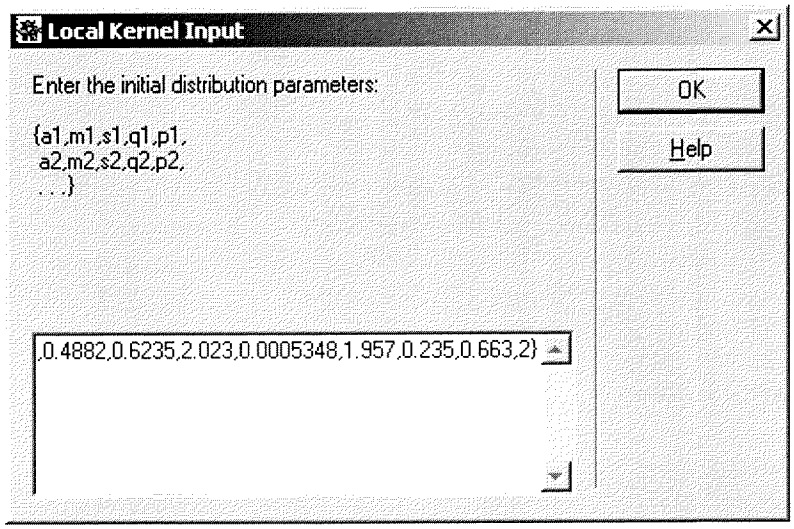

Perform a component analysis (2 SGG functions)

The model is now much more complex and the search for a stable solution needs more than 50 iterations. A warning message appears and you are asked to stop or continue for other 50 steps. Finally a stable solution is reached. The distribution parameters of the combustion product did not change more than 10% with respect to the initial values, and the model is now compatible with the measurements within the measurement errors. The solution of this component analysis is accepted, since it is compatible with the magnetic properties assumed initially for the combustion products.

Back to the program example

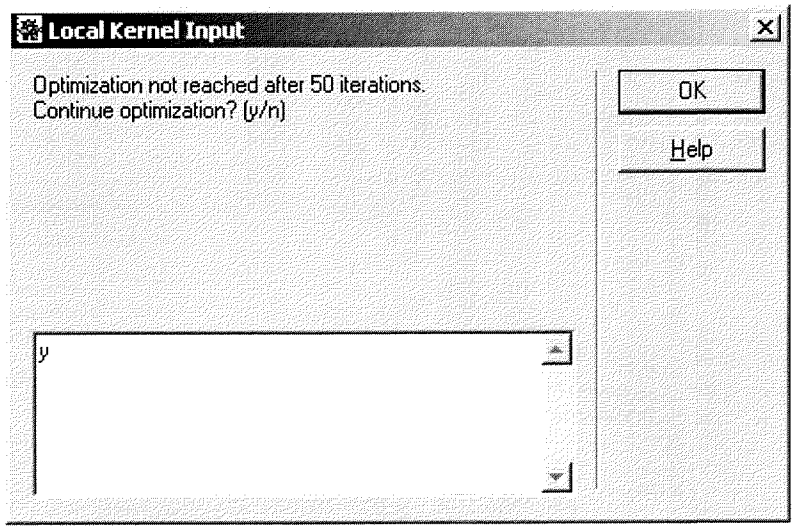

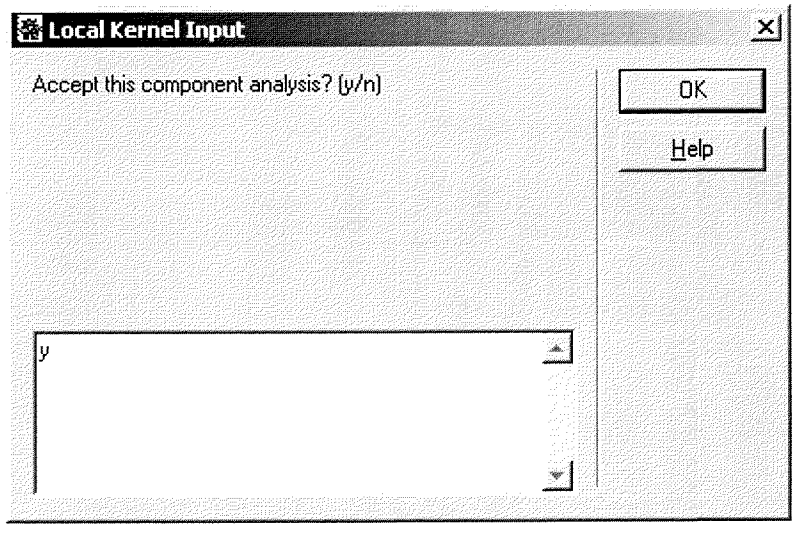

Perform a systematic solution search

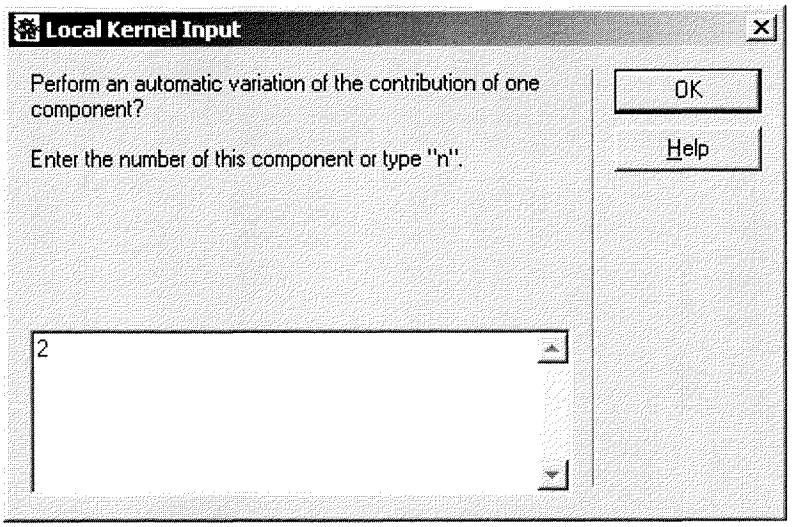

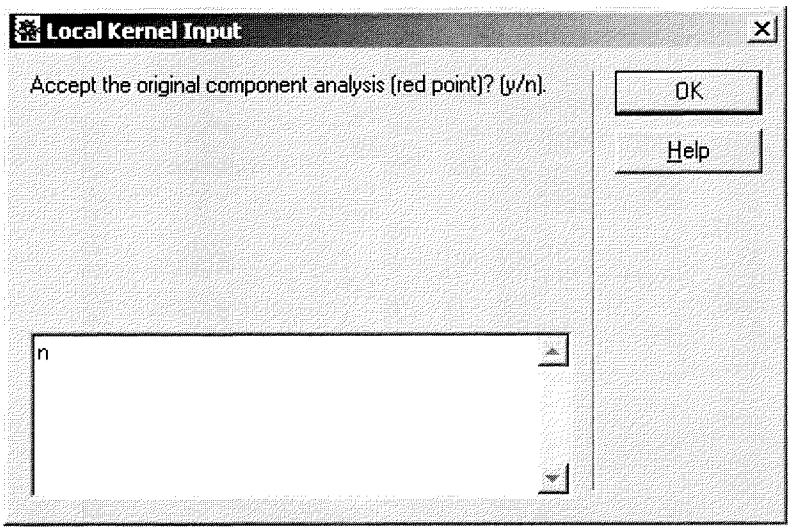

Stable solutions of the component analysis correspond to local minima of the merit function. The merit function can have several local minima for a given finite mixture model. One among them is a global minimum as well, and is usually considered as the acceptable solution. A solution which corresponds to a global minimum of the merit function is attained if the initial model is chosen to be close enough to the acceptable solution. Since this solution is usually unknown in advance, a sufficient number of initial models has to be tested in order to ensure that at least one will converge to a global minimum of the merit function. If you try 5 initial values for each parameter of a model with two SGG functions, you should perform $5^{10} = 10^7$ optimizations! GECA performs a selected search for a global minimum of the merit function, starting with the result of the last component analysis as initial model. You can select one end-member function, whose amplitude a will be increased and decreased in steps of 1/100 of the total sample magnetization, starting form the solution of the last component analysis. After each step, the new solution is taken as an initial model for the next component analysis. As a result, the merit function is plotted for all possible amplitudes of the selected SGG function. In the program example, the last solution of the component analysis (red point) is close to the global minimum of the merit fuction. The sharp steps of the merit function are an effect of the sudden convergence of some distribution parameters to a different local minimum. You are asked to accept the solution of the last component analysis, indicated by a red point, if it corresponds to a global minimum of the merit function.

Back to the program example

Choose initial distribution parameters from the systematic solution search

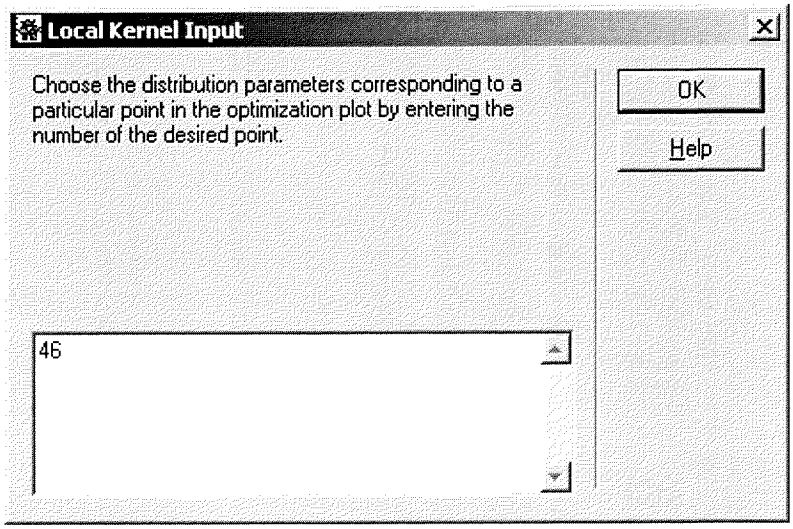

You can check the distribution parameters which corresponds to various values of the merit function previously plotted. The merit function was calculated for 100 points (black dots in the last plot, every 10th point is gray). You can enter the number of the point which corresponds to a particular value of the merit function you are interested in. In this way you can explore the solutions which correspond to various local minima and to the global minimum of the merit function. This option is particularly useful in the case that several local minima exist, which are close to the global minimum. Due to the measurement errors, a meaningful solution could be given by one of these local minima. You may evaluate differnet solutions with some independent informations about the coercivity distribution expected for the individual magnetic components. In the program example, point number 46 is entered, which corresponds exactly to the global minimum of the merit function.

Back to the program example

Perform a component analysis (representing a global minimum)

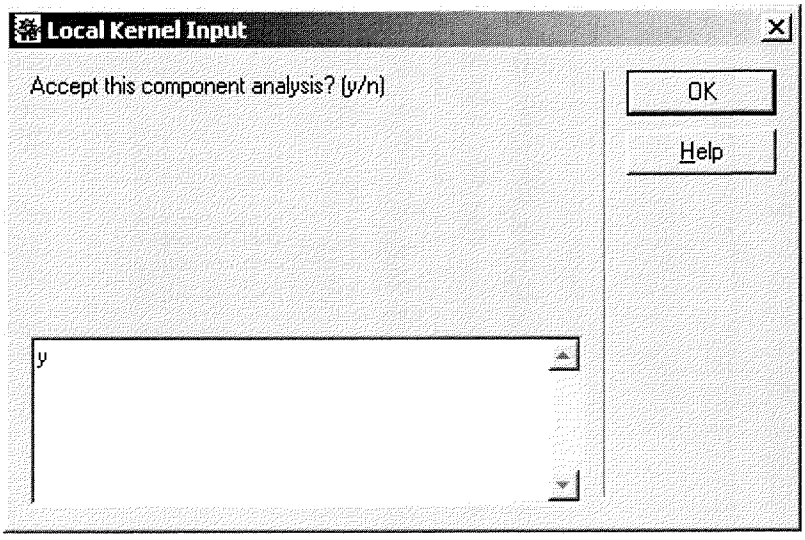

The set of distribution parameters which corresponds to a global minimum of the merit function is taken as initial model for the last component analysis. In the program example, this is the final solution, which represents a finite mixture model which is compatible with the measurements and with independent informations about the properties of the individual magnetic components. In other cases you may not accept this solution and enter a set of initial parameters which corresponds to other values of the merit function, until a satisfacting result is obtained.

Back to the program example

Perform an error estimation

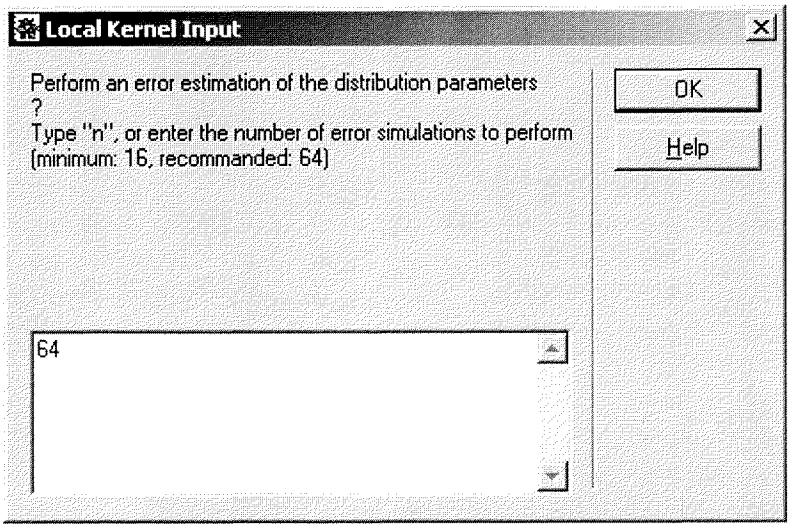

You can choose to perform an error estimation of the last component analysis. GECA will perform the error estimation by adding a random noise signal to the measured coercivity distribution. The standard deviation of the noise signal is chosen to be identical with the estimated measurement error for each value of the field. The new "noisy" coercivity distribution is fitted with the same set of end-member functions used for the last component analysis, whose solution is taken as the initial model. The result of the component analysis performed on the "noisy" coercivity distribution differs slightly from the result of the component analysis performed on the original coercivity distribution. The process of adding and adequate noise component to the original data and fitting the resulting coercivity distribution is repeated several times. GECA calculates the standard deviation of the component analysis results for each distribution parameter. These standard deviations are taken as an error estimation. At the same time, some statistical properties of the end-member functions are calculated as well, together with the related errors. The error estimation performed by GECA is quite time consuming, therefore you can choose the number of iterations to perform. With 64 iterations, an accuracy of 12% is expected for the error estimation. The relative accuracy of the error estimation, expressed in %, is given by $100/\sqrt{n}$, where n is the number of iterations used. The error estimation performed by GECA takes into account the effect of the measurement errors on a set of distribution parameters which is related to a particular local minimum of the merit function. The effect of measurement errors on the convergence of the component analysis to parameters which correspond to other local minima of the merit function is not considered. Therefore, the error estimation performed by GECA has to be cosidered as a lower limit for the real error of each parameter. Finally, all distribution parameters are displayed together with the estimated errors. Additionally, statistical parameters like the dispersion parameter DP, the mean, the skewness and the kurtosis are displayed with the related errors. The result of the component analysis is plotted again, together with the confidence limits of each end-member function. Finally, the normalized end-member distributions are plotted, together with their confidence limits. The area under the curve of each end-meber distribution is equal to one in this last plot.

Back to the program example

Save the component analysis results in a log file

You can save the component analysis results to the log file `components.txt`. You will find this file in the same folder where the program package CODICA is installed. The log file contains the results of all component analysis you decided to save, in form of a list of distribution parameters and statistics for each end-member distribution. The error estimation of each parameter is stored as well, if you decided to run an error estimation with GECA. An example of the content of the log file is displayed below.

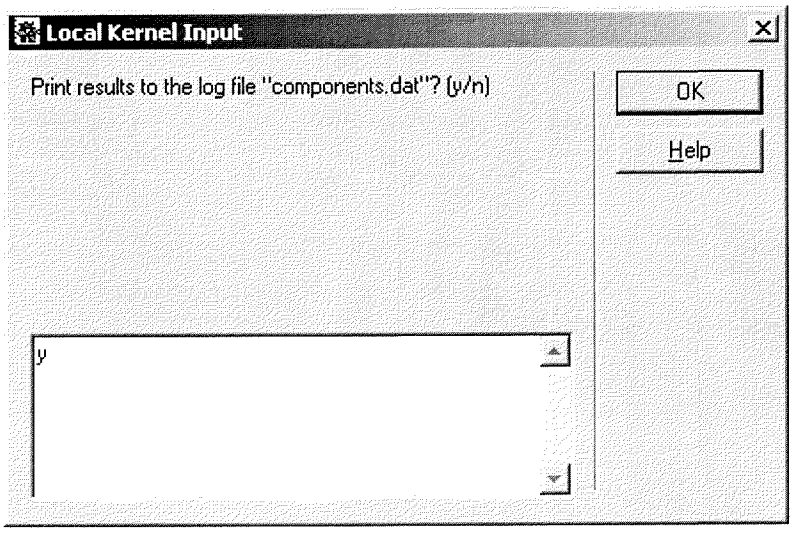

components.txt - Editor

Datei Bearbeiten Format ?

file name	a1	+/-	MDF1	+/-	s1	+/-	q1	+/-	p1	+/-	DP1
WDKarm.slog	0.0007989		0.00002064		1.428	0.01136	0.4739	0.002868		0.5562	0.004€

Back to the program example

Save the end-members to a file

The end-member distributions, together with their confidence limits, can be stored in a separated file as a list of colums with the numerical values of each function. The file will have the same name as the file where the original data for the coercivity distribution were stored, with extention `.cum`. This file will be stored in the same directory as the data file. An example is given below.

Back to the program example

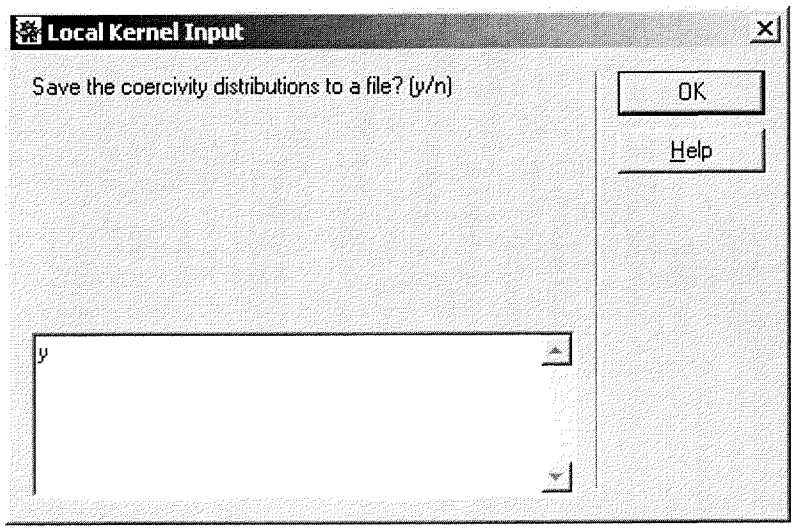

WDKarm.comp - WordPad

Datei Bearbeiten Ansicht Einfügen Format ?

field comp.	#1 abs. error	comp. #2	abs. error
-0.62572	1.67553e-6 2.18e-8	2.46818e-24	5.81e-23
-0.623455	1.69239e-6 2.19e-8	2.66975e-24	6.24e-23
-0.621189	1.7094e-6 2.21e-8	2.88759e-24	6.69e-23
-0.618924	1.72657e-6 2.22e-8	3.123e-24	7.18e-23
-0.616658	1.7439e-6 2.23e-8	3.37737e-24	7.7e-23

Drücken Sie F1, um die Hilfe aufzurufen.

Cautionary note

GECA 1.0 has been tested more than 500 times with coercivity distributions of various artificial and natural samples and the most different combinations of initial parameters. Nevertheless, there is a remote possibility that particular uncommon data or parameter sets will produce evaluation problems. In this case, blue-written warning messages appear on the *Mathematica* front-end. If more than one of these messages is displayed, you may force-quit the Kernel of *Mathematica* as follows: in the top menu bar choose Kernel → Quit Kernel → Local. You can also exit from GECA at any time just by typing "abort" in any input prompt window.
In case of problems, write to the author (Ramon Egli) at the address given in the `install.txt` file of the installation packet or at the beginning of the source code file `Codica.m`. Please save and send a copy of the Mathematica session you were using when the problem arised, together with the data file you analyzed with GECA.

References

Egli, R., Analysis of the field dependence of remanent magnetization curves, *J. Geophys. Res.*, *102*, doi 10.1029/2002JB002023, 2003.

Heslop, D., M. J. Dekkers, P. P. Kruiver and I. M. H. Oorschot, Analysis of isothermal remanent magnetization acquisition curves using the expectation-maximization algorithm, *Geophys. J. Int.*, *148*, 58-64, 2002.

Kruiver, P. P., M. J. Dekkers, and D. Heslop, Quantification of magnetic coercivity components by the analysis of acquisition curves of isothermal remanent magnetization, *Earth Planet. Sci. Lett.*, *189*, 269-276, 2001.